



Multiscale simulations of intergranular fracture initiation in face-centered cubic metals and alloys : influence of the localised plastic slip deformation

Bertrand Sicaud

► To cite this version:

Bertrand Sicaud. Multiscale simulations of intergranular fracture initiation in face-centered cubic metals and alloys : influence of the localised plastic slip deformation. Mechanics of materials [physics.class-ph]. Sorbonne Université, 2020. English. NNT : 2020SORUS444 . tel-03662476

HAL Id: tel-03662476

<https://theses.hal.science/tel-03662476>

Submitted on 9 May 2022

HAL is a multi-disciplinary open access archive for the deposit and dissemination of scientific research documents, whether they are published or not. The documents may come from teaching and research institutions in France or abroad, or from public or private research centers.

L'archive ouverte pluridisciplinaire **HAL**, est destinée au dépôt et à la diffusion de documents scientifiques de niveau recherche, publiés ou non, émanant des établissements d'enseignement et de recherche français ou étrangers, des laboratoires publics ou privés.

Sorbonne Université

École doctorale Sciences mécaniques, acoustique, électronique & robotique
de Paris (ED 391, SMAER)

CEA SACLAY - DEN/DANS/DMN/SRMA/LC2M

Multiscale simulations of intergranular fracture initiation in face-centered cubic metals and alloys: influence of the localised plastic slip deformation

Par Bertrand SICAUD


Thèse de doctorat de l'Université Paris Sorbonne

Dirigée par Maxime SAUZAY et encadrée par Laurent VAN BRUTZEL

Présentée et soutenue publiquement le 17 septembre 2020

Devant un jury composé de :

M. Peter HOSEMAN, Professeur, University of California, Berkeley	Rapporteur
M. Miroslav ČERNÝ, Professeur, Brno University of Technology	Rapporteur
Mme. Anne TANGUY, Professeur, INSA Lyon	Examinatrice
M. Dominique LEGUILLON, Directeur de recherche, CNRS-Université Paris Sorbonne	Examineur
M. Thierry COUVANT, Ingénieur de Recherche, EDF R&D	Examineur
M. Laurent VAN BRUTZEL, Ingénieur de Recherche, CEA Saclay	Examineur
M. Maxime SAUZAY, Ingénieur de Recherche, CEA Saclay	Examineur

    Except where otherwise noted, this work is licensed under <http://creativecommons.org/licenses/by-nc-nd/3.0/>

Contents

1	Context and motivation	7
1.1	Intergranular stress corrosion cracking of austenitic stainless steels used in nuclear power reactor	9
1.2	Irradiation assisted stress corrosion cracking of austenitic SS	12
1.2.1	Various approaches to better understand a complex phenomenon .	12
1.2.2	Influence of irradiation on the SCC of austenitic stainless steels . .	15
1.3	Mechanical properties of grain boundaries and metal/oxide interfaces . .	24
1.4	Conclusion: toward multiscale simulations through bottom-up or top-down approaches	30
2	Multiaxial behaviour of FCC nickel bicrystals at the atomic scale	32
2.1	Motivations and purposes	34
2.2	Molecular dynamics simulations of FCC bicrystal systems for the investigation of CSL symmetric tilt grain boundaries behaviour	35
2.2.1	Formation of the [100] symmetric tilt grain boundaries	36
2.2.2	Atomic structure, mechanical description and energy of the grain boundaries	38
2.2.3	Uniaxial tensile loadings	45
2.2.4	Multiaxial tensile loadings	47
2.3	From dislocation nucleation to grain boundary decohesion	50
2.3.1	Preliminary results	50
2.3.2	Influence of the multiaxiality : a behaviour transition	53
2.3.3	Influence of the temperature and strain rate on the behaviour of the $\Sigma 5$ grain boundary	59
2.3.4	Influence of the shearing deformation on the $\Sigma 5$ grain boundary behaviour	60
2.3.5	Behaviour of the different CSL grain boundaries	62
2.4	Summary of the results and conclusion	64
2.4.1	Results	64
2.4.2	Conclusion	65

CONTENTS

3	Homogeneous and heterogeneous dislocation nucleation: influence of the strain multiaxiality	66
3.1	Homogeneous and heterogeneous dislocation nucleation in FCC metals . . .	68
3.2	Dislocation nucleation from the CSL symmetric tilt grain boundaries . . .	69
3.2.1	Influence of the grain boundary local atomic stress field	69
3.2.2	Dislocation nucleation from the $\Sigma 5$ grain boundary and its restriction through stress multiaxiality	73
3.3	Further computations, comparisons and discussion	81
3.3.1	The Frenkel model and the onset of a stacking fault	82
3.3.2	Molecular static computation of the generalised stacking fault energy curve	86
3.3.3	Influence of the lattice deformation on the nucleation of partial dislocations	90
3.3.4	Influence of the temperature	97
3.4	Summary of the results and conclusion	100
3.4.1	Results	100
3.4.2	Conclusion	101
4	Grain boundaries failure under homogeneous stress state	102
4.1	Grain boundaries decohesion	104
4.2	Critical stresses and Griffith energies of the different grain boundaries . .	104
4.2.1	Axial critical stress for the decohesion of the grain boundaries . . .	104
4.2.2	Griffith energies of the grain boundaries	107
4.2.3	The coupled criterion for the onset of intergranular cracking	110
4.3	Strain localisation at the grain boundaries	114
4.3.1	Thickness of the grain boundaries based on their intrinsic excess energy	115
4.3.2	Apparent Young modulus of the homophase interfaces	120
4.4	Local debonding of the grain boundary phase	127
4.4.1	Influence of the disclination atomic volumes	127
4.4.2	The universal binding energy relation	133
4.4.3	Local criterion for the onset of grain boundary decohesion	138
4.5	Summary of the results and conclusion	146
4.5.1	Results	146
4.5.2	Conclusion	149
5	Stress concentrations and crack initiation at grain boundaries: the V-notch problem	150
5.1	Intergranular stress concentrations	152
5.2	Experimental results for the failure of CSL grain boundaries in nickel chromium alloy	153
5.3	Bottom-up approaches for the prediction of intergranular fracture initiation at a V-notch	158

CONTENTS

5.3.1	Stress and energy thresholds for the onset of a finite crack increment considering a coupled criterion	158
5.3.2	Finite element computation of fracture initiation using a cohesive zone model	167
5.4	A top-down approach for the prediction of intergranular fracture initiation	173
5.4.1	Method	174
5.4.2	Results for the $\Sigma 5$ [03 1] grain boundary	178
5.5	Comparison of the three approaches for different V-notch angles	185
5.6	Results for the $\Sigma 5$ [0 $\bar{1}$ 2] and $\Sigma 3$ [1 1 1] grain boundaries	187
5.7	Summary of the results and conclusion	192
5.7.1	Results	192
5.7.2	Conclusion	193
6	Discontinuous slip bands model for low stacking fault energy metals and alloys	194
6.1	Intergranular stress concentrations at plastic slip band or clear band impacts	196
6.2	Experimental characterisation of plastic slip bands in a 316L stainless steels	200
6.2.1	Material and method	200
6.2.2	Preliminary observation and measurements	205
6.2.3	Statistical characterisation of slip bands	213
6.3	Discussion	232
6.3.1	Thickness and plastic slip strain of slip bands and clear bands . . .	233
6.3.2	Interband spacing and plastic slip strain	237
6.4	Summary of the results and conclusion	241
6.4.1	Results	241
6.4.2	Conclusion	242
7	Intergranular fracture initiation in unirradiated and irradiated stainless steels	244
7.1	Introduction	247
7.2	Finite element computations of intergranular stress fields in the vicinity of slip bands or clear bands	249
7.2.1	Microstructures	249
7.2.2	Constitutive elastoplastic laws	252
7.2.3	Expected intergranular stress fields and scale effect	254
7.2.4	Computed stress fields for one or several slip bands	258
7.3	Criterion for intergranular crack initiation and multiscale chaining	265
7.3.1	Application of the coupled criterion: a bottom-up approach	265
7.3.2	Bottom-up and top-down approaches for the failure of several CSL nickel grain boundaries	268
7.4	Application of the multiscale model and comparison with experimental data	281
7.4.1	Molecular dynamics inputs for predicting the fracture of oxidized grain boundaries	281

CONTENTS

7.4.2	Selection of experimental data	283
7.4.3	Application of the model	285
7.4.4	Results and discussion	287
7.5	Summary of the results and conclusion	291
7.5.1	Results	291
7.5.2	Conclusion	292
8	Conclusion and perspectives	293
8.1	Conclusion	294
8.2	Perspectives	296
	Appendices	304
A	Universal binding energy relation model	305
B	Tensile test	308
C	Stress field solutions at intergranular slip band(s) or clear band(s) impacts	310
D	Multiscale model of the macroscopic remote stress for intergranular fracture initiation at clear channels impact	313

1

Context and motivation

In this first chapter, a brief overview of the industrial and scientific context of this thesis is provided in order to propose several relevant points of development to be undertaken. In that regard a plan of the thesis is delivered in the concluding part of this chapter. More comprehensive elements of bibliography are provided in each of the corresponding chapters. Therefore, these elements shall not be presented here in order to merely focus on the irradiation assisted stress corrosion cracking of austenitic stainless steels used in the nuclear industry which essentially constitute an intergranular fracture phenomenon.

1. CONTEXT AND MOTIVATION

Contents

1.1 Intergranular stress corrosion cracking of austenitic stainless steels used in nuclear power reactor	9
1.2 Irradiation assisted stress corrosion cracking of austenitic SS	12
1.2.1 Various approaches to better understand a complex phenomenon	12
1.2.2 Influence of irradiation on the SCC of austenitic stainless steels	15
1.2.2.1 Radiation induced segregation and irradiation hardening	15
1.2.2.2 Preponderant influence of localised deformation	18
1.2.2.3 Stress field at channel/grain boundary intersection . .	22
1.3 Mechanical properties of grain boundaries and metal/oxide interfaces	24
1.4 Conclusion: toward multiscale simulations through bottom-up or top-down approaches	30

1. CONTEXT AND MOTIVATION

1.1 Intergranular stress corrosion cracking of austenitic stainless steels used in nuclear power reactor

As of today, civilian nuclear power programs rely on the technological feasibility of exploiting the nuclear fission phenomenon. Specifically, the energy resulting from the fission of uranium ^{235}U nuclei is partly converted by nuclear reactors for its consumption on electrical power grids.

In 2020, the light water reactors (LWR) represents the most common nuclear reactor concept among the overall 443 reactors worldwide, comprising 300 pressurised water reactors (PWR) and 65 boiling water reactors (BWR) [IAEA, 2020].

As illustrated in figure 1.1 for the case of a PWR, LWRs operate through the use of water as a heat transfer medium. For PWRs, in particular, the original combustion of the fuel (pellets of UO_2 piled in zirconium-based alloy claddings) induces a temperature increase of the liquid water circulating in the primary circuit under a pressure of 155 bar. This energy is then converted in a secondary circuit through a steam generator and a turbine-generator system, thus providing the power grid with electricity, the best medium for energy transport and distribution.

High temperatures of about 300 °C and heavy neutron radiations resulting from the fission reactions therefore characterise the harsh environment of a PWR vessel. BWRs essentially follow the same energetic cycle, with the notable exception that the liquid water entering into the reactor vessel is directly boiled in the vessel, therefore reducing the two preceding circuits to only one circuit. Although the water chemistry and the overall design of this two LWRs differ, in both cases the materials used for their conception have to endure drastic in-service conditions due to potential corrosion, neutron irradiation and mechanical solicitations.

Austenitic Stainless Steels (SS) are widely used for that purpose, as illustrated in figure 1.1.

In particular, solution annealed 304L (18Cr10Ni) and cold-worked (CW 15 %) 316 (17Cr11Ni) austenitic SS are employed for the baffle/former plates (figure 1.2b) and for the baffle/former bolts (figure 1.2c) respectively.

As presented in figure 1.2a which illustrates the vessel internals of a typical PWR, the baffle (vertical) and former (horizontal) plates take part of the lower internals. This group of structural elements insure the support of the reactor core (gathering the fuel assemblies) and preserve the cooling flow as intended near the core. The baffle/former bolts simply provide the liaison between the plates. Dimensions of these bolts can be appreciated in the upper picture of figure 1.2d.

Due to their proximity to the core and since in-service inspections of the lower internals are limited, these components are particularly exposed to the above exploitation conditions for a significant amount of time. In PWRs, irradiation doses up to 80-100 dpa (displacement per atom) can be evaluated for these components after 40 years [Tanguy and Hure, 2016, Féron et al., 2012], as illustrated in the upper picture of figure 1.2b. Such doses can obviously induce significant modifications of the material microstructure

1. CONTEXT AND MOTIVATION

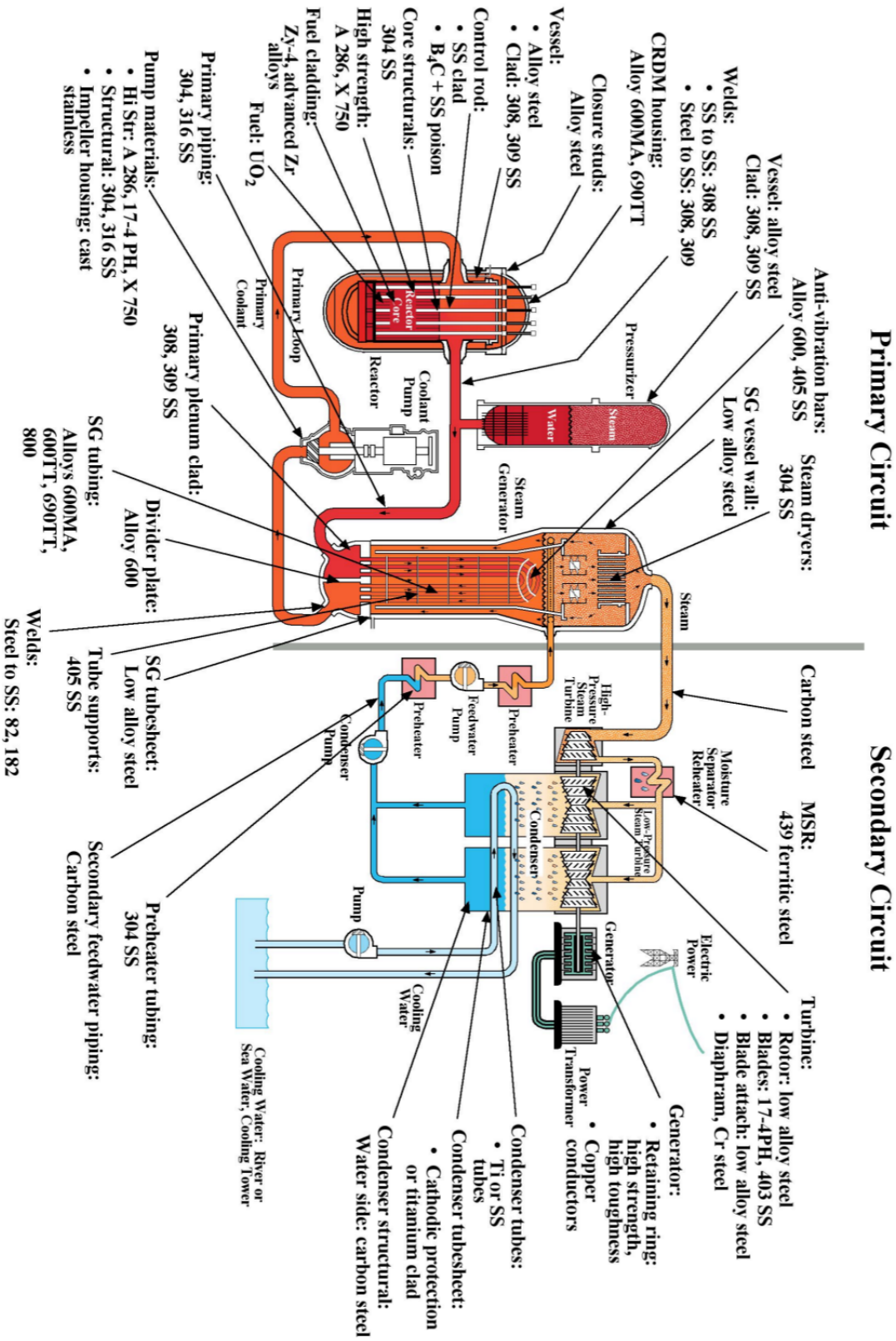


Figure 1.1: Scheme of a PWR along with an overview of the materials employed for some of its components (from Steahle et al. [Féron and Staehle, 2016]). Abbreviation: stainless steels (SS).

1. CONTEXT AND MOTIVATION

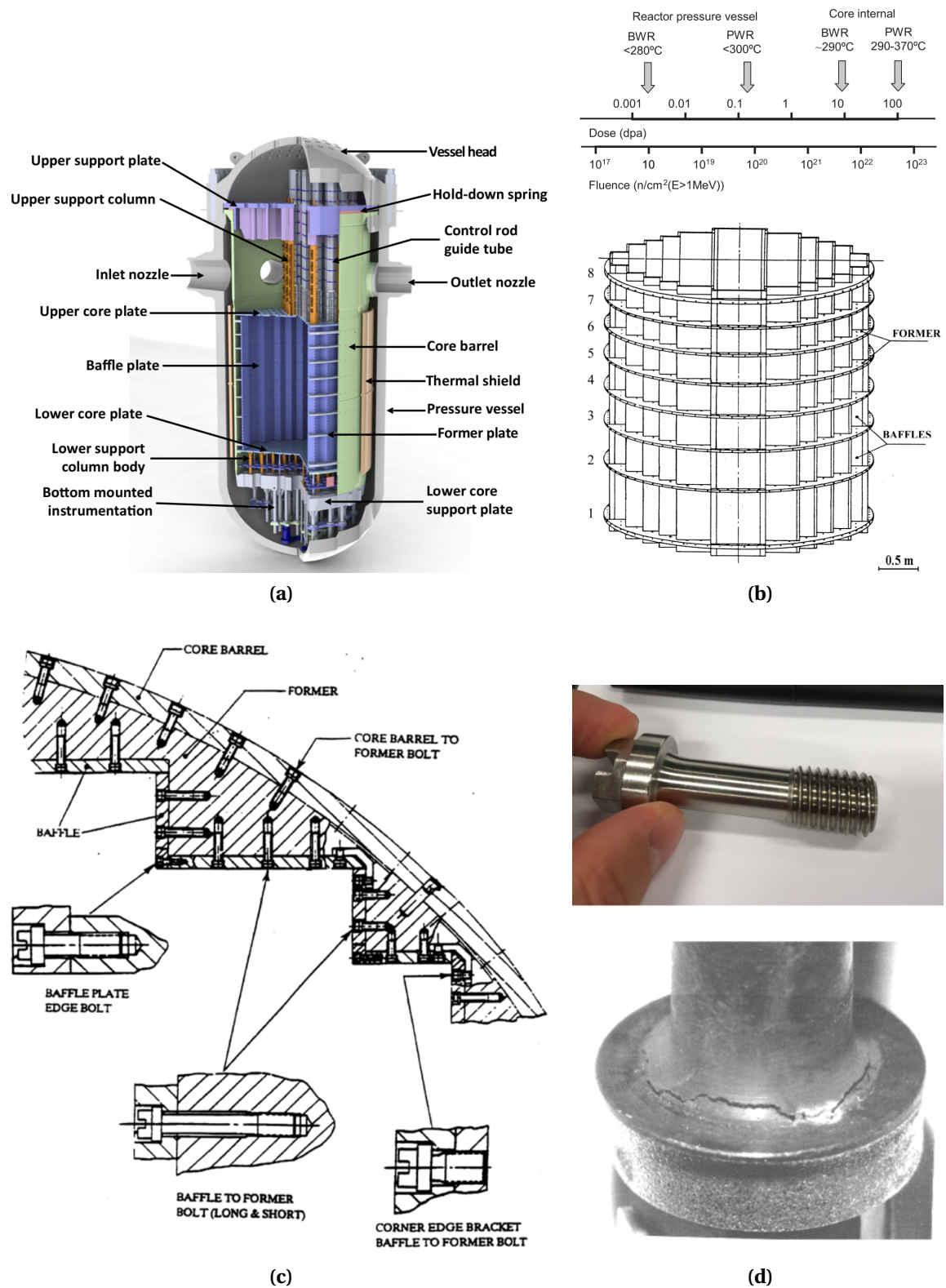


Figure 1.2: Exploded view of a typical PWR vessel with its internals (1.2a) [ANS, 2019]. Irradiations doses of PWR and BWR internals and vessel after 40 years of service [Fukuya et al., 2013] and scheme of the baffle and former plates lower internals (1.2b) [Edwards et al., 2001]. Scheme of the baffle to former bolts (1.2c) and related picture of unfractured [EDF, 2018] and fractured [Thomas and Bruemmer, 2002] bolt (1.2d).

1. CONTEXT AND MOTIVATION

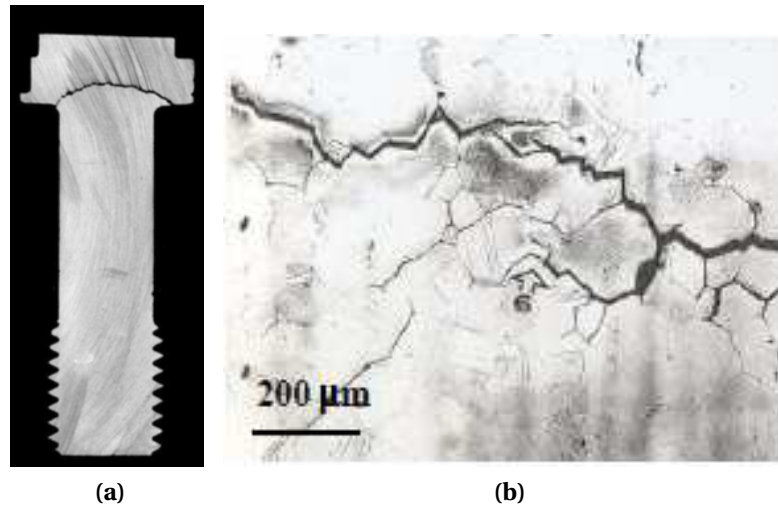


Figure 1.3: Tihange PWR fractured bolt by IGSCC (1.3a and 1.3b) [Thomas and Bruemmer, 2002].

and microchemistry without mentioning the impact on the water chemistry and all its consequences on the alloys chemical interaction with this environment.

Despite good feedbacks on austenitic SSs use in LWRs [Féron et al., 2012] over several decades, in-service failures of reactor components by irradiation assisted stress corrosion cracking (IASCC) have been evidenced since the 1960s for stainless steels fuel cladding and more extensively since the 1980s-1990s for baffle/former bolts [Was, 2007b]. The lower picture of figure 1.2d provides an observation of this later case concerning a fractured bolt from the Tihange PWR in Belgium [Thomas and Bruemmer, 2002].

More specifically, an intergranular stress corrosion cracking (IGSCC) phenomenon has been clearly evidenced, as shown on more detailed observations of fractured bolts in figures 1.3a and 1.3b. Since then, periodic controls of this lower internal components on several PWRs have revealed further failures by IASCC with significant damage behaviour variations according to numerous factors, inducing a need to better understand and predict this phenomenon.

1.2 Irradiation assisted stress corrosion cracking of austenitic SS

1.2.1 Various approaches to better understand a complex phenomenon

IASCC is a complex and multi-physical phenomenon, involving numerous synergistic effects. This last point is illustrated by the diagram of figure 1.4. Understanding IASCC requires the consideration of the main phenomena occurring at the confluence of four

1. CONTEXT AND MOTIVATION

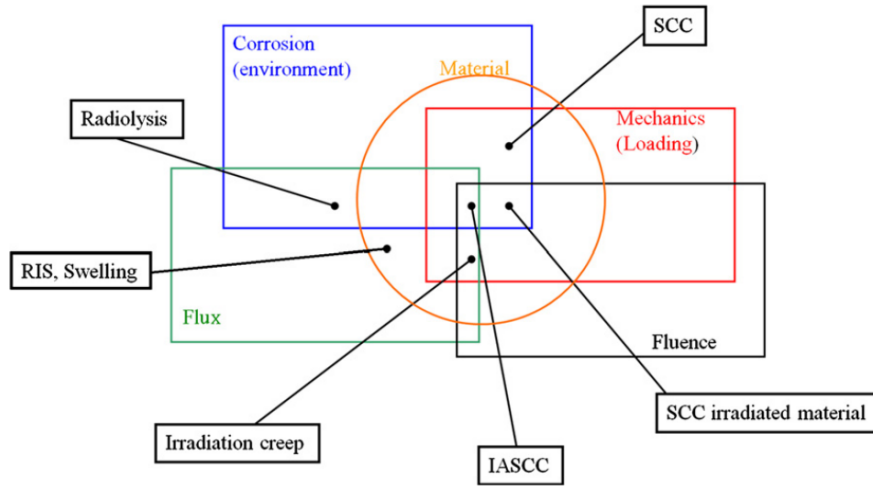


Figure 1.4: Venn diagram of the different factors and phenomenon involved in IASCC [Tanguy, 2011].

groups of key influential factors and their interactions: the material, the mechanical solicitation, the environment and the irradiation (gathering the fluence and the neutron flux).

In that context, significant efforts have been engaged through numerous studies following three main axes [Tanguy, 2011]: IASCC in-situ testing in reactors, stress corrosion cracking (SCC) testing on neutron pre-irradiated materials employing corrosion loops (simulated PWR or BWR environments), SCC testing on representative materials (replacing for example neutron radiation by ion irradiations, or irradiation hardening by mechanical hardening). As clearly underlined by figure 1.4, these three respective approaches treat different aspects of the problem with a decreasing degree of representativeness but also decreasing costs and an increasing degree of control over the numerous parameters.

This strategy has permitted to derive IASCC sensitivity criteria based on empirical curves. Such an example of data set resulting from numerous constant loadings using O-rings, C-rings and tensile testing up to fracture of 316 and 304 austenitic SS at different irradiation dose, is presented in figure 1.5 in terms of stress (in yield stress percent) to failure or non failure of the as-irradiated alloy. After a significant irradiation dose, a 50 % yield stress loading is taken as a first-hand criterion from an engineering perspective (black line in figure 1.5). However, a large data scattering is clearly evidenced. Moreover, these kind of curves are depending on the numerous factors cited above. In consequence they do not provide an intrinsic information.

In parallel, focusing on more physical aspects has also permitted to perform numerous parametric studies with higher parameters control [Jiao et al., 2005, Jiao et al., 2007, Jiao and Was, 2010, Jiao and Was, 2011, Le Millier, 2014, Cissé et al., 2013, Gupta et al., 2016, Fukuya et al., 2008b, Nishioka et al., 2008], thus significantly increasing

1. CONTEXT AND MOTIVATION

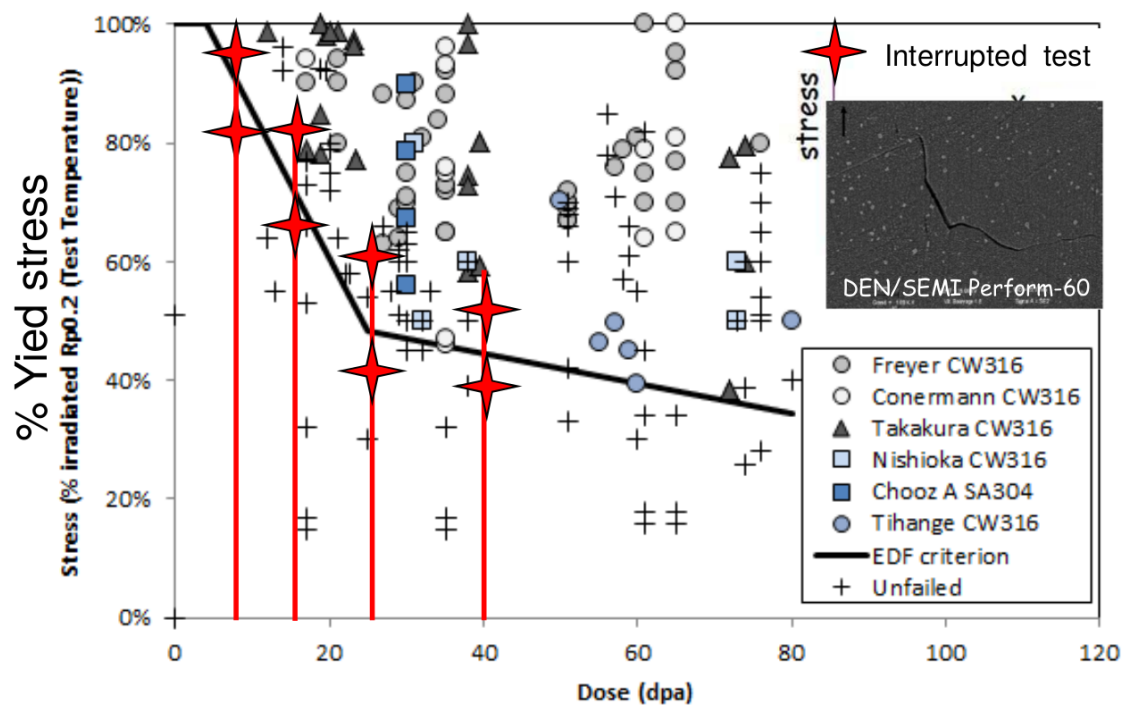


Figure 1.5: IASCC empirical curve of the critical stress to fracture according to the irradiation dose, along with CEA strategy of interrupted tests of interest around the industrial criterion [Tanguy and Hure, 2016, Féron et al., 2012].

1. CONTEXT AND MOTIVATION

our understanding of some parts of the overall phenomenon. In particular SCC testing of neutron-irradiated or proton-irradiated austenitic SSs using slow strain rate tensile test (SSRT) has been undertaken in order to better understand the initiation part of the IGSCC. This aspect is for example illustrated (figure 1.5) by the work carried out at CEA using corrosion loops in hot cells [Féron et al., 2012].

However, to this day, no model permits to predict successfully both the initiation and/or the propagation part of IASCC, the difficulty clearly residing in the synergistic effects of this multi-physical phenomenon.

1.2.2 Influence of irradiation on the SCC of austenitic stainless steels

Following the SCC tests on neutron or proton irradiated austenitic SSs, important breakthroughs have been achieved in the last decades. In particular, a strong endeavour has been dedicated to the determination of the most influential factors involved in SCC of irradiated austenitic stainless steels, this strategy being intended to tackle the behaviour complexity previously exposed. It should be reminded here that this kind of studies discards any influence of irradiation on the environment and merely focusses on the potential impacts of irradiation on the materials properties (through changes of its microstructure and its microchemistry) and subsequently on the IGSCC behaviour under simulated PWR, BWR or inert environments.

The main results from these studies are summarised in the next subsections.

1.2.2.1 Radiation induced segregation and irradiation hardening

The difficulties of the above endeavour resides into the multiple effects of irradiation on austenitic SS that have been correlated with the same rate (according to the irradiation dose) to the intergranular cracking phenomenon observed during the SCC tests: radiation induced segregation, irradiation hardening, localised deformation [Was, 2007b, Fukuya, 2013]. These correlations are summarised in figure 1.6 from the work of Was et al. with arbitrary units as indicator of each factor occurrence. Hence the raising problem to clearly discriminate one or several predominant effect(s) over IASCC.

1.2.2.1.1 Radiation induced segregation Radiation induced segregation (RIS) of austenitic SS is a well-known phenomenon related to a local modification of the microchemistry of the grain boundaries due to irradiation. It mainly results in a chromium depletion and a nickel enrichment in the close vicinity (within distances of roughly 10 nm) of grain boundaries. Figure 1.7a typically illustrates this effect in the case of a CW316 austenitic SS neutron-irradiated (PWR) to 35 dpa at 310 °C. Complementary to the correlations between the increase of the chromium depletion with the increase of IASCC susceptibility, a modification of the mechanical properties (strength) of grain boundaries was pointed out as one of the possible explanations for the IASCC initiation phase. It is also noted that the chromium concentration constitute an important factor

1. CONTEXT AND MOTIVATION

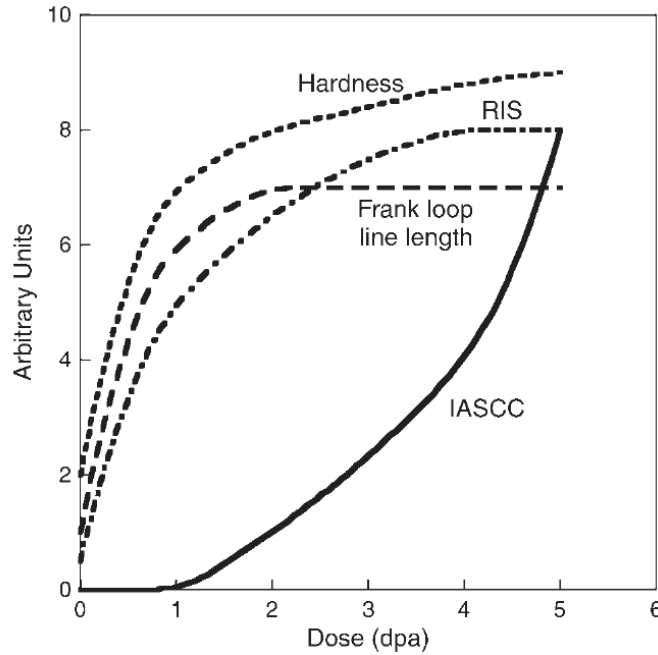


Figure 1.6: IASCC correlations with radiation induced segregation, hardness and Frank loop defects [Was and Andresen, 2007].

for the passivation of the alloy (i.e. the formation of an oxide thin protective layer) [Fukuya et al., 2013] leading to suggestions that RIS might participate to the IGSCC propagation phase through enhanced corrosion mechanisms at grain boundaries.

However, annealing experiments of irradiated austenitic SSs [Was, 2003] have shown that in given annealing conditions for which RIS was kept steady, the IASCC phenomenon was mitigated well before, as illustrated in figure 1.7b.

1.2.2.1.2 Hardness A second well-known effect of the increase of the irradiation dose on austenitic SS is the significant increase of the yield stress, the decrease of ductility, along with the increase of the hardness. Figure 1.8 typically illustrates this first two points with the typical stress-strain curves of a 304L stainless steel irradiates between 0 and 3.4 dpa [Pokor, 2002]. Other studies show that, at doses between 5 and 10 dpa, a saturation of the yield stress at a 900–1000 MPa threshold (with respect to the dose) is reached for similar 316 austenitic SS [Fukuya et al., 2013].

It is also known that the yield stress increase is linearly correlated to the hardness. These modifications of the mechanical properties of the material with irradiation are explained by the underlying mechanisms involved at the microstructure level.

Transmission electron microscopy (TEM) observations of irradiation austenitic SSs have evidenced radiation induced defaults such as dislocation loops, vacancies, cavities (or helium bubbles) and precipitates (depending on the irradiation dose), with a preponderance of the interstitial dislocation loops (or Frank loops) [Edwards et al.,

1. CONTEXT AND MOTIVATION

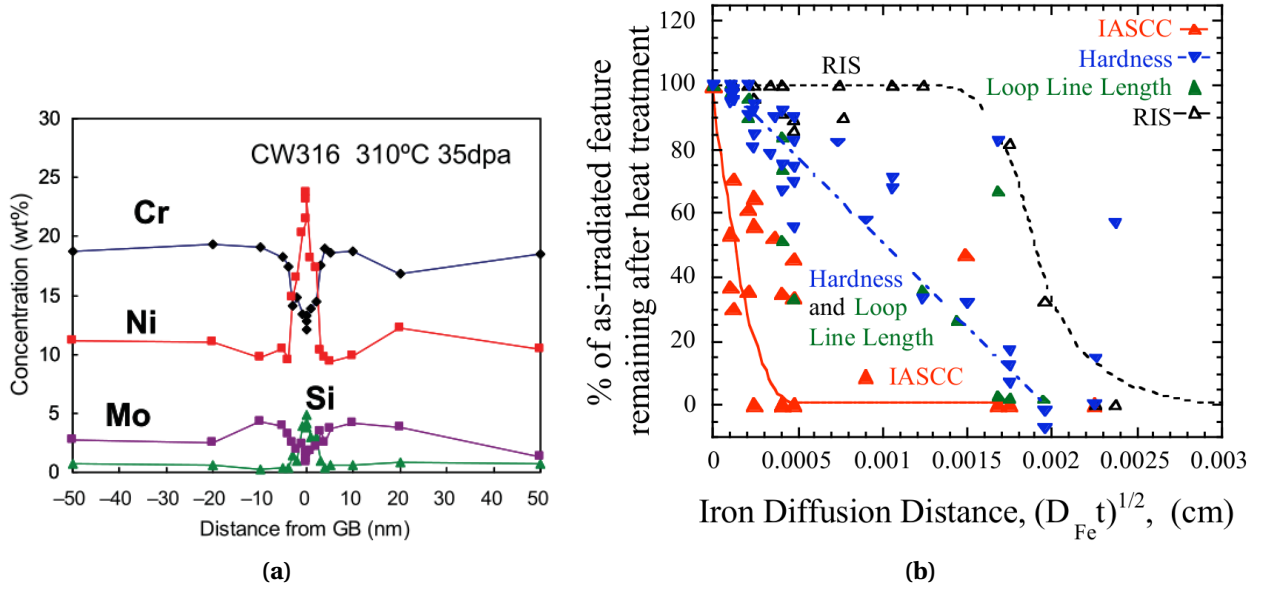


Figure 1.7: Typical RIS concentration GB profiles at a PWR-irradiated type 316 austenitic SS to 35 dpa [Fukuya, 2013]. Mitigation of RIS, dislocation loops and hardness according to the extent of final annealing for several 316 and 304 austenitic SSs, primarily irradiated to doses between 1 and 35 dpa [Was, 2003] and subjected to SCC testing.

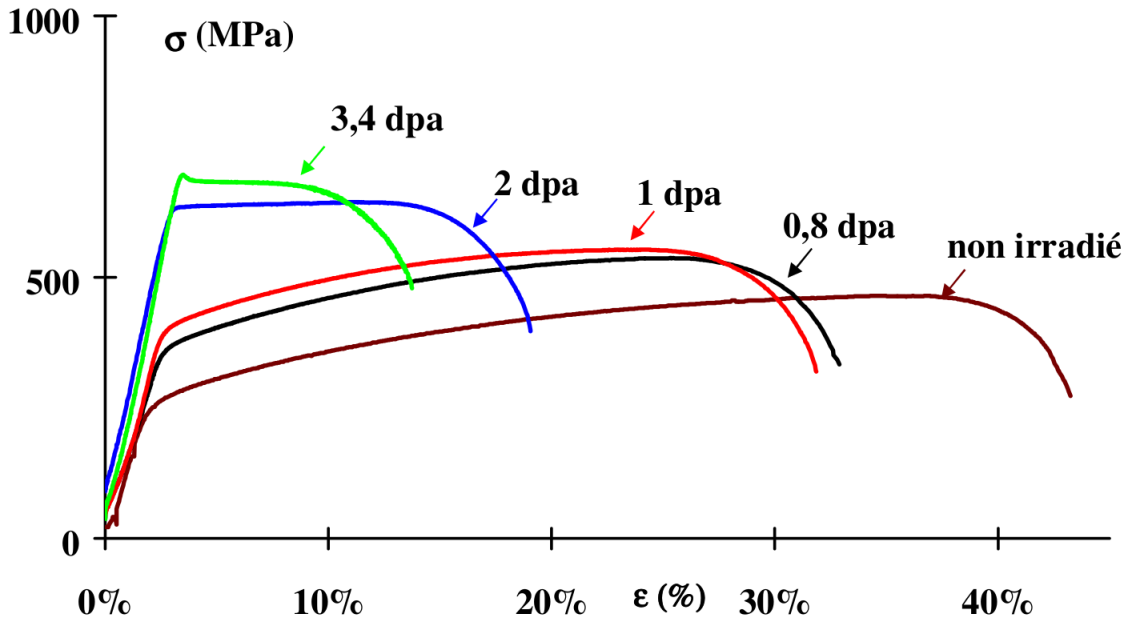


Figure 1.8: Effects of irradiation on typical stress-strain curves of a 304L austenitic SS [Pokor, 2002].

1. CONTEXT AND MOTIVATION

2003, Fukuya et al., 2013]. In particular, it was shown that these dislocation loops are fine (between 5 nm and 20 nm) and dense.

Both the increase of the yield stress and the increase of the hardness, result from the impingement by these irradiation induced defects of the moving dislocations during plasticity.

However, complementary studies have also shown that hardening alone does not provide a relevant correlation: keeping a constant hardness values by either mechanical hardening on unirradiated austenitic SS or irradiation hardening on the same material, the IASCC susceptibility was only recorded in the case of the irradiated material.

It was then pointed out that irradiation constitutes a necessary condition, and that the irradiation microstructure is at the bottom of the story ; RIS, the hardness or the yield stress increase representing secondary correlating factors.

1.2.2.2 Preponderant influence of localised deformation

An other important consequence of irradiation is the modification of the deformation mode from the onset of plasticity: a localisation of plastic slip deformations or dislocation channelling (i.e. a concentration of the plastic deformations in so-called channels) is clearly evidenced in figure 1.9. In comparison to unirradiated materials, these channel are less numerous and gather significantly larger plastic deformations (flow of dislocations) with almost no dislocation gliding outside these channels due to a high density of irradiation defects.

TEM studies [Bailat et al., 2000, Sauzay et al., 2010, Jiao et al., 2007] of neutron or proton irradiated austenitic SS microstructure have revealed a very specific mechanism for the formation of these features: irradiation defects such as Frank loop or precipitates are sheared and eliminated by preliminary gliding dislocations, clearing the way and facilitating subsequent dislocations flows [Was, 2007b]. As a result, clear bands with very few defects left can be evidenced, as illustrated by the different TEM observations in figure 1.9. In summary, these TEM contrasts conveniently provide the traces of the dislocations flows history.

It should be noted that this deformation mode have already been observed before in other metallic materials [Sharp, 1967, Victoria et al., 2000].

Was et al. [Was, 2007b, Jiao et al., 2005] have evidenced an intensification of the slip strain in these clear bands with the increase of the irradiation dose measuring the surface step heights of emerging clear bands using atomic force microscopy (AFM). Values above 100 % slip deformation was retained as a noticeable illustration of localised deformation.

Observations show that these clear bands actually cross the entire grain and therefore intersect grain boundaries where intense shearing may or may not be accommodated by the interface, leading to various behaviour: slip transmission in the adjacent grain, ledge or step formation, grain boundary sliding and so on.

Figure 1.9c shows for example a TEM observation of a deformation step induced by the shearing of a grain boundary by the intersection of a channel.

1. CONTEXT AND MOTIVATION

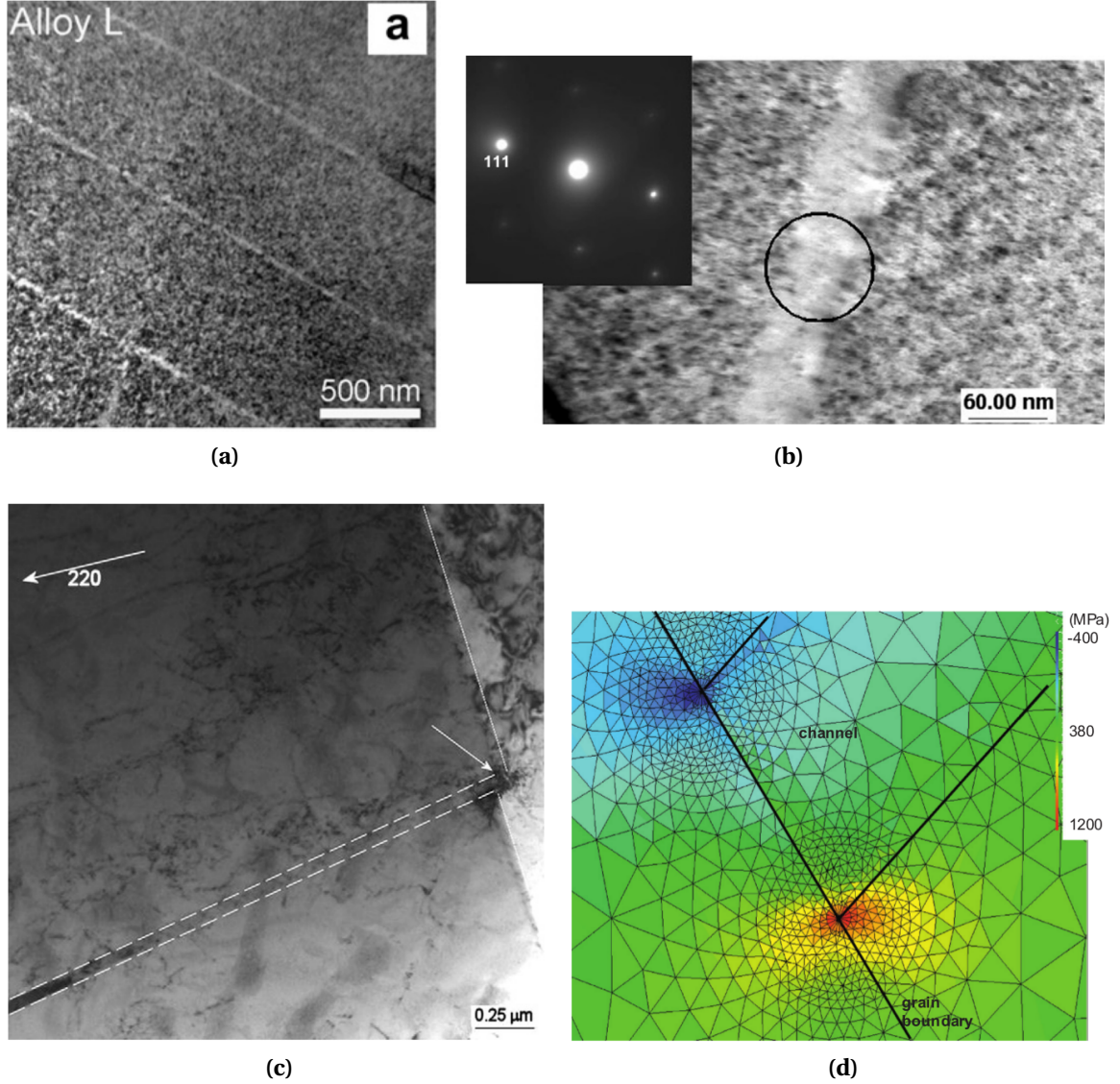


Figure 1.9: TEM observations of clear bands for: a 304 austenitic SS with Cr and Ni addition, irradiated to 5 dpa and strained to 7 % (1.9a) [Jiao et al., 2007] ; a 304L austenitic SS irradiated to 0.16 dpa (1.9b) with a GB slip step induced by intense shearing in the channel (1.9c) [Sauzay et al., 2010]. Crystal plasticity FE computations of the intergranular stress field in the vicinity of a clear band/GB intersection (1.9d) [Sauzay and Moussa, 2013].

1. CONTEXT AND MOTIVATION

Eventually, the interaction between channel and grain boundary can lead to microcrack nucleation as evidenced by numerous studies [Gupta et al., 2016, McMurtry et al., 2011, Jiao and Was, 2008, Le Millier, 2014, Nishioka et al., 2008, Onchi et al., 2003, West and Was, 2013] carried out using slow strain rate tensile test of various irradiated austenitic SSs in either simulated PWR, BWR or inert environment (i.e. SCC testing on pre-irradiated materials). Some observations extracted from these studies are provided in figures 1.10 and establish a causality between the intersection of clear bands at grain boundaries and intergranular cracking initiations.

In particular, Onchi et al. [Onchi et al., 2003] have performed fractography observations after IG failure of an irradiated 304L pulled under inert environment. The authors have shown that IG fracture occurred without any presence of PWR or BWR environment. Furthermore, as illustrated by the related fractographies in figure 1.12d, linear features probably resulting from the interactions of clear bands with grain boundaries were evidenced.

Nishioka et al. [Nishioka et al., 2008] have further confirmed the direct influence of clear bands/grain boundary interactions during slow strain rate tensile tests under inert environment, as evidenced by their observations reported in figure 1.10c.

These studies therefore reveal that the environment does not constitute a necessary condition for IG fracture. In contrast, they clearly underline the importance of dislocation channelling for the occurrence of intergranular cracking initiations. Nevertheless, it is admitted that the influence of the environment is clearly detrimental [Fukuya et al., 2011] during SCC testings.

Finally, in a comprehensive parametric study, Jiao et al. [Jiao and Was, 2011] have quantitatively shown that localized deformation constitutes the most influential factor on IASCC. The authors used a IASCC correlation strength factor S_{IASCC} to compare the influences of RIS, hardness, the stacking fault energy and localised deformation:

$$S_{IASCC} = \frac{L_{total} - L_{mixed}}{L_{total}} \quad (1.1)$$

by plotting the measured crack length per unit (representative of IASCC susceptibility) against a representative indicator for the different factors in the case of seven different austenitic SSs, proton irradiated to 1 and 5 dpa, and slow rate tensile tested at 1 % and 3 % deformations under either simulated BWR or argon environments. Using these data, a subsequent definition of three IASCC susceptibility zones for each factor, yields the extended lengths L_{total} and L_{mixed} and the corresponding correlation strength factor as illustrated in figure 1.11a.

The following coefficients were found: $S_{IASCC} = 0.0-0.4$, 0.54, 0.5 and 0.88 for respectively the RIS (using GB chromium concentration measure of the study and results of literature), the hardness, the stacking fault energy and localised deformation (using the channel height measured by AFM, as illustrated in figure 1.11b).

Following these studies, it was clearly agreed that the localization of the plastic deformation play a major role in the IASCC phenomenon.

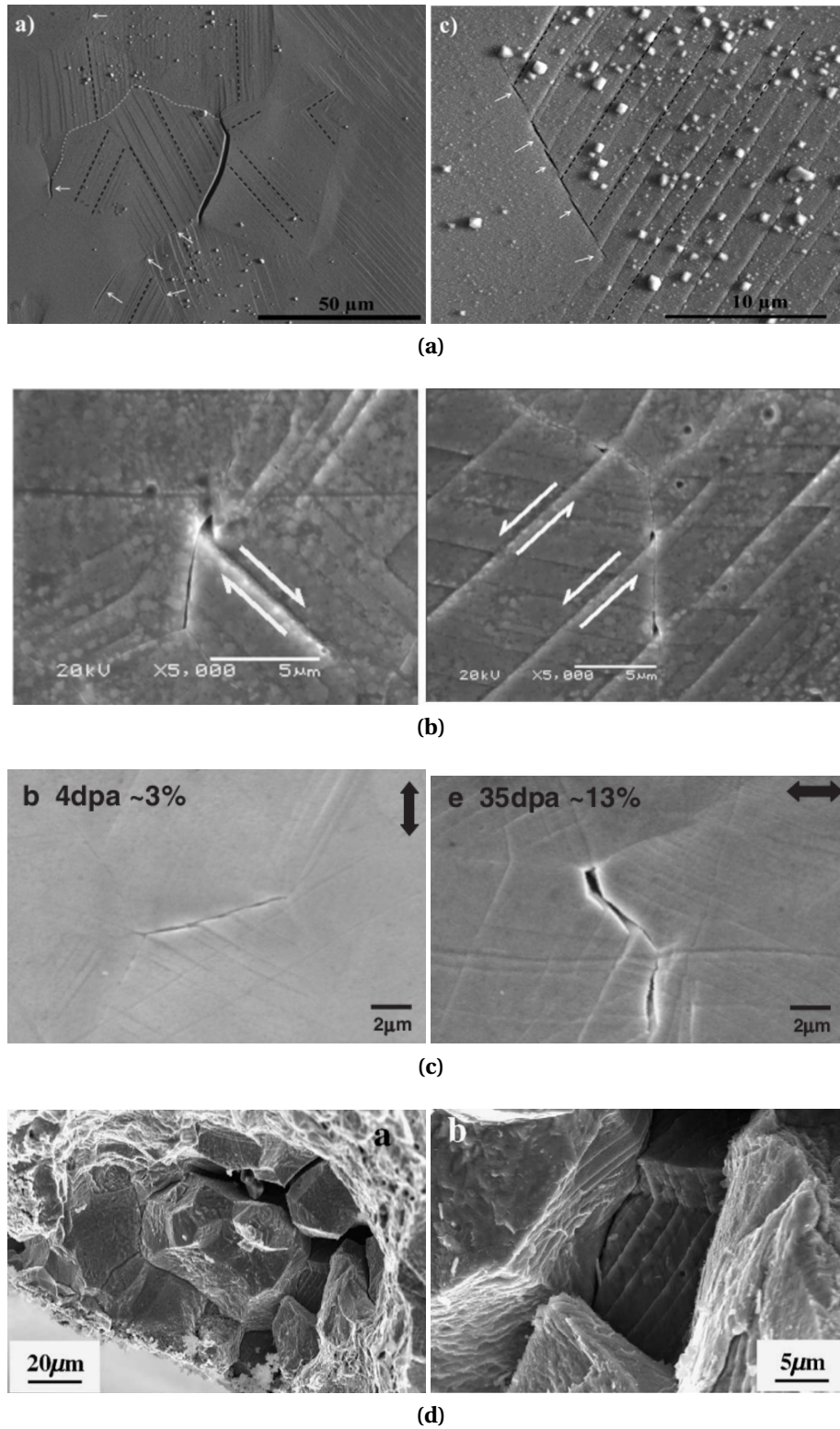


Figure 1.10: SEM observations at free surfaces showing clear band/grain boundary interactions after interrupted SSRT on: a 304L austenitic SS proton-irradiated to 5 dpa pulled at 4 % plastic deformation under simulated PWR environment (1.10a) [Gupta et al., 2016], a 18Cr12Ni austenitic SSs proton-irradiated at 5 dpa and pulled at 9 % deformation under simulated BWR environment (1.10b) [McMurtrey and Was, 2012], a CW316 austenitic SSs pulled under inert environment (1.10c) [Nishioka et al., 2008], SEM fractography of a 304 austenitic SS irradiated to $1.2 \times 10^{21} \text{ ncm}^{-2}$ pulled under inert environment (1.12d) [Onchi et al., 2003].

1. CONTEXT AND MOTIVATION

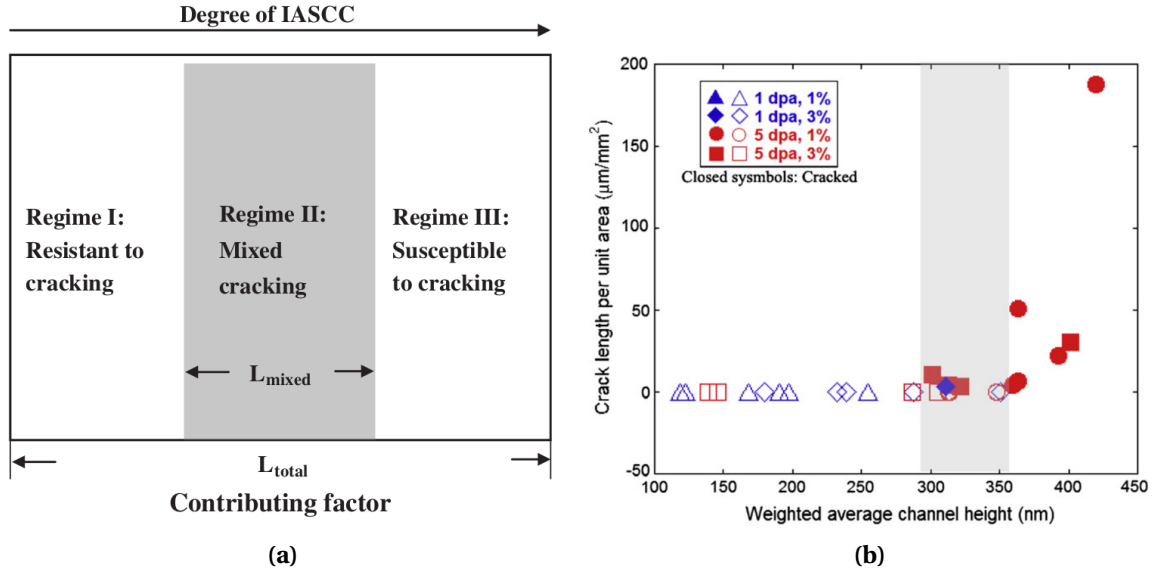


Figure 1.11: Scheme of IASCC susceptibility zones defined by [Jiao and Was, 2011] using the crack length per unit area to assess the correlation strength of various influential factors (1.11a) such as the localised deformation using the channel height measured by AFM (1.11b).

1.2.2.3 Stress field at channel/grain boundary intersection

Following the above results, additional key elements involving dislocation channelling and improving our understanding of IASCC have been highlighted.

Importantly, it has been remarked that IGSCC occurs more frequently at the discontinuous channels/grain boundary intersection, i.e. clear bands that do not transmit to the adjacent grain through the grain boundary. Observations and results of [Le Millier, 2014], reported in figure 1.12, illustrate this point with a statistical study of the IG fracture frequency of several austenitic SS at different irradiation doses and interrupted tensile deformation, according to three categories of channel/grain boundary interaction: discontinuous clear bands, continuous clear bands (i.e. with slip transmission) and no clear bands (see figures 1.12b, 1.12c and 1.12a respectively). The higher frequency of IG cracking at discontinuous clear bands is readily explained by the fact that IG stress concentrations are probably more pronounced in this particular case than in any other cases for which accommodation of the plastic slip may induce more stress relieves through slip transmissions.

In consequence, discontinuous clear bands/grain boundaries intersections have been the subject of several studies trying to decipher and quantify related intergranular stress fields induced by these shearing channels using either finite element computations [Sauzay and Moussa, 2013, Sauzay and Vor, 2013] or high resolution electron back scattered diffraction (HR-EBSD) [Johnson et al., 2016]. These studies have shown

1. CONTEXT AND MOTIVATION

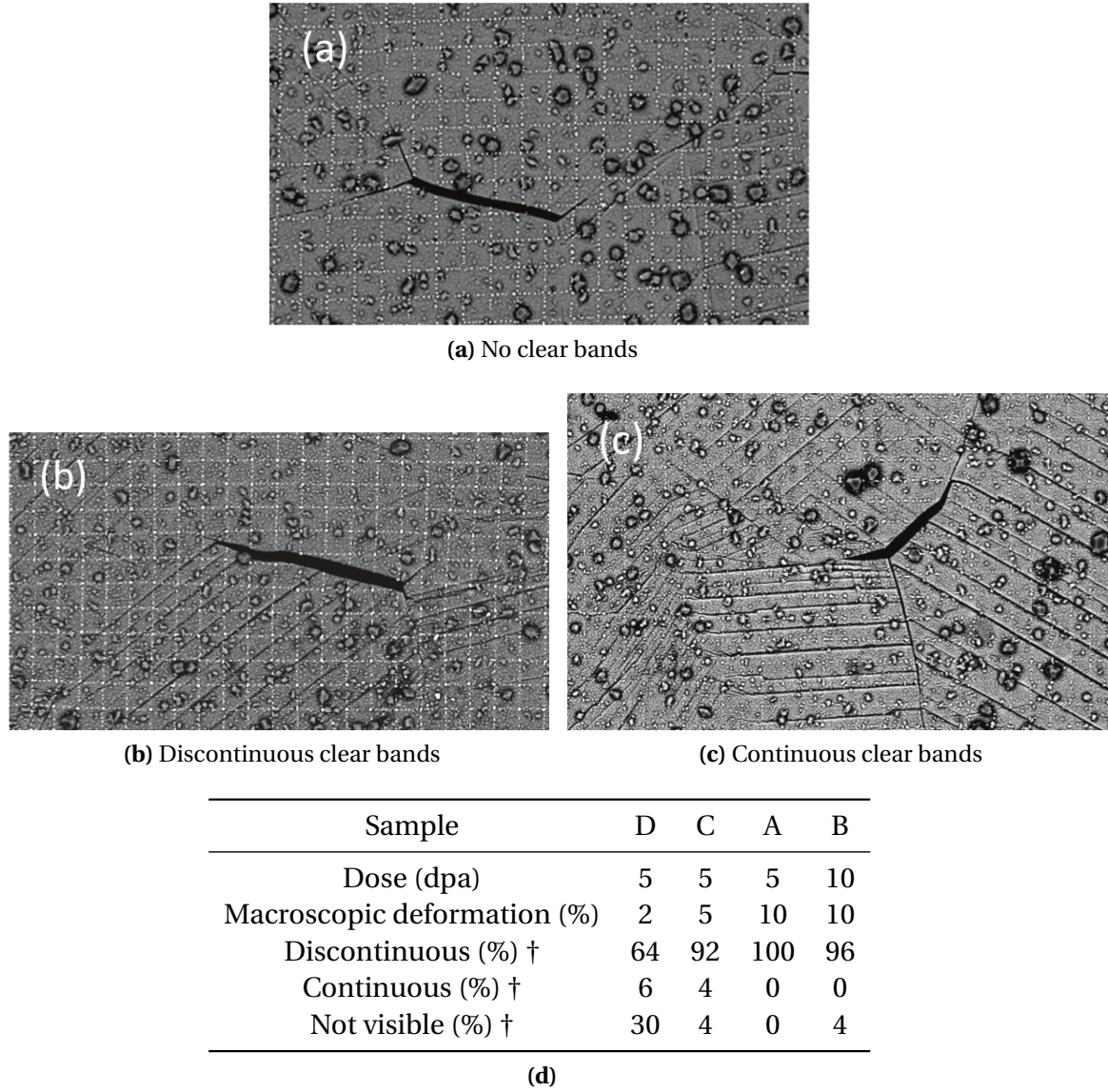


Figure 1.12: Results of the statistical study performed by [Le Millier, 2014] on proton-irradiated austenitic stainless steels, quantifying the crack frequency related to three categories of channel/grain boundary interactions: no clear band (1.12a), discontinuous clear bands (1.12b), and continuous clear bands (1.12c).

1. CONTEXT AND MOTIVATION

that stress concentrations at discontinuous clear bands intersections are quantitatively evidenced. More specifically, it has been underlined that the intergranular normal stress component may constitute a key factor, which motivates its intervention should one consider a criterion to predict IGSCC initiation.

As stressed out by the quantitative studies of Sauzay et al. [Sauzay and Moussa, 2013, Sauzay and Vor, 2013], proposing a critical stress multiscale model for intergranular cracking, using a coupled criterion for fracture initiation:

- The pile-up theory generally used to model channel/grain boundary intersections [Was, 2007a, Fukuya et al., 2011, Jiao et al., 2005, Johnson et al., 2016] as arrays of dislocations piling at grain boundaries in one atomic slip plane, is clearly not suited for a predictive model using atomistic data.
- A multiscale model based on the stress concentrations obtained at channel or slip band/grain boundary intersection needs at least two intrinsic mechanical parameters of fracture for the interface: a critical energy and a critical stress.

IGSCC studies are now completed by more thorough quantification studies of grain boundaries strength and material behaviour characterisation at smaller scales, aiming to access to more physical characterisation and more predictive models.

1.3 Mechanical properties of grain boundaries and metal/oxide interfaces

In the continuity of the preceding sections, a succinct and non exhaustive presentation of some results and current methodologies related to the study of interfaces behaviour and mechanical properties is provided in this last section.

Advances in experimental techniques such as high-resolution characterisation methods (atom probe tomography, HR-EBSD, FIB 3D slicing, HR-TEM) or micromechanical testing have allowed the consideration of new perspectives to better understand the underlying mechanisms of materials at smaller scales [Lozano-Perez et al., 2014].

For example, in the case of a 304L austenitic SS exposed to a simulated PWR environment, the influence of cold-work and applied stress on the oxidation behaviour has been studied using FIB 3D slicing. Preferential oxidation of grain boundaries and slip bands have been clearly evidenced through nm-resolution 3D reconstruction of the inner oxide layer, as presented in figure 1.13a. In particular, the size of the 3D reconstructions have permitted the access to a statistical quantification of the oxidation depth on the grains surface and at grain boundaries. Significant depth variations were found along the GBs, justifying the statistical representation. The effect of cold-work (CW) and applied stress was underlined with mean GB oxide depths of about 200 nm and 400 nm for the samples with no CW, no applied stress and both CW and applied stress respectively.

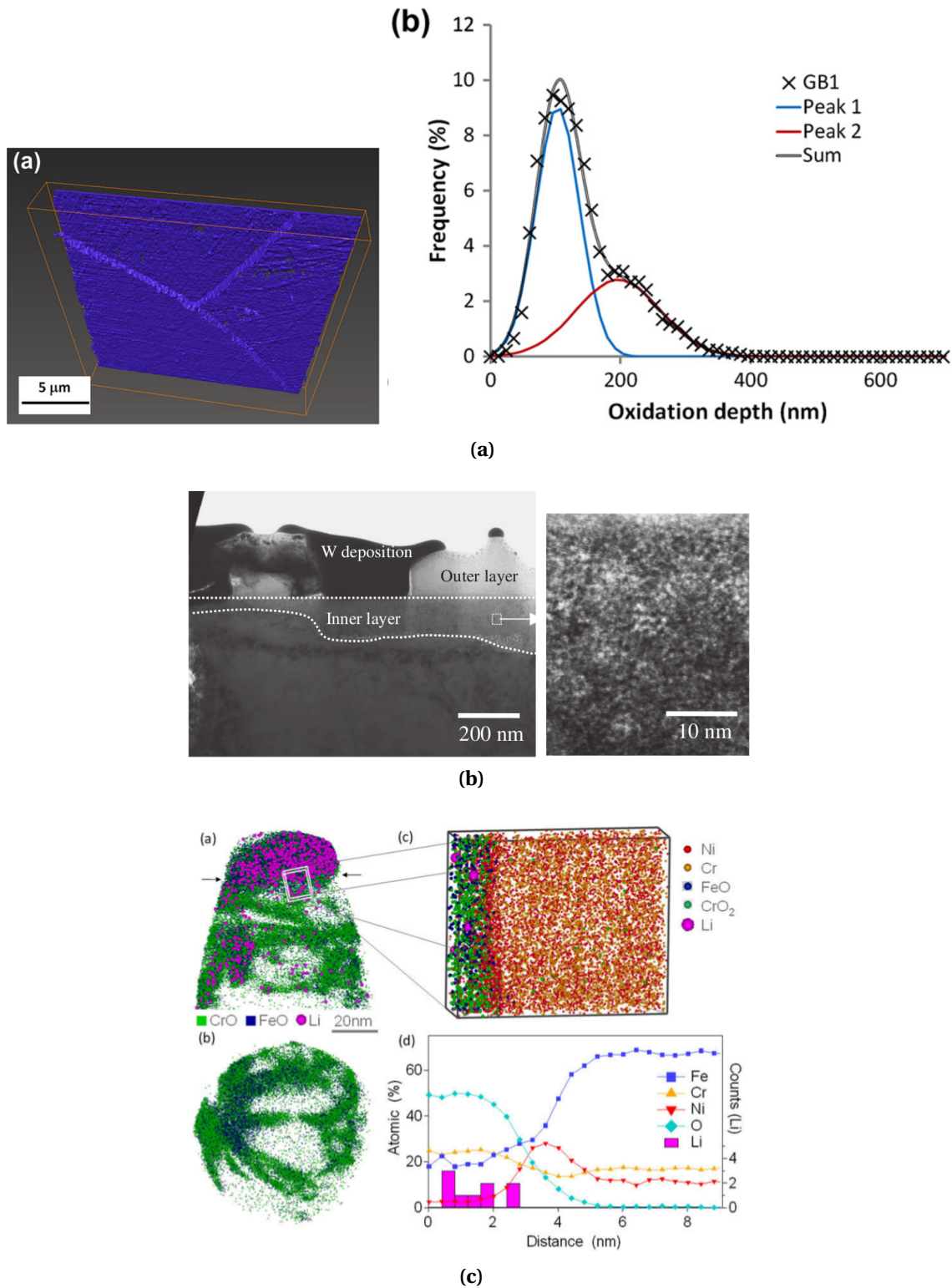


Figure 1.13: Focused ion beam 3D slicing reconstruction of the inner layer of an oxidised 304L austenitic SS and related statistical assessment of the oxidation depth along one grain boundary (1.13a), adapted from [Lozano-Perez et al., 2012a]. TEM observation of the duplex structure of the oxide scale formed on a oxidised 316 austenitic SS (1.13b) [Terachi et al., 2008]. Atom probe tomography performed on in the vicinity of the inner oxide layer metal/oxide interface of an oxidised CW 316 (1.13c) [Lozano-Perez et al., 2010].

1. CONTEXT AND MOTIVATION

Concerning the oxidation of austenitic SSs in a simulated PWR environment, it is now well-known [Dumervil et al., 2016, Terachi et al., 2008, Lozano-Perez et al., 2014] that the oxide scale developed is composed of a duplex structure: an outer Fe-rich oxide layer and an inner Cr-rich oxide layer with spinel structures of Fe_3O_4 and $(\text{Ni,Fe})_2\text{Cr}_2\text{O}_4$ respectively. Figure 1.13b shows a typical TEM observation [Terachi et al., 2008] of such an oxide structure formed on a 316 austenitic SS after exposure to a simulated PWR environment, with a focus on the metal oxide interface revealing fine nanometric grains.

Atom probe tomography (APT) carried out on a tip extracted at the inner layer metal/oxide interface of a 20 %CW 316 austenitic SS exposed to a simulated PWR environment have brought atomic resolution information on the interface structure [Lozano-Perez et al., 2010]. As shown in figure 1.13c, the authors have evidenced an oxide network below the inner layer. This network is linked to the dislocation production during CW at the surface, therefore confirming the influence of cold-working on the oxidation mechanism.

Finally, the recent advances in the FIB techniques have allowed the development of novel micromechanical tests such as microcantilever bending or microtensile tests. The micromechanical tests constitute valuable and promising techniques for nuclear materials testing for several reasons:

- The mechanical behaviour recorded during the test can be associated with in-situ observation of the microstructure, thus permitting the authors to directly decipher the related underlying mechanisms.
- A focus on the local features of interest such as grain boundaries or other interfaces can be achieved, thus allowing a better understanding of the potential microstructural events through a better control of the experiment.
- Novel access to phenomena and mechanical properties of irradiated materials
- The significant reduction of radioactive volume of material to perform mechanical characterisations, thus greatly facilitating the handling of irradiated samples.
- Ion-irradiated samples give access to low activation materials for convenient manipulations. However, the irradiated affected zones are generally limited to the surface of the sample with shallow depths, thus limiting the relevance of mechanical testing. Small-scale testing clearly allow to tackle this issue by only focusing on small volume at the surface of interest.

For example Dugdale et al. [Dugdale et al., 2013] have achieved a mechanical characterisation of an oxidised grain boundary in a nickel-based alloy previously exposed to a simulated PWR primary water environment, by using microcantilevers bending and finite element computations with a cohesive zone model (CZM). Figure 1.14a [Dugdale et al., 2013] illustrates the process: through a fitting procedure of the maximum stress of the CZM, a local strength of 1.35 GPa is assessed for this interface.

1. CONTEXT AND MOTIVATION

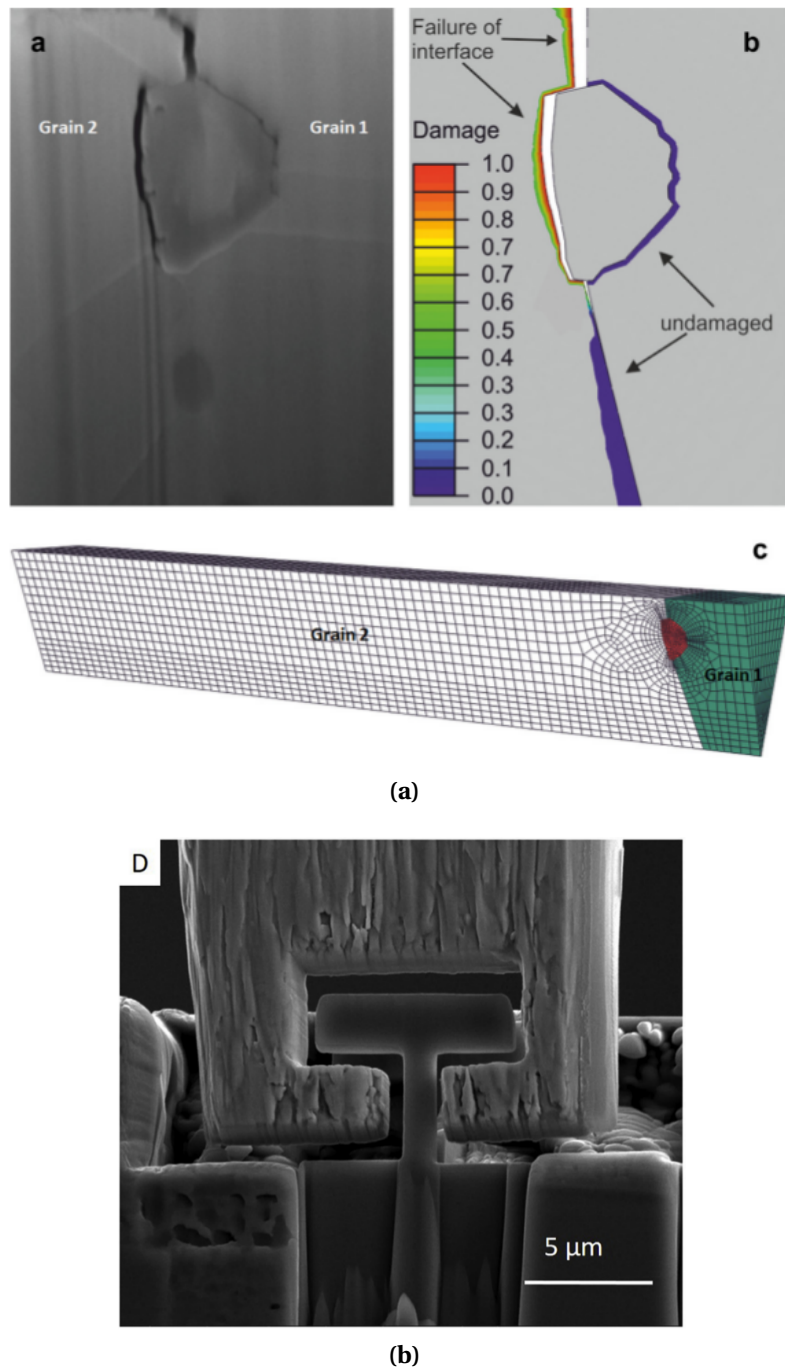


Figure 1.14: Partial fracture of an oxidised grain boundary in a 600 nickel-based alloy using microcantilever bending, FIB and finite element computation for the assessment of the interface strength (1.14a) [Dugdale et al., 2013]. Apparatus used for the microtensile test carried out on a 304L austenitic SS proton-irradiated to 10 dpa (1.14b) [Vo et al., 2017].

1. CONTEXT AND MOTIVATION

Vo et al. [Vo et al., 2017] have also shown that microtensile tests (illustrated in figure 1.14b) constitute a relevant method to characterise the behaviour of irradiated materials. With limited volumes of material, microtensile curves of a 304L austenitic SS proton-irradiated to 10 dpa, have provided yield stresses and strain-to-failure in agreement with macro-tensile tests. A similar method could be employed on bicrystal specimens, thus providing complementary information on the strength of grain boundaries in irradiated materials.

As concluded by P. Hosemann in his review [Hosemann, 2018], current experimental studies tend toward mechanical testing on smaller volumes while the increase of computer performances now allows to consider atomistic simulations with larger volumes of materials. One can hope that this progression may lead to a bridge between the experimental scales and the modelling scales.

In order to appreciate the remaining gap between these two scales (microscopic and atomic scales), some atomistic computational results of bicrystals tensile testing are now presented.

Ab initio GB cleavage computations of Černý et al. [Černý et al., 2019] on a pure Ni $\Sigma 5$ (2 1 0) grain boundary provide several stress-strain curves related to different loading models, as presented in figure 1.15a. In some of these models, the cleavage plane is arbitrarily chosen in the vicinity of the grain boundary. The related supercell used for these computations is adjoined in the same figure.

Additionally, results of molecular dynamics computations of tensile tests carried out on various FeCr_2O_4 (spinel) oxide grain boundaries are presented in figure 1.15b. The maximum stresses correspond to the grain boundary debonding, as illustrated in the case of a $\Sigma 5$ (2 1 0) grain boundary in the same figure.

In both cases, the recorded maximum tensile stresses, which could be referred to the ideal cleavage strength of the interfaces, are at least one order of magnitude higher than what could be expected from experimental assessments. This might obviously be partly explained by the small volumes considered for these simulations which are ideally free of defects (precipitates, dislocations and so on) that could potentially trigger critical events at significantly lower stresses.

This effect could be compared to the yield stress increase phenomenon observed when considering the compression of nanopillars for which the dislocations density drastically decreases. These simulations are clearly not too far from a certain realism. Moreover, this kind of simulations does provide intrinsic mechanical properties of interfaces that are not yet accessible by any other means.

Nevertheless, the use of this data for engineering model is still very limited, since a bridge between atomic and microscopic scales is not clearly established yet.

1. CONTEXT AND MOTIVATION

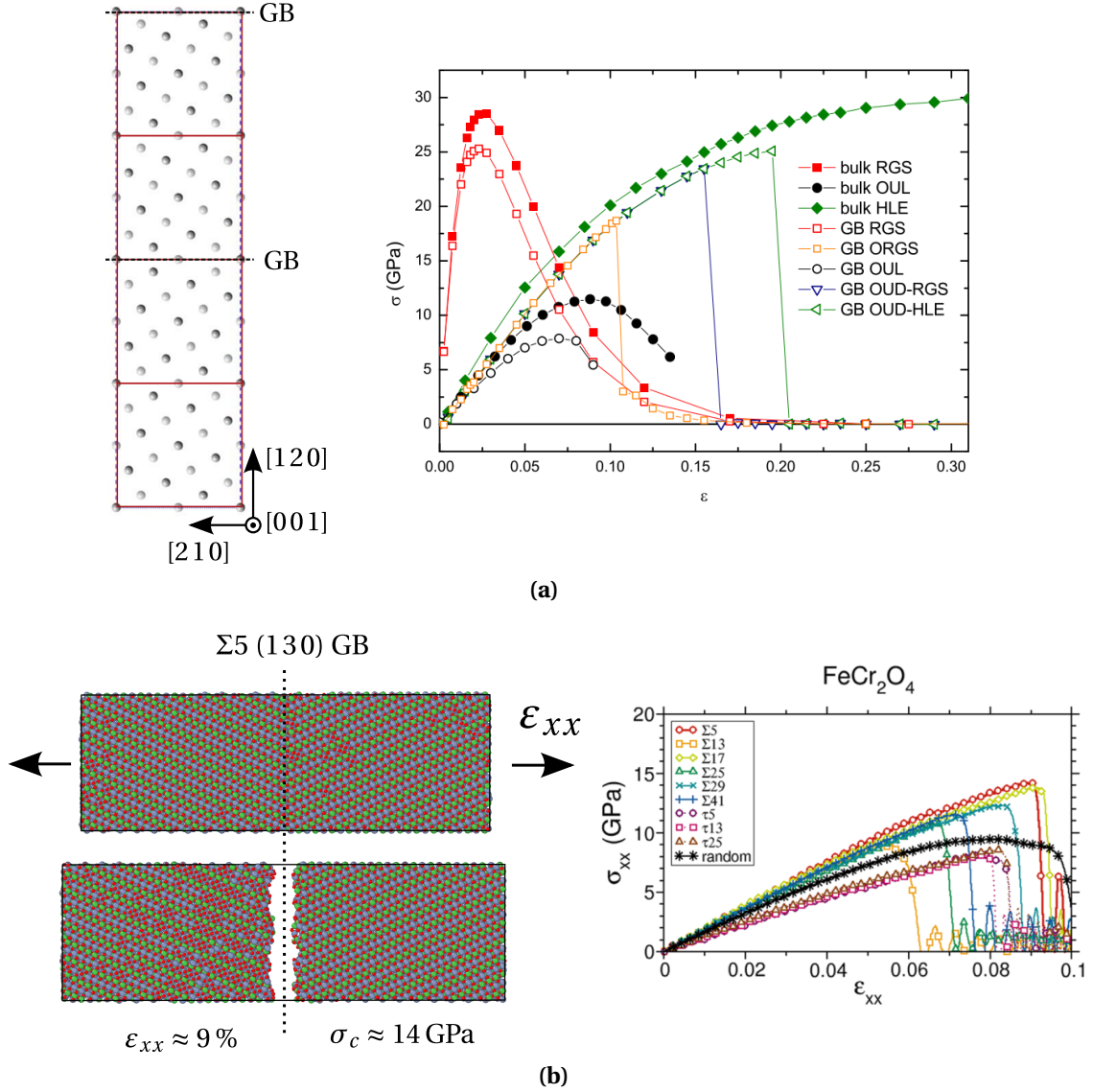


Figure 1.15: Ab initio computational supercell containing a $\Sigma 5$ (210) GB and the related stress-strain curves obtained using different loading models (1.15a) [Černý et al., 2019]. Molecular dynamics tensile test simulations performed on several spinel-type oxide FeCr_2O_4 CSL grain boundaries (1.15b) with the illustration of one periodic simulation box (left picture, for the $\Sigma 5$ (031) GB) and the tensile curves of all the studied GBs (right picture) (1.15b) [Van Brutzel et al., 2019].

1.4 Conclusion: toward multiscale simulations through bottom-up or top-down approaches

Far from being exhaustive, this chapter was intended to highlight three points from the current context regarding the understanding and the prediction of the IG cracking phenomenon of irradiated austenitic SSs:

- More physically-based prediction models are still needed in complement of the empirical criteria that are currently available.
- The major influence of the localisation of the plastic deformation is now clearly established. However a quantification of this mechanism influence that could lead to better predictive models, is not yet achieved.
- The need of grain boundaries and metal/oxide interface mechanical properties is highlighted here. However, the use of these inputs in dedicated multiscale models is not clearly established yet.

In this thesis, these points are approached by proposing the use of a multiscale model based on finite element computations in conjunction with molecular dynamics simulations for the assessment of grain boundaries mechanical properties. In that regard, the following steps are undertaken:

- In **chapter 2**, multiaxial loadings are carried out on pure nickel GBs through molecular dynamics simulations in order to decipher GBs behaviour in FCC metals. Pure nickel is chosen as a FCC material model.
- **chapter 3** and **chapter 4** focus on the interpretation of the results of **chapter 2**, since a competition between GB dislocation nucleation and GB decohesion is found. These two behaviours and the transition in between are treated in these two chapters respectively.
- **chapter 5** proposes a first example for the use of the atomistic results of **chapter 2** at the upper scale, in the context of a the simulation of V-notches located at grain boundaries. In that regard, two multiscale approaches are introduced: a bottom-up approach using either a coupled criterion or a cohesive zone model for fracture initiation, and a top-down approach using molecular dynamics GB computations informed by finite element simulations.
- In **chapter 6**, it is proposed to present and partly justify a geometrical model of plastic slip bands or clear bands of finite thickness in low stacking fault energy alloys. An experimental assessment of this geometrical model is undertaken using atomic force microscopy coupled with EBSD data after interrupted tensile tests on an unirradiated 316 austenitic SS. The contrast between irradiated and

1. CONTEXT AND MOTIVATION

unirradiated deformation mode of various austenitic SSs is underlined through a comparative study as it could partly explain the IG cracking behaviour.

- Finally, [chapter 7](#) focuses on the physical justification and the use of the multiscale model proposed by Sauzay et al., involving the finite element computations of slip band(s) or clear band(s)/ grain boundary interaction stress fields and the use of a coupled criterion for intergranular cracking initiation in conjunction with GBs mechanical properties assessed by MD simulations. The bottom-up and top-down approaches, introduced in [chapter 5](#), and the data on the geometrical model gathered in [chapter 6](#) are used for this purpose.

2

Multiaxial behaviour of FCC nickel bicrystals at the atomic scale

In this chapter, the mechanical behaviour of various bicrystals is investigated through molecular dynamics computations. Loadings consisting in normal straining to the grain boundary plane coupled with transverse straining, are applied to the related bicrystals in the case of numerous CSL tilt symmetric $[100]$ grain boundaries in pure nickel using an EAM potential developed by Mishin.

For each grain boundary, several tensile loadings are carried out for different transverse/normal (T/N) strain ratios. The influence of the shear strain is also considered in the case of a $\Sigma 5 [0\bar{1}2]$ grain boundary.

An increase of the T/N strain ratio is correlated to the increase of the normal critical stress triggering either Shockley partial dislocation nucleations from the grain boundary or GB brittle decohesion as a progressive behaviour transition is observed between the two phenomena.

For all the considered grain boundaries, it is found that as the strain ratio increases from one tensile test to another, the first occurrence of the GB crack initiation occurs as the critical stress saturates to a constant value, which may correspond to a GB intrinsic parameter of fracture. The adjunction of shear straining reveals a similar influence of the coupled transverse straining for the $\Sigma 5 [0\bar{1}2]$ grain boundary but with a significant decrease of this critical stresses.

Contents

2.1 Motivations and purposes	34
2.2 Molecular dynamics simulations of FCC bicrystal systems for the investigation of CSL symmetric tilt grain boundaries behaviour	35
2.2.1 Formation of the [100] symmetric tilt grain boundaries	36
2.2.2 Atomic structure, mechanical description and energy of the grain boundaries	38
2.2.2.1 Application of the structural unit model	38
2.2.2.2 Mechanical description with the structural unit/grain boundary dislocation model	41
2.2.2.3 Grain boundary energies	43
2.2.3 Uniaxial tensile loadings	45
2.2.4 Multiaxial tensile loadings	47
2.2.4.1 Transverse strains	47
2.2.4.2 Transverse and shear strains	49
2.3 From dislocation nucleation to grain boundary decohesion	50
2.3.1 Preliminary results	50
2.3.2 Influence of the multiaxiality : a behaviour transition	53
2.3.3 Influence of the temperature and strain rate on the behaviour of the $\Sigma 5$ grain boundary	59
2.3.4 Influence of the shearing deformation on the $\Sigma 5$ grain boundary behaviour	60
2.3.5 Behaviour of the different CSL grain boundaries	62
2.4 Summary of the results and conclusion	64
2.4.1 Results	64
2.4.2 Conclusion	65

2.1 Motivations and purposes

The investigation of the grain boundaries mechanical behaviour at the atomic scale is of particular interest for the prediction of intergranular fracture initiation in metals and alloys.

Many experimental observations at the microstructure scale report the formation of plastic slip bands impacting grain boundaries and leading to a wide variety of phenomena: slip band transmission (direct or indirect) [Lim and Raj, 1985, Cui et al., 2014], strong elastic deformations (and related stresses) in the neighbouring grain without plasticity [Britton and Wilkinson, 2012, Johnson et al., 2016, Genée, 2017, Genée et al., 2017], or GB crack nucleation [Lee and Vermilyea, 1971, Cui et al., 2014, Jiao and Was, 2008, Jiao and Was, 2011, McMurtrey et al., 2015]. Additionally, dislocation emission from the grain boundaries through slip band interactions [Genée et al., 2017] or ledges [Kurzydowski et al., 1984, Murr, 1981, Malis et al., 1972] has been extensively observed. Finally, grain boundary sliding (i.e. the local shearing of the interface) is also accounted for as an influential deformation mode linked to slip band interactions [Linne et al., 2019] with the grain boundaries.

Numerical computations based on the finite element method [Sauzay and Moussa, 2013, Sauzay and Vor, 2013] or discrete dislocation dynamics simulations [Gururaj et al., 2015] reveal strong multiaxial stress fields in the vicinity of impinged slip bands or pile-ups at grain boundaries.

This variety of intergranular behaviours and the multiaxiality of the related stress states encourage further investigations of the grain boundaries intrinsic behaviour.

At the atomic scale, uniaxial tensile and compressive loadings are extensively considered for the study of heterogeneous dislocation nucleations at grain boundaries [Tschopp et al., 2008, Spearot et al., 2005, Spearot et al., 2007b, Zhang et al., 2014] or homogeneous dislocation nucleation in single crystals [Tschopp et al., 2007, Spearot et al., 2007b, Cai et al., 2018]. Shearing deformations (or stress) are also widely considered for the grain boundaries behaviour and reveal deformation mode such as GB sliding through atomic shuffling, GB motion or fracture [Cahn et al., 2006, Sansoz and Molinari, 2005, Spearot et al., 2004, Zhang et al., 2015].

Larger computations on nanocrystalline aggregates [Van Swygenhoven et al., 1999, Van Swygenhoven et al., 2002, Van Swygenhoven, 2002, Yamakov et al., 2002, Yamakov et al., 2003] provide insight into the polycrystal behaviours involving the coupled behaviour of multiple grain boundaries under complex loadings. Grain boundary sliding, intergranular fracture initiation and dislocation nucleations are reported.

However, to our knowledge, few atomistic studies cover the intrinsic behaviour of isolated grain boundaries subjected to multiaxial loadings [Wyman et al., 2017, Černý et al., 2016, Černý et al., 2019].

In this chapter, the choice is made to focus on such aspect for several CSL tilt symmetric $\langle 100 \rangle$ grain boundaries in pure nickel through molecular dynamics simulations.

A first part introduces the methods implemented for this investigation from the for-

2. MULTIAXIAL BEHAVIOUR OF FCC NICKEL BICRYSTALS AT THE ATOMIC SCALE

mation of the thirteen grain boundaries to the application of the uniaxial and multiaxial loadings. A second part presents the results obtained and focuses on the observation of a progressive behaviour transition from the nucleation of dislocations at the grain boundary to the pure debonding of the interface according to the variation of the strain state applied. The influence of the temperature and the strain rate is further investigated.

A comprehensive discussion of the results obtained in this chapter and further related computations are provided in chapters 3 and 4.

2.2 Molecular dynamics simulations of FCC bicrystal systems for the investigation of CSL symmetric tilt grain boundaries behaviour

The mechanical behaviour of thirteen symmetric tilt [100] grain boundaries of pure nickel is investigated through molecular dynamics (MD) simulations using the code LAMMPS [LAMMPS, , Plimpton, 1995].

A semi-empirical potential proposed by Mishin [Mishin, 2004] is used to model atomic interactions in pure FCC nickel. This potential is based on the embedded-atom method (EAM) [Daw and Baskes, 1984] and is shown to reproduce with a rather good agreement (as presented in table (2.1) and (4.1)): the ratios between the elastic constants, the intrinsic stacking fault energy (SFE), the cohesive energy and the lattice parameter. Further verification at 300 K confirm the diminution of the elastic constants with the increase of the temperature even if a perfect agreement is not found with experimental measurements. The tool OVITO [OVITO, , Stukowski, 2009] provides atomic visualisations and various analysis modules such as: the common neighbour analysis (CNA) and the dislocation extraction algorithm (DXA) [Stukowski et al., 2012], allowing the detection of the crystallographic structure and the detection of dislocation lines with their Burgers vector.

	C_{11} (GPa)	C_{12} (GPa)	C_{44} (GPa)	γ_{SF} (mJm ⁻²)
EAM (0 K) [Mishin, 2004]	241.3	150.8	127.3	134
EAM (300 K) †	224	138	121	
Exp. (300 K) [Huntington, 1958]	246.5	147.3	124.7	-
Exp. (4 K) [Alers et al., 1960]	261.2	150.8	131.7	-
Exp. (300 K) [Alers et al., 1960]	250.8	150	123.5	-

Table 2.1: Elastic constants of pure nickel referenced by Mishin [Mishin, 2004] at 0 K and calculated here (†) at 300 K using the EAM potential of Mishin [Mishin, 2004] and comparison with experimental data [Mishin, 2004, Alers et al., 1960, Huntington, 1958]

2. MULTIAXIAL BEHAVIOUR OF FCC NICKEL BICRYSTALS AT THE ATOMIC SCALE

In this part, the formation of the simulated grain boundaries in their bicrystal configurations is primarily described before developing the method of mechanical investigation of the chosen systems.

2.2.1 Formation of the [1 0 0] symmetric tilt grain boundaries

The subsequent mechanical investigation is carried out on bicrystal systems allowing the application of homogeneous loadings in order to investigate the intrinsic grain boundaries behaviour (without any influence of strain or stress gradients).

Thirteen coincident site lattice (CSL) [1 0 0] symmetric tilt grain boundaries are selected among the comprehensive list provided by Mikura [Mykura, 1980]. This choice is made in order to obtain a wide range of Σ ratios, yet simple enough to ease the basic understanding of the underlying mechanism of the grain boundaries behaviour. Furthermore, the structure of those selected grain boundaries are additionally studied and validated in the literature [Sutton et al., 1995, Rittner and Seidman, 1996, Cahn et al., 2006], thus allowing possible comparisons with the present study. Table 2.2 references the different chosen grain boundaries and the dimensions of each initial box considered for the atomistic simulations involving the related N_{GB}^{at} number of particles.

CSL grain boundaries are chosen for their periodic lattice allowing the use of periodic boundaries conditions on the MD box in every directions of space. This choice implies the presence of two grain boundaries in the simulation box, as illustrated by the bicrystal in figure 2.1b containing two $\Sigma 5$ [0 $\bar{1}$ 2] grain boundaries.

From this optimised configuration at 0 K, an MD relaxation is carried out for 40 ps with a time step of 1 fs in the NPT isothermic, isobaric ensemble with prescribed temperature and stress components values of 300 K and 0 MPa respectively. It is verified that the temperature and the stress components converges toward the prescribed values at the end of the relaxation.

In the present and following chapters, the same coordinate system (\mathbf{e}_x , \mathbf{e}_y , \mathbf{e}_z), as presented on figures 2.1a and 2.1b, is adopted systematically for the bicrystal systems. The y coordinate denotes the distance from the grain boundary in the normal direction \mathbf{e}_y while the x and z coordinates are related to the transverse directions \mathbf{e}_x and \mathbf{e}_z in the grain boundary plane.

The box dimensions are employed such that the restriction preventing autointeractions due to periodic boundary conditions is respected : $L_x, L_y, L_z > 2r_{cut-off}$, with $r_{cut-off} = 0.5168\text{nm}$ the cut-off radius of this potential [Mishin, 2004] for pure nickel.

The size of the boxes is optimised in order to minimise the computational costs and to allow numerous computations, permitting the coverage of a large panel of sollicitations for this study. Furthermore, the different boxes possesse similar dimensions whatever the Σ ratio.

The parameters and the method employed for the formation of the modeled atomic structure of the chosen grain boundaries are now described more thoroughly.

Grain boundaries possesse nine degrees of freedom, five of which can generally be

2. MULTIAXIAL BEHAVIOUR OF FCC NICKEL BICRYSTALS AT THE ATOMIC SCALE

Σ	θ	\mathbf{n}_I	L_x (nm)	γ_{GB}^{300K} (mJ m ⁻²)	$N_{GB}^{at.}$	d_{GB}^{disl} (Å)	SU
101	11.42°	[0101]	10.61	991	28872	17.6	CD ⁷ .CD ⁷
25	16.26°	[071]	7.47	1152	14160	12.5	CDDDD
13	22.62°	[051]	8.97	1275	24960	9.0	CDD
17	28.07°	[041]	8.71	1341	19392	7.3	CD.CD
5	36.87°	[031]	7.79	1339	15568	5.5	C
29	43.60°	[052]	7.58	1443	14656	4.0 (5.5) †	BC.BC
29	46.40°	[073]	8.04	1478	16560	4.0 (5.5) †	BBC
5	53.13°	[0 $\bar{1}$ 2]	7.87	1357	16000	3.84	B.B
17	61.93°	[053]	8.21	1283	17216	4.93	ABB
25	73.74°	[043]	8.80	979	19760	8.7	AAB.AAB
41	77.32°	[054]	9.01	880	20704	11.1	AAAB.AAAB
61	79.61°	[065]	8.25	765	17328	13.8	A ⁴ B.A ⁴ B
85	81.20°	[076]	9.74	711	24240	16.1	A ⁵ B.A ⁵ B

Table 2.2: MD initial configurations of the thirteen CSL symmetric [100] tilt grain boundaries. With $L_y = 2L_x$, $L_z = 1.48$ nm and $\phi_G = \frac{L_y}{2} - d_0$. The distance between the minority units (or the predominant unit for favoured grain boundaries) is denoted d_{GB}^{disl} , † for the $\Sigma 29$ GBs, the first and second distance are obtained between the B->B and C->B units respectively

obtained by experiment [Priester, 2006] from the knowledge of the rotation between the two grains (described by the rotation angle θ and the related unit vector \mathbf{e}_θ along the rotation axis) and the orientation of the grain boundary plane through the unit normal vector \mathbf{n}_I (or \mathbf{n}_{II}) in the referential of the upper grain (I) (or lower grain (II)). Those macroscopic parameters constitute inputs for the atomic models used for the simulation. In the case of symmetric tilt grain boundaries, only two macroscopic degrees of freedom are necessary, however, for clarifications, all grain boundaries parameters are referenced in table 2.2.

The four remaining degrees of freedom are subsequently obtained, using energy minimisations via the conjugate gradient algorithm. At first, the atomic plane of the grain boundary is determined by selecting the least-energy configuration after iterative atomic layer deletions in the \mathbf{e}_y direction and systematic energy minimisation with atomic relaxation in the same direction perpendicular to the grain boundary plane.

The γ -surface method [Vitek, 1968, Mishin and Farkas, 1998] is then employed for the determination of the least-energy configuration according to the in-GB plane displacements in the \mathbf{e}_x and \mathbf{e}_z directions of one grain over the other within the CNID lattice.

(a) Atomic structure and cell of the CSL GB

(b) Periodic box used for MD computations

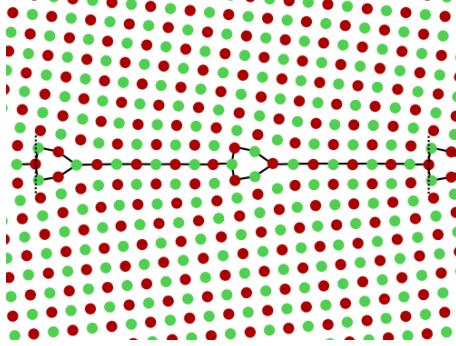
2.2.2 Atomic structure, mechanical description and energy of the grain boundaries

The atomic structures of the grain boundaries are presented figure 2.1 along with their decomposition in structural unit patterns. The structural unit (SU) model [Sutton et al., 1995] is applicable here with the four elementary units A, B, C and D, displayed figure 2.1n. The obtained structures are validated by the literature [Sutton et al., 1995, Cahn et al., 2006, Tschopp et al., 2008].

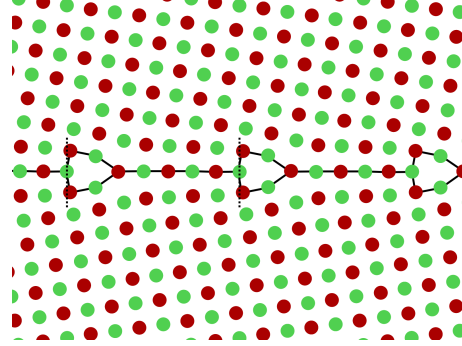
Due to their periodicity in the $[100]$ direction, the grain boundaries can be described by only two atomic planes indicated by the red and green colors for the $[100]$ and for the $[200]$ crystallographic planes respectively. Indeed, it is reminded here that, despite the 2D projections of figures 2.1, the atomic description of the grain boundaries spans over the two preceding planes.

38

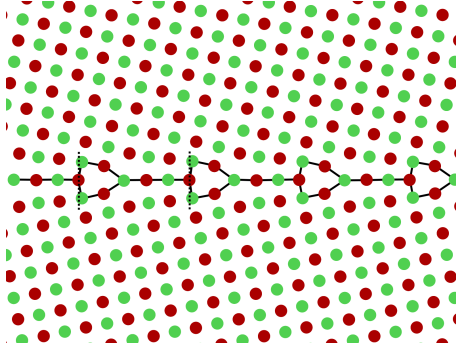
2. MULTIAXIAL BEHAVIOUR OF FCC NICKEL BICRYSTALS AT THE ATOMIC SCALE



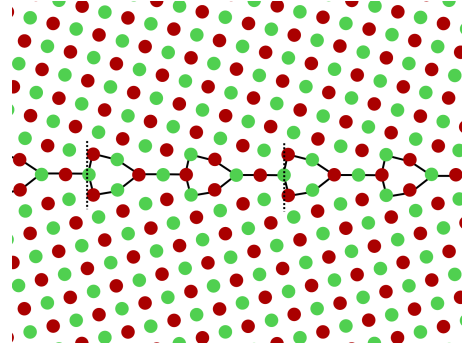
(a) $\Sigma 101$ $[0101]$ $\theta = 11.42^\circ$ $|CD^7.CD^7|$



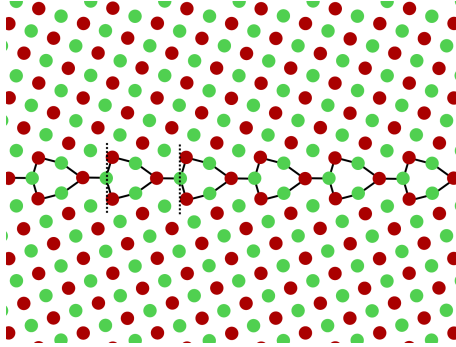
(b) $\Sigma 25$ $[071]$ $\theta = 16.26^\circ$ $|CDDDD|$



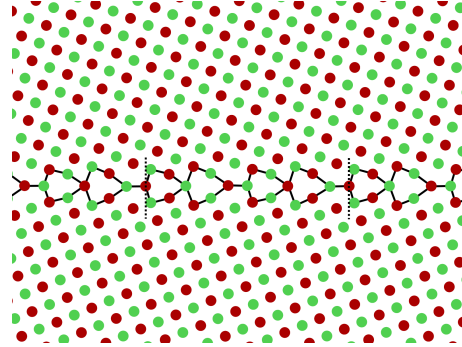
(c) $\Sigma 13$ $[051]$ $\theta = 22.62^\circ$ $|CDD|$



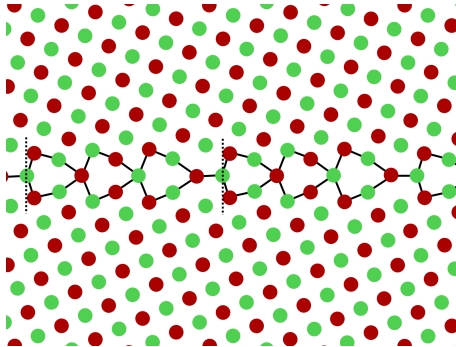
(d) $\Sigma 17$ $[041]$ $\theta = 28.07^\circ$ $|CD.CD|$



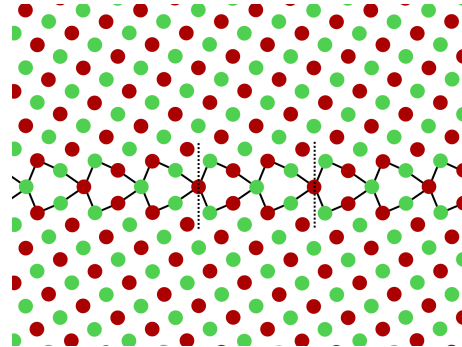
(e) $\Sigma 5$ $[031]$ $\theta = 36.87^\circ$ $|C|$



(f) $\Sigma 29$ $[052]$ $\theta = 43.60^\circ$ $|BC.BC|$



(g) $\Sigma 29$ $[073]$ $\theta = 46.40^\circ$ $|BBC|$



(h) $\Sigma 5$ $[0\bar{1}2]$ $\theta = 53.13^\circ$ $|B.B|$

2. MULTIAXIAL BEHAVIOUR OF FCC NICKEL BICRYSTALS AT THE ATOMIC SCALE

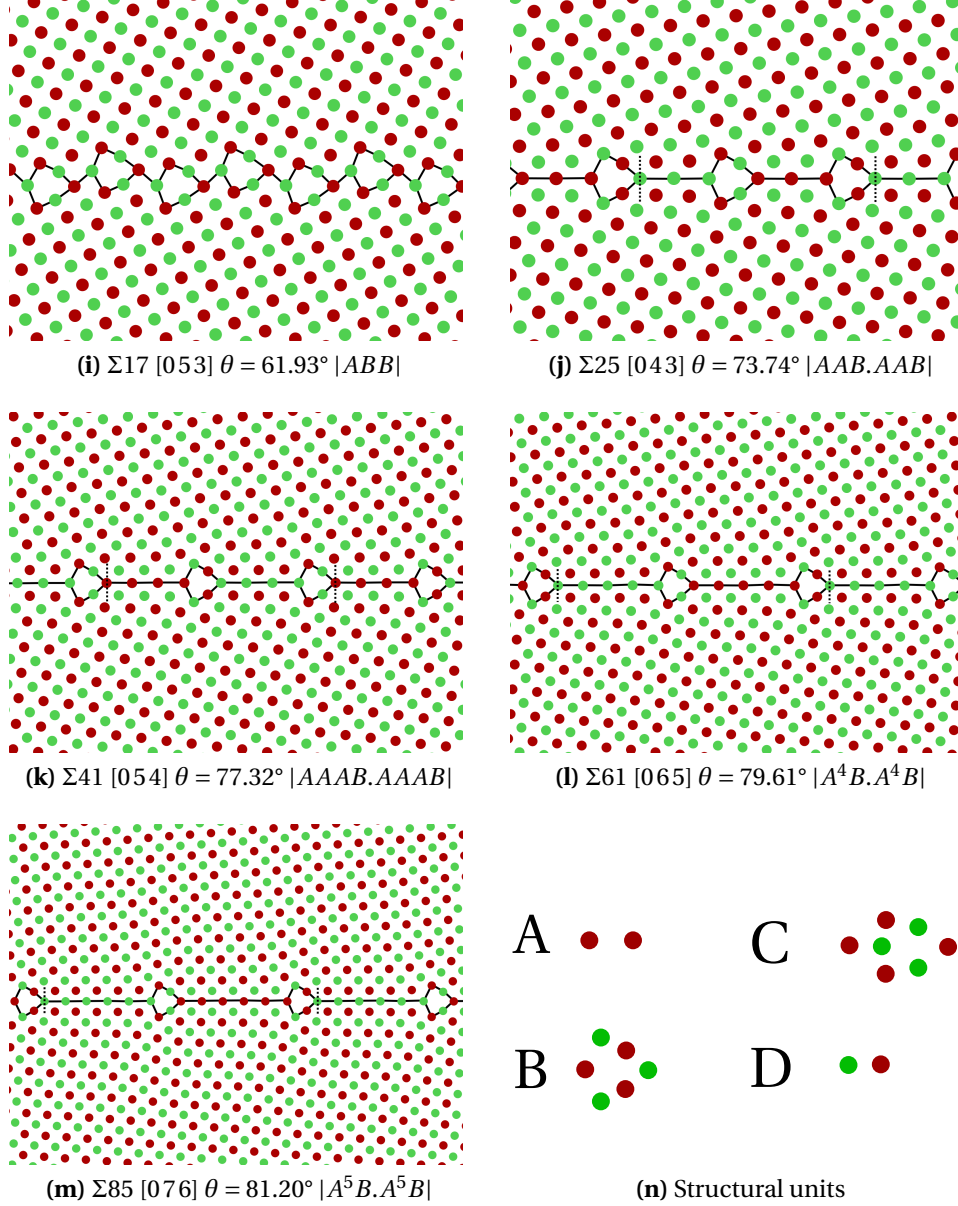


Figure 2.1: Atomic structure of the 13 CSL grain boundaries and identification of the structural unit patterns. ● indicates the [100] plane and ● indicates the [200] plane. The vertical bar indicates the repetition of the pattern and the dot a reversal of the elementary unit between the two planes.

2. MULTIAXIAL BEHAVIOUR OF FCC NICKEL BICRYSTALS AT THE ATOMIC SCALE

parison of their mechanical behaviour may ease possible correlations. The two other favored grain boundaries related to the A and D units corresponds to the $\Sigma 1$ [011] ($\theta = 90^\circ$) and $\Sigma 1$ [010] ($\theta = 0^\circ$) single crystals and are not considered here.

As explained more extensively in [Sutton et al., 1995, Priester, 2006] a hierarchical description of the atomic structure of the grain boundaries is therefore recovered here. The very first level of this description can be illustrated by the unit C which can be described as follow: $C = BD$.

2.2.2.2 Mechanical description with the structural unit/grain boundary dislocation model

In conjunction with the preceding atomic description, a characterisation of the grain boundaries through a mechanical description focusing on the local stress fields is considered.

It is known that grain boundaries are the location of intrinsic stress concentrations as a result of the necessary accommodations between the two grain lattices. Atomic stress fields of several grain boundaries are plotted in figure 2.2 and provide an illustration of such accommodations with subgrain boundaries localised at the isolated structural units (for the $\Sigma 101$ and $\Sigma 85$ GBs) between the regions of good lattice matching.

The structural unit/grain boundary dislocation (SU/GBD) model [Sutton et al., 1983] stipulates that for GBs with a large SU period, composed of isolated units (say C for the exemple of the $\Sigma 101$) embedded among a sequence of predominant units (say D with the same exemple), secondary intrinsic GB dislocation cores can be assimilated to the minority units along the interface. Those dislocations possesse a Burgers vector that can be decomposed with the DSC lattice primitive vectors related to the favoured grain boundary of the predominant unit.

Figure 2.2 shows the exemple of the $\Sigma 101$ [0101] grain boundary obtained after the first MS relaxation at 0 K (top pictures) and composed of a C unit embedded in an array of seven D units.

An intrinsic dislocation with a Burgers vector of $\mathbf{b}_0 = \frac{a_0}{\sqrt{101}} [0\bar{1}0\bar{1}]$ (in the upper grain referential) is identified through a Frank circuit (via the DXA of OVITO) and can be clearly correlated to the C unit as illustrated in figure 2.2. The Burgers vector indeed corresponds to the unit vector $-\mathbf{b}_{\text{DSC}} = a_0[0\bar{1}0]$ of the $\Sigma 1$ [010] DSC lattice in the original referential.

The related stress field is illustrated with the $\sigma_{yy}^{\text{at.}}$ atomic stress component as derived from LAMMPS and could be approximated by the classical array of edge dislocations (seperated from each other with a distance d_{GB}) stress field as derived by Hirth and Lothe within the isotropic linear elasticity framework [Hirth and Lothe, 1982]:

$$\sigma_{yy}^{\text{edge}} = \frac{2\pi\mu b_0 y}{(1-\nu)(d_{\text{GB}}^{\text{disl}})^2} \exp\left(\frac{-2\pi y}{d_{\text{GB}}^{\text{disl}}}\right) \sin\left(\frac{2\pi x}{d_{\text{GB}}^{\text{disl}}}\right) \quad (2.1)$$

2. MULTIAXIAL BEHAVIOUR OF FCC NICKEL BICRYSTALS AT THE ATOMIC SCALE

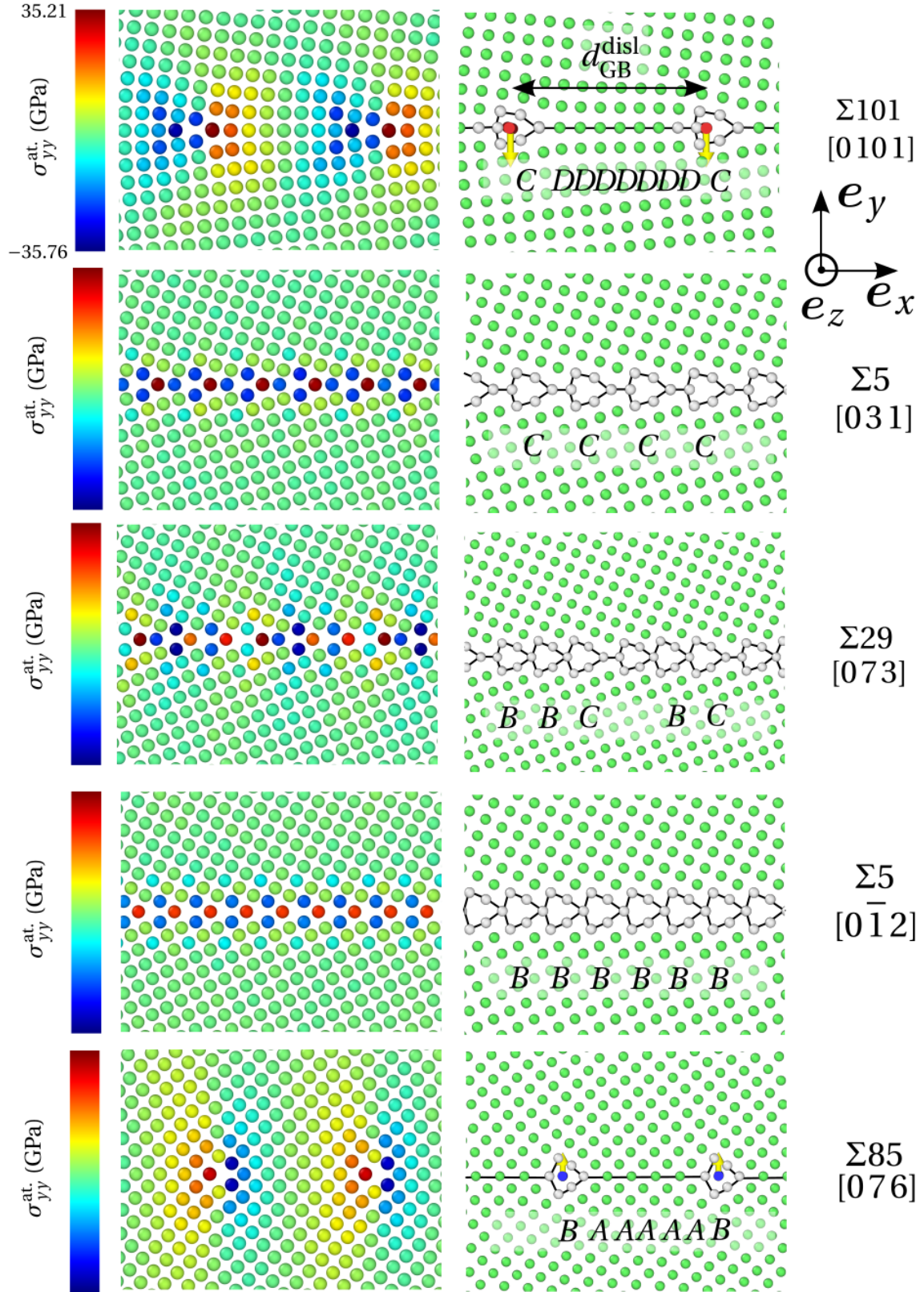


Figure 2.2: Mechanical descriptions of the $\Sigma 101$ [0101], $\Sigma 5$ [031], $\Sigma 29$ [073], $\Sigma 5$ [01̄12], $\Sigma 85$ [076]

2. MULTIAXIAL BEHAVIOUR OF FCC NICKEL BICRYSTALS AT THE ATOMIC SCALE

$$\tau_{xy}^{\text{edge}} = \frac{2\pi\mu b_0 y}{(1-\nu)(d_{\text{GB}}^{\text{disl}})^2} \exp\left(\frac{-2\pi y}{d_{\text{GB}}^{\text{disl}}}\right) \cos\left(\frac{2\pi x}{d_{\text{GB}}^{\text{disl}}}\right) \quad (2.2)$$

with b_0 the amplitude of the Burgers vector (here equal to $a_0 = 3.52 \text{ \AA}$), μ the isotropic shear modulus, ν the Poisson coefficient, and $d_{\text{GB}}^{\text{disl}}$ the distance between the dislocations along the interface as presented on the $\Sigma 101$ GB top right figure 2.2.

The same verification is carried out for the $\Sigma 85$ $[076]$ GB, featuring a Burgers vector of $\frac{a}{\sqrt{2}\sqrt{85}}[076]$ in the upper grain referential (or $\frac{a}{2}[011]$ in the initial referential of $\Sigma 1$ $[011]$).

The same dislocation cores are identified for the $\Sigma 25$, $\Sigma 13$, $\Sigma 17$ GBs on one hand with a Burgers vector of $a[0\bar{1}0]$ and for the $\Sigma 17$, $\Sigma 41$, $\Sigma 61$ on the other hand with a Burgers vector of $\frac{a}{2}[011]$. For those grain boundaries, the distance $d_{\text{GB}}^{\text{disl}}$ (as referenced in table 2.2) between the minority units (or the associated secondary dislocations) are significant enough to enable the identification. The following geometrical relation is verified furthermore for these grain boundaries:

$$d_{\text{GB}}^{\text{disl}} = \frac{b_0}{2 \sin\left(\frac{\Delta\theta}{2}\right)} \quad (2.3)$$

with $\Delta\theta$ the difference of angle between the grain boundary considered and the favoured grain boundary related to the predominant unit (i.e. the A or D units corresponding to the $\Sigma 1$ $[011]$ or $\Sigma 1$ $[010]$ grain boundaries respectively).

From the evolution of the stress field according to the rotation angle θ as depicted in figure 2.2 with the same color scale for all the grain boundaries, it is expected that the preceding mechanical description will not stand as the distance between the dislocations cores shrinks. However, as advanced in the literature [Priester, 2006], it is clear that the atomic structure still induces local stresses inherent to the GB geometry, even though their description are not accessible otherwise than by simulation.

2.2.2.3 Grain boundary energies

The grain boundary energies obtained from the previous calculations of GB formations at 300 K are listed in table 2.2 and plotted in figure 2.3 according to the rotation angle θ .

Those computed values result from a simple energetic balance deducting the mean potential energy of the grains from the potential energy of a slab containing one of the grain boundaries after full relaxation of the system and using averaged energies over 10 ps in the NPT ensemble, as expressed by equation (2.4). Care is taken to select the boundaries of the slab far enough from the GB plane such that the extent of the GB excess energy (that will be presented later on in chapter 4 for the $\Sigma 5$ $[0\bar{1}2]$) is encompassed in the slab for each chosen grain boundary.

$$\gamma_{\text{GB}}^{300\text{K}} = \frac{\langle E_{\text{slab,GB}}^{\text{p}} \rangle_{\tau}^{\text{NPT}} - N_{\text{slab,GB}}^{\text{at.}} \langle \bar{E}_{\text{bulk}}^{\text{p, at.}} \rangle_{\tau}^{\text{NPT}}}{A} \quad (2.4)$$

2. MULTIAXIAL BEHAVIOUR OF FCC NICKEL BICRYSTALS AT THE ATOMIC SCALE

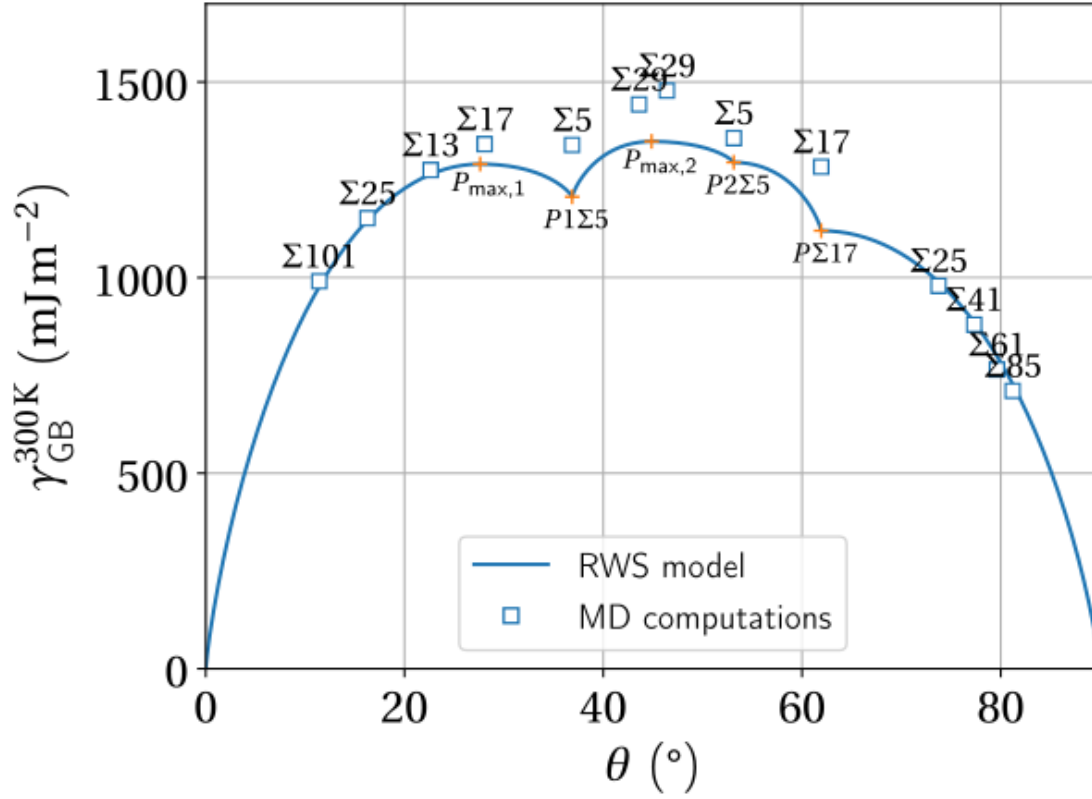


Figure 2.3: Energies of the thirteen CSL symmetric tilt $[100]$ grain boundaries according to their misorientation angle and Read-Shockley-Wolf extended model of grain boundary energy, fitted by [Bulatov et al., 2014]

with A the grain boundary plane surface, $E_{\text{slab,GB}}^{\text{p}}$ the potential energy of the slab containing one of the grain boundaries, $N_{\text{slab,GB}}^{\text{at}}$ the number of atoms contained in the slab $\bar{E}_{\text{bulk}}^{\text{p, at}}$ the mean value of the atomic potential energy of a pack of atoms situated far away from the grain boundaries area and $\tau = 10$ ps.

The computed grain boundary energies present the same variations as numerous comparable studies of $\langle 100 \rangle$ symmetrical tilt grain boundaries in FCC metals [Gertsman et al., 1989, Wolf, 1990, Bulatov et al., 2014] which partly validates the GB atomic configurations obtained with this potential.

The classical extended formula of Read-Schockley-Wolf (RWS) [Read and Shockley, 1950, Wolf, 1989] in the case of $\langle 100 \rangle$ tilt grain boundaries in FCC metal is also plotted on figure 2.3:

$$\gamma_{\text{GB}}^{\text{tot}}(\theta) = \begin{cases} \gamma_{\text{GB}}^{+,i}(\theta) & \forall \theta \in [\theta^{i-1}, \theta^i] \text{ if } \tilde{\gamma}^i > \tilde{\gamma}^{i-1} \\ \gamma_{\text{GB}}^{-,i}(\theta) & \forall \theta \in [\theta^{i-1}, \theta^i] \text{ if } \tilde{\gamma}^i < \tilde{\gamma}^{i-1} \end{cases} \quad (2.5)$$

2. MULTIAXIAL BEHAVIOUR OF FCC NICKEL BICRYSTALS AT THE ATOMIC SCALE

$$\begin{aligned}\gamma_{GB}^{+,i}(\theta) &= \gamma_{\text{RGB}} \left[\tilde{\gamma}^{i-1} + (\tilde{\gamma}^i - \tilde{\gamma}^{i-1}) f_{\text{RSW}}(\xi^+) \right] & \xi^+ &= \frac{\theta - \theta^{i-1}}{\theta^i - \theta^{i-1}} \\ \gamma_{GB}^{-,i}(\theta) &= \gamma_{\text{RGB}} \left[\tilde{\gamma}^i + (\tilde{\gamma}^{i-1} - \tilde{\gamma}^i) f_{\text{RSW}}(\xi^-) \right] & \xi^- &= \frac{\theta^i - \theta}{\theta^i - \theta^{i-1}} \\ f_{\text{RSW}}(\xi) &= \sin\left(\frac{\pi}{2}\xi\right) \left(1 - a \log\left(\sin\left(\frac{\pi}{2}\xi\right)\right)\right)\end{aligned}$$

with $\gamma_{\text{RGB}} = 1445 \text{ mJ m}^{-2}$ the surface energy of a hypothetical random grain boundary [Bulatov et al., 2014], $a = 0.5$ and $\gamma_{GB}^{+,i}(\theta)$ or $\gamma_{GB}^{-,i}(\theta)$ the branches of the total function γ_{GB}^{tot} defined between the interpolation points referenced in table 2.3. The same values derived by Bulatov et al. [Bulatov et al., 2014] for pure nickel and referenced in table 2.3 are employed in our case. Those parameters are coming from a fitting procedure based on numerous GB energy data of Olmsted et al. [Olmsted et al., 2009] for pure nickel using an other EAM potential and therefore permit by comparison a validation of the grain boundary configurations formed with the potential of Mishin for pure nickel [Mishin, 2004].

Even if a satisfying agreement is found for the low angle grain boundaries, a slight discrepancy is evidenced between 30° and 60° . The reasons for these discrepancies may be linked to the relaxation procedure employed and the potential used.

Coordinates	$P_{\text{max},1}$	P1Σ5	$P_{\text{max},2}$	P2Σ5	PΣ17
θ^i (°)	27.62	36.87	44.86	53.13	61.93
$\tilde{\gamma}^i$	0.893	0.835	0.933	0.896	0.775

Table 2.3: Interpolation points for the use of the RWS extended model [Bulatov et al., 2014]

2.2.3 Uniaxial tensile loadings

From the initial configurations of the Σ5 $[0\bar{1}2]$ grain boundary previously obtained, two types of loading are primarily attempted. In both cases, an uniaxial tensile loading is applied in the direction perpendicular to the grain boundary plane.

For the following simulations, when strain components are assessed or imposed, they correspond to the components of the engineering strain tensor ϵ of the box which is deduced from the box lengths and tilt angles. The global stress tensor σ of the box is computed with the virial stress and the kinetic energy contribution:

$$\sigma_{ij} = \frac{1}{V} \left(\frac{1}{2} \sum_k^N \sum_{l \neq k}^{N-1} r_i^{kl} f_j^{kl} + \sum_k^N m^k v_i^k v_j^k \right) \quad (2.6)$$

with V the volume of the box containing the N atoms. For each atom k , m^k and v_i^k represent respectively the mass of the atom and the i th component of the velocity vector

2. MULTIAXIAL BEHAVIOUR OF FCC NICKEL BICRYSTALS AT THE ATOMIC SCALE

\mathbf{v}^k . For the virial contribution, r_i^{kl} represents the i th component of the interatomic distance vector $\mathbf{r}^{kl} = \mathbf{r}^l - \mathbf{r}^k$ and f_j^{kl} , the j th component of the force \mathbf{f}^{kl} acting on atom k due to its interaction with atom l .

An uniaxial stress loading is primarily, carried out. A deformation of the box along the y axis (perpendicular to the grain boundary plane) is imposed with a strain rate $\dot{\epsilon} = 1.0 \times 10^8 \text{ s}^{-1}$, a temperature of 300 K and a timestep $\Delta t = 1 \text{ fs}$. The σ_{yy} stress component is let free while the other components of the stress tensor are set to 0 GPa. Every stress components are computed during the simulations from equations 2.6.

Here, it is obvious that thermodynamically speaking, the sollicitation induces a non equilibrium state ; and from the limited computation time that is affordable in MD simulations, it also obvious that the strain rates employed are several orders of magnitude higher than mechanical sollicitations typically imposed at higher scales. The influence of the strain rate shall be assessed later on.

At the n^{th} step of the simulation, the stress and strain components are theoretically imposed as follow (using matrix notations) with a relaxation in the isobaric-isothermic ensemble (NPT) at 300 K:

$$[\boldsymbol{\epsilon}] = \begin{bmatrix} \epsilon_{xx} & \gamma_{xy} & \gamma_{xz} \\ - & n\dot{\epsilon}\Delta t & \gamma_{yz} \\ - & - & \epsilon_{zz} \end{bmatrix} \quad [\boldsymbol{\sigma}] = \begin{bmatrix} 0 & 0 & 0 \\ - & \sigma_{yy} & 0 \\ - & - & 0 \end{bmatrix}$$

It is reminded here that the controled stress components are not strictly equal to zero but fluctuates around the prescribed values. Here, it is indeed verified that all the stress components except the tensile stress σ_{yy} are indeed negligible and fluctuate with a very weak amplitude during the tensile loading. The non-diagonal strain components are also verified to be negligible and negative values of the transverse strain components ϵ_{xx} and ϵ_{zz} are logically found, as induced by the Poisson effect.

Although widely used in atomistic studies imposing mechanical loadings through MD or ab initio calculations [Spearot et al., 2007b, Borovikov et al., 2017, Singh et al., 2019, Barbé et al., 2018, Janisch et al., 2010], this type of sollicitation does not necessarily agree with all the stress state that could be expected, particularly at grain boundaries in polycrystals.

It is believed that the mechanical behaviour of nanowires with or without grain boundaries [Cao et al., 2008, Weinberger and Cai, 2012], featuring such free surfaces, should differ from what is expected here for bicrystals with periodic boundaries.

An uniaxial strain loading is also carried out on the same $\Sigma 5$ grain boundary. For this second tensile test, the same initial configuration is used and the same axial deformation of the box is imposed. As opposed to the previous loading, every components of the strain tensor are now imposed to zero except the tensile strain component ϵ_{yy} . The stress tensor is computed every 0.1 ps. The stress and strain components are thus imposed as follow with a relaxation in the canonical ensemble (NVT) at 300 K:

2. MULTIAXIAL BEHAVIOUR OF FCC NICKEL BICRYSTALS AT THE ATOMIC SCALE

$$[\epsilon] = \begin{bmatrix} 0 & 0 & 0 \\ - & n\dot{\epsilon}\Delta t & 0 \\ - & - & 0 \end{bmatrix} \quad [\sigma] = \begin{bmatrix} \sigma_{xx} & \tau_{xy} & \tau_{xz} \\ - & \sigma_{yy} & \tau_{yz} \\ - & - & \sigma_{zz} \end{bmatrix}$$

Once again it is verified that τ_{xy} , τ_{xz} and τ_{yz} are negligible. As expected the transverse stress components are positive since the Poisson effect is now fully restrained. Indeed, a constant grain boundary section is imposed during the tensile loading, therefore inducing, with the chosen periodic boundaries and the tensile sollicitation, an increase of the transverse components of the atomic forces and interatomic distances contributing to the corresponding transverse stress components (as illustrated by equations (2.6)).

The tensile curves $\sigma_{yy} - \epsilon_{yy}$ of these two uniaxial loadings are plotted figure 2.6a and described in the next section.

Interestingly, those first results indicate a very different behaviour as the nucleation of a partial nucleation is observed for the uniaxial tensile stress which contrast with the grain boundary decohesion featuring very limited plasticity in the case of the uniaxial tensile strain. Those preliminary results shall be presented more thoroughly later.

It is expected of those simple loadings not be sufficient to provide realistic stress and strain states, as typically experienced by grain boundaries in bicrystals or polycrystals. The influence of the stress state has to be considered if a better understanding of the mechanical behaviour of those interfaces (or their related single crystal counterparts) is to be achieved, as underlined by the work of Pokluda et al. [Pokluda et al., 2015] and Cerny et al. [Černý et al., 2016, Černý et al., 2019, Černý and Pokluda, 2007, Černý et al., 2010] on ab initio computations on single crystals and bicrystals,

The mechanical behaviour of the selected grain boundaries are now fully investigated using multiaxial tensile loadings. This choice is further motivated by the fact that the stress or strain states at the impact of slip bands inducing stress concentrations are obviously not expected to be uniaxial.

2.2.4 Multiaxial tensile loadings

2.2.4.1 Transverse strains

In order to fully characterise the behaviour of the $\Sigma 5$ $[0\bar{1}2]$ CSL grain boundary, various strain states are now imposed through the use of additional transverse deformations ϵ_{xx} and ϵ_{zz} during the tensile loadings at 300 K.

It is expected here to get access to the transition between the two critical behaviours previously evidenced. As will be justified later on, it is believed that if the decohesion of the grain boundary is to be obtained before the nucleation of dislocations: decreasing progressively the differences between the principal stress components should permit to postpone the onset of plasticity and vice versa.

Using periodic boundary conditions and controlling the strain tensor components between the different loadings permit to indirectly vary the principal stress components,

2. MULTIAXIAL BEHAVIOUR OF FCC NICKEL BICRYSTALS AT THE ATOMIC SCALE

and more importantly their ratios. The assumption is made here, that the coordinate system ($\mathbf{e}_x, \mathbf{e}_y, \mathbf{e}_z$) corresponds to the principal coordinate system of the stress tensor. This hypothesis should be systematically verified or approached later on by verifying systematically the negligible values of the shear stress components τ_{xy} , τ_{xz} and τ_{yz} .

Therefore, transverse strain ratios α_ε and β_ε are chosen as inputs to control the strain state as follow (through the use of the NVT ensemble at 300 K):

$$[\boldsymbol{\varepsilon}] = \begin{bmatrix} \alpha_\varepsilon \varepsilon_{yy} & 0 & 0 \\ - & n \dot{\varepsilon} \Delta t & 0 \\ - & - & \beta_\varepsilon \varepsilon_{yy} \end{bmatrix} \quad [\boldsymbol{\sigma}] = \begin{bmatrix} \sigma_{xx} & \tau_{xy} & \tau_{xz} \\ - & \sigma_{yy} & \tau_{yz} \\ - & - & \sigma_{zz} \end{bmatrix}$$

Controlling the strain state is chosen for convenient reasons since it only requires to intervene on the MD box dimensions. Deformed boxes are schematically represented at an arbitrary time step on figure 2.4 for positive or negative α_ε and β_ε strain ratios in order to illustrate the solicitations to be imposed. A positive or negative transverse ratio would then correspond to an extension or a reduction of the grain boundary section in the corresponding transverse direction during the loading. Mixed positive and negative ratios are also attempted as a strong anisotropy is expected for FCC nickel with a Zener ratio of about 2.81, assessed with this potential at 300 K (see table 2.1).

Adopting this method should allow the exploration of a large panel of probable diagonal stress state.

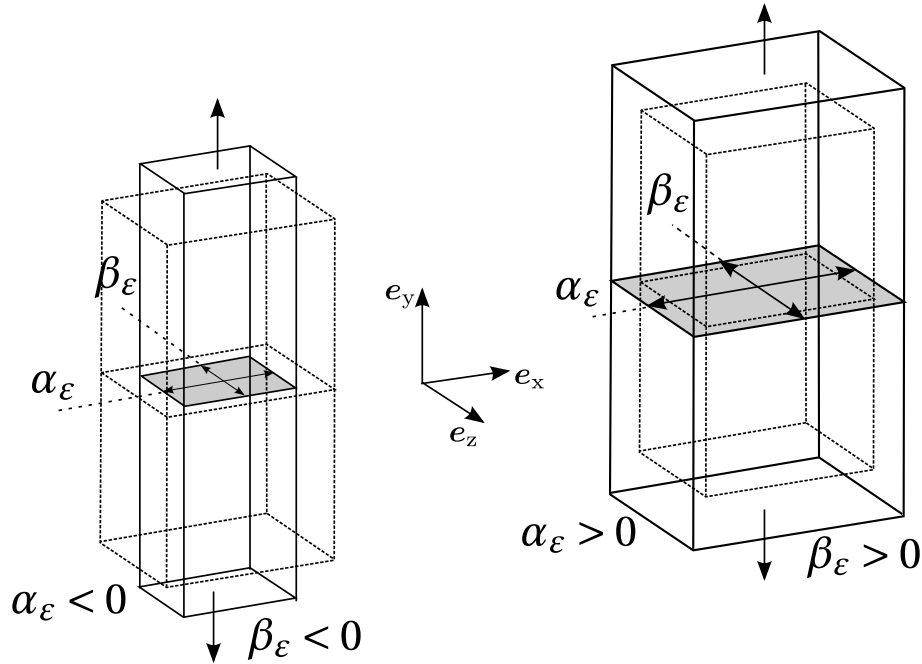


Figure 2.4: Scheme of a deformed box (plain lines) in the case of negative (left) and positive (right) $\alpha_\varepsilon, \beta_\varepsilon$ ratios. The initial undeformed box is represented in dotted lines.

For the $\Sigma 5$ $[0\bar{1}2]$ grain boundary, the strain ratios are imposed between -0.3 and 0.3

2. MULTIAXIAL BEHAVIOUR OF FCC NICKEL BICRYSTALS AT THE ATOMIC SCALE

with a 0.05 step. Therefore, 169 different tensile loadings are systematically applied on the initial configuration permitting to cover a wide range of grain boundary behaviours. The same loadings are performed on every listed grain boundaries, however for lisibility purposes, only 13 out of the 169 loadings are presented later on. For comparison purposes, the same 13 loadings are also performed on a single crystal adopting the same orientation as the upper grain adjacent to the $\Sigma 5$ $[0\bar{1}2]$ grain boundary. Typical stress-strain curves are shown in figure 2.7a for the $\Sigma 5$ grain boundary. Non-diagonal components of the strain tensor are imposed to zero and every components of the stress tensor are computed. It is verified that non-diagonal components are once again negligible during the tensile loadings. The same strain ratio $\dot{\epsilon}$ and timestep Δt are used as before.

Supplementary loadings are performed in the case of the $\Sigma 5$ grain boundary at temperatures of 10 K, 150 K and 573 K in order to assess possible thermoactivation process. The influence of the strain rate $\dot{\epsilon}$ is also considered at the lower values of $1.0 \times 10^7 \text{ s}^{-1}$ and $1.0 \times 10^6 \text{ s}^{-1}$ for temperatures of 300 K and 573 K.

Finally, for every grain boundary among the list provided in table 2.2, the same multiaxial tensile loadings are performed at 300 K on single crystals possessing the same orientation as the upper grains for each related bycristal and using similar box dimensions. This may help to decorelate the influence of the adjacent grains behaviour.

2.2.4.2 Transverse and shear strains

Multiaxial tests are attempted by adjunction of a shear strain in the case of the $\Sigma 5$ $[0\bar{1}2]$ grain boundary. The shear strain component γ_{xy} is controlled through the η_ϵ ratio as follows (at an arbitrary step n):

$$[\epsilon] = \begin{bmatrix} \alpha_\epsilon \epsilon_{yy} & \eta_\epsilon \epsilon_{yy} & 0 \\ - & n \dot{\epsilon} \Delta t & 0 \\ - & - & \beta_\epsilon \epsilon_{yy} \end{bmatrix}$$

Illustration of a deformed MD box is also provided in figure 2.5 with a positive value of the shear/normal (S/N) strain ratio η_ϵ . The transverse strain ratios α_ϵ and β_ϵ are kept equal and vary between -0.3 and 0.3. The cases with $\alpha_\epsilon = 0$ then corresponds to a pure shear deformation of the bicrystal. The S/N strain ratio η_ϵ is varied between 0.2 and 0.8 with a 0.2 step.

The $\Sigma 5$ central grain boundary of the related bicrystal in figure 2.2h clearly reveals a asymetrical structure with respect to the \mathbf{e}_x direction (i.e. a mirror asymmetry with respect to the plane of normal direction \mathbf{e}_x). However it is logically supposed here that the direction of shear straining should not influence the behaviour of the symmetric tilt grain boundaries contained in the bicrystal. Indeed, for one of the grain boundaries (at the centre of the bicrystal for example), positive and negative values (at equal absolute values) of the η_ϵ ratio, will clearly induce symmetrically equivalent loadings. This is directly linked to the twining nature of the grain boudnary and shall obviously not be the case in the general case (asymmetrical grain boundaries for example).

2. MULTIAXIAL BEHAVIOUR OF FCC NICKEL BICRYSTALS AT THE ATOMIC SCALE

Nevertheless, one negative value of the ratio is also attempted to verified this assumption.

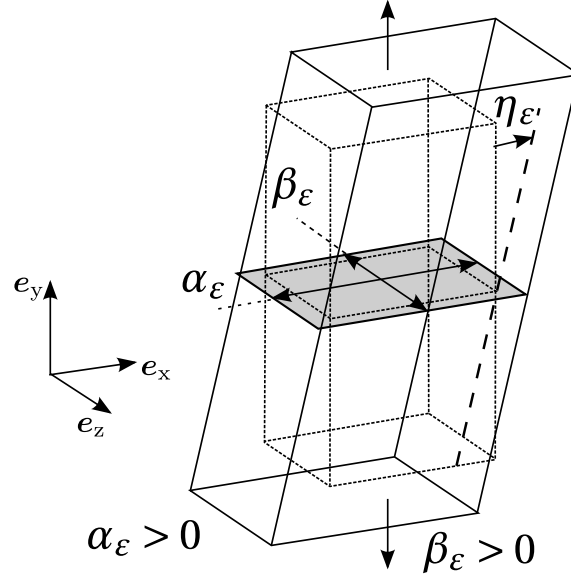


Figure 2.5: Scheme of a deformed MD box (plain lines) in the case of positive α_ϵ , β_ϵ ratios with the adjunction of shear straining through the η_ϵ ratio. The initial undeformed box is respresented in dotted lines.

2.3 From dislocation nucleation to grain boundary decohesion

2.3.1 Preliminary results

Stress-strain curves ($\sigma_{yy} - \epsilon_{yy}$) are shown figure 2.6a for the two uniaxial tensile loadings of the $\Sigma 5$ $[0\bar{1}2]$ grain boundary.

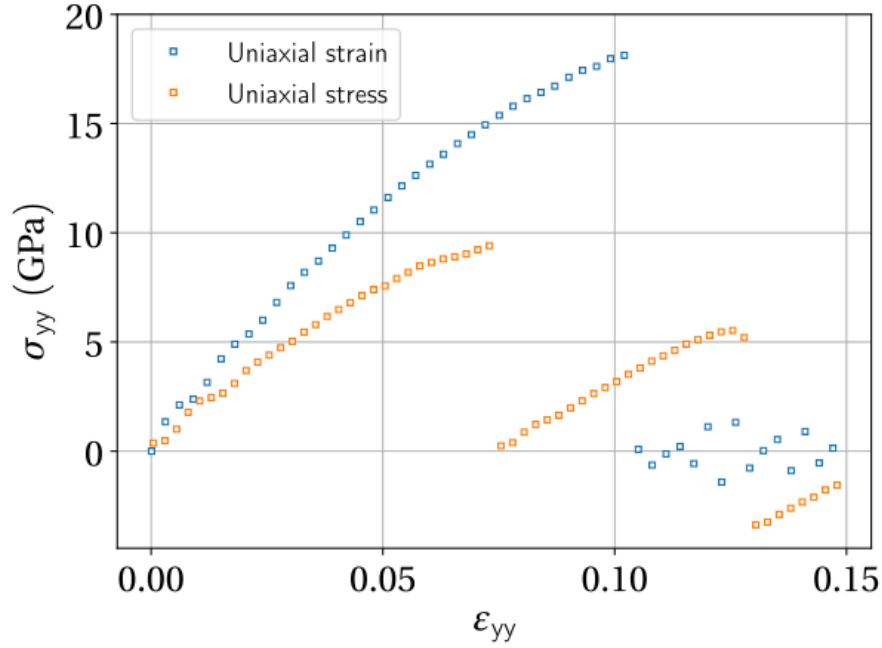
Both curves display a monotonic progressions until a maximum stress is reached ; three parts can be qualitatively identified.

A first part relating the stress and strain with a linear relation. This part represents the linear elastic behaviour at small strains of the bicrystal system involving the two grain boundaries and their adjacent grains.

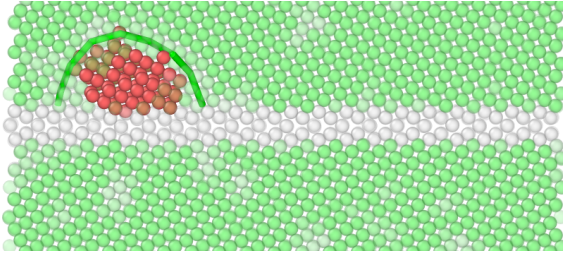
The initial slope is the lowest for the uniaxial stress tensile loading. Assuming an homogenised behaviour of the bicrystal throught a 4th order tensor C , the Hooke's law allows to express the major principal stress σ_{yy} for the uniaxial stress loading (NPT ensemble) and for the uniaxial strain loading (NVT ensemble), as follow:

$$\sigma_{yy}^{\text{NPT}} = C_{yyxx}\epsilon_{xx} + C_{yyyy}N\dot{\epsilon}\Delta t + C_{yyzz}\epsilon_{zz}$$

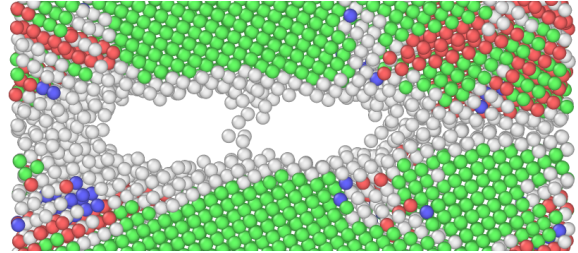
2. MULTIAXIAL BEHAVIOUR OF FCC NICKEL BICRYSTALS AT THE ATOMIC SCALE



(a)



(b) Uniaxial tensile stress



(c) Uniaxial tensile strain

Figure 2.6: Engineering stress-strain curves of the $\Sigma 5$ $[0\bar{1}2]$ grain boundary under uniaxial tensile stress state or uniaxial tensile strain state (2.6a). Dislocation nucleation from the grain boundary for an uniaxial stress state at maximum stress (2.6b) ; atom transparency is used for visibility purposes. Grain boundary decohesion for an uniaxial strain state at maximum stress (2.6c).

2. MULTIAXIAL BEHAVIOUR OF FCC NICKEL BICRYSTALS AT THE ATOMIC SCALE

$$\sigma_{yy}^{\text{NVT}} = C_{yyyy} N \dot{\epsilon} \Delta t$$

where it is verified that the apparent elasticity coefficients C_{yyyy} , C_{yyxx} and C_{yyzz} are all positives. Since it is expected that the transverse deformations ϵ_{xx} and ϵ_{zz} display negative values for the uniaxial tensile stress loading (the Poisson effect is enabled in that case), one should logically expects a lower principal stress value for the same tensile deformation ϵ_{yy} applied in the case of the uniaxial tensile strain loading.

A second part of the curve features a non-linear evolution. In order to clarify the nature of this evolution, charge and discharge loadings with a direction switch at deformation magnitudes located in the range of this non-linear area of the curves have been carried out. As expected, no residual strain or stress is recorded at rest after discharge, indicating that this non-linearity is not related to an irreversible phenomenon.

This evolution is clearly related to the the departure from the small deformation hypothesis. Here, it could be roughly explained considering the interatomic interactions modeled in those simulations using a semi-empirical potential. Indeed, it is understandable that from the simplified example of two atoms interacting with one another, the departure from a parabolically-shaped potential well would induce a non-linear relation between the interaction force and the interatomic distance for a sufficient deformation. It is reminded here that the force field \mathbf{f} is directly deduced from the space gradient of the total potential energy:

$$\mathbf{f} = -\nabla E_{\text{tot}}^p$$

The case presented herein is obviously more complexe as a lattice specifically oriented and involving around 15000 atoms is considered for the system of interest. However it is clear that this simple explanation also holds in that case. Further formal description of this non-linear elasticity could be of interest but is not in the scope here.

Finally, a sudden stress relaxation characterised by a clear drop constitutes the final part of the curves. The maximum stresses before the drops are, as previously described, in direct correlation with a critical phenomenon for both loadings. We will therefore refer to it as the critical stress σ_{yy}^c throughout the rest of the document.

As shown in figure 2.6b, in the case of the uniaxial stress loading the maximum stress and its later drop corresponds to the nucleation of a $\langle 112 \rangle$ Schokley partial dislocation from the grain boundary clearly identified here by the DXA algorithm. The related stacking fault is outlined by the two atomic planes in the hexagonal close-packed configuration as observed in red on figure 2.6b.

A subsequent stress increase followed by another drop indicates that further deformation is accomodated by the nucleation of a second dislocation from the grain boundary. However, due to the small grain sizes and the periodic boundary conditions, this part of the curve is not physically representative of the grain boundary behaviour since at this stage, emitted dislocations already interact with the neighbouring grain boundary and/or with each other. It is chosen, in the following sections, to focus on the first critical phenomenon occuring at the first maximum stress. The occurrence of the

2. MULTIAXIAL BEHAVIOUR OF FCC NICKEL BICRYSTALS AT THE ATOMIC SCALE

first dislocation nucleation from the grain boundary or the GB decohesion is reasonably supposed to be independant of the simulation box dimensions ; further validation will be provided on this particular point later on.

In the case of the uniaxial strain loading, the relaxation drop corresponds to a local decohesion of the grain boundary as shown in figure 2.6c. The newly formed crack then propagates further on few time steps with some induced plasticity at its tips. After decohesion, stress oscillations are reported. They are linked to the elastic discharge of the two grains acting like springs and dissipating their accumulated energy stored during the applied loading.

It is interesting to notice the difference of behaviour between the two types of loading as the propensity to dislocation nucleation from the grain boundary or its decohesion seems to be correlated to a difference of critical stress with values of 9.3 GPa and 18.2 GPa for the uniaxial stress and the uniaxial strain loadings respectively. Since both critical events take place at the grain boundary, it is assumed that they represent an intrinsic behaviour of the interface and shall therefore be studied further.

From the above observations, it seems that the stress state has a strong influence on the mechanical behaviour of the grain boundary. Further investigation of those critical phenomena is carried out with the analysis of the results obtained from the multiaxial tensile loadings simulations. It is expected that this method should allow to explore a larger panel of stress states and may help to identify a possible transition from one behaviour to an other.

2.3.2 Influence of the multiaxiality : a behaviour transition

Tensile curves of the bicrystal comprising the two $\Sigma 5$ $[0\bar{1}2]$ grain boundaries subjected to multiaxial loadings are presented figure 2.7a for which loadings with equal T/N strain ratios ($\alpha_\varepsilon = \beta_\varepsilon$) are selected among the 169 loading curves available. In those specific cases and for lisibility purposes, only the α_ε ratio will be further mentionned when talking about both ratios.

Once again, three parts can be identified on every curves.

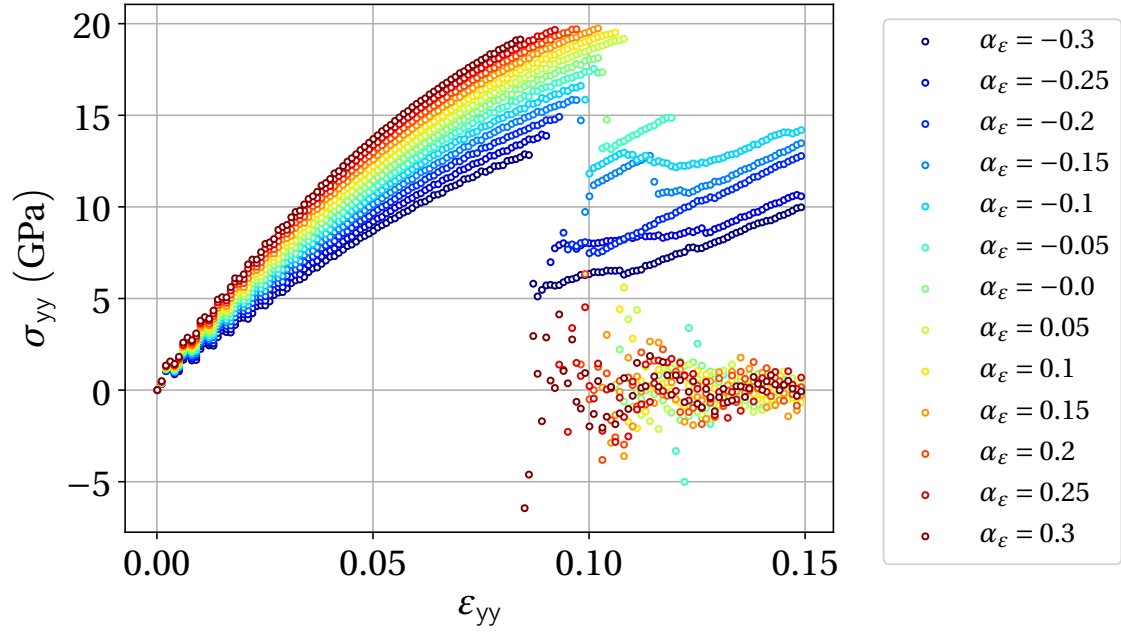
The progressive increase of the linear apparent elastic modulus with the increase of the α_ε ratios is easily understandable in the context of linear elasticity, as once again, the major principal stress component σ_{yy} can be drawn from the Hooke's law for every performed multiaxial tensile loading:

$$\sigma_{yy} = \left[\alpha_\varepsilon (C_{yyxx} + C_{yyzz}) + C_{yyyy} \right] N \dot{\varepsilon} \Delta t$$

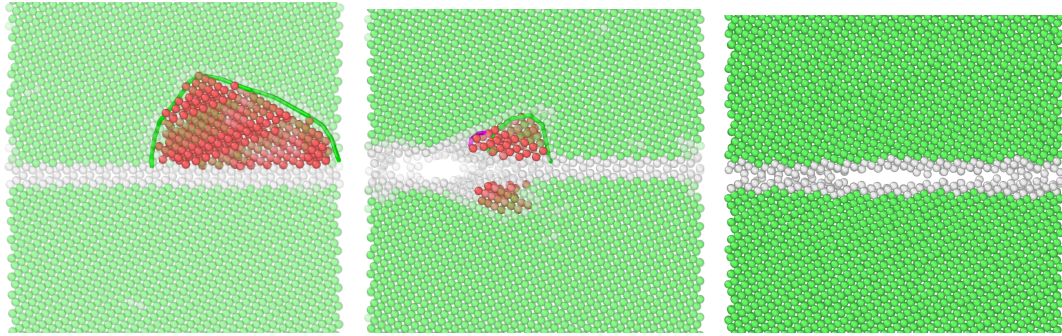
where the axial deformation component $\varepsilon_{yy} = N \dot{\varepsilon} \Delta t$ at step N is small enough to fall into the linear part of the curve. Once again, since it is verified that the elastic component C_{yyxx} and C_{yyzz} are positives, an increase of the α_ε would logically results in an increase of the apparent elastic modulus in the tensile direction.

Weak oscillations of the stress components are recorded at the beginning of the tensile loadings. They are associated with periodic elastic flexion of the bicrystal at very

2. MULTIAXIAL BEHAVIOUR OF FCC NICKEL BICRYSTALS AT THE ATOMIC SCALE



(a)



(b) $\alpha_\varepsilon = \beta_\varepsilon = -0.25$

(c) $\alpha_\varepsilon = \beta_\varepsilon = 0.05$

(d) $\alpha_\varepsilon = \beta_\varepsilon = 0.25$

Figure 2.7: σ_{yy} - ε_{yy} tensile curves of the $\Sigma 5$ $[0\bar{1}2]$ grain boundary under multiaxial strain state at $\alpha_\varepsilon = \beta_\varepsilon$ ratios varying between -0.3 and 0.3 with a 0.05 step (2.7a). Grain boundary behaviour from dislocation nucleation to decohesion for $\alpha_\varepsilon = -0.25$ (2.7b), 0.05 (2.7c) and 0.25 (2.7d). The common neighbour analysis references atoms in FCC lattice structure (in green), HCP lattice structure (in red) and in non identified lattice structure (in white) ; atom transparency is used for visibility purposes.

2. MULTIAXIAL BEHAVIOUR OF FCC NICKEL BICRYSTALS AT THE ATOMIC SCALE

low amplitude due to the initial configuration which is not fully relaxed at the prescribed temperature despite further extent of the relaxation times during the GB formation.

It is believed that those oscillations have no impact on the critical behaviour as an attenuation of this regime is clearly obtained far before the critical stress is reached (figure 2.7a).

A clear monotonic variation of the critical stress is reported. As the α_ϵ ratio varies between -0.3 and 0.3, an increase of the critical stress can be observed until the occurrence of a saturation characterised by a plateau on figure 2.7a for $\alpha_\epsilon \geq 0$.

Figures 2.7b, 2.7c and 2.7d show the atomic configurations at the critical stresses for $\alpha_\epsilon = -0.25, 0.05$ and 0.25 respectively.

It is shown here, that the occurrence of the plateau is directly correlated to the systematic decohesion of the grain boundary. Before that saturation, the critical stresses reported herein corresponds to the nucleation of a partial dislocation from the grain boundary.

Furthermore, a very clear and progressive behaviour transition is observed: from the nucleation of a dislocation at the grain boundary (figure 2.7b) to a brittle and neat decohesion of the grain boundary (figure 2.7d) without any dislocations emission at highest values of α_ϵ .

In between, a progressive restriction of the dislocation emissions is identified as the α_ϵ ratio increases. The appearance of the saturation stress is directly correlated to the nucleation of a crack characterised by blunted tips with previous emission of partial dislocations swiftly resorbed as the decohesion occurs. It is followed by a propagation of the crack with dislocations nucleated from the front tips as shown in figure 2.7c. In which cases, it is verified that subsequent dislocations are emitted by the newly formed blunted crack under a subsequent propagation regime.

As illustrated in figures 2.7c and 2.7d, a qualitative progression of the crack morphology is identified, from a rather blunted crack tip at $\alpha_\epsilon = 0$ to a very neat crack tip at higher ratios. It is interesting to note that all the decohesions at the origin of those different crack morphologies are happening at a constant critical stress of about 19.6 GPa. A decrease of the critical strain ϵ_{yy}^c is obtained when the plateau is reached as opposed to its increase when only dislocation nucleations are obtained as shown in figure 2.7a.

For the plateau where the grain boundary decohesion is systematically occurring, the decrease of the critical strain with the transverse strain ratio may be explained by the increase of the apparent elastic modulus as previously described. The constant critical stress for grain boundary decohesion will therefore be reached earlier (i.e. for a smaller critical axial deformation).

An inverse variation is obtained for the critical strain for dislocation nucleation. This variation shall be described later in chapter 3.

It is now proposed to focus on the loading cases for which $\alpha_\epsilon \neq \beta_\epsilon$. Critical stresses are systematically reported for the 169 tensile loadings in the $(\alpha_\epsilon, \beta_\epsilon)$ T/N ratios space and displayed on a color map figure 2.8a. In each cases, different markers are used to

2. MULTIAXIAL BEHAVIOUR OF FCC NICKEL BICRYSTALS AT THE ATOMIC SCALE

indicate the decohesion of the grain boundary (crosses), the dislocation nucleation occurrence at the grain boundary (circles), and the mixed behaviours featuring a dislocation nucleation prior to the decohesion (squares). A dashed line links the cases of equal transverse/normal ratios treated before.

This qualitative classification is obtained from the systematic critical configuration observations and their automatic post-treatment using the python interface of OVITO and its DXA module [OVITO,]. The classification factors are qualitatively defined as previously described for the three loadings shown on figure 2.7c at the critical stresses.

Those supplementary results confirm the plateau observed before, as a clear saturation is correlated with the decohesion of the grain boundary. Contour plots are added with a step of 0.8 GPa and seem to confirm that the border line delimiting the grain boundary decohesion area for a critical stress of about 19.2 GPa is correlated to the 2D evolution of the critical stress in the dislocation nucleation zone.

A clear anisotropy effect is observed, as an increase of the α_ϵ ratio does not necessarily induces a decohesion of the grain boundary unlike the increase of the β_ϵ ratio. This is clearly linked to the evolution of the critical stress prior to the decohesion area. It is reminded here that the \mathbf{e}_x and \mathbf{e}_z directions, related to the transverse α_ϵ and β_ϵ ratios respectively, are parallel to the crystallographic directions $[021]$ (for the upper grain and the $[02\bar{1}]$ direction for the lower grain) and $[100]$. It is reminded that the anisotropy coefficient obtained with this potential is at about 2.8 which should partly explained this behaviour.

A three dimensional representation of the critical stress in the $(\alpha_\epsilon, \beta_\epsilon)$ ratios space is also provided in figure 2.8b . It reveals that the dislocation nucleation surface could be fairly well approximated by a linear relation with the transverse ratios. This evolution seems to indicate that the critical stress for dislocations nucleation from this particular grain boundary may be linked to a rather simple relation involving the deformation components of the cristal lattice.

The critical stresses and strains for the $\Sigma 5 [01\bar{2}]$ grain boundary and the related single crystal subjected to the same $\alpha_\epsilon = \beta_\epsilon$ ratios loadings at 300 K are reported figures 2.9a and 2.9b.

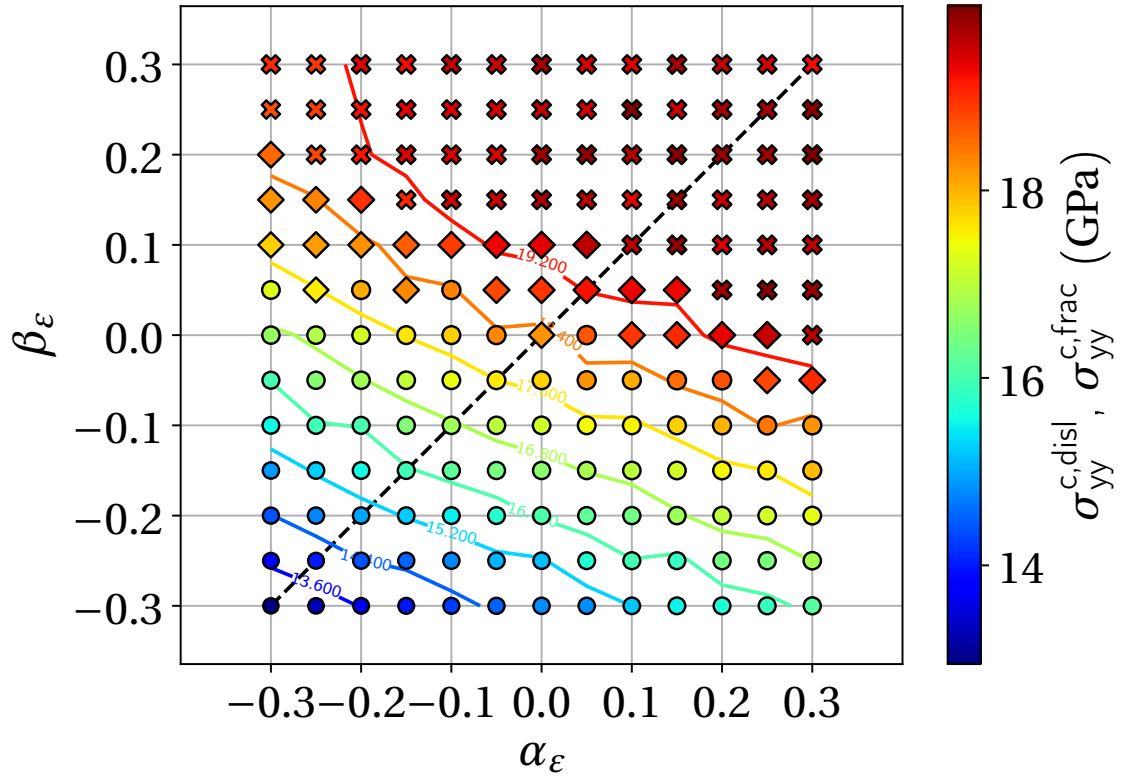
For now on, the critical events are only classified in terms of the first occuring phenomenon ; therefore crack initiations preceded by dislocation emissions are considered to be dislocation nucleation events according to the chronological order.

Those results seems to indicate that the nucleation of partial dislocations might not be influenced by the presence of the chosen grain boundary as similiar critical stresses are found (mostly for negative transverse strain ratios).

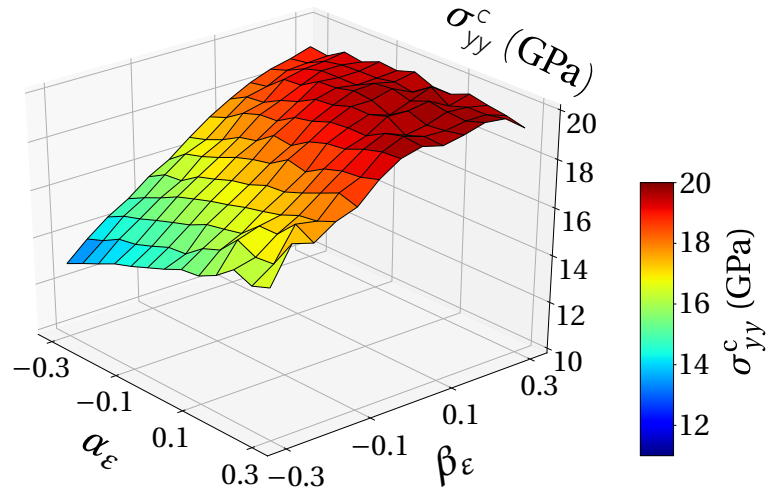
However, it is clear that in the grain boundary case, every dislocations is emitted from the interface whereas an homogeneous dislocation nucleation is reported for the single crystal. This might explain the slight discrepancies of the critical strain found on figure 2.9b for negative transverse ratios.

As the GB decohesion area is approached for larger ratios, it is interesting to note the difference between the critical stress plateau and the monotonic linear evolution of

2. MULTIAXIAL BEHAVIOUR OF FCC NICKEL BICRYSTALS AT THE ATOMIC SCALE



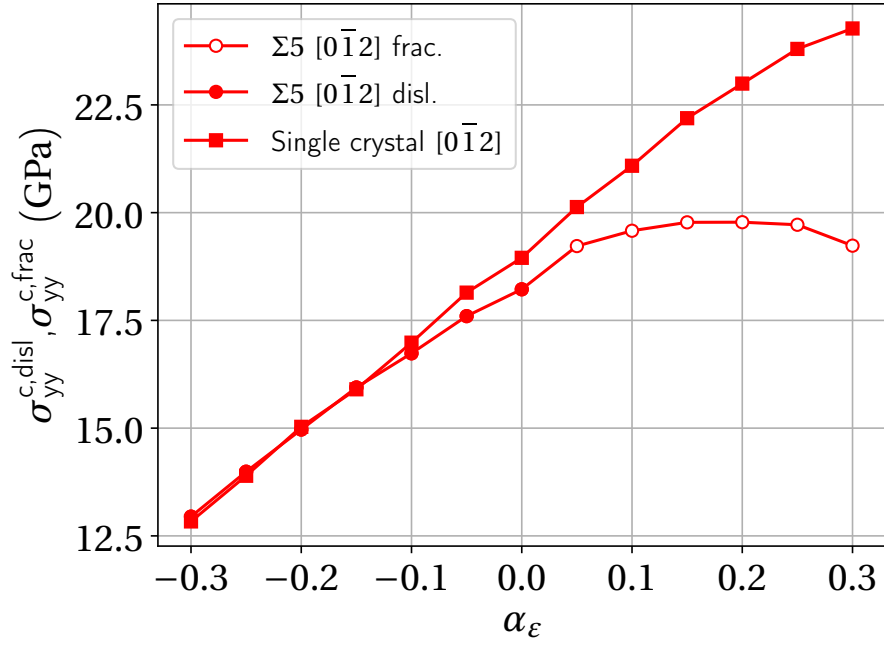
(a)



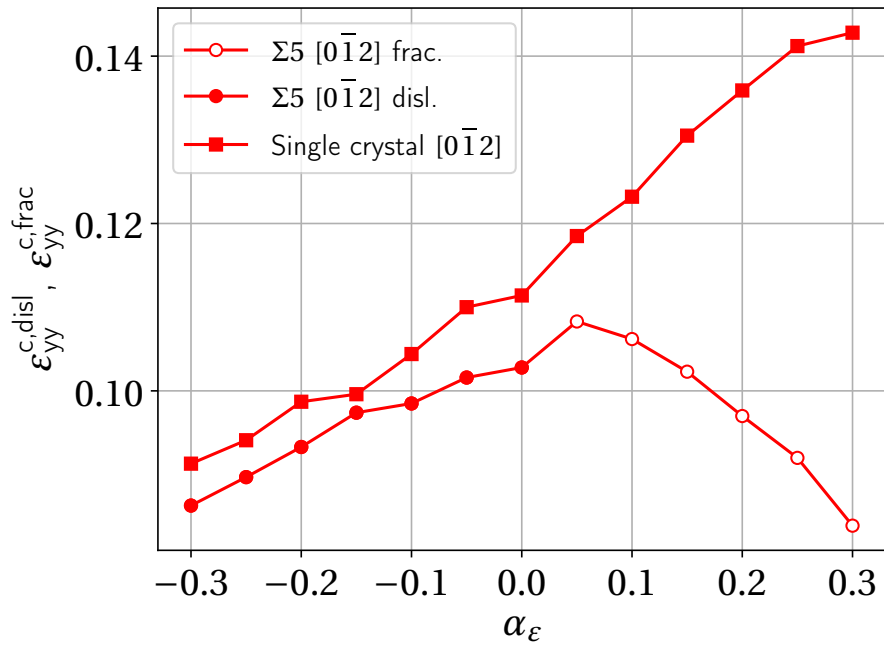
(b)

Figure 2.8: Critical stress map $\sigma_{yy}^c(\alpha_\epsilon, \beta_\epsilon)$ triggering either dislocation nucleation from the grain boundary (circle), dislocation nucleation and decohesion (square) or decohesion without dislocations (crosses) (2.8a) and its three dimensional representation (2.8b).

2. MULTIAXIAL BEHAVIOUR OF FCC NICKEL BICRYSTALS AT THE ATOMIC SCALE



(a)



(b)

Figure 2.9: Critical stress σ_{yy}^c and critical strain ϵ_{yy}^c obtained during the multiaxial tensile tests at 300 K on the $\Sigma 5$ $[0\bar{1}2]$ grain boundary and on the bulk oriented according to the $[0\bar{1}2]$ direction for the y-tensile axis

2. MULTIAXIAL BEHAVIOUR OF FCC NICKEL BICRYSTALS AT THE ATOMIC SCALE

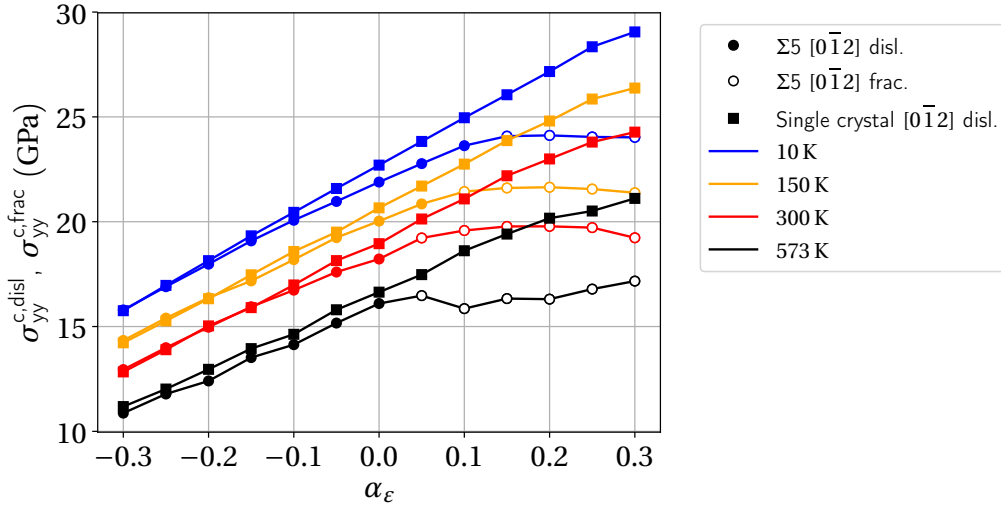


Figure 2.10: Critical stress σ_{yy}^c obtained during the multiaxial tensile tests at 10 K, 150 K, 300 K and 573 K for the $\Sigma 5$ $[0\bar{1}2]$ GB and for the related single crystal.

the critical stress in the case of the single crystal. Once again, only partial dislocation nucleations are observed in this later case.

2.3.3 Influence of the temperature and strain rate on the behaviour of the $\Sigma 5$ grain boundary

The influence of the temperature and strain rates are now considered in the case of the same $\Sigma 5$ $[0\bar{1}2]$ grain boundary and the same single crystal under multiaxial loading with equal transverse strain ratios for supplementary temperatures of 10 K, 150 K and 573 K and at a strain rate of $1.0 \times 10^8 \text{ s}^{-1}$. Results of the critical stress are presented along with the preceding results at 300 K on figure 2.10.

A thermoactivation of the critical behaviours is clearly evidenced with the global decrease of the critical stress values for both dislocation nucleations (for the single crystal and the grain boundary) and the GB decohesions, identified by filled and unfilled markers respectively. A drop of about 6–8 GPa can be evaluated between 10 K and 573 K whatever the loading applied. Interestingly, the GB decohesion area expands slightly with temperature despite the seemingly constant decrease of the critical stress whatever the applied strain ratios (i.e. whatever the induced behaviour). It indicates that, in this particular case, the GB decohesion is favored by an increase of the temperature which seems to contradict the usual intuition that plasticity and the related ductile fracture phenomena are generally favored with temperature. This may point toward different underlying thermoactivation mechanisms between GB decohesion and heterogeneous dislocation nucleation considering multiaxiality. Once again, only homogeneous partial dislocation nucleation with similar linear increases of the critical stress are reported

2. MULTIAXIAL BEHAVIOUR OF FCC NICKEL BICRYSTALS AT THE ATOMIC SCALE

for the single crystal whatever the temperature. The influence of the grain boundary, inducing heterogeneous dislocation nucleation, seems again negligible whatever the temperature.

The strain rate influence is illustrated for the $\Sigma 5$ GB at 300 K and 573 K on figures 2.11a and 2.11b respectively. A clear decrease of the critical stress with the decrease of the strain rate is evidenced.

The influence of the strain rate (on the ranges explored here) is evidently weaker than the temperature influence.

The difference of the critical stresses does not exceed 1 GPa for 300 K and 2 GPa for 573 K. At 573 K, a wider repartition is logically obtained with respect to the results at 300 K.

It is clear that the temperature and the strain rates induce a coupling effect which can logically be related to the increase of the probability of reaching energetical barriers triggering GB decohesion: thermal atomic motions are obviously promoted by temperature and are more likely to reach earlier (at a lower strain ϵ_{yy}) the critical thresholds with slower strain variations. Strangely, the decreasing strain rate seems more influential on the GB decohesion than on the heterogeneous dislocation nucleation.

2.3.4 Influence of the shearing deformation on the $\Sigma 5$ grain boundary behaviour

Critical stress results extracted from the tensile curves of the combined transverse and shear strain multiaxial loadings are reported in figure 2.12 in the case of the $\Sigma 5$ $[0\bar{1}2]$ grain boundary at 300 K.

It appears from those results that the added shear strain has a detrimental effect over the strength of the grain boundary for both dislocation nucleations and decohesions. At a ratio η_ϵ of 80 %, a clear drop of about 3 GPa is recorded for the constant critical stress triggering the GB decohesion.

It is also interesting to note that the shear strain does not modify the influence of the transverse strains ratios since similar variations (according to the $\alpha_\epsilon = \beta_\epsilon$ ratios) are evidenced. However, a restriction of the GB decohesion area (i.e. an increase of the transverse ratios threshold for decohesion) is observed with η_ϵ higher than 20 %.

This last point would suggest that despite the decrease of the critical stress to GB decohesion with the adjunction of shear strain, dislocation nucleation seems to be promoted.

For every explored loadings, no grain boundary migration are observed prior to the registered critical stress.

Finally, it is also confirmed that the shear strain direction does not influence the behaviour of the bicrystal as demonstrated by the red curve in figure 2.12 for a S/N ratio of -60 %. As already suggested, it is related to the twinning nature of this particular grain boundary and this should not be expected in the general case.

2. MULTIAXIAL BEHAVIOUR OF FCC NICKEL BICRYSTALS AT THE ATOMIC SCALE

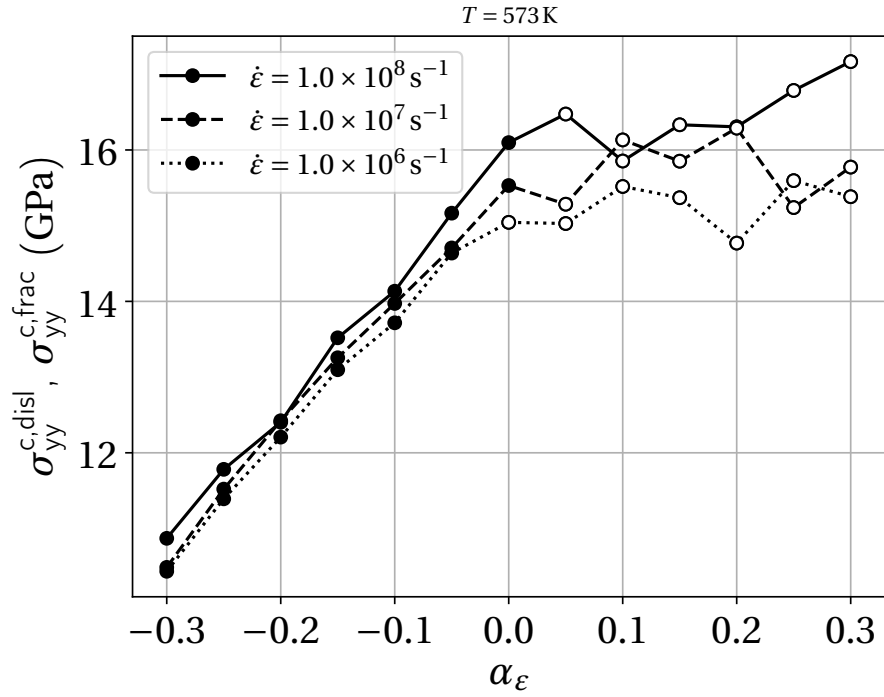
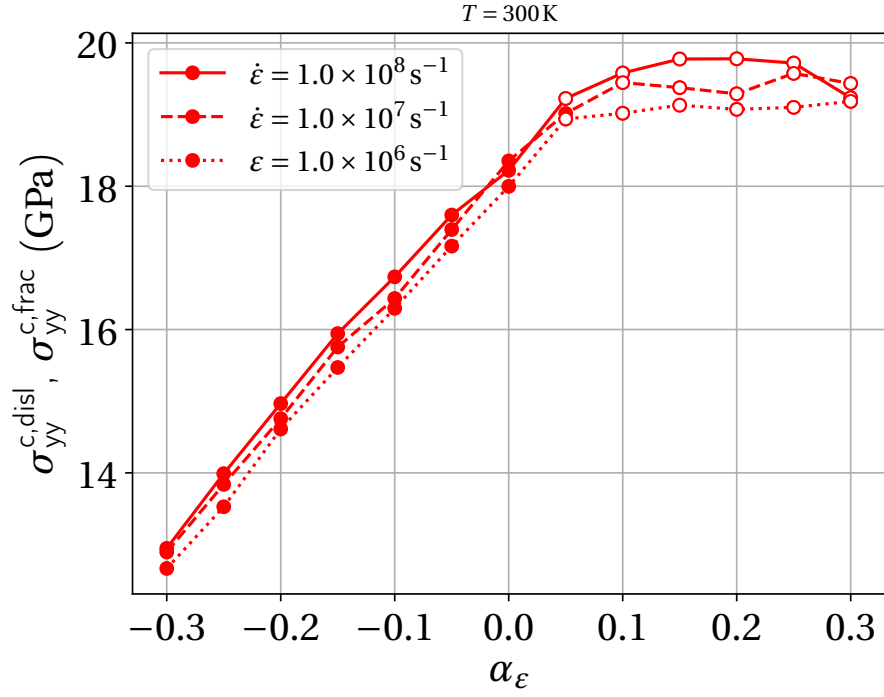


Figure 2.11: Critical stress for the $\Sigma 5$ $[0\bar{1}2]$ at 300 K (figure 2.11a) and 573 K (figure 2.11b) for strain rates of $1.0 \times 10^8 \text{ s}^{-1}$, $1.0 \times 10^7 \text{ s}^{-1}$ and $1.0 \times 10^6 \text{ s}^{-1}$.

2. MULTIAXIAL BEHAVIOUR OF FCC NICKEL BICRYSTALS AT THE ATOMIC SCALE

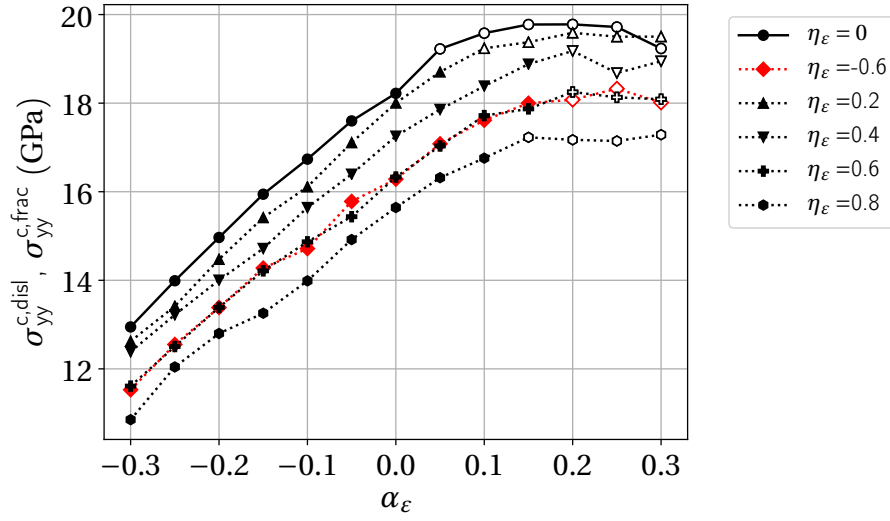


Figure 2.12: Critical stress σ_{yy}^c obtained during the multiaxial tensile tests coupling the influence of the shear straining on the $\Sigma 5$ $[0\bar{1}2]$ through the shear/normal strain ratio η_ϵ varying between 0 and 0.8. The results for the negative value of the S/N ratio $\eta_\epsilon = -0.6$ is reported with the red curve. The transverse/normal strain ratios $\alpha_\epsilon = \beta_\epsilon$ are taken between -0.3 and 0.3.

2.3.5 Behaviour of the different CSL grain boundaries

Further insight is obtained from the results of the same multiaxial loadings on the twelve other grain boundaries at 300 K.

The critical stresses triggering either dislocation nucleation or GB decohesion are reported for equal transverse deformation ratios in figure 2.13. The same progressive transition from dislocation nucleation to GB decohesion is observed with the appearance of a critical saturation for all the grain boundaries studied with the slight exception of the $\Sigma 101$ $[0101]$ and $\Sigma 25$ $[071]$ grain boundaries which mostly experience decohesion. Similar slopes are observed in the partial dislocation area for most of the grain boundaries except for the $\Sigma 5$ $[031]$ grain boundary.

A unique critical stress for the grain boundaries decohesion can be fairly identified in each cases by the mean value of the plateau. Further results and a more comprehensive discussion about the origins of these behaviours and their variation according to the grain boundary structure are provided in chapter 3 for the dislocation nucleation mechanism and in chapter 4 for GB decohesion.

2. MULTIAXIAL BEHAVIOUR OF FCC NICKEL BICRYSTALS AT THE ATOMIC SCALE

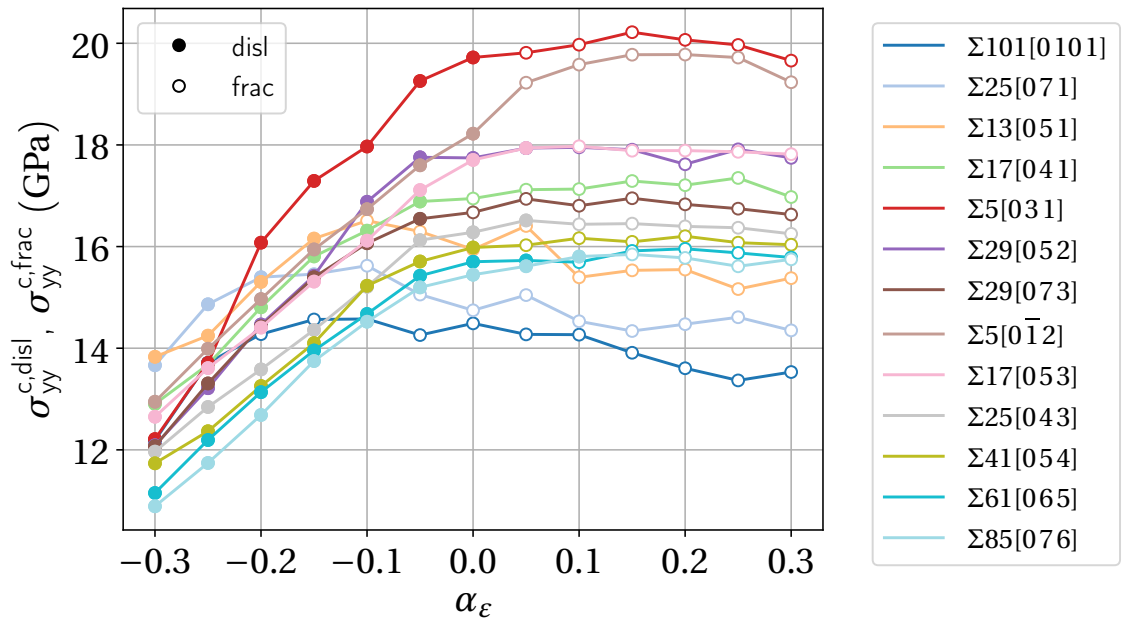


Figure 2.13: Critical stress variation $\sigma_{yy}^c(\alpha_\epsilon)$ for the thirteen CSL symmetric [100] tilt grain boundaries referenced in table 2.2. The empty markers indicate grain boundary decohesions without any dislocation nucleation, the filled markers indicate nucleation of dislocations from the grain boundary with or without grain boundary decohesion.

2.4 Summary of the results and conclusion

2.4.1 Results

In this section 2.3, the following results are found:

- Uniaxial stress and uniaxial strain tensile loadings applied on the $\Sigma 5$ $[0\bar{1}2]$ grain boundary at room temperature (300 K) show a clear difference of behaviour as the nucleation of a partial dislocation is obtained in the first case at a maximum stress of $\sigma_{yy}^{c,disl} = 9.3$ GPa, whereas a grain boundary decohesion with limited plasticity is evidenced in the second case at a higher maximum stress of $\sigma_{yy}^{c,frac} = 18.2$ GPa
- Multiaxial strain loadings on the same $\Sigma 5$ $[0\bar{1}2]$ grain boundary indicate a clear influence of the transverse deformation strain ratios α_ϵ and β_ϵ with a progressive behaviour transition of the grain boundary. An increase of those deformation ratios, induces a logical restriction of incipient plasticity with an increase of the critical stress to dislocation nucleation $\sigma_{yy}^{c,disl}$. In fine, the tensile strain multiaxility leads to the appearance of a critical stress plateau correlated to the systematic decohesion of the grain boundary without any dislocation nucleation.
- Results obtained through the variation of the simulation temperature and strain rate evidently points toward a thermoactivation mechanism. The increase of the temperature has the most detrimental effect over the critical stress to GB decohesion and further induces an increase of the GB decohesion area. Counter-intuitively, the temperature therefore promote GB fracture initiation.
- The adjunction of a shear deformation does not modify the influence of the transverse straining on the $\Sigma 5$ $[0\bar{1}2]$ grain boundary. But a clear decrease of the critical stress for GB decohesion is evidenced despite a reduction of the GB decohesion area. No GB migration or GB sliding is observed.
- A comparison of the multiaxial behaviour of the $\Sigma 5$ $[0\bar{1}2]$ and related single crystal, reveals that the critical stress for GB decohesion may represent an intrinsic parameter of the interface as only dislocation nucleation is obtained for the single crystal case.
- Results of the multiaxial loadings on the other grain boundaries show the same trends as systematic increase of the critical stress to dislocation nucleation $\sigma_{yy}^{c,disl}$ and a critical stress plateau correlated to the grain boundary decohesion is found.

2.4.2 Conclusion

In this chapter, a method consisting in varying purposely the multi-axiality of the strain (or stress) state applied on several bicrystals is used in order to explore the behaviour of CSL symmetric tilt grain boundaries in FCC metals, seeking for intergranular fracture initiations and its related mechanisms.

The multi-axiality of intergranular loadings shows a significant influence over the behaviour of the chosen grain boundaries in terms of mechanisms and related critical stresses. The importance of considering the grain boundary as a possible source of dislocation, depending on the loading conditions, is underlined. The study confirms the importance of considering the full strain (or stress) state for assessing the probability of grain boundaries failure. This part also provides mechanical fracture properties of thirteen grain boundaries which are supposed inherent to the homophase interface.

These preliminary considerations focusing on multi-axial strain loadings applied homogeneously on FCC bicrystals appears to constitute a prerequisite, should more advanced characterisations of grain boundaries failure be undertaken at upper scales in simulation or experimental studies.

The origins of the different behaviours observed are the scope of chapters 3 and 4.

3

Homogeneous and heterogeneous dislocation nucleation: influence of the strain multiaxiality

This chapter focuses on the dislocation mechanism observed in the single crystals and in the bicrystals previously studied under multiaxial loadings.

Particular attention is paid to the case of the $\Sigma 5$ $[0\bar{1}2]$ GB from which partial dislocation nucleations are recorded for critical resolved shear stresses similar to its related single crystal.

A systematic analysis of the activated slip systems and their related critical resolved shear stress is undertaken in that case. Non-Schmid effects are observed at this atomic scale as a criterion for dislocation nucleation based on the best oriented slip system for slip is not verified.

The underlying mechanisms for homogeneous dislocation nucleation in the related single crystal (of the $\Sigma 5$ GB) under multiaxial loading is investigated. A classical stress state analysis fully explains the confined plasticity previously observed with the increase of the transverse/normal strain ratios and the observed increase of the critical principal stress for dislocation nucleation. This explanation should encompass any system considered at this scale.

Paradoxically, results show that the confined plasticity is accompanied by a decrease of the critical resolved shear stress for dislocation nucleation. This result is further explained by the influence of the lattice deformation occurring during a given strain (or stress) state over the shape of the generalised stacking fault energy curve.

Therefore, a competition between the decrease of the resolved shear stress, restraining dislocation nucleation and the decrease of the critical resolved shear stress promoting plasticity is therefore underlined for the multiaxial loadings.

3. HOMOGENEOUS AND HETEROGENEOUS DISLOCATION NUCLEATION: INFLUENCE OF THE STRAIN MULTIAXIALITY

Contents

3.1 Homogeneous and heterogeneous dislocation nucleation in FCC metals	68
3.2 Dislocation nucleation from the CSL symmetric tilt grain boundaries	69
3.2.1 Influence of the grain boundary local atomic stress field	69
3.2.2 Dislocation nucleation from the $\Sigma 5$ grain boundary and its restriction through stress multiaxiality	73
3.2.2.1 Activated slip systems	74
3.2.2.2 Variation of the critical resolved shear stress	77
3.3 Further computations, comparisons and discussion	81
3.3.1 The Frenkel model and the onset of a stacking fault	82
3.3.1.1 The Frenkel model	82
3.3.1.2 Applicability	84
3.3.1.3 Generalised stacking fault energy curve and critical resolved shear stress for heterogeneous and homogeneous dislocation nucleation	85
3.3.2 Molecular static computation of the generalised stacking fault energy curve	86
3.3.3 Influence of the lattice deformation on the nucleation of partial dislocations	90
3.3.4 Influence of the temperature	97
3.4 Summary of the results and conclusion	100
3.4.1 Results	100
3.4.2 Conclusion	101

3. HOMOGENEOUS AND HETEROGENEOUS DISLOCATION NUCLEATION: INFLUENCE OF THE STRAIN MULTIAXIALITY

3.1 Homogeneous and heterogeneous dislocation nucleation in FCC metals

Grain boundaries are often regarded as sinks for lattice dislocations [Pumphrey and Gleiter, 1974, Pond and Smith, 1977] or as barriers for dislocation transmission [Sangid et al., 2011, Kacher et al., 2014].

Inversely, it has been evidenced from in situ straining experiments that grain boundaries can also act as sources of dislocations when local intergranular stress fields develop at stress concentrator sites such as triple points, GB extrinsic dislocations, ledges or kinks [Murr, 1974, Murr, 1981, Kurzydowski et al., 1984, P. H. Pumphrey, 1975].

In pure nickel, partial and perfect dislocation emissions from grain boundaries has been observed during in situ testing at premacroyield deformations [Singh and Tangri, 1970, Malis et al., 1972]. Once again, the origins of the emissions were linked to intergranular stress concentrators such as grain boundary dislocations.

In that respect, slip bands impacting grain boundaries should also be regarded as potential mechanical triggers for dislocation emission.

Recently, Genée et al. [Genée et al., 2017] have shown that discontinuous slip band interactions with grain boundaries after a monotonic tensile test on a nickel-base alloy lead to numerous intergranular behaviours, including the formation of a plastic zone without slip transmission in the adjacent grain or the initiation of a microcrack.

In the context of assessing intergranular failure for prediction purposes, the full mechanical behaviour of grain boundaries should be modeled. In particular, the emission of dislocations from the interface constitutes one of the key feature that needs to be understood for that matter.

For that matter, atomistic simulations allow to undertake convenient studies of the intrinsic behaviour of perfect grain boundaries with a decorrelation of any local stress concentrations.

Homogeneous and heterogeneous dislocation nucleation (in a single crystal and from a grain boundary, respectively) has been extensively treated for FCC metals by atomistic simulation studies. Molecular dynamics simulations of various loadings applied on bicrystal systems [Tschopp et al., 2008, Zhang et al., 2014, Spearot et al., 2007a], single crystals [Tschopp et al., 2007, Spearot et al., 2009, Cai et al., 2018] or nanocrystalline metals [Van Swygenhoven et al., 1999, Van Swygenhoven et al., 2002, Van Swygenhoven and Derlet, 2008, Yamakov et al., 2002, Yamakov et al., 2003] in copper, aluminium or nickel provide the following points of interest:

- Shockley partial or perfect dislocation nucleation is widely observed with a significant influence of the stacking fault energy as metals featuring the lowest SFE are more prone to extended partial dislocation emission.
- The activated slip systems does not feature the highest Schmid factors.

3. HOMOGENEOUS AND HETEROGENEOUS DISLOCATION NUCLEATION: INFLUENCE OF THE STRAIN MULTIAXIALITY

- A directionality of the critical resolved shear stress is underlined for the determination of the activated slip system.
- Non-Schmid effects are often recorded as the normal stress component in the activated slip system referential also shows a significative influence over the dislocation nucleation process. It is generally found that: the higher the stress component normal to the slip plane, the lower the critical resolved shear stress (i.e. the easier the dislocation nucleation).
- The influence of the generalised stacking fault energy curve over dislocation nucleation is strongly suggested.
- Significant discrepancies between heterogeneous and homogeneous dislocations nucleations are found. In some particular cases, the propensity to heterogeneous dislocation nucleation can be correlated to the appearance of one elementary structural unit.

Additionally, molecular static and ab initio studies clearly demonstrate the importance of the stress state over the generalised stacking fault energy curve [Andric et al., 2019, Ogata et al., 2002] linked to the ideal shear strength of the material.

It has been shown before that the strain multiaxiality logically restrains the dislocation nucleation both in bicrystals and in single crystals (chapter 2). In order to clarify the observed behaviour in that context, a comprehensive study of the dislocation nucleation is provided in this chapter.

It is chosen to primarily focus on the discrepancies between heterogeneous and homogeneous dislocation nucleation in the selected grain boundaries of chapter 2 with a particular emphasis on the $\Sigma 5$ $[0\bar{1}2]$ grain boundary.

Further insight is provided through the consideration of the generalised stacking fault energy curve and its variation according to the lattice deformation which is directly correlated to the critical resolved shear stress (CRSS) variation recorded in the case of the $\Sigma 5$ $[0\bar{1}2]$ and its related single crystal.

3.2 Dislocation nucleation from the CSL symmetric tilt grain boundaries

3.2.1 Influence of the grain boundary local atomic stress field

Results from the multiaxial loadings presented in chapter 2 at 300 K and for transverse/normal strain ratios of $\alpha_\epsilon = \beta_\epsilon = -0.25$ in the case of the thirteen grain boundaries and their related single crystals are presented figure 3.1. All the critical stresses correspond to heterogeneous or homogeneous dislocation nucleations except in the cases of the $\Sigma 101$ and $\Sigma 25$ $[071]$ GBs for which they correspond to the propagation of a prenucleated dislocation.

3. HOMOGENEOUS AND HETEROGENEOUS DISLOCATION NUCLEATION: INFLUENCE OF THE STRAIN MULTIAXIALITY

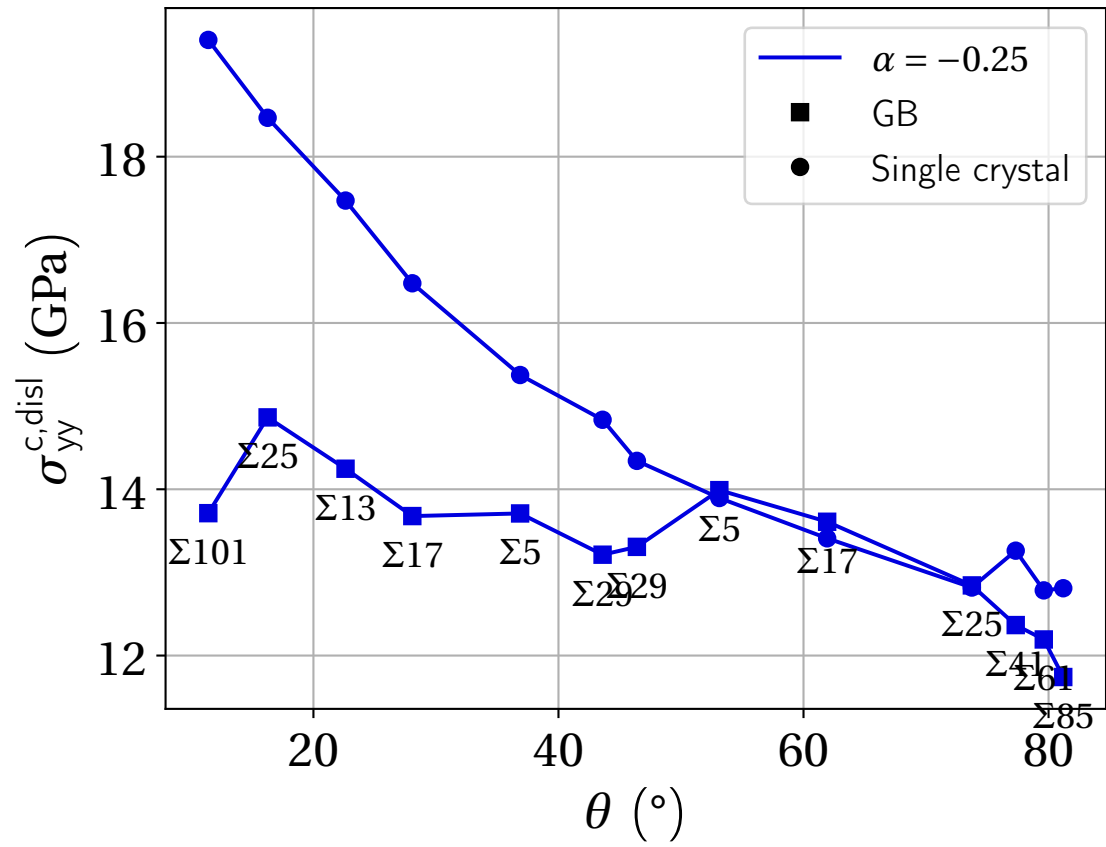


Figure 3.1: Critical stress σ_{yy}^c for dislocation nucleation at $\alpha_\varepsilon = -0.25$ for the thirteen grain boundaries and their related single crystals (3.1).

3. HOMOGENEOUS AND HETEROGENEOUS DISLOCATION NUCLEATION: INFLUENCE OF THE STRAIN MULTIAXIALITY

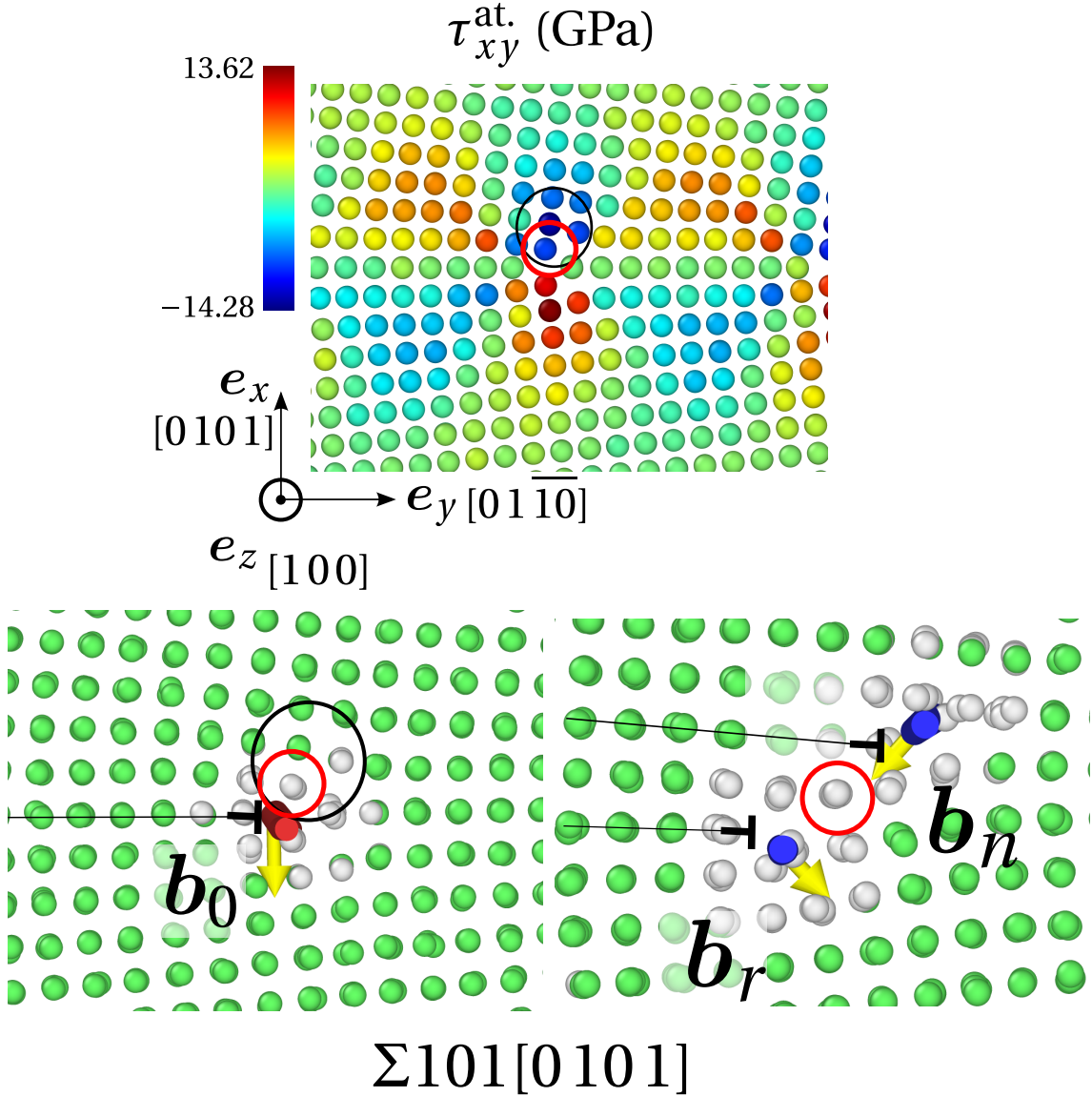


Figure 3.2: Initial configuration of the $\Sigma 101$ [0 10 1] at 0 K with the plot of the atomic shear stress field $\tau_{xy}^{\text{at.}}$ (top picture). Mechanism for the dislocation nucleation from the $\Sigma 101$ [0 10 1] GB at $\alpha_\varepsilon = -0.25$ (bottom pictures). Initial configuration at 300 K and the intrinsic GB dislocation (bottom left picture). Configuration of the grain just after the nucleation and before propagation of the dislocation (bottom right picture). The dislocation lines (along the [100] axis) are indicated in red for the intrinsic GB dislocation (left bottom picture), and in blue for the nucleated and residual dislocations (right bottom picture).

3. HOMOGENEOUS AND HETEROGENEOUS DISLOCATION NUCLEATION: INFLUENCE OF THE STRAIN MULTIAXIALITY

Clear discrepancies between bicrystals and single crystal are evidenced for $\theta < 50^\circ$, with lower values of the critical stresses for heterogeneous dislocation nucleation at grain boundaries. This effect is not surprising as grain boundaries are the location of atomic stress concentrations [Priester, 2013, Read and Shockley, 1950, Bollmann, 1970] and are therefore intrinsically prone to trigger critical events. More unanticipated is the negligible discrepancies observed between the $\Sigma 5$ $[0\bar{1}2]$, $\Sigma 17$ $[053]$ and $\Sigma 25$ $[043]$ grain boundaries and their related single crystals.

For the example of the $\Sigma 101$ $[0101]$ GB, the nucleation of an edge dislocation is observed and can clearly be correlated to the intrinsic grain boundary edge dislocation triggering the nucleation event significantly before the maximum stress is reached, as presented on the bottom picture of figure 3.2. The propagation of the nucleated dislocation leaving a residual dislocation happens subsequently as the first stress drop is recorded. As already stated before, a Burgers vector $\mathbf{b}_0 = \frac{a}{\sqrt{101}}[0\bar{1}01]$ is recorded for the intrinsic GB dislocation, indicated in red. The residual and nucleated edge dislocations, indicated in blue, feature respectively the Burgers vectors $\mathbf{b}_r = \frac{a}{2\sqrt{101}}[0911]$ and $\mathbf{b}_n = \frac{a}{2\sqrt{101}}[0\bar{1}19]$ in the upper grain referential. The conservation of the Burgers vector is logically verified here, as the following equality holds:

$$\mathbf{b}_0 = \mathbf{b}_r + \mathbf{b}_n$$

The nucleation mechanism is illustrated on figure 3.2: the local shearing of the dark-circled area and the motion of the red-circled atom can be identified as the origin. The plot of the atomic shear strain component field $\tau_{xy}^{\text{at.}}$ at 0 K on the initial GB configuration clearly reveals that the highest shear stress are recorded in the preceding circled areas which further underlines the role of the intrinsic stresses of the grain boundary as a precursor for critical mechanisms.

It is obvious that the grain boundaries and their atomic structures or their description at the stress level are involved in the process of heterogeneous dislocation nucleation as already evidenced [Tschopp et al., 2008, Shimokawa, 2010]. However, the prediction of such mechanism according to the nature of the grain boundary constitute obviously a challenging task since every interface has to be studied separately. Here, no clear tendency can be decipher according to the rotation angle of the grain boundary or their SU descriptions given in table 2.2 unlike the monotonic decrease of the homogeneous dislocation nucleation for the single crystals. In these later cases, a geometrical tendency is evidenced and could be related to the changing orientation of the primary slip system with respect to the tensile direction. Nevertheless, a decrease of the critical stress $\sigma_{yy}^{\text{c,disl}}$ discrepancy between the grain boundary and its single crystal can be noted.

Those results also confirm that the $\Sigma 5$ $[0\bar{1}2]$ grain boundary is a particular case since only few other grain boundaries ($\Sigma 17$ $[053]$ and $\Sigma 25$ $[043]$) display similar critical stress with respect to their single crystal counterpart. The reasons of these similar critical stress values is not obvious at first sight.

Finally, it is observed that, except for the particular case of the $\Sigma 101$ $[0101]$ and $\Sigma 25$ $[071]$, only Shockley partial dislocation are nucleated from the grain boundaries. The

3. HOMOGENEOUS AND HETEROGENEOUS DISLOCATION NUCLEATION: INFLUENCE OF THE STRAIN MULTIAXIALITY

$\Sigma 101$ and $\Sigma 25$ GBs both feature a near perfect dislocation nucleation. It is interesting to note that for some GBs the slip plane of the propagating partial dislocation is oriented in such way that possible interactions with intrinsic grain boundary dislocation are induced resulting in complex dislocation propagations in the grain. In the cases of the $\Sigma 25$ [043] to the $\Sigma 85$ [076] GBs, the partial dislocation nucleation clearly originates from the intrinsic GB perfect dislocations which therefore dissociate into two partial. Those final remarks further illustrate the complexity of heterogeneous dislocation nucleation as every grain boundary features its own particular mechanism.

Nevertheless, the underlying mechanisms for heterogeneous and homogeneous partial dislocation nucleations should share a common ground as in both cases the resulting process consist in similar $\{111\}$ plane gliding with the onset of a stacking fault (if no perfect dislocation is directly emitted).

3.2.2 Dislocation nucleation from the $\Sigma 5$ grain boundary and its restriction through stress multiaxiality

A systematic study of the dislocation nucleation behaviour of the $\Sigma 5$ [0 $\bar{1}$ 2] is now proposed in order to supplement the preceding results. For every multiaxial tensile loadings performed at 300 K and inducing the nucleation of a partial dislocation, the first appearance of the dislocation is detected through the use of the DXA algorithm of OVITO. The frequency of configuration sampling in LAMMPS is high enough during the loading, so that the very first appearance of the dislocation can clearly be identified on the computed configurations. The Burgers vector assessed by the DXA algorithm is used to identify the slip system activated for each cases.

Figure 3.4a shows the identification of the first slip systems activated for each related $(\alpha_\varepsilon, \beta_\varepsilon)$ loading using the arbitrary slip systems notations presented in table 3.1 for the possible $\frac{1}{6} \langle 112 \rangle$ Shockley partial dislocations. Care is taken to consider in which grain the dislocation is emitted ; the indication of the referred grain is specified by the upper left roman numbers I (upper grain) or II (lower grain).

The critical resolved shear stress for the emission of the dislocation from the grain boundary is computed in each case using the preceding identification of the slip system and the critical stress state in the corresponding grain:

$$\tau_{nm}^{c,disl} = \mathbf{m}_s \boldsymbol{\sigma}^{c,disl} \mathbf{n}_s \quad (3.1)$$

with \mathbf{m}_s and \mathbf{n}_s the gliding and normal unit vectors corresponding to the activated slip system s identified in each cases. Figure 3.4b also shows the same map with the computation of the normal component of the stress vector acting on the slip plane:

$$\sigma_{nn}^{c,disl} = |\mathbf{n}_s \boldsymbol{\sigma}^{c,disl} \mathbf{n}_s|$$

Notations used for the slip planes are also referenced in table 3.1, and further illustrated by the Thompson tetrahedra in figure 3.3.

3. HOMOGENEOUS AND HETEROGENEOUS DISLOCATION NUCLEATION: INFLUENCE OF THE STRAIN MULTIAXIALITY

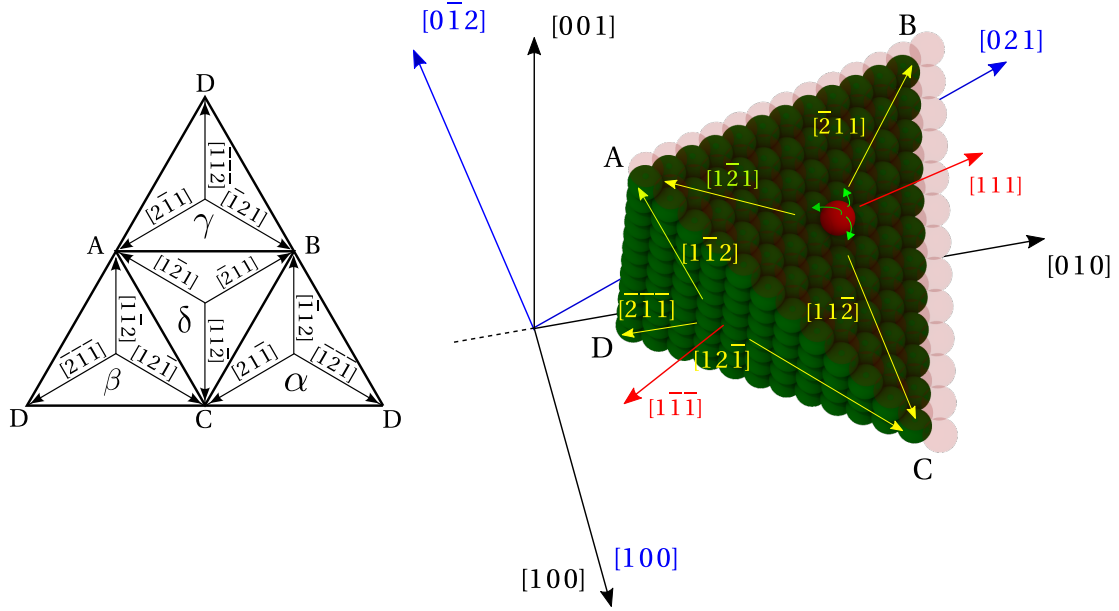


Figure 3.3: Thompson tetrahedra referencing the directions of glide for Shockley partial dislocation nucleation

In this section, it is proposed to focus on a comparison with the Schmid criterion, generally used for assessing the activation of the primary slip system:

$$\max_{s \in \{1..12\}} |\tau_s| \geq \tau^c$$

where τ_s is the resolved shear stress (RSS) on the slip systems s and τ_c the critical resolved shear stress which is considered to be solely related to the material.

3.2.2.1 Activated slip systems

Four slip systems (with identification number 3, 4, 9 and 11 as referenced in table 3.1) are identified with a rather sporadic appearance. However it is observed here that the slip systems 3 and 4 appear systematically when the partial dislocation is emitted in the lower grain, the same remarks hold for the systems 9 and 11 for the upper grain. It is reminded here that the grain boundary is symmetric, therefore inducing an equal probability of dislocation nucleation in the lower or the upper grain. Furthermore, systems 3 and 4 (or 9 and 11) are equivalent slip systems with respect to the lower (or upper) grain tensile axis orientation. This two points explain this apparently random repartition of activated slip systems. In the single crystal case, the same activated slip systems 9 and 11 of the upper grain are systematically reported as the same orientations are considered.

Since the misorientation axis of the grain boundary is the $[100]$ crystal axis, this geometrical equivalence forming slip system couples with the same resolved shear

3. HOMOGENEOUS AND HETEROGENEOUS DISLOCATION NUCLEATION: INFLUENCE OF THE STRAIN MULTIAXIALITY

$\#_n$	$\#_m$	$\sqrt{3}\mathbf{n}_s$	$\sqrt{6}\mathbf{m}_s$
δ	1	[1 1 1]	[1 1 $\bar{2}$]
	2		[1 $\bar{2}$ 1]
	3		[$\bar{2}$ 1 1]
β	4	[1 $\bar{1}$ $\bar{1}$]	[$\bar{2}$ $\bar{1}$ $\bar{1}$]
	5		[1 $\bar{2}$ $\bar{1}$]
	6		[1 $\bar{1}$ $\bar{2}$]
α	7	[$\bar{1}$ 1 $\bar{1}$]	[$\bar{1}$ $\bar{2}$ $\bar{1}$]
	8		[$\bar{1}$ 1 2]
	9		[2 1 $\bar{1}$]
γ	10	[$\bar{1}$ $\bar{1}$ 1]	[$\bar{1}$ $\bar{1}$ $\bar{2}$]
	11		[2 $\bar{1}$ 1]
	12		[1 $\bar{2}$ 1]

Table 3.1: Notations of the twelve slip systems for the Shockley partial dislocations in FCC metals or alloys. The directions for the slip systems are specifically chosen to respect the criterion for admissible gliding [Cai et al., 2018].

stress is verified for the other slip systems as evidenced on figure 3.5 which will be presented later on.

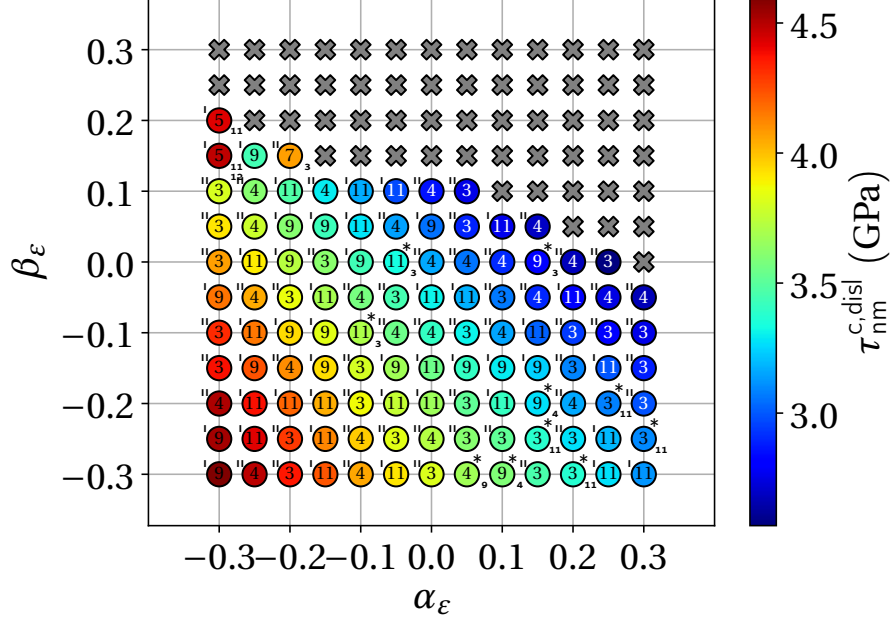
In some rather rare cases, two emitted dislocations are identified in the two grains as the sampling do not permit to identify which dislocation is nucleated first. Those cases are denoted with an asterisk in the upper right corner of the mark on the same figure and the second slip system is also indicated in the lower right corner.

Further verifications indicate that in the three cases $(\alpha_\varepsilon, \beta_\varepsilon) = (-0.3, 0.15)$; $(-0.3, 0.2)$; $(-0.2, 0.15)$ (upper left area of figure 3.4a), the partial dislocations are in fact emitted from the tip of a pre-crack nucleated at the grain boundary. Therefore, those cases are not linked to a pure dislocation nucleation.

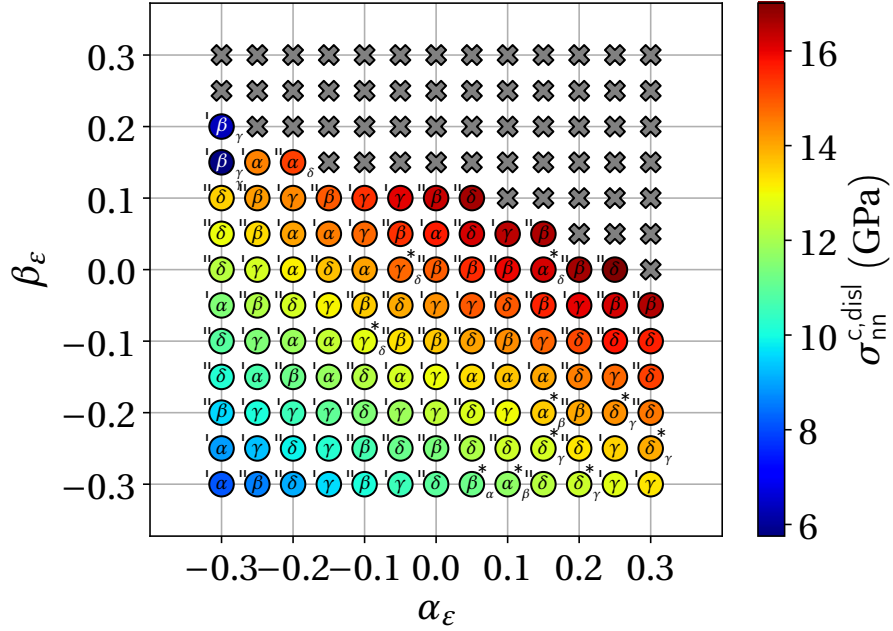
Resolved shear stresses (RSS) at the critical moment of the dislocation nucleation are systematically reported on figure 3.5 for every slip systems and for the loading cases $\alpha_\varepsilon = -0.3, -0.2, -0.1, 0$ and 0.05 along with the critical resolved shear stress reported for the observed activated slip systems (squared marks). It is reminded here that all the RSS are computed using equation 3.1, choosing the grain in which the dislocation nucleation is evidenced. Following this reminder, it is to be noted that the cases $\alpha_\varepsilon = 0$ and 0.05 displayed in figure 3.5, are obtained for the second lower grain (denoted Gr. II) as the other ones are obtained for the first upper grain. This explained the apparent RSS discontinuity for on given slip system between $\alpha_\varepsilon = -0.1$ and 0 .

As previously noted, it is here logical to obtain equivalent couples of slip systems with equal resolved shear stresses for geometrical reasons linked to the orientation of

3. HOMOGENEOUS AND HETEROGENEOUS DISLOCATION NUCLEATION: INFLUENCE OF THE STRAIN MULTIAXIALITY



(a)



(b)

Figure 3.4: Critical resolved shear stress $\tau_{nm}^c = \mathbf{m}_s \boldsymbol{\sigma}^c \mathbf{n}_s$ (3.4a) and normal critical stress $\sigma_{nn}^c = |\mathbf{n}_s \boldsymbol{\sigma}^c \mathbf{n}_s|$ (3.4b) for the first dislocation nucleation from the grain boundary on the s slip system, for each multiaxial tensile test according to its $(\alpha_\epsilon, \beta_\epsilon)$ ratio. Each slip system s is identified by its arbitrary notations referenced in table 3.1

3. HOMOGENEOUS AND HETEROGENEOUS DISLOCATION NUCLEATION: INFLUENCE OF THE STRAIN MULTIAXIALITY

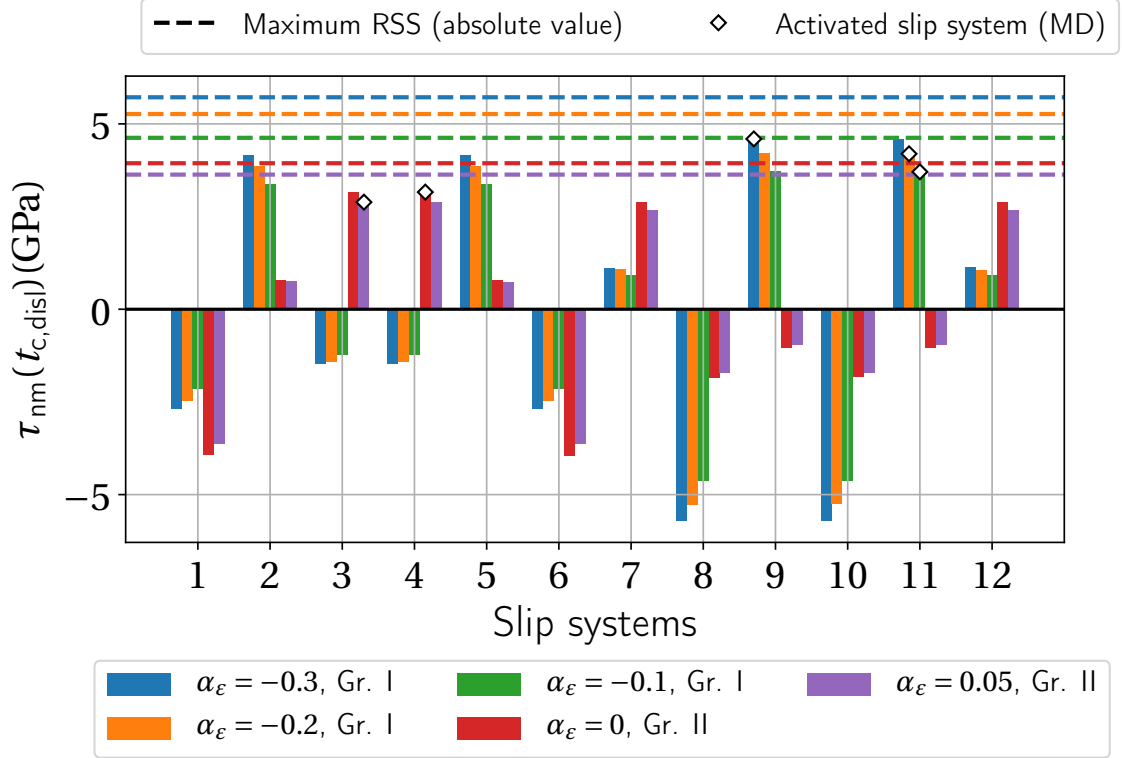


Figure 3.5: Resolved shear stress on each slip system at maximum σ_{yy}^c stress for ratios $\alpha_\epsilon = \beta_\epsilon = -0.3, -0.2, -0.1, 0$ and 0.05 .

the slip systems with respect to the tensile axis.

It is observed that a Schmid criterion is not sufficient to predict the nucleation of partial dislocations as in every cases presented here, the first activated slip system does not feature the maximum resolved shear stress (in absolute value) but the second one. However it should also be noted that the slip systems presenting the higher Schmid factor also display a negative value of the resolved shear stress for the selected directions of slip (table 3.1) which are purposely chosen. This particular points will be addressed more extensively in the next section. It is verified that this remark also holds for every loadings in the $(\alpha_\epsilon, \beta_\epsilon)$ space.

3.2.2.2 Variation of the critical resolved shear stress

Figure 3.6a shows the variation of the critical resolved shear stress on the 11th slip system in the $\alpha_\epsilon = \beta_\epsilon$ cases for the $\Sigma 5$ $[0\bar{1}2]$ and the single crystal with the same orientation of the tensile axis. This variation is equivalent to the values extracted from the diagonal of the graph displayed in figure 3.4a as the four slip systems 3, 4, 9 and 11 are all equivalent as previously explained.

From figures 3.4a and 3.6a, it is clear that the critical resolved shear stress displays a

3. HOMOGENEOUS AND HETEROGENEOUS DISLOCATION NUCLEATION: INFLUENCE OF THE STRAIN MULTIAXIALITY

decreasing variation from around 4.5 GPa to 2.5 GPa with the increase of the transverse strain ratios ($\alpha_\varepsilon, \beta_\varepsilon$). As expected from previous results, a similar trend with negligible discrepancies are obtained in the case of the single crystal.

An inverse variation is observed for the critical stress normal to the slip plane with an increase from around 8.5 GPa to 17 GPa as observed on figure 3.4b.

The variation of the resolved shear stress on the 11th slip plane is also displayed in figure 3.6b according to the axial stress σ_{yy} for the single crystal case and for the different $\alpha_\varepsilon = \beta_\varepsilon$ cases. It is reminded that for the single crystal, only dislocation nucleation are recorded at $\sigma_{yy}^{c,dislo}$, corresponding to the end points in figure 3.6b. Those variations clearly illustrate the effect of the transverse straining.

At the same axial stress σ_{yy} , the resolved shear stress is decreased by the increase of the α_ε and β_ε ratios.

Although this constitutes a well-known effect, further explanation are provided in the following paragraph as a reminder. This point can be easily explained and illustrated by a Mohr's circle representation of the Cauchy stress. Figure 3.7 shows such representation for the critical stress state at $\alpha_\varepsilon = \beta_\varepsilon = -0.3, 0$. and 0.3 along with the decrease of the maximum shear stress which is deduced in the principal coordinate system through:

$$|\tau_{\max}| = \frac{1}{2}(\sigma_1 - \sigma_3)$$

where σ_1 and σ_3 correspond to the maximum and minimum stresses in the principal coordinate system (i.e. here, the coordinate system $(\mathbf{e}_x, \mathbf{e}_y, \mathbf{e}_z)$ as explained before). As denoted on figure 3.7 the following correspondance are found to plot the Mohr's circles in each cases:

$$\sigma_1^c \equiv \sigma_{yy}^c \quad \sigma_2^c \equiv \sigma_{zz}^c \quad \sigma_3^c \equiv \sigma_{xx}^c$$

The diminution of the difference between the maximum and minimum principal stresses with the increase of the strain ratios logically induces a decrease of the absolute value of the maximum shear stress τ_{\max} . A fortiori, a probable decrease of the absolute value of the resolved shear stresses τ_s whatever the slip system s considered may be suggested since by definition:

$$|\tau_s| \leq |\tau_{\mathbf{n}_s}| \leq |\tau_{\max}| \quad \forall s \in \{1..12\}$$

This decrease is further confirmed by the plot of the critical stress state representation $(\sigma_{\mathbf{n}_{11}}^c, \tau_{\mathbf{n}_{11}}^c)$ choosing the normal vector \mathbf{n}_{11} of the 11th slip system plane. It is reminded here that:

$$\sigma_{\mathbf{n}_{11}}^c = \mathbf{T}^c(\mathbf{n}_{11}) \cdot \mathbf{n}_{11} \quad \tau_{\mathbf{n}_{11}}^c = \|\mathbf{T}^c(\mathbf{n}_{11}) - \sigma_{\mathbf{n}_{11}}^c \mathbf{n}_{11}\|$$

with $\mathbf{T}^c(\mathbf{n}_{11}) = \boldsymbol{\sigma}^c \cdot \mathbf{n}_{11}$ the constraint vector on the 11th slip system plane.

The emission of dislocations is therefore postponed with the increase of the α_ε and β_ε ratios as a further increase of the axial stress σ_{yy} and axial strain ε_{yy} is necessary for reaching the critical resolved shear stress to dislocation nucleation.

3. HOMOGENEOUS AND HETEROGENEOUS DISLOCATION NUCLEATION: INFLUENCE OF THE STRAIN MULTIAXIALITY

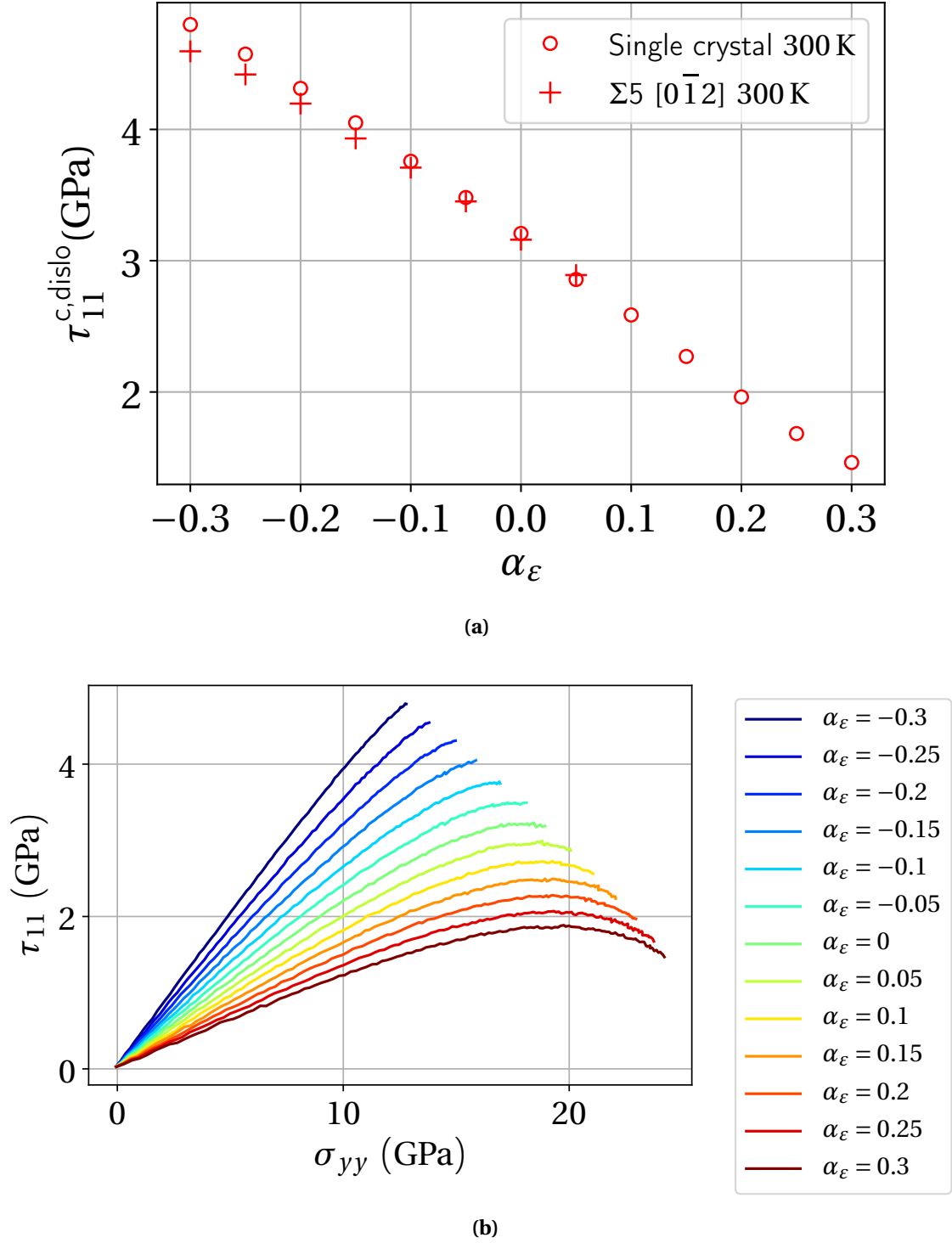


Figure 3.6: Variation of the critical resolved shear stress for the $\Sigma 5$ GB and the single crystal with the same orientation (3.6a). Variation of the resolved shear stress on the 11th slip system for the single crystal [0 $\bar{1}$ 2], according to the $\alpha_\epsilon = \beta_\epsilon$ ratios.

3. HOMOGENEOUS AND HETEROGENEOUS DISLOCATION NUCLEATION: INFLUENCE OF THE STRAIN MULTIAXIALITY

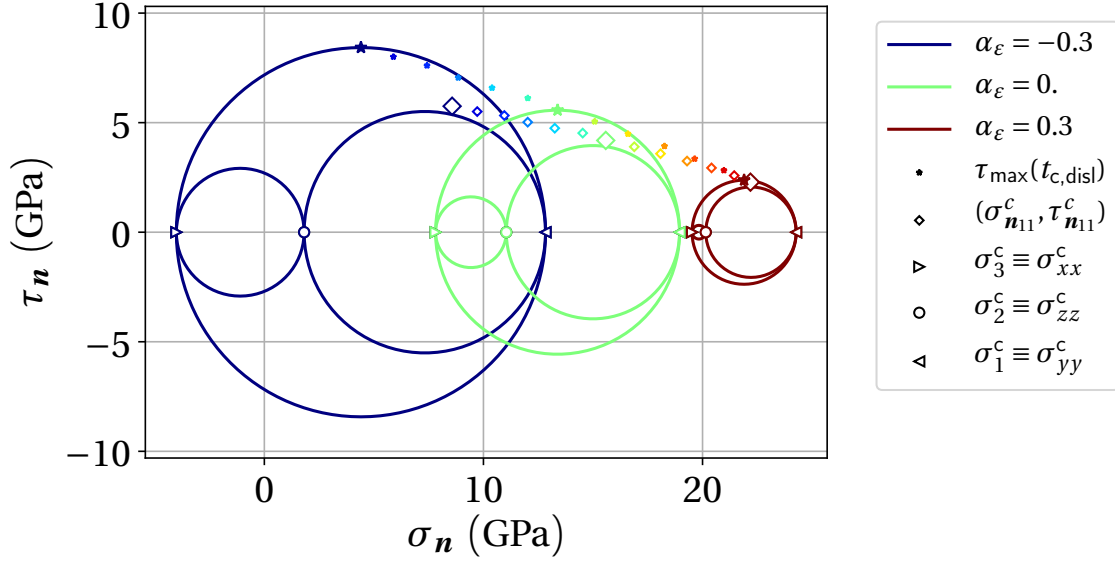


Figure 3.7: Mohr representation of the critical stress state at homogeneous dislocation nucleation in the cases of $\alpha_\varepsilon = \beta_\varepsilon = -0.3, 0$ and 0.3 . The maximum shear stress τ_{\max} and the actual stress state for the 11th slip system are displayed in black and red respectively for every multiaxial loading cases (from $\alpha_\varepsilon = -0.3$ (left) to $\alpha_\varepsilon = 0.3$ (right)).

This fully explains the increase of the critical stress $\sigma_{yy}^{c, \text{disl}}$ and critical strain $\varepsilon_{yy}^{c, \text{disl}}$ previously observed on figures 2.9, 2.10 for the single crystal. This should also explain the similar variations observed for all the grain boundaries on figure 2.13 as the same loadings are applied. Indeed the abovementioned reasoning holds whatever the system considered (i.e. single crystal or grain boundary) since no specification related to the system considered is implied. This confined plasticity effect should therefore also be valid at this scale and on any grain boundary.

Now, as the same variation can be observed for the GB case and assuming a constant critical stress for the GB decohesion (as previously observed whatever the loading cases), this trend also explains the complete disappearance of plasticity to the profit of the GB fracture at some high enough deformation ratios α_ε . Therefore, it is here suggested that the GB dislocation nucleation and decohesion are independent phenomena despite their common dependence over the nature of the grain boundary itself.

Nevertheless, the decreasing variation of the critical resolved shear stress $\tau_{nm}^{c, \text{disl}}$ (figure 3.6a or 3.4a) with the transverse ratios clearly contrasts with this increase of the critical stress normal to the grain boundary plane $\sigma_{yy}^{c, \text{disl}}$. Indeed, this last trend would indicate that dislocation nucleation is facilitated with the increase of the α_ε and β_ε ratios but it has clearly been shown that the incipient of plasticity is actually postponed.

It is interesting to note that the adjunction of transverse strains (and a fortiori the increase of transverse stresses) has therefore two competing effects with a predominant effect of the resolved shear stress decrease over the multiaxial behaviour of the grain

3. HOMOGENEOUS AND HETEROGENEOUS DISLOCATION NUCLEATION: INFLUENCE OF THE STRAIN MULTIAXIALITY

boundary (decrease of the critical resolved shear stress). This eventually leads to the grain boundary decohesion.

Assuming the same decrease of the resolved shear stress but a much stronger decreasing effect of the critical resolved shear stress may have led to an inverse variation (decrease) of the critical strain to dislocation nucleation if we relate to the tensile curves presented figure 2.7a. Following this reasoning, this hypothetical situation could have postponed the grain boundary decohesion to the point where only dislocation nucleation would have been observed as the grain boundary critical stress for decohesion would have never been attained or at least severely postponed.

The understanding of the critical resolved shear stress variation would then be of great importance if one wants to describe the frontier between those two behaviours.

Figures 3.4a and 3.4b also indicate an influence of the stress normal to the slip plane over the critical resolved shear stress as evolutions presented on figures 3.4a and 3.4b are clearly correlated. Similarly to the remarks of Spearot et al. [Spearot et al., 2008], it is found here that the increase of the normal stress to the slip plane may induce a decrease of the critical resolved shear stress, therefore inducing a significant non-Schmid effect.

Further discussion will be provided on that matter in the following section.

Once again, it appears that in the single crystal case, the resolved shear stress corresponds with negligible discrepancies to the results here obtained for the grain boundary. This remarks and the preceding results seem to indicate that the dislocation nucleation mechanism is almost not influenced by the presence of the $\Sigma 5$ GB $[0\bar{1}2]$. However, it is important to stress once again that this remarks only holds for this particular grain boundary in pure nickel as already shown before. This particular point has been studied extensively by Tschopp et al. [Tschopp et al., 2008] in copper and aluminium on several bicrystals and their single crystals counterparts under tensile and compressive loadings. The authors clearly show numerous discrepancies between the single crystals and the related bicrystal cases.

3.3 Further computations, comparisons and discussion

Based on the previous results and from an engineering point of view, the aim of this part is to achieve a partial understanding toward a general prediction of the bicrystal behaviour as illustrated by the scheme figure 3.8 where critical steps are highlighted in red and grey. A finality would therefore consists in the prediction of the transition observed between the dislocation nucleation zone and the grain boundary decohesion, at least for the $\Sigma 5$ $[0\bar{1}2]$.

As stated before, understanding the variation of the critical resolved shear stress in the case of the $\Sigma 5$ $[0\bar{1}2]$ grain boundary is of particular interest here.

To this extent, it is proposed to focus on the so called shear strength of the material considered here and its variation with regard to the lattice deformation. A first reminder of the Frenkel model and the generalised stacking fault energy curve are presented.

3. HOMOGENEOUS AND HETEROGENEOUS DISLOCATION NUCLEATION: INFLUENCE OF THE STRAIN MULTIAXIALITY

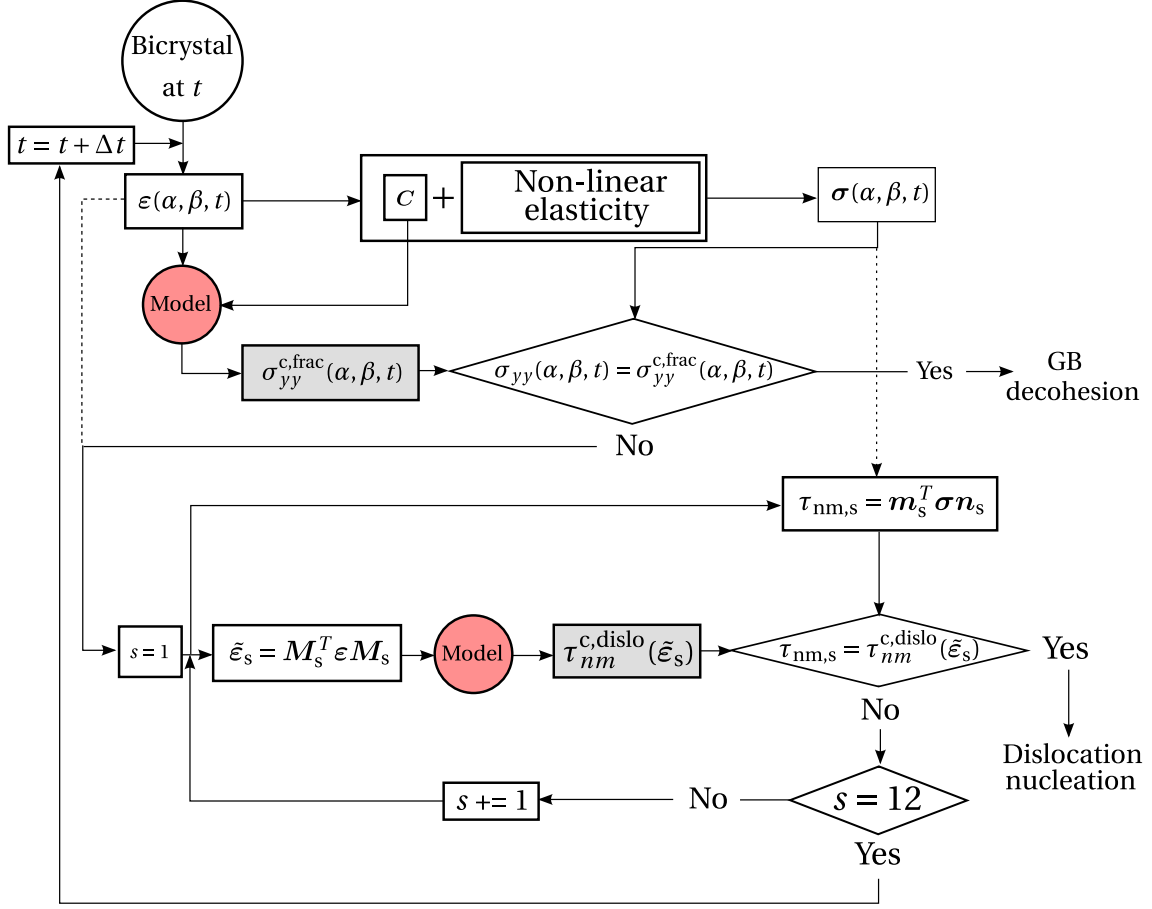


Figure 3.8: Proposed scheme to describe the critical behaviour of the bicrystal for dislocation nucleation or grain boundary decohesion. The $\tilde{\epsilon}_s$ matrix corresponding to the strain state in the related s slip system referential and related to the strain components in the referential of the bicrystal through the change of basis M_s .

3.3.1 The Frenkel model and the onset of a stacking fault

3.3.1.1 The Frenkel model

From previous results (figures 2.9a, 3.6a), it is clear that the mechanism for dislocation nucleation for the grain boundary or for the single crystal should be quite similar in terms of critical resolved shear stresses, at least for the $\Sigma 5$ $[0\bar{1}2]$ GB. It is therefore proposed to focus on the case of this particular single crystal ($[0\bar{1}2]$ tensile axis), which permits to decorelate the influence of the grain boundary.

It is reminded that in FCC systems, Shockley partial dislocations glide in $\langle 111 \rangle$ crystallographic planes inducing a displacement in the directions $\langle 112 \rangle$ as it propagates through the matrix.

It is well known that this amount of displacement can be assessed by a Burgers

3. HOMOGENEOUS AND HETEROGENEOUS DISLOCATION NUCLEATION: INFLUENCE OF THE STRAIN MULTIAXIALITY

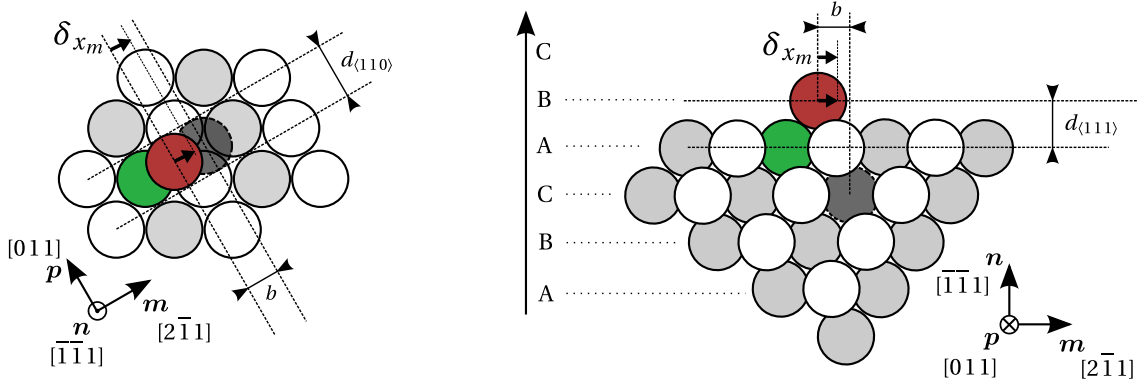


Figure 3.9: Scheme for the onset of a stacking fault leading to the nucleation of a Shockley partial dislocation. The 11th slip system referential ($[2\bar{1}1]$, $[011]$, $[\bar{1}\bar{1}1]$) is arbitrarily chosen for the exemple.

circuit around the dislocation core revealing a displacement of one Burgers vector $\mathbf{b} = \frac{a}{6} \langle 112 \rangle$, with a the lattice parameter of the material considered (equal to a_0 the initial lattice parameter at the undeformed state).

As previously observed, the nucleation of a Shockley partial dislocation can also be seen as the formation of an intrinsic stacking fault delimited by the partial dislocation which expend in order to accomodate the deformation.

In 1926, the Frenkel model [Frenkel, 1926] was used in an attempt to understand the underlying mecanism of plasticity, trying to assess an ideal shear strength depending on the material considered. The application of the Frenkel model mainly consisted in considering the plastic deformation as the gliding of an entire atomic plane relatively to an other one in a specific direction [Hull and Bacon, 2011].

Figure 3.9 represents a similar situation for the case of the onset of an intrinsic stacking faults where the atom in red is adopting the same rigid translation as the entire atomic planes above which is to be glided in the $\langle 112 \rangle$ direction over the $\langle 111 \rangle$ atomic plane underneath.

The result being the nucleation of a Shockley partial dislocation and the onset of an intrinsic stacking fault as the regular piling patern in the $\langle 111 \rangle$ direction ABCABC switches to a defaulted stacking sequence ABCACA as illustrated on the right scheme of figure 3.9.

As underlined by Cai et al. [Cai et al., 2018] and as illustrated by this scheme, it is quite clear that some directions of gliding are energetically much more demanding rendering them not admissible (e.g. the gliding direction with the red atom passing above the green atom). This particular point is, a priori, not taken into account in a Schmid criterion, preferably used for dislocation propagation which significantly differs from the situation herein. The related admissible gliding directions previously already considered in chapter 2 are listed in table 3.1 and partially illustrated on figure 3.3 for two gliding planes.

3. HOMOGENEOUS AND HETEROGENEOUS DISLOCATION NUCLEATION: INFLUENCE OF THE STRAIN MULTIAXIALITY

In his model, Frenkel proposed to approximate the energetical landscape in a particular direction of gliding with the two first terms of a Fourier development. He could deduced a theoretical critical shear stress τ_{Frenkel}^c requiered for one atomic plane to cross energetical barriers with an elastic hypothesis via the shear modulus μ in the same direction and considering an undeformed state of the lattice (the full developpment can be found in [Kelly and MacMillan, 1986, Hull and Bacon, 2011]).

In the example of the configuration depicted figure 3.9 for the onset of a stacking fault, the following formulation illustrates the above reasoning:

$$\gamma(\delta_{x_m}) = \frac{\mu b^2}{4\pi^2 d} \left(1 - \cos \frac{2\pi \delta_{x_m}}{b} \right) \quad (3.2)$$

$$\tau(\delta_{x_m}) = \frac{d\gamma}{d\delta_{x_m}} = \frac{\mu b}{2\pi d} \sin \frac{2\pi \delta_{x_m}}{b} \quad (3.3)$$

$$\tau_{\text{Frenkel}}^c = \max_{\delta_{x_m}} \tau(\delta_{x_m}) = \frac{\mu b}{2\pi d} \quad (3.4)$$

δ_{x_m} being the distance traveled in the gliding direction ($\mathbf{m} \propto \langle 112 \rangle$) by the upper $\langle 111 \rangle$ atomic layer over the lower atomic layer, b the norm of the Burgers vector of the partial dislocation or the distance to travel for a full formation of the stacking fault, d the $\langle 111 \rangle$ interplane spacing, $\gamma(\delta_{x_m})$ the normalised energetical landscape in the gliding direction or generalised stacking fault energy curve and $\tau(\delta_{x_m})$ the assossiated shear stress (necessary for the gliding process). It is from equation 3.4 that is derived the well-known approximation $\tau^c \approx \frac{\mu}{10}$. Indeed the quantity $\frac{b}{2\pi d}$ can be reduced to the ratio $\frac{1}{2\pi\sqrt{2}} \approx \frac{1}{9}$, considering that $b = \frac{a}{\sqrt{6}}$ and $d = \frac{a}{\sqrt{3}}$.

At the time, it was pointed out that the model prediction clearly indicated discrepancies of several orders of magnitude with values of critical shear stress in GPa as only few MPa seemed to be necessary for the onset of plasticity.

Later on, the dislocation model provided a clear explanation of this discrepancies. Those linear defects, evidenced experimentaly, successfully described cristal plasticity and its underlying mecanisms at the atomic scale. One of the explanation for the discrepancies of the Frenkel model rises from the fact that shearing by the gliding of an atomic plane was obviously much more energetically demanding than the propagation of a linear defect already present in the matrix.

3.3.1.2 Applicability

As pointed out by Hull and Bacon [Hull and Bacon, 2011] but also widely observed experimentaly, it is interesting to note that in the case of mechanical sollicitations on nanopillars or microtensile sample, the onset of plasticity is obtained with increasing values of the yield stress with magnitudes approaching the Frenkel estimatation. References of micro compression or micro tensile tests can illustrate this particular point for irradiated or non irradiated materials [Hosemann, 2018]. These size effects are to be partly interpreted in the context of a decreasing density of glissile dislocations in

3. HOMOGENEOUS AND HETEROGENEOUS DISLOCATION NUCLEATION: INFLUENCE OF THE STRAIN MULTIAXIALITY

the matrix for decreasing volumes of material and a higher probability for dislocation nucleation from surfaces.

A similar context can be found in nanoindentation experiments. Assessment of critical resolved shear stresses between (2.12 ± 0.43) GPa and (4.29 ± 0.42) GPa are found by Tokuda et al. [Tokuda et al., 2018] for a $\Sigma 3$ $(1\bar{1}0)$ $[111]$ grain boundary and in the bulk (respectively) of a pure aluminium bicrystal sample from the first pop-in occurring during nanoindentation testings.

Isamu et al. [Isamu and Tsurekawa, 2019] have conducted similar experiments on a pure nickel bicrystal. They have found critical resolved shear stresses of (3.34 ± 0.24) GPa and (3.76 ± 0.29) GPa for a $\Sigma 3$ grain boundary and in the bulk respectively.

The MD computed values presented figure 3.4a between 2.5 GPa and 4.5 GPa (mean value of 3.5 GPa) for the critical resolved shear stress show a rather good agreement with those experimental values even if the performed simulations are obviously not directly comparable.

Indeed, multi-scale simulations of nanoindentation [Tadmor et al., 1999] using the so-called quasicontinuum method [Tadmor et al., 1996a, Tadmor et al., 1996b], have shown different plasticity mechanisms at the atomic scale induced by a nanoindentation sollicitation, from nanotwinning to partial dislocation nucleations. However this measurement still quantitatively indicates a satisfying agreement which roughly validates the use of the Mishin potential used for pure nickel [Mishin, 2004].

3.3.1.3 Generalised stacking fault energy curve and critical resolved shear stress for heterogeneous and homogeneous dislocation nucleation

As already stressed, the generalised stacking fault energy (GSFE) curve, directly linked to the onset of the stacking fault and partly approximated by the Frenkel model (equation 3.2), is of particular importance for the understanding of partial dislocation nucleation in FCC metals.

In 1992, Rice [Rice, 1992] used a similar approach for his model of dislocation nucleation at the crack tip, considering the unstable stacking fault energy (first peak of the GSFE curve) as an important parameter. In that case, the stress state is obviously not homogeneous as stress concentrations are involved. However it is obvious that a distinction has to be made between the imposed stress (induced here by the mechanical loading and the presence of the crack) and the necessary stress to be imposed for the onset of plasticity.

In our case the critical resolved shear stress should originates from the same mechanism previously described and, as already implied, the GSFE curve has to be considered for the prediction of the homogeneous partial dislocation nucleation.

It is expected that the case of heterogeneous partial dislocation nucleation from the grain boundary should also follow this mechanism. In that context, the discrepancies observed by Tschopp et al. [Tschopp et al., 2008] between the two cases for certain grain boundaries could be related to local stress (or strain) inherent to the interface as already illustrated in chapitre 2. Should one be able to quantify those residual atomic stresses,

3. HOMOGENEOUS AND HETEROGENEOUS DISLOCATION NUCLEATION: INFLUENCE OF THE STRAIN MULTIAXIALITY

it is suggested here that the prediction of dislocation nucleation may follow the same approach presented before in figure 3.8, but considering a pre-stressed state.

This framework is also indicated should one wonder if the onset of intergranular cracking induced by clear bands or slip bands impacts is expected at the atomic scale. Indeed, for the volumes of material considered here (typically the volumes of the simulated bicrystals and single crystals), it would seem appropriate to envision a very low density of dislocations already present in the matrix ; the extreme case being the perfect crystals used in the present MD simulation models.

With that respect, the occurrence of either dislocation nucleation at the grain boundary or decohesion of the grain boundary should be considered even if the critical stresses involved in both cases are several order of magnitude higher than the resolved shear stresses for dislocation gliding.

A presentation of the GSFE curve, as obtained by the chosen semi-empirical potential, is now proposed in order to get access to the basic understanding of the simulation results obtained earlier in this chapter for the dislocation nucleation in the $[0\bar{1}2]$ single crystal case.

3.3.2 Molecular static computation of the generalised stacking fault energy curve

The GSFE curve at 0 K is obtained by molecular static computations consisting in iteratively displacing by an amount δ_{x_m} , one block of atoms over another atomic block in one of the admissible $\langle 112 \rangle$ directions of gliding (as referenced in table 3.1) and in one of the $\langle 111 \rangle$ atomic planes. As illustrated on figure 3.9, the 11th slip system is chosen arbitrarily with the crystallographic directions $[2\bar{1}1]$, $[\bar{1}\bar{1}1]$ and $[011]$.

Periodic boundary conditions are used according to the $[2\bar{1}1]$ and $[011]$ directions. The total potential energy γ , normalised by the section of the system is recorded at each displacement δ_{x_m} .

The GSFE curve is displayed by the blue points on figure 3.10a and the related shear stress - displacement curve is obtained by the first derivative of the GSFE and shown on figure 3.10b. It is verified that the unstable stacking fault energy $\gamma_{us} = 298 \text{ mJ m}^{-2}$ and the intrinsic SF energy $\gamma_{SF} = 134 \text{ mJ m}^{-2}$ as indicated by Mishin [Mishin, 2004] with this potential, are recovered here. They are respectively derived from the energies of the first energetical barrier and at the second local minimum for which a distance of one Burgers vector amplitude b is covered resulting in the stacking fault formation (site identified by the dark grey atoms situated two atomic plane underneath, figures 3.9 and 3.12).

The unstable stacking fault energy, corresponds to the energetical saddle point attained at approximately $\delta_{x_m} = \frac{b}{2}$ (red atom passing by the white atoms on the upper left schemes, figures 3.9 and 3.12).

The Frenkel model, is applied with the values of the Burgers vector amplitude $b = \frac{a}{\sqrt{6}}$ and interplane spacing $d_{\langle 111 \rangle} = \frac{a}{\sqrt{3}}$ obtained from the lattice parameter $a = a_0 = 3.52 \text{ \AA}$ at 0 K. A shear modulus μ of 57.6 GPa in the $([2\bar{1}1], [\bar{1}\bar{1}1], [011])$ crystalline referential is

3. HOMOGENEOUS AND HETEROGENEOUS DISLOCATION NUCLEATION: INFLUENCE OF THE STRAIN MULTIAXIALITY

obtained from the cubic elastic constants of the potential at 0 K: C_{11} , C_{12} and C_{44} listed in table 2.1 and the following formulation [Kelly and MacMillan, 1986]:

$$\mu = \frac{3C_{44}(C_{11} - C_{12})}{4C_{44} + C_{11} - C_{12}}$$

The evolution of the model is also plotted figures 3.10a and 3.10b. A very good approximation of the critical resolved shear stress is found with a discrepancy of about 8 % between the computed value $\tau_{0K}^{c,dislo} = 6.0$ GPa and the prediction of the Frenkel model $\tau_{Frenkel}^{c,dislo} = 6.5$ GPa. This discrepancy is certainly related to the omission of further terms in the Frenkel development of the GSFE.

MacKenzie proposed in 1949 [Kelly and MacMillan, 1986] to describe more thoroughly the GSFE by adding further terms in the developpement considering the presence of atomic sites C_0 , A , P , B and C_2 along the $\langle 112 \rangle$ direction as illustrated figure 3.11, with the following formulation:

$$U(x) = K \left[\cos\left(\frac{2\pi x}{3}\right) + \alpha \cos\left(\frac{4\pi x}{3}\right) + \beta \cos\left(\frac{6\pi x}{3}\right) \right] \quad (3.5)$$

with $Ub \equiv \gamma$, $x = x_m + 1 = \frac{\delta_{x_m}}{b} + 1$. Imposing a flat slope for $U(x)$ at $x = 0, 1, 2$ and 3 yields the following expression of $\tau(x) = \frac{dU}{dx}$ with $\alpha = 0.5$:

$$\tau(x) = \frac{2\pi K}{3} \sin\left(\frac{2\pi x}{3}\right) \left(1 + 2 \cos\left(\frac{2\pi x}{3}\right)\right) \left(1 - 3\beta + 6\beta \cos\left(\frac{2\pi x}{3}\right)\right) \quad (3.6)$$

with K a constant linked to the shear modulus via the same elastic fit of Frenkel described before at $\delta_{x_m} = 0$:

$$\frac{d\tau}{d\gamma}(x=1) = \mu = \frac{2\pi^2}{3} K \frac{d}{b} (1 - 6\beta) \quad (3.7)$$

with $\gamma = \frac{x}{a} = \frac{x}{bd}$ and the fitting parameter β . This β parameter possesses a critical value of $\frac{1}{8}$ for which the energy at point P is zero which correspond to the disappearance of the energy barrier.

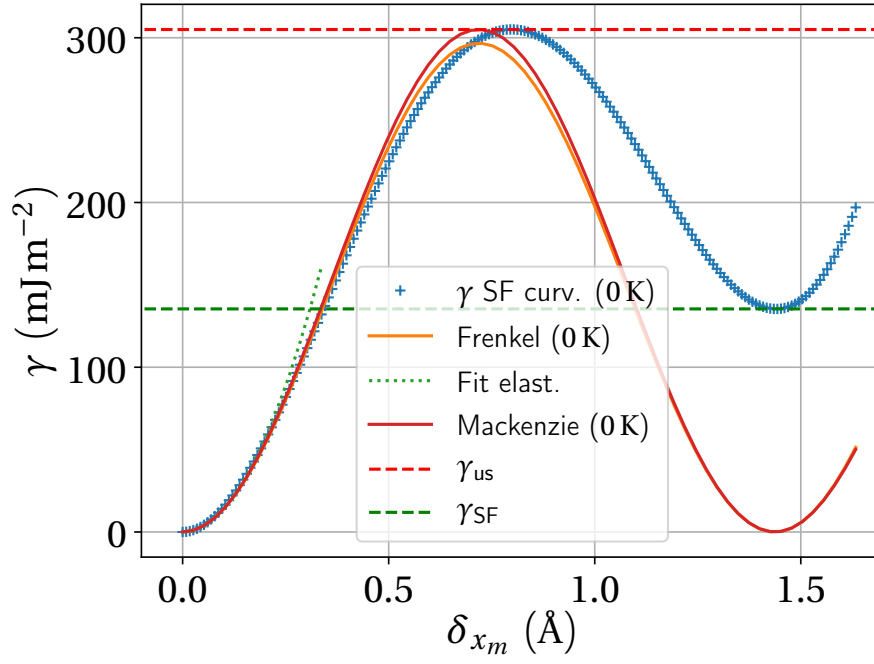
This simple reasoning led to the well-known approximation $\tau_{MacKenzie}^{c,dislo} \approx \frac{\mu}{30}$, which actually constitutes a lower limit. With the preceding value of μ , this estimation provides therefore the most conservative value of the critical shear stress at 0 K, $\tau_{MacKenzie}^{c,dislo} = 1.92$ GPa in our particular case, which is obviously too conservative for our concern.

It is chosen to fit the β parameter so that the unstable stacking fault energy (which is assumed to be a material property, here derived by the potential of Mishin) is recovered at the first energetical peak of the model for $x = \frac{3}{2}$:

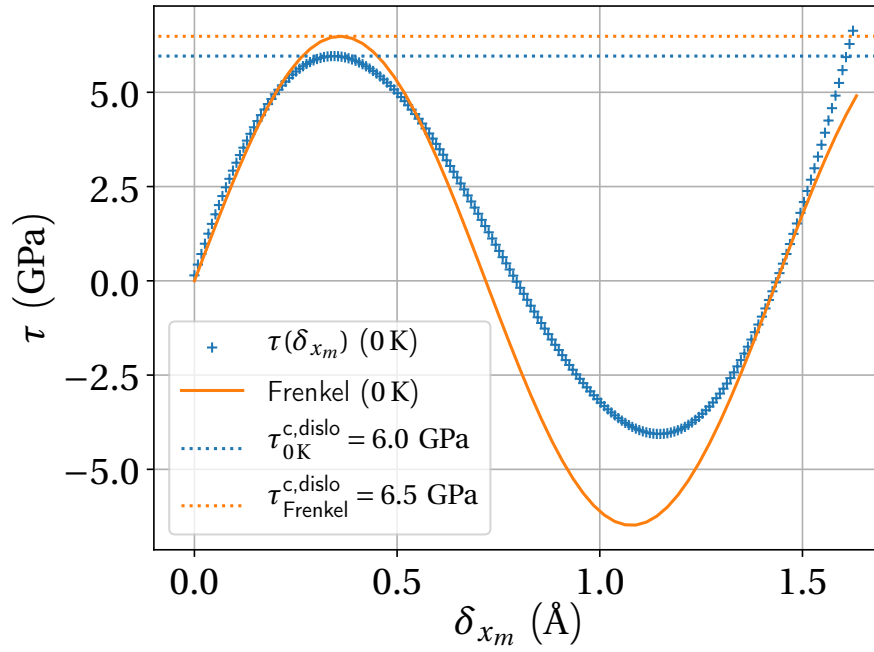
$$U\left(\frac{3}{2}\right) - U(1) = \frac{\gamma_{us}}{b}$$

The obtained comparison with the MacKenzie model is provided on figure 3.10a, however this application does not provide a better prediction. Similarly to the Frenkel model,

3. HOMOGENEOUS AND HETEROGENEOUS DISLOCATION NUCLEATION: INFLUENCE OF THE STRAIN MULTIAXIALITY



(a)



(b)

Figure 3.10: Stacking fault energy curve by molecular static with pure Ni Mishin potential and comparison with the Frenkel model (figure 3.10a). Shear stress deduced from direct derivation of the SF energy curve (figure 3.10b).

3. HOMOGENEOUS AND HETEROGENEOUS DISLOCATION NUCLEATION: INFLUENCE OF THE STRAIN MULTIAXIALITY

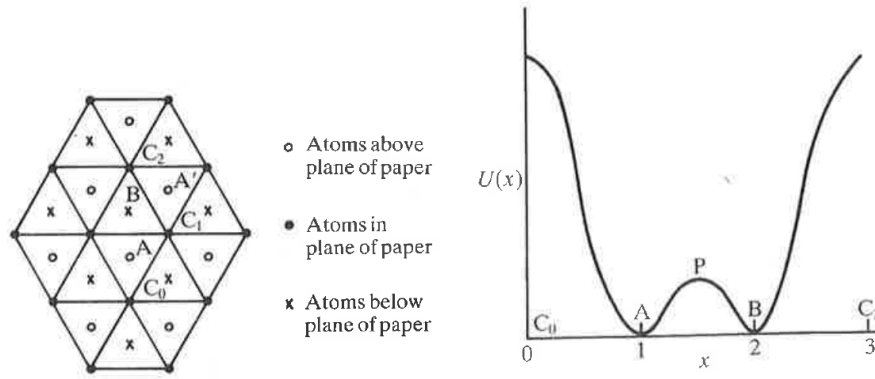


Figure 3.11: Figures extracted from Kelly and MacMillan [Kelly and MacMillan, 1986], illustrating three $[1\ 1\ 1]$ (for example) FCC planes with the following directions $\overrightarrow{C_0 C_2} \equiv [1\ 1\ \bar{2}]$, $\overrightarrow{AA'} \equiv [1\ 0\ \bar{1}]$ (left) and the MacKenzie model of the curve $U(x)$ with $U = \gamma b$ and $x = x_m + 1$

the MacKenzie model does not permit to reach the correct abscissa of the first energetical barrier related to the unstable stacking fault energy which seems to be an essential parameter for partial dislocation nucleation as already pointed out by several authors [Rice, 1992, Van Swygenhoven and Derlet, 2008]. The reasons may be partly linked to the fact that the 2nd atomic layer underneath the moving block is not described in the Fourier or the MacKenzie development and in particular, the site at $x = 2$ (above the grey atom two planes underneath on figure 3.9)

Therefore, the preceding models illustrates the importance of the unstable stacking fault energy for the description of the onset of partial dislocations. The values predicted constitute good approximations, and the underlying mechanisms of dislocation nucleation is directly correlated to the deducted value of $\tau^{C,dislo}$ at the inflexion point through the onset of the stacking fault.

However, one of the hypothesis of those formulations considering an undeformed lattice should be reconsidered in our case. Indeed, it has already been shown that the transverse/normal strain ratios α_ϵ and β_ϵ induce consequent variations of the critical resolved shear stress. Furthermore, it is logical to consider a non-negligible impact of the lattice deformation over the γ - surface of the $\langle 1\ 1\ 1 \rangle$ planes: as illustrated on figure 3.12 and based on the preceding GSFE curve, it is easily conceivable that the stretching of interatomic distances with lattice deformations might have a significative impact on the GSFE curve and thus on the related critical resolved shear stress.

Atomistic studies [Andric et al., 2019, Cai et al., 2018] show the influence of the stress or strain state over the GSFE curve with both non negligible variations of the intrinsic stacking fault energy and the unstable stacking fault energy. Cai et al. [Cai et al., 2018] has recently pointed out the importance of the lattice deformation as one main contributor to the CRSS variations. The authors also point forward the necessity to consider specific directions for the possible glides along the $\langle 1\ 1\ 2 \rangle$ directions in

3. HOMOGENEOUS AND HETEROGENEOUS DISLOCATION NUCLEATION: INFLUENCE OF THE STRAIN MULTIAXIALITY

order to take into account non-Schmid effects for partial dislocation nucleation. As already explained, this particular point has been taken care of and further explains the activated slip systems observed on figure 3.5 in the dislocation analysis section 3.2.2. The non-Schmid effect can clearly be explained here by the negative value of the maximum resolved shear stress obtained using the admissible direction for this slip system. It indicates that the shearing of the planes is occurring in the opposite direction and therefore is less likely to happen as opposed to the second slip system which is effectively activated first.

These admissible directions should be systematically taken into account for the twelve slip systems considered.

Finally, in order to explain the variations of the CRSS with the lattice deformation, a comparison is proposed between the CRSS based on the MS computations of the GSFE curves $\tau_{SF}^{c,dislo}(\epsilon^c(\alpha_\epsilon, \beta_\epsilon))$ taking into account a lattice pre-deformation extracted from the preceding MD computations just before dislocation nucleation, and the corresponding $\tau_T^{c,dislo}$ as obtained previously by the former MD computations on the single crystal at temperatures $T = 10$ K, 150 K and 300 K.

3.3.3 Influence of the lattice deformation on the nucleation of partial dislocations

From the MD computations on the $[0\bar{1}2]$ single crystal at different temperatures presented in the preceding chapter, partial dislocation nucleations have been once again evidenced with the same activated slip system.

Figure 3.12 illustrates the lattice deformations in the referential of the 11th activated slip system $(\mathbf{m}_{11}, \mathbf{p}_{11}, \mathbf{n}_{11})$ computed just before dislocation nucleation. Figure 3.13 shows the evolution of the six components of the critical deformations at the dislocation nucleation point as function of the α_ϵ ratio. For instance, the deformation components in the (\mathbf{p}, \mathbf{m}) plane is computed as follows:

$$\epsilon_{mm} = \mathbf{m}_{11}^T \boldsymbol{\epsilon} \mathbf{m}_{11}$$

$$\epsilon_{pp} = \mathbf{p}_{11}^T \boldsymbol{\epsilon} \mathbf{p}_{11}$$

$$\gamma_{pm} = \mathbf{m}_{11}^T \boldsymbol{\epsilon} \mathbf{p}_{11}$$

The other components are similarly obtained. In the following developments, the subscript of the 11th slip system shall be further omitted for lisibility purposes.

The effective deformation component ϵ_{mm} are also evaluated from the MD computation results by referencing systematically the Burgers vectors amplitudes b in every cases after just after the dislocation nucleation and by comparison with the initial Burgers vector b_0 :

$$\epsilon_{mm}^{MD} = \frac{b - b_0}{b_0}$$

3. HOMOGENEOUS AND HETEROGENEOUS DISLOCATION NUCLEATION: INFLUENCE OF THE STRAIN MULTIAXIALITY

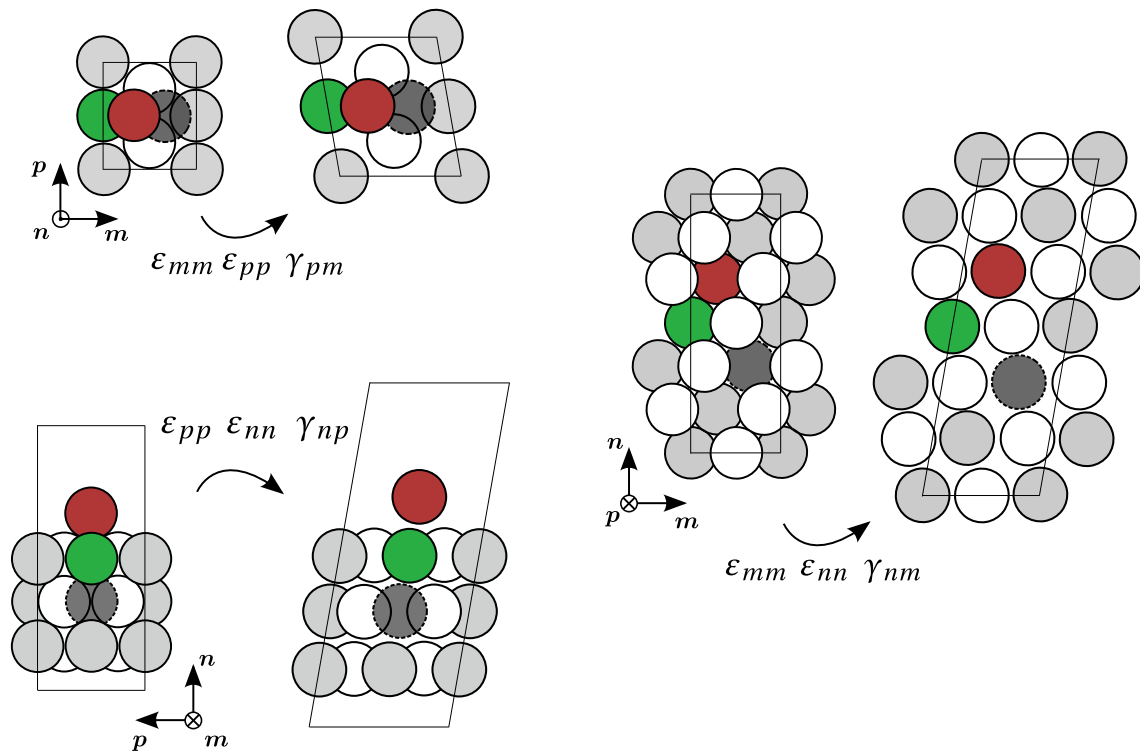


Figure 3.12: Schemes of the deformed cristalline lattice in the slip system referential in relation with the creation of a stacking fault. Only in-plane deformations are represented, with respectively the $\langle 111 \rangle$, $\langle 110 \rangle$ and $\langle 112 \rangle$ planes (clockwise).

3. HOMOGENEOUS AND HETEROGENEOUS DISLOCATION NUCLEATION: INFLUENCE OF THE STRAIN MULTIAXIALITY

The DXA algorithm of OVITO is purposely used. Indeed, it provides the effective measure of b as a Burgers circuit is applied on the nucleated dislocation.

Similarly, a measure of the $[\bar{1}\bar{1}1]$ interplane spacing $d_{[\bar{1}\bar{1}1]}$ is carried out on the configuration just before the dislocation nucleation using the projection of atomic coordinates on the updated normal direction \mathbf{n} after deformation and pics detection. As before the initial distance d_0 is used for computing the normal deformation ε_{nn} .

Figures 3.13a and 3.13e show a good agreement between the projected values and the actual assessment using the computed configurations. It is therefore considered that the projection values for the other components are indeed valid. Those plots clearly show a strong variability of strain deformations just before dislocation nucleation for the different loading cases. Deformations between 0 % and 13 % are registered with the highest values for the components acting on the normal plane ε_{nn} and γ_{nm} and non negligible values for the other components. This clearly indicates that the lattice deformations are not negligible whatever the component considered, and as this assessment is obtained for the activated slip system, it is also mandatory to study their effect on the critical resolved shear stress.

Systematic molecular static computations of GSFE curves are then performed as before, but with a pre deformed lattice using the strain tensors already extracted from the MD computations and expressed in the 11th activated slip system referential.

Two types of simulation are used: a first one using only strain diagonal components ε_{ii} , and a second one using the full description of the strain tensor adding the shear deformation components γ_{ij} (in the slip system referential).

Those two sets of calculations, allow an interesting comparison for the determination of predominant deformation effects. It is reminded here that those simulations are now performed in static at 0 K but taking into account critical deformations recorded for MD computations at different temperature. This procedure allows to get rid of potential thermal activation effects and therefore strengthen the comparison with the MD results.

The computed critical resolved shear stresses for both sets of simulations and considering the deformations at 10 K are presented figure 3.14a along with the shear stress evolution curves figure 3.14b computed from the related stacking fault energy curves considering the full strain tensors pre-deformations. On this last figure, it is logical that the first point of the curve originates from a position close to the CRSS as the considered pre-deformation states are obtained just before dislocation nucleation. A decrease of the CRSS characterised by the local maximum of the curves is identified with the increase of the $\alpha_\varepsilon = \beta_\varepsilon$ ratios as expected from the previous results.

Comparison figure 3.14a of the computed values of $\tau_{10K}^{c,dislo}$ for both sets of MS simulations with the MD values registred before on single crystal and bicrystal reveals a very good agreement in terms of evolution and amplitudes for both sets. It is clear that the diagonal deformations are playing a major role for describing the decreasing evolution of the CRSS, however it is also clear that considering the full strain tensor is here mandatory in order to obtain more accurate values. Indeed, discrepancies of about 20 %

3. HOMOGENEOUS AND HETEROGENEOUS DISLOCATION NUCLEATION: INFLUENCE OF THE STRAIN MULTIAXIALITY

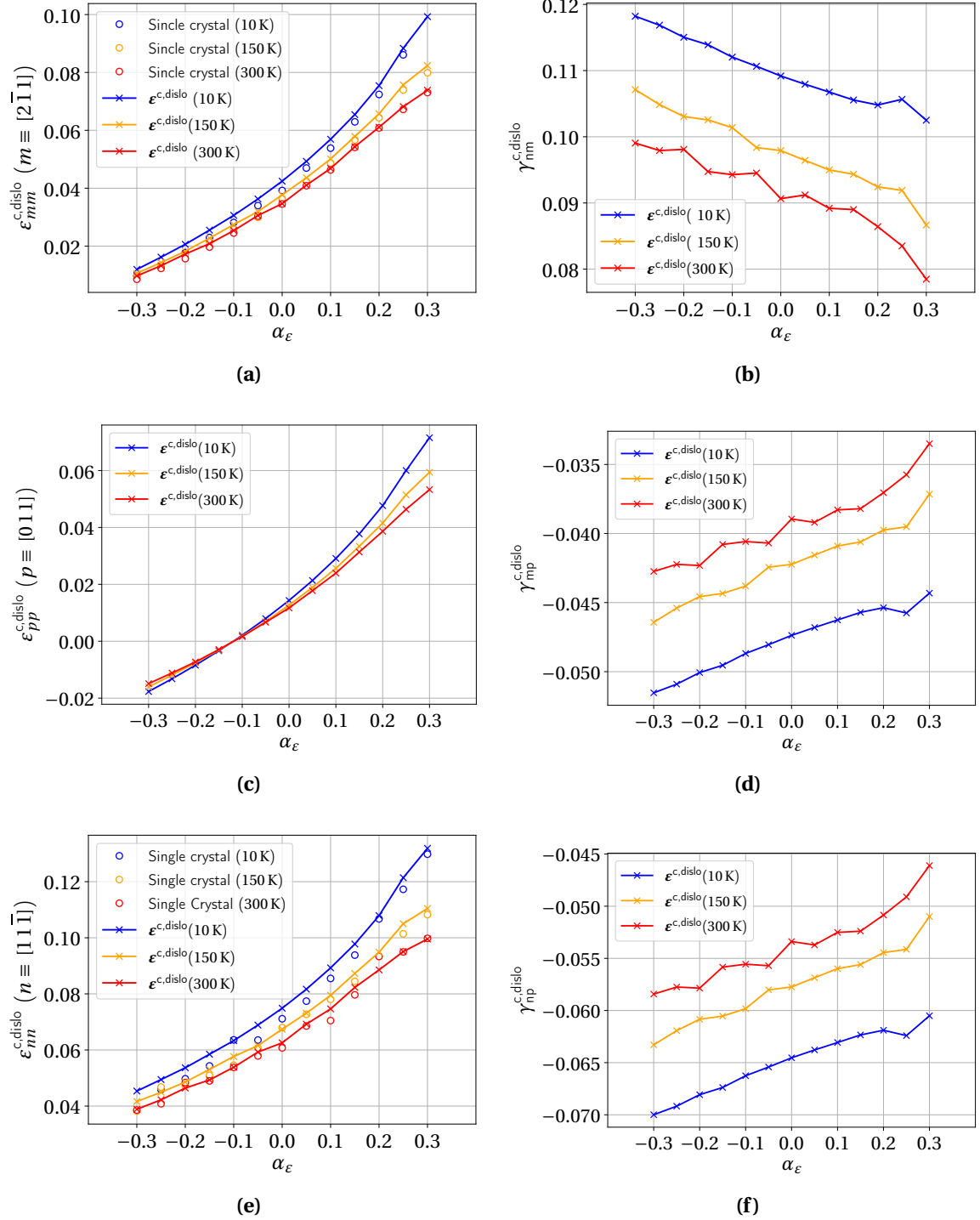


Figure 3.13: Critical deformations to dislocation nucleation in the activated slip system referential for the single crystal and for the different loadings $\alpha_\varepsilon = \beta_\varepsilon$ with transverse ratios in the single crystal referential.

3. HOMOGENEOUS AND HETEROGENEOUS DISLOCATION NUCLEATION: INFLUENCE OF THE STRAIN MULTIAXIALITY

are registered for the $\alpha_\varepsilon = -0.3$, considering only diagonal strain deformations. This last figure therefore demonstrates the importance of considering lattice deformation for the assessment of the CRSS as variations between 6 GPa and 1.5 GPa are clearly reproduced here. The final discrepancies observed are certainly due to the thermal activation which are quite weak at 10 K. This last point will be discussed further in the next paragraph on the influence of temperature.

In conclusion, a model for the prediction of homogeneous dislocation nucleation in the single crystal case near 0 K necessitates to take into account the accurate description of the stacking fault energy curve with the full lattice deformation influence.

The models of Frenkel or Mackenzie provides fairly good approximation considering an undeformed lattice, but even in that case, it is observed that the first energetical barrier cannot be described accurately which directly impacts the computed CRSS at the inflexion point.

A more accurate analytical model would necessitate to define an elementary unit cell that should be representative enough for achieving the description of the first energetical barrier and its variation with deformation. A second pre-requisite for this model would be to achieve a description of the energetical landscape in the 2D space for the $\langle 111 \rangle$ plane. It would allow to take into account the influence of all the components of the strain tensor. This second point could be reached if a further analytical developement of the energetical landscape is carried out in the 3D space taking into account the presence of the atomic sites located in the predefined elementary cell. The extension of the development would then depends on the accuracy needed for the final prediction of the critical resolved shear stress $\tau^{c,dislo}$.

A more straightforward methodology consists in performing a complete map of the CRSS depending on the different strain components influence.

In order to gain more insight into the variations of the CRSS according to the lattice deformation, the same MS calculations are therefore performed as before, but using this time numerous different pre-deformation states by varying independently only three diagonal components ε_{mm} , ε_{pp} and ε_{nn} between -15% and 15% with a step of 1% .

The influence of the shear deformation components are not taken into account here as it is clear that the diagonal components have the major impact on the CRSS variation.

Furthermore taking into account the influence of the six strain components would necessitate a very large number of calculations. Here only $31^3 = 29791$ stacking fault energy curve assessments are obtained from those MS computations. It is obvious that ab initio computations would provide more accurate and physically-based assessments for this particular purpose, but it is also clear that the computational costs of performing such a task would not be reasonable in comparison.

The corresponding variations of the CRSS are displayed figure 3.15 for four normal pre-deformations $\varepsilon_{nn} = 0\%$, 5% , 10% and 15% in the $(\varepsilon_{mm}, \varepsilon_{pp})$ pre-deformation space.

The CRSS globally decreases with the increase of each deformation components. However this is not always the case as figure 3.15a clearly shows an increase of the

3. HOMOGENEOUS AND HETEROGENEOUS DISLOCATION NUCLEATION: INFLUENCE OF THE STRAIN MULTIAXIALITY

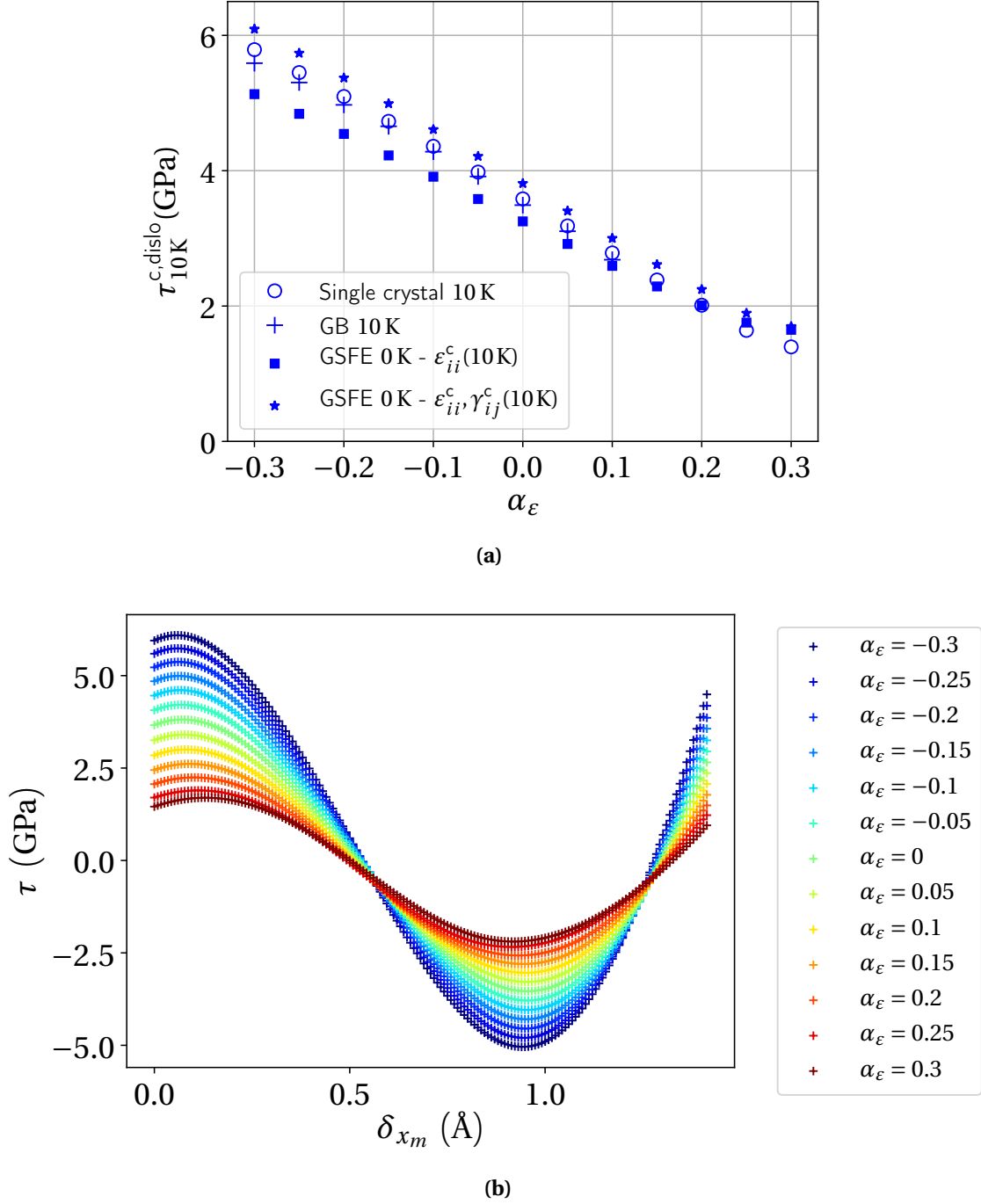


Figure 3.14: Comparison between $\tau_{SE,10K}^{c,dislo}(\epsilon)$ obtained by molecular static computations (using either ϵ_{ii} deformation components or ϵ_{ii} and γ_{ij} components) and molecular dynamics results of dislocation nucleation in the single crystal and in the bicrystal cases at 10 K (3.14a). Shear stress curves computed from the SFE curves at 0 K with the full predeformation obtained from the single crystal MD simulations at 10 K (3.14b).

3. HOMOGENEOUS AND HETEROGENEOUS DISLOCATION NUCLEATION: INFLUENCE OF THE STRAIN MULTIAXIALITY

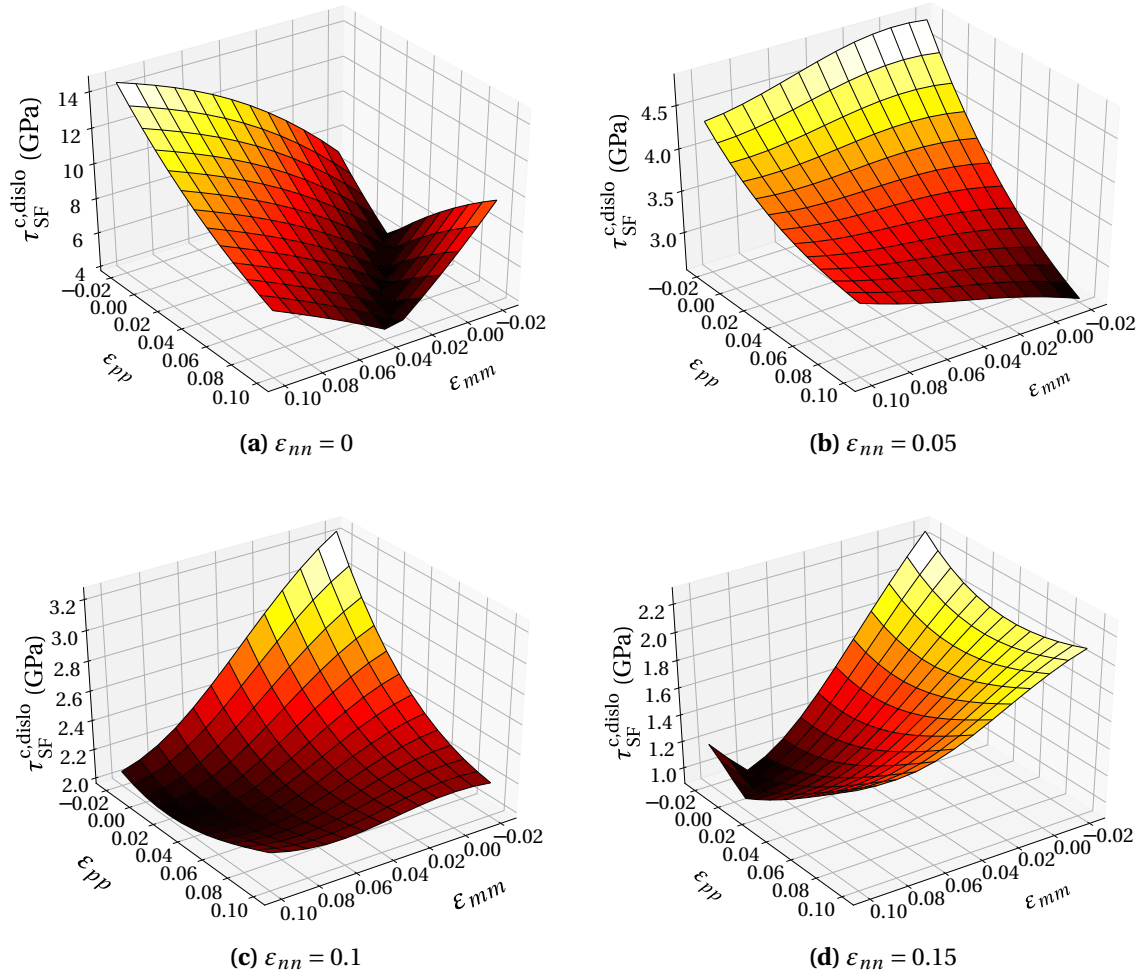


Figure 3.15: Parametrical characterisation of the critical resolved shear stress $\tau_{SF}^{c,dislo}(\epsilon_{ii})$, only varying ϵ_{bb} , ϵ_{pp} and ϵ_{nn} deformations with molecular static computations of SF curves.

3. HOMOGENEOUS AND HETEROGENEOUS DISLOCATION NUCLEATION: INFLUENCE OF THE STRAIN MULTIAXIALITY

CRSS with an increase of the deformation in the $\langle 112 \rangle$ direction for $\varepsilon_{nn} = 0$. This trend tends to reverse with the increase of the normal deformation. This observation can be easily understood considering figure 3.12 without the consideration of the shear deformations. Indeed, at $\varepsilon_{nn} = 0$, the deformation in the direction of glide ε_{bb} will energetically induce a deeper well and therefore more effort to escape it. As the normal deformation increases this influence will logically diminish as the increasing interplane distance $d_{\langle 111 \rangle}$ limits the digging of the well.

The global decrease of the CRSS with the increase of ε_{pp} can be explained for low normal deformations by the decrease of the unstable stacking fault energy at the first energetical barrier. As illustrated by the upper left scheme of figure 3.12 (without consideration of the shear deformations), the passage of the red atom travelling in the $\langle 112 \rangle$ direction will be eased by the increasing spacing between white atoms as ε_{pp} increases. This trend will again tends to disappear as the normal strain increases.

The influence of the normal deformation is similar. The global decrease of the CRSS can be explained by the less energetic passage in the gliding direction from $\delta_{xm} = 0$ to the saddle point.

From those results it can be concluded that the influence of the normal strain deformation (or the normal stress) on the CRSS is quite significant as observed before by several authors [Spearot et al., 2008, Ogata et al., 2002, Cai et al., 2018]. However, it is also clear that the transverse deformations induce significant variations as drops between 1 GPa (figure 3.15d) and 10 GPa (figure 3.15a) are registred. This constitutes variations of at least 50 % as evidenced by figure 3.15d for exemple, or even larger for low normal deformations with a drop of around 70 % at $\varepsilon_{nn} = 0$.

From a prediction point of view, it is also doubtful that a simple analytical model could encompass those influences as high lattice deformations would necessitate much more information than a simple use of linear elasticity as employed by the Frenkel and MacKenzie models. Furthermore, it is clear that taking those high deformations into account is mendatory in our case considering the values previously assessed at different temperatures just before the onset of partial dislocations (figure 3.13).

Here, it is therefore proposed to rely on the numerous computations performed by molecular statics since a step of 1 % is small enough to allow a rather good prediction of the CRSS with a linear interpolation between the data points.

In conclusion, the principal advantage of this method relies on the fact that the obtained data set is usable for every slip system and at any global deformation state which is quite advantageous in the context presented before, in figure 3.8. However, those computations are performed at 0 K and clearly neglect thermal activated mechanisms. Therefore, it is finally proposed to focus on the influence of the temperature.

3.3.4 Influence of the temperature

In this last section, the influence of the temperature over the CRSS is considered for 10 K, 150 K and 300 K.

3. HOMOGENEOUS AND HETEROGENEOUS DISLOCATION NUCLEATION: INFLUENCE OF THE STRAIN MULTIAXIALITY

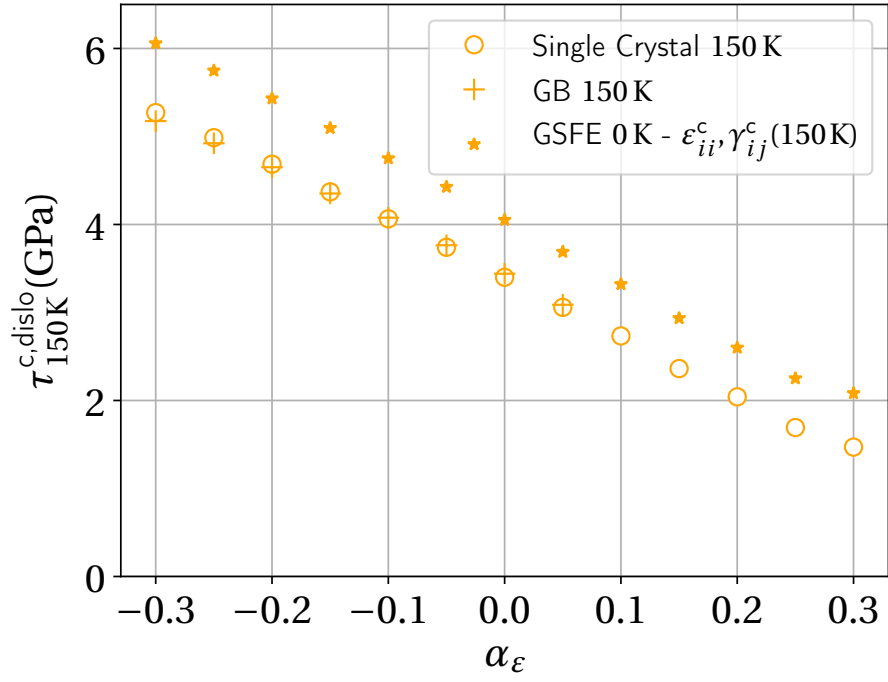
Figures 3.14, 3.16a and 3.16b present the results of the MD computations at respectively 10 K, 150 K and 300 K on the $\Sigma 5$ $[0\bar{1}2]$ grain boundary and the corresponding single crystals. A comparison with the results obtained from MS computations of the stacking fault energy curve considering the full strain tensor just before dislocation nucleation for different loading cases is also provided on the same figures.

As already noted for the results at 10 K, a decreasing variation of the CRSS is reproduced for every temperature, which once again points toward the necessity to consider the lattice deformation as a major contributor. It is also noted that this variation is almost not modified by the temperature as similar slopes for the MS results are obtained from the three data sets.

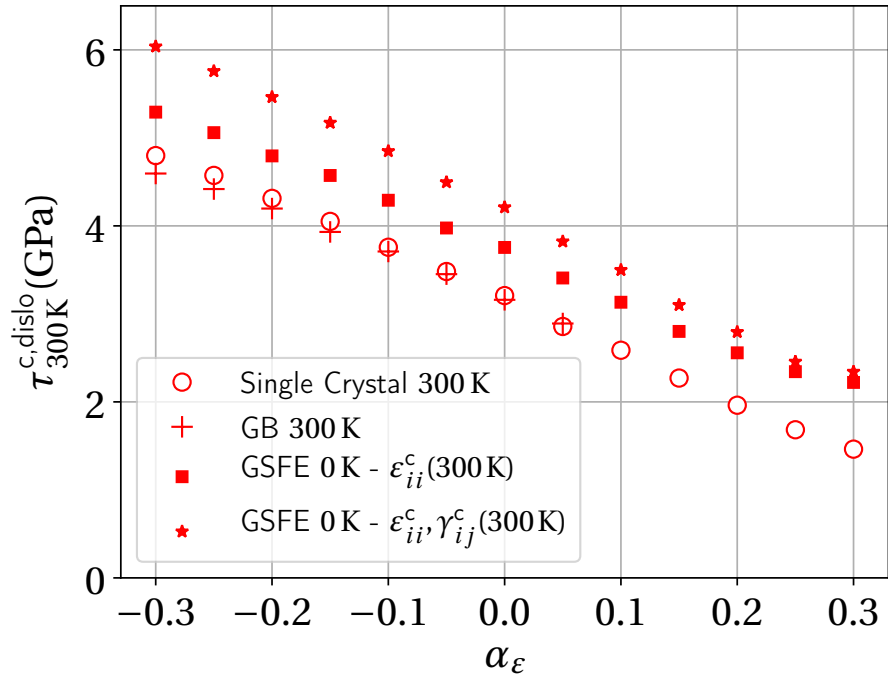
However, it is clear that a drop $\Delta\tau_T$ of the CRSS is evidenced with the increase of the temperature. The larger the discrepancy, the easier the dislocation is nucleated, as compared to the case with no thermal atomic motions (MS computation of the SF energy curves).

For each temperature a mean CRSS drop $\overline{\Delta\tau_T}$ over the α_ϵ ratios can be assessed revealing non negligible values of around 0.25 GPa, 0.65 GPa and 1.0 GPa for 10 K, 150 K and 300 K respectively. A thermal activation mechanism is clearly identified.

3. HOMOGENEOUS AND HETEROGENEOUS DISLOCATION NUCLEATION: INFLUENCE OF THE STRAIN MULTIAXIALITY



(a)



(b)

Figure 3.16: Comparison between $\tau_{SE,150K}^{c,dislo}(\epsilon)$, $\tau_{SE,300K}^{c,dislo}(\epsilon)$ and MD computations at 150 K and 300 K

3. HOMOGENEOUS AND HETEROGENEOUS DISLOCATION NUCLEATION: INFLUENCE OF THE STRAIN MULTIAXIALITY

3.4 Summary of the results and conclusion

3.4.1 Results

In this chapter, the following results are found:

- Heterogeneous and homogeneous dislocation nucleations (from the grain boundary or from the single crystal) clearly feature significant discrepancies in terms of critical stresses depending on the grain boundary considered but with no apparent geometrical correlation.
- Those discrepancies might be explained by the atomic GB stress fields, although their analytical description is not possible with the preceding GB mechanical or atomic description through the SU/GBD or SU models.
- Shockley partial dislocation nucleations are recorded for all the grain boundaries except for the $\Sigma 101$ and $\Sigma 25$ $[071]$ GBs which triggers near perfect dislocations nucleation. Only partial dislocations loops are emitted in the single crystals.
- The $\Sigma 5$ $[0\bar{1}2]$, $\Sigma 17$ $[053]$ and $\Sigma 25$ $[043]$ feature the same critical stress as their related single crystals.
- A more thorough investigation of the dislocation nucleation behaviour of the $\Sigma 5$ $[0\bar{1}2]$ indicates that a Schmid criterion cannot be used for the prediction of the activated slip system. This result can be explained by the admissible directions of gliding which should systematically be taken into account for a dislocation nucleation criterion.
- The confined plasticity effect previously observed along the increase of the critical stress to dislocation nucleation $\sigma_{yy}^{c,disl}$ with the increase of the transverse strain ratios $\alpha_\epsilon = \beta_\epsilon$ is logically explained by a simple stress state analysis underlying the importance of multiaxiality over the intergranular behaviour.
- A decrease of the critical resolved shear stress with the increase of the transverse/normal strain ratios is found, which seems to contradict the confined plasticity previously evidenced. A competition between the two effects (decrease of both the RSS and CRSS) is therefore evidenced.
- The variation of the critical resolved shear stress is fully explained by the deformation of the crystal lattice resulting in a significative variation of the related CRSS at the inflexion point.
- This effect of the lattice deformation cannot be described by the simple analytical models of Frenkel or MacKenzie and necessitates to take into account the full deformation tensor components in the slip systems referentials. In particular, the

3. HOMOGENEOUS AND HETEROGENEOUS DISLOCATION NUCLEATION: INFLUENCE OF THE STRAIN MULTIAXIALITY

diagonal strain components possess a major influence over the CRSS variation even if the effect of the non-diagonal components are non negligible.

- A numerical molecular static assessment of the GSFE curve and its variation according to the deformation can be achieved once for all and conveniently used for the prediction of partial dislocation nucleation in single crystals whatever the tensile axis. Its application is obviously restricted to the applications at 0 K as a non negligible thermoactivation mechanisms is evidenced.

3.4.2 Conclusion

The preliminary results of chapter 2 concerning the intergranular dislocation nucleation behaviour are fully explained and discussed in this chapter.

The homogeneous dislocation nucleation prediction in single crystals can be undertaken considering the modified Schmid criterion as proposed by Cai [Cai et al., 2018] along with the variation of the CRSS with the lattice deformation. This last effect clearly necessitates one set of atomistic simulations assessing the GSFE and its variations (only once, for all slip systems) considering a suitable potential.

The heterogeneous dislocations nucleation prediction in the perfect GB cases considered here is clearly restrained by the complexity of the GB structures and its related local atomic stress field. The mechanical description presented in chapter 2 is clearly not applicable to any grain boundary (specifically for the high angle GBs) and a general prediction would necessitate a case-by-case study with therefore no prediction value.

It appears that the prediction of the frontier between the dislocation nucleation and the GB decohesion zones whatever the grain boundary considered (in the framework of the scheme proposed in figure 3.8) shall require a more thorough study since it is clear that the dislocation nucleation prediction is mandatory for this purpose.

However, the similar multiaxial behaviours observed for a majority of the grain boundaries considered in chapter 2 indicate that the different effects explicitated here (e.g. the well-known multiaxial confined plasticity effect applicable at this scale, leading to GB decohesion) in the case of the $\Sigma 5$ $[0\bar{1}2]$ GB (and its related single crystal) should also be effective for any interface.

This key feature appears to be necessary for the assessment of the intergranular behaviour at slip bands/grain boundaries impacts with a possible competitive effect between GB fracture initiation and incipient plasticity as observed experimentally for discontinuous slip bands. It may also have implications for possible comparisons with experimental micro mechanical testing. The validity of the chosen potential is roughly confirmed by experimental comparison with nanoindentation mechanical tests on pure nickel grain boundaries.

4

Grain boundaries failure under homogeneous stress state

This chapter primarily focuses on the origins of the bicrystals failure observed previously by GB decohesion during the multiaxial loadings.

An important variation of the axial critical stress according to the rotation angle of the grain boundaries is evidenced with a seemingly geometrical correlation by pieces. It is shown that the atomistic description of the interface, is mandatory to explain this trend.

It is also found that the local volumic expansion recorded on the grain boundaries initial configuration and during the loading at particular disclination sites, constitutes a key point to understand and predict the elementary mechanism at the origin of the full GB decohesion.

In that respect, the prediction of the disclination debonding at grain boundaries can be envisioned in the context of the universal binding energy relation (UBER) of Rose et al., relating the cohesive energy of metals according to their changing lattice parameter. Comparison between the UBER model, constituting an input of the MD computations, and the disclination cohesive energy curve agrees reasonably well. Concerning the debonding of grain boundaries in metals, it is therefore suggested that their description as homophase interfaces should be primarily considered, as opposed to heterophase interfaces for which a separation of two naturally defined surface planes is generally pictured for the same matter.

The grain boundaries under study are finally described as predamaged phases of finite thickness featuring degraded apparent elastic modulus with respect to the bulk. This rather pragmatic description could be employed at upper scale in a continuum framework using the axial critical stress previously recorded, along with the assessed Griffith energies in a couple criterion for fracture initiation.

4. GRAIN BOUNDARIES FAILURE UNDER HOMOGENEOUS STRESS STATE

Contents

4.1 Grain boundaries decohesion	104
4.2 Critical stresses and Griffith energies of the different grain boundaries	104
4.2.1 Axial critical stress for the decohesion of the grain boundaries . . .	104
4.2.2 Griffith energies of the grain boundaries	107
4.2.3 The coupled criterion for the onset of intergranular cracking . . .	110
4.2.3.1 Paradox of the bar failure considering an energy criterion	110
4.2.3.2 Predominance of the stress criterion for the failure of the bicrystals under homogeneous stress state	112
4.3 Strain localisation at the grain boundaries	114
4.3.1 Thickness of the grain boundaries based on their intrinsic excess energy	115
4.3.2 Apparent Young modulus of the homophase interfaces	120
4.4 Local debonding of the grain boundary phase	127
4.4.1 Influence of the disclination atomic volumes	127
4.4.2 The universal binding energy relation	133
4.4.3 Local criterion for the onset of grain boundary decohesion . . .	138
4.4.3.1 Debonding mechanism and elementary representative volume	138
4.4.3.2 Comparison to the UBER model of Rose et al.	142
4.5 Summary of the results and conclusion	146
4.5.1 Results	146
4.5.2 Conclusion	149

4. GRAIN BOUNDARIES FAILURE UNDER HOMOGENEOUS STRESS STATE

4.1 Grain boundaries decohesion

In this chapter, a first part is dedicated to describe the previously observed GB fracture phenomenon through the derivation of critical stresses and critical energies. A second part focuses on a geometrical characterisation of the grain boundaries with a finite thickness assessment based on the excess energy of the interface. A grain boundary phase can then be described with its related critical fracture properties, featuring degraded apparent elastic modulus with respect to the adjacent bulks. A final part deals with the debonding mechanism observed at the origin of the bicrystal failure in the optic a possible prediction.

4.2 Critical stresses and Griffith energies of the different grain boundaries

The axial critical stresses $\sigma_{yy}^{c, \text{frac}}$ and the critical energies γ_c , obtained from the previous calculations presented in chapter 2, are here related to the geometrical description and to the atomic structure of the grain boundaries. The possibility to consider the axial critical stress, triggering the failure of the bicrystal, as a GB intrinsic parameter of fracture is further discussed.

4.2.1 Axial critical stress for the decohesion of the grain boundaries

The axial critical stresses $\sigma_{yy}^{c, \text{frac}}$ previously presented in figure 2.13 (2), for all the grain boundaries decohesions considering all the transverse/normal strain ratios α_ϵ and β_ϵ , are reported in figure 4.2 according to the rotation angle θ . The seemingly constant values (according to the multiaxial loading) of this critical stress, are evaluated in each GB case by the mean value over the saturation plateau previously described.

This plateau is further illustrated in figure 4.1 for seven grain boundaries, spanning the entire range of rotation angles from the $\Sigma 101$ to the $\Sigma 85$ GBs. In each cases, it is confirmed that the saturation plateau is related to the GB decohesion. In the cases of the $\Sigma 101$ [0101], $\Sigma 25$ [071] and $\Sigma 13$ [051] GBs, featuring the smallest rotation angles, a slight decrease of the critical stress can be decipher with the increase of the strain ratios, although the variation is rather weak. This point can be appreciated more quantitatively in figure 2.13 of chapter 2.

The extent of the GB decohesion zone, identified by a negligible space gradient on the $(\alpha_\epsilon, \beta_\epsilon)$ maps, clearly depends on the rotation angle. A positive transverse strain ratios does not constitute a necessary condition for GB decohesion as obviously illustrated by the cases of the $\Sigma 101$ and $\Sigma 13$ GBs which essentially experience fracture. Nevertheless, it is clear that for all the grain boundaries considered here, this last condition seems to be a sufficient one.

4. GRAIN BOUNDARIES FAILURE UNDER HOMOGENEOUS STRESS STATE

These critical stress maps are plotted with the same stress scale and the height of the plateaus clearly illustrates the variation observed in figure 4.2.

A rather large repartition of the critical stresses for GB decohesion is observed in figure 4.2 from around 14.0 GPa to 20 GPa.

The beginning of a geometrical correlation seems to be observed even if the exact evolution of the critical stress is apparently not trivial. A rough symmetrical trend around the rotation angle $\theta = 45^\circ$ could be guessed with rather low values for the lowest and the highest rotation angles and an increase toward the 45° angle with the exception of the $\Sigma 29$ grain boundaries.

From figures 4.1 and 4.2 and the above remark, a first-hand conclusion would therefore point toward the low angle grain boundaries as the weakest interfaces (for bicrystal fracture) and the most prone to decohesion (as opposed to the most prone to heterogeneous dislocation nucleation) since they display the lowest critical stresses with the most extended GB decohesion areas.

Nevertheless, an incomplete conclusion when comparing two grain boundaries strength, would be to consider that the GB featuring the highest Σ coefficient possesses the lowest critical stress and hence is the most prone to fracture, which is apparently not always the case here. This trend would only seem to be verified for the grain boundaries with very high Σ values with respect to the very low Σ grain boundaries. In these cases, the highest Σ value is actually linked to the smallest rotation angles.

More reliably, it is observed that the evolution of the structural unit description should rather be considered. From table 2.2 or figures 4.1 and 4.2, that three branches of the critical axial stress evolution $\sigma_{yy}^{c, \text{frac}}(\theta)$ can be considered separately and related to:

1. The connection between C and D or C and C elementary structural units from the $\Sigma 101$ [0 10 1] to the $\Sigma 5$ [0 3 1] grain boundary.
2. The appearance of the connection between the B and C or B and B structural units for the two $\Sigma 29$ grain boundaries.
3. The disappearance of the C unit and the presence of the B unit for $\Sigma 5$ [0 $\bar{1}$ 2], along with the A unit from the $\Sigma 17$ [0 5 3] to the $\Sigma 85$ [0 7 6] grain boundaries.

These branches are further indicated by different colours in figure 4.2.

These connections are commonly called disclinations [Gertsman et al., 1989, Nazarov et al., 2000] and shall be described further in section 4.4.1.

Then it is clear that considering only the macroscopic degrees of freedom are not sufficient to explain the observed variation here. The atomic structure and therefore the microscopic degrees of freedom of the grain boundary that can only be obtained by high-resolution transmission electron microscopy or computation, should also intervene.

Furthermore, it is reminded that the grain boundaries considered are all $\langle 100 \rangle$ symmetric GBs. Therefore, at this stage, we can not affirm that the atomic structure of the interface is a predominant factor for assessing the strength of the wide variety of homophase interfaces [Priester, 2006, Tschopp and McDowell, 2007].

4. GRAIN BOUNDARIES FAILURE UNDER HOMOGENEOUS STRESS STATE

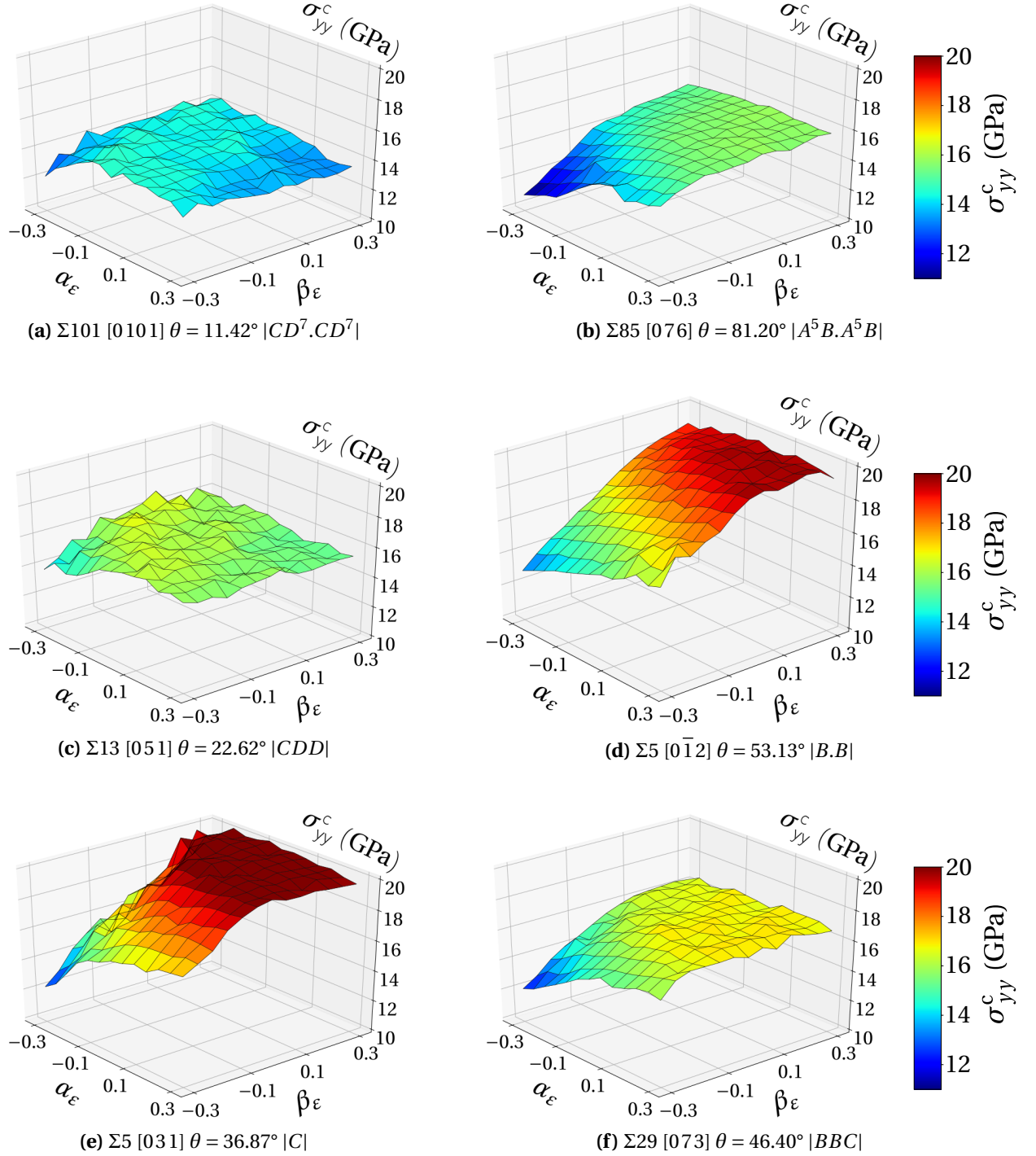


Figure 4.1: 3d maps of the critical stress in the $(\alpha_\epsilon, \beta_\epsilon)$ space for seven grain boundaries covering the entire range of rotation angles θ , from the top left to the top right figures (anticlockwise).

4. GRAIN BOUNDARIES FAILURE UNDER HOMOGENEOUS STRESS STATE

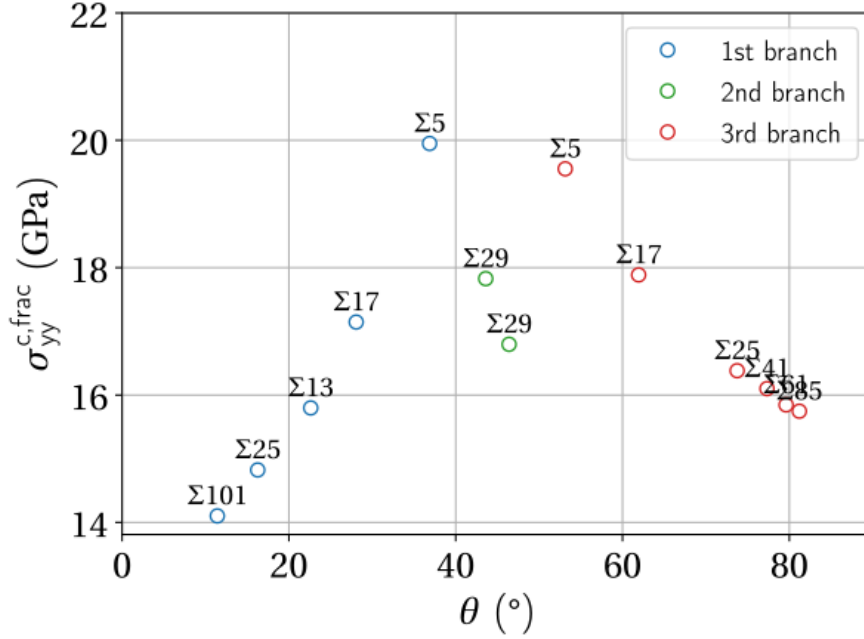


Figure 4.2: Axial critical stress $\sigma_{yy}^{c,frac}$ of the thirteen CSL symmetric [100] tilt grain boundaries according to the rotation angle θ .

However, if this influence is confirmed, the structural unit model should certainly present a valuable asset for prediction purposes.

4.2.2 Griffith energies of the grain boundaries

From a prediction point of view, the energetic aspect of fracture can also be considered. This aspect has been successfully employed for many years using Linear Elastic Fracture Mechanics (LEFM) since the work of Griffith [Griffith, 1921] considering a pre-existing crack (which is however not the case here) and relying on a critical energy γ_c (or Griffith energy) assumed to be a material property. Griffith defines the energy release rate G as the differential form of the energy balance between the thermodynamic equilibrium after and before the propagation of the crack:

$$G = \lim_{\delta A \rightarrow 0} -\frac{\delta W}{\delta A} = -\frac{dW}{dA}$$

where δW corresponds to the amount of work restituted to the system for the onset of a finite size area increment δA ; in the case of a crack, the propagation occurs by an infinitesimal crack extension dA .

The propagation of the crack is then thermodynamically admissible, provided that this energy rate contributes at least to the formation of two surfaces from the initial

4. GRAIN BOUNDARIES FAILURE UNDER HOMOGENEOUS STRESS STATE

state, represented by an amount of energy per surface γ_c :

$$G \geq \gamma_c \quad (4.1)$$

which constitutes the energy criterion of Griffith in the case of a pre-existing crack. In the more generalised case considered in Finite Fracture Mechanics (FFM) [Taylor et al., 2005], a discrete amount of crack surface increment is assumed and the differential form of the energy criterion in equation 4.1 is dropped:

$$-\frac{\delta W}{\delta A} \geq \gamma_c \quad (4.2)$$

This allows to successfully treat the problem of fracture initiation at the tip of notches which LEFM is unable to predict, as will be seen in chapter 5.

The critical energy γ_c is at the basis of the energy criterion in LEFM or in FFM and therefore need to be considered carefully. For our purpose, a critical energy per unit area γ_c related to the grain boundary decohesion can be computed here. Following the assumption of Griffith and employing a simple balance at the thermodynamic equilibria after and before decohesion:

$$\gamma_c = 2\gamma_s - \gamma_{GB} \quad (4.3)$$

where γ_{GB} is the initial grain boundary energy per surface area and $2\gamma_s$ the energy per unit area of the two newly created surfaces.

The above assessment is obtained from the GB decohesion cases (with $\alpha_\varepsilon = \beta_\varepsilon$) with the same slabs already used before to compute the grain boundaries energy.

It is reminded that these slabs include atoms with atomic potential energy significantly diverting from the mean potential energy of the bulk and therefore contributing to the grain boundary excess energy. This point shall be specified more thoroughly in section 4.3.

The borders of the slabs (denoted + and - for the upper and lower boundaries) are marked by selecting from the initial undeformed configuration, fifty atoms featuring the closest y coordinates to the location of the initial prescribed boundaries y_{slab}^\pm along the direction normal to the GB plane. Since we only consider symmetric grain boundaries here, the slab is selected so that $y_{slab}^- = -y_{slab}^+$ considering the grain boundary plane at $y = 0$. Care is obviously taken to effectively select the grain boundary to be fractured since it is reminded that the bicrystal contains two grain boundaries with equal probability of fracture.

This method permits to follow the deformation of the slab with the same number of atoms and ultimately allows to encompass the two created surfaces after decohesion and full relaxation of the system.

The total excess energy (relatively to the bulk) is computed during the different loading cases using a similar differential operation as previously employed for the assessment of the grain boundary energy:

$$\Gamma(t) = \frac{E_{slab}^p(t) - N_{slab}^{at.} \bar{E}_{bulk}^{p, at.}(t)}{A}$$

4. GRAIN BOUNDARIES FAILURE UNDER HOMOGENEOUS STRESS STATE

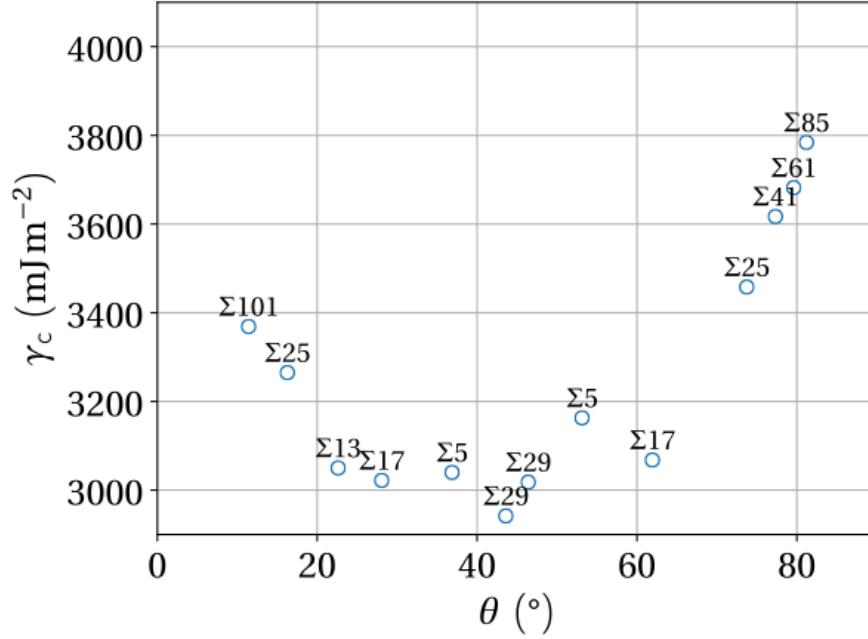


Figure 4.3: Critical energy (or Griffith energy) γ_c of the thirteen CSL symmetric [100] tilt grain boundaries according to the rotation angle θ .

The assessment of the critical energy for the GB decohesion is then obtained from the energy balance of equation 4.3 with the grain boundary energy previously computed (as referenced in chapter 2) and the energy of the two created surfaces:

$$2\gamma_s = \langle \Gamma(t \gg t_{c, \text{frac}}) \rangle_\tau$$

where $t \gg t_{c, \text{frac}}$ indicates the time when full relaxation is obtained, far away from the critical time of decohesion.

It is found that the surface energy varies slightly with the $\alpha_\varepsilon = \beta_\varepsilon$ ratios for which the GB decohesion is effectively obtained. This variation is clearly due to the surface deformations imposed by the different prescribed transverse strain ratios still active after decohesion. It is therefore chosen to rely on the data obtained with $\alpha_\varepsilon = \beta_\varepsilon$ close or equal to zero for which no extra mechanical work is added to the final value after the GB decohesion.

Figure 4.3 presents the results of the GB critical energies for the thirteen grain boundaries according to their rotation angle θ . The values vary between around 2.9 Jm^{-2} and 3.8 Jm^{-2} .

Again, a geometrical evolution seems to be drawn, and the same three branches as observed before on the critical stress evolution figure 4.2 can be distinguished here even if a clear trend cannot be established.

The highest strength related to highest critical energies (and considering now solely

4. GRAIN BOUNDARIES FAILURE UNDER HOMOGENEOUS STRESS STATE

a energy criterion for bicrystal fracture), are observed for the grain boundaries featuring the highest and the lowest rotation angle. This remark, clearly contrasts with the preceding results obtained on the critical stresses for which the inverse trend is derived. Grain boundaries showing the lowest critical stresses for decohesion do not feature the lowest critical energies. Interestingly, grain boundaries with the lowest critical stresses do not show the highest critical energies either which is illustrated with the example of the Σ 101 [0101] grain boundary.

This remark seems to show that these two properties are complementary for the understanding of the decohesion behaviour of these grain boundaries in terms of strength.

In order to provide more insight, following this last remark and the presented results, a criterion of fracture is further considered and discussed in the next subsection.

4.2.3 The coupled criterion for the onset of intergranular cracking

4.2.3.1 Paradox of the bar failure considering an energy criterion

To illustrate and to understand the use and the validity of the previous mechanical assessments (i.e. $\sigma_{yy}^{c, \text{frac}}$ and γ^c) it is proposed to primarily consider the simple problem of the failure of an isotropic and homogeneous bar in the continuum framework of linear elasticity.

Leguillon [Leguillon, 2002] used this very example to illustrate the need to consider a coupled criterion for the onset of cracking in a generalised vision considering both a critical stress and a critical energy to attain. The author presents the following paradox to underline the inability of a unique energy criterion to account for fracture initiation. It is reported here for illustration purposes.

The above mentioned problem of the failure of an elastic bar of length L , surface S and young modulus Y , loaded under a monotonic tensile loading with an applied uniaxial stress Σ_{yy} , is considered. The figure 4.4 illustrates the problem, just before and after the failure.

A simple energy balance provides the energy released for failure $-\delta W$ as follows:

$$-\delta W = -(W_2 - W_1) = \frac{1}{2} SL \frac{\Sigma_{yy}^2}{Y}$$

with W_2 and W_1 the work brought to the system after and before failure respectively, with the fact that $W_2 = 0$ since subsequent loading after failure will obviously not contribute to the potential energy of the system. Following solely an energy criterion, the failure of the bar is therefore obtained when a critical energy is attained:

$$\frac{1}{2} L \frac{\Sigma_{yy}^2}{Y} \geq \gamma_c$$

or simply:

$$\Sigma_{yy} \geq \sqrt{\frac{2\gamma_c Y}{L}} \quad (4.4)$$

4. GRAIN BOUNDARIES FAILURE UNDER HOMOGENEOUS STRESS STATE

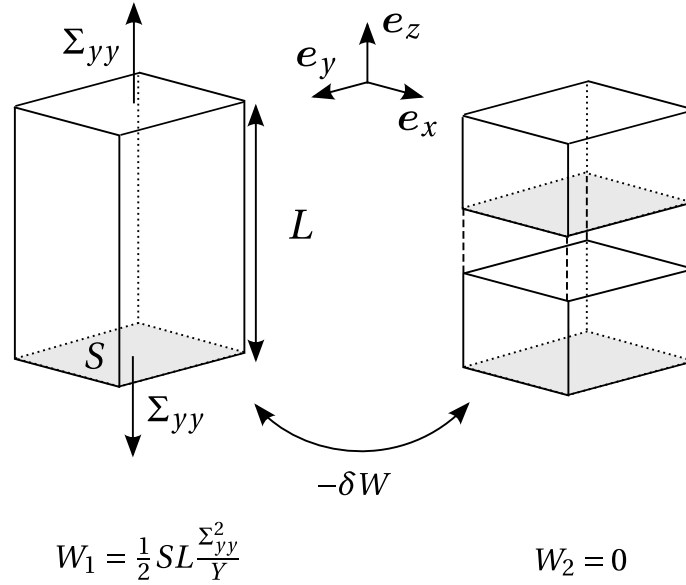


Figure 4.4: Failure of a bar under an uniaxial tensile stress Σ_{yy} .

From this application of the energy criterion, Leguillon rightfully exposes the following paradox: should we increase the length of the bar at will, a failure could be obtained for an infinitesimal stress loading, which is clearly never observed.

The above paradox can be resolved considering that an additional stress criterion is also fulfilled:

$$\Sigma_{yy} \geq \sigma_c \quad (4.5)$$

with σ_c a critical stress defined as a material property of fracture. In that particular case, this last criterion is predominant over the energy criterion, which meanwhile, should also be respected.

Following this coupled criterion (illustrated here in that particular example with equations 4.4 and 4.5), the Griffith theory is also encompassed since in the case of the propagation of a pre-crack under a given loading, the energy criterion would prevail over the stress criterion which is always respected since a stress singularity is expected in front of the crack.

It is suggested here, that the bicrystal cases treated before in MD have to respect this coupled criterion for the onset of fracture with a predominance of the stress criterion.

Of course, the bicrystal simulation considered presents several discrepancies with respect to the above mentioned problem hypothesis:

1. The boundary conditions are clearly different as no free surfaces are considered for the bicrystal since periodic boundaries are used in every direction of space. However, in both cases, no stress concentration develops under an applied loading.
2. The bicrystal is obviously not homogeneous and not isotropic, however there

4. GRAIN BOUNDARIES FAILURE UNDER HOMOGENEOUS STRESS STATE

is no arguments for which these two points should render the above reasoning inapplicable.

3. As shown before in chapter 2, linear elasticity cannot be assumed considering the deformations at which the decohesions of the bicrystals are obtained. But once again, this point should not tackle the comparison intended here.

Therefore, it is proposed to justify that the critical axial stresses obtained before represent intrinsic fracture properties of the interfaces by using an assimilation to the above problem of the bar failure.

4.2.3.2 Predominance of the stress criterion for the failure of the bicrystals under homogeneous stress state

From the previous computations of the multiaxial loadings leading to the fracture of the $\Sigma 5$ $[0\bar{1}2]$ GB (i.e. with $\alpha_\varepsilon \geq 0.05$ or with the case $\alpha_\varepsilon = 0$ which also experiences decohesion after a first dislocation nucleation without propagation), the mechanical work per surface unit γ , brought to the bicrystal, is recorded through the mechanical loading applied to the system:

$$\gamma = \frac{W}{A} = \frac{1}{A} \left(\int_0^\varepsilon \boldsymbol{\sigma} : d\boldsymbol{\varepsilon} \right) V = L \left(\int_0^\varepsilon \boldsymbol{\sigma} : d\boldsymbol{\varepsilon} \right) \quad (4.6)$$

considering the bicrystal as one homogenised phase, with L , A and V the length, the section area and the volume of the box respectively, $\boldsymbol{\sigma}$ the global stress tensor, $\boldsymbol{\varepsilon}$ the global strain tensor and W the mechanical work at a computed step.

In the approximation of linear elasticity at small deformations, the mechanical work features a quadratic form considering the elasticity tensor of the Hooke's law:

$$\gamma = L \frac{1}{2} \boldsymbol{\varepsilon} : \mathbf{C} : \boldsymbol{\varepsilon} \quad (4.7)$$

The balance of the potential energy of the system ΔE^p between the computed steps and the initial configuration is plotted on figure 4.5a:

$$\Delta E^p = E^p - E_0^p$$

Lets now consider in each α_ε cases, a configuration before decohesion (denoted κ_1) and a configuration after the full decohesion (denoted κ_2), as illustrated in figure 4.5b ; the decohesions being clearly evidenced by the energy drops in figure 4.5a.

For a κ_1 configuration, the difference of potential energy ΔE_1^p boils down to the mechanical work brought to the system W_1 by the axial and transverse deformations. The quadratic form of equation 4.7 is evidently illustrated on figure 4.5a at small deformations and with, most probably, some discrepancies, at higher deformations for which non-linear elasticity has been evidenced in chapter 2.

4. GRAIN BOUNDARIES FAILURE UNDER HOMOGENEOUS STRESS STATE

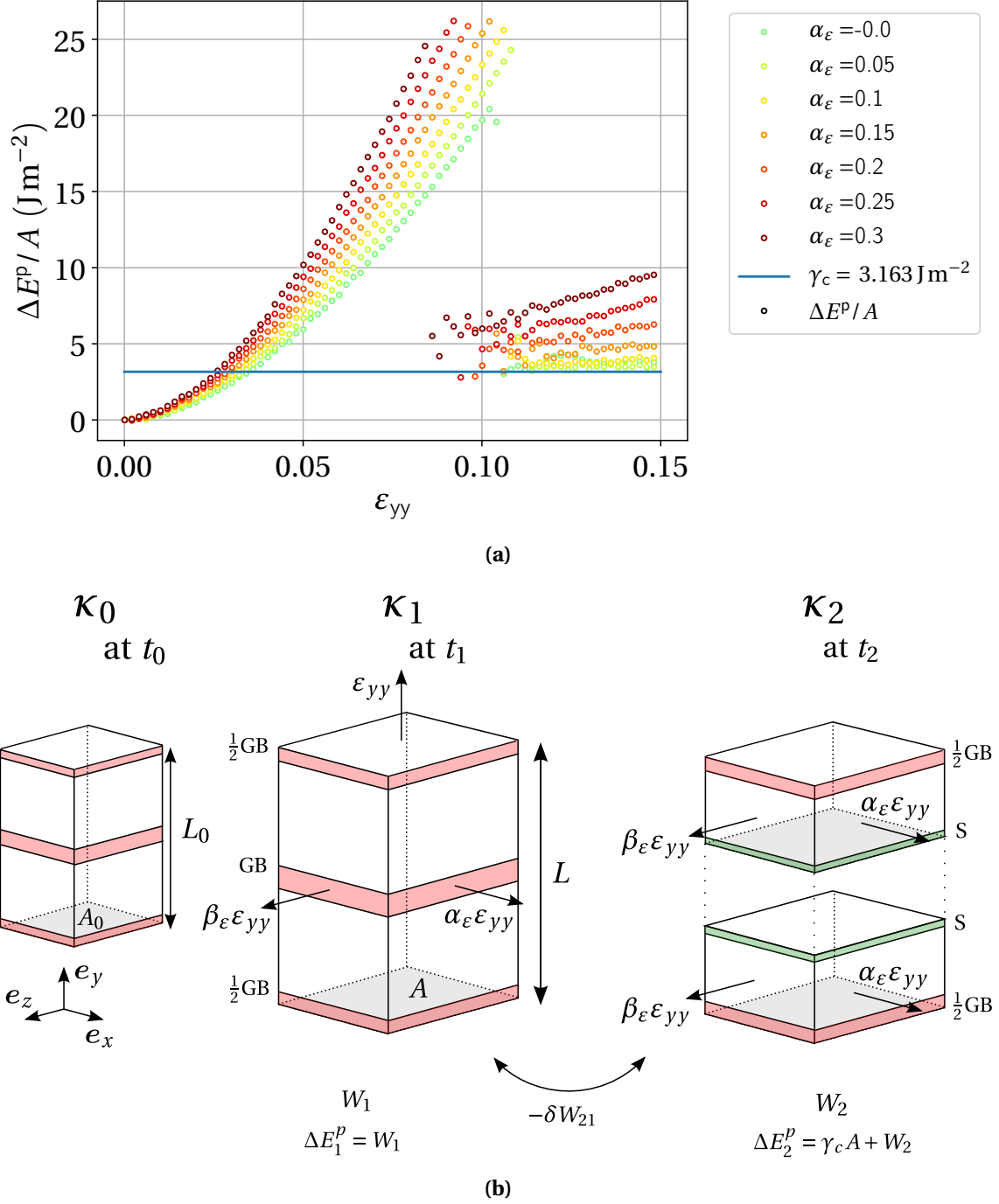


Figure 4.5: Evolution the total potential energy balance between the current and the initial state κ_0 of the bicrystal containing two $\Sigma 5$ $[0\bar{1}2]$ grain boundaries during the different loadings $\alpha_\epsilon = \beta_\epsilon$ leading to decohesion (4.5a). Scheme for the energy balance of the bicrystal between the configuration before fracture κ_1 and after κ_2 (4.5b).

4. GRAIN BOUNDARIES FAILURE UNDER HOMOGENEOUS STRESS STATE

Considering a configuration κ_2 , after decohesion, the difference of potential energy can be accounted for by the sum of the energy necessary for the creation of two surfaces from the initial grain boundary and the mechanical work W_2 due to the transverse deformations:

$$\Delta E_2^p = \gamma_c A + W_2$$

with $\gamma_c = 2\gamma_S - \gamma_{GB}$.

For the case $\alpha_\varepsilon = 0$, the critical energy γ_c is therefore recovered in figure 4.5a since no transverse deformation is induced by the loading. For the other cases, an energy surplus is therefore logically found just after the drop, which further increases with subsequent transverse deformations.

Therefore, at $\alpha_\varepsilon = 0$, the loss of energy $-\delta W_{21}$ can be assimilated to the curve observed since:

$$-\delta W_{21} = W_1 = \Delta E_1^p$$

It is then clear from figure 4.5a that the Griffith criterion is verified for this case (and also for every cases with $\alpha_\varepsilon > 0$) when failure occurs since:

$$\frac{W_1}{A} \geq \gamma_c$$

However, it can be seen from figure 4.5a that the criterion is also verified well before failure.

Following equation 4.6 and the energy criterion, it is finally clear that by increasing the grain size at will, one could obtain a failure at an infinitesimal loading since the criterion boils down to:

$$\int_0^\varepsilon \boldsymbol{\sigma} : d\boldsymbol{\varepsilon} \geq \frac{\gamma_c}{L}$$

which is obviously improbable.

Therefore, similarly to the case of the bar failure, it is suggested that the use of a unique energy criterion for the prediction of the bicrystal failure is not viable.

It is rightfully assumed that a stress criterion is predominant in the case of the bicrystal failure under an homogeneous stress state. In conclusion, this last statement encourages the use of the preceding computed critical axial stress $\sigma_{yy}^{c, \text{frac}}$ as an intrinsic GB property of fracture.

4.3 Strain localisation at the grain boundaries

Previous results show that for certain transverse deformation ratios, a decohesion is obtained when for the same ratios only dislocation nucleations are observed for their single crystals counterparts.

This observation indicates that the presence of the grain boundary induces a weak link in the bicrystal, which will break at some critical stress outstripping any other critical event in the bulk.

4. GRAIN BOUNDARIES FAILURE UNDER HOMOGENEOUS STRESS STATE

In particular, it has been suggested before that the grain boundaries feature degraded mechanical properties with respect to the adjacent grains. To support this statement, it is often observed that grain boundaries are the localisation of strong deformations or GB sliding. Grain boundary segregation is also clearly an indicator that these homophase interfaces constitute the location of higher free volumes.

The relation between a geometrical description of the grain boundary and their elastic behaviour is proposed and discussed in this section 4.3, based on a definition of the grain boundary as a phase of finite thickness possessing its own mechanical properties.

4.3.1 Thickness of the grain boundaries based on their intrinsic excess energy

Figure 4.6 presents the potential energy per atom in the vicinity of the $\Sigma 5$ $[0\bar{1}2]$ grain boundary after its formation and annealing at 300 K. As briefly mentioned in chapter 2 when computing the GB energies, a GB excess energy is observed relatively to the energy of the adjacent grains. Quite naturally, a grain boundary thickness relying on this local excess energy seems to be appropriate to describe the extent of a GB phase. It is therefore proposed to focus on the assessment of this geometrical property.

The related total excess energy Γ can be formulated here by its summation formulation over a system of N atoms containing only one grain boundary and normalised by the GB section A :

$$\Gamma = \frac{1}{A} \sum_i^N \Delta E_i^{\text{p.at.}} \quad \Delta E_i^{\text{p.at.}} = E_i^{\text{p.at.}} - \bar{E}_{\text{bulk}}^{\text{p.at.}}$$

with $E_i^{\text{p.at.}}$ the potential energy of the atom i , $\bar{E}_{\text{bulk}}^{\text{p.at.}}$ the mean potential energy per atom of the bulk and $\Delta E_i^{\text{p.at.}}$ the excess energy per atom. Following the preceding definition, it is clear that the excess energy per atom in the bulk (i.e. far enough from the vicinity of the grain boundary) is zero. Therefore any system of N atoms can be considered for the computation, provided that it contains the full extent of the grain boundary. It is also clear, as described before, that the grain boundary energies previously calculated correspond to this GB excess energy.

This excess energy per atom is represented in figure 4.7a against the y_i coordinate of the atom i perpendicularly to the grain boundary plane. This gain in potential energy results from the atomic structure of the grain boundary as interatomic distances increase or shrink in its core with local lattice distortions covering several atomic layers.

This GB extent may be pictured as a defected zone, presenting a certain amount of excess free volumes related to a certain amount of damage relatively to the bulk. This consideration has already been suggested by [Spearot et al., 2007b] through a proposed definition of a damage internal variable based on the first-neighbour coordination number of the grain boundary atoms, therefore trying to account for initial porosity.

4. GRAIN BOUNDARIES FAILURE UNDER HOMOGENEOUS STRESS STATE

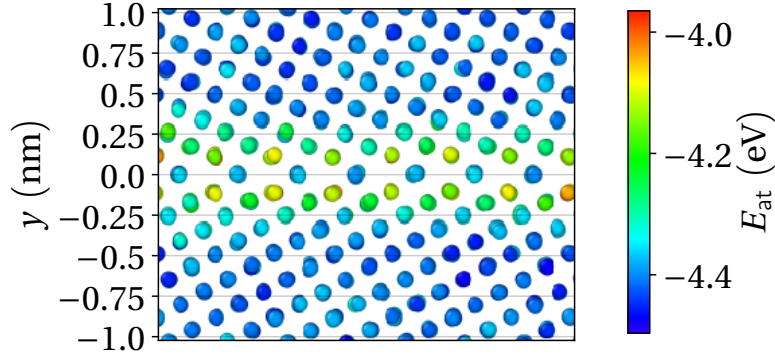


Figure 4.6: Potential energy per atom in the vicinity of the $\Sigma 5$ $[0\bar{1}2]$ grain boundary according to the atomic coordinates y perpendicular to the grain boundary plane.

The aforementioned thickness can be clearly discerned for the case of the $\Sigma 5$ $[0\bar{1}2]$ GB case, however more complex structures, such as the $\Sigma 101$ GB, necessitate a more thorough description as evidenced in figure 4.8a. In the following paragraphs, it is proposed to rely on a same procedure for the determination of the grain boundaries thickness, based on the observed excess energies. In that respect, a reliable comparison between the different grain boundaries may be obtained in fine.

The successive atomic layers piling in the y axis direction and observed in the figures 4.7a and 4.8a, can clearly be located through a peak detection plotted in figures 4.7b and 4.8b along with a discrete cumulative probability based on the excess energy per atom:

$$P(y_i) = \frac{1}{\Gamma} \sum_{j/y_j \leq y_i}^i \Delta E_j^{\text{p, at.}}$$

where the notation $j/y_j \leq y_i$ suggests a summation over every atom j with a coordinate y_j lower or equal to y_i .

In order to obtain a formal comparison between the various grain boundaries, the cumulative distribution function of a classical normal distribution is chosen to be fitted on the preceding discrete cumulative distribution:

$$P(y) = \frac{1}{v\sqrt{2\pi}} \int_{-\infty}^y e^{-\frac{t^2}{2v^2}} dt$$

with the variance v , recorded for every grain boundary in the table, figure 4.9. These discrete and fitted probabilities of GB crossing are plotted in figures 4.7b and 4.8b for the $\Sigma 5$ $[0\bar{1}2]$ and the $\Sigma 101$ $[0101]$ GBs at 300 K after averaging the atomic positions and energies over time.

A grain boundary thickness t_{GB} is then obtained, considering arbitrarily a 98 % Γ excess energy between the upper and lower bounds of the GB phase, defined symmetrically from the median at 50 % Γ (i.e. between the quantiles at 1 % Γ and 99 % Γ). Discrete

4. GRAIN BOUNDARIES FAILURE UNDER HOMOGENEOUS STRESS STATE

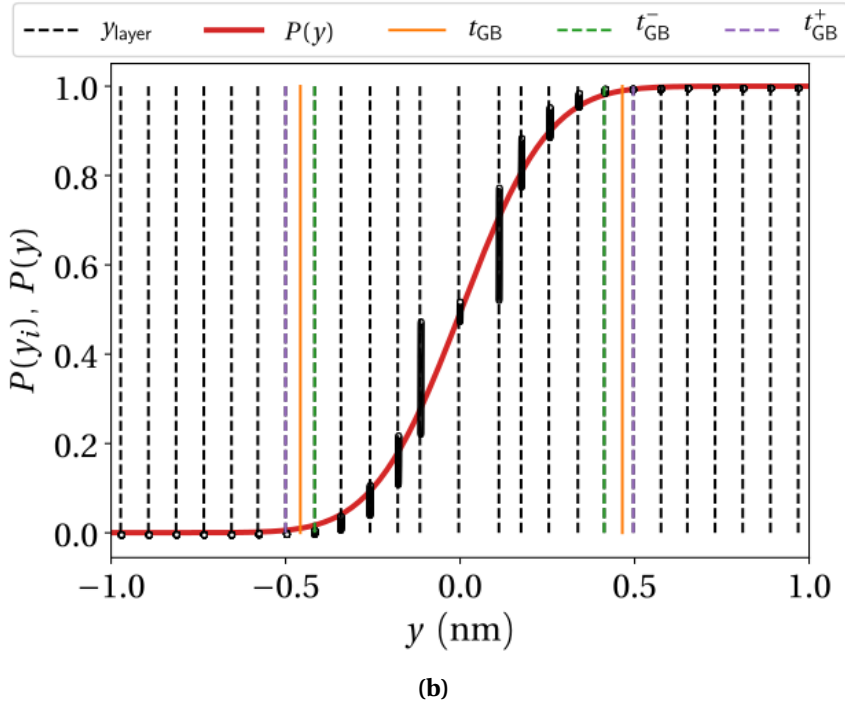
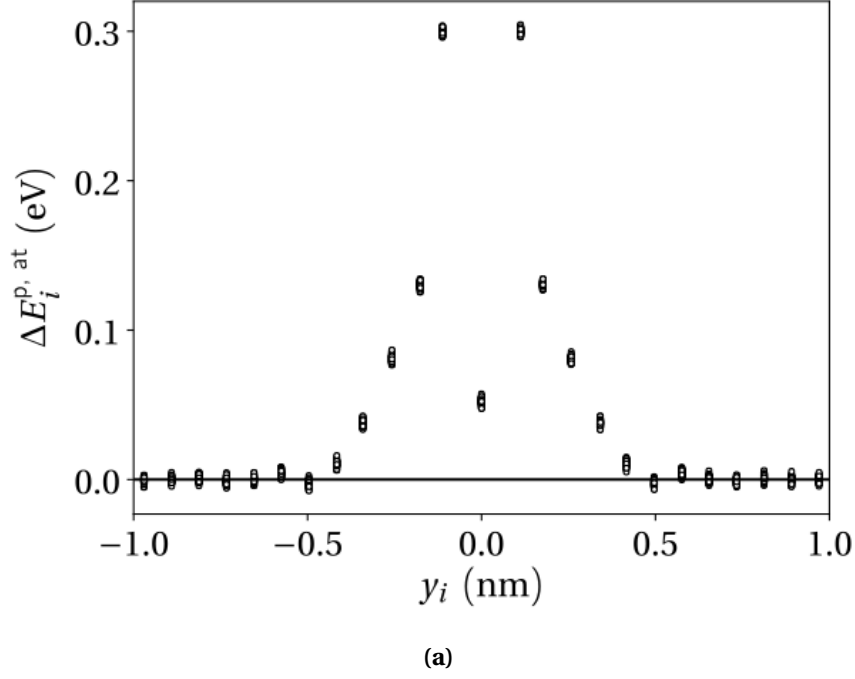


Figure 4.7: Excess energy per atom in the vicinity of the $\Sigma 5$ $[0\bar{1}2]$ grain boundary according to the atomic coordinates y perpendicular to the grain boundary plane (4.7a). Corresponding cumulative probability and atomic layer pic detection (4.7b), the yellow lines delimit the 98 % excess energy area, the green and purple lines delimit the corresponding lower and upper atomic layers.

4. GRAIN BOUNDARIES FAILURE UNDER HOMOGENEOUS STRESS STATE

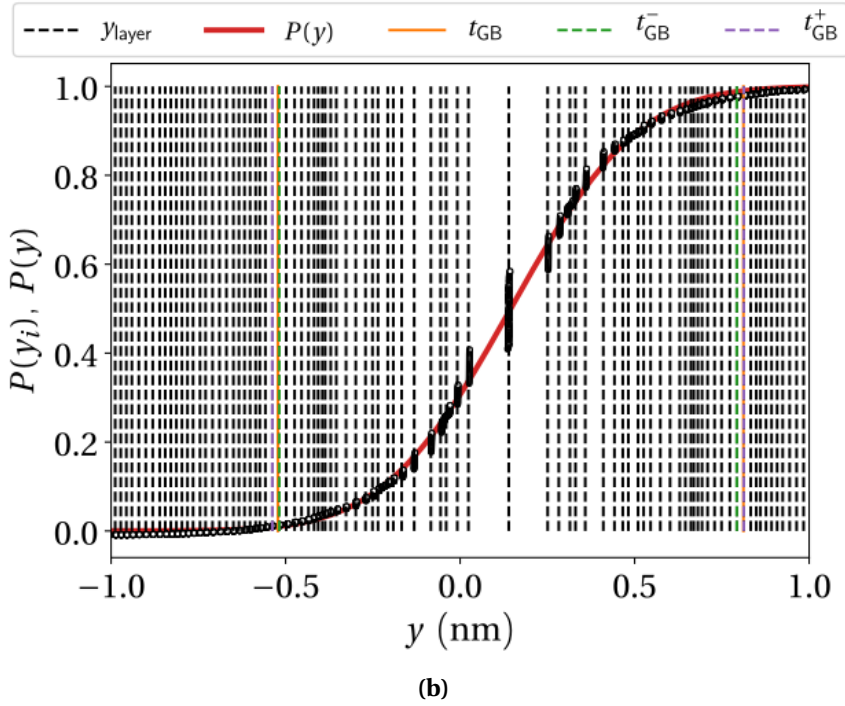
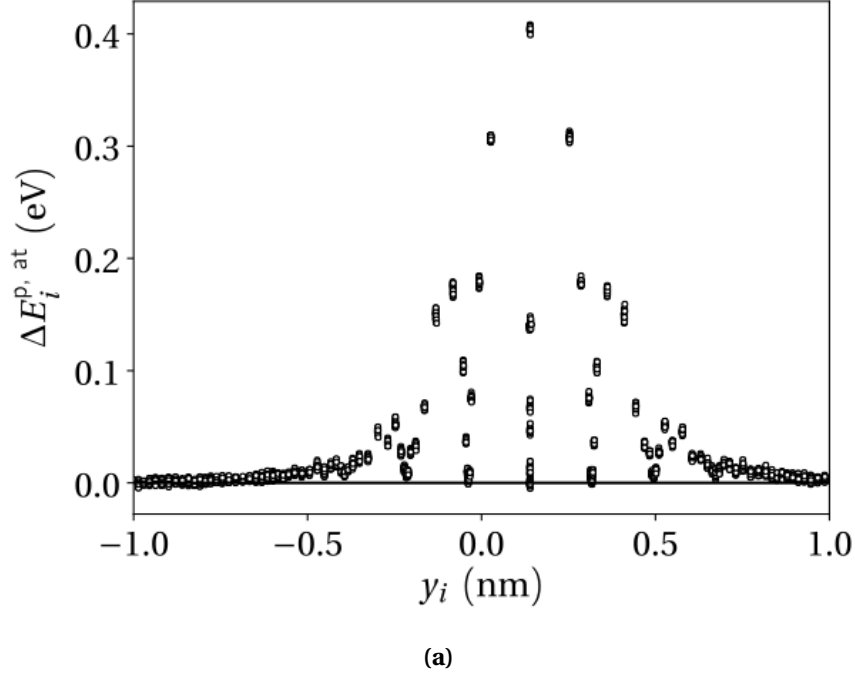


Figure 4.8: Excess energy per atom in the vicinity of the $\Sigma 101$ [0 10 1] grain boundary according to the atomic coordinates y perpendicular to the grain boundary plane (4.8a). Corresponding cumulative probability and atomic layer pic detection (4.8b), the yellow lines delimit the 98 % excess energy area, the green and purple lines delimit the corresponding lower and upper atomic layers.

4. GRAIN BOUNDARIES FAILURE UNDER HOMOGENEOUS STRESS STATE

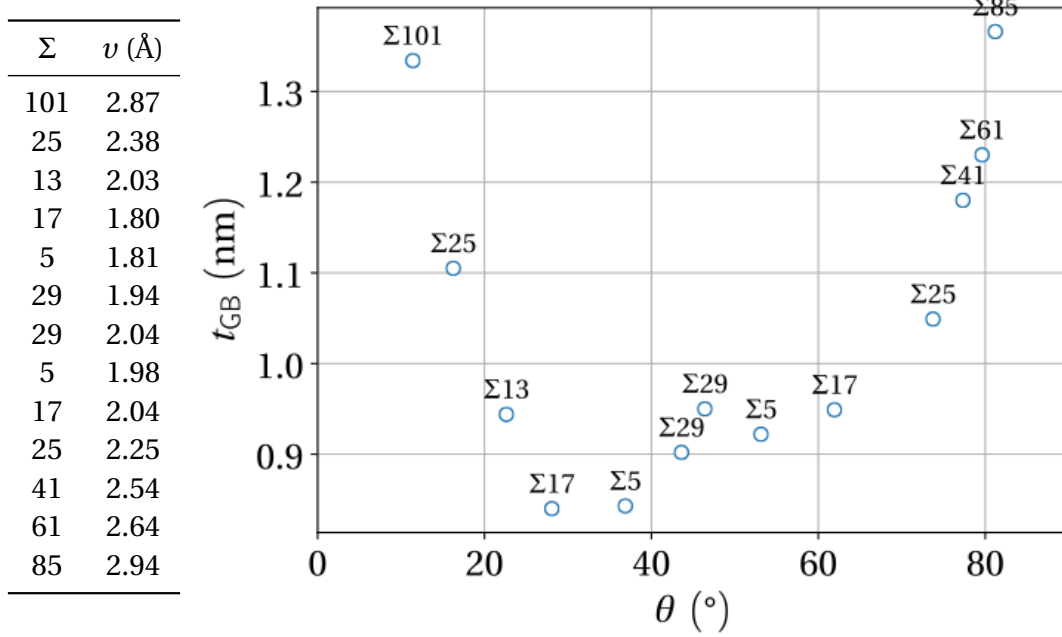


Figure 4.9: Energy-based thickness for the thirteen CSL symmetric [100] tilt grain boundaries according to the rotation angle θ .

boundaries related to the atomic layers can also be recorded based on the preceding characterisation and considering the atomic layers above and below the preceding upper and lower bounds leading to minimum and maximum atomic thicknesses t_{GB}^- and t_{GB}^+ . These different boundaries are plotted in figures 4.7b and 4.8b. Similar characterisations are carried out for the other grain boundaries ; the resulting thickness assessments are plotted in figure 4.9 according to the rotation angle θ of the grain boundaries.

Once again a geometrical trend is clearly evidenced as grain boundaries featuring the lowest and highest rotation angles clearly show the thickest GB phase extents. This observation can certainly be explained by the mechanical description of the grain boundaries by arrays of intrinsic dislocations for which the extent of the local strain (or stress) field clearly diminishes from one grain boundary to an other with the decreasing distance between the dislocations d_{GB}^{disl} (as previously assessed in chapter 2) accompanied by the related variation of the rotation angle θ .

It is not surprising to note that the inverse variations recorded for the grain boundary energies in figure 2.3 and the critical energy variation in figure 4.3, are strongly linked to the above trend, although the correlation is not straightforward. The aforementioned definition is clearly based on the energetic description of the grain boundary. And it is also reminded that the Read-Shockley-Wolf modified model, describing the GB energy variations, is originally based on the energetic description of the edge dislocations wall. Shimokawa [Shimokawa, 2010], in his molecular dynamic study of $\langle 112 \rangle$ grain boundaries in aluminium, also described similar variations for the distances the author

4. GRAIN BOUNDARIES FAILURE UNDER HOMOGENEOUS STRESS STATE

arbitrarily defined by the extent of the stress lobes induced by the intrinsic GB edge dislocations.

This GB thickness definitions, which neglects the energy gradient along the grain boundary planes, may not fully represent the GB geometry, particularly for low angle boundaries with increasing intrinsic dislocation distances.

However, for upperscale considerations where the atomic description is not directly considered in such details, it is quite convenient to be able to define grain boundaries as homogeneous phases possessing their own geometrical and mechanical properties. Such a mechanical characterisation is further developed and supported in the next subsection.

4.3.2 Apparent Young modulus of the homophase interfaces

As already implied, it is suggested that the distorted atomic structures of the GBs phase induce a degradation or more generally a modification of the mechanical properties with respect to the adjacent grains. The description of grain boundaries as pre-damaged phases may partly explain the failure localisation of the bicrystal at grain boundaries acting as a weak links. For the same axial stress, the localisation of the axial strain would be expected at the grain boundaries rather than in the adjacent bulks, should the above statement be verified.

To support this assumption, the assessment of apparent elastic moduli of the grain boundaries based on the GB thicknesses obtained before is undertaken in this final subsection for the thirteen grain boundaries.

In a continuum framework (that shall be justified in our case since a discrete medium is under focus), the bicrystals can be considered as a succession of piling phases, namely the grains (G) and the grain boundaries (GB), featuring different mechanical properties as pictured in figure 4.10.

If one considers a given mechanical loading (uniaxial or multiaxial) applied on this layered structure, the axial deformation ϵ^{layer} of any arbitrary layer of thickness t_L , encompassing at least one GB phase of thickness t_{GB} can be expressed through a classical rule of mixture:

$$\epsilon^{\text{layer}} = \frac{t_{\text{GB}}}{t_L} \epsilon^{\text{GB}} + \left(\frac{t_L - t_{\text{GB}}}{t_L} \right) \epsilon^{\text{G}} \quad (4.8)$$

with ϵ_{GB} and ϵ_{G} the axial deformations of the grain boundary and grain phases respectively. The axial stress σ_{yy} is here conserved along the tensile axis:

$$\sigma_{yy} = C_{yy}^{\text{GB}} \epsilon^{\text{GB}} = C_{yy}^{\text{G}} \epsilon^{\text{G}} = C_{yy}^{\text{layer}} \epsilon^{\text{layer}} \quad (4.9)$$

with C_{yy}^{layer} , C_{yy}^{GB} and C_{yy}^{G} the apparent elastic moduli of the layer in the y axis direction, of the grain boundary and grain phases respectively.

4. GRAIN BOUNDARIES FAILURE UNDER HOMOGENEOUS STRESS STATE

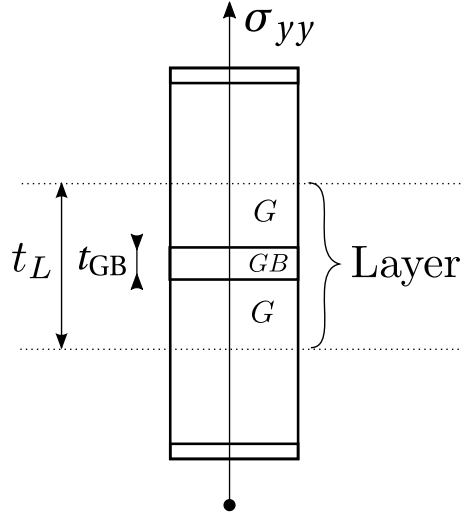


Figure 4.10: Scheme of the bicrystal system as a composite material with two phases: the grain (G) and the grain boundary (GB). The variable t_L represents the thickness of an arbitrary layer regrouping N_L atomic layers.

Equations 4.8 and 4.9 therefore imply the following formulation depending on the layer thickness t_L considered:

$$C_{yy}^{\text{layer}}(t_L) = \frac{1}{\frac{t_{GB}}{t_L} \left(\frac{C_{yy}^G - C_{yy}^{GB}}{C_{yy}^G C_{yy}^{GB}} \right) + \frac{1}{C_{yy}^G}} \quad (4.10)$$

In order to confirm the preceding description of the bicrystal in a continuum framework at small deformations, it is proposed to record, during the multiaxial loading cases $\alpha_\varepsilon = \beta_\varepsilon$ of the $\Sigma 5$ $[0\bar{1}2]$ GB, the axial deformation of the atomic layers, previously evidenced by their discrete coordinates y_i^+ and y_i^- (for any layer i).

Figure 4.11a shows the initial configuration of the $\Sigma 5$ GB at 300 K, with a colour identification of the first ten atomic layers.

In order to track each atomic layer during the deformation, fifty atoms are pre-selected on the initial configuration for their proximity to the layer boundaries at y_i^+ and y_i^- coordinates and tracked at each computed steps.

An evolution of the layer boundaries coordinate is therefore obtained by the mean value of the pre-selected atoms during the loadings, giving access to the related mean axial displacements of the upper and lower boundaries $u_{y,i}^+$ and $u_{y,i}^-$.

The deformation of each layer is then computed using their initial thickness:

$$\varepsilon_{yy}^{\text{layer } i} = \frac{u_{y,i}^+ - u_{y,i}^-}{t_i}$$

Using the same tracking method, the energy-based definition of the interface boundaries are also followed during the loadings.

4. GRAIN BOUNDARIES FAILURE UNDER HOMOGENEOUS STRESS STATE

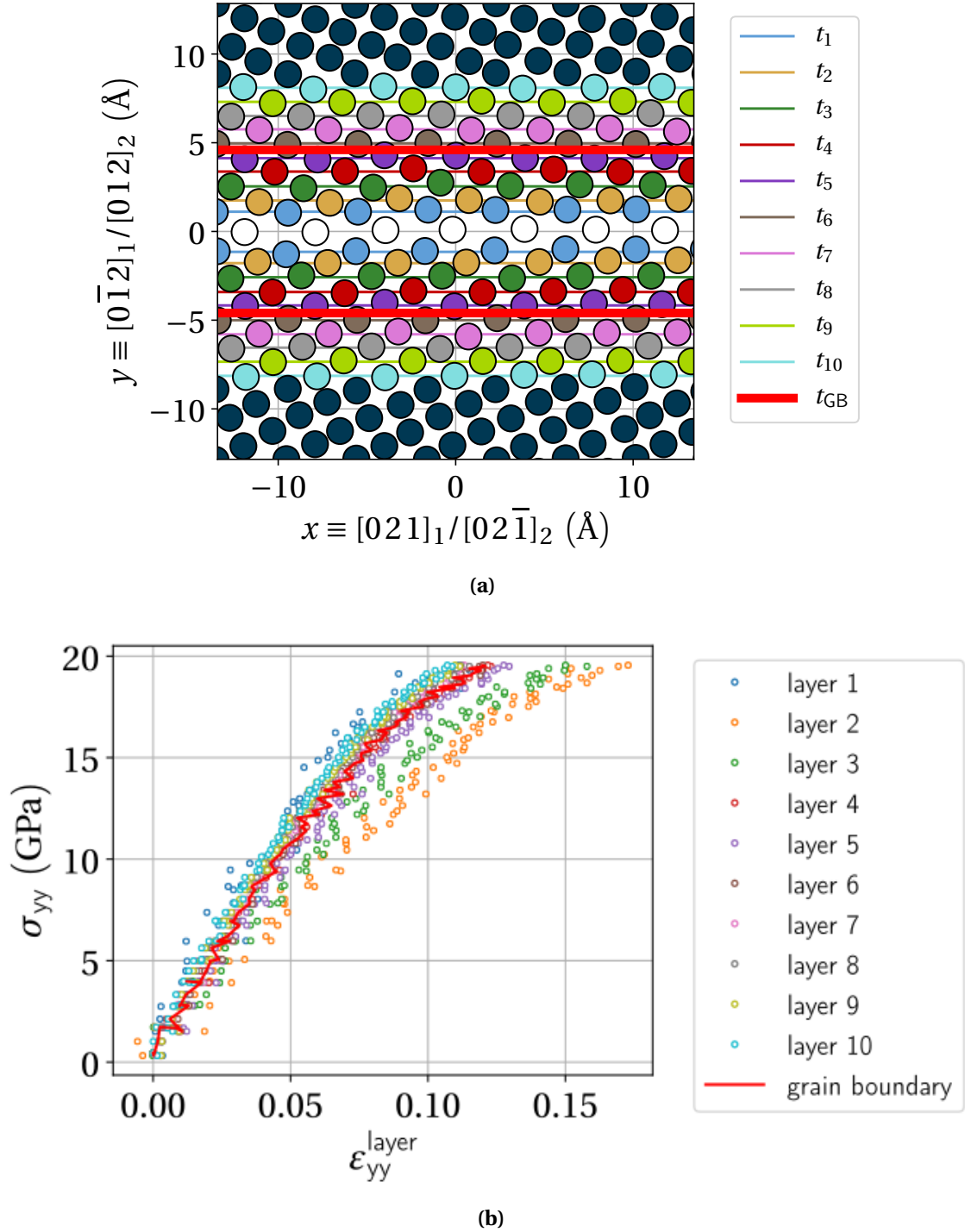


Figure 4.11: Identification of the atomic layers on the initial averaged configuration of the $\Sigma 5$ $[0\bar{1}2]$ GB at 300 K in the y axis direction. The grain boundary layer previously identified is specified by the thick red lines (4.11a). Atomic layers tensile curves. The tensile curve of the grain boundary is specified by the red line (4.11b).

4. GRAIN BOUNDARIES FAILURE UNDER HOMOGENEOUS STRESS STATE

Local atomic tensile curves are derived in each loading cases considering the global axial stress σ_{yy} as previously recorded on the MD box. Figure 4.11b presents such tensile curves in the case $\alpha_\epsilon = \beta_\epsilon = 0$ for the first ten layers illustrated in figure 4.11a.

From this plot, a degradation of the apparent elastic moduli (initial slope) can be deciphered in the vicinity of the GB core. A progressive increase and a subsequent saturation of the initial slopes are identified beyond the reach of the GB thickness identified by the red curve.

The apparent elastic moduli C_{yy} for the different loadings are computed using the initial slopes of the different tensile curves and plotted against the initial layers thickness of the first twenty pre-identified atomic layers in figure 4.12a (in circle markers). The previously observed increase and saturation of the elastic moduli are clearly evidenced.

Identifying the elastic moduli of the grain boundary C_{yy}^{GB} with the initial slope obtained with the tensile curves of the energy-based GB layer of thickness t_{GB} (square markers), the theoretical elastic moduli at a layer thickness t_L is plotted on the same figure using the law of mixture of equation 4.10. For the applications, the apparent elastic moduli of the grain C_{yy}^G is obtained by separate calculations on the related single crystal with the same multiaxial loadings. The same increasing trend is clearly reproduced, which confirms the approximation made on the continuum description of the bicrystals as a composite material. It also clearly illustrates the degradation of the elastic moduli in the vicinity of the grain boundary as a recorded value of around $C_{yy}^{GB} = 170$ GPa for the grain boundary contrasts with the value of around $C_{yy}^G = 260$ GPa obtained for the bulk at $\alpha_\epsilon = 0$, revealing a 35 % decrease of the apparent elastic modulus.

The beginning of the saturation observed for the first twenty layers clearly reveals that increasing the layer thickness t_L logically leads to the recovery of the elastic moduli of the bicrystal (close to the elastic moduli of the bulk). This trend can be further appreciated in figure 4.12b presenting the atomic tensile curves of the grain boundary and the twentieth layer along with the tensile curve of the bicrystal.

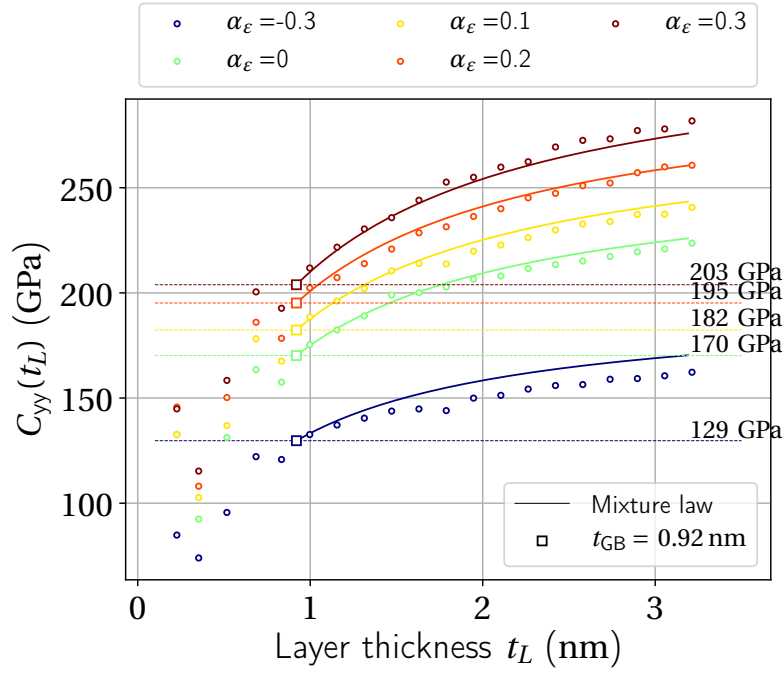
Now considering a larger grain size and with regard to equation 4.10, the thickness $t_{L,X\%}$ for the $X\%$ recovery of the bulk elastic moduli in terms of GB layer number (of unit thickness t_{GB}) is given by:

$$\frac{t_{L,X\%}}{t_{GB}} = \frac{X}{100 - X} \frac{C_{yy}^G - C_{yy}^{GB}}{C_{yy}^{GB}} \quad (4.11)$$

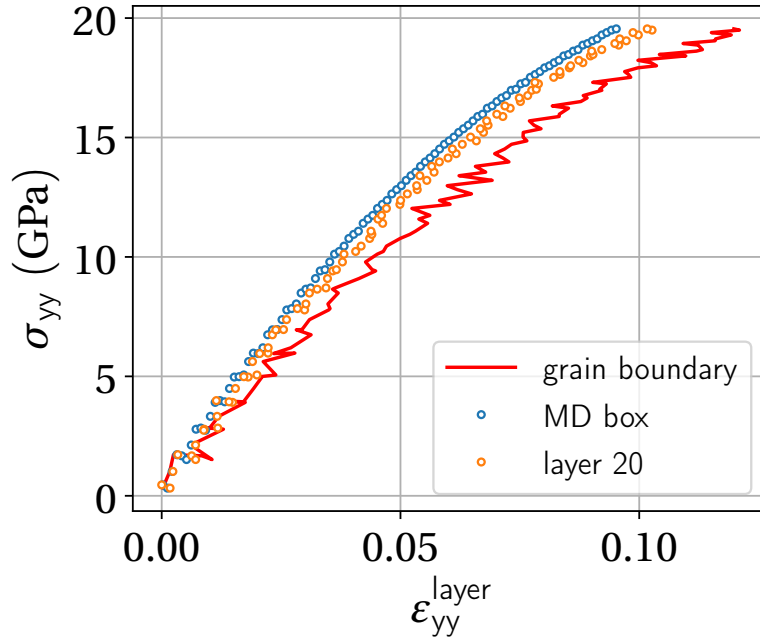
For the example of the $\Sigma 5$ $[0\bar{1}2]$ grain boundary (with an initial thickness $t_{GB} = 9.2\text{\AA}$), a layer of around 58 times the GB thickness is required to recover 99 % of the elastic modulus corresponding to a thickness of about 53 nm, but only around 5 times for a 90 % recovery, corresponding to a thickness of about 4.8 nm. This first-hand assessment suggests that the influence of the grain boundary is, from a mechanical point of view, very localised and should not be detected at the micron scale even though the values assessed here are clearly not negligible at the atomic scale.

The observed increase of the apparent elastic moduli of the layers in figure 4.12a with the increase of the $\alpha_\epsilon = \beta_\epsilon$ ratios, obviously results from the elastic behaviour within the

4. GRAIN BOUNDARIES FAILURE UNDER HOMOGENEOUS STRESS STATE



(a)



(b)

Figure 4.12: Comparison between the apparent elastic moduli of the layers for the $\Sigma 5$ $[0\bar{1}2]$ grain boundary at different $\alpha_\epsilon = \beta_\epsilon$ ratios and the variations obtained by the law of mixture taking into account the GB thickness t_{GB} (4.12a). Tensile curves of the 20th and GB layers along with the bicrystal curve (4.12b).

4. GRAIN BOUNDARIES FAILURE UNDER HOMOGENEOUS STRESS STATE

multiaxial loading applied, as already exposed before in chapter 2. It is chosen to further rely on the GB elastic moduli for $\alpha_\varepsilon = \beta_\varepsilon = 0$ (uniaxial strain) as an intrinsic mechanical property of the grain boundary.

Following these results for the $\Sigma 5$ GB, it is chosen to assess the GB apparent elastic moduli of the other grain boundaries from the tensile curves recorded on the bicrystals and their related single crystals in the $\alpha_\varepsilon = \beta_\varepsilon = 0$ cases. A mixture law (through equations 4.8 and 4.9) and the previously assessed GB thickness are used for the assessment:

$$C_{yy}^{GB} = t_{GB} \left(\frac{L_y}{2C_{yy}^{bi.}} - \frac{\phi_G}{C_{yy}^G} \right)^{-1} \quad (4.12)$$

with $C_{yy}^{bi.}$ the initial slope extracted from the tensile curves of the bicrystals, L_y its initial length and $\phi_G = \frac{1}{2}L_y - t_{GB}$ the grain size. The computed values are displayed in figure 4.13, along with the related values obtained on the same loadings applied on the single crystals. A value of 164 GPa is obtained for the $\Sigma 5$ GB which closely agrees with the value of 170 GPa, previously assessed from the layer tracking method. It is therefore believed that the above formulation may reasonably provide a reliable assessment.

The degradation of the apparent elastic moduli is here clearly evidenced for all the grain boundaries. Once again no clear geometrical tendency seems to hold which contrasts with the variation for the single crystals clearly linked to the crystals orientation with respect to the tensile axis. In the previous continuum description of the interfaces, these results further encourage to describe the core of the grain boundary as a predamaged phase which could be characterised by a damage variable D_{GB} :

$$D_{GB} = 1 - X_{GB} \quad \text{with } X_{GB} = \frac{C_{yy}^{GB}}{C_{yy}^G}$$

The computed values are displayed in the table figure 4.13, for all the grain boundaries. A quite significant mean value of around 35 % damage can be deduced over the grain boundaries considered with a maximum value of 43 % for the $\Sigma 13$ [051] and $\Sigma 17$ [041] GBs and a minimum value of 16 % for the $\Sigma 85$ [076] GB.

Using the simple assessment of equation 4.11, the thicknesses for 70 %, 80 % and 90 % bulk elastic modulus recovery are plotted in figure 4.14 for the thirteen GBs to provide a general idea of the extent of the GBs mechanical influence.

Once again, the computed values are significant at the atomic scale, but a strong localisation of the deformation at the micron scale should be concluded here, since a maximum distance of around 3 nm from the grain boundaries is registered for a rather weak 10 % damage.

However, it should be pointed out once more that the interfaces considered here are symmetric CSL tilt grain boundaries which present rather simple atomic structures. In the case of asymmetric tilt grain boundaries in copper FCC metal simulated by MD simulations, much more complex grain boundary structures have been evidenced [Tschopp and McDowell, 2007, Tschopp et al., 2008] with extended stacking faults originating

4. GRAIN BOUNDARIES FAILURE UNDER HOMOGENEOUS STRESS STATE

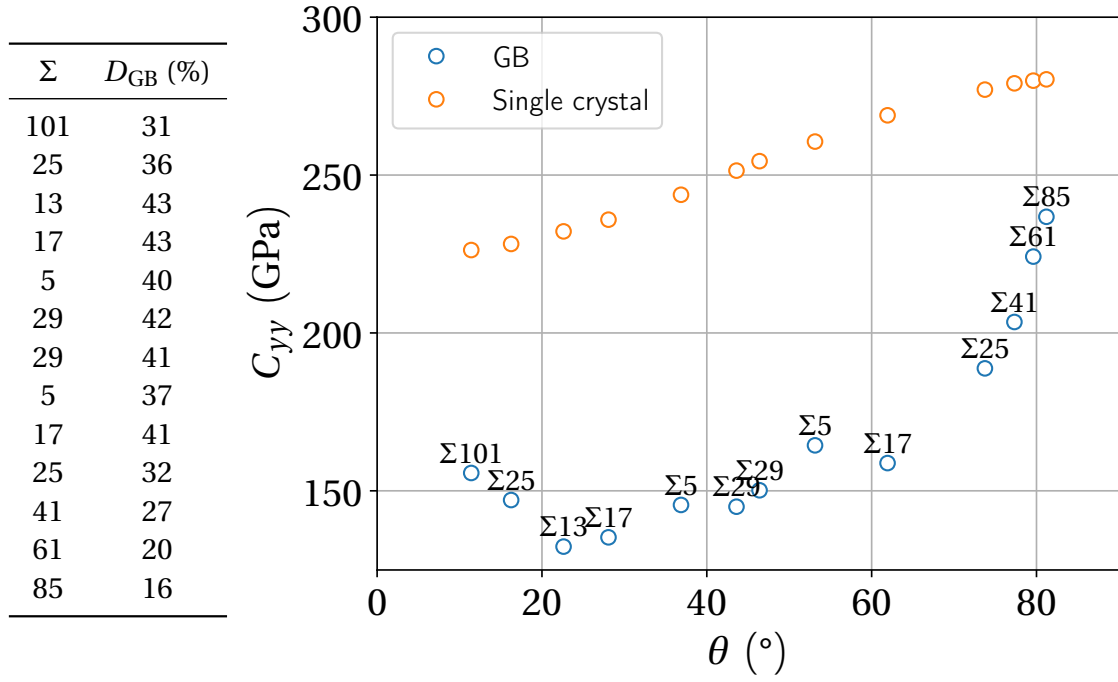


Figure 4.13: Apparent elastic modulus based on a mixture law for the thirteen CSL symmetric [100] tilt grain boundaries according to the rotation angle θ .

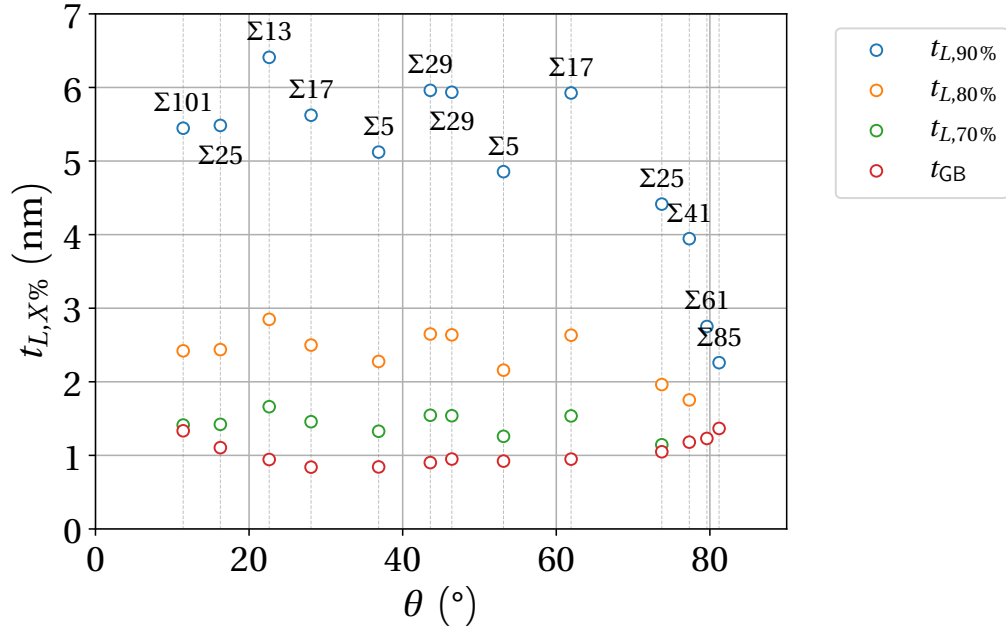


Figure 4.14: Thicknesses for the 70 %, 80 % and 90 % bulk elastic modulus recovery in the vicinity of the thirteen CSL grain boundaries

4. GRAIN BOUNDARIES FAILURE UNDER HOMOGENEOUS STRESS STATE

from the grain boundaries. In the case of regular polycrystals very few is known about the exact structures of the general grain boundaries and a more extended mechanical influence may be expected in comparison to the perfect structures considered here.

The above section has focused on a grain boundary description as a predamaged phase with respect to its adjacent grains which may partly explain the localisation of the bicrystal fracture at GBs.

However, nothing is said about the exact origins of the observed simulated GB decohesion nor is explained the geometrical variation of the critical axial stress to GB decohesion. The reasons may lie on the fact that the above energetically-based description of the grain boundaries as homogenised phases does not take into account the local atomic description of the interface.

As previously shown at the beginning of this chapter, the critical axial stresses recorded here, for which it has been suggested that they originate from an intrinsic GB property, are clearly correlated to the grain boundaries atomic structure. Furthermore, it has been shown that a criterion based solely on a rather globalised (at the bicrystal scale considered here) energy-based property such as the critical energy does not fully describes the fracture phenomenon observed for the bicrystals and that a second stress criterion was needed as suggested by Leguillon et al. [Leguillon, 2002].

The next section of this chapter therefore proposes to deal with the above remaining questions.

4.4 Local debonding of the grain boundary phase

In this final section, a link between the axial critical stress previously recorded for the bicrystals and the atomic structures of the grain boundaries is further suggested and supported.

The GB decohesion phenomenon is put in the context of the universal binding energy relation in metals, constituting an assumption on which the EAM potential of Mishin is based on.

In this framework, the observed GBs decohesion may be related to a unique debonding mechanism whatever the grain boundary structure considered, therefore permitting to better understand the geometrical variation of the axial critical stress of the bicrystal loaded under homogeneous stress states.

4.4.1 Influence of the disclination atomic volumes

Concerning the extraction of an elementary mechanism for GB decohesion, the observation of the $\Sigma 101$ debonding is quite revealing and easy to decipher as the bad fit regions are very localised and distant from one another along the GB plane. Indeed, figures 4.15b, 4.15d and 4.15e present several steps leading to the full decohesion of the bicrystal related to the debonding of the $\Sigma 101$ [0101] GB during the multiaxial

4. GRAIN BOUNDARIES FAILURE UNDER HOMOGENEOUS STRESS STATE

loading at $\alpha_\varepsilon = 0.15$. Figure 4.15c shows the related tensile curve of the bicrystal with the chronological indication of the preceding steps.

It is reminded in figure 4.15a, that the $\Sigma 101$ can be described by a succession of $|CD^7.CD^7|$ patterns. The C unit can be clearly identified by the common neighbour analysis indicating the white atoms departing from the regular FCC configurations of the green atoms.

At the maximum axial critical stress $\sigma_{yy}^c = 14.0 \text{ GPa}$ is recorded the first step (1) considered at the origin of the decohesion process. A void nucleation is observed almost simultaneously at every disclinations between the elementary units C and D . However, it should be noted that the precise moment at the origin of the void nucleation is quantitatively difficult to determined and might actually be located before the recorded peak.

A voids coalescence is observed subsequently (step 2 in figure 4.15d), just a few time steps later, as the axial stress decrease indicates the beginning of the relaxation phase.

The full decohesion in step 3 (figure 4.15e) is finally obtained almost instantaneously afterwards.

From this description of the $\Sigma 101$ GB debonding mechanism, two points could be proposed for a better understanding of the simulated phenomenon:

- The void nucleation at the origin of the decohesion process seems to be triggered by the local extension of the atomic volume in the vicinity of the disclinations between C and D elementary units. The fact that the use of the multiaxial loadings eases the onset of fracture may be linked to a criterion based on the reaching of an atomic critical volume while the dislocation nucleation is postponed for other mechanical reasons (as already exposed in chapter 3).
- The description of all the grain boundaries considered here in terms of similar elementary units D , C , B and A , may suggest a common mechanism for GB decohesion, paving the way to decipher the geometrical trend of the GB axial critical stress previously observed. It is reminded here that the C elementary unit can also be described by the adjunction of D and B units, for readability purposes the C notations is further conserved when needed.

In order to confirm these rather qualitative suggestions, it is proposed to focus more thoroughly on the atomic volume of the initial configurations of the thirteen grain boundaries at 0 K.

The assessment of atomic volumes is obtained on these configurations using the Voronoi analysis of OVITO [OVITO,] through the determination of the Voronoi cell at each atomic site and its related volume.

The Voronoi cell for a given atom, corresponds to the space region incorporating any point closest to the related atomic position than any other atoms, as illustrated in two dimensions by the upper scheme in figure 4.16.

4. GRAIN BOUNDARIES FAILURE UNDER HOMOGENEOUS STRESS STATE

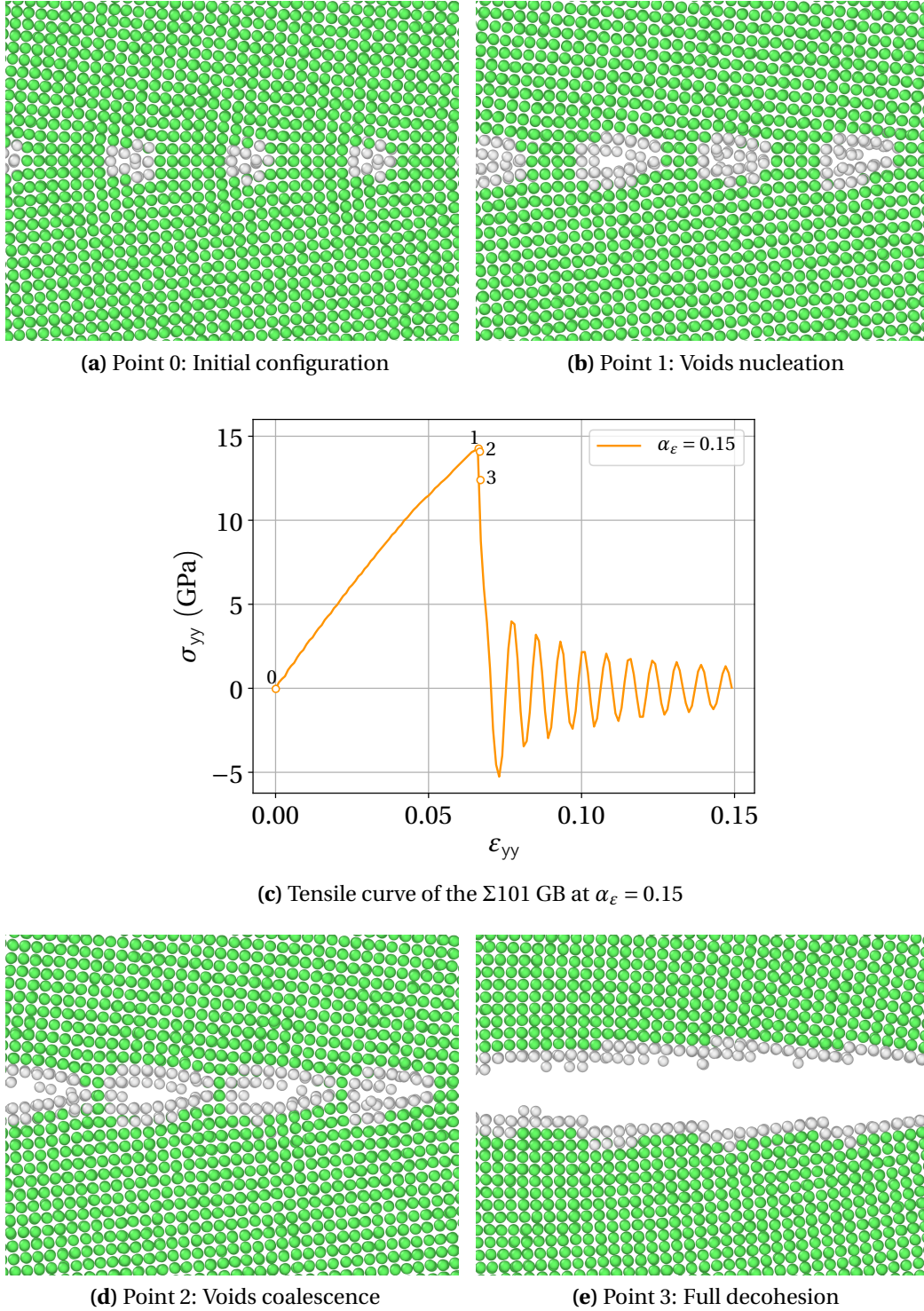


Figure 4.15: Tensile curve of the $\Sigma 101$ [0 10 1] GB at 300 K (4.15c) during the multiaxial loading at $\alpha_\epsilon = 0.15$ and visualisation of the different steps of the decohesion mechanisms (4.15a, 4.15b, 4.15d, 4.15e)

4. GRAIN BOUNDARIES FAILURE UNDER HOMOGENEOUS STRESS STATE

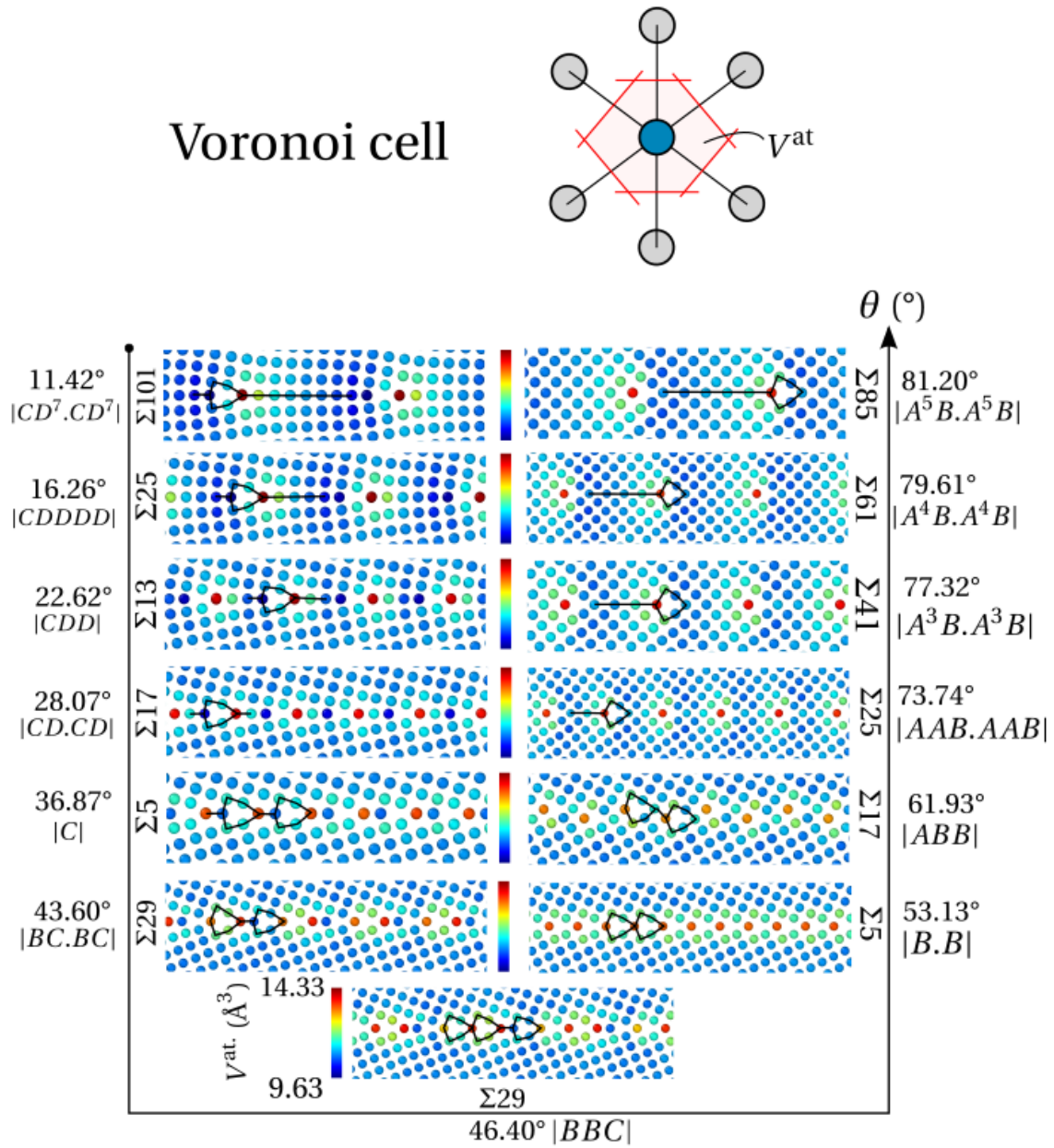


Figure 4.16: Atomic volume discrete field on the thirteen grain boundaries initial configurations according to their rotation angle θ . Part of the structural unit patterns are trace in plain lines.

4. GRAIN BOUNDARIES FAILURE UNDER HOMOGENEOUS STRESS STATE

The discrete field of Voronoi volumes is represented with the same scale on the initial configuration of the thirteen grain boundaries in figure 4.16 according to the rotation angle θ from the left top picture to the right top picture (anticlockwise).

Systematic local maxima of the atomic volume field are clearly evidenced at the disclinations between:

1. the C and D elementary units, for the $\Sigma 101$ to the $\Sigma 5$ $[03\ 1]$ GBs
2. the B and C or B and B units for the two $\Sigma 29$ GBs
3. the B and B or A and B units for the $\Sigma 5$ $[0\bar{1}\ 2]$ to the $\Sigma 85$ GB with the exception of the $\Sigma 17$ $[05\ 3]$.

which is directly correlated to the points made at the beginning of this chapter concerning a possible link between the critical axial stresses and the GB atomic structures. The switch of the maximum atomic volume sites according to the θ angle, along with the variation of the maximum atomic volume amplitude can be clearly deciphered. The largest maximum atomic volume among all the grain boundaries is evidenced for the $\Sigma 101$ GB.

Motivated by this last remark, the above debonding mechanism of the $\Sigma 101$ GB and its related critical axial stress constituting the lowest among all the other grain boundaries, the inverse variation of the maximum atomic volumes is plotted in figure 4.17 according to the rotation angle θ .

The resulting trend is clearly similar to the variation recorded for the axial critical stresses of the bicrystal in figure 4.2, although some discrepancies are observed for the third branch from the $\Sigma 17$ to the $\Sigma 85$ GBs with a seemingly upward translation with respect to the two previous branches.

These results confirm the aforementioned points: the GB decohesion mechanisms and the related critical stress of the bicrystals are intrinsically linked to the local atomic volumes of the disclination sites and their evolution during the loading whatever the grain boundary considered.

To fully complete this statement, figure 4.18 shows some of the steps leading to decohesion at 300 K and $\alpha_\varepsilon = \beta_\varepsilon = 0$ for the $\Sigma 25$ and $\Sigma 29$ GBs and at $\alpha_\varepsilon = 0.05$ for the $\Sigma 41$ GB. Each chosen GB belongs to one of the three distinctive branches described before. The disclination sites can be identified through the atomic volume discrete fields plotted during the loadings with the same scale; the void nucleation and coalescence in the final step are clearly correlated to these initial sites with a net increase of the maximum atomic volume.

It is therefore confirmed that the origins of intergranular fracture in the bicrystals under study, should be described on the basis of a criterion involving a local property intrinsic to the GB atomic structure.

From this ascertainment, it is supposed that contrarily to the decohesion of heterophase interfaces for which the separation of two atomic planes constitutes the underlying mechanism, the debonding of the homophase interfaces considered here,

4. GRAIN BOUNDARIES FAILURE UNDER HOMOGENEOUS STRESS STATE

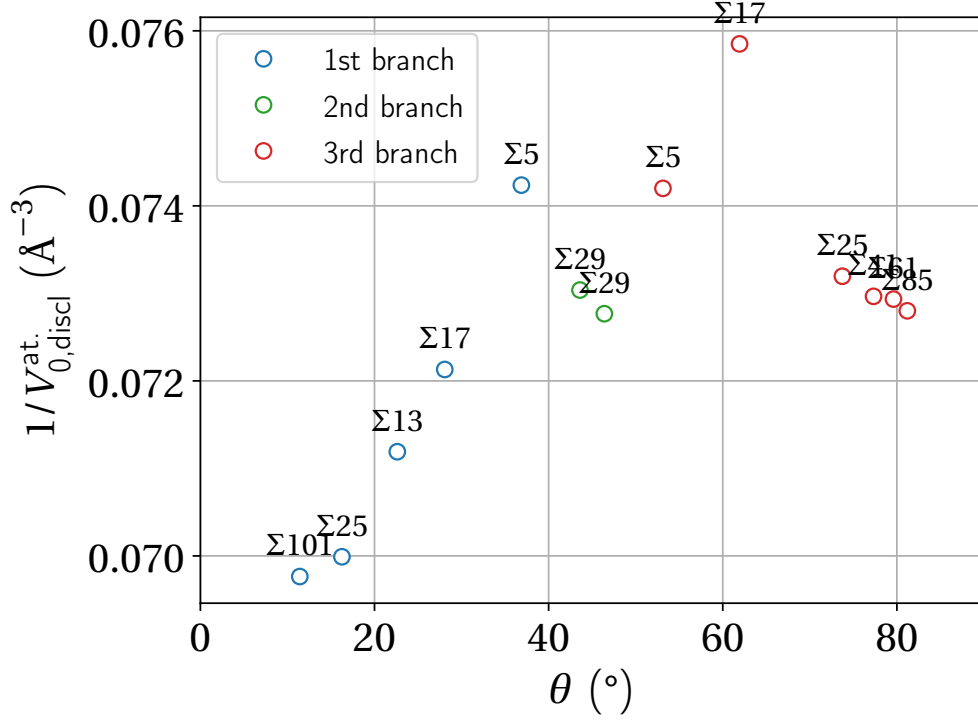


Figure 4.17: Maximum atomic volumes recorded at disclinations sites for the thirteen grain boundaries according to the rotation angle θ (4.17).

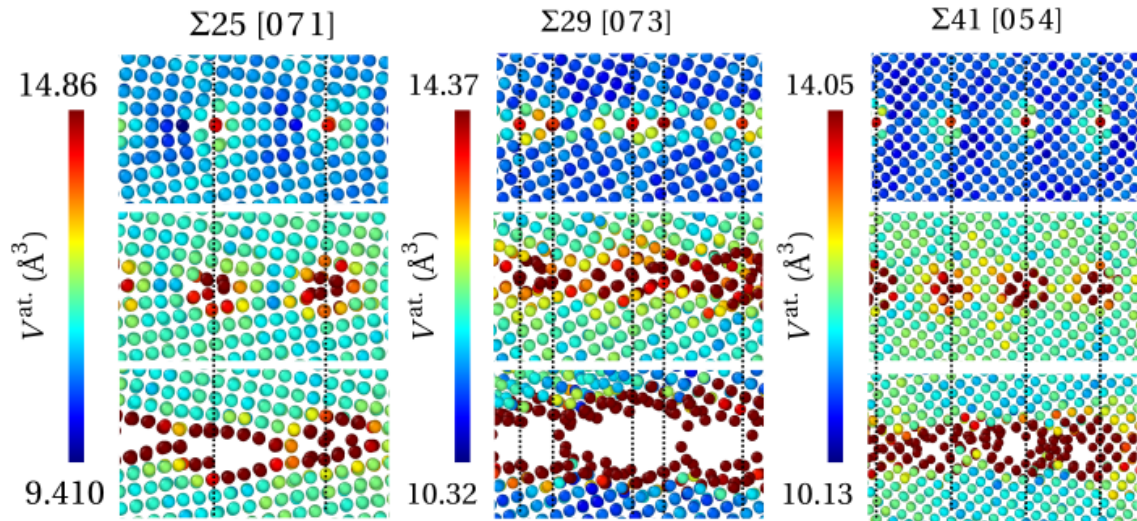


Figure 4.18: Debonding steps of the $\Sigma 25$ [071], $\Sigma 29$ [073] and $\Sigma 41$ [054] GBs, along with the atomic volume discrete fields. Disclination location are further marked by dotted lines.

4. GRAIN BOUNDARIES FAILURE UNDER HOMOGENEOUS STRESS STATE

is based on the local volume expansion at the disclination sites featuring initially the largest atomic volume at rest.

Comparatively to the generalise stacking fault energy curve for the onset of partial dislocations, the cohesive energy curve for bulk metals, relating the bulk energy with its volume expansion, should therefore constitute a milestone for understanding GB decohesion.

4.4.2 The universal binding energy relation

In the 1980s, Rose et al. [Rose et al., 1981, Rose et al., 1983, Rose et al., 1984] evidenced a universality of the debonding behaviours for a wide variety of bulk metals, interfaces and diatomic molecules through the determination of two scaling parameters in their ab initio computations: an energy and a length scale parameter ; the so-called universal binding energy relation (UBER) model was proposed.

The aforementioned behaviours are characterised by a binding-energy-distance curve at 0 K featuring the variation of the cohesive energy of the system considered against the related definition of a separation distance variable.

Considering the example of the cohesive energy E of bulk metals, Rose et al. have shown that choosing: the cohesive energy per atom at rest E_0 , a separation distance δ based on the average volume per atom and a length scale l defined as the critical separation at the inflexion point of the different binding curves, the following universal scaled energy form E^* could be fairly well identified for every material considered as shown by the author's plot reproduced in figure 4.19a [Rose et al., 1983]:

$$\frac{E(r_{WS})}{-E_0} = E^*(a^*) = -(1 + a^*)e^{-a^*} \quad (4.13)$$

$$a^* = \frac{\delta}{l} \quad (4.14)$$

$$\delta = r_{WS} - r_{WS,0} \quad (4.15)$$

$$l = \sqrt{\frac{-E_0}{\left(\frac{d^2 E}{dr_{WS}^2}\right)_{\delta=0}}} \quad (4.16)$$

where the radius r_{WS} is obtained from the mean Wigner-Seitz volume V (Voronoi volume per atom):

$$r_{WS} = \left(\frac{3}{4\pi} V\right)^{\frac{1}{3}} \quad (4.17)$$

with $r_{WS,0}$ the value of the above radius at rest, considering the lattice parameter a_0 at equilibrium:

$$r_{WS,0} = \left(\frac{3}{4\pi} V_0\right)^{\frac{1}{3}} \quad V_0 = \frac{a_0^3}{4} \quad (4.18)$$

4. GRAIN BOUNDARIES FAILURE UNDER HOMOGENEOUS STRESS STATE

The value of the second derivative of the cohesive energy at the origin was computed by Rose et al. within linear elasticity through the bulk modulus B :

$$\left(\frac{d^2 E}{dr_{\text{WS}}^2} \right)_{\delta=0} = 12\pi B r_{\text{WS},0} \quad (4.19)$$

More insight of the above formulation are given in appendix A. A third order formulation was originally proposed [Rose et al., 1984] through a final fit with the metal thermal expansion within the scope of reproducing the compressive behaviour of various metals:

$$E^*(a^*) = -(1 + a^* + 0.05(a^*)^3)e^{-a^*} \quad (4.20)$$

The first-order relation is however often used.

The universality found and characterised by $E^*(a^*)$ was physically justified [Banerjee and Smith, 1988] from the common exponential dependence of the host electronic density at atomic sites and its relation with the energy per atom. This rather empirical relation, although considered to be physically reliable as confirmed by numerous ab initio calculations [Hayes et al., 2004, Barbé et al., 2018, Černý et al., 2016, Lazar and Podloucky, 2008, Janisch et al., 2010], is sometimes used in the fitting procedure of semi-empirical potentials.

For our concern, the EAM potential of Mishin [Mishin et al., 2001] for pure nickel used for this study is, in part, fitted on this particular relation using experimental measurements [Kittel and McEuen, 1996, Simmons and Wang, 1971] (gathered in table 4.1) for the cohesive energy E_0 , the lattice parameter a_0 and the bulk modulus B . Therefore, the UBER model constitutes an assumption made at the origin of every MD computation performed herein. It is important to remind that the most rigorous way to obtain the cohesive energy curve is to perform ab initio computations and that the universal formulation of Rose et al. still constitutes a fitted model which may be considered to be, however, fairly reliable.

Reference	E_0 (eV)	a_0 (Å)	B (GPa)	l (Å)	P_c (GPa)	V_c (Å)
EAM (0 K) [Mishin, 2004]	-4.45	3.52	181.	0.276	29.13	16.52
Exp. [Kittel and McEuen, 1996]	-4.45	3.52	-	-	-	-
Exp. [Simmons and Wang, 1971]	-	-	181.0	-	-	-
Exp. [Rose et al., 1983]	-	-	-	0.27	-	-
Ab initio [Černý et al., 2016]	-	-	-	-	29.3	-

Table 4.1: Cohesive energy, lattice parameter,

The EAM fit on the UBER model, is further illustrated by the cohesive energy curve in figure 4.19b (blue markers). This plot is obtained from a simple molecular static computation of the volume expansion at 0 K of a bulk with the same potential for pure nickel. The fitted properties referenced in table 4.1 are clearly recovered here. The

4. GRAIN BOUNDARIES FAILURE UNDER HOMOGENEOUS STRESS STATE

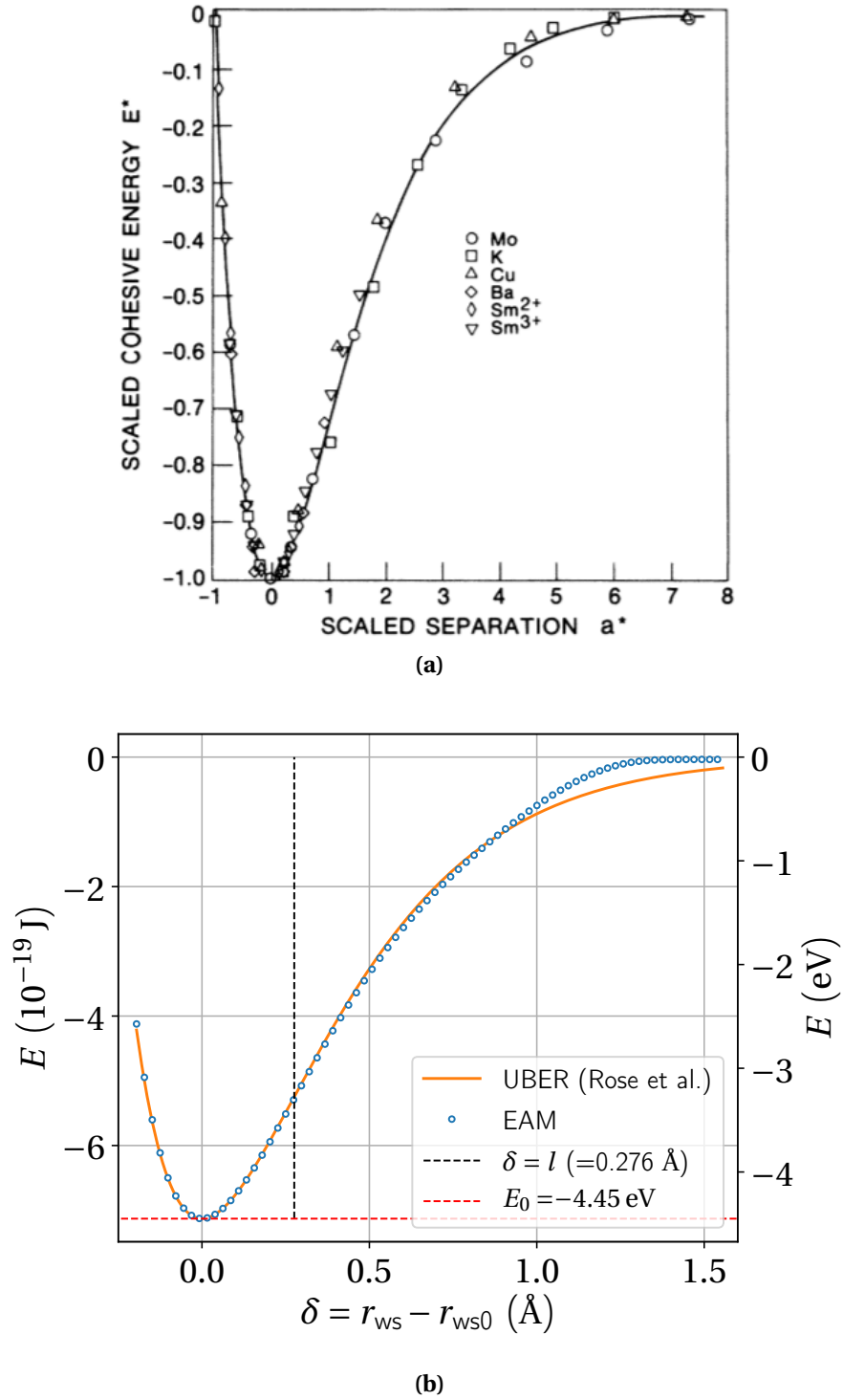


Figure 4.19: Universal Binding energy relation identified by Rose et al. for a wide variety of bulk metals (reproduced from [Rose et al., 1983]) (4.19a). Cohesive energy curve of the EAM potential of Mishin [Mishin, 2004] fitted on the UBER model (4.19b).

4. GRAIN BOUNDARIES FAILURE UNDER HOMOGENEOUS STRESS STATE

first order UBER model of equation 4.13 is also plotted (orange line) with the same properties. A logical correspondence with the computed values of the EAM potential is recovered. The inflexion point can be identified with the length scale parameter value of $l = 0.276 \text{ \AA}$ using equation 4.16. This value was previously obtained by [Rose et al., 1983] using the experimental references of table 4.1.

A pressure-volume relation can be derived from the UBER model through the first derivation of the cohesive energy with respect to V , the mean volume per atom:

$$P(V) = \frac{-E_0}{4\pi l r_{WS}^2} a^* e^{-a^*} \quad (4.21)$$

and the maximum (critical) pressure $P_c = P(V_c)$ is obtained at the critical volume:

$$V_c = \frac{4}{3}\pi r_c^3 \quad (4.22)$$

$$r_c = r_{WS,0} - \frac{l + r_{WS,0} - \sqrt{(l + r_{WS,0})^2 + 4lr_{WS,0}}}{2} \quad (4.23)$$

from the derivatives of the pressure-volume function. Further details can be found in appendix A. The obtained critical pressure $P_c = 29.13 \text{ GPa}$ is fairly similar to the result of ab initio computation of [Černý et al., 2016] recording a value of 29.3 GPa . It is to be noted, however, that the reference value of Černý et al. is obtained using a rigid grain shift loading. Therefore the bulk volume expansion performed here in molecular static may not be directly comparable. Nevertheless, the order of magnitude is still in a fairly good agreement which partly validates the use of this potential for decohesion simulations.

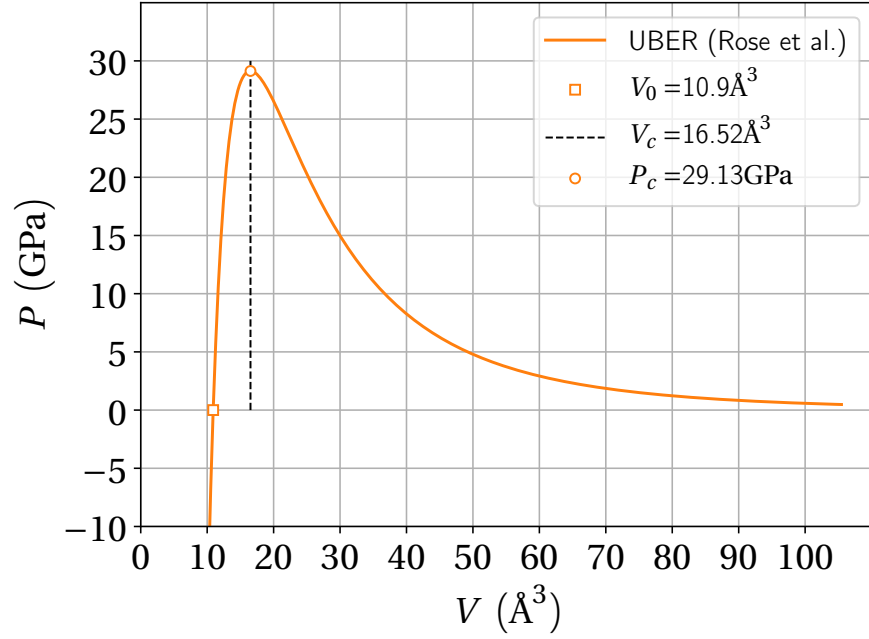
It is remarked here that the pressure P is previously derived from an energy per atom and the corresponding pressure-volume curve could therefore be related to an averaged behaviour per atom.

In that context, it is suggested to compare the UBER model with the triaxial stress per atom $\sigma_{m,discl}^{at.}$ at the previously identified disclination sites for every GB initial configuration at 0 K according to their related atomic volume.

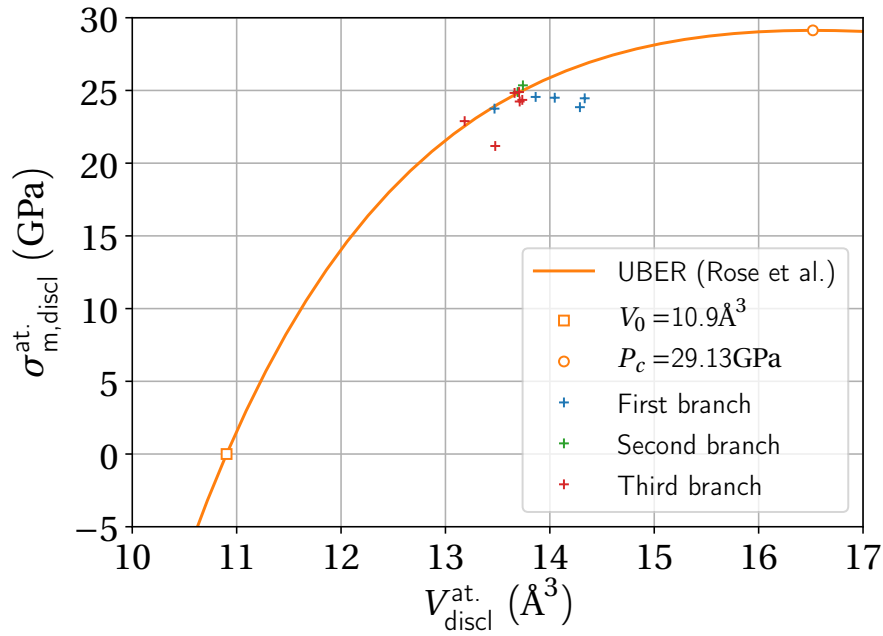
This comparison is motivated by the preceding correlation concerning the influence of the atomic volume on the final critical stress for which no direct explanation was provided. Furthermore, it was clearly shown before that a common ground should be expected for all the grain boundaries in terms of local debonding behaviour with regard to the previous geometrical trends observed. It is here suggested that this common ground should partly originates from the universal binding energy relation on which the potential is based on, and more specifically on the critical pressure P_c previously derived. A disclination site induces a local volume expansion of the neighbouring lattice, with respect to the initial bulk atomic sites. It is therefore suggested that a triaxial pre-stress of the disclination sites could be roughly predicted from the UBER model, should the above remark be valid.

Figure 4.20b presents such comparison. Several grain boundaries match the model although others show clear discrepancies.

4. GRAIN BOUNDARIES FAILURE UNDER HOMOGENEOUS STRESS STATE



(a)



(b)

Figure 4.20: Pressure-volume curve derived from the model of Rose et al. in figure 4.19b (4.20a). Triaxial stress per atom according to the related atomic volume at weak disclination sites from the initial configuration at 0 K of the thirteen grain boundaries and correspondance with the UBER pressure-volume variation (4.20b).

4. GRAIN BOUNDARIES FAILURE UNDER HOMOGENEOUS STRESS STATE

These discrepancies are expected since it is obvious that the coordination and more specifically the atomic radial distribution of a disclination atomic site differs in comparison to a bulk atom embedded in a FCC environment. However, it is also clear that the local behaviour can be closely related to the UBER model for the bulk.

A stress criterion for GB decohesion would then rely on the reaching of the critical pressure P_c (or the related critical volume V_c) from an intrinsic atomic triaxial pre-stress.

In the above consideration, the grain boundary is therefore preferentially viewed as an **homophase** interface in metals rather than a **general interface**. This last group of surface defects clearly has to compose with a wide variety of behaviour originating from different types of chemical bondings at the interface. For the example of heterophase interfaces, Rose et al. have proposed to rely on the distance of separation between the interface planes of the two phases which can be defined rather naturally. This same procedure may be used for grain boundaries with simple atomic structures featuring a flat surface plane. However, it becomes rather difficult to apply for more complex interfaces such as asymmetric grain boundaries or GBs featuring extended stacking faults. In the case of grain boundaries, it is clear that a problem rises from the definition of the interface plane which has to be rather arbitrary.

It is proposed here, for grain boundaries, to primarily consider a definition of the separation distance based on the atomic volumes as previously shown in this chapter. This view seems essentially more natural and avoids the above obstacle.

4.4.3 Local criterion for the onset of grain boundary decohesion

In this final subsection, it is finally proposed to confirm the previous assumption concerning the GB debonding mechanism based on the UBER model for the volume expansion of metals, during multiaxial loadings.

In order to limit the influence of temperature, different multiaxial loadings applied on the $\Sigma 5$ $[0\bar{1}2]$ at 10 K are considered. Transverse/normal strain ratios of $\alpha_\epsilon = \beta_\epsilon = 0.15$, 0.3 and 0.8 are used and configurations are recorded every 100 fs near the decohesion event in order to catch the debonding mechanism.

A loading in two phases is employed to ease the comparison with the UBER model: a compression is primarily carried out, followed by a regular tensile test. For both phases, the same strain ratios are kept constant. The compression is purposely used in order to catch a plausible elastic behaviour at the disclination sites since a pre-distorted volume is intrinsically recorded. Care is taken to performed the compression phase without any irreversible alteration of the initial configuration like grain boundary migration or disconnection step nucleation.

4.4.3.1 Debonding mechanism and elementary representative volume

For every loading, the weakest disclination site leading to the first local debonding is qualitatively detected and indicated by the red atom on one of the atomic plane in the z direction as shown in figure 4.21b. Two atomic planes are shown in this figure, with the

4. GRAIN BOUNDARIES FAILURE UNDER HOMOGENEOUS STRESS STATE

white and light green atoms on the same plane and the grey and dark green atoms on the underlying plane.

The atomic stress diagonal components $\sigma_{ij}^{\text{discl.}}$ of the weakest disclination atomic site are recorded according to the axial stress computed on the bicrystal σ_{yy} and plotted in figure 4.21a for the $\alpha_\varepsilon = 0.15$ case.

As already recorded in chapter 2, a rather constant critical axial stress of about 23.6 GPa is obtained once again whatever the loading applied. However, a slight decrease from 24.1 GPa at $\alpha_\varepsilon = 0.15$ to 23.1 GPa at $\alpha_\varepsilon = 0.8$ is to be noted. This value agrees rather satisfyingly with the ab initio results at 0 K of [Černý et al., 2016] for the exact same grain boundary in pure nickel, recording a 25.3 GPa maximum tensile stress after a rigid grain shift loading. This discrepancy could be explained by the fact that this later loading induces a constant strain ratios of 0 in both transverse directions while a 0.15 ratio is employed here, which would agree with the slight decrease observed before. It is also reminded here that the MD computations are performed at 10 K, which could induce slight thermoactivation effect. The discrepancy could also be explained by the use of a semi-empirical potential and the MD method which are obviously not as physically reliable as ab initio calculations.

From figure 4.21a, it is clear that the atomic axial stress displays larger values than the recorded axial stress of the bicrystal with a seemingly parabolic shape. The atomic stress drop (whatever the component) at constant axial stress indicates the original debonding event happening before the failure of the bicrystal by void coalescence. In the case of the $\Sigma 5$ [0 1 2], this debonding event is almost concomitant with the full GB decohesion since the disclination atomic sites are closely located along the GB plane. This is not always true since for some cases, further slight increase of the loading is necessary for the void coalescence. However this concomitance is observed very frequently for the grain boundaries considered here.

It is interesting to note that a maximum axial atomic stress, indicating local stress relaxations, is recorded well before the decohesion event. A debonding criterion based on this atomic axial stress would therefore not be indicated here.

The elementary mechanism of debonding, cross-marked on figure 4.21a, is shown by the sequence of configurations 1 to 5 (further abbreviated {1..5}) in figure 4.21b where the dotted horizontal line indicates the GB plane.

The debonding is clearly happening by the irreversible displacement of the atomic disclination site therefore inducing a local void nucleation immediately spreading further.

This local mechanism seems to qualitatively agree with the procedure employed by [Černý et al., 2016] for the rigid grain shift loading for which a cleavage plane is chosen between the GB plane and the first neighbouring plane. It is clear that, in comparison, the debonding is primarily localised at only one disclination site. However, due to the atomic structures considered here with the GB plane essentially composed of disclination sites, the comparison seems to be valid.

On the initial configuration of the grain boundary, several representative elemen-

4. GRAIN BOUNDARIES FAILURE UNDER HOMOGENEOUS STRESS STATE

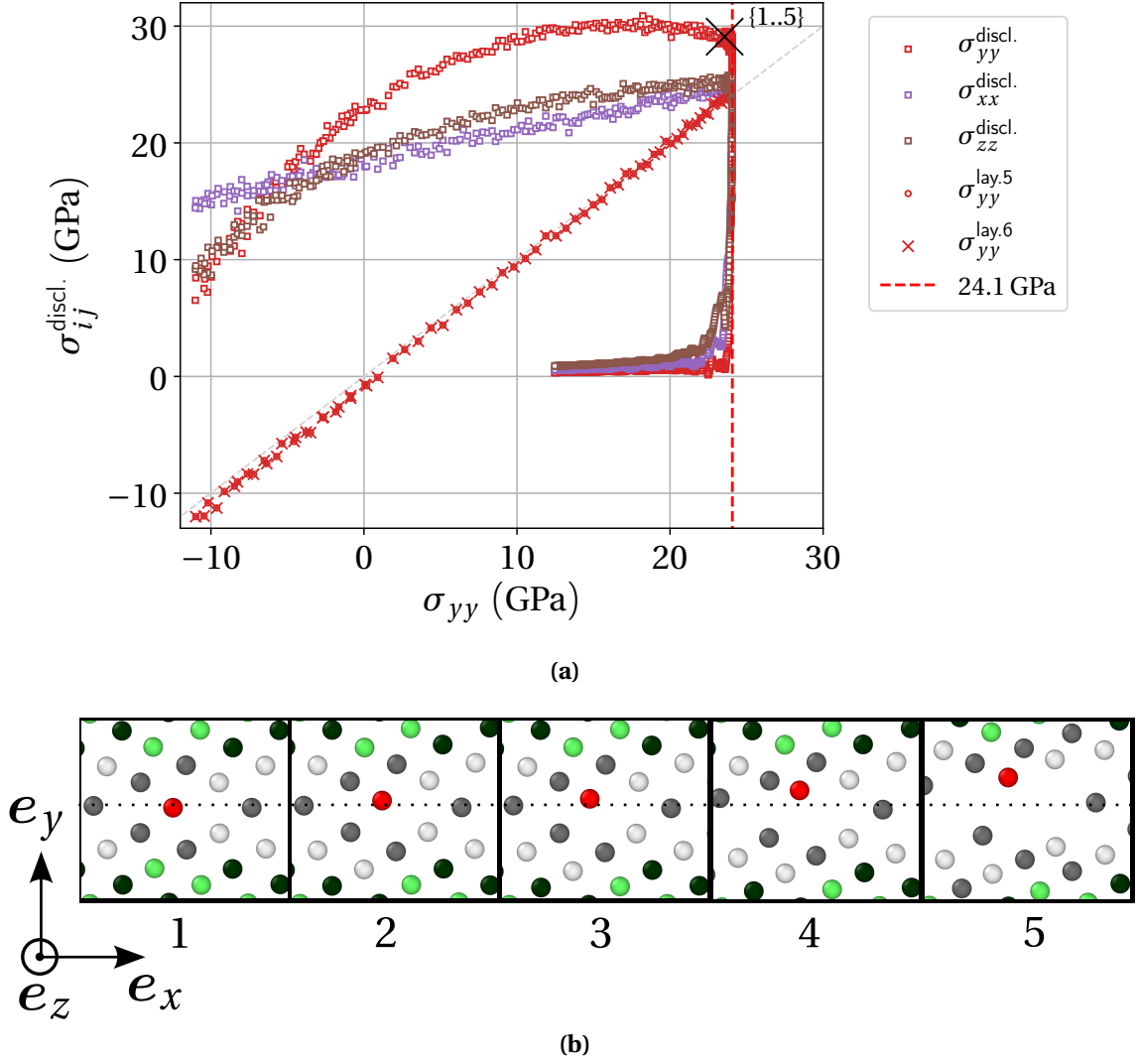


Figure 4.21: Atomic stress diagonal components at the weakest disclination site and on elementary representative volumes according to the axial stress of the bicrystal related to the $\Sigma 5$ $[0\bar{1}2]$ during the $\alpha_\varepsilon = 0.15$ multiaxial loading (4.21a). Related debonding mechanism observed at the weakest disclination atomic site (in red) identified on one localised atomic plane (according to the direction z) with a duration of a few time steps $\Delta t = 100$ fs. The grain boundary or the bulk are identified by atoms in white and grey, or green and dark green according to the atomic plane $[200]$ or $[100]$ in the z direction (4.21b).

4. GRAIN BOUNDARIES FAILURE UNDER HOMOGENEOUS STRESS STATE

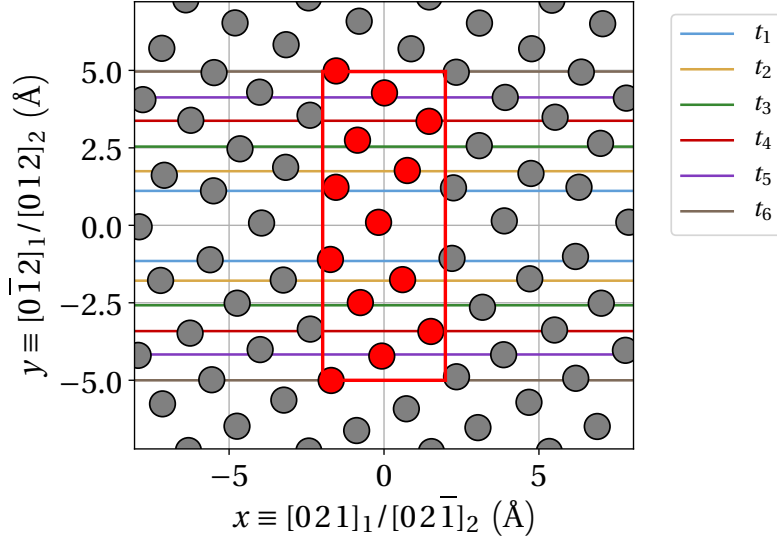


Figure 4.22: Representative elementary volume of atoms in red, used for the computation of the atomic axial stress for the layer six.

tary volumes (REV) of atoms surrounding the weakest disclination site are defined in relation with the atomic layers of thickness t_i between the y_i^+ and y_i^- coordinates. The transverse dimensions Δ_x and Δ_z of the REV are chosen so that a periodicity is achieved with regard to the GB atomic structure. Since a succession of B elementary units are composing the entire $\Sigma 5$ grain boundary, and since the CSL period is composed of only two B elementary units, the following dimensions are used for selecting only one B elementary unit in the REV:

$$\Delta_x = \frac{1}{2} \frac{a_0}{\sqrt{5}}$$

$$\Delta_z = a_0$$

An illustration of the REV for $i = 6$ is given in figure 4.22. Hence, for $i = 0$, the disclination site is recovered. For every REV i , the axial stress $\sigma_{yy}^{\text{lay},i}$ at a given time step is simply assessed through the summation of the virial and kinetic contributions of every REV atoms with respect to the REV volume $V^i = t_i \Delta_x \Delta_z$.

Results for $i = 5$ and 6 are plotted in figure 4.21a with a lower sampling, for readability purposes. It is clearly shown that the axial stress of the box is recovered between these two layers, which corresponds to the GB thickness evaluated before.

From this later result, two points can be made in order to prepare the case of heterogeneous loadings, yet to come (e.g. the impact of a slip band with a grain boundary):

- An REV can be intrinsically defined for the $\Sigma 5$ grain boundaries, since a periodicity and an homogeneous repartition of the disclination sites permit to link the local and global stresses at the interface plane. This might be more complicated for more complex grain boundaries.

4. GRAIN BOUNDARIES FAILURE UNDER HOMOGENEOUS STRESS STATE

- Provided that such a REV can be defined, it is suggested that its dimensions could be defined on the thickness t_{GB} and the atomic periodicity of the disclination sites involved in the GB debonding.
- Then, a definition of such a REV may allow the use of the axial critical stress of the bicrystals for a stress criterion at higher scales, provided that the computed GB normal stress to compare, be roughly homogenised on the REV dimensions (in the case of finite element computations for example).

4.4.3.2 Comparison to the UBER model of Rose et al.

The potential energy per atom of the disclination site and the average potential energy per atom of a slice gathering bulk atoms is recorded during the loading according to the related atomic volumes. The energies variation are plotted in figures 4.23a and 4.23b according to the separation distance δ based on the above atomic volume as already indicated before by equations 4.15 and 4.17.

In both cases (bulk and disclination) and for every loading performed, the model of Rose et al. on which the EAM potential is based on, can clearly describe the cohesive energy variation in the elastic regime (figure 4.23a). The energy shift of the local minima points, featuring a $\Delta\delta_{GB}$ separation distance from each other, could be related to the difference of atomic neighbours radial distribution ; the disclination indicating a lower energy configuration in compression than the bulk atoms at rest.

However, the energy variations are evidently similar. This might be explained by the fact that the relation between the energy and the host electronic density at the atomic sites, empirically modelled here by the EAM potential, varies in the same manner whatever the atomic surrounding. Further similar verification would however be needed for the other grain boundaries disclination sites as the same curves may not be recovered in the general case. Moreover, this should also need to be validated by ab initio calculations which obviously represents a more indicated tool to this matter.

It can be remarked that, for the bulk atoms, the full curve is actually displayed in figure 4.23a as the decohesion is indeed occurring at the disclination sites while the bulk atoms are still in the elastic regime.

The same match with the model of Rose et al. is obtained in figure 4.23b for a great part of the cohesive energy curve related to the disclination, despite slight discrepancies. It is obvious that at some point during the loading, the creation of a new surface, as a result of the disclination debonding, clearly departs from the entire isolation of a bulk atom through volume extension. Hence the differences observed here between the model and the disclination cohesive energy curve, concerning:

- The final energy plateau directly linked to the energy of the disclination atom in the newly created surface environment and therefore not completely isolated.
- The critical length scale at the inflexion point of the model which clearly diverges from the critical length at the debonding mechanism observed in MD.

4. GRAIN BOUNDARIES FAILURE UNDER HOMOGENEOUS STRESS STATE

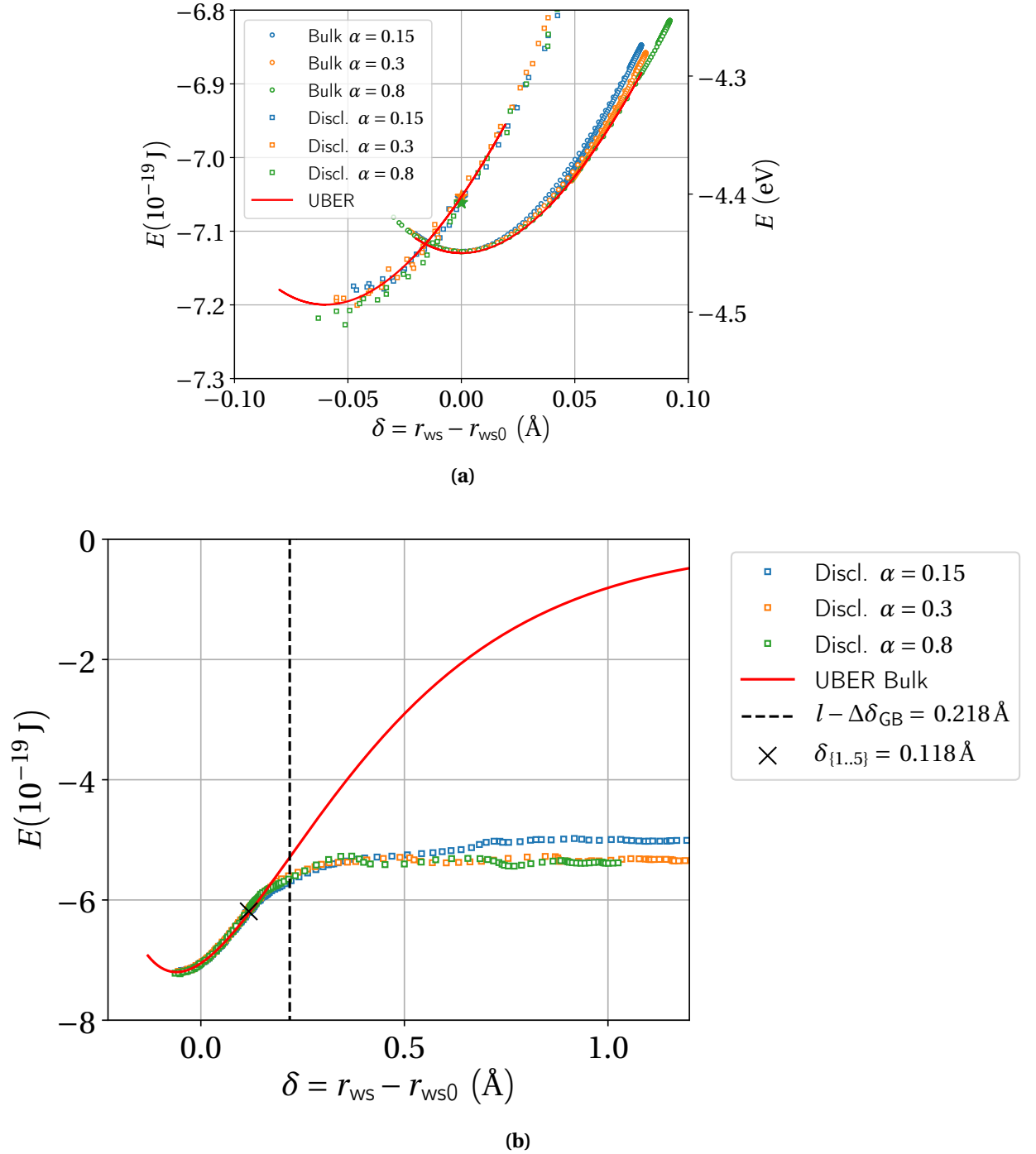


Figure 4.23: Energy per atom of the bulk and the weakest disclination site according to the volume-based definition of the separation variable δ during the $\alpha_\varepsilon = \beta_\varepsilon = 0.15, 0.3$ and 0.8 loading cases in the elastic regime (4.23a). Full cohesive energy curve for the disclination site and comparison with the UBER model (4.23b).

4. GRAIN BOUNDARIES FAILURE UNDER HOMOGENEOUS STRESS STATE

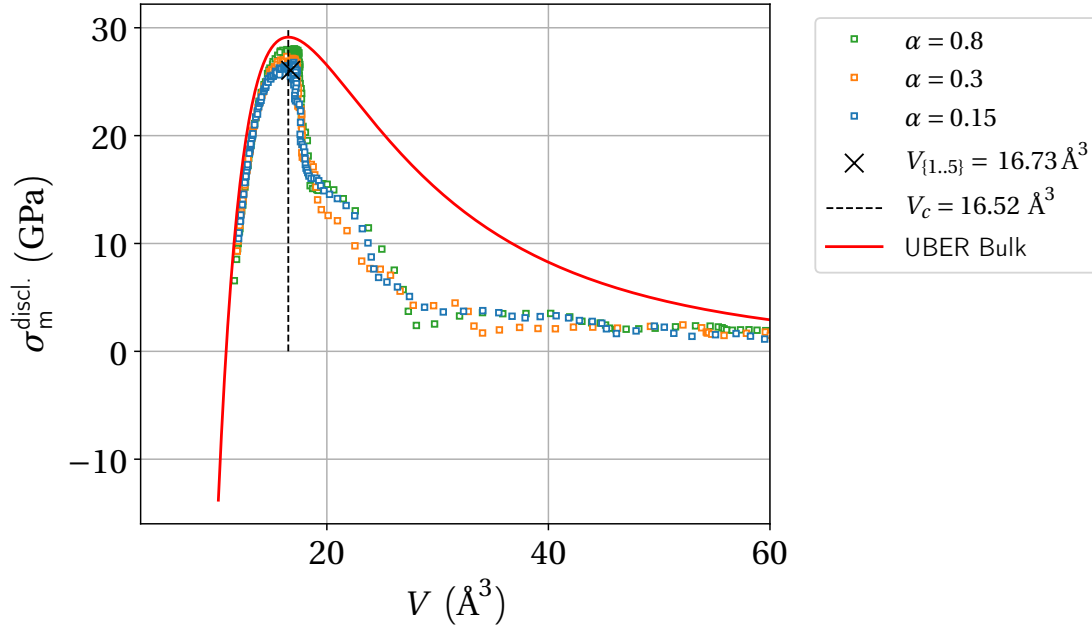


Figure 4.24: Variation of the triaxial atomic stress at the weakest disclination site according to the related atomic volume with a comparison to the pressure-volume derived from the UBER model. The debonding sequence {1..5} is indicated by the cross mark.

The separation distance δ chosen here, may not be physically representative of the debonding event.

A comparison between the pressure-volume relation derived from the UBER model in equation 4.21 and the atomic triaxial stress variation according to the atomic volume for the three $\alpha_\epsilon = 0.15, 0.3$ and 0.8 loadings, is finally proposed in figure 4.24.

Once again, the variations are very similar despite some discrepancies that might be explained by the above remarks. The critical stress value of 29.1 GPa slightly overestimates the values ranging from 26.8 GPa to 28.0 GPa (at $\alpha_\epsilon = 0.15$ and 0.8) by 8.0 % and 3.7 % respectively.

It is also interesting to note that a rather low variation of the critical triaxial atomic stress is reported between $\alpha_\epsilon = 0.15$ and $\alpha_\epsilon = 0.3$ with related values of 26.8 GPa and 27.3 GPa respectively. This might explain the seemingly constant value of the axial critical stress previously recorded for the $\Sigma 5 [0 \bar{1} 2]$ in chapter 3, illustrated by the plateau in the $(\alpha_\epsilon, \beta_\epsilon)$ space. Should the same behaviour be confirmed on the wide variety of the weakest grain boundaries disclination sites and considering the universality of the debonding mechanism previously shown in figure 4.18, this later remark might be extrapolated further, with caution, to all the grain boundaries.

Ultimately, a fairly good agreement is also found in figure 4.24, between the critical volume V_c predicted by equation 4.23 and the atomic volume $V_{\{1..5\}}$ at the debonding event.

4. GRAIN BOUNDARIES FAILURE UNDER HOMOGENEOUS STRESS STATE

This later observation may once again, point toward a debonding criterion based a critical volume or a related critical triaxial stress, even if the same verifications should be carried out for all the grain boundaries. A clear physical causality have yet to be deciphered for that matter. As stated before, these result would necessitate ab initio computations for that matter.

In conclusion, assuming a debonding criterion based on the reach of a local critical volume or a critical atomic triaxial stress (approximated in the UBER theory of Rose et al.), several points would still need clarifications in order to achieve a prediction of the axial critical stress for bicrystals failure, based on their geometrical or atomistic characterisation:

- The initial atomic volume at the disclination sites according to the atomic structure and geometry of the related grain boundary.
- The relation between the atomic volume variation at the disclination sites and the applied strain state. Or, alternatively the relation between the atomic triaxial stress at the disclination sites and the stress state applied on the bicrystal.

Should the above points be clarified, and based on the previous results of this chapter, the following stress criterion formulation could then be proposed in the context of the UBER model:

$$\sigma_{yy} \geq \sigma_{yy}^{c, \text{frac}} \quad (4.24)$$

$$\sigma_{yy}^{c, \text{frac}} = f(\text{GB}, P_c, \sigma_m^{0, \text{discl.}}) \quad (4.25)$$

$$\sigma_m^{0, \text{discl.}} \approx P(V_{0, \text{discl.}}^{\text{at.}}) \quad (4.26)$$

where $\sigma_{yy}^{c, \text{frac}}$ is the usual axial critical stress, $P(V)$ the pressure function derived from the UBER model in equation 4.21, P_c the related maximum critical pressure at the critical volume V_c , $\sigma_m^{0, \text{discl.}}$ and $V_{0, \text{discl.}}^{\text{at.}}$ the initial atomic triaxial stress and volume at the weakest disclination sites and f a relation, yet to be found, between the remote and the local stress which will depend on the grain boundary and the stress gap between the initial and critical triaxial atomic stresses.

Such a formulation seems however difficult to envision without any molecular dynamics or ab initio computation.

4.5 Summary of the results and conclusion

4.5.1 Results

In this chapter, the following results are found:

- Axial critical stresses for GB decohesion ranging from 14 GPa to 20 GPa are recorded. A geometrical correlation between this critical stress and the GB rotation angle θ is partly evidenced. However, the GB macroscopic degrees of freedom are not sufficient to describe this trend and it is shown that the atomic structure of the grain boundaries have to be considered for that matter, with an obvious influence of particular disclinations.
- The low angle grain boundaries feature the lowest critical axial stresses and are the most prone to GB decohesion and the less prone to GB heterogeneous dislocation nucleation.
- The Griffith energies display, in comparison, an inverse variation. No conclusion can be derived concerning the grain boundary strength based on either a critical stress or a critical energy as both mechanical properties seems to be complementary.
- The bicrystal failure is consistent with a coupled criterion for fracture as proposed by Leguillon. It is clearly shown that a unique energy criterion only represents a necessary condition, while a second stress criterion is predominant to describe the bicrystal failure, and therefore clearly needed. With that regard, the axial critical stress is then considered as an intrinsic GB mechanical property for the decohesion of the bicrystal under homogeneous stress state.
- A definition of the grain boundary as a phase of finite thickness featuring degraded mechanical properties is proposed at this scale. Grain boundaries thicknesses are naturally assessed, based on their intrinsic excess energy. Values between about 0.9 nm to 1.35 nm are recorded. Not surprisingly, the variation of this energy-based thickness follow the same trend as the critical energy or the inverse trend of the GB energy ; this should be explained by the mechanical description of the grain boundaries in terms of intrinsic GB dislocations.
- Apparent elastic modulus are derived from this preceding thickness assessment using a law of mixture. This method is shown to be fairly satisfying and valid using an atomic layer by layer tracking during the various multiaxial loadings applied on the $\Sigma 5$ [012] GB. Degraded values of around 65 % (mean value) of the elastic modulus of the related single crystals are found for the GBs under study.
- The above results confirm the validity of considering the GBs as predamaged phases in a continuum framework. The degraded mechanical properties of the

4. GRAIN BOUNDARIES FAILURE UNDER HOMOGENEOUS STRESS STATE

GB phase induce a strain localisation which may partly explain the location of the bicrystal failures at grain boundaries. However, the extent of the grain boundaries mechanical influence is very localised, as a 90 % of the apparent Young modulus is recovered at a distance of at most 3 nm from the interface.

- Based on the observed elementary mechanisms of GBs decohesion through void nucleation and coalescence, a presumption for the origin of the GBs debonding, based on the local expansion of atomic volume at the GBs is advanced.
- A correlation is found between the initial atomic volumes at the weakest disclination sites and the critical axial stresses recorded. The link between the previous critical stress variation and the structural unit description is therefore clarified.
- The EAM potential used here for pure nickel is partly fitted on the universal binding energy relation of Rose et al., describing the variation of the cohesive energy of metals with respect to their volume expansion. It is shown that the triaxial pre-stress at disclination sites on the initial GB configuration can be recovered by the UBER model from the knowledge of their initial atomic volume.
- The elementary debonding mechanism at the origin of the void nucleation is identified at the weakest disclination atomic site. The cohesive energy curve and the related triaxial stress-volume variation at the weakest disclination site can be recovered by the UBER model. The discrepancies observed might be explained by the neighbouring atomic radial distribution and the resulting creation of two surfaces instead of an entire atomic isolation. A critical pressure of 29.1 GPa expected by the model overestimates slightly by 4 % to 8 % the recorded MD values. A good agreement is found between the predicted and actual value of the critical volume for debonding which confirms the previous presumption. These results underline the importance of considering the grain boundaries as homophase interfaces whose behaviour can be strongly related to the behaviour of the bulk in the adjacent grains.
- A prediction of the axial critical stress solely based on a geometric or an atomic description of the GB seems difficult to obtain without MD or ab initio simulations.
- Should the axial critical stresses be used at upper scales for prediction purposes, the previously described homogenised view of the grain boundary as a separate phase of finite thickness t_{GB} with its own mechanical properties could be adopted. However, care should be taken to consider a succession of representative elementary volume along the interface plane for a reliable comparison with computed stress value normal to the GB plane.
- A summary of the GB intrinsic properties assessed in this chapter are gathered in the following table [4.2](#)

4. GRAIN BOUNDARIES FAILURE UNDER HOMOGENEOUS STRESS STATE

Σ	θ	\boldsymbol{n}	$\gamma_{\text{GB}}^{300\text{K}}$	$\sigma_{yy}^{\text{c,frac}}$ (GPa)	γ^{c} (mJm ⁻²)	t_{GB} (nm)	C_{yy}^{GB} (GPa)	$V_{0,\text{discl}}^{\text{at}}$	$d_{\text{GB}}^{\text{disl}}$ (Å)	SU
101	11.42°	[0101]	991	14.0	3369	1.33	155.6	14.334	17.6	$CD^7.CD^7$
25	16.26°	[071]	1152	14.8	3265	1.11	147.1	14.288	12.5	CDDDD
13	22.62°	[051]	1275	15.8	3050	0.94	132.3	14.047	9.0	CDD
17	28.07°	[041]	1341	17.1	3022	0.84	135.3	13.864	7.3	CD.CD
5	36.87°	[031]	1339	19.9	3040	0.84	145.5	13.470	5.5	C
29	43.60°	[052]	1443	17.8	2949	0.90	145.0	13.692	4.0 (5.5)	BC.BC
29	46.40°	[073]	1478	16.8	3018	0.95	150.2	13.742	4.0 (5.5)	BBC
5	53.13°	[012]	1357	19.6	3163	0.92	164.4	13.477	3.84	B.B
17	61.93°	[053]	1283	17.9	3068	0.95	158.8	13.184	4.93	ABB
25	73.74°	[043]	979	16.4	3458	1.05	188.8	13.662	8.7	AAB.AAB
41	77.32°	[054]	880	16.1	3617	1.18	203.5	13.705	11.1	AAAB.AAAB
61	79.61°	[065]	765	15.8	3682	1.23	224.2	13.711	13.8	A ⁴ B.A ⁴ B
85	81.20°	[076]	711	15.7	3784	1.37	236.8	13.736	16.1	A ⁵ B.A ⁵ B

Table 4.2: Summary of the intrinsic properties of the thirteen CSL symmetric [1 0 0] tilt grain boundaries. θ : rotation angle, \boldsymbol{n} : crystallographic normal direction to the GB plane in the upper grain, $\gamma_{\text{GB}}^{300\text{K}}$: GB energy at 300 K, $\sigma_{yy}^{\text{c,frac}}$: axial critical stress of the bicrystal, γ^{c} : Griffith energy, t_{GB} : GB thickness, C_{yy}^{GB} : GB apparent elastic modulus, $V_{0,\text{discl}}^{\text{at}}$: initial atomic volume at the weakest disclination sites, $d_{\text{GB}}^{\text{discl}}$: distance between the GB disclinations, SU: structural unit GB description.

4. GRAIN BOUNDARIES FAILURE UNDER HOMOGENEOUS STRESS STATE

4.5.2 Conclusion

In an attempt to complete the scheme presented in figure 3.8, the grain boundary decohesion phenomenon observed in chapter 2 is treated in this chapter, from a prediction perspective based on the geometrical and atomistic description of the grain boundaries.

The geometrical variation by pieces, of the critical stress to GB decohesion is observed and explained according to the GB rotation angle θ . With that respect, the local atomic volume of the grain boundaries disclinations at rest and during the multiaxial loading constitute a key point. The elementary mechanism of GB disclination debondings by local volume expansion followed by a quasi-simultaneous voids coalescence is at the origin of the bicrystal failure.

With that regard, and considering the universality of the cohesive behaviour of metals under volume expansion to be respected a priori, the disclination cohesive behaviour of any grain boundaries considered could be described by the related UBER model. For a given grain boundary, the seemingly constant value of the axial critical stress, whatever the applied loading considered, should also be explained by the rather weak variation of the critical triaxial disclination stress related to the UBER model.

It is then strongly suggested that such perfect grain boundaries should be primarily envisioned as homophase interfaces, clearly linked to their bulk behaviour with respect to their cohesive properties, rather than regular interfaces naturally defined by two separating surface planes during decohesion.

From a more pragmatic point of view, the consideration of grain boundaries as homogenised phases is suggested and supported. It brings a convenient way to model grain boundaries at the upper scales where heterogeneous loadings can be expected in a continuum framework. This method obviously contrasts with the atomic nature of the grain boundaries considered at this scale and its validity shall be verified further in the subsequent chapters. For that matter, GBs geometrical and mechanical properties to be used in the next chapters, are summarised in table 4.2.

5

Stress concentrations and crack initiation at grain boundaries: the V-notch problem

In this chapter, the fracture initiation of grain boundaries is considered with a multiscale approach taking into account heterogeneous loadings.

In this regard, the previous approach considering the modelisation of grain boundaries as homogenised interfaces, with two main properties of fracture at the atomic level, is fully reused through two bottom-up approaches in the context of the V-notch problem at the continuum level: the application of a coupled criterion for fracture initiation and the use of a cohesive zone model in finite element computations.

These approaches are completed and physically validated, by a so-called top-down approach which consists in performing the inverse scale transition from finite element computations at the microscopic scale to molecular dynamics simulations at the atomic scale. To this extent the FE2AT method is conveniently used. It also brings qualitative and quantitative support for the preceding endeavour initiated in chapters 2, 3 and 4. In particular, the relevance of the bicrystal multiaxial simulations, providing a thorough characterisation of the grain boundaries behaviour, is clearly highlighted in this chapter.

The coherency of the multiscale approaches is validated by a comparison to experimental results in full awareness of the the gap of scale between the simulations and the experimental assessment. In that respect, a bridge between those scales is proposed, based, as a first step, on the predominant influence of intergranular stress concentrations.

5. STRESS CONCENTRATIONS AND CRACK INITIATION AT GRAIN BOUNDARIES: THE V-NOTCH PROBLEM

Contents

5.1 Intergranular stress concentrations	152
5.2 Experimental results for the failure of CSL grain boundaries in nickel chromium alloy	153
5.3 Bottom-up approaches for the prediction of intergranular fracture initiation at a V-notch	158
5.3.1 Stress and energy thresholds for the onset of a finite crack increment considering a coupled criterion	158
5.3.1.1 Problem of the V-notch and related solutions	158
5.3.1.2 The coupled criterion	160
5.3.1.3 Application for the CSL grain boundaries	163
5.3.2 Finite element computation of fracture initiation using a cohesive zone model	167
5.3.2.1 Method	168
5.3.2.2 Results for the $\Sigma 5$ [03 1] grain boundary	169
5.4 A top-down approach for the prediction of intergranular fracture initiation	173
5.4.1 Method	174
5.4.2 Results for the $\Sigma 5$ [03 1] grain boundary	178
5.4.2.1 Stress field and debonding mechanism	178
5.4.2.2 Prediction of crack initiation	183
5.5 Comparison of the three approaches for different V-notch angles . .	185
5.6 Results for the $\Sigma 5$ [0$\bar{1}$ 2] and $\Sigma 3$ [1 1 1] grain boundaries	187
5.7 Summary of the results and conclusion	192
5.7.1 Results	192
5.7.2 Conclusion	193

5. STRESS CONCENTRATIONS AND CRACK INITIATION AT GRAIN BOUNDARIES: THE V-NOTCH PROBLEM

5.1 Intergranular stress concentrations

Grain boundaries in polycrystal alloys or metals are the location of a wide variety of intergranular stress concentrators such as: precipitates, oxide penetrations, triple junctions, ledges, twin band, slip band or clear channel (in irradiated materials) impacts. These stress concentrators originate from the microstructure of the material and appears during its manufacturing or its loading history (e.g. mechanical, thermal and environmental loadings). Unless purposely engineered and manufactured otherwise, it can be rightfully assumed that metallic materials always feature such intergranular stress concentrators which are therefore intrinsic to the material.

These features clearly deviates from the perfect grain boundaries structures that are commonly treated in atomistic simulations.

The discrepancies of several orders of magnitude, observed between the critical stresses typically assessed at the macroscale from experiments or simulations, and the the strength of bicrystal derived at the atomic scale from MD or ab initio computations, might be predominantly related to this stress concentrators.

From this point of view, bridging these two scales could be of particular interest for a better understanding of intergranular failure.

In this chapter, the problem of the V-notch is treated in the context of the prediction for intergranular fracture initiation, using simulations at the atomic scale and at the microscopic scale.

It is intended to illustrate several approaches that can be undertaken for intergranular cracking modeling at different scales. For that matter, the problem of the V-notch, which has already been under focus by several authors [Leguillon, 2002, Henninger, 2007], is chosen as a preliminary exercise before focusing on the problem of discontinuous slip band impacts at grain boundaries in the next chapter.

Tensile testing performed on notched samples at grain boundaries represents a convenient way to assess intergranular fracture initiation properties at the microscale. Such an experimental study, performed by [Suzuki et al., 2011] on several CSL grain boundaries, is primarily reported. The related results bring an experimental basis on which we rely to compare and discuss the subsequent simulations intended in this chapter.

Within the Finite Fracture Mechanics framework, the couple criterion for the prediction of fracture initiation, as briefly mentioned in chapter 4, is then reviewed and employed in the context of the V-notch problem at a grain boundary. For that purpose, the MD results of chapters 3 and 4 are employed in a first bottom-up approach.

This theoretical basis is further compared and supported by two multiscale approaches:

- A second bottom-up approach using finite element simulations with cohesive zone models (CZM) parameterised by the MD results on bicrystals failure.
- A top-down approach using molecular dynamics simulations on predeformed

5. STRESS CONCENTRATIONS AND CRACK INITIATION AT GRAIN BOUNDARIES: THE V-NOTCH PROBLEM

V-notched GB configurations from the displacement fields obtained at the microscale with finite element computations.

5.2 Experimental results for the failure of CSL grain boundaries in nickel chromium alloy

Suzuki et al. have proposed an experimental assessment for the strength of several coincident site lattice grain boundaries in a Ni-20Cr alloy using microtensile tests [Suzuki et al., 2011] on notched samples.

The CSL bicrystals have been obtained by diffusion bonding of two single crystals according to the desired directions using electron back scattered diffraction measurements to determine the relative orientation of the crystal lattices.

As illustrated by figure 5.1a, extracted from the original article, samples with notches have been manufactured from the bicrystals, in order to actually trigger the grain boundaries failure.

The dimensions of the microtensile specimen are further specified by the author and reported on figure 5.1a. The two notches have a depth of 300 μm , and from the information provided by the authors, the notches opening angle can be assessed at about 10°, assuming a perfect V-notch. The apparatus used for the machining is a femtosecond laser ; further information concerning the notch shape are not provided but it is logically assumed to depart from a perfect V-notch shape. This geometrical hypothesis could be quite significant here, whether the notch is considered at the microscale or at the atomic scale.

However, this simplification allows to consider simple sample geometries for the simulations intended latter on. Electropolishing is further employed on the sample before performing the tensile tests.

Far from being exhaustive with the above description, a more thorough description of the protocol for the sample preparation can be found in the original article [Suzuki et al., 2011].

Microtensile tests are subsequently performed on the specimens at room temperature and at a strain rate of about $8.3 \times 10^{-4} \text{ s}^{-1}$.

Among the chosen CSL grain boundaries, the $\Sigma 5 \langle 100 \rangle (310)$ and $\Sigma 5 \langle 100 \rangle (210)$, as also studied by MD simulations in chapters 2, 3 and 4, are of particular interest. This study allows a convenient opportunity to compare the previous simulation results with these experimental assessments. In this section, we will therefore mainly focus on these two grain boundaries. The $\Sigma 3 (111)$ coherent twin boundary, which can be particularly common in polycrystal alloys, also constitutes an interesting point of comparison.

Interestingly, transgranular fracture are mainly obtained in the case of the $\Sigma 5 (210)$ and the $\Sigma 3 (111)$ grain boundaries while intergranular fracture are exclusively reported in the case of the $\Sigma 5 (310)$ grain boundaries.

Scanning electron microscopy observations of fractured samples for a $\Sigma 3 (111)$ and

5. STRESS CONCENTRATIONS AND CRACK INITIATION AT GRAIN BOUNDARIES: THE V-NOTCH PROBLEM

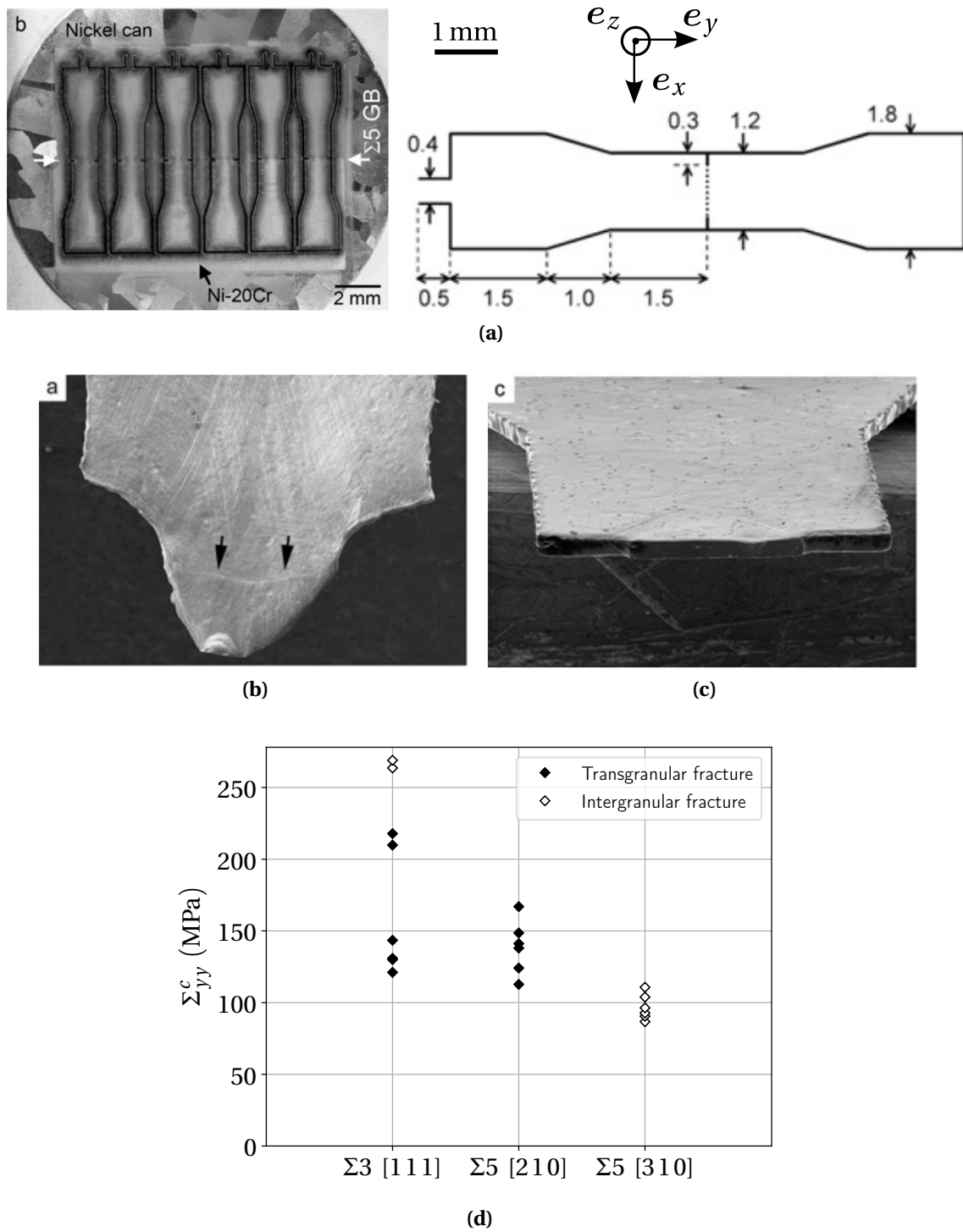


Figure 5.1: Figures reproduced from [Suzuki et al., 2011]: the notched samples of manufactured $\Sigma 5$ Ni-20Cr bicrystal (5.1a) ; quotations are in mm, SEM observations after the transgranular and intergranular fracture of $\Sigma 3$ (111) and $\Sigma 5$ (310) bicrystal samples respectively (5.1b and 5.1c), microscopic critical stresses to fracture in the case of the $\Sigma 3$ (111), $\Sigma 5$ (210) and (310).

5. STRESS CONCENTRATIONS AND CRACK INITIATION AT GRAIN BOUNDARIES: THE V-NOTCH PROBLEM

$\Sigma 5$ (3 1 0) are provided by the authors and reported here on figures 5.1b and 5.1c to illustrate these two behaviours.

A similar fracture behaviour to the $\Sigma 3$ grain boundary presented in figure 5.1b is assumed for the $\Sigma 5$ (2 1 0), as fractography observations are not provided for this grain boundary.

The failure of the $\Sigma 3$ bicrystal can clearly be attributed to a ductile fracture originating from the notches where a stress concentration is purposely induced. The grain boundary is evidently not impacted as the crack initiates at the notch and propagates in the adjacent grain. However, a non negligible GB alteration is observed, probably due to the plastic deformation evidenced by the slip traces (close to the arrows in figure 5.1b). It is supposed that the ductile failure of the $\Sigma 5$ (2 1 0) might present a slightly different fracture pattern due to the different orientation of the slip systems.

The failure of the $\Sigma 5$ (3 1 0) bicrystal, observed in figure 5.1c, clearly contrasts with the above description as a neat brittle fracture has propagated along the grain boundary. With regard to the MD computations of the preceding chapters, it is obvious that the fracture path might not perfectly follow the grain boundary plane at the atomic scale. However, the figure 5.1c is quite compelling and a clear influence of the grain boundary over the failure of the sample can be concluded.

The remote critical stresses obtained at failure for the $\Sigma 3$ and the $\Sigma 5$ grain boundaries are deduced from the data presented by the authors and displayed in figure 5.1d.

It is interesting to note that the $\Sigma 5$ (2 1 0) ductile failure is observed at remote critical stresses noticeably larger than in the case of the $\Sigma 5$ (3 1 0). A 50 % strength increase of the $\Sigma 5$ (2 1 0) GB over the $\Sigma 5$ (3 1 0) can be roughly deduced from the averaged values of about 150 MPa and 100 MPa respectively. A larger data repartition is also evidenced for the $\Sigma 5$ (2 1 0) GB.

In the case of the $\Sigma 3$ grain boundary, the critical stresses to transgranular fracture are significantly higher with a larger repartition in comparison to the $\Sigma 5$ GBs. The mixed transgranular and intergranular fractured samples display the largest critical stresses at about 260 MPa.

As a first approach, it is now proposed to think qualitatively on the molecular dynamics results obtained in the preceding chapters for the $\Sigma 5$ [0 $\bar{1}$ 2] and $\Sigma 5$ [03 1] GBs with respect to the above results of Suzuki et al. Additionally, the GB formation and the same multiaxial tensile tests employed in the preceding chapters are performed on a $\Sigma 3$ [1 1 1] bicrystal at 300 K within the strain plane hypothesis ($\beta_\epsilon = 0$). Its well recognisable atomic structure is shown on figure 5.2a through a common neighbour analysis (top picture) and its related atomic stress field (bottom picture) at 10 K using the same scale previously employed in figure 2.2 of chapter 2. From this figure, it is clear that the $\Sigma 3$ GB has almost no mechanical influence with respect to the bulk in comparison to the grain boundaries of chapter 2. And the results of the multiaxial tests confirm this point, as only homogeneous dislocation nucleations are obtained (see figure 5.2b for $\alpha_\epsilon = 0$) randomly in the bulk or at the grain boundary for the α_ϵ range explored.

The critical stresses obtained by the previous MD computations on $\Sigma 5$ bicrystals are

5. STRESS CONCENTRATIONS AND CRACK INITIATION AT GRAIN BOUNDARIES: THE V-NOTCH PROBLEM

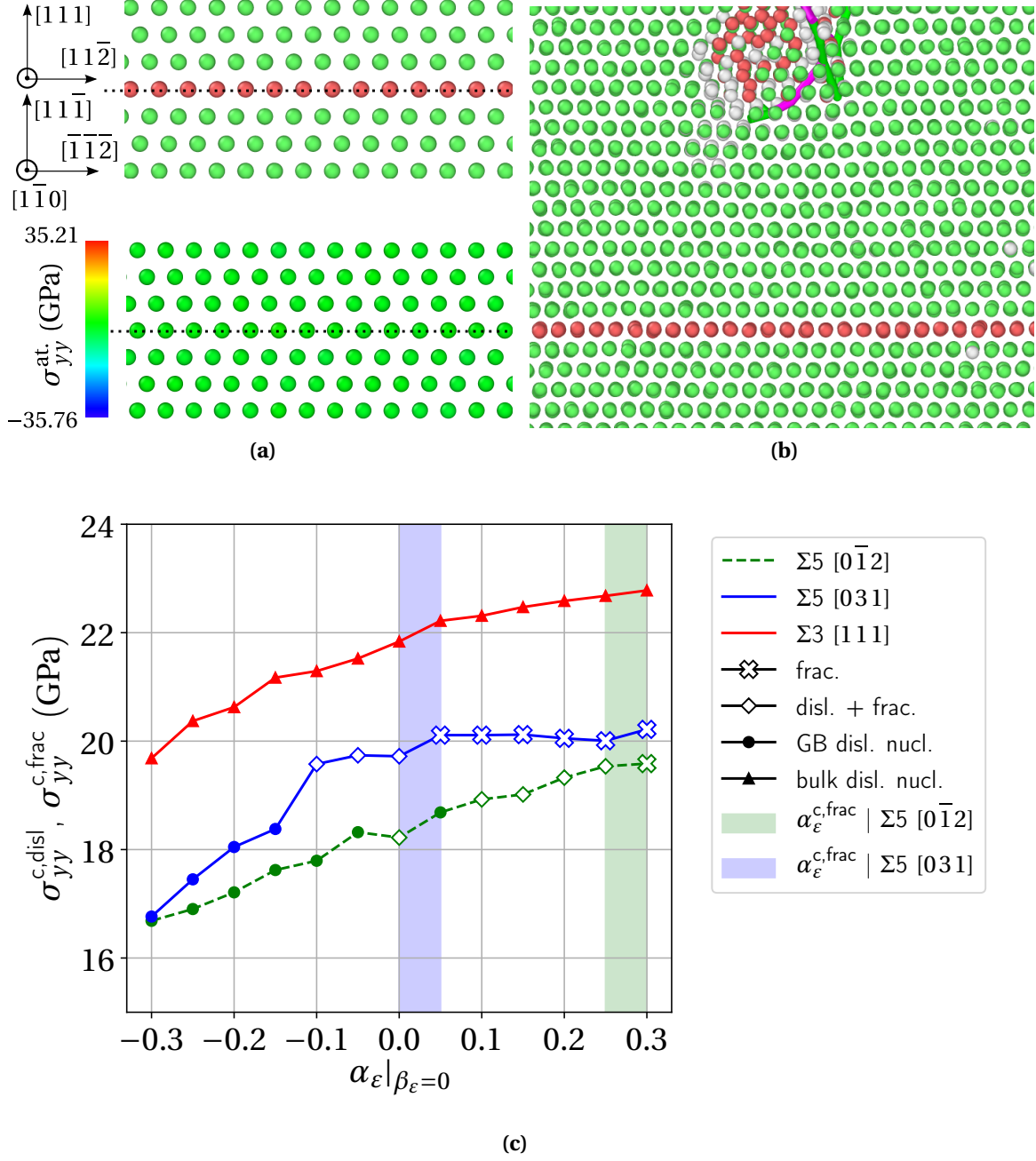


Figure 5.2: Atomic stress field and atomic structure (with a common neighbour analysis: FCC atoms in green and HCP atoms in red) of the $\Sigma 3$ $\langle 110 \rangle$ $[111]$ grain boundary at 10 K (5.2a). Homogeneous dislocation nucleation in the bulk during the multiaxial tensile of the $\Sigma 3$ GB at 300 K and at $\alpha_\epsilon = \beta_\epsilon = 0$ (5.2b). MD critical stresses for the $\Sigma 5$ $[0\bar{1}2]$ and $[031]$, obtained at 300 K for $\beta_\epsilon = 0$ and according to the α_ϵ strain ratio (5.2c). Full circle and triangle markers indicate a dislocation nucleation while the void square and cross markers indicate a GB decohesion with and without dislocation nucleation respectively.

5. STRESS CONCENTRATIONS AND CRACK INITIATION AT GRAIN BOUNDARIES: THE V-NOTCH PROBLEM

extracted from figures 4.1d and 4.1e and plotted on figure 5.2c by considering the plane strain hypothesis (for which $\beta_\varepsilon = 0$). The present results for the $\Sigma 3$ grain boundary are also displayed.

From these results, two points can be noted:

1. Not surprisingly, it can be pointed out first that the critical stresses between the MD results on the bicrystals and the experimental assessment on the notched samples show discrepancies by several orders of magnitude. As proposed in the introduction of this chapter, this first point could be predominantly explained by the presence of the notches, inducing a strong stress concentration at the grain boundary. Of course, the difference of scale considered here is noticeable, and it is clear that a direct comparison would have to be taken with caution.
2. Secondly, the results of figure 5.2c suggest that the $\Sigma 5$ $[0\bar{1}2]$ grain boundary model is the most prone to GB dislocation nucleation at stresses significantly lower than the critical stress to fracture of the $\Sigma 5$ $[031]$ (at the same α_ε deformation ratios). To illustrate this comparison, the α_ε range at which the critical behaviour shows a transition between dislocation nucleation with fracture and the fracture without any dislocation nucleation is stressed further on figure 5.2c by the colored area.

This qualitative observation seems to roughly agree with the experimental results. However, an inverse trend is evidenced for the critical stresses recorded from the experiment: the $\Sigma 5$ (210) notched samples display higher remote critical stresses as already stated before.

Once again, it is clear that the difference of scale should be accounted for, rendering a direct comparison between the present simulations and the experiment rather tricky.

Indeed, the fracture behaviour observed by Suzuki et al. results from a crack initiation and its full propagation on a $300\mu\text{m}$ distance (from both sides of the sample). It can be easily imagined that a ductile fracture propagation in the grain would necessitate more energy and therefore more stress with respect to a brittle intergranular fracture propagation.

Therefore, the MD results on bicrystals and the experimental measurements on the notched samples may not be contradictory. The MD simulations only consider the initiation of the critical events at time and space scales that do not match the experimental observations. Hence, the apparent contradiction presented above is actually not surprising.

The same remark holds for the $\Sigma 3$ GB. It can be easily imagined that the homogeneous dislocation nucleations observed in MD can result in a transgranular cracking propagation at the microscopic scale with a ductile mechanism. In this case, the MD critical stresses recorded for dislocation nucleation are significantly higher than for the other $\Sigma 5$ GBs. However, as stated before, care is needed in such comparison with regard to the time and space scale differences.

5. STRESS CONCENTRATIONS AND CRACK INITIATION AT GRAIN BOUNDARIES: THE V-NOTCH PROBLEM

In this chapter, it is therefore proposed to bridge the two preceding scales in order to decipher some common grounds between the experimental results and the MD assessment of GBs strength. Methods are proposed, in an attempt to bring some insight to that matter by treating independantly the two aforementioned points.

The first of this two points is addressed in the two sections.

5.3 Bottom-up approaches for the prediction of intergranular fracture initiation at a V-notch

Following the critical stress discrepancies observed between the microscopic scale and the atomic scale, the presence of the notches is assumed to have a major influence as a stress concentrator on the microscopic critical stress to fracture initiation. In this section, it is therefore proposed to assess this influence. As stated before, the problem of the V-notch is considered as a relevant model for that matter despite the strong geometrical simplifications involved.

5.3.1 Stress and energy thresholds for the onset of a finite crack increment considering a coupled criterion

5.3.1.1 Problem of the V-notch and related solutions

The problem of the fracture initiation prediction at a V-notch tip is now briefly summarised in the context of Finite Fracture Mechanics and the coupled criterion already addressed in chapter 4.

The following paragraphs are essentially based on the following references [Leguillon, 2002, Leguillon and Sanchez-Palencia, 1987, Henninger, 2007].

Lets consider, in the continuum framework, a monotonic tensile sollicitation on a V-notched specimen featuring a notch angle ω . For this problem, isotropic linear elasticity and plane strain hypothesis are assumed. Figure 5.3 illustrates this problem, showing the configurations just before (κ_1) and after (κ_2) a finite crack initiation of unknown length a . The monotonic tensile loading consists in an imposed displacement at the edges of the sample.

A polar coordinate system $(\mathbf{e}_r, \mathbf{e}_\theta)$, with the origin \mathcal{O} at the tip of the notch, is often adopted for this kind of problem for which orthoradial solutions are expected. However, it is known for this problem geometry that the fracture initiation is occurring at an angle of $\theta_c = \pi - \frac{\omega}{2}$ as depicted figure 5.3. Furthermore, if a grain boundary is considered at the tip of the notch along this particular direction, it can be rightfully assumed that the fracture will initiate along the interface featuring diminished cohesive properties with respect to the bulk.

It is therefore proposed to consider the Cartesian coordinate system $(\mathbf{e}_x, \mathbf{e}_y)$, conserving the same origin. In order to keep the same notations of the above references, the

5. STRESS CONCENTRATIONS AND CRACK INITIATION AT GRAIN BOUNDARIES: THE V-NOTCH PROBLEM

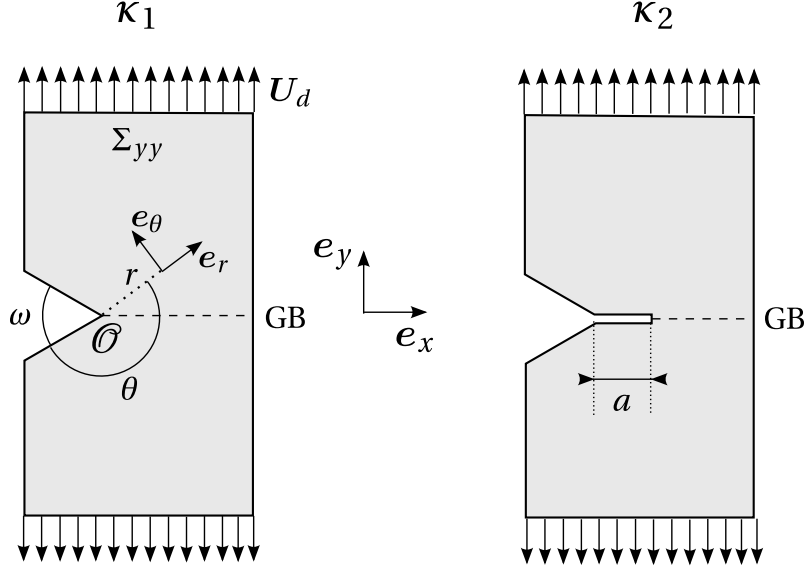


Figure 5.3: Problem of the fracture initiation at the V-notch tip \mathcal{O} along a grain boundary (dashed line).

distance $r \equiv x$ from the tip of the notch is adopted.

The displacement field, solution of the so-called outer problem illustrated on configuration κ_1 in figure 5.3, gives rise to a singular stress field. It can be described by the following predominant term along the direction of θ_c angle, in the vicinity of the tip:

$$\mathbf{U}(r) = \mathbf{U}(\mathcal{O}) + Kr^\lambda \mathbf{u}(\theta_c) + .. \quad (5.1)$$

where, K and λ are the generalised intensity factor and the singularity exponent respectively. Further terms are considered negligible in this development, provided that the distance r is kept small enough.

The λ exponent has been demonstrated to respect the following condition:

$$\frac{1}{2} \leq \lambda \leq 1 \quad (5.2)$$

Several λ values are reported from [Leguillon, 2002] in table 5.1 for different ω angles of the notch.

The $\omega = 0$ configuration evidently corresponds to the case of the perfect crack.

The generalised intensity factor K , like the intensity factor in LEFM, is proportional to the remote applied stress Σ_{yy} induced by the imposed displacement \mathbf{U}_d . $\mathbf{U}(\mathcal{O})$ corresponds to the rigid body displacement of the tip.

In linear elasticity, a singular stress field in front of the tip can be deduced from equation 5.1:

$$\sigma_{yy}(r) = Kr^{\lambda-1} s_{yy}(\theta_c) + .. \quad (5.3)$$

5. STRESS CONCENTRATIONS AND CRACK INITIATION AT GRAIN BOUNDARIES: THE V-NOTCH PROBLEM

$\omega(^{\circ})$	λ	$\overline{\mathcal{A}}$
0	0.5	5.670
30	0.502	5.648
60	0.513	5.416
90	0.545	4.900
120	0.616	4.040

Table 5.1: Variation of the singularity exponent and the geometrical normalised coefficient $\overline{\mathcal{A}}$.

where the geometrical variation $s_{yy}(\theta)$ can be conveniently normalised along the direction of θ_c angle: $s_{yy}(\theta_c) = 1$. The singular stress field of the perfect crack is here recovered for $\lambda = \frac{1}{2}$. For $\lambda > \frac{1}{2}$, a weaker singularity is obtained. From the values of table 5.1, it is clear that a monotonic increase of the λ exponent is evidenced according to the ω angle. Therefore, the larger the angle of the notch, the weaker the singularity.

Considering now the energetical balance between the state κ_2 for which a crack increment a is initiated and state κ_1 , the energy release to the system $-\delta W$ has been demonstrated to be predominantly approximated by:

$$-\frac{\delta W}{A} = \gamma(a) = K^2 \mathcal{A}(\omega) a^{2\lambda-1} + .. \quad (5.4)$$

where A is the surface of the newly created crack and \mathcal{A} is a geometrical coefficient depending on ω and the Young modulus Y . Several values of this coefficient are reported for a unitary Young modulus in table 5.1 from [Henninger, 2007], such that $\overline{\mathcal{A}} = \mathcal{A} Y$.

The prediction of fracture initiation therefore consists in the determination of the two unknowns K_c and a_c which represent the critical generalised intensity factor (proportional to the critical remote stress Σ_{yy}^c) and the critical (finite) crack increment at which the crack initiation is triggered.

5.3.1.2 The coupled criterion

Leguillon proposes to set and solve the above problem using a coupled criterion in conjunction with equations 5.3 and 5.4. This criterion provides two independant equations in relation with two properties of fracture: a critical stress σ_c and a critical energy γ_c .

The fracture initiation occurs when the threshold stress σ_c is attained on a certain distance from the tip of the notch. In the same time, the threshold energy γ_c also has to be reached on a finite crack length. For the weak singularity cases at $\lambda > \frac{1}{2}$, an infinitesimal fracture would indeed be impossible since the energy available for this event to happen (i.e. the energy release rate G) is null.

5. STRESS CONCENTRATIONS AND CRACK INITIATION AT GRAIN BOUNDARIES: THE V-NOTCH PROBLEM

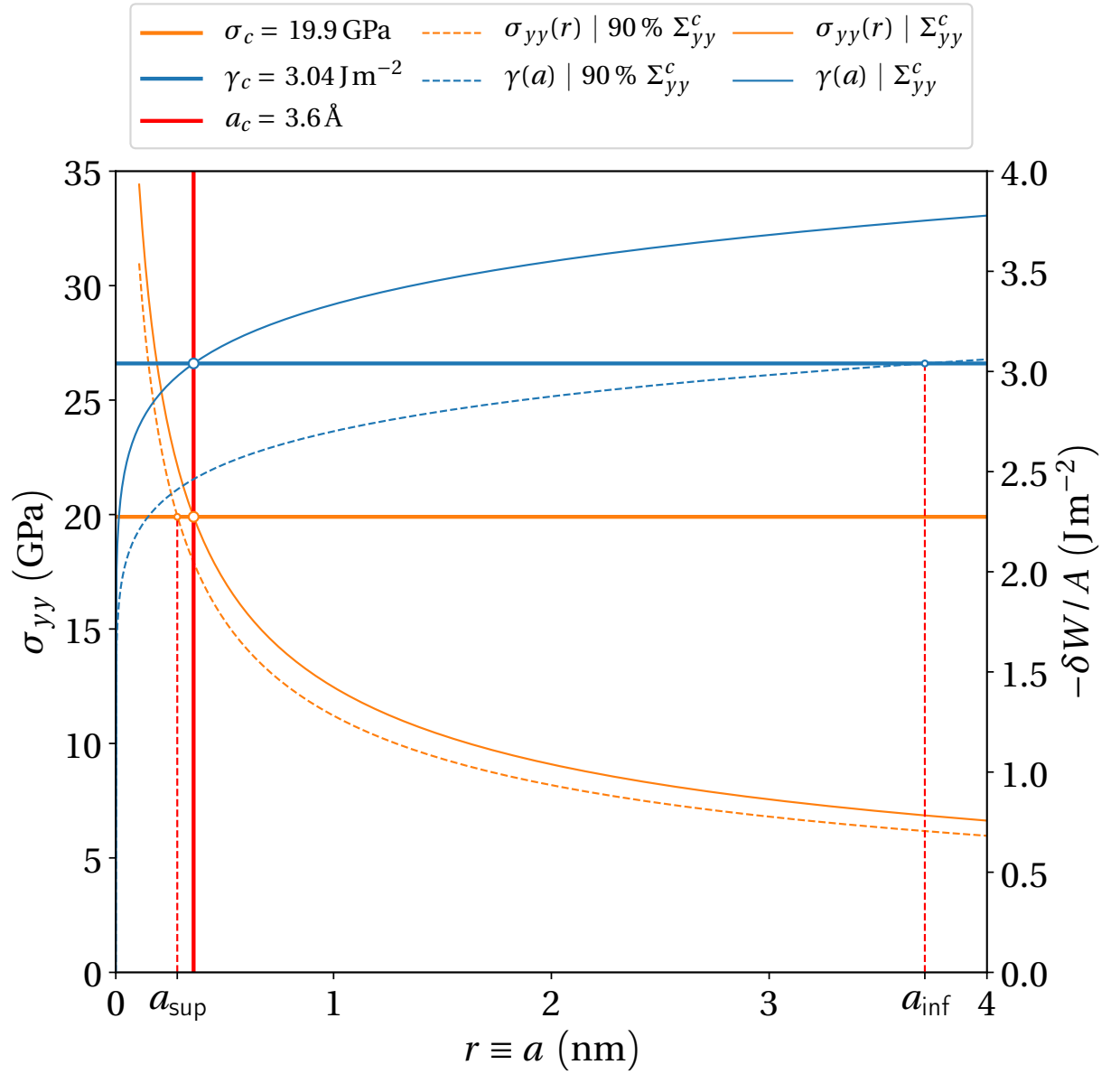


Figure 5.4: Illustration of the coupled criterion in the case of the $\Sigma 5$ [031] grain boundary ($\sigma_c = 19.9 \text{ GPa}$ and $\gamma_c = 3.04 \text{ Jm}^{-2}$).

5. STRESS CONCENTRATIONS AND CRACK INITIATION AT GRAIN BOUNDARIES: THE V-NOTCH PROBLEM

This criterion can be formulated as follows:

$$\begin{cases} \sigma_{yy}(r) \geq \sigma_c \\ \gamma(a) \geq \gamma_c \end{cases} \quad (5.5)$$

$$\quad (5.6)$$

where the equivalence between the distance r and the crack increment length a can be made for notation coherency: $r \equiv a$.

At a given remote applied stress Σ_{yy} (or its related generalised intensity factor K), the stress criterion of equation 5.5 and the stress solution in front of the notch (equation 5.3) provides an upper bound a_{sup} for the crack increment:

$$a_{\text{sup}} = \left(\frac{K}{\sigma_c} \right)^{\frac{1}{1-\lambda}} \quad (5.7)$$

with $s_{yy}(\theta_c) = 1$. Meanwhile, at the same loading, the energy criterion of equation 5.6 and the energy variation of equation 5.4 yields a lower bound a_{inf} :

$$a_{\text{inf}} = \left(\frac{\gamma_c}{\mathcal{A} K^2} \right)^{\frac{1}{2\lambda-1}} \quad (5.8)$$

A finite crack initiation is therefore rendered possible when the critical remote stress Σ_{yy}^c is attained such that $a_{\text{sup}} = a_{\text{inf}} = a_c$. Then, the solution of the above system of equations is:

$$\begin{cases} a_c = \frac{\gamma_c}{\mathcal{A} \sigma_c^2} \\ K_c = \left(\frac{\gamma_c}{\mathcal{A}} \right)^{1-\lambda} \sigma_c^{2\lambda-1} \end{cases} \quad (5.9)$$

$$\quad (5.10)$$

For the sake of illustration, the criterion is applied in figure 5.5 for the 90 % Σ_{yy}^c and Σ_{yy}^c stresses, using a $\Sigma 5$ [03 1] grain boundary ($\sigma_c = 19.9$ GPa, $\gamma_c = 3.04$ J m⁻²), a Young modulus $Y = 228$ GPa (Voight average for a nickel polycrystal with the C_{ij} values at 300 K of chapter 2) and a notch angle of $\omega = 120^\circ$.

The application shows that a crack increment of $a_c = 3.6$ Å is triggered.

Regardless of the validity of this application at the atomic scale, it is confirmed that the crack increment a_c is indeed small enough such that the predominance of the terms in equations 5.3 and 5.4 still holds.

Meanwhile, this coupled criterion conveniently encompasses the specific cases of:

- The perfect crack ($\omega = 0^\circ$, $\lambda = \frac{1}{2}$) for which equation 5.4 and 5.6, do not yield any lower bound. Hence, the propagation of the crack with an infinitesimal crack length is admissible. Then, the coupled criterion reduces to the Griffith criterion. The energy criterion is preponderant while the stress criterion is always respected.
- The wall ($\omega = 180^\circ$, $\lambda = 1$) for which equation 5.3 and 5.5 do not yield any upper bound. The singular stress field disappear and the predominant criterion is the stress criterion, as evidenced by the bicrystals failure of chapter 4.

5. STRESS CONCENTRATIONS AND CRACK INITIATION AT GRAIN BOUNDARIES: THE V-NOTCH PROBLEM

Finally, it has been pointed out by Leguillon [Leguillon, 2002] that the energy release rate of the initiated crack of length a_c exceeds the critical energy γ_c for the $\lambda > \frac{1}{2}$ cases. Indeed, using equation 5.4, this energy rate can be computed by derivation:

$$G(a_c) = 2\lambda\gamma_c \quad (5.11)$$

This means that, considering a weak singularity, the initiated crack is in an unstable equilibrium and shall therefore propagates.

5.3.1.3 Application for the CSL grain boundaries

The application of the coupled criterion is now proposed in comparison to the experimental results of Suzuki et al. This first multiscale approach consists in a bottom-up scale transition between the MD results at the atomic scale and the upper scale characterisation of the stress field in front of the notch. For that matter, finite element computations are performed with Cast3M [CAST3M,] using 2D meshes of V-notch samples, considering a plane strain hypothesis. The dimensions employed are reproduced from the bicrystal samples used by Suzuki et al. in figure 5.1a. One mesh and its dimensions are presented in figure 5.5 with the notch angle of $\omega = 10^\circ$. Only half of the sample is meshed considering the symmetry of the problem with the adequate zero displacement conditions at the bottom ($U_x = 0$) edge, which represents the axe of symmetry. Zero displacement conditions are applied at the left ($U_y = 0$) edges, while free surfaces at the top edges are considered. The loading is imposed with a monotonic displacements time evolution at the right edges. The strain rate is somewhat meaningless considering the imposed linear elastic behaviour.

An orthoradial refined mesh is used at the tip of the notch with a mesh size of $\Delta_x = 5.5 \text{ \AA}$. This size is chosen to respect the prescribed disclination distance presented in the conclusion of chapter 4 for the case of the $\Sigma 5 [031]$ grain boundary. At the tip of the notch, a refinement disc of radius 26.4 nm, featuring this constant refined mesh size Δ_x , is used for all the meshes (see top picture of the figure 5.5). Additionnaly, three other notch angles: $\omega = 60^\circ, 90^\circ$ and 120° are considered. For the $\omega = 10^\circ$ and 90° cases, refined meshes with a size $\Delta_x = 2 \text{ \AA}$ are also used to verify the mesh size influence with regard to the convergeance of the computations.

Isotropic linear elasticity is employed with a Young modulus of 228.4 GPa and a Poisson coefficient of 0.272. These values are obtained from a Voigt average [Hirth and Lothe, 1982] using the MD nickel elastic coefficients C_{ij} at 300 K of chapter 2:

$$\begin{aligned} \mu &= \frac{1}{5}(C_{11} - C_{12} + 3C_{44}) \\ \nu &= \frac{1}{2} \left(\frac{C_{11} + 4C_{12} - 2C_{44}}{2C_{11} + 3C_{12} + C_{44}} \right) \\ Y &= 2(\nu + 1)\mu \end{aligned}$$

5. STRESS CONCENTRATIONS AND CRACK INITIATION AT GRAIN BOUNDARIES: THE V-NOTCH PROBLEM

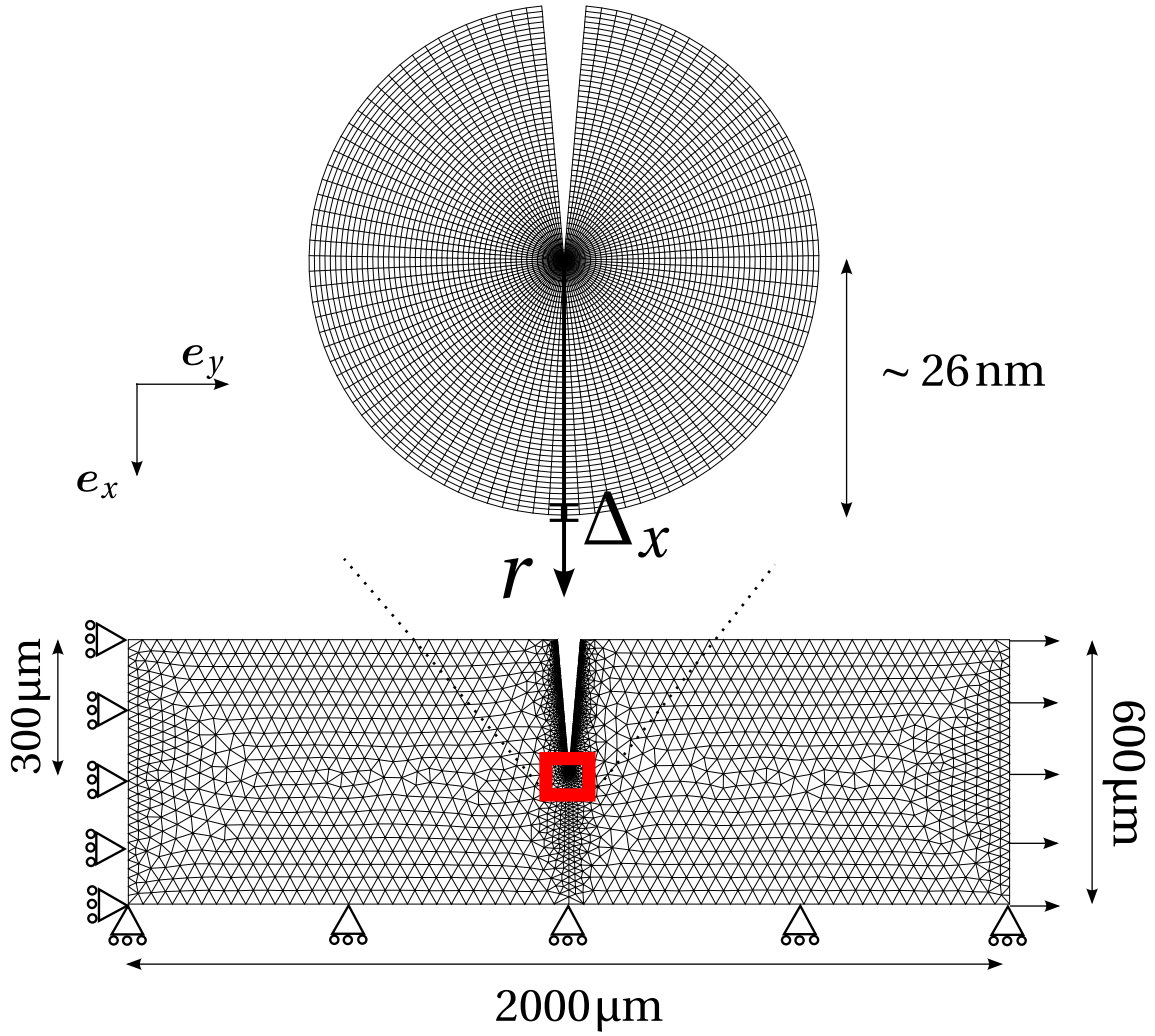


Figure 5.5: Full mesh of the V-notch sample using the sample quotation of Suzuki et al. as referenced in figure 5.1a. The refinement disc at the tip of the notch features a radius of about 26 nm according to the mesh size Δx .

5. STRESS CONCENTRATIONS AND CRACK INITIATION AT GRAIN BOUNDARIES: THE V-NOTCH PROBLEM

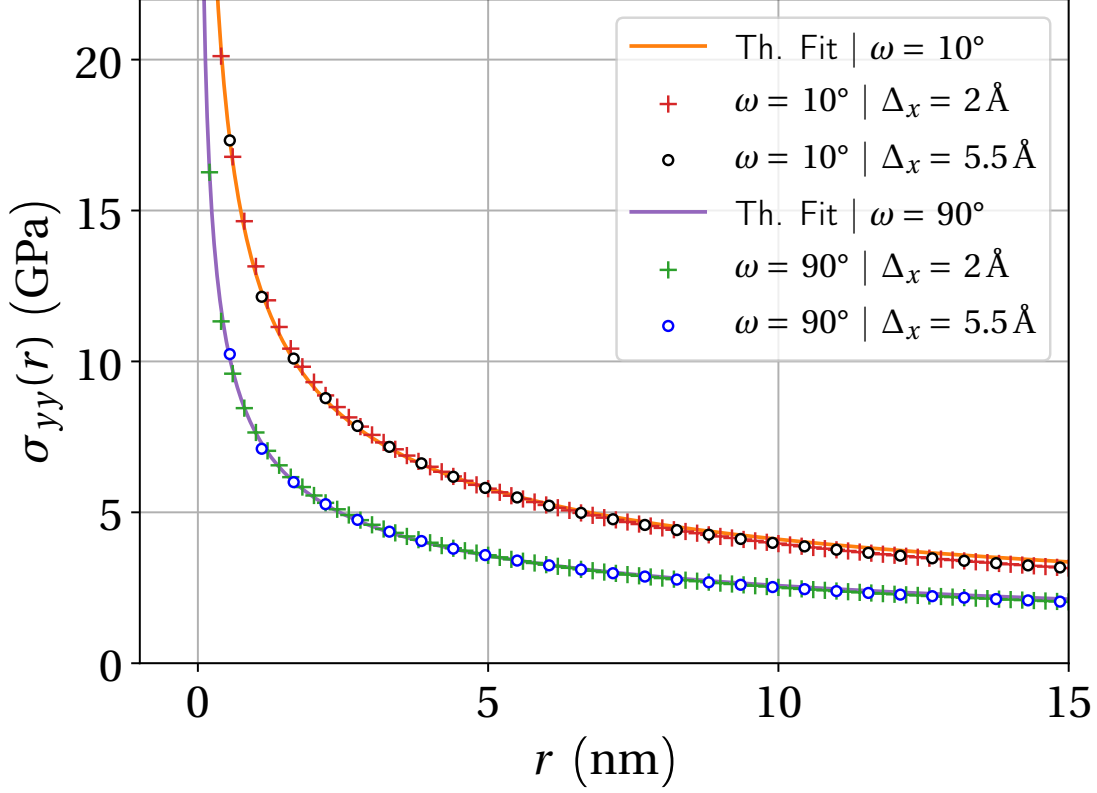


Figure 5.6: Stress profiles obtained by finite element computations at the remote stress of $\Sigma_{yy} = 27.36$ MPa along with the theoretical fit used from equation 5.3.

These simple computations are consistent with the application of the coupled criterion specified earlier but the elastic anisotropy of nickel (≈ 2.8) is not taken into account for this first-hand application. Stress profiles are systematically extracted along the θ_c direction, at several time steps for registered remote axial stresses Σ_{yy} between 0 MPa and 40 MPa.

The stress profiles at $\Sigma_{yy} = 27.36$ MPa are plotted in figure 5.6 for $\omega = 10^\circ$ and 90° cases, and the two refined mesh sizes $\Delta_x = 5.5 \text{ \AA}$ and 2 \AA . For both angles, the independance of the mesh size is obtained. It is rightfully supposed that a mesh size of 5.5 \AA is therefore sufficient here.

The exponents of table 5.1 are approximately recovered from the stress profiles, through a fitting precEDURE using equation 5.3.

The influence of the notch angle ω through the singularity exponent can clearly be observed in figure 5.6. As expected, a much weaker singularity is obtained as ω and incidently λ increase. The generalised stress intensity factor K is also identified with respect to the remote axial stress Σ_{yy} over all the registered time steps.

Equation 5.10 is then used in the case of the four ω angles and the thirteen nickel

5. STRESS CONCENTRATIONS AND CRACK INITIATION AT GRAIN BOUNDARIES: THE V-NOTCH PROBLEM

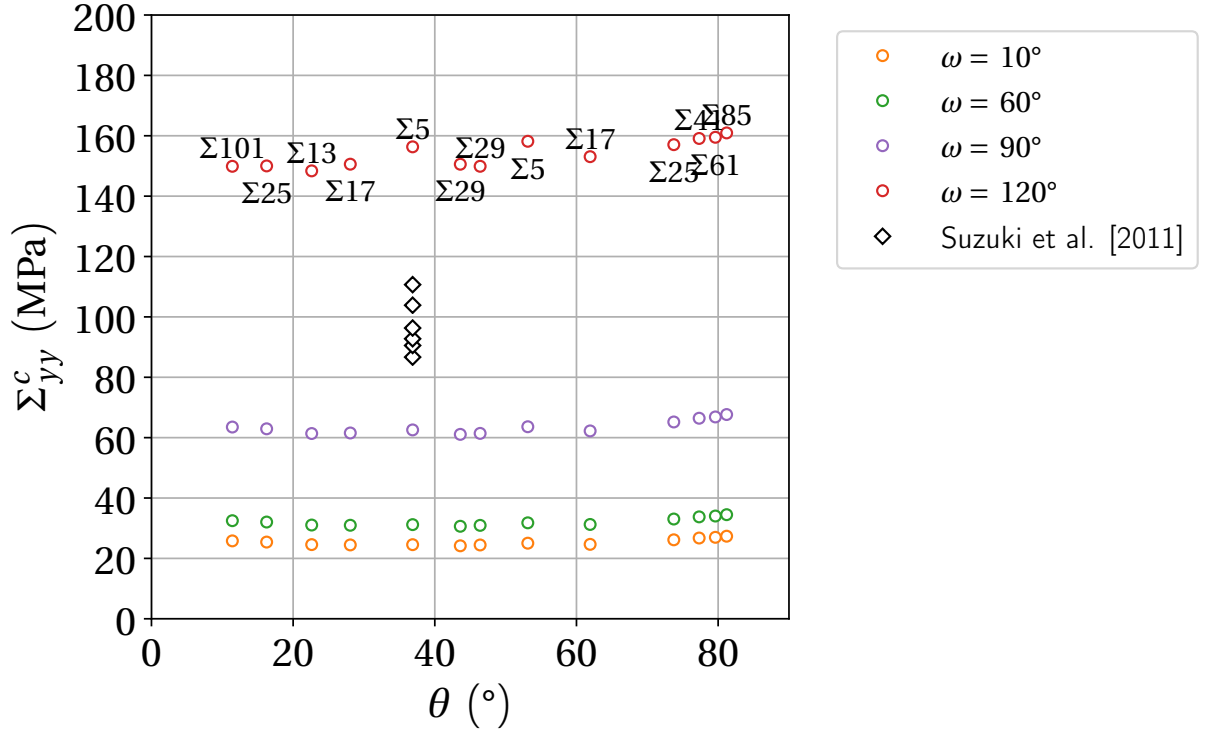


Figure 5.7: Application of the coupled criterion for the thirteen CSL nickel grain boundaries in the case of the notch angles $\omega = 10^\circ$, 60° , 90° and 120° .

grain boundaries through their (σ_c, γ_c) fracture properties. The predictions are plotted in figure 5.7 according to the θ angles of the grain boundaries. Results of Suzuki et al. are also plotted for comparison purposes.

For the $\Sigma 5$ [031] grain boundary at $\omega = 10^\circ$, a remote critical stress of 24.6 MPa is obtained at the previously assessed 3.6 \AA critical crack length.

Firstly, this application suggests that the nature of the grain boundary is not as influential as the V-notch geometry. This point might be in adequation with the experimental observations, as Suzuki et al. have recorded rather similar critical stresses between the CSL fractured grain boundaries.

Secondly, these results clearly display a fairly good agreement with the experimental results as similar orders of magnitude are obtained.

This model of the V-notch seems to yield a coherent comparison and therefore confirms the major influence of this kind of stress concentrator. It may partly explain the discrepancies typically observed between the atomic scale and the microscale.

An 80 % gap is still roughly recorded for the $\Sigma 5$ [031] GB with regards to the experimental values. Once again, the V-notch geometry used herein constitutes a significant assumption with that regard since a rather blunted notch would be expected at this scale. Furthermore, it is reminded that the comparison is here carried out between pure

5. STRESS CONCENTRATIONS AND CRACK INITIATION AT GRAIN BOUNDARIES: THE V-NOTCH PROBLEM

nickel in MD and a Ni-20Cr alloy, which may further explain some of the discrepancies observed.

However, this prediction presents a lower bound which is in fact quantitatively coherent. Indeed, it is reminded that the critical remote stress predicted here concerns the initiation of a crack at the atomic scale. The experimental critical stresses are obtained for the complete failure of the sample over its 300 μm half-width. It is several orders of magnitude higher than the initiation of the 3.5 \AA crack length evaluated before. The prediction is therefore coherent since a full propagation of the initiated crack on the entire length of the sample would logically necessitate further increase of the axial remote stress.

A direct comparison would therefore be valid considering simulations at the atomic scale, if a propagation over microscale distances (and the related time scale) was possible in molecular dynamics, which is not the case.

However, despite the current limitations of the MD simulations, the fracture propagation behaviour of grain boundaries at the atomic scale still remains under scrutiny. Current efforts focus on the transition between simulations at different scales [Yamakov et al., 2006, Dingreville et al., 2017, Barrows et al., 2016], trying to derive cohesive zone models (CZM) at the atomic scale for upper scale simulations. A rather similar but coarser approach is undertaken in the next subsection in order to propose the beginning of a solution concerning the above issue. This second approach also presents the opportunity of comparing the preceding predictions with the results of an other fracture model.

5.3.2 Finite element computation of fracture initiation using a cohesive zone model

A cohesive zone model (CZM) based on the bicrystal MD results is used as a second bottom-up approach within finite element computations.

From a physical point of view, the use of a CZM is coherent with the description of the grain boundaries (or any interface) debonding. Indeed, like the description of the cohesive behaviour at the atomic scale (see chapter 4), these models permits to take into account stress relaxation processes once a maximum stress is reached. In consequence, it also avoids the rather non-physical view of singular stress fields conveniently accepted by the theory.

From a pragmatic point of view, this kind of models allows to obtain a direct prediction of fracture initiation. For our purposes, it also permits to consider the anisotropy of pure nickel directly in the finite element computation with cubic elasticity.

Furthermore, a CZM is particularly suitable here, since it allows to encompass both the initiation of fracture and its propagation. However, this may constitute a strong simplification since it is supposed here that the only use of the bicrystal results can cover both processes.

Finally, the equivalence between the coupled criterion and the use of a CZM has

5. STRESS CONCENTRATIONS AND CRACK INITIATION AT GRAIN BOUNDARIES: THE V-NOTCH PROBLEM

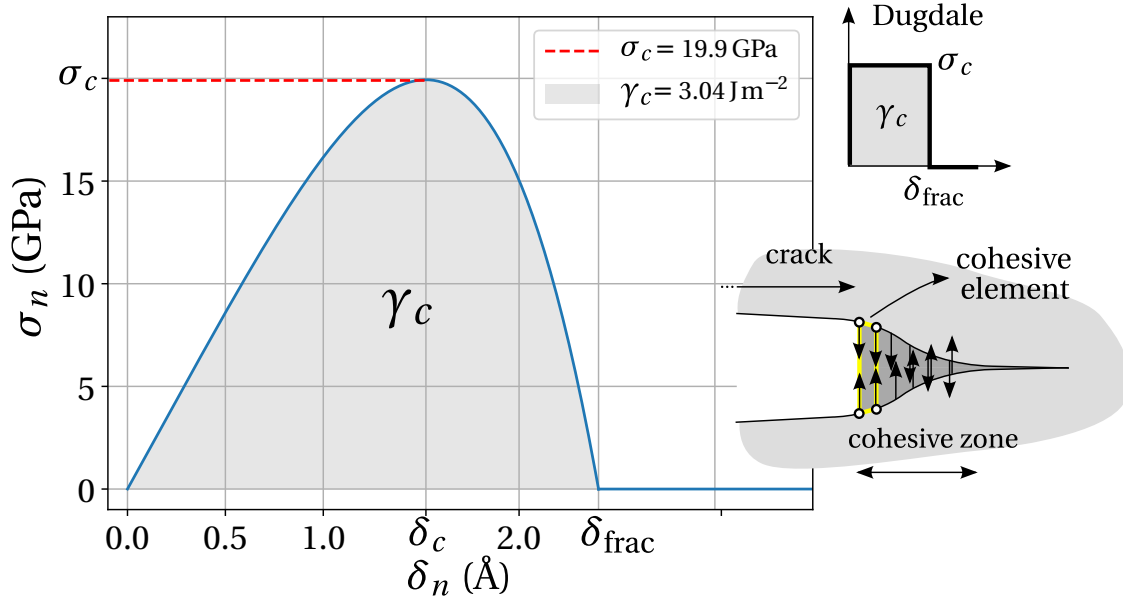


Figure 5.8: The Hinte CZM model implemented in Cast3M and the Dugdale model (left and upper right respectively), along with the schematisation of the related cohesive zone in the continuum framework in front of a crack (lower right).

been demonstrated [Henninger, 2007, Henninger et al., 2007] using a Dugdale model [Dugdale, 1960]. A comparison with the coupled criterion is therefore also intended here.

In the remaining of this section, it is chosen to mainly focus on the case of the $\Sigma 5$ [031] grain boundary from a prediction perspective.

5.3.2.1 Method

Like the coupled criterion, two properties of fracture (for example the critical stress σ_c and the critical energy γ_c) are used in a CZM to simulate the damage behaviour of materials.

In the continuum framework, these models consist in the non-linear description of the cohesive behaviour of the material in the area of splitting surfaces as represented on the right scheme in figure 5.8.

For example, the Dugdale model simulates the onset of a cohesive zone through constant return forces on the lips of the opening damaged zone when a critical stress σ_c is reached (see the upper right scheme of figure 5.8). Concomittent with the initiation or the propagation of a crack, the failure then occurs at a displacement δ_{frac} , when the critical energy γ_c is reached.

For our purpose, the hinte model of Cast3M is employed, only considering a mode I fracture with the stress component σ_n and the opening length (or displacement jump)

5. STRESS CONCENTRATIONS AND CRACK INITIATION AT GRAIN BOUNDARIES: THE V-NOTCH PROBLEM

δ_n normal to the interface. This simplified cohesive model is formulated as follows:

$$\sigma_n = K_n [1 - D] \delta_n \quad (5.12)$$

$$D = \begin{cases} \left[\frac{\alpha}{\alpha + 1} \left(\frac{\gamma_{el}}{\gamma_c} \right) \right]^\alpha & \text{if } \delta_n < \delta_c \\ 1 & \text{otherwise} \end{cases} \quad (5.13)$$

$$\gamma_{el} = \frac{1}{2} K_n \delta_n^2 \quad (5.14)$$

with D , a damage internal variable. The elastic behaviour at small displacements is modeled through the rigidity coefficient K_n . For our purpose, the apparent Young modulus of the grain boundary and its thickness assessed before, are used directly:

$$K_n = \frac{C_{yy}}{t_{GB}} \quad (5.15)$$

The α parameter permits to set the damage evolution of the interface, described by equation 5.13, such that the maximum stress σ_c is reached considering the critical energy γ_c .

The displacement to complete fracture δ_{frac} then follows, along with the critical displacement δ_c when the maximum stress is reached:

$$\delta_{frac} = \sqrt{2 \frac{\alpha + 1}{\alpha} \frac{\gamma_c}{K_n}} \quad \delta_c = \left(\frac{1}{2\alpha + 1} \right)^{\frac{1}{2\alpha}} \delta_{frac} \quad (5.16)$$

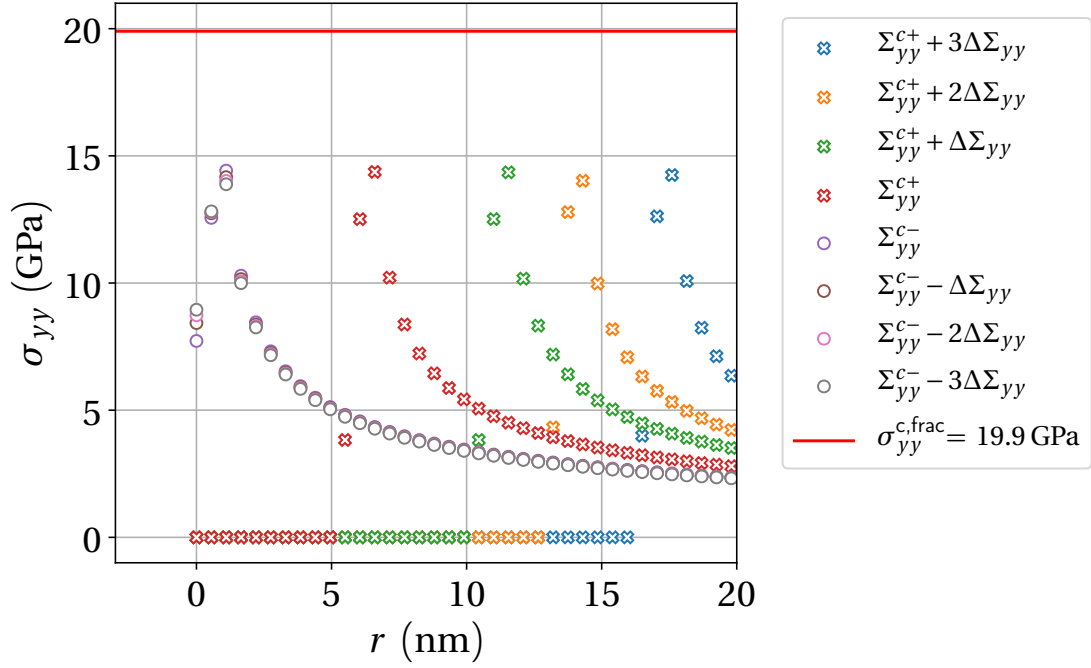
The parametrisation of the model is illustrated in figure 5.8 for the case of the $\Sigma 5$ [03 1] grain boundary using the MD data of table 4.2.

Unlike the Dugdale model, this model allows to take into account a progressive stress relaxation. However, it is expected that the shape of the CZM has a minor influence on the fracture initiation prediction. Like the coupled criterion, the fracture process is only described by the reach of these two properties whatever the path.

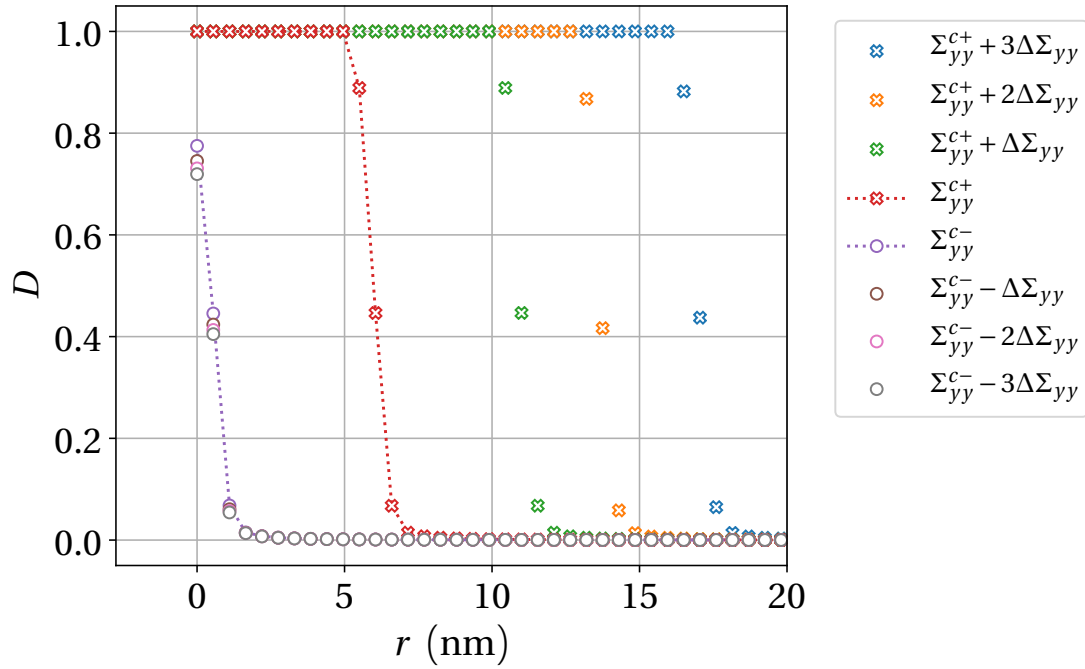
5.3.2.2 Results for the $\Sigma 5$ [03 1] grain boundary

Using the finite element method, the cohesive zone is modeled by 2D cohesive elements placed at the interface as roughly represented in figure 5.8. As illustrated, these elements are composed of four nodes, two nodes at each side of the interface. These elements are introduced in the meshes illustrated by figure 5.5 along the interface. For a first application, the $\omega = 10^\circ$ case is treated. The cohesive behaviour of the $\Sigma 5$ [03 1] is modelled. A monotonic tensile loading is applied with the same computation parameters described before considering a mesh size of $\Delta_x = 5.5 \text{ \AA}$. Cubic elasticity is employed with the elasticity coefficients of chapter 2 and the corresponding crystalline orientations of the grains.

5. STRESS CONCENTRATIONS AND CRACK INITIATION AT GRAIN BOUNDARIES: THE V-NOTCH PROBLEM



(a)



(b)

Figure 5.9: Stress and damage profiles along the cohesive elements computed at several time steps around the crack initiation event.

5. STRESS CONCENTRATIONS AND CRACK INITIATION AT GRAIN BOUNDARIES: THE V-NOTCH PROBLEM

In order to derive the remote critical stress precisely enough and to ease the computation convergence, a time step Δt is chosen so that a remote stress step $\Delta \Sigma_{yy}$ of around 0.1 MPa is achieved.

Normal stress and damage profiles extracted along the nodes of the cohesive elements are plotted in figure 5.9 for time steps surrounding the initiation of the crack at the tip of the V-notch.

The remote stresses just before and just after the fracture initiation are computed at around $\Sigma_{yy}^{-c} = 21.6$ MPa and $\Sigma_{yy}^{+c} = 21.7$ MPa respectively. These results are in a rather good agreement with the coupled criterion prediction of 24.6 MPa. The two methods yield similar results and in that particular case, the influence of anisotropy does not greatly impact the prediction.

For the sake of illustration, the σ_{yy} stress field is plotted shortly after the crack initiation ($\Sigma_{yy}^{+c} + 3\Delta \Sigma_{yy}$) on the deformed configuration in figure 5.10a.

From figure 5.9, it can clearly be seen that at Σ_{yy}^{+c} , a 5 nm long crack is computed which is approximately one order of magnitude higher than the coupled criterion prediction of 3.6 Å for the critical crack length. Following the precedent remark concerning the theoretical energy release rate $G(a_c)$ of the initiated crack (equation 5.11), this result is not surprising. Indeed, an unstable equilibrium of the newly created crack is expected considering that $\omega > 0^\circ$. The observed profile may result in the initiation and the propagation of the crack.

A cohesive zone can be clearly identified before failure ($\Sigma_{yy} \leq \Sigma_{yy}^{-c}$) by the distance over which significant damage values and relaxed stresses are recorded. A length of at most $2\Delta_x$ (11 Å) before failure can be clearly deciphered. It partly agrees with a crack initiation length significantly lower than the observed crack length at Σ_{yy}^{+c} .

However, in the eventuality that the critical crack increment of 3.6 Å can actually be recovered in the simulation, the mesh size of 5.5 Å, chosen for its coherency with the MD results (conclusions of chapter 4), is rather restrictive.

In order to verify this point and the independance of the computed solution with respect to the mesh size, computation with meshes featuring Δ_x values of 2 Å and 1.5 Å are also carried out.

An additional computation is employed with the initial mesh size $\Delta_x = 5.5$ Å and a time step one hundred time lower, in order to assess its influence.

All the results are plotted on figure 5.10b, with the evolution of the crack length (as measured with elements featuring a damage $D = 1$) according to the remote stress recorded. It is clear that the mesh size and the timestep have a minor influence on the critical stress to initiation. However, it is also manifest that the crack propagation strongly differs between the different simulations.

To keep a certain coherency with regards to the atomic structure of the grain boundary, the 5.5 Å mesh size would be preferable.

However, considering the propagation of the crack on the 300 µm half-length of the sample with a refined mesh of 5.5 Å all along the interface seems rather tricky with regards to the convergence of such computation and the related costs. Since the crack

5. STRESS CONCENTRATIONS AND CRACK INITIATION AT GRAIN BOUNDARIES: THE V-NOTCH PROBLEM

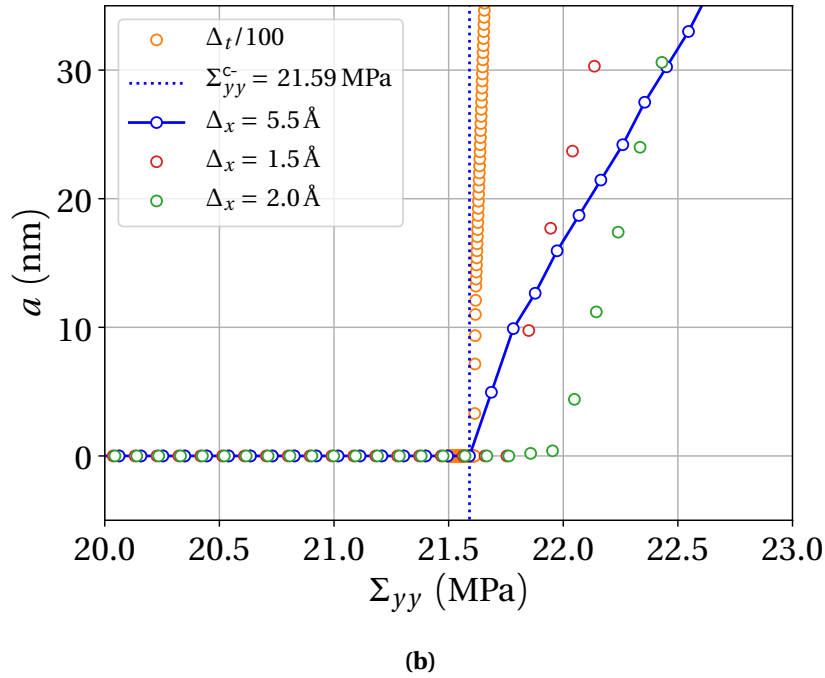
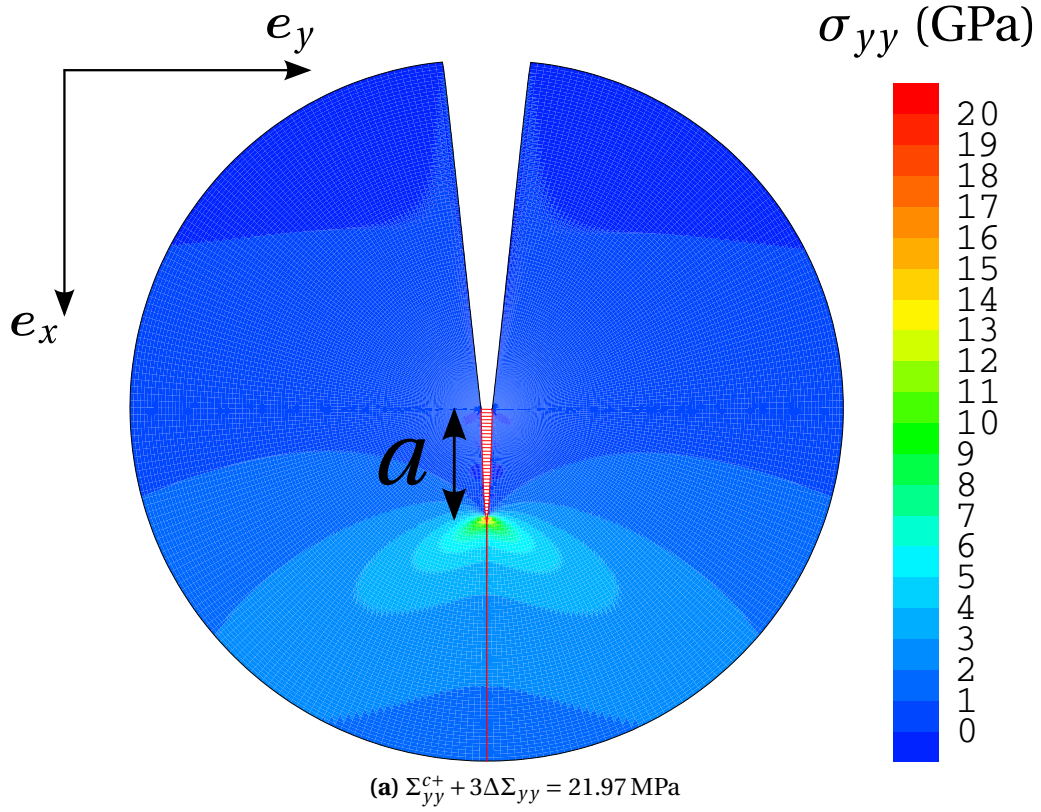


Figure 5.10: Normal stress field σ_{yy} on the deformed configuration at $\Sigma_{yy}^{c+} + 3\Delta\Sigma_{yy}$ with the propagation of the newly created crack (5.10a). Crack length evolution a according to the remote stress Σ_{yy} for the three meshes and two timesteps employed (5.10b).

5. STRESS CONCENTRATIONS AND CRACK INITIATION AT GRAIN BOUNDARIES: THE V-NOTCH PROBLEM

initiation is the main interest here, this point will not be further investigated.

Nevertheless, it is clear that in order to achieve a direct comparison with the experiment, all the while considering microscopic scale simulations informed by atomistic inputs, a more thorough investigation is needed in order to take into the crack propagation process.

In this subsection, it is shown that a CZM parametrised by MD results could be conveniently used at the microscopic scale for predicting crack initiation. These models present a certain interest from an engineering point of view even if a more thorough investigation would be needed with regard to the behaviour of the propagated crack at grain boundaries.

Meanwhile, using such model involves the hypothesis of an intergranular fracture mechanism. However, it has been shown in chapter 3 that a larger variety of mechanisms can be expected at grain boundaries during a monotonic and homogeneous multiaxial loading. Similarly, different GB mechanisms could be expected in the presence of the singular stress field previously described. Despite the scale effects involved, the experimental observations of Suzuki et al. also show different mechanisms resulting in the notched samples failure.

A complementary and comparative investigation at the atomic scale is therefore proposed in the next subsection in order to bring more insight. In that regard, molecular dynamic simulations informed by finite element computations of V-notched samples are used.

Provided that the results of this atomistic simulations agree with the results of the bottom-up approaches, a coherency of the predictions would be demonstrated. It would further validate the multiscale scheme based on the assessment of the fracture properties of grain boundaries at the atomic scale.

Finally, performing such MD simulations could qualitatively confirms the debonding mechanisms observed on bicrystals (see chapter 4), should the grain boundaries fracture initiation be achieved.

5.4 A top-down approach for the prediction of intergranular fracture initiation

An opposite approach is now undertaken following a top-down scale transition. It consists in performing MD simulations on deformed configurations deduced from FE computations.

For that matter, the FE2AT method introduced by [Möller et al., 2013] is widely employed and adapted for our purpose. The related code, developed and provided by A. Prakash, J.Möller and E.Bitzek is conveniently used. The following paragraphs, which are based on the above reference, merely summarise the main steps and purpose of the method. More details can be found in the original publication.

5. STRESS CONCENTRATIONS AND CRACK INITIATION AT GRAIN BOUNDARIES: THE V-NOTCH PROBLEM

5.4.1 Method

The FE2AT method consists in providing atomistic simulation with initial and boundary conditions determined by finite element computations. More precisely the finite element contribution mainly comes from providing the MD computations with the elastic solution of a particular loaded structure. Here, the configurations treated in MD and FE simulations are geometrical equivalents. The predeformed configurations resulting from the quasi-static loading steps constitute an initial guess, close enough to the minimum energy configurations subsequently obtained by relaxation at the atomic scale.

The FE computations can then be conveniently used to treat complex problems involving anisotropic media which could not be analytically solved as easily. This particular point may not be as necessary for the case of the V-notch problem since analytical solutions of the related problems already exist. However it becomes essential in the problem of slip band impacts at grain boundaries which is not as well-known. The MD simulations are then employed to take into account the mechanisms and processes at the atomic scale that departs from this initial configuration.

With this process, a multiscale scheme can be easily envisioned in the case of the V-notched samples with FE computations similar to the simulations already performed before. Local stress fields, reaching the appropriate MD critical stresses as illustrated in figure 5.6, can then be considered at the atomic scale for remote stresses close to the experimental assessments.

However, it should be noted that this process constitutes a one-way coupling (chain-ing?). The history of the material is indeed not considered at each FE loading steps since the FE computations are not informed by MD data on atomic scale events that could potentially occurs before the applied loadings.

The following paragraphs present and illustrate this three steps method, adapted in the case of a $\Sigma 5$ [03 1] grain boundary at a V-notched sample with a notch angle of 10° .

1. The first step consists in reproducing the equivalent MD configuration to the refined mesh carried out before in the continuum framework in figure 5.5. For that matter, only the refined disc of 26.4 nm radius, needs to be considered. For this step, a $\Sigma 5$ [03 1] grain boundary is formed and relaxed at 300 K with zero stress components and with the same EAM potential of Mishin [Mishin, 2004] for pure nickel. An equivalent V-notch disc configuration is then carved from the relaxed configuration, as illustrated in figure 5.11a. The tip of the notch is placed at one disclination atomic location. The atomic structure of the notch is provided on the same figure along with the atomic volume field identifying the disclination sites at maximum volumes (further marked by vertical lines). A peripheral zone of the disc (in red on the figure) is marked in the optic of the subsequent atomic relaxation to be performed. Its purpose shall be explained later on. A significant thickness ($> 2r_{\text{cutoff}}$) of the box is used in the z direction in order avoid autointeractions.

5. STRESS CONCENTRATIONS AND CRACK INITIATION AT GRAIN BOUNDARIES:
THE V-NOTCH PROBLEM

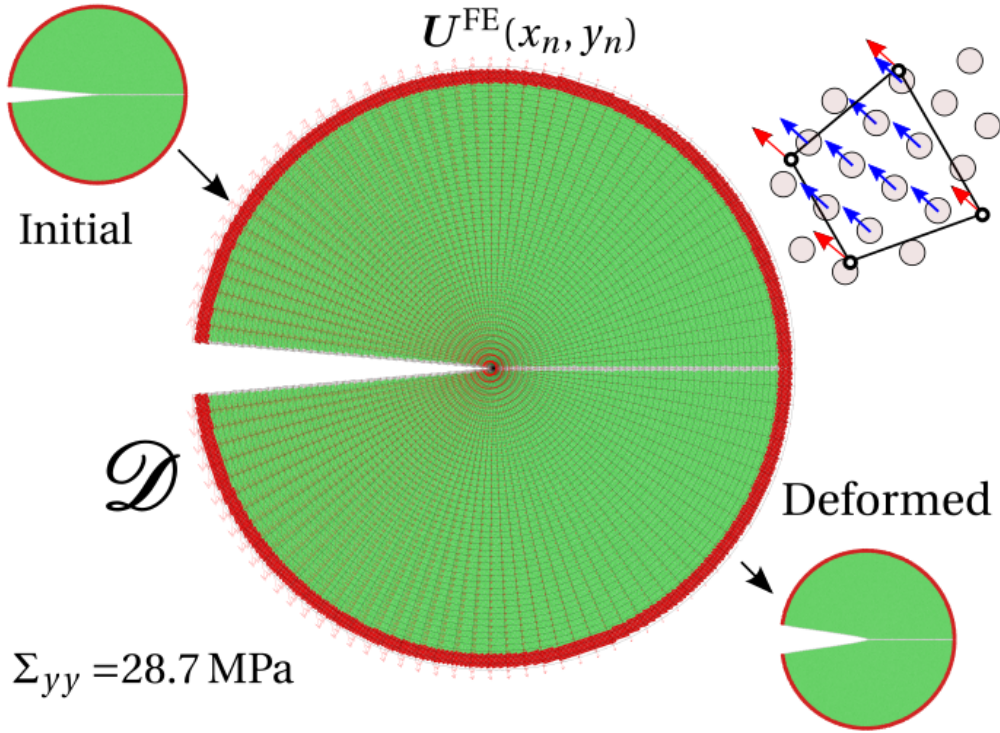
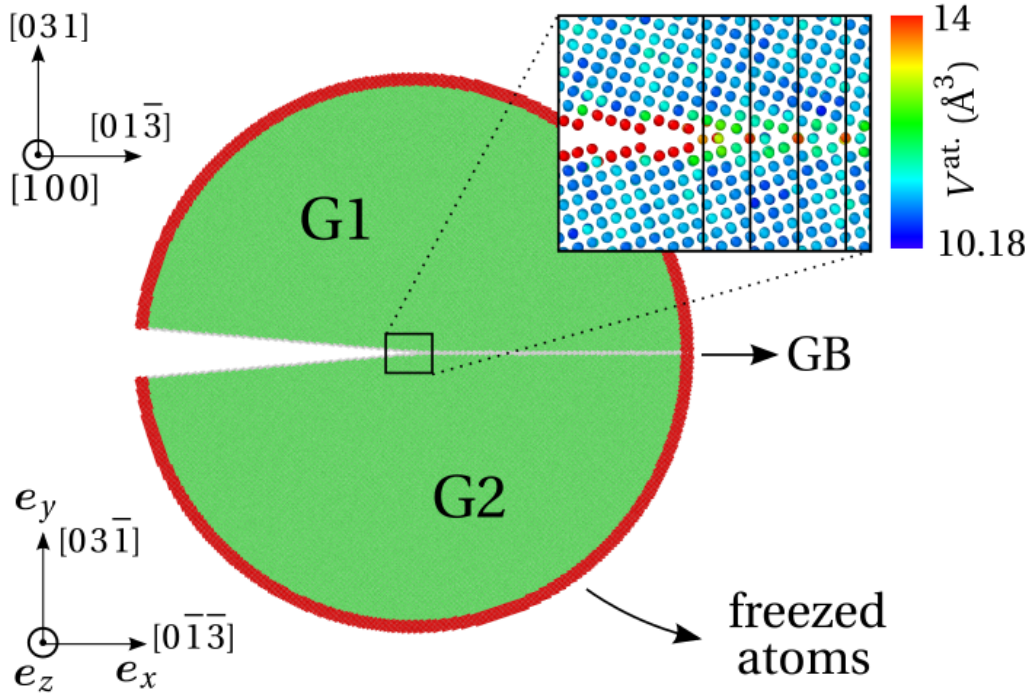


Figure 5.11: Step 1 and step 2 of the top-down approach consisting in the formation of the V-notch sample from a first MD computation at 300 K (5.11a) and the interpolation of the nodal displacements computed by FE analysis (5.11b).

5. STRESS CONCENTRATIONS AND CRACK INITIATION AT GRAIN BOUNDARIES: THE V-NOTCH PROBLEM

2. The second step of the process deals with the obtention of preformed configurations from the FE simulations. A 2D FE computation is performed with the same mesh illustrated before in this chapter. For this simple computation, cubic elasticity is employed using the same elasticity coefficients obtained with the MD potential at 300 K in chapter 2. The plane strain hypothesis is also assumed. The displacement fields $\mathbf{U}(x_n, y_n)$, computed at the nodes n of Cartesian coordinates x_n and y_n , are extracted on the refined disc at every loading steps. For convenient purposes related to subsequent data processings, an equivalent displacement field is arbitrarily deduced using the constant averaged displacement vector integrated over the disc domain \mathcal{D} at every loading step:

$$\mathbf{U}^{\text{FE}}(x_n, y_n) = \mathbf{U}(x_n, y_n) - \frac{1}{S_{\mathcal{D}}} \int_{\mathcal{D}} \mathbf{U}(x, y) dS$$

where the above integration is performed numerically with Cast3M. This displacement field \mathbf{U}^{FE} incidently yields the same strain field as the original field \mathbf{U} since a constant (in space) vector is subtracted for a given loading step. For the example, the resulting vector field for a remote stress of $\Sigma_{yy} = 28.7$ MPa is plotted in figure 5.11b on the refinement disc superimposed to the MD initial configuration.

As illustrated on the upper right scheme of figure 5.11b, the atomic displacements are then imposed by interpolation of the nodal displacement fields using the shape functions of each nodes of the finite element assigned to each atomic positions (see [?] for further details). A deformed configuration is finally obtained at this stage.

Following the preceding $\Sigma 5$ [03 1] example at 28.7 MPa, the related atomic stress field $\sigma_{yy}^{\text{at.}}$ (see chapter 1) resulting from the deformed configuration is displayed in figure 5.12 along with the FE stress field computed at the same loading. Despite some noises observed due to the thermal motion, the MD atomic stress fields qualitatively agree with the elastic solution. Furthermore a convincing quantitative comparison could also be deciphered. However, such comparison is not completely viable since an atomic stress field (defined on single atoms) can hardly be compared to a continuum stress field.

3. The final step of the process consists in the MD relaxation of the deformed structure within the NVT ensemble at 300 K with fixed box dimensions in every space directions. This relaxation is coherent with the plane strain hypothesis used in the FE computation. As stated before, the deformed structure is considered to bring initial and boundary conditions to the atomistic simulation. The relaxation is performed to approach the minimum energy configuration from that initial state. For that matter, the atoms belonging to the peripheral area of the disc (previously delimited in red on figure 5.11a) are freezed through a zero velocity condition while only the atoms in the enclosed elastic area (in green) are relaxed during the process. The thickness of the freezed area is purposely chosen to

5. STRESS CONCENTRATIONS AND CRACK INITIATION AT GRAIN BOUNDARIES:
THE V-NOTCH PROBLEM

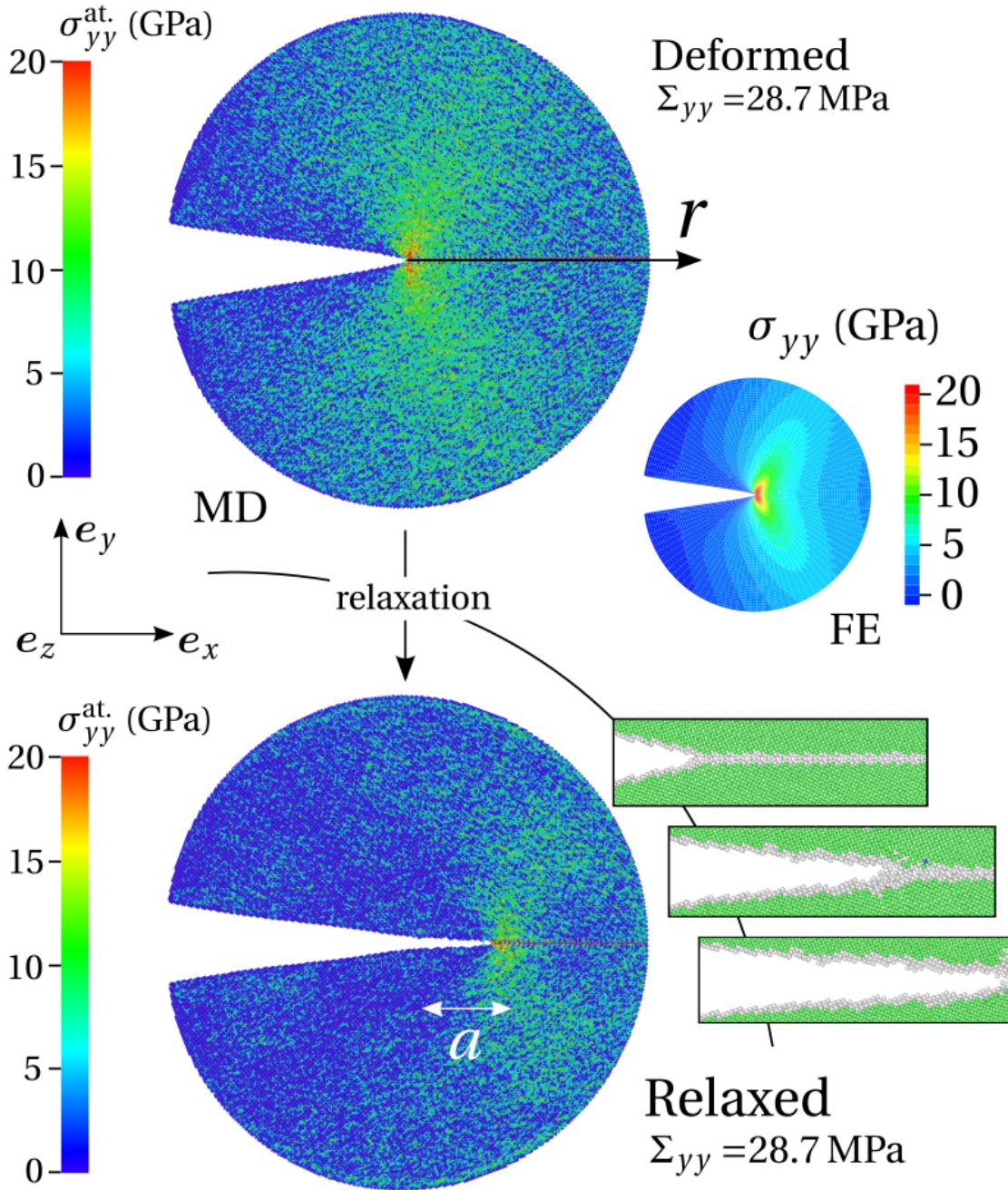


Figure 5.12: Step 3 of the top-down approach illustrated in the case of the $\Sigma 5$ [031] grain boundary at a remoted stress of 28.7 MPa. Atomic stress field compared to the FE computed stress field (up). Relaxation process of the deformed configuration and atomic stress field on the minimum energy configuration after full relaxation (down).

5. STRESS CONCENTRATIONS AND CRACK INITIATION AT GRAIN BOUNDARIES: THE V-NOTCH PROBLEM

avoid any free surface influence on the elastic body thus mimicking its relaxation as embedded in a virtual matrix. This permits to effectively apply the boundary conditions prescribed by the FE computation. The relaxation is performed for 20 ps, therefore permitting to achieve the minimum energy configuration at the prescribed upper scale loading.

This third step is finally applied on the atomic configuration of the $\Sigma 5$ [03 1] GB at 28.7 MPa. Several MD steps of the relaxation are shown in the lower right part of figure 5.12. The initiation and propagation of a crack at the grain boundary without any dislocation nucleation is clearly evidenced by the common neighbour analysis. The final step of the relaxation at 20 ps is displayed in the lower left part of the figure, along with the axial atomic stress field $\sigma_{yy}^{\text{at.}}$. The crack front can be located by the related stress concentration at a distance a of the initial notch tip.

5.4.2 Results for the $\Sigma 5$ [03 1] grain boundary

5.4.2.1 Stress field and debonding mechanism

A validation of the stress field applied to the MD configuration of the $\Sigma 5$ [03 1] GB is now undertaken for the same loading case (28.7 MPa). The mechanism of the crack initiation and propagation is also described. It is important to remind that this propagation is observed during the MD relaxation at a constant prescribed loading which may certainly be higher than the actual remote critical stress to crack initiation.

In order to obtain comparable stress profiles, boxes of atoms are defined on the initially deformed configuration along the grain boundary and around the disclination atomic sites as represented in the vicinity of the notch tip on figure 5.13a (arrows for the disclinations sites and red and blue atoms for the successive boxes). The boxes definition follows the representative elementary volume (REV) previously envisioned in chapter 3. These REV conveniently encompass the periodicity of the grain boundary atomic structure using the thickness of the $\Sigma 5$ [03 1] t_{GB} (0.84 nm) and the periodic distance between the disclination sites $d_{\text{GB}}^{\text{discl.}}$ (0.55 nm). For this example, a REV typically gathers at least fifty atoms, thus allowing a proper and comparable definition of a local stress around the disclination sites $\sigma_{yy}^{\text{discl.}}$ (see chapter 1) through a classical formulation:

$$\sigma_{ij}^{\text{discl.}} = \frac{1}{V^{\text{discl.}}} \left(\frac{1}{2} \sum_k^{N_d} \sum_{l \neq k}^{N_d-1} r_i^{kl} f_j^{kl} + \sum_k^{N_d} m^k v_i^k v_j^k \right) \quad (5.17)$$

$$\text{and} \quad V^{\text{discl.}} = t_{\text{GB}} d_{\text{GB}}^{\text{discl.}} L_z$$

similarly to the definition of the global stress on bicrystals in chapter 2 (with the virial and kinetic contribution), and here adapted on the REV. L_z denotes the thickness of the box in the z direction and N_d the number of atoms in each box.

Following this definition, axial stress profiles $\sigma_{yy}^{\text{discl.}}(r)$ are plotted in figure 5.13b according to the disclination sites r coordinates and at different time steps of the

5. STRESS CONCENTRATIONS AND CRACK INITIATION AT GRAIN BOUNDARIES: THE V-NOTCH PROBLEM

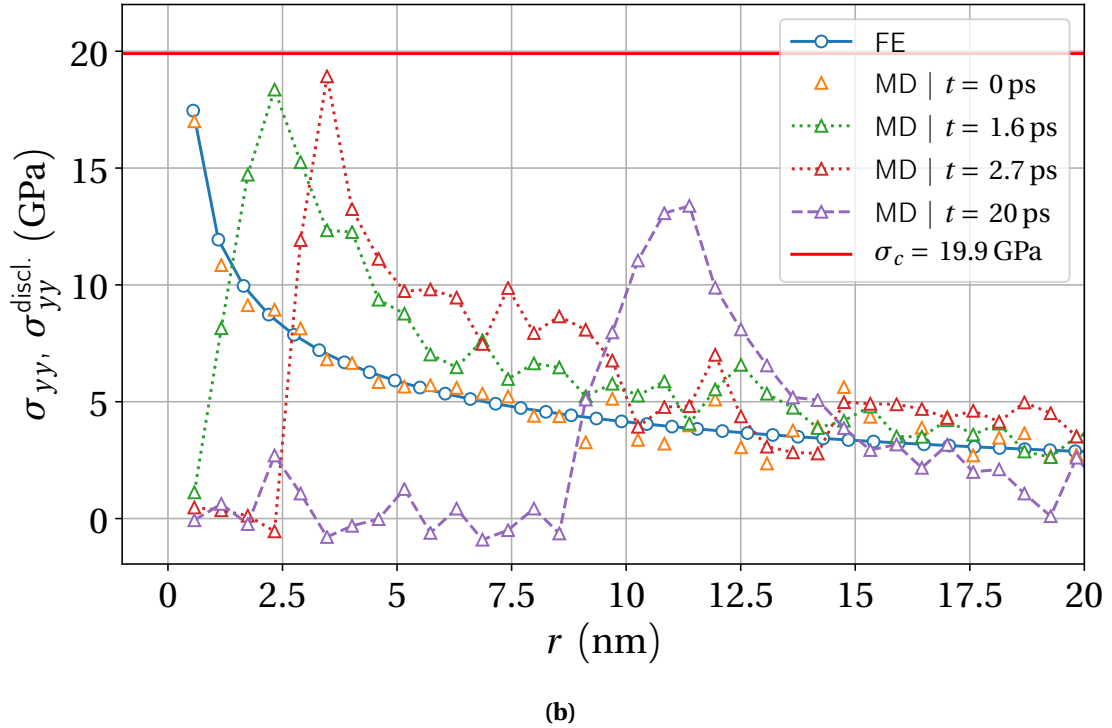
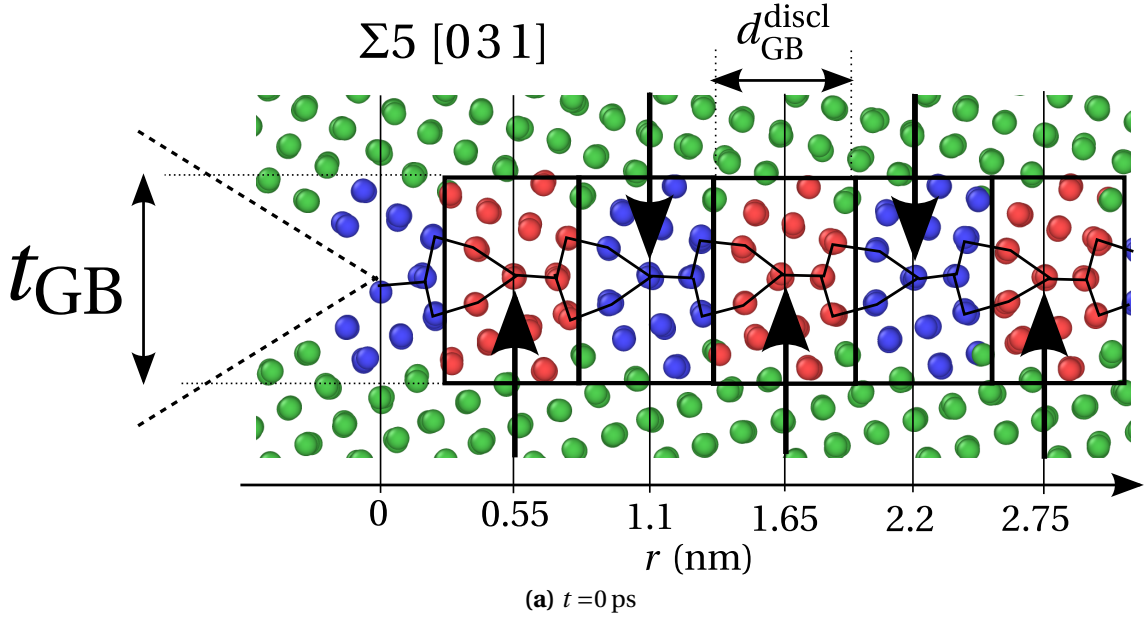


Figure 5.13: Definition of the successive representative elementary volumes in the vicinity of the V-notch tip and along the grain boundary (5.13a). Corresponding stress profiles at $\Sigma_{yy} = 28.7$ MPa obtained from equation 5.17 applied on the same REV atoms at various MD steps, along with FE stress profiles at the same axial remote stress.

5. STRESS CONCENTRATIONS AND CRACK INITIATION AT GRAIN BOUNDARIES: THE V-NOTCH PROBLEM

relaxation. The first disclination box at the tip of the notch is not taken into account since it encompasses a significant part of the notch.

For the initial deformed configuration at $t = 0$ ps the MD profile clearly agrees with the stress profiles extracted from the FE computation. At the final step ($t = 20$ ps), the propagated crack observed in figure 5.12 can be identified by the zero stresses recorded at the newly created free surfaces. With regard to these preliminary results, the validity of the above stress definition at the atomic scale is confirmed and shall be systematically used from now on.

On the intermediate stress profiles recorded at 1.6 ps and 2.7 ps, the crack initiation along with an equivalent of a cohesive zone can be deciphered.

Atomic configurations in the vicinity of the notch tip are displayed at several time steps of the relaxation in figures 5.14 and 5.15. The Voronoi atomic volume and the arrows ease the localisation of the disclination sites. These figures clearly illustrate the same debonding mechanisms observed before in chapter 4. It is reminded that in the case of the bicrystal these mechanisms were directly linked to the reach of a local critical stress. This result confirms the utility of the previous bicrystal simulation as the critical stress of 19.9 GPa is clearly attained and correlates with a subsequent stress relaxation. This further agrees with the formation of a cohesive zone ahead of the crack. This mechanism confirms and validates the use of a CZM to simulate the crack initiation and propagation processes at this scale. This point is further confirmed by the intermediate stress profiles of figure 5.13 in conjunction with the related configurations in figures 5.15b and 5.15d which clearly correlates the formation of the crack and the presence of the cohesive zone with significant stress relaxation once the critical stress is reached.

5. STRESS CONCENTRATIONS AND CRACK INITIATION AT GRAIN BOUNDARIES: THE V-NOTCH PROBLEM

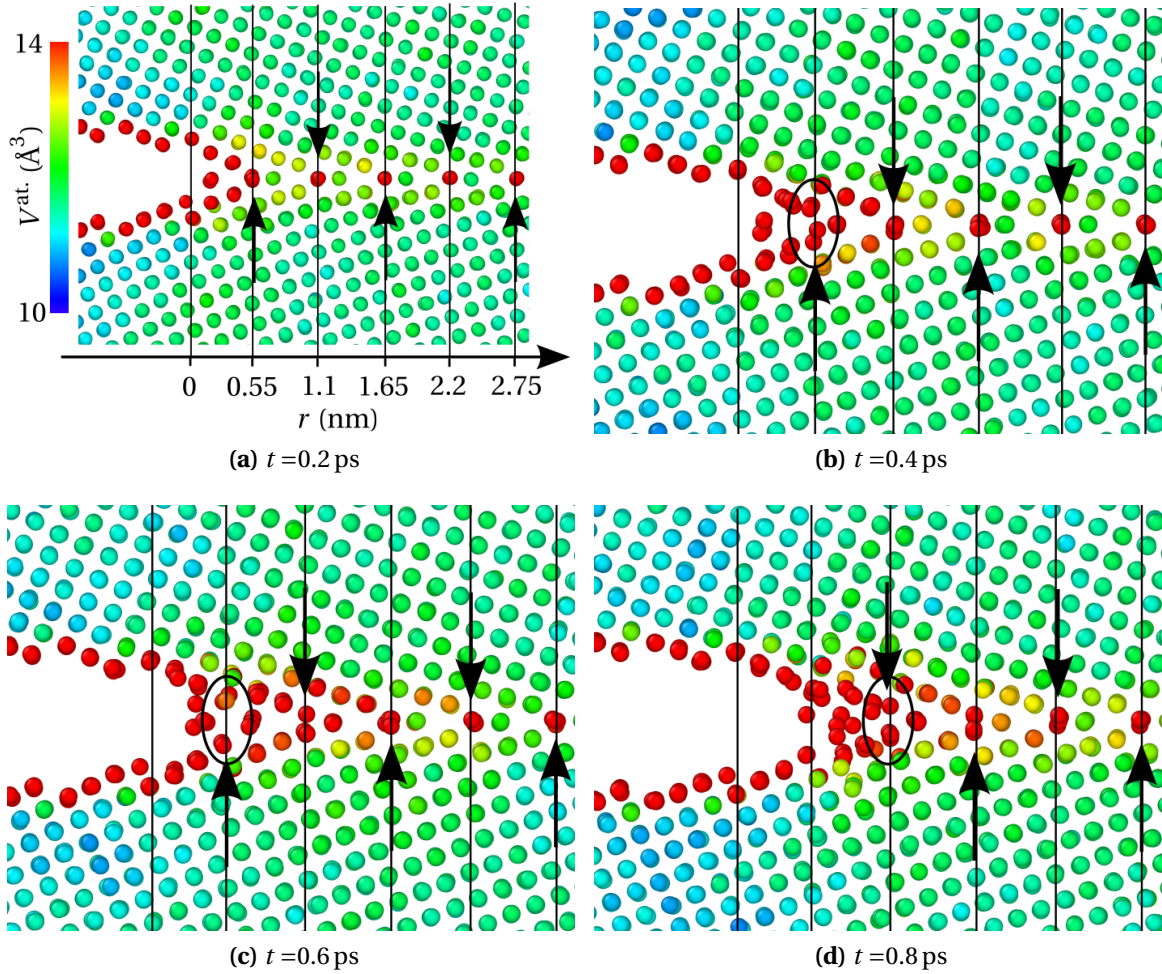


Figure 5.14: Atomic configurations plotted with the atomic volume field, at different time step during the relaxation at $\Sigma_{yy} = 28.7$ MPa. The same scale is used for every configuration. The arrows and lines indicate the location of the atomic disclination sites. The circle markers identify the debonding of the disclination sites.

5. STRESS CONCENTRATIONS AND CRACK INITIATION AT GRAIN BOUNDARIES: THE V-NOTCH PROBLEM

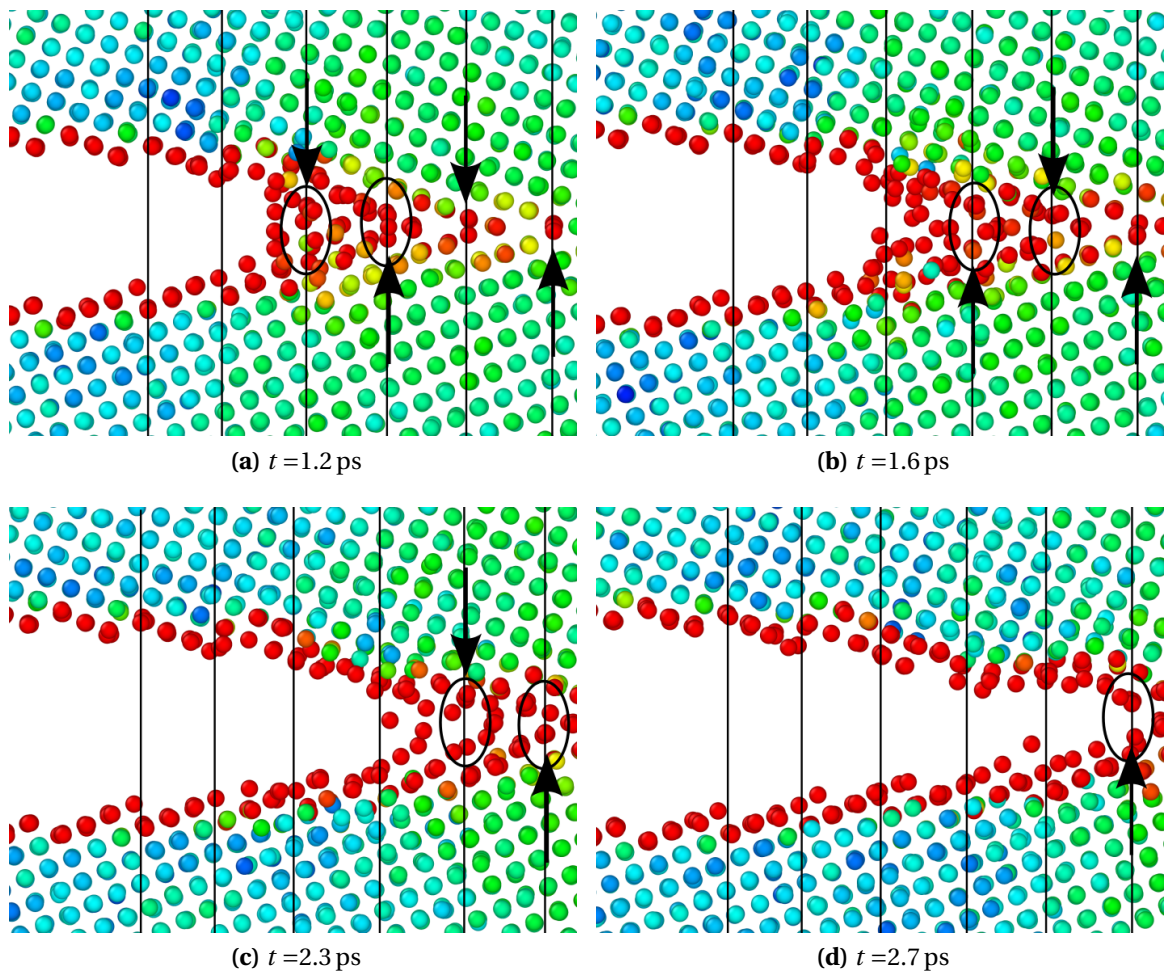


Figure 5.15: MD steps following the figure 5.14.

5. STRESS CONCENTRATIONS AND CRACK INITIATION AT GRAIN BOUNDARIES: THE V-NOTCH PROBLEM

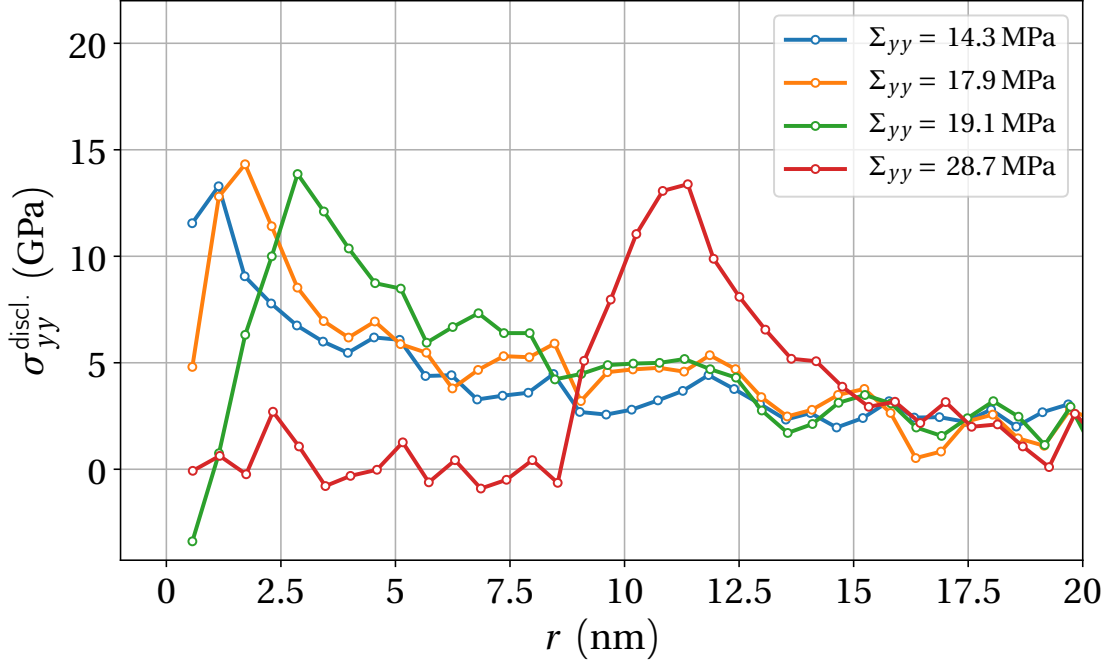


Figure 5.16: MD stress profiles $\sigma_{yy}^{\text{discl.}}(r)$ at the remote stress referenced in figure 5.17 on the fully relaxed configuration.

5.4.2.2 Prediction of crack initiation

A prediction of the remote critical stress to crack initiation is now undertaken by performing further top-down simulations on the same sample at different axial remote stress Σ_{yy} . For this part, the same procedure is applied, and only the final configuration after full relaxation are now considered. It is reminded however that between the different loadings, the history of the material is not taken into account. The representativity of the relaxed configuration should be taken with caution.

It is indeed assumed here that these final states at the prescribed Σ_{yy} remote stresses could be equivalent to the results that would be typically obtained by a full time scale MD simulation (i.e. an imposed remote stress loading from 0 to Σ_{yy}). This later case is obviously not possible considering the time scale restrictions of molecular dynamics simulations (duration between at most 1 ns to 1 μ s).

In full knowledge of this assumption and using the same disclination boxes of atoms, several relaxed configurations are displayed in figure 5.17 at different loading steps with a qualitative identification of a possible crack length a and a cohesive zone extension Δ_{coh} . The related axial stress profiles are plotted in figure 5.16. The initiation of a crack is recorded at the axial remote stress of 19.1 MPa on more than 1.1 nm. Once again, the identification of a finite crack initiation length of about 0.36 nm (as predicted by the coupled criterion) seems rather difficult to achieve here. But this does not invalidate the

5. STRESS CONCENTRATIONS AND CRACK INITIATION AT GRAIN BOUNDARIES: THE V-NOTCH PROBLEM

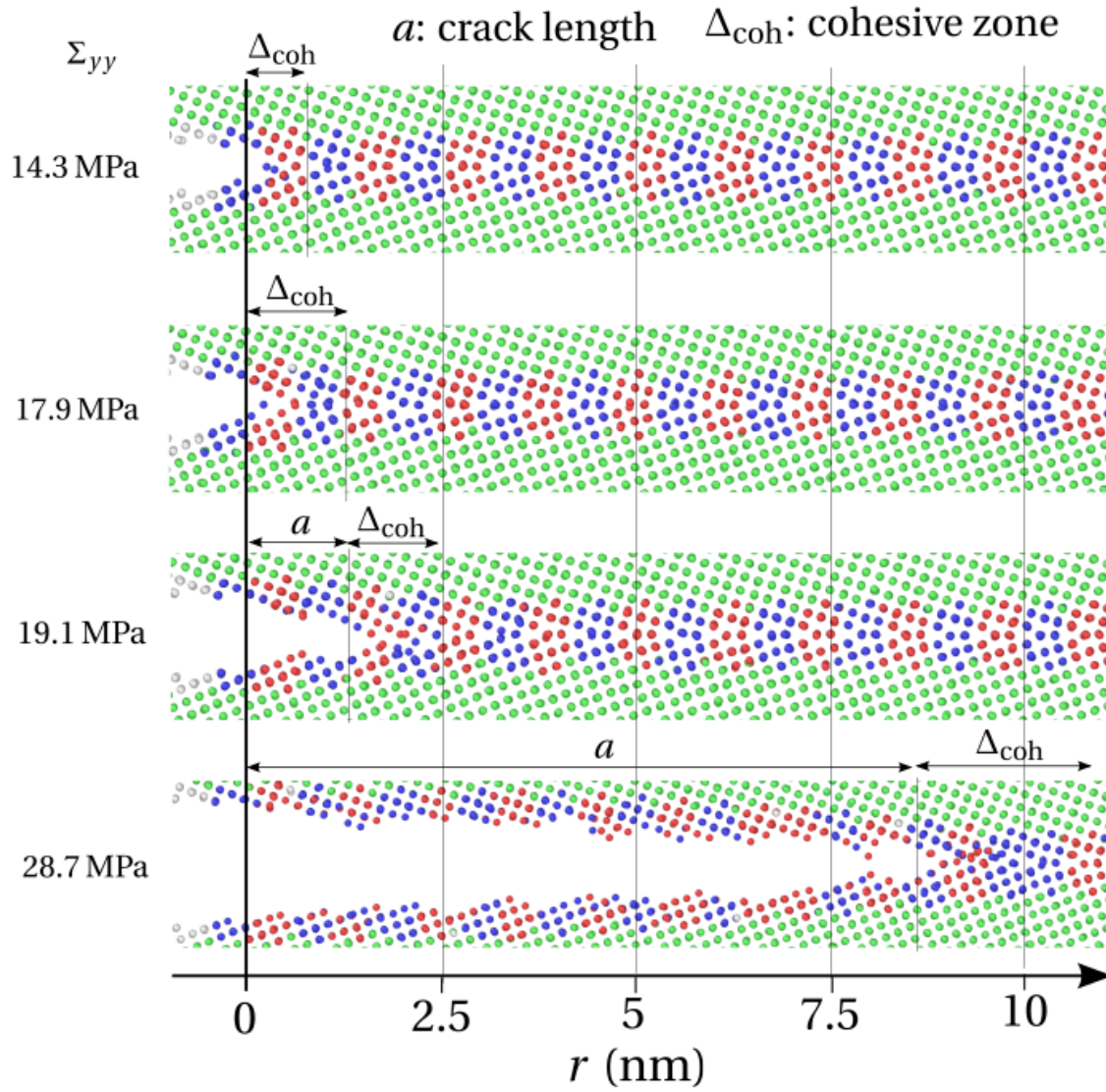


Figure 5.17: Fully relaxed configurations obtained by different top-down simulations performed at different remote stress Σ_{yy} . The crack length a and the extent distance of the cohesive zone Δ_{coh} are further identified.

5. STRESS CONCENTRATIONS AND CRACK INITIATION AT GRAIN BOUNDARIES: THE V-NOTCH PROBLEM

use of such criterion. It is also interesting to note that, as illustrated, no significant crack initiation or dislocation nucleation event is observed before this loading. This point is more thoroughly verified by performing several simulation points at lower remote stresses. This result agrees rather satisfyingly with the coupled criterion and CZM predictions of about 24.6 MPa and 21.7 MPa respectively. The presence of a cohesive zone, with significant debonding of the disclination sites, is once again correlated to a significant axial stress relaxation as similarly observed on the previous CZM stress profiles of figure 5.9a.

In conclusion, this first $\Sigma 5$ [031] example clearly illustrates and confirms the relevance of the top-down approach.

The coherency between the different approaches (bottom-up and top-down) is also demonstrated here in the case of the $\omega = 10^\circ$ notch angle.

5.5 Comparison of the three approaches for different V-notch angles

In order to partly validate the use of a coupled criterion for fracture initiation at the atomic scale, a final comparison between the three approaches is now performed on samples with increasing notch angles.

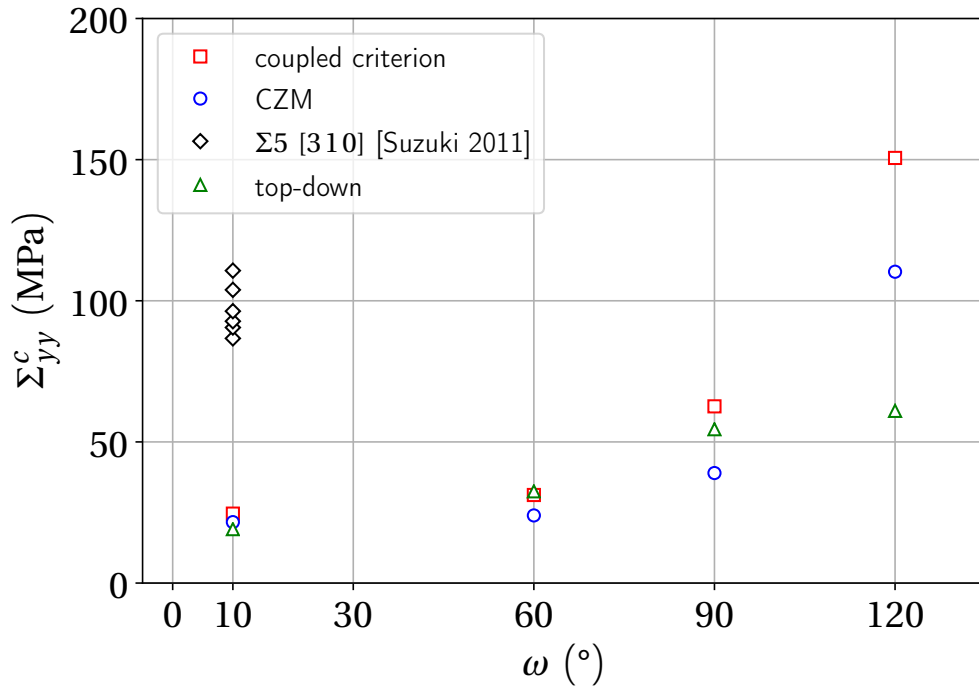
The case of the $\Sigma 5$ [031] grain boundary is reconsidered with the additional notch angles of 60° , 90° and 120° .

The same procedure, described before with the same hypothesis related to the three approaches, are employed and adapted considering these notch angles. The results of the different predictions are plotted in figure 5.18a according to the ω angle along with the experimental results of Suzuki et al.

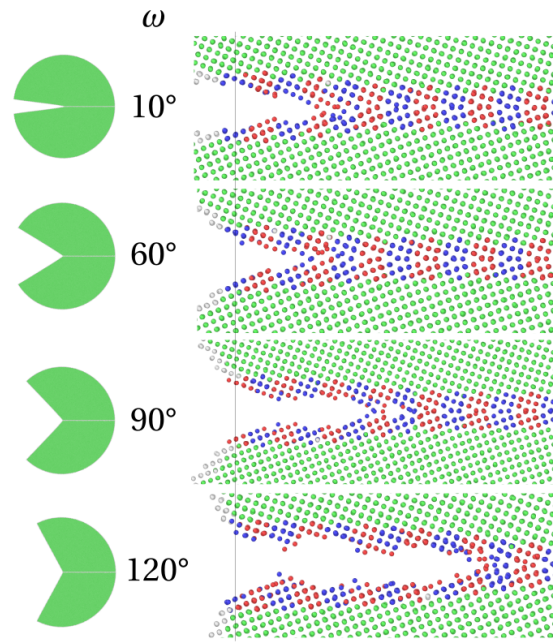
The shape of the critical stress evolution (or critical generalised intensity factor) computed by [Leguillon, 2002] is roughly recovered here for the application of the coupled criterion and the CZM with a satisfying agreement. The top-down approach also yields similar predictions for the 10° , 60° and 90° samples. Significant discrepancies are recorded at 120° , specifically for the top-down approach which shows a rather flat evolution after $\omega = 90^\circ$. However, it is suspected that this result does not discard the validity of the coupled criterion at this scale, considering the satisfying evolution for the lower angles. In particular the V-notch tip geometry set out at this scale may not strictly satisfy certain requirements which are not completely apparent here. It is to be reminded that for the bicrystal cases treated before, which here would correspond to the case $\omega = 180^\circ$, the critical remote stress Σ_{yy}^c is equal to the critical stress σ_c assessed at about 19.9 GPa. Logically, a significant increase of the critical remote stress Σ_{yy}^c is expected with the increase of the ω angle, which contradicts the above discrepancy.

Finally, for the top-down simulations, an illustration of the final relaxed configurations at which the first crack is clearly detected (at Σ_{yy}^c) is provided in figure 5.18b according to the ω angle. It is clear that the propagation distance of the newly created

5. STRESS CONCENTRATIONS AND CRACK INITIATION AT GRAIN BOUNDARIES: THE V-NOTCH PROBLEM



(a)



(b)

Figure 5.18: Prediction of the critical remote stress Σ_{yy}^c for the three bottom-up and top-down approaches, according to the different notch angles (5.18a). Corresponding fully relaxed configuration at the critical remote stress for the top-down approach (5.18b).

5. STRESS CONCENTRATIONS AND CRACK INITIATION AT GRAIN BOUNDARIES: THE V-NOTCH PROBLEM

crack also increases with the ω angle. This observation may be explained by the increase of the energy release rate $G(a_c)$ of the newly created crack with the increase of the exponent λ (and equivalently by the increase of the ω angle). This final result further complete the above agreements.

It is therefore concluded that the coupled criterion can be applied for a prediction of crack initiation at the atomic scale considering homogeneous and heterogeneous loadings on grain boundaries. However care should be taken with regards to certain atomic aspects that may need to be more thoroughly considered.

A final remark can be made concerning the coherency between the experimental results and the different approaches. Despite some clear discrepancies that can easily be explained by some scale effects, it is interesting to note that the same orders of magnitude are found by the predictions using values assessed at the atomic scale. The scale transition obtained here seems to be quite effective from the quantitative and qualitative points of view.

In a final section, it is proposed to address the second point presented at the beginning of this chapter (paragraph 5.2), concerning the grains boundaries behaviour observed experimentally by Suzuki et al. Some insight are provided, regarding the different failure behaviours that may be expected in the simulations by taking into account intergranular heterogeneous stress fields.

5.6 Results for the $\Sigma 5$ $[0\bar{1}2]$ and $\Sigma 3$ $[111]$ grain boundaries

The top-down approach is here conveniently employed on the same $\Sigma 5$ $[0\bar{1}2]$ and $\Sigma 3$ $[111]$ grain boundaries treated by Suzuki et al. Once again, it is assumed that the $\omega = 10^\circ$ V-notch may provide a relevant model.

For the FE part, similar meshes (as presented in figure 5.5) are employed by adapting the mesh refinement size at the tip of the notch according to the grain boundary case considered.

Remote critical stresses for intergranular fracture or dislocation nucleation are presented in figure 5.19 for the three grain boundaries treated, along with the results of Suzuki et al.

For the $\Sigma 3$ grain boundary, only dislocation nucleations are recorded from the V-notch tip whatever the loading stress considered. The first nucleation is obtained at a critical stress of 31.3 MPa. This result is coherent with the experimental assessment even if, once again, a direct comparison should be considered with caution. However, from a qualitative point of view a common ground can be deciphered. Indeed, a ductile behaviour is observed in the top-down simulations with a transgranular fracture. Figure 5.20 depicts the initiation of transgranular cracking at a much higher remote stress of 95.3 MPa. Several MD steps recorded during the relaxation clearly illustrate the ductile mechanism involved in this fracture behaviour with a significant amount of dislocation nucleation from the tip of the notch. This result further agrees qualitatively

5. STRESS CONCENTRATIONS AND CRACK INITIATION AT GRAIN BOUNDARIES: THE V-NOTCH PROBLEM

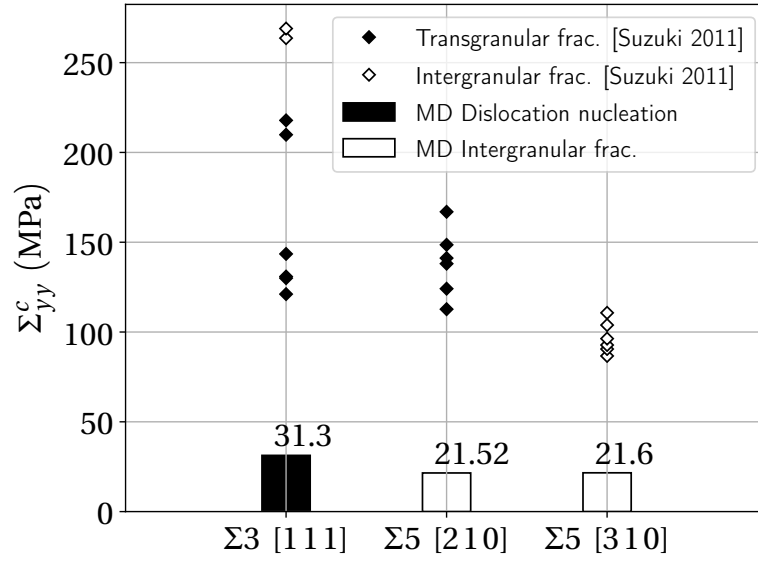


Figure 5.19: Remote critical stress predicted by the top-down approach for either dislocation nucleation or intergranular fracture along with the experimental results of Suzuki et al. for the $\Sigma 3$ [111], $\Sigma 5$ [012] and $\Sigma 5$ [031] grain boundaries.

with the behaviour characterisation of the $\Sigma 3$ [111] bicrystal under multiaxial loadings performed at the beginning of this chapter. As already observed, the presence of the grain boundary does not seem to influence the dislocation nucleation process as the fracture propagation mainly proceeds in the bulk.

In comparison, the $\Sigma 5$ [012] and $\Sigma 5$ [031] grain boundaries clearly display a brittle behaviour with a neat intergranular fracture as illustrated by figure 5.21 for the case of the $\Sigma 5$ [012] GB at $\Sigma_{yy} = 35$ MPa. Slightly lower critical stress to fracture initiation are assessed at 21.52 MPa and 21.6 MPa. Again these results agree with the previous behaviour characterisation on bicrystals presented in figure 5.2c:

- It was shown that the critical stress to dislocation nucleation for the $\Sigma 3$ grain boundary was higher than the critical stress to grain boundary decohesion without dislocation for the two $\Sigma 5$ grain boundaries
- For the two $\Sigma 5$ grain boundaries, the critical stress were quantitatively similar.
- Finally, the α_ε ratios recorded here in the vicinity of the tip of the notches considered in FE computations exceeds 0.8 in each grain boundary cases. This is in agreement with the behaviour map of figure 5.2c.

These points further validate the MD approach on bicrystals presented in chapters 2, 3 and 4.

However, a behaviour discrepancy can be noted in the case of the $\Sigma 5$ [012] grain boundary between the simulation and the experimental results. In the latter case,

5. STRESS CONCENTRATIONS AND CRACK INITIATION AT GRAIN BOUNDARIES:
THE V-NOTCH PROBLEM

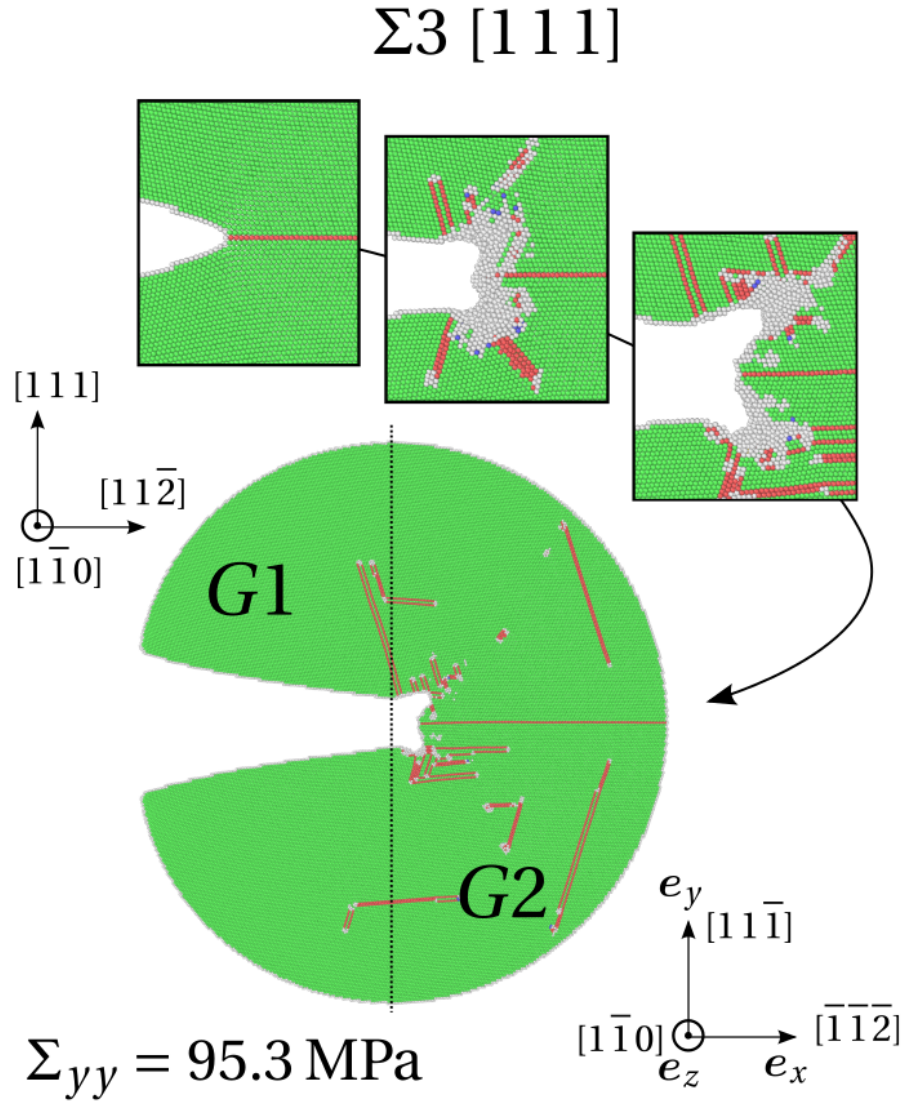


Figure 5.20: Transgranular fracture behaviour observed during the several relaxation steps of the $\Sigma 3 [111]$ grain boundary for the top-down simulation at $\Sigma_{yy} = 95.3 \text{ MPa}$. The common neighbour analysis indicates the crystallographic structure of the atoms: HCP (red), FCC (green), unidentified (white). Partial dislocations path can be identified by the line of HCP atoms.

5. STRESS CONCENTRATIONS AND CRACK INITIATION AT GRAIN BOUNDARIES: THE V-NOTCH PROBLEM

transgranular fracture is predominantly observed. This discrepancy would be difficult to explain thoroughly but it is easy to imagine that the geometry of the tip used in MD or other scale effects could be at the origin of this discrepancy.

Finally, as evidenced in figure 5.19, the top-down predictions are logically lower than the experimental assessments. A justification was already proposed before. This discrepancy obviously results from the difference of space and time scale considered as the MD critical remote stress characterise at most the cracking initiation and propagation over nanometer distances. An increase of the remote stress is therefore expected for the complete failure of the samples.

More interestingly, the comparative behaviour observed in MD between the $\Sigma 3$ and the $\Sigma 5$ GBs seems to agree with the evolution of the critical stresses observed experimentally according to the grain boundary. The ductile mechanism, evidenced for the $\Sigma 3$ on figure 5.20 at 95.3 MPa, limits the propagation of the crack. In comparison, a longer crack propagation is observed (figure 5.21) for the $\Sigma 5$ $[0\bar{1}2]$ grain boundary at a significantly lower remote stress of 35 MPa.

In conclusion, the validity of the top-down method is further confirmed as quantitative and qualitative agreement are found. These results confirm that the $\Sigma 3$ twin boundaries do not predominantly influence the fracture behaviour. It indirectly supports the intergranular fracture mechanism proposed in chapter 4, since negligible atomic volumes (and therefore intrinsic atomic stresses) correlates with the absence of intergranular fracture.

5. STRESS CONCENTRATIONS AND CRACK INITIATION AT GRAIN BOUNDARIES:
THE V-NOTCH PROBLEM

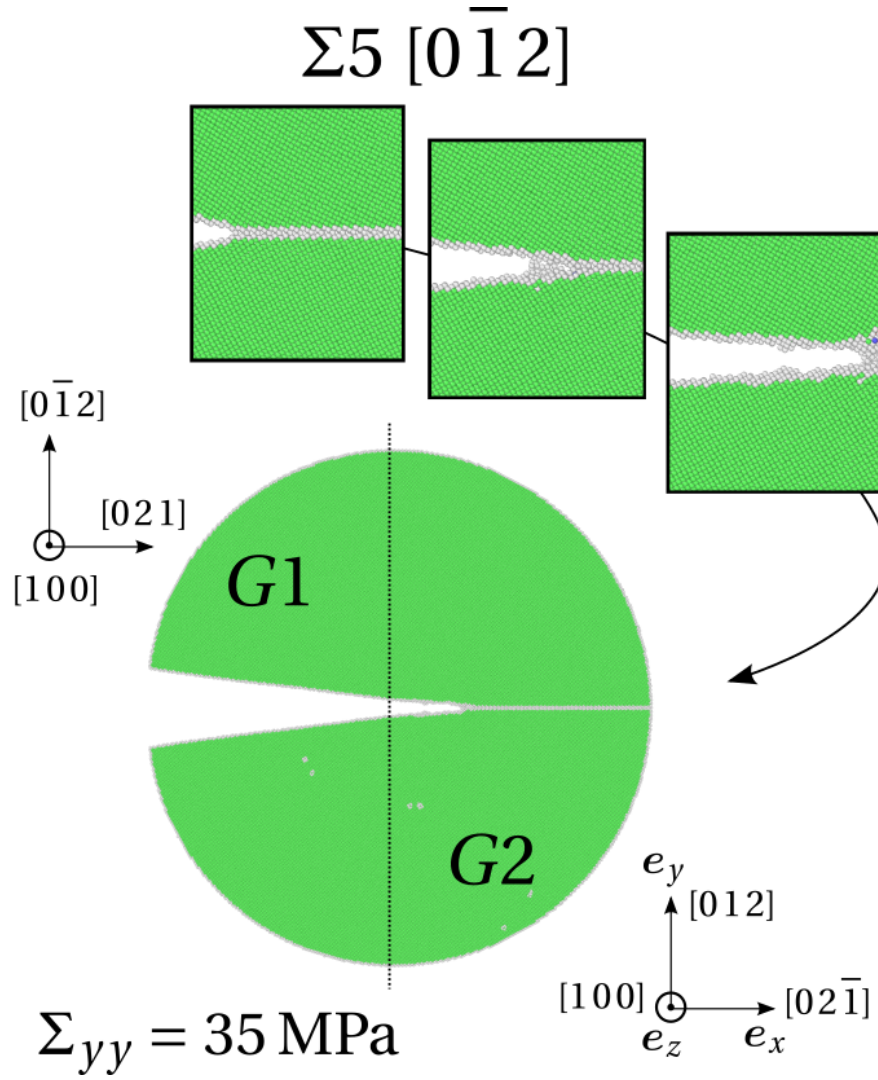


Figure 5.21: Intergranular fracture behaviour observed during the several relaxation steps of the $\Sigma 5 [0 \bar{1} 2]$ grain boundary for the top-down simulation at $\Sigma_{yy} = 35 \text{ MPa}$.

5.7 Summary of the results and conclusion

5.7.1 Results

In this chapter, the following results are found:

- The homogenised phase view of the grain boundaries, as suggested in the conclusion of chapter 4, is successfully employed here to predict the crack initiation at a V-notch sample. Two bottom-up approaches are used: a coupled criterion and a CZM in finite element computations at the continuum level. Similar results are found between the two methods for the case of the $\Sigma 5$ [031] grain boundary and for a notch angle of 10° .
- The application of the coupled criterion to the grain boundaries studied in the preceding chapters reveals a predominant influence of the V-notch geometry at the microscopic scale through the notch angle. Comparatively, the properties of fracture σ_c and γ_c (i.e. the nature or structure of the chosen nickel grain boundaries), shows significantly less influence on the critical remote stress prediction for fracture initiation.
- A top-down approach validates the above predictions at the atomic scale in the case of an heterogeneous stress field. The FE2AT method is successfully used for this purpose.
- An intergranular fracture mechanism is evidenced at the atomic scale for the $\Sigma 5$ [031] grain boundary. This mechanism is coherent with the modelisation proposed by the CZM as a cohesive zone is clearly identified by the significant stress relaxations once the critical stress σ_c is locally reached on representative elementary volumes, as proposed in chapter 4. It also agrees with the bicrystals assessments and debonding mechanism previously obtained for the multiaxial homogeneous loadings.
- The validity of a coupled criterion for crack initiation is partly demonstrated using the three approaches. Similar predictions are found for V-notch angles between 10° and 90° with an increasing variation of the critical remote stress related to increasingly weaker singularities. Significant discrepancies are found for the case of the 120° angle.
- A quantitative and qualitative coherency is found between the experimental assessments of Suzuki et al. and the three multiscale simulations for the $\Sigma 5$ [031] GBs and the top-down approach for the $\Sigma 3$ [111], $\Sigma 5$ [0 $\bar{1}$ 2] GBs.

At first, the same orders of magnitude are reproduced by the different multiscale approaches. Lower bound are logically found for the remote critical stresses predicted by the simulation for nanoscale crack initiation and propagation.

5. STRESS CONCENTRATIONS AND CRACK INITIATION AT GRAIN BOUNDARIES: THE V-NOTCH PROBLEM

Secondly, similar behaviours are found as a ductile transgranular fracture is simulated for the $\Sigma 3$ [1 1 1] grain boundary at seemingly higher remote stresses than the remote critical stresses for the intergranular fractures of the $\Sigma 5$ [0 $\bar{1}$ 2] and $\Sigma 5$ [0 3 1] grain boundaries.

5.7.2 Conclusion

In this chapter, the relevance of the previous MD studies carried out in chapters 2, 3 and 4, is clearly illustrated by several multiscale predictions of intergranular crack initiation under heterogeneous loadings.

The coherency found between the experimental and the simulation results, validates the transition carried out between the atomic scale and the microscopic scale. Based on the results of this chapter, it is believed that the systematic presence of stress concentrators at grain boundaries may constitute a predominant factor to explain the large gap observed between the critical stresses assessed at the different scales.

Although more relevant for complex anisotropic problems of fracture, the cohesive zone models constitute a convenient tool from an engineering point of view. The use of atomistic data in conjunction with these models may however need more thorough developments for computations at the upper scale, in particular concerning the simulation of crack propagation.

The use of a coupled criterion for the fracture initiation prediction at the atomic scale is believed to be adequate, despite the significant discrepancies found that might be related to the multiscale simulations performed here. This point is important since the generality of this criterion may allow to treat a large extent of different stress concentrations from a prediction point of view. The discontinuous slip band (or clear bands for irradiated materials) impacting grain boundaries constitutes, for that matter, a particular case of interest here.

In the next chapters, this point is further investigated, by relying on the present results and conclusions.

6

Discontinuous slip bands model for low stacking fault energy metals and alloys

In this chapter, an experimental assessment of the thickness, the interband spacing and the plastic slip strain of slip bands in a typical 316L austenitic stainless steels is proposed to support the use of a multiscale model for the prediction of intergranular fracture initiation.

The necessity to cross atomic force microscopy measures with grain orientation data, as obtained by EBSD, is stressed further in this study.

Elements are provided to identify the principal factors that could explain the sensitivity of irradiated austenitic stainless steels to intergranular cracking, as compared to their unirradiated counterpart predominantly subjected to transgranular fracture.

In particular, an extensive comparison to other similar studies on irradiated and unirradiated stainless steel is provided in order to derive comparative elements.

In that regard, the plastic slip strain constitute the relevant indicator to characterise the degree of localised deformation. A comparison of the interband spacing between slip bands and clear bands constitute a key factor that could explain the propensity to intergranular fracture in irradiated stainless steels.

6. DISCONTINUOUS SLIP BANDS MODEL FOR LOW STACKING FAULT ENERGY METALS AND ALLOYS

Contents

6.1 Intergranular stress concentrations at plastic slip band or clear band impacts	196
6.2 Experimental characterisation of plastic slip bands in a 316L stainless steels	200
6.2.1 Material and method	200
6.2.1.1 Material and sample	200
6.2.1.2 Tensile tests	201
6.2.1.3 Atomic force microscopy	203
6.2.2 Preliminary observation and measurements	205
6.2.2.1 AFM results	205
6.2.2.2 Slip band geometry	207
6.2.2.3 Importance of the grains orientation	211
6.2.3 Statistical characterisation of slip bands	213
6.2.3.1 Electron back scatter diffraction	213
6.2.3.2 Grain selection	216
6.2.3.3 Material behaviour	217
6.2.3.4 Interrupted tensile test	220
6.2.3.5 Slip band surface relief measurement	221
6.3 Discussion	232
6.3.1 Thickness and plastic slip strain of slip bands and clear bands .	233
6.3.1.1 Slip bands and clear bands thickness	233
6.3.1.2 Dislocation channelling	235
6.3.2 Interband spacing and plastic slip strain	237
6.3.2.1 Influence of the irradiation	237
6.3.2.2 Influence of the stacking fault	239
6.3.2.3 Influence of the grain size	239
6.4 Summary of the results and conclusion	241
6.4.1 Results	241
6.4.2 Conclusion	242

Acknowledgement

For this chapter, many contributors are thanked for their help: J. Hazan for the samples and their preparation procedure for EBSD along with the first loaded sample (denoted Int-1), F. Barcelo and A. Gangloff for the EBSD acquisitions and samples preparation, B. Arnal for the FIB platinum deposits, E. Pons, L. Ziolek and J.-L. Flamand for the tensile tests and Cindy L. Rountree for all the AFM measurements.

6.1 Intergranular stress concentrations at plastic slip band or clear band impacts

Among the different intergranular stress concentrators in metallic irradiated material, the interaction between clear bands and grain boundaries in irradiated stainless steels is of particular interest for the prediction of the irradiation assisted stress corrosion cracking (IASCC) phenomenon.

In unirradiated materials, emerging plastic slip bands are commonly observed during the onset and the development of plastic deformations. They result from the flows of numerous dislocations gliding in their plastic slip plane.

In irradiated materials, the presence of radiation induced defaults, such as Frank loops [Jiao et al., 2007] or voids, impinge the dislocations. These defaults are eventually recombined by the gliding dislocations when sufficient resolved shear stresses are reached. As a result, clear bands or clear channels, almost entirely free of defects, can be evidenced as reported by transmission electron microscopy studies [Jiao and Was, 2010, Sauzay et al., 2010, Sharp, 1967].

Concerning IASCC, it has been clearly shown by numerous studies [Jiao and Was, 2008, Nishioka et al., 2008, Fukuya et al., 2008a, Fukuya et al., 2008b, Le Millier, 2014, Gupta et al., 2016] that irradiated austenitic stainless steels experience intergranular cracking during slow strain rate tensile (SSRT) tests when exposed to either inert or oxidising environments.

In particular, microcrack initiations detected during interrupted tensile tests at grain boundaries are directly correlated to the impact of clear bands [Jiao and Was, 2008] as typically observed by SEM in the lower left picture of figure 6.1. Jiao et al. [Jiao and Was, 2011] have demonstrated the preponderant influence of localised plastic deformations over the intergranular cracking phenomenon among other factors such as radiation induced segregation or radiation hardening.

Meanwhile, McMurtrey et al. and Le Millier et al. [?, Le Millier, 2014] have recorded a higher frequency of intergranular microcrack initiations at discontinuous clear bands, for which plasticity is not significantly activated in the neighbouring grain.

In comparison, transgranular ductile fracture is predominantly observed in unirradiated austenitic stainless steels. Only highly pre-strained materials subsequently pulled using SSRT testing under oxidising environment are susceptible to transgranular

6. DISCONTINUOUS SLIP BANDS MODEL FOR LOW STACKING FAULT ENERGY METALS AND ALLOYS

stress corrosion cracking [Couvant et al., 2005].

In that context, it is believed that a prediction of intergranular cracking in stainless steels based on models involving predominantly localised plasticity could be achieved by focusing on the intergranular stress field induced by discontinuous slip bands and clear bands. In particular, deciphering the transition from transgranular to intergranular cracking between unirradiated and irradiated materials could enlighten and confirm the underlying mechanism involved in IASCC, considering either inert or oxidising environments.

Recently, an experimental assessment of the intergranular stress field recorded at the impact of a discontinuous clear channel using high resolution electron back scatter diffraction (HR-EBSD), have been carried out on a proton irradiated stainless steel after SSRT testing in argon environment [Johnson et al., 2016]. The authors strongly suggest that the intergranular normal stress represents a key indicator for intergranular cracking initiation. This method, previously used in plastically deformed titanium [Britton and Wilkinson, 2012], provides a characterisation of the stress concentration induced by slip bands or clear bands with a resolution of several hundred nanometres.

For both studies, stress concentrations are successfully compared to the pile-up model originally introduced by Eshelby [Eshelby et al., 1951], and extensively used ever since [Stroh, 1957, Smith and Barnby, 1967, Johnson et al., 2016, Britton and Wilkinson, 2012, Gururaj et al., 2015]. This analytical model consists in describing the impinged slip bands or clears bands, as arrays of dislocations sliding under an applied shear stress in a single slip plane and piling on the grain boundary (see upper left scheme of figure 6.1). The spacing between dislocations in the plane are determined by the equilibrium between the applied loading and the repulsion forces between the dislocations. The theoretical stress field is computed in the linear elasticity hypothesis by a summation of the stress fields of each piling dislocations. Like a perfect crack loaded in mode II, its formulation proposes a $r^{-\frac{1}{2}}$ evolution of the stress field along the grain boundary using a cylindrical coordinate system:

$$\sigma_{nn}^{\text{pile-up}}(r, \theta) = h(\theta) \langle f\Sigma - \tau_0 \rangle \left(\frac{L^{\text{pile-up}}}{r} \right)^{\frac{1}{2}} + \Sigma_{nn}^{\infty} \quad (6.1)$$

$$\Sigma_{nn}^{\infty} = \Sigma \cos(\alpha_{GB})^2$$

with r the distance from the impact of the pile-up along the grain boundary, $L^{\text{pile-up}}$ the length of the pile-up considered to be half of the grain size, $f\Sigma - \tau_0$ the effective remote shear stress considering the Schmid factor f , the remote stress Σ , the initial critical resolved shear stress τ_0 and Σ_{nn}^{∞} the intergranular normal stress far away from the impact. Finally the geometrical prefactor follows the formulation $h(\theta) = \frac{3}{2} \sin(\theta) \cos(\frac{\theta}{2})$ with:

$$\theta = \frac{\pi}{2} + \alpha_{GB} - \alpha_{SB} \quad (6.2)$$

considering the α_{SB} angle between the tensile axis and the inclination of the slip band and the α_{GB} angle between the GB normal direction and the tensile axis (see figure 6.1).

6. DISCONTINUOUS SLIP BANDS MODEL FOR LOW STACKING FAULT ENERGY METALS AND ALLOYS

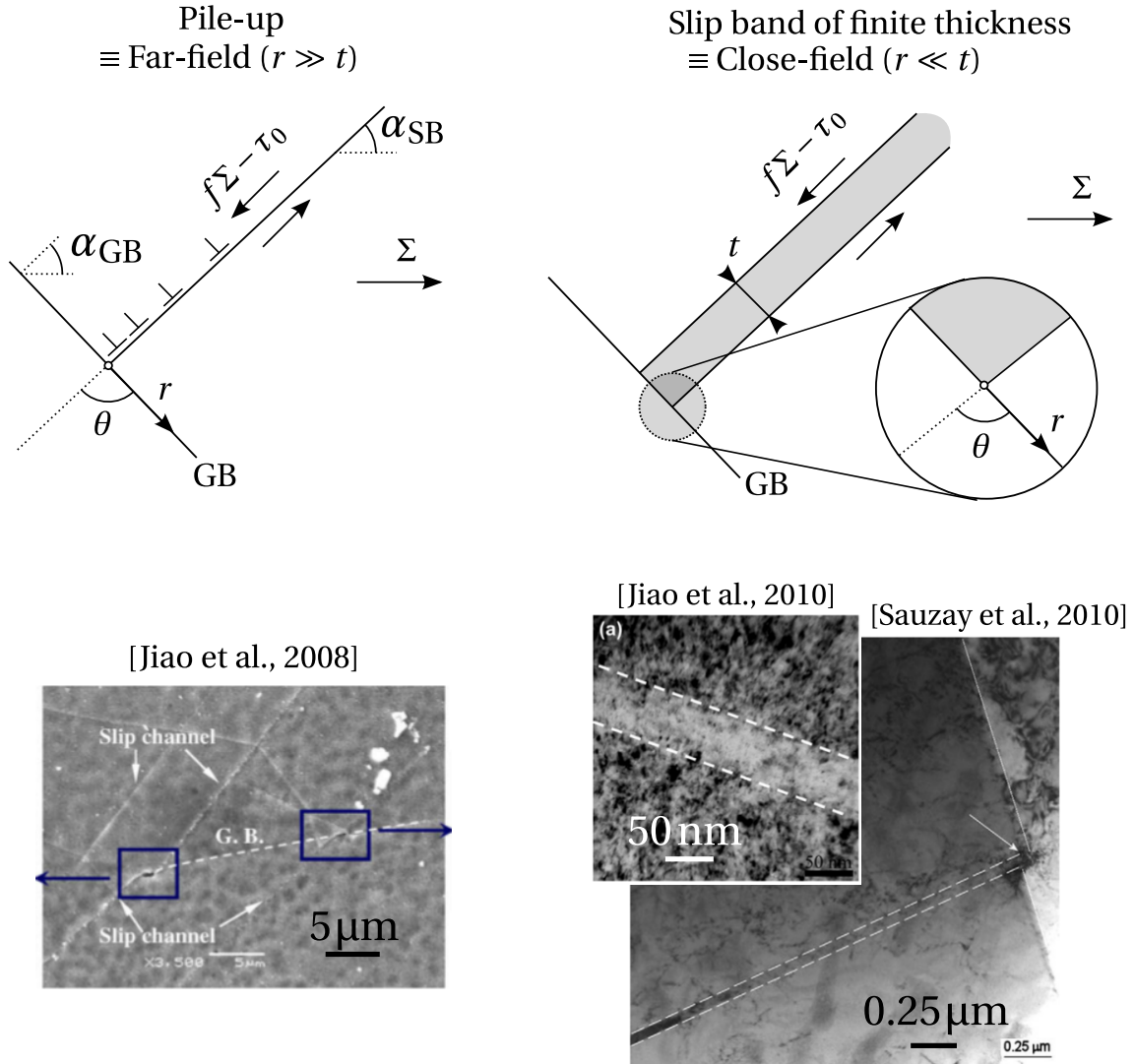


Figure 6.1: Comparison between the pile-up model and the finite thickness slip band model (top pictures) along with the SEM observation of Jiao et al. [Jiao and Was, 2008] (15Cr 12Ni SS alloy, 5 dpa, 1 %) compared to the TEM observation at a higher resolution of [Jiao and Was, 2011] (18Cr 12Ni SS alloy, 5 dpa, 7 %) and [Sauzay et al., 2010] (304L SS alloy, 0.16 dpa)

6. DISCONTINUOUS SLIP BANDS MODEL FOR LOW STACKING FAULT ENERGY METALS AND ALLOYS

This model presents a convenient way to assess a critical remote stress to intergranular crack initiation using the Griffith theory (see chapter 5) and grain boundaries mechanical properties at the atomic scale.

However, it has been shown by Sauzay et al. [Sauzay and Moussa, 2013, Sauzay and Vor, 2013] that the comparison between such application and experimental results leaves strong discrepancies.

In particular, it was pointed out that the clear bands typically observed in irradiated stainless steels by transmission electron microscopy actually display a finite thickness t of about 50 nm [Jiao and Was, 2010, Sauzay et al., 2010] as displayed by the lower right TEM observations of figure 6.1. These results are therefore clearly in contradiction with the use of the pile-up model at the atomic scale, for modelling the intergranular stress field of slip bands and clear bands.

Based on these observations, Sauzay et al. have performed a change of scale considering the close-field solution of the intergranular normal stress field in the vicinity of a slip band of finite thickness as depicted by the upper right picture in figure 6.1. Following this multiscale approach, a parametric study has been carried out using the finite element method. A semi-analytical model has been proposed to characterise the intergranular normal stress field σ_{nn} :

$$\sigma_{nn}(r, \theta) = A_{nn}(\theta) \langle f\Sigma - \tau_0 \rangle \sqrt{\frac{L}{t}} \left(\frac{t}{r} \right)^{1-\lambda} + \Sigma_{nn}^{\infty} \quad (6.3)$$

with the geometrical prefactor $A_{nn}(\theta)$ only depending on the θ angle. The length L of the slip band (or clear band) is considered to be equal to the grain size as numerous SEM observations have shown that dislocation channels cross the entire grain.

Following this asymptotic expansion to the close-field, for which the distances r considered are much lower than the slip band (or clear band) thickness denoted t (e.g. typically $r < \frac{t}{10}$), a matching solution with the far-field solution far away from the impact (i.e. $r \gg t$) has to be respected in between. This far-field solution can then clearly be assimilated to the pile-up solution through an evolution with a 0.5 exponent. But, more importantly, the parametrical studies of Sauzay et al. clearly evidence a singularity exponent $1 - \lambda$ lower than 0.5 with values around 0.25.

Considering the values measured for the thickness of the clear bands, it is clear that the use of GB properties of fracture at the atomic scale is more coherent within the close-field scale considered in the multiscale model of equation 6.3.

As pointed out by Leguillon and extensively mentioned in chapter 5, the exponent of the singularity characterised by Sauzay et al., at this scale, prevents the use of the Griffith theory for a prediction of intergranular fracture.

Therefore, the same approach used in chapter 5 for the V-notch can be rightfully undertaken here, in the context of Finite Fracture Mechanics and a coupled criterion for the prediction of intergranular fracture initiation.

A complementary investigation comparing slip bands stress field and clear bands stress field is then proposed with the same approach, in order to decipher a possible

6. DISCONTINUOUS SLIP BANDS MODEL FOR LOW STACKING FAULT ENERGY METALS AND ALLOYS

quantitative evidence of the localised plastic deformation effect over intergranular cracking.

To support this approach, detailed and used in the next chapter, it is proposed in this chapter to focus on an experimental assessment of the slip band thickness and the interband spacing in an unirradiated 316L austenitic stainless steels loaded at different plastic deformations.

Thanks to the contrast induced by the channelling of dislocations sweeping irradiation defaults (mainly Frank loops) in irradiated materials, the clear bands thickness can be readily characterised by TEM observations (see figures 6.1). However, little is known about the slip bands geometry in unirradiated materials. Indeed, unlike clear bands, no bulk traces providing subsequent evidence of the history of the plastic deformation, are detectable in that case.

Should the above approach be undertaken for irradiated and unirradiated materials through a comparative and quantitative study, it is clear that the use of the model of equation 6.3 necessitates a characterisation of the slip bands geometry (thickness, interband spacing and plastic slip strain in the band).

For that purpose, electron back scatter diffraction and Atomic Force Microscopy (AFM) are employed. It is to be noted that the AFM method, providing a high resolution record of surface relief, has already been used for the characterisation of emerging slip bands in a similar alloy [Menard, 2005, Aubert et al., 2010, Aubert et al., 2012]. These studies have provided statistical data concerning apparent interband spacings and step heights.

However, neither the thickness of the slip bands nor the actual interband spacing in the bulk has been taken into account.

It should be finally noted that the underlying mechanisms for the formation of the clear bands and the formation of the slip bands are not fully understood yet, despite recent breakthroughs [Gussev et al., 2015, Marano et al., 2019]. Therefore, in this chapter, it is chosen to focus on the early appearance of the slip bands at low plastic deformations.

6.2 Experimental characterisation of plastic slip bands in a 316L stainless steels

6.2.1 Material and method

6.2.1.1 Material and sample

A 316L austenitic stainless steels is used for this experimental characterisation. The related composition of the alloy is provided in table 6.2a and its bigger grains size distribution is presented in figure 6.2c from the EBSD data collected subsequently (see subsection 6.2.3.1) by taking into account the $\Sigma 3$ twin GBs. Despite a mean grain size value of about 40 μm , the material clearly displays a large amount of significantly large

6. DISCONTINUOUS SLIP BANDS MODEL FOR LOW STACKING FAULT ENERGY METALS AND ALLOYS

grains with values reaching at least $300\text{ }\mu\text{m}$. A second averaged grain size weighted by the surface ratios of the grains can be evaluated at $170\text{ }\mu\text{m}$ [Hazan, 2019] along with a log-normal distribution that is partly illustrated in figure 6.2c. These significantly large grains facilitate the AFM acquisitions intended later on. Manufacturing details and texture data of the present alloy are more comprehensively provided by Hazan [Hazan, 2019].

The stacking fault energy (SFE) of the alloy can be estimated at 30.4 J m^{-2} using Pickering's correlation for austenitic stainless steels [Pickering, 1976]. This low value is characteristic of a planar material for which plasticity is preferentially localised with very restrained cross slips and only few slip systems activated. In comparison, copper, nickel and aluminium feature higher SFEs with values of roughly 50 J m^{-2} , 130 J m^{-2} and at least 150 J m^{-2} respectively, the from DFT data [Andric et al., 2019]. In particular, it is well-known that aluminium displays a more homogeneous plasticity.

Flat specimens featuring an initial cross-sectional area of $1\text{ mm} \times 2\text{ mm}$ and an initial gauge length of $L_0 = 8\text{ mm}$ (see figure 6.2b) are used for the monotonic tensile tests listed in the table of figure 6.2b. These dimensions allow to take into account a representative amount of grains (about 5000 grains) while facilitating the EBSD acquisitions.

6.2.1.2 Tensile tests

A first interrupted tensile test, denoted Int-1, is performed and provided by J. Hazan [Hazan, 2016] at a macroscopic plastic deformation of 17.4 %. The monotonic tensile test is carried out at room temperature in air with a constant strain rate of $2.7 \times 10^{-5}\text{ s}^{-1}$. The deformed sample is conveniently used for a first-hand AFM characterisation of several slip bands in one grain.

A more thorough investigation is then considered using samples denoted Fra and Int-2 for which a fracture test and two interrupted tensile tests at 1 % and 2 % plastic deformations are performed with a strain rate of $2.0 \times 10^{-5}\text{ s}^{-1}$ at room temperature. The Fra tensile test provides the representative behaviour of the material necessary for the subsequent interrupted tensile tests on the Int-2 specimen by using the same tensile apparatus. From the Int-2 specimen, EBSD and AFM data are crossed in order to characterise geometrically the emerging slip bands developed for each plastic deformation. The tensile tests are carried out using a Instron 4507 testing system with a 20 kN load cell, as displayed in figure 6.2d.

In the case of the Int-1 and Int-2 specimens, a mirror polishing of the surface is carried out before the tensile tests in order to obtain a surface state prone to AFM measurements and in the later case (Int-2) necessary for the EBSD acquisition. The polish consists of a mechanical and an electrochemical polishing with the following steps: (1) a first and a second polishing with a paper grade 600 ($26\text{ }\mu\text{m}$) and 1200 ($15\text{ }\mu\text{m}$), (2) a third and a fourth polishing with a diamond spray $3\text{ }\mu\text{m}$ and $1\text{ }\mu\text{m}$ and (3) an electropolishing (70 % ethanol, 20 % ethylene glycol monobutyl ether, 10 % perchloric acid solution).

Due to the size of the sample the traditional strain assessment by extensometry is

6. DISCONTINUOUS SLIP BANDS MODEL FOR LOW STACKING FAULT ENERGY METALS AND ALLOYS

Cr	Ni	Mo	Mn	Si	Co	N	P	C	S	Fe
16.543	10.093	2.044	1.288	0.335	0.132	0.048	0.034	0.022	0.002	bal.

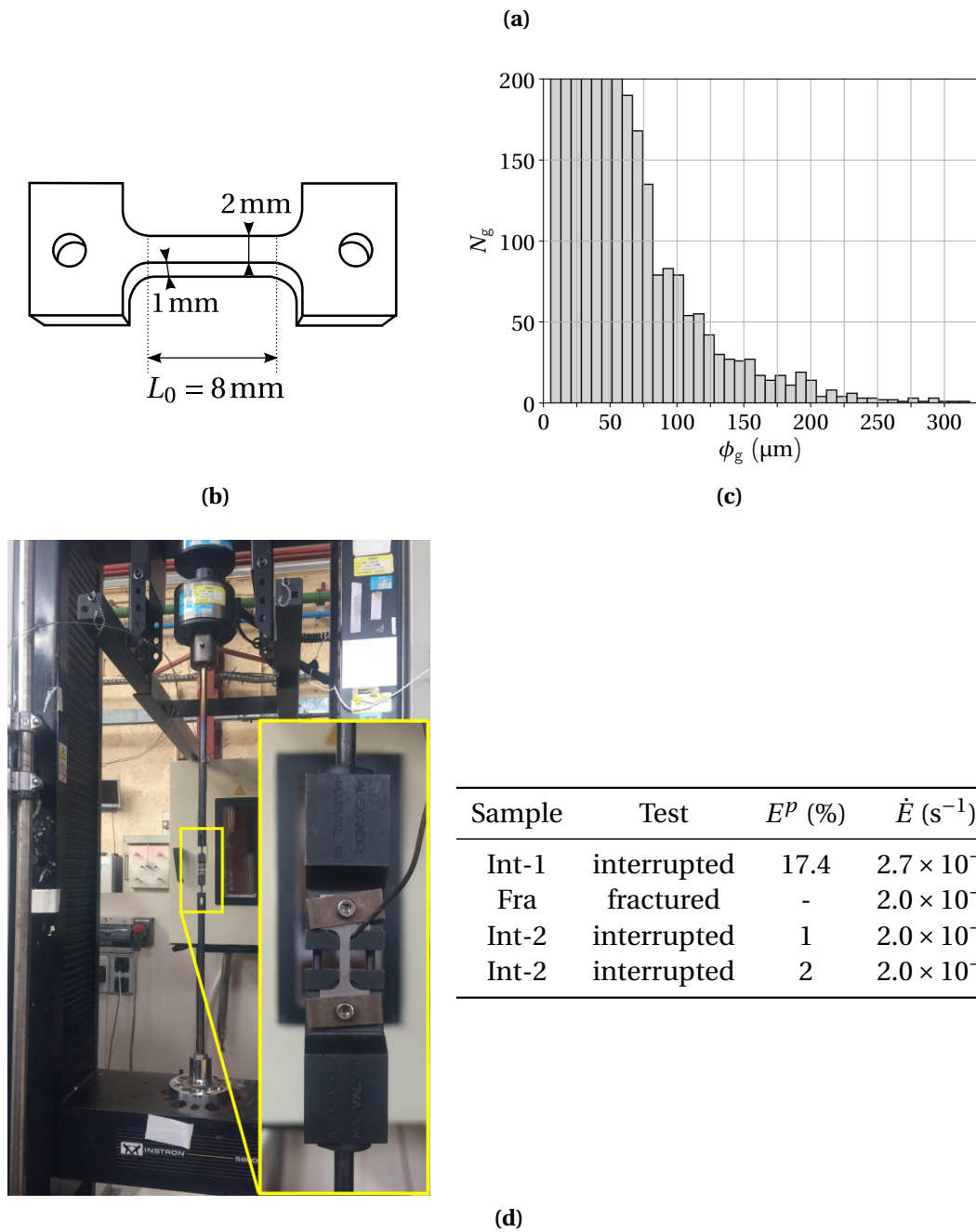


Figure 6.2: Composition (wt %) of the 316L austenitic stainless steel (6.2a) and the grain size distribution (6.2c). N_g : number of grains. Dimensions of the samples (6.2b) used for the listed tensile tests and tensile apparatus (6.2d). E^P : interrupted macroscopic plastic deformation. \dot{E} : strain rate.

6. DISCONTINUOUS SLIP BANDS MODEL FOR LOW STACKING FAULT ENERGY METALS AND ALLOYS

rendered impossible here with the apparatus (figure 6.2d). After polishing, platinum deposit lines are therefore drawn on each side of the gauge area (length L_0) of the Int-2 sample using a focused ion beam (FIB). These marks allow a direct strain measurement of the gauge area after deformation by referencing the initial length in between the marks. It also conveniently provides reference points to localise the grains of interest for the AFM measurements.

6.2.1.3 Atomic force microscopy

Introduced in the late 1980s [Binnig et al., 1986], the atomic force microscope provides, among other material characterisation, topographic measurements reaching an atomic resolution.

The AFM apparatus basically consists in a tip fixed at the end of a cantilever, which probes the surface of a sample. The tip moves over the surface of a sample via a piezo system. As this is occurring, a laser reflects off the cantilever and onto a photodiode (figure 6.3). A feedback system moves the tip up or down to maintain the position of the laser dot on the photodiode. This provides the topography of the surface.

Two standard acquisition modes exist to probe the surface relief: contact and non-contact modes. In contact mode, the tip is in contact with the surface and the feedback system moves the tip up or down to maintain a constant deflection. In non-contact mode or tapping mode, the tip oscillates over the surface. As the tip moves over the surface, the feedback system aims to maintain a constant oscillation, and in turn a constant tip surface distance. A new mode of operation coined PeakForce Tapping mode is between the two others. This mode of operation taps the surface with a constant force and treats the approach and retract curves at every pixel giving nano-mechanical information.

A Bruker Dimension Icon Nanoscope V provides detailed information via the topography of the slip bands located within one or several grains for the two samples Int-1 and Int-2. These measurements use a ScanAsyst-Air probe from Bruker (see top left picture provided by Bruker [Bruker,] and displayed in figure 6.3). The spec parameters of the tip are: tip radius of 2 nm; front angle (FA) of $(15.0 \pm 2.5)^\circ$; back angle (BA) of $(25.0 \pm 2.5)^\circ$, side angle (SA) of $(17.5 \pm 2.5)^\circ$ and height (h_{tip}) of 5 μm (as referenced in figure 6.3). The AFM software records both the trace and retrace to help minimize tip effects. The mode of operation was Peak-Force QNM with the "Peak Force Setpoint" set to 5 nN to minimize wearing of the tip. When imaging, care was taken not to be parallel to the slip bands traces.

The \mathbf{e}_x scanning direction is chosen along the tensile axis \mathbf{e}_f as displayed, on the top right picture of figure 6.3, by the AFM optics during scanning of the Int-2 at 1 % plastic deformation.

It is also verified that the tip configuration respects the angular limitation of measurement already mentioned by Menard [Menard, 2005] in the case of emerging slip bands. As depicted in the lower left scheme of figure 6.3, the tip angle in the scanning

6. DISCONTINUOUS SLIP BANDS MODEL FOR LOW STACKING FAULT ENERGY METALS AND ALLOYS

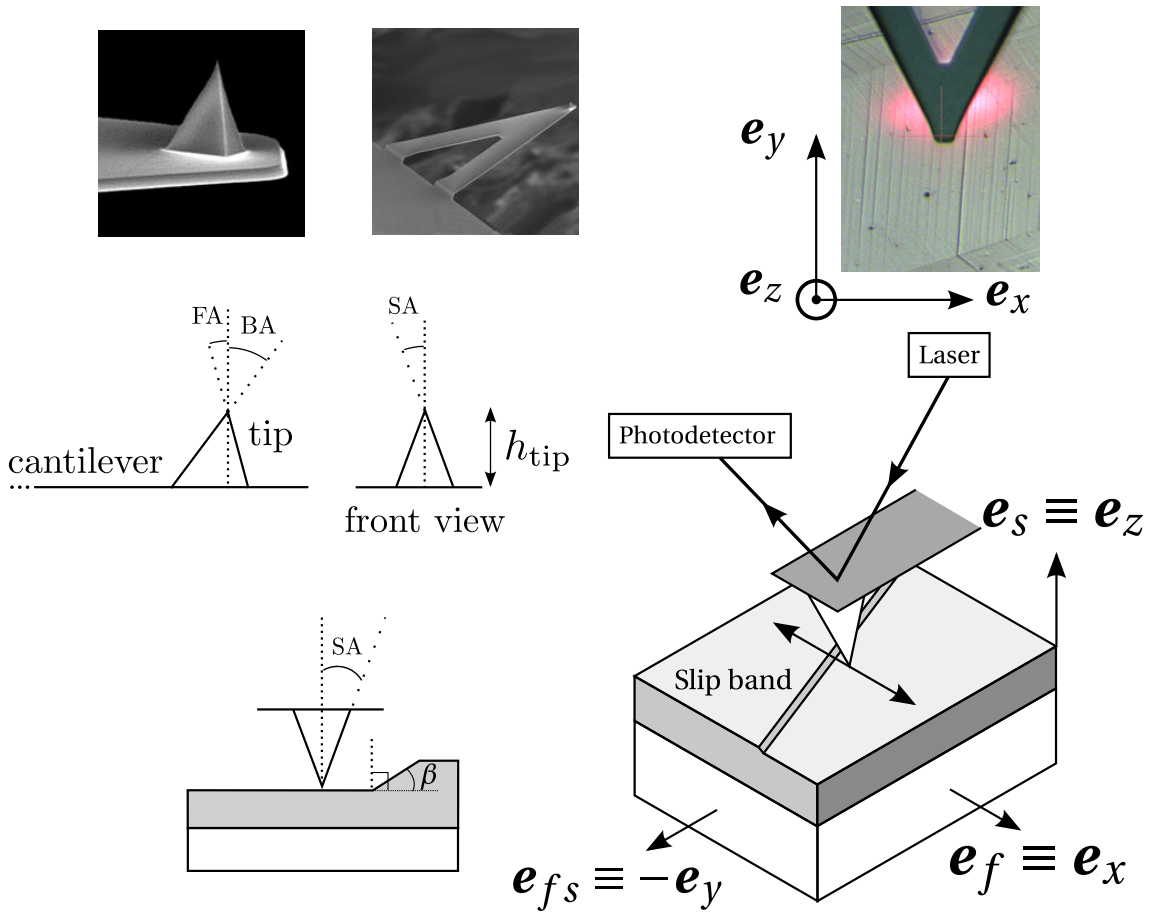


Figure 6.3: Tip and cantilever [Bruker,] used for the AFM acquisitions (top left picture). Engaged tip during the Int-2 sample scanning of one grain after 1 % deformation (top right picture). Schemes of the AFM apparatus (bottom right picture) and scheme of the angle condition for measurement (bottom left picture).

6. DISCONTINUOUS SLIP BANDS MODEL FOR LOW STACKING FAULT ENERGY METALS AND ALLOYS

direction has to be lower than the $90^\circ - \beta$ angle, β being the inclination angle of the slip band surfaces.

From the previous assessment of 50 nm for the clear bands thickness in a typical 304L irradiated stainless steels [Sauzay et al., 2010] (see figure 6.1), it is assumed that a larger thickness should be expected for a similar unirradiated material. Therefore $20\mu\text{m} \times 20\mu\text{m}$ or $10\mu\text{m} \times 10\mu\text{m}$ acquisition windows are scanned with a pixel resolution of about 20 nm ($1024\text{px} \times 1024\text{px}$ or $512\text{px} \times 512\text{px}$ scanning windows respectively), thus allowing to obtain enough data points to resolved the slip bands surface delimiting the apparent thickness.

6.2.2 Preliminary observation and measurements

A first attempt to decipher slip band surface relief is proposed here by focusing on the Int-1 deformed sample at 17.4 % plastic deformation. A geometrical model of slip bands is then supported, based on these observations.

6.2.2.1 AFM results

Due to the coarse-grain microstructure of the material, the optical microscope of the AFM allows to select conveniently a grain featuring a single slip system identified by the surface slip traces (see figure 6.4a). It is interesting to note that Hazan [Hazan, 2019, Hazan, 2016] has observed that, for the same material deformed at 17 % plastic deformation, roughly 70 % of the grains feature single slip (single trace). It is here assumed that only one slip system is predominantly activated in the slip plane. This low stacking fault material therefore displays a low number of activated slip systems in the grains, even under a significant plastic deformation.

This observation provides a key element toward the geometrical modelisation of slip bands in plastically deformed polycrystals. A rather rightful approximation could therefore consists in considering only single plastic slip planes predominantly activated for a majority of the grains.

The Nanoscope post-treatment software by Bruker facilitates the identification of the slip bands surfaces on the selected grain displayed in figure 6.4a. Figure 6.4b depicts $10\mu\text{m} \times 3.52\mu\text{m}$ strip of the slip bands imaged by the AFM. Clearly the sharp features in the surface (characterised by steep slopes) correspond to slip bands protruding from the surface. At first glance, there are six large scale slip bands as further identified on figure 6.5.

Figure 6.5 displays a height profile with two scales to enhance the visualisation. This profile is obtained from an average of several slices orthogonal to the slip line (i.e. along direction of the green arrow in figures 6.4). Table 6.1 references the apparent thickness \tilde{t} , inclination angle β and step height \tilde{h} of the slip surfaces to the horizontal line as extracted for each band from the AFM profile.

It is interesting to remark that a profile displaying the same length and height scale would appear rather flat considering the weak inclination angles ($\beta = 3\text{--}10^\circ$) or

6. DISCONTINUOUS SLIP BANDS MODEL FOR LOW STACKING FAULT ENERGY METALS AND ALLOYS

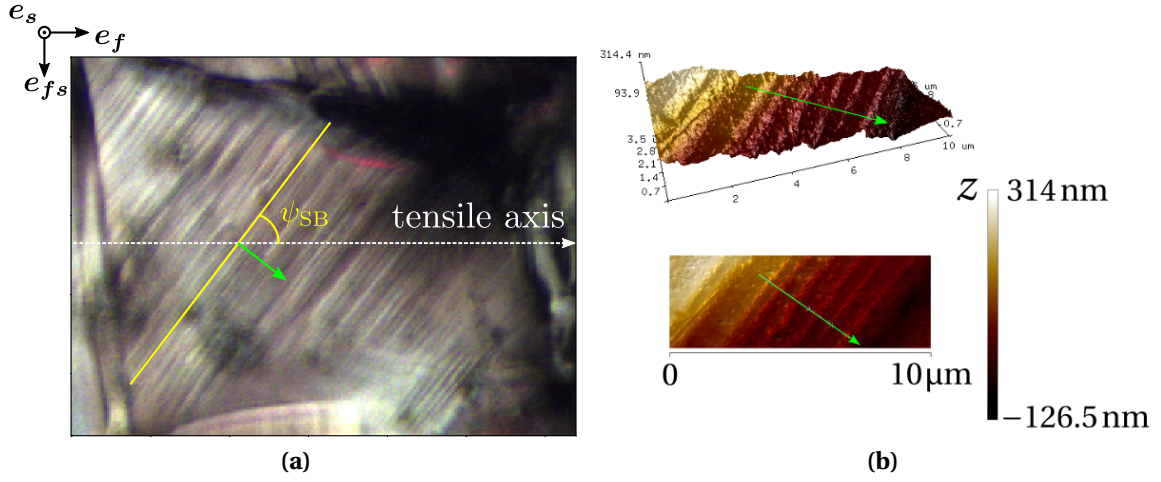


Figure 6.4: AFM measurements on the Int-1 sample after 17.4 % plastic deformation. Optical view of the grain selected for AFM measurements (a) and scan acquisition of the surface height z as recorded by AFM (b). The tensile axis (white), the slip band line (yellow) and the orthogonal direction profile (green) as referenced in the figures.

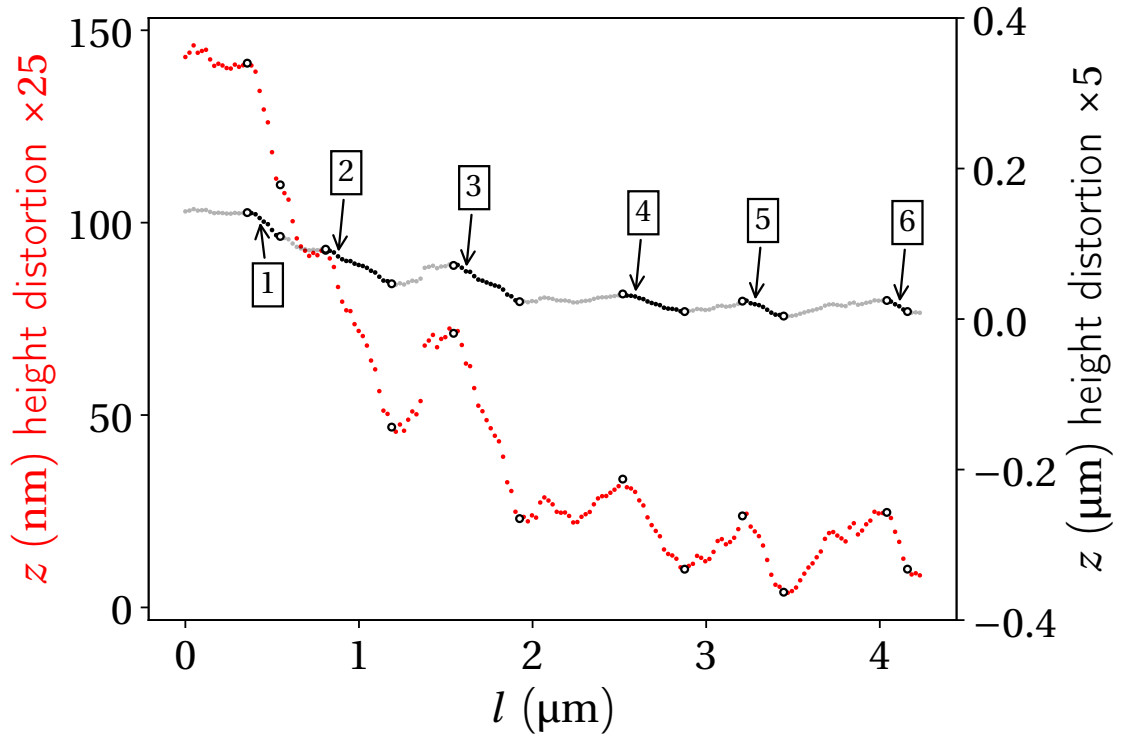


Figure 6.5: AFM surface height measurements z after 17.4 % macroscopic plastic deformation from the extracted orthogonal profile (figure 6.4b), l being the coordinate along this profile. Each point correspond to a measured value. Two height distortion plots are employed for readability purposes. The steeper slopes indicate the slip band surfaces.

6. DISCONTINUOUS SLIP BANDS MODEL FOR LOW STACKING FAULT ENERGY METALS AND ALLOYS

band #	\tilde{t} (nm)	β (°)	\tilde{h} (nm)	t (nm) †	
				ω_{SB} (°)	
				45	35
1	170	10.5	31	96	119
2	361	6.8	43	223	269
3	362	7.8	49	219	266
4	311	3.8	21	204	242
5	216	5.4	20	138	164
6	142	4.7	12	91	109

Table 6.1: Apparent thickness measurements \tilde{t} , step height \tilde{h} and slip bands surface inclination angle β from AFM data. Assessment of the true thickness t using equation 6.9 and considering type B slip bands (†) (see figures 6.10) featuring ω_{SB} angles (see figures 6.6) of 45° and 35° for Schmid factors of 0.5 and 0.47 respectively.

equivalently the rather weak step heights at about 30 nm in average. The angle limitation mentioned before is here verified. The use of the AFM, providing a high resolution in the z-direction, is also clearly justified to resolve the step heights. It can also be noticed that the in-plane resolution of around 24 nm is high enough so that around five data points can be roughly obtained for each slip band relief.

The apparent thickness values obtained around 270 nm on average is clearly higher than the measured values of 50 μm obtained for clear bands, which would further illustrate the localised deformation effect induced by irradiation. However, it should be stressed that this present measurement is obtained at a significantly higher plastic strain (with regard to the 1 % deformation for the irradiated material [Jiao and Was, 2010]) on only six slip bands in one grain. Furthermore, the apparent thickness \tilde{t} does not correspond to the actual slip band thickness t as depicted on the scheme in figure 6.6. The thickness t could actually feature significantly large discrepancies with respect to the apparent thickness, depending on the orientation of the grains. A comprehensive measurement would then necessitates the determination of the normal direction to the slip plane (denoted \mathbf{n}) which can readily be assessed by EBSD measurements. These particular points will be addressed later on with a more thorough investigation performed on the Int-2 sample.

Based on this first hand characterisation and following the modelling approach of Sauzay et al. [Sauzay et al., 2010, Sauzay and Moussa, 2013, Sauzay and Vor, 2013], a geometrical model of the slip band is now presented.

6.2.2.2 Slip band geometry

Geometrically, a slip band can be modelled as a polyhedron with two parallel faces assimilated to the associated plane of the primary slip system of the grain. Figure 6.6 depicts a first scheme suggesting a simplified representation of a slip band (or a clear band) activated during plastic deformation.

6. DISCONTINUOUS SLIP BANDS MODEL FOR LOW STACKING FAULT ENERGY METALS AND ALLOYS

As already introduced before, the Cartesian coordinate system $(\mathbf{e}_f, \mathbf{e}_s, \mathbf{e}_{fs})$ is conveniently chosen, \mathbf{e}_f being parallel to the tensile axes of the specimen, \mathbf{e}_s being the normal vector to the sample initial surface plane and $\mathbf{e}_{fs} = \mathbf{e}_f \wedge \mathbf{e}_s$ as indicated in the figure.

In this model, an emerging slip band in its grain (see the lower scheme (3) of figure 6.6) is partially described by five parameters:

1. three orientation parameters. As argued before, it can be assumed that only one slip system is activated during the plastic deformation. It is then relevant to confound the orientation of the slip band with the orientation of the corresponding primary slip system related to the orientation of its grain. The unit normal vector of the slip plane and the unit slip vector of this system (\mathbf{n}, \mathbf{m}) , are therefore directly related to the orientation of the slip band.

A dislocation gliding in that slip system possesses a Burgers vector $\mathbf{b} = b\mathbf{m}$, with b its magnitude.

2. its thickness t representing the minimum distance between the two parallel faces of the polyhedron.
3. the plastic slip strain field γ_{SB}^p in the band. As illustrated in the lower scheme (1) in figure 6.6 and further observed by SEM or TEM, the slip bands cross the entire grain in which they are activated. Their activation results from a significant number of dislocations crossing the grain and inducing a gliding deformation quantified by the plastic slip strain field γ_{SB}^p . This field is not homogeneous throughout the band and its determination generally requires finite element calculations (e.g. [Sauzay et al., 2010] for 2D plane strain calculations). As a first approximation, the surface displacement \mathbf{u}_{SB} in the gliding direction \mathbf{m} , as referenced in the lower scheme (3) in figure 6.6, can be related with the mean value $\overline{\gamma_{SB}^p}$ of this plastic strain field in the band and the thickness t :

$$\mathbf{u}_{SB} \approx t \overline{\gamma_{SB}^p} \mathbf{m} \quad (6.4)$$

The emerging surface of the band in this model is therefore approximately determined by the plastic strain and the thickness t . For a given plastic deformation, knowing the number of emerging dislocations N_{disl} would also yield the surface step displacement magnitude: $u_{SB} = N_{disl} b$.

Following this model, a full description of the slip band would necessitate the information of the initial transverse faces of the polyhedron (as depicted in scheme (1) of figure 6.6). With the exception of the slip band surface, this information would be inaccessible by non-destructive experimental means. This aspect is therefore not considered here.

The parameter of this geometrical model are varying during the loading, according to the plastic slip strain in the band, the lattice rotation of the grain and the thickness variation of the band during the onset of dislocations mobility.

6. DISCONTINUOUS SLIP BANDS MODEL FOR LOW STACKING FAULT ENERGY METALS AND ALLOYS

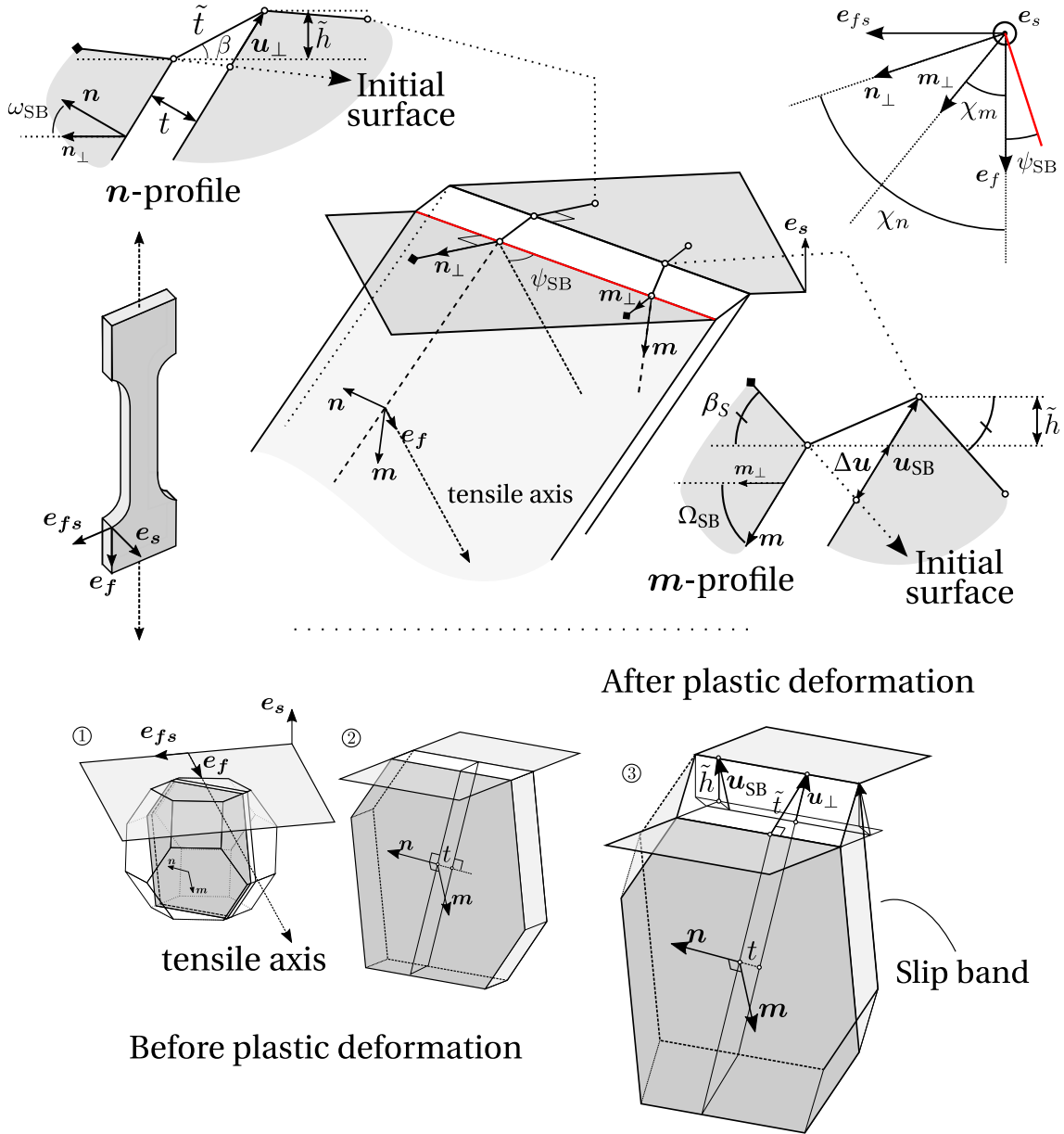


Figure 6.6: Scheme of one emerging slip band after activation (upper picture). The AFM profile provides the steps height $\tilde{h} = \tilde{t} \sin(\beta)$. The \mathbf{n} -profile and \mathbf{m} -profile contains the normal vector \mathbf{n} to the slip plane and the unit slip vector \mathbf{m} respectively. Geometrical model of one slip band (lower picture). Schemes (1) and (2) depict the volume of material to be irreversibly deformed when a slip band (3) is activated through the onset of plasticity, during the tensile test. The band is considered to cross the entire grain (1).

6. DISCONTINUOUS SLIP BANDS MODEL FOR LOW STACKING FAULT ENERGY METALS AND ALLOYS

Following this description and considering a profile orthogonal (further denoted **n**-profile) to the slip trace of an activated slip band (as depicted in the upper scheme of figure 6.6), the relation between the apparent thickness \tilde{t} and the step height \tilde{h} simply follows:

$$\tilde{h} = \tilde{t} \sin(\beta) \quad (6.5)$$

The surface slip trace angle with respect to the tensile axis is denoted ψ_{SB} as already illustrated in figure 6.4a. The normal vector **n** to the slip plane can also be described in the basis ($\mathbf{e}_f, \mathbf{e}_s, \mathbf{e}_{fs}$):

$$\mathbf{n} = \cos(\omega_{SB}) \sin(\psi_{SB}) \mathbf{e}_f + \sin(\omega_{SB}) \mathbf{e}_s + \cos(\omega_{SB}) \cos(\psi_{SB}) \mathbf{e}_{fs} \quad (6.6)$$

where the ω_{SB} angle is the inclination of the slip plane normal direction with respect to the horizontal plane (\mathbf{e}_s normal vector) for an **n**-profile. Assuming the normal vector **n** to be known, the ω_{SB} and ψ_{SB} angles can be simply determined (see equation 6.6):

$$\omega_{SB} = \arcsin(\mathbf{n} \cdot \mathbf{e}_s) \quad (6.7)$$

$$\psi_{SB} = \arcsin\left(\frac{\mathbf{n} \cdot \mathbf{e}_f}{\cos(\omega_{SB})}\right) \quad (6.8)$$

Here, it is clear that $\omega_{SB} \neq \frac{\pi}{2}$ for obvious reasons, preventing that $\cos(\omega_{SB}) = 0$.

A **n**-profile contains the normal vector and gives access to the thickness t of the slip band through:

$$t = \tilde{t} \cos(\beta + \omega_{SB}) \quad (6.9)$$

Similarly, an **m**-profile performed as depicted in figure 6.6, gives an assessment of the step displacement \mathbf{u}_{SB} , provided that the slip direction **m** is known and the angle of the adjacent surface β_s is negligible:

$$\Omega_{SB} = \arcsin(\mathbf{m} \cdot \mathbf{e}_s) \quad (6.10)$$

$$\mathbf{u}_{SB} \approx \frac{\tilde{h}}{\sin(\Omega_{SB})} \mathbf{m} \quad (6.11)$$

with the Ω_{SB} angle, the inclination of the slip direction with respect to the horizontal plane (normal \mathbf{e}_s). The division by 0 is clearly avoided in equation 6.11 for obvious physical reasons. Should the angle β_s of the adjacent surface be significant, a correction $\Delta \mathbf{u}$ of the slip band displacement would have to be taken into account as presented in figures 6.6. In that case, by defining the unit slope vector **s** and the apparent thickness vector after displacement \mathbf{t}_m as illustrated in figure 6.7, the slip band displacement \mathbf{u}_{SB} would readily be obtained by projection of \mathbf{t}_m along the slope vector **s** on the slip vector **m**:

$$\mathbf{u}_{SB} = \frac{(\mathbf{t}_m \cdot \mathbf{m}) - (\mathbf{t}_m \cdot \mathbf{s})(\mathbf{s} \cdot \mathbf{m})}{1 - (\mathbf{s} \cdot \mathbf{m})^2} \mathbf{m} \quad (6.12)$$

This point shall be verified later on. Additionally, in order to facilitate the AFM profiles, χ_n and χ_m can be defined (see upper right scheme of figure 6.6) as the angles between the tensile axis and the orthogonal projections (along \mathbf{e}_s) \mathbf{n}_\perp and \mathbf{m}_\perp of vectors **n** and **m** respectively.

6. DISCONTINUOUS SLIP BANDS MODEL FOR LOW STACKING FAULT ENERGY METALS AND ALLOYS

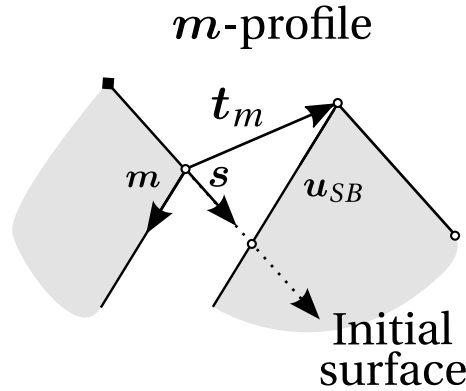


Figure 6.7: Scheme of an m -profile featuring the slope of the matrix surface s outside the slip band, the vector after displacement t_m and the slip vector m for the determination of the displacement u_{SB} .

6.2.2.3 Importance of the grains orientation

In order to give an idea of the discrepancies that could be encountered between the apparent thickness \tilde{t} and the real thickness t , a simple numerical application is now provided. The AFM data of the six bands previously measured for the preliminary observation (table 6.1) and equation 6.9 are used for that purpose. Since EBSD data are not available for this first observation, type B slip bands are considered as an example (see the following section and figure 6.10 for the corresponding definition of type B slip bands).

Of course, it is obvious from figure 6.4, that the type B slip bands assumption is incorrect since a surface trace angle of about 60° can be deciphered. However, it is assumed that the results of this application may not strongly differ by considering another orientation.

Finally, Schmid factors between 0.47 and 0.5 are proposed for the application, corresponding, with the above considerations, to ω_{SB} values of 35° and 45° . This range of Schmid factors is typically very common for non-textured polycrystals. Results of the application are displayed in table 6.1. Significant discrepancies can be noted with roughly 20–45 % variation between the apparent thickness and the actual (hypothetical) thickness. Furthermore, a non-negligible discrepancy can also be remarked between a Schmid factor of 0.47 and 0.5.

This simple application therefore justifies the need to determine the orientation of the grains in order to get access to reliable assessments. It can also be pointed out that the same discrepancy ratios (20–45 %) are applicable to the discrepancies that can be expected between apparent and actual interband spacings. This point is particularly important since most AFM and SEM studies of slip bands only consider apparent assessments of this latter parameter.

Following the above model and considerations, the geometrical characterisation of a statistical number of slip bands in several grains is envisioned by performing EBSD

6. DISCONTINUOUS SLIP BANDS MODEL FOR LOW STACKING FAULT ENERGY METALS AND ALLOYS

and AFM measurements.

6. DISCONTINUOUS SLIP BANDS MODEL FOR LOW STACKING FAULT ENERGY METALS AND ALLOYS

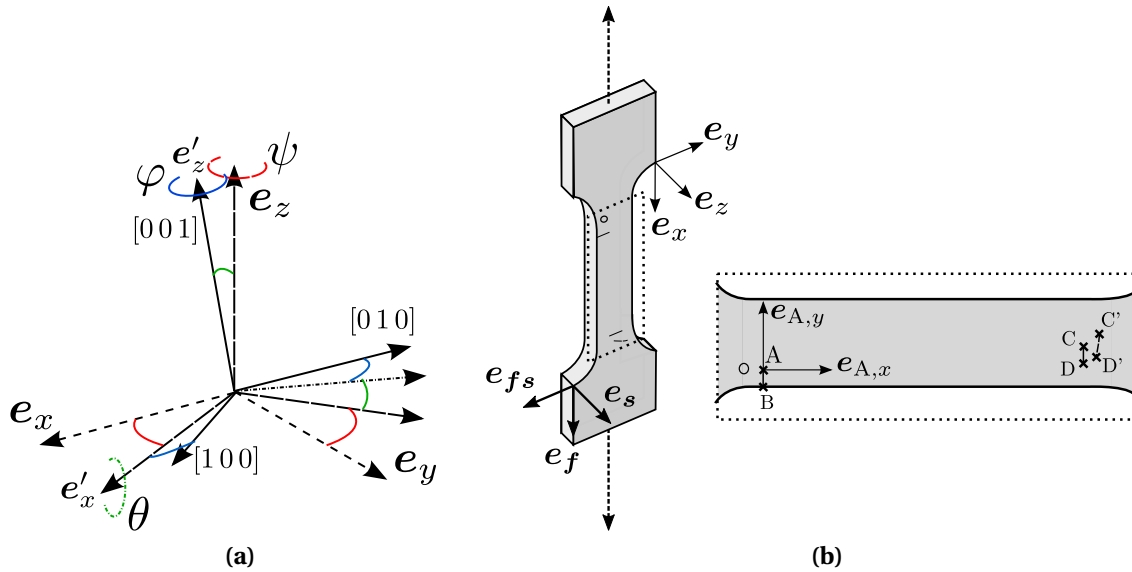


Figure 6.8: Euler's angle in the (e_x, e_y, e_z) referential as assessed by EBSD for the orientation of the crystallographic axis $[100]$, $[010]$ and $[001]$ (6.8a). Scheme of the sample with the two marks of platinum deposit AB, CD and the scratch C'D' (6.8b)

6.2.3 Statistical characterisation of slip bands

This section primarily focuses on the Int-2 sample EBSD analysis before the subsequent interrupted tensile tests and the related AFM acquisitions. The material behaviour is briefly illustrated with the tensile test to fracture carried out on the Fra sample while helping to set up the interrupted tensile tests performed on the Int-2 sample.

6.2.3.1 Electron back scatter diffraction

Electron back scatter diffraction (EBSD) is a characterising technique commonly used to relate the crystallographic orientation of a material with its microstructure [Wilkinson and Britton, 2012]. Briefly, EBSD consists in the detection and analysis of the diffracted patterns resulting from the anisotropic retrodiffusion of an electron beam targetting the sample surface to analyse.

More precisely, EBSD is performed within a scanning electron microscope (SEM) providing a monochromatic electron beam focused on a small portion of the sample surface. From their interactions with the material surface (layers of about 40 nm), a portion of the primary electrons are back scattered from the sample surface. Some are preferentially diffused according to the crystallographic planes of the materials following the Bragg condition. An EBSD detector composed of a phosphor screen coupled with a CCD camera, resolves this back scatter beam resulting in band patterns commonly called Kikuchi patterns.

6. DISCONTINUOUS SLIP BANDS MODEL FOR LOW STACKING FAULT ENERGY METALS AND ALLOYS

From the indexing of these patterns, the identification and orientation of the crystallographic plane for a portion of the sample surface can be deduced with respect to a referential of measure. Using SEM, an EBSD map can then be obtained by scanning a prescribed area of the sample surface. The surface of sample to analyse is significantly tilted to provide a good quality for the detected Kikuchi patterns.

This technique is used for our purpose to perform a complete EBSD map of one face of the Int-2 sample before any tensile loading. A JEOL JSM-7001F SEM is used for that purpose with a Bruker Quantax e-Flash EBSD camera in conjunction with the related software Channel5 for the data analysis. Considering the large grain size expected for this material, a resolution of 5 μm per pixel is used, allowing to sufficiently resolved grain while optimising the time of acquisition.

The measured crystallographic orientations of the grains are provided by the Euler's angles ψ , θ , ϕ with respect to the referential coordinate system $(\mathbf{e}_x, \mathbf{e}_y, \mathbf{e}_z)$ as illustrated in figures 6.8a and 6.8b.

The resulting EBSD map is displayed on the upper picture in figure 6.9 with the Euler's angle contrast.

The two FIB deposits and a reference scratch can be deciphered from both side (left and right) of the sample gauge. As indicated on figure 6.8b, the marks are indexed AB, CD and C'D' respectively and shall be conveniently used later on to spot the coordinates of the grains to be analysed and to roughly assess the macroscopic plastic deformation imposed by the interrupted tensile loadings. Regarding this last point, care has been taken to place the platinum deposits in the gauge area, therefore avoiding the transition area between the shoulders of the sample where plastic deformations can localise during deformation. The reference point A is chosen as the origin in order to facilitate the localisation of the grains analysed by AFM between the different deformations.

From this map, a rather homogeneous orientation field is recorded within each grains with a maximum disorientation of about 1° . Therefore, the averaged value on each grain can be rightfully assumed to represent the orientation of the grain with a $\pm 0.5^\circ$ dispersion.

For each grain, the $(\mathbf{n}_s, \mathbf{m}_s)$ unit vectors related to the twelve slip systems s of the FCC crystallographic configuration can be expressed in the $(\mathbf{e}_x, \mathbf{e}_y, \mathbf{e}_z)$ referential system. For the example of the unit slip vector \mathbf{m}_s :

$$[\mathbf{m}_s]_{xyz} = \mathbf{R}(\mathbf{e}'_z, \varphi) \mathbf{R}(\mathbf{e}'_x, \theta) \mathbf{R}(\mathbf{e}_z, \psi) [\mathbf{m}_s]_0 \quad (6.13)$$

$$\mathbf{e}'_x = \mathbf{R}(\mathbf{e}_z, \psi) \mathbf{e}_x \quad (6.14)$$

$$\mathbf{e}'_z = \mathbf{R}(\mathbf{e}'_x, \theta) \mathbf{e}_z \quad (6.15)$$

with $[\mathbf{m}_s]_0$ the unit slip vector in the crystallographic referential of the grain ($\frac{1}{\sqrt{2}} \langle 110 \rangle$ twelve vectors for \mathbf{m} and $\frac{1}{\sqrt{3}} \langle 111 \rangle$ vectors for \mathbf{n} in the FCC crystallographic system) and $\mathbf{R}(\mathbf{e}, \psi)$ the rotation matrix of angle ψ according to the \mathbf{e} axis.

Using these data, the Schmid factors f_{sch} related to the identified primary slip system (\mathbf{n}, \mathbf{m}) of each grain can be determined and mapped as shown in the lower picture of

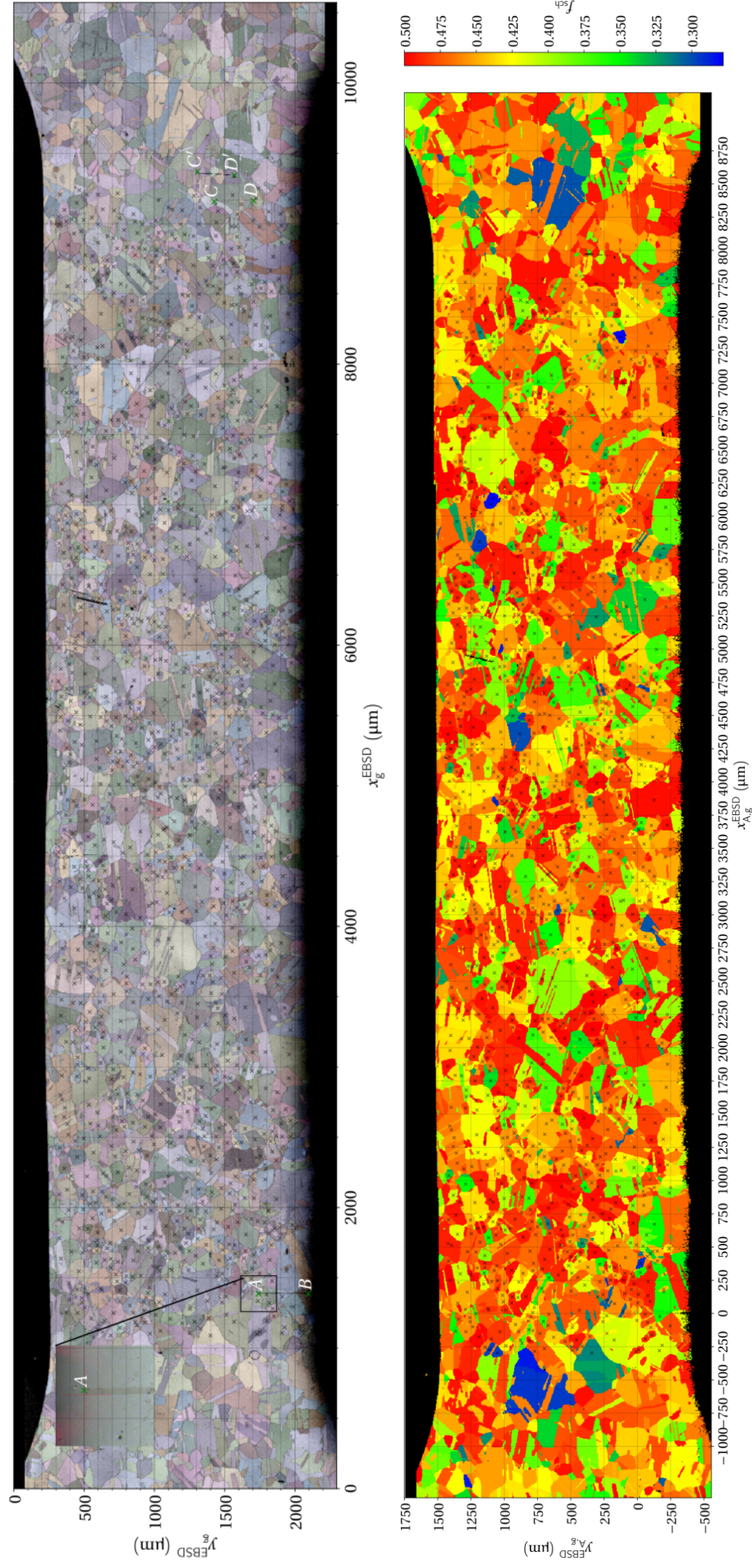


Figure 6.9: EBSD maps by Euler's angle contrast (upper) and by schmid factors (lower). The marks AB, CD and C'D' are further located along with the grains featuring a grain size superior to 50μm

6. DISCONTINUOUS SLIP BANDS MODEL FOR LOW STACKING FAULT ENERGY METALS AND ALLOYS

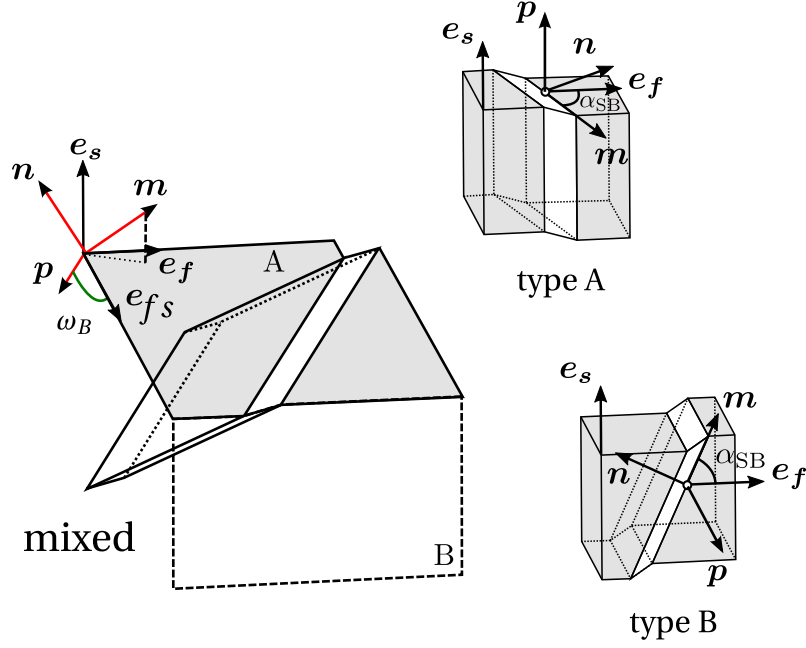


Figure 6.10: Type A and type B configurations of the emerging slip bands according to the specific orientation of \mathbf{n} and \mathbf{m} with $\mathbf{p} = \mathbf{m} \wedge \mathbf{n}$.

figure 6.9. It is reminded that:

$$f_{\text{sch}} = \max_{s \in \{1, \dots, 12\}} [\mathbf{m}_s]_{xyz} \cdot [\mathbf{e}_f \otimes \mathbf{e}_f] \cdot [\mathbf{n}_s]_{xyz} \quad (6.16)$$

considering the related matrix with the tensile axis according to the unit vector \mathbf{e}_f :

$$[\mathbf{e}_f \otimes \mathbf{e}_f] = \begin{bmatrix} 1 & 0 & 0 \\ 0 & 0 & 0 \\ 0 & 0 & 0 \end{bmatrix}$$

6.2.3.2 Grain selection

In the optic of the AFM acquisitions, six grains are selected from the EBSD map following two criteria:

1. The grains featuring the largest grain size are primarily listed in order to facilitate their localisation by the AFM optical microscope when needed. Among the largest grain sizes, three grains featuring the highest Schmid factors are preferred in order to obtain activated slip bands at low deformations. Care is taken to also select grains with secondary slip system with significantly low Schmid factor with respect to the primary slip system in order to avoid their activation thus facilitating the AFM data analysis. The denoted grains: 3b, 6b and 15b are listed in table 6.2.

6. DISCONTINUOUS SLIP BANDS MODEL FOR LOW STACKING FAULT ENERGY METALS AND ALLOYS

Grain	ϕ_g (μm)	f_{sch}	ω_B ($^\circ$)	$\psi_{\text{SB}}^{\text{EBSD}}$ ($^\circ$)	$\psi_{\text{SB}}^{\text{AFM}}$ ($^\circ$)	ω_{SB} ($^\circ$)	Ω_{SB} ($^\circ$)	χ_n ($^\circ$)	χ_m ($^\circ$)
3b	305	0.495	8.71	-78.2	-79.5	43.0	46.2	-168.2	-1.8
6b	292	0.498	49.9	-51.0	-50.8	29.1	25.1	39.0	144.1
15b	257	0.488	10.2	84.8	85.6	50.0	38.7	174.8	12.3
1g	68	0.495	0.3	89.7	88.6	49.1	47.3	179.7	-0.4
2g	81	0.487	1.4	-89.0	-88.5	51.6	-38.4	1.0	1.7
3g	149	0.498	2.2	-87.5	-87.6	42.7	40.9	-177.5	1.9

Table 6.2: Selected grains from the EBSD map, according to the grain size, the Schmid factor and the ω_B angle.

2. Three other grains are selected based on their specific orientation with respect to the tensile axis and the surface plane.

Theoretically, a slip band can be characterised as a type A slip band when its normal and slip vectors (\mathbf{n}, \mathbf{m}) belong to the surface plane of normal \mathbf{e}_s . Similarly, when these vectors belongs to the plane ($\mathbf{e}_f, \mathbf{e}_s$) defined along the tensile axis and perpendicular to the surface, the slip band is of type B. Any slip band can be characterised as a mixed between these two types as illustrated in figure 6.10. For our concern, the simulation of type A or type B slip bands by finite element analysis greatly simplifies the computation within a 2D plane stress or plane strain hypothesis respectively. Furthermore, it has been shown that type B slip bands feature the highest plastic slip [Sauzay and Gilormini, 2002] and could therefore potentially trigger the highest stress concentrations. Slip bands close to the type B are therefore preferentially selected in order to get access to comparable experimental data when considering the most conservative configurations in the FE simulations to come. For that purpose, the ω_B angle, defined as the angle between the vector $\mathbf{p} = \mathbf{m} \wedge \mathbf{n}$ and the vector \mathbf{e}_{fs} , provide an appropriate indicator: the lowest the angle the closest to the type B slip band (at $\omega_B = 0$). The three grains featuring the lowest ω_B angles are therefore selected and denoted: 1g, 2g and 3g, as referenced in table 6.2.

The other reference angles $\psi_{\text{SB}}^{\text{EBSD}}$, ω_{SB} , Ω_{SB} , χ_n and χ_m , as derived by EBSD are also comprehensively listed in table 6.2.

The $\psi_{\text{SB}}^{\text{AFM}}$ angles, as measured subsequently by the AFM acquisition at 1 % plastic deformation (Int-2), are here listed for verification purposes and will be detailed later on.

The tensile tests performed on the Fra and Int-2 samples are now described.

6.2.3.3 Material behaviour

The experimental curve of the tensile test to fracture performed on the Fra sample is displayed at low deformations in figure 6.11 (dotted line). The tensile test is performed

6. DISCONTINUOUS SLIP BANDS MODEL FOR LOW STACKING FAULT ENERGY METALS AND ALLOYS

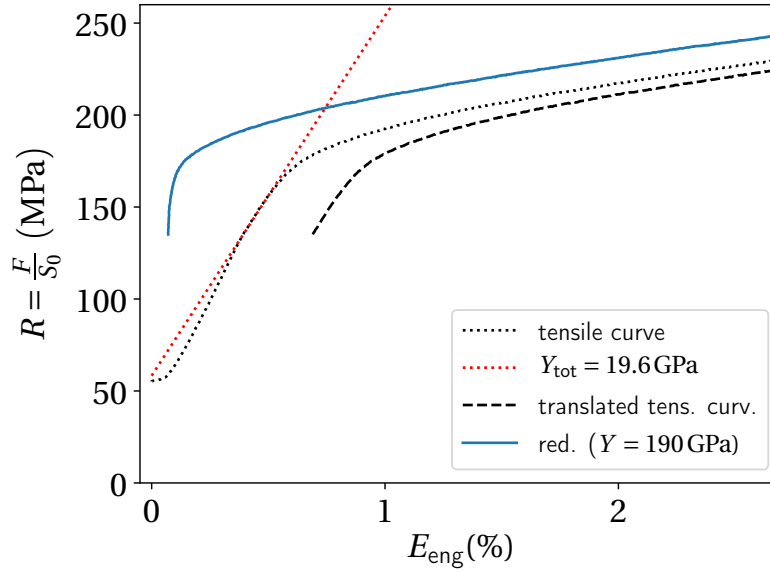


Figure 6.11: Experimental engineering tensile curve (dotted line), translated to match the origin (dashed line) and corrected using the total young modulus Y_{tot} to yield the material engineering curve (blue line).

by controlling the traverse displacement U_{tot} . The engineering stress R is measured using the initial section S_0 and the force F recorded, while the engineering strain is obtained from the initial length of the sample gauge L_0 and the imposed displacement U_{tot} :

$$R = \frac{F}{S_0} \quad E_{\text{eng}} = \frac{U_{\text{tot}}}{L_0}$$

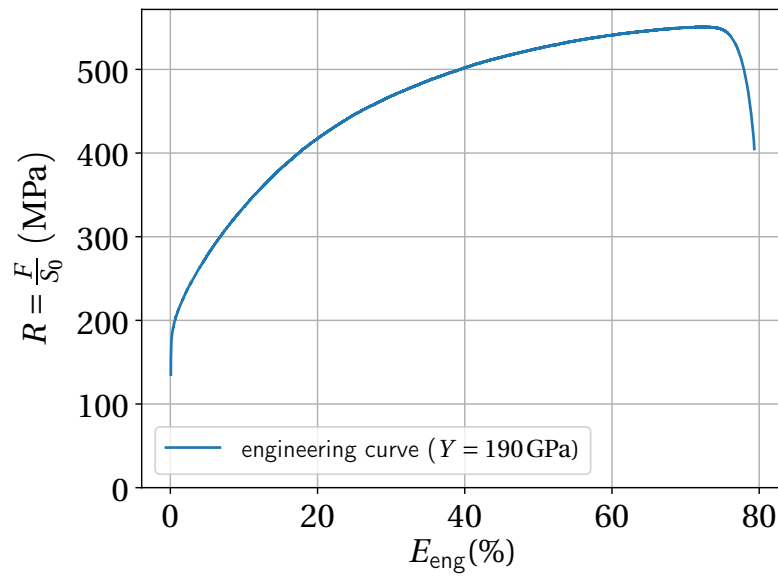
From the raw data, the pre-loading of about 50 MPa can be deciphered, but most importantly a total Young modulus of 19.6 GPa taking into account the complete loading apparatus is indexed when a clear slope can be identified as illustrated further by the red line in figure 6.11. This modulus is not surprisingly far below the expected Young modulus of the material expected between 185–200 GPa.

A translated experimental curve is derived from the original curve in order to match the origin (dashed line in figure 6.11). This curve taking into account the apparent rigidity of the apparatus is subsequently and conveniently used for the subsequent interrupted tensile test on the Int-2 sample in order to prescribe effectively the plastic deformation intended, using the same apparatus. It is indeed reminded here that a direct measurement of the gauge deformation by extensometry is discarded due to the geometry of the samples (see figure 6.2d).

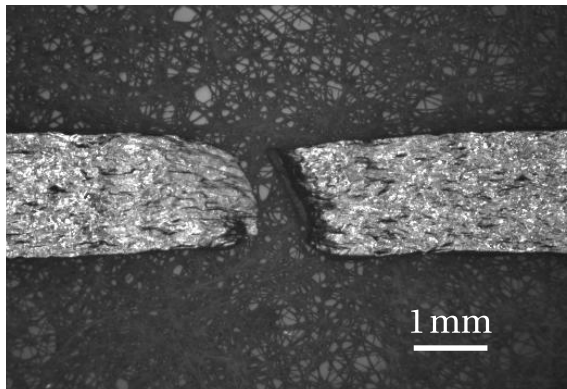
The engineering tensile curve of the material is then obtained by redressing the experimental curve, considering a Young modulus of 190 GPa (see appendix B).

The full engineering curve (R, E_{eng}) is displayed in figure 6.12a. It is reminded that the test is carried out at room temperature and for a strain rate of $2 \times 10^{-5} \text{ s}^{-1}$. From

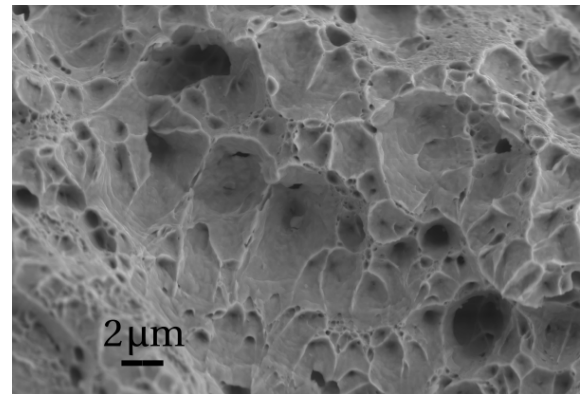
6. DISCONTINUOUS SLIP BANDS MODEL FOR LOW STACKING FAULT ENERGY METALS AND ALLOYS



(a)



(b)



(c)

Figure 6.12: Engineering tensile curve of the material (6.12a). Observation of the ductile fracture profile by the optical microscope (6.12b) and related SEM fractography (6.12c)

6. DISCONTINUOUS SLIP BANDS MODEL FOR LOW STACKING FAULT ENERGY METALS AND ALLOYS

Sample	$\dot{\epsilon}$ (s ⁻¹)	$R_{p0.2}$ (MPa)	R_m (MPa)	A_{gt} (%)	A (%)
Flat	2×10^{-5}	187	551	74.4	79.9
Cyl-1 (CEA K87)	2×10^{-3}	222	591	63.0	75.6
Cyl-2 (CEA K87)	2×10^{-3}	221	589	61.7	75.7

Table 6.3: Material characteristics extracted from the tensile test on the Fra sample and compared to the tensile test performed on Cyl-1 and Cyl-2 for the same material.

this curve, the material characteristics listed in table 6.3 can be extracted and compared to two other tensile tests performed at CEA (J.-L. Flamand DEN/DMN/SRMA/LC2M) [Hazan, 2019] on the same material, at room temperature, for a strain rate of $2.0 \times 10^{-3} \text{ s}^{-1}$ and using cylindrical samples (5 mm in diameter).

The related notations are the following: $R_{p0.2}$ is the yield stress at 0.2 % plastic deformation, R_m the ultimate tensile stress or maximum stress obtained at the total deformation A_{gt} and A the deformation at failure of the sample.

By comparison, it has to be noted that the $R_{p0.2}$ extracted from the Fra sample clearly shows a significant drop of about 16 % with respect to the two other samples. Furthermore, a higher ductility can also be deciphered along with a slight decrease of the ultimate stress. This could be related to the significant strain rate discrepancy.

Not surprisingly, the complete failure of the sample is obtained by ductile fracture after striction as observed by optical or scanning electron microscopy in figures 6.12b and 6.12c (void nucleation and coalescence).

The interrupted tensile tests are now performed on the Int-2 sample.

6.2.3.4 Interrupted tensile test

From the translated experimental curve of figure 6.11, total displacement of the traverse to impose can be deduced in order to obtain 1 % and 2 % plastic deformations of the Int-2 sample. It is to be noted that that these plastic deformations actually comprises all the irreversible deformations that can occurs along the loading line. In that respect, it is rightfully assumed that the plastic deformation of the loading apparatus are negligible, however the stress concentration induced by the shoulders of the sample obviously contributes to a non negligible amount.

The final plastic deformation at rest is therefore roughly measured after each deformation using the platinum deposits and the scratch as depicted in figures 6.8 and 6.9.

The interrupted tensile curves plot with the cumulative plastic deformation E_p , are displayed in figure 6.13.

A 1.0 % plastic deformation is obtained from the tensile curve while a 0.8 % deformation is roughly measured by the optical microscope between the referenced marks indicating that about 0.2 % plastic deformation can be accounted for in the shoulders of the sample. To compensate this discrepancy, the second tensile test is performed using

6. DISCONTINUOUS SLIP BANDS MODEL FOR LOW STACKING FAULT ENERGY METALS AND ALLOYS

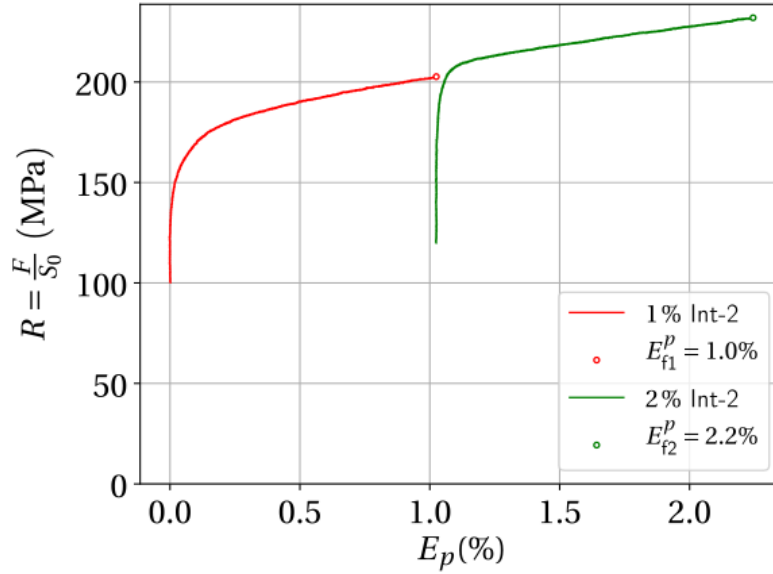


Figure 6.13: Interrupted tensile test curves of the Int-2 sample plot using the cumulative plastic deformation E_p .

a 1.2 % plastic deformation increment. A 2.0 % plastic deformation is finally measured through the markers in the gauge after this final increment.

6.2.3.5 Slip band surface relief measurement

At each deformation, AFM acquisitions are performed on the selected grains listed in table 6.2.

An observation of the sample surface after 0.8 % plastic deformation in the gauge is provided in the upper picture of figure 6.14 with the localisation of the selected grains. Parallel slip band networks can be clearly identified in numerous grains. The lower picture of figure 6.14 illustrate the AFM localisation of four grains using the optical microscope of the AFM. From these observations and from the subsequent acquisitions, the angle of the slip traces ψ_{SB}^{AFM} are measured and listed in table 6.2. The values previously deduced by EBSD are in good agreement, as also illustrated by the \mathbf{n}_\perp and \mathbf{m}_\perp axis in the lower pictures of figure 6.14. The AFM acquisition areas are further illustrated by the black markers on the pictures.

The AFM acquisitions of the same spot localised on the grain 3b, are illustrated in figures 6.15a and 6.15b for 0.8 % and 2 % plastic deformations respectively. The emerging slip bands are identified and numbered, revealing at least 21 slip bands with at least 9 slip bands recovered at the two deformations.

A 250×250 nm (512×512 px) acquisition is also provided at 2 % plastic deformation with a subnanometric resolution (about 0.5 nm per pixel), focusing on one of the emerging slip band. The corresponding 3D representation in figure 6.15b is displayed with a

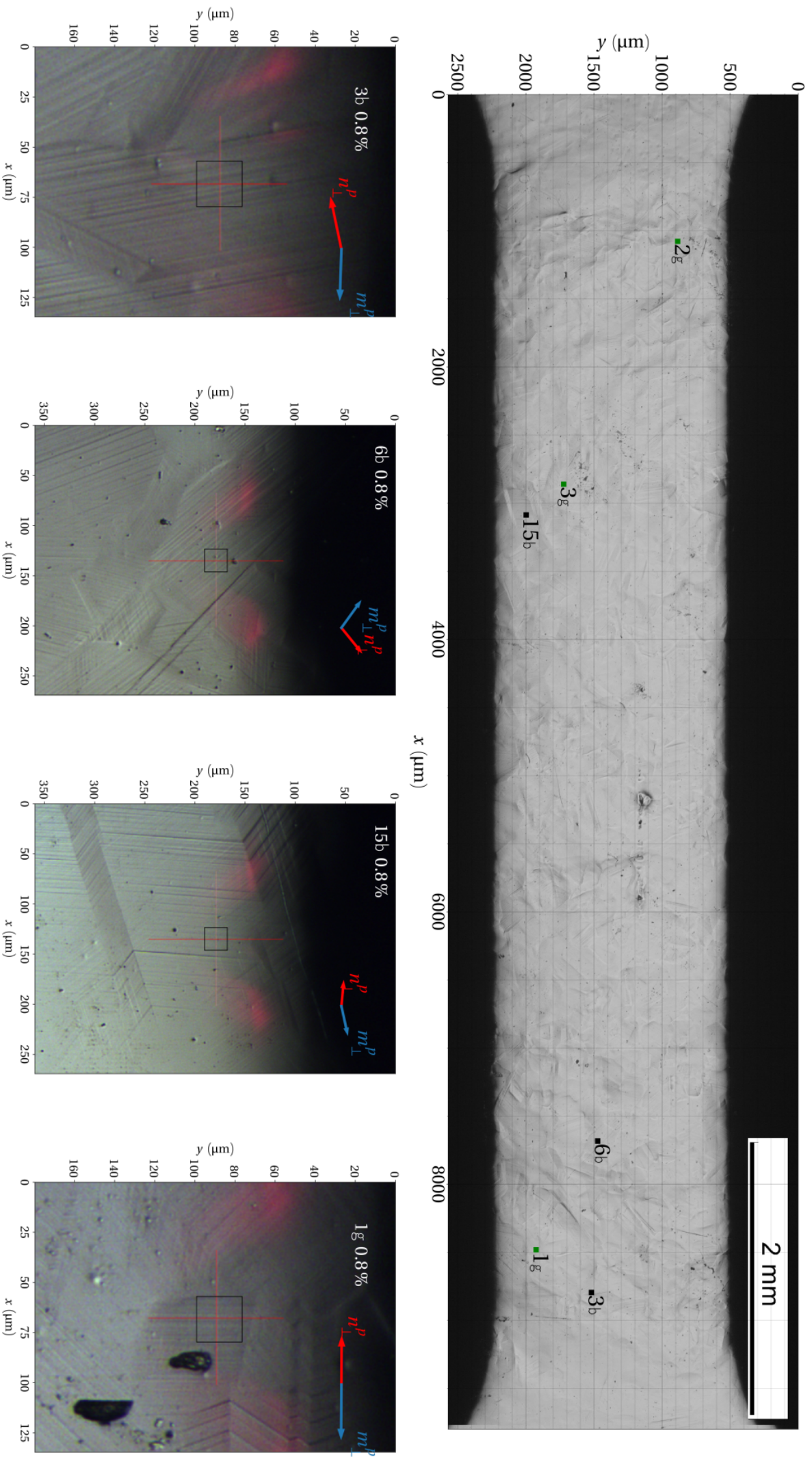


Figure 6.14: Surface of the sample after 0.8 % plastic deformation along with the localisation of the selected grains (upper picture). AFM acquisition screen (black boxes) for four grains after 0.8 % plastic deformation (lower pictures). Orthogonal projections of the n and m vectors of the primary slip system are obtained from EBSD data.

6. DISCONTINUOUS SLIP BANDS MODEL FOR LOW STACKING FAULT ENERGY METALS AND ALLOYS

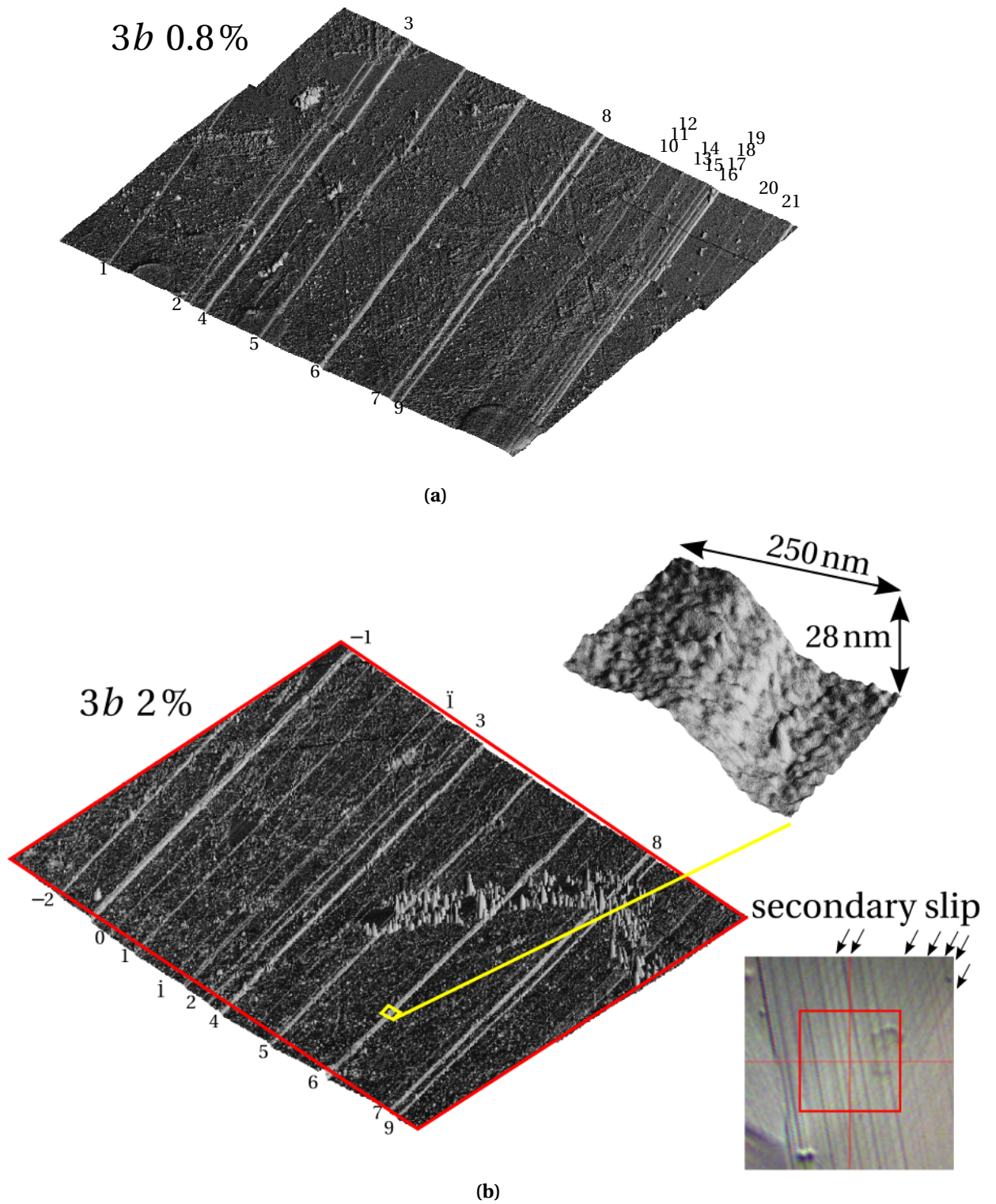


Figure 6.15: AFM acquisitions for the 3b grain at 0.8 % (6.15a) and 2 % plastic deformations (6.15b) with the identification of the same slip bands (1 to 9).

6. DISCONTINUOUS SLIP BANDS MODEL FOR LOW STACKING FAULT ENERGY METALS AND ALLOYS

dilated z-axis as referenced by the dimensions of the step.

These results confirm the non negligible thickness of the slip bands. These reliefs obviously result from a large amount of emerging or departing dislocations at (or from) the surface on several slip planes. Even if the resolution and the surface state may not enable a clear visualisation at this scale, those slip planes seems to be rather homogeneously scattered in the band as a smooth profile can be deciphered on the single band acquisition in figure 6.15b.

Interestingly, it can be remarked that on the $20 \times 20 \mu\text{m}$ acquisitions, clusters of one or several slip bands are organised rather regularly with seemingly constant distances in between. These clusters are regularly observed on the six grains treated here. In particular, clusters of slip bands following the pattern of three slip bands close together (as illustrated by the slip bands group 2-3-4, 7-8-9 or 10-11-12) are quite common.

Between 0.8 % and 2 %, almost no new slip bands are produced on the primary slip system with the exception of the two slip bands denoted $\dot{1}$ and $\ddot{1}$ in figure 6.15b. This observation would suggest that the increment of plastic deformation imposed here, could have been accommodated primarily by an intensification of the deformation in the pre existing slip bands rather than by slip band multiplications.

However, this observation is obtained on a small portion of one grain. Furthermore, it should be noticed on figure 6.15b, that a secondary slip system is triggered even if the corresponding steps are very tenuous and should not be significantly accounted for in the plastic deformation of the grain.

From the AFM data, n-profiles and m-profiles are extracted for the six selected grains at 0.8 % and for the grain 3b at 2 %. The figures 6.16, 6.17 and 6.18 illustrate this approach for the grain 3b at 0.8 %. The same method of extraction is employed automatically for all the grains using the gwyddion software [Nečas and Petr, 2012] and its python interface.

At first, several orthogonal n-profiles (denoted A, D, G and M, along the \mathbf{n}_{\perp} direction) are carried out by averaging the profile over a thickness of about $1.3 \mu\text{m}$ as illustrated on figure 6.16 by the shaded areas. As the thickness of the band may vary along the trace, the profiles are extracted by covering a distance along the the slip traces of at least $10 \mu\text{m}$ to obtain a more representative data set. As already presented before, the slip band can then be spotted rather easily on these profiles. The A, D and G profiles are displayed in figure 6.17 along with the identification of the slip band surfaces. The thickness of the slip bands t and the corresponding interband spacing d can then be readily obtained from equation 6.9 coupling the EBSD data. Final average values of t and d are obtained for each slip bands using the four profiles.

The m-profiles are performed along the \mathbf{m}_{\perp} direction for each clusters of slip bands as illustrated by the white boxes on figure 6.16. For each box, several profiles are extracted in parallel to the slip trace on $1 \mu\text{m}$ and an average of these profiles is subsequently performed as illustrated for two clusters of slip bands in figures 6.18. Several averaging boxes are used for each cluster, thus allowing as before a more representative data set to be averaged subsequently for each band.

6. DISCONTINUOUS SLIP BANDS MODEL FOR LOW STACKING FAULT ENERGY METALS AND ALLOYS

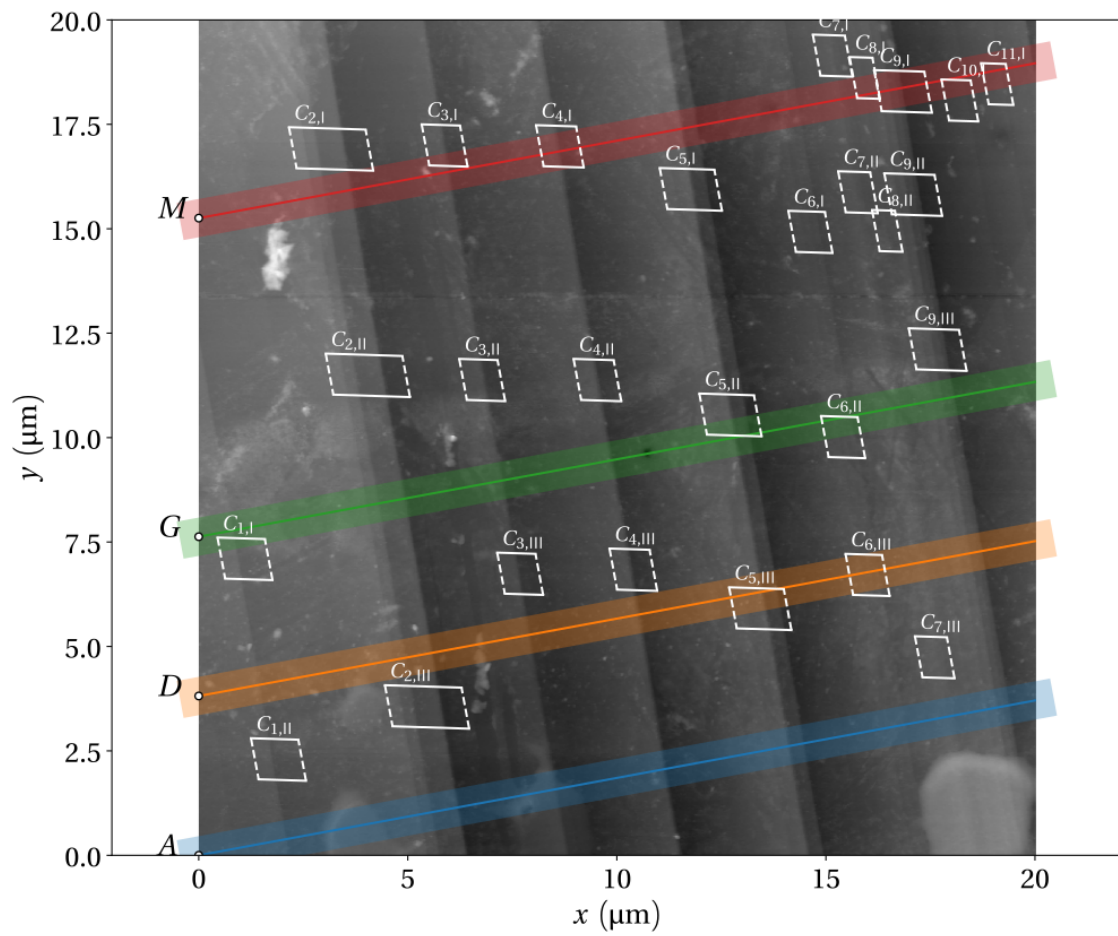


Figure 6.16: AFM acquisition of the grain 3b at 0.8 % plastic deformation showing the n-profiles denoted A, D, G and M and the m-profile boxes assigned to each clusters of slip bands.

6. DISCONTINUOUS SLIP BANDS MODEL FOR LOW STACKING FAULT ENERGY METALS AND ALLOYS

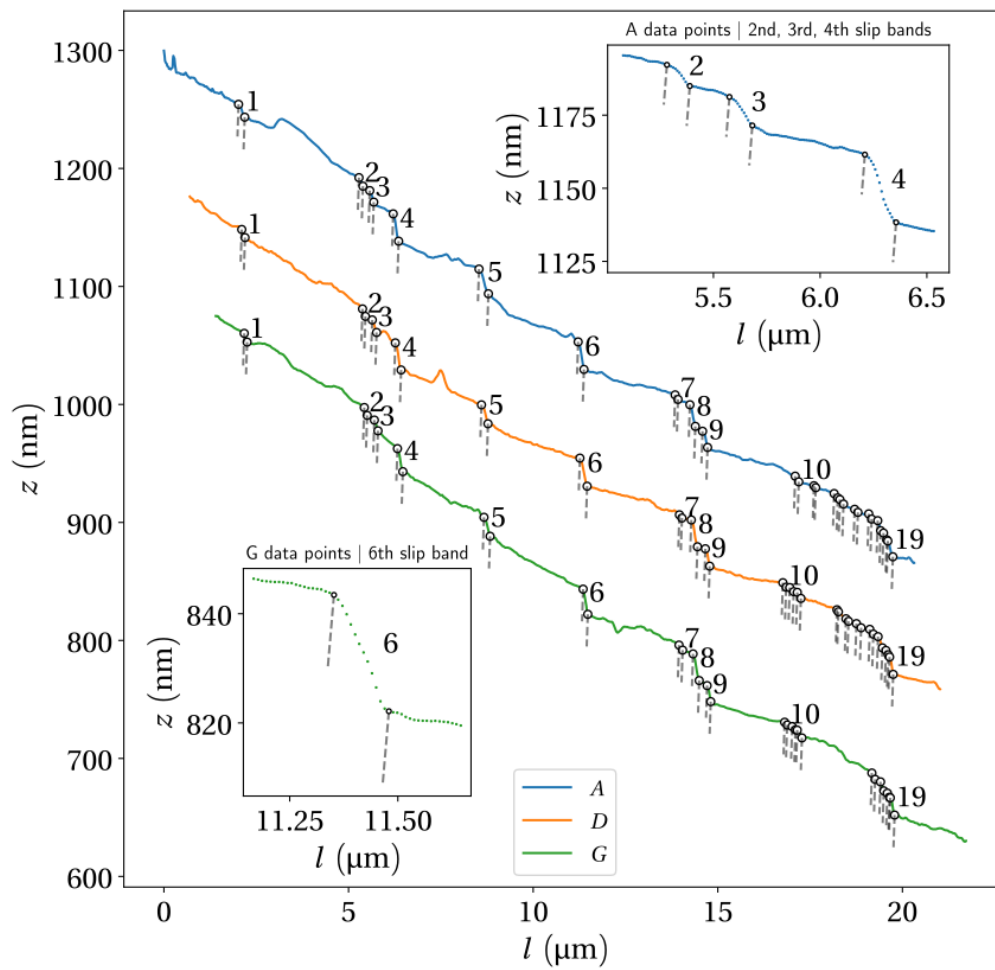


Figure 6.17: n-profiles extracted and averaged over a thickness of 1.3 μm . Details of the slip bands localisation are provided for the 2nd, 3rd and 4th slip bands of the A profile and for the 6th slip band of the G profile.

6. DISCONTINUOUS SLIP BANDS MODEL FOR LOW STACKING FAULT ENERGY METALS AND ALLOYS

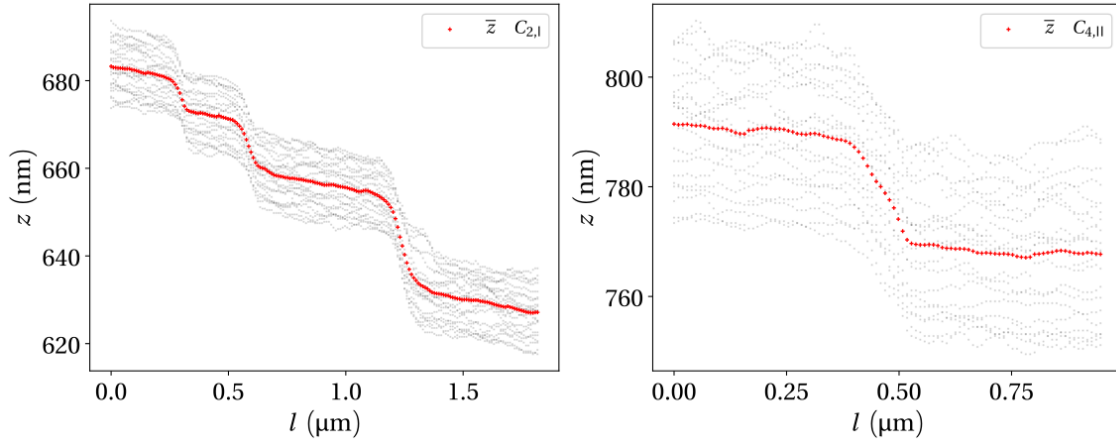


Figure 6.18: m-profiles obtained on the $C_{2,I}$ and $C_{4,II}$ clusters of slip bands 1-2-3 and 6 respectively. Grey points represent the profiles obtained on each boxes over the $1\ \mu\text{m}$ thickness, and the red points represent the averaged profiles over the boxes.

From these profiles, the magnitude of the step displacement vector u_{SB} , and subsequently the plastic strain deformation γ_{SB}^p , can be deduced from equations 6.12 and 6.4 respectively. Here, it is quite clear that the initial slope of the surface is not completely negligible, hence the use of equation 6.12.

Figures 6.19a and 6.19b presents the results obtained for the slip bands thickness t (blue bars), interband spacings d (orange bars) and plastic slip γ^p (green bars) on the grain 3b at 0.8 % and 2 % (diamond, circle and square markers respectively) plastic deformation. The same notations of the slip bands referenced in figure 6.15 are used. Slip band thickness values between about 40–140 nm and interband spacings between 0.05–1.75 μm are recorded.

For the grain 3b (and subsequently for all the other grains), the averaged values of these parameters (t and d) are referenced in table 6.4 at 0.8 % and 2 %. These results seem to bring further arguments in favour of an intensification of the plastic slip strain in the bands during the deformation increment since mean values of 11 % and 17 % are reported at 0.8 % and 2 % macroscopic plastic deformation respectively. Furthermore the thickness of the slip bands seems to be conserved while the mean interband spacing is only slightly reduced, probably due to the appearance of the slip bands denoted $\dot{1}$ and $\ddot{1}$ revealing only few slip band multiplications.

However, it is clear that only the 21st and 14th slip bands considered for the two deformations are not sufficient, statistically speaking, to be able to clearly support the above point for the entire grain and more extensively for any grain. In addition, the population of slip bands considered for both cases are still significantly different despite the tracking of 9 common slip bands.

Finally, it can be noticed on figure 6.19a that between 0.8 % and 2 %, the thickness of the slip bands seem to be lowered by a significant gap for several bands, which should

6. DISCONTINUOUS SLIP BANDS MODEL FOR LOW STACKING FAULT ENERGY METALS AND ALLOYS

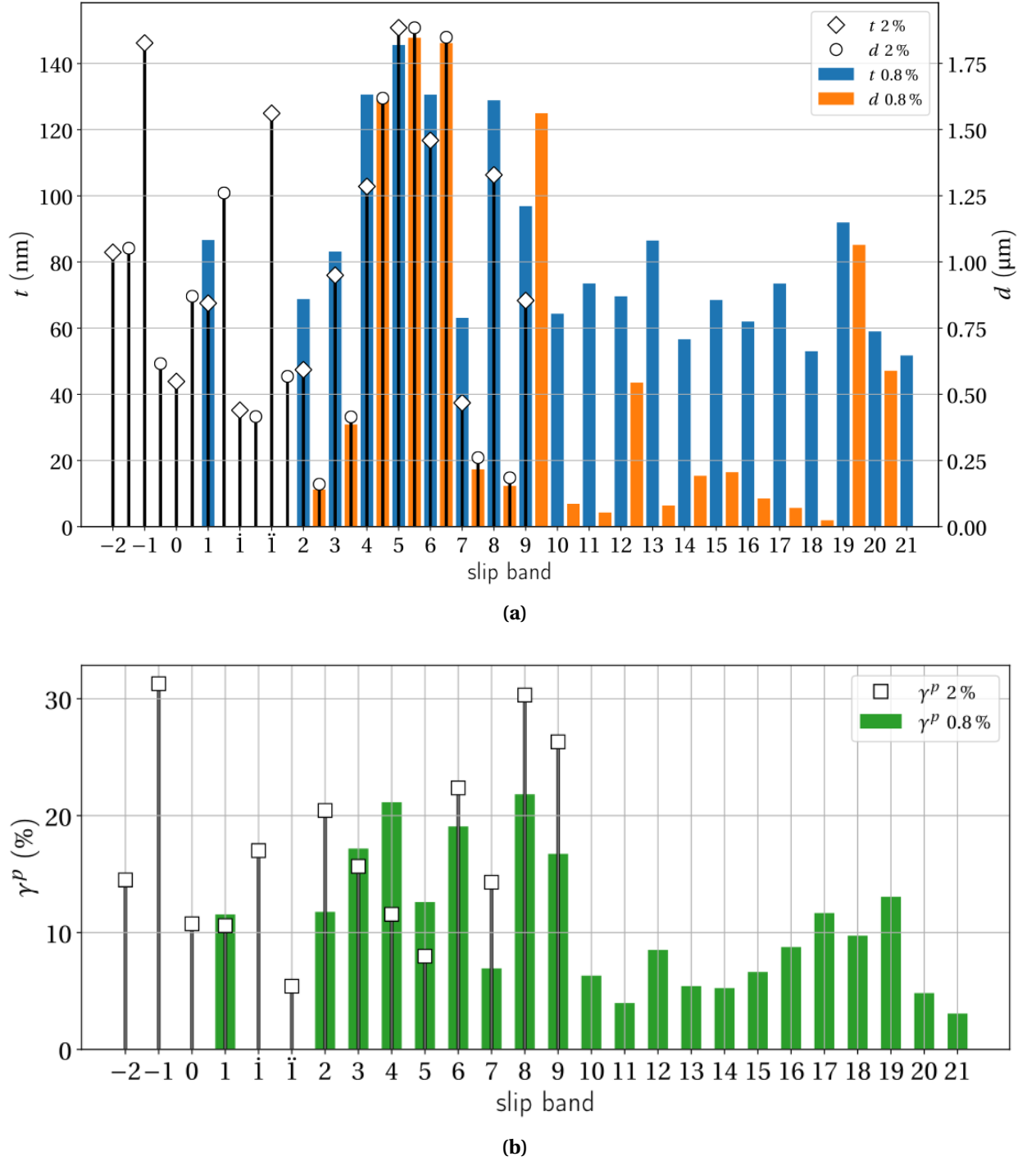


Figure 6.19: Slip band thickness t and interband spacing d for the grain 3b at 0.8 % and 2 % plastic deformations (6.19a) and the corresponding slip band plastic slip strain γ^p (6.19b).

6. DISCONTINUOUS SLIP BANDS MODEL FOR LOW STACKING FAULT ENERGY METALS AND ALLOYS

Ref.	Irr. (dpa)	SFE (mJm ⁻²)	n_G ϕ_G (μm)	n_{SB}	E^p (%)	\dot{E} (s ⁻¹)	\bar{t} (nm)	\bar{d} (μm)	\bar{h} (nm)	$\overline{\gamma_{SB}^p}$ (%)
† (RT)	0	30.4	1 305 (3b)	21	0.8	2.0×10^{-5}	83	0.86	9	11
			1 305 (3b)	14	2		86	0.66	15	17
			1 292 (6b)	23	0.8		73	0.83	4	18
			1 257 (15b)	15	0.8		52	0.67	3	10
			1 68 (1g)	14	0.8		50	0.70	6	14
			1 81 (2g)	24	0.8		60	0.34	5	15
			1 149 (3g)	9	0.8		50	0.54	3	6
			6 192	106	0.8		64	0.63	5	13
A (RT)	0	31.1	17 140	975	2	1.0×10^{-3}	-	0.85	10	-
			16 140	1115	10			0.66	16	
			10 140	459	2	1.0×10^{-6}		1	12	
			11 300	330	2	1.0×10^{-3}		1.57	19	
			22 300	977	10			0.88	23	
B (RT)	0	31.1	13 ‡ 140	660 ‡	3	1.0×10^{-3}	-	0.88 ‡	19 ‡	-
					10			0.60 ‡	16 ‡	
			13 ‡ 300		3			1.37 ‡	65 ‡	
					10			0.78 ‡	88 ‡	
C (288 °C)	1	27.5	10 -	50-100	3	3.5×10^{-7}	-	4.42	130	-
	5.5							3.74	285	
	1	40.5						3.63	60	
	5.5							3	223	
	1	59.7						3.55	50	
	5.5							3	117	

Table 6.4: AFM statistical results and comparison with several AFM studies of literature. Notations: †: this study, SFE (stacking fault energy), n_G : number of grains, n_{SB} : number of slip bands, \bar{X} : mean value of the X variable, ‡: estimated from literature data. References: A [Menard, 2005], B [Aubert et al., 2010], C [Jiao et al., 2005]

6. DISCONTINUOUS SLIP BANDS MODEL FOR LOW STACKING FAULT ENERGY METALS AND ALLOYS

not be expected. This discrepancy can be easily explained by the significant uncertainty over the thickness assessment using the previous method. Indeed, it is reminded that the n-profiles and m-profiles have a resolution of roughly 10 nm. Therefore, identifying slip bands with either N points or N+2 points, which seems to constitute a quite reasonable source of uncertainty considering the profiles of figures 6.17, yields a discrepancy of about 20 nm. This is typically the magnitude of the discrepancies observed in figure 6.19a.

This obviously induces a very sensitive assessment with respect to the measured value which could be comparatively detrimental here, should one wants to evidence slip band thickness variations between small macroscopic deformation increments.

Not to mention the fact that the averaged profiles cumulated over 4 μm along the slip traces and for different spots between the two macroscopic deformations, may not be sufficient enough for this comparison. It is indeed clear that the variations between the measured thicknesses along the same slip traces differ significantly with respect to the small values of the slip bands thickness evidenced here.

This will impact even more the assessment of the corresponding plastic slip strain presented in figure 6.19b since similar methods are used for the thickness and displacement steps assessments. In particular, it can be noticed that the assessments obtained on slip bands 4 and 5 display roughly 30–50 % lower values of plastic strain slip between 0.8 % and 2 % which could be partly related to the above explanation.

Thus, no clear conclusion can be drawn from these measures of the same slip bands on only one grain and it is obvious that a more thorough investigation would be needed to obtain a more statistically representative population of slip bands involving more macroscopic plastic deformation increments and more grain acquisitions.

Should a more statistical approach be followed, this method appears to be sufficient to evaluate relevant orders of magnitude for characterising the slip bands network during deformation and therefore to provide possible points of comparison with irradiated materials.

Despite a significant uncertainty of the measures, such approach is undertaken using the same method for the assessment of 106 slip bands scattered over the six selected grains.

The mean values of t , d and γ^p are reported for the five other grains at 0.8 % plastic deformations, along with the mean apparent step height \bar{h} . The latter measures are readily obtained from the n-profiles as depicted in figure 6.6.

Probability density (normed) functions of the variables t , d , \bar{h} and γ^p are displayed in figures 6.20a, 6.20b, 6.20c and 6.20d respectively from the assessment over the six grains at 0.8 %.

From table 6.4, it is clear that the mean thickness values of the slip bands does not strongly differ from one grain to an other with a final mean value over the six grains of 64 nm. However the repartition displayed in figure 6.20a, evidences a non negligible amount of slip bands featuring thicknesses between 25–90 nm with, in addition, a non negligible distribution tail between 100–150 nm.

6. DISCONTINUOUS SLIP BANDS MODEL FOR LOW STACKING FAULT ENERGY METALS AND ALLOYS

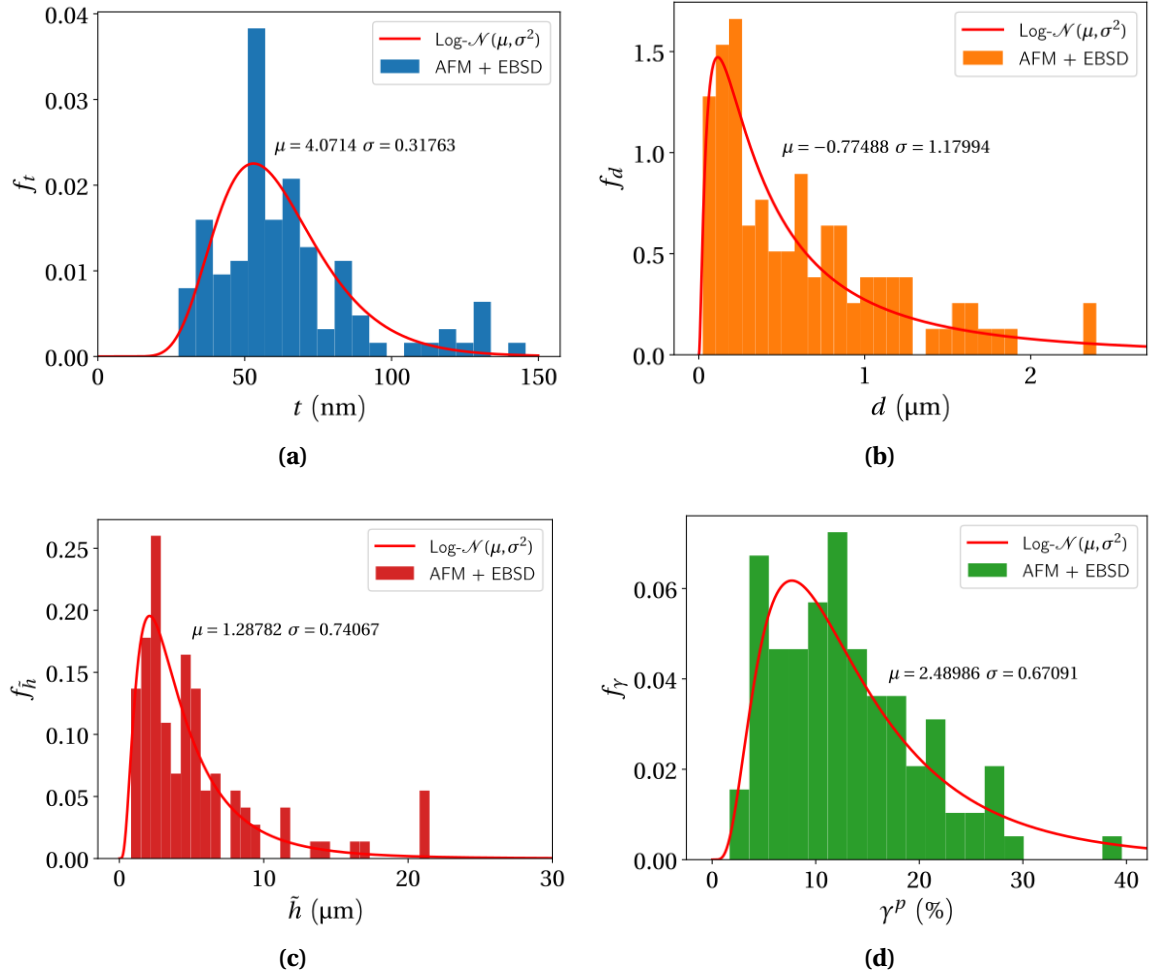


Figure 6.20: Probability density function of the parameters t , d , \tilde{h} and γ^p assessed over the six grains with a population of 106 slip bands at 0.8 % deformation.

6. DISCONTINUOUS SLIP BANDS MODEL FOR LOW STACKING FAULT ENERGY METALS AND ALLOYS

Similarly, the plastic slip strain repartition clearly evidences large amount of slip bands featuring between 5–22 % deformation whereas a mean value of only 13 % is obtained. Following the model of Sauzay et al. in equation 6.3, one can easily imagine that the slip bands which are the most prone to trigger intergranular fracture should feature the highest plastic slip strain values. From figures 6.19a and 6.15, it is clear that the thickest slip bands display the highest plastic slip strains (with the example of the slip bands denoted 4,5,6, 8 and 9). From a model perspective, a focus should therefore be preferentially made over these particular slip bands which seems to be at the centre of the clusters previously observed. However, it is also clear that the lower thicknesses slip bands (60–80 nm) feature non negligible deformation with the example of the slip bands 1, 2 and 3 featuring about 13 % plastic slip strain. Therefore, this later population should not be discarded, which is even more true considering that it appears the most frequently (figure 6.20a).

The distribution of the interband spacing and the step height are less spread with high pick frequencies around rather low values of about 0.25 μm and 3 nm respectively. These picks are related to the lowest thickness slip bands population. Meanwhile a non negligible amount of slip bands can be evidenced with higher values of interband spacing between 0.25–1.5 μm .

It was pointed out by Menard [Menard, 2005] and Aubert et al. [Aubert et al., 2010] that the interband spacing and the step height in a typical 316L unirradiated austenitic stainless steel follows a lognormal distribution: $d \sim \text{Log-}\mathcal{N}(\mu, \sigma^2)$. It is reminded that the related probability density function (PDF) f_d follow the formulation of a normal distribution with a change of variable:

$$f_d(x) = \frac{1}{x\sigma\sqrt{2\pi}} \exp\left(-\frac{(\ln(x) - \mu)^2}{2\sigma^2}\right) \quad (6.17)$$

with the variable $y = \ln(x)$ following a normal distribution $\mathcal{N}(\mu, \sigma)$. The related expectancy $\mathbb{E}(d)$ is given by:

$$\mathbb{E}(d) = \exp\left(\mu + \frac{\sigma^2}{2}\right) \quad (6.18)$$

A lognormal distribution fit through the mean value μ and the standard deviation σ is performed using the least square method on the four experimental distributions. The fitted parameters and the corresponding functions are displayed in figure 6.20. A fairly good agreement is recovered for the interband spacing in figure 6.20b and the step height in figure 6.20c as indicated by Menard et al. The distributions of the slip bands thickness and plastic slip strain do not display such a satisfying agreement.

6.3 Discussion

Following these results, it is proposed to carry out a comparison with several AFM and SEM studies of literature concerning slip bands characterisation in typical 316L

6. DISCONTINUOUS SLIP BANDS MODEL FOR LOW STACKING FAULT ENERGY METALS AND ALLOYS

unirradiated stainless steels [Menard, 2005], [Aubert et al., 2010] (denoted studies A and B respectively) and clear bands characterisation in three proton irradiated stainless steels [Jiao et al., 2005] (denoted study C). The related results are gathered in table 6.4, along with the different testing conditions (temperature, strain rate, macroscopic plastic deformation, number of grains and number of slip bands).

6.3.1 Thickness and plastic slip strain of slip bands and clear bands

6.3.1.1 Slip bands and clear bands thickness

For each of these studies (A, B and C), slip band thickness and plastic slip strain assessments are not provided due to insufficient resolution or biased measurements [Was and Jiao,].

Despite a significant uncertainty of measure, the present study (denoted †) brings a first assessment of slip bands thickness in a 316L austenitic stainless at low macroscopic plastic deformations. The mean value of 64 nm in this unirradiated material seems to suggests a similar thickness to the clear band TEM assessment of about 50 nm previously reviewed. However, it is clear that the most predominant slip bands in terms of plastic slip strains, rather feature thicknesses above 100 nm. In that regard, a more statistical characterisation of clear band thickness would be needed to draw a relevant comparison at the same plastic deformation.

Nonetheless, it is quite clear that these results support the finite thickness approach proposed by Sauzay et al. for both unirradiated and irradiated stainless steels. This related model and the present AFM observations appear to enter in contradiction with the usual single pile-up model (see figure 6.21) which is often conveniently employed [Aubert et al., 2016, Britton and Wilkinson, 2012]. However, the pile-up model which may be less representative and therefore coherent at the lower scales (atomic scale) considered in the multiscale approach.

Two other models considering slip bands with finite thickness would differ from their repartition of the gliding planes in which dislocations emerge at the surface as depicted by the two right schemes (2 and 3) of figure 6.21.

A first discrete model (scheme 2) would propose an heterogeneous repartition of the gliding planes separated by a non negligible distance $d_{\text{pile-up}}$. It would therefore results a rather discrete plastic slip strain field as depicted by the scheme 2 of figure 6.21.

The present AFM observation (see figure 6.15b) would rather support the second model (scheme 3) featuring a more homogeneously deformed slip band (i.e. from the preceding model: $d_{\text{pile-up}} \rightarrow d_{\{111\}}$, with $d_{\{111\}}$ the distance between two FCC slip planes). TEM observations of deformed irradiated stainless steels also seem to support this model. Indeed, it can often be remarked that clear bands are mostly free of irradiation defects (see figure 6.1), which could probably be induced by a flow of dislocations homogeneously recombining most of the defects.

However, the underlying mechanisms for single slip bands and single clear bands formation is still not completely understood.

6. DISCONTINUOUS SLIP BANDS MODEL FOR LOW STACKING FAULT ENERGY METALS AND ALLOYS

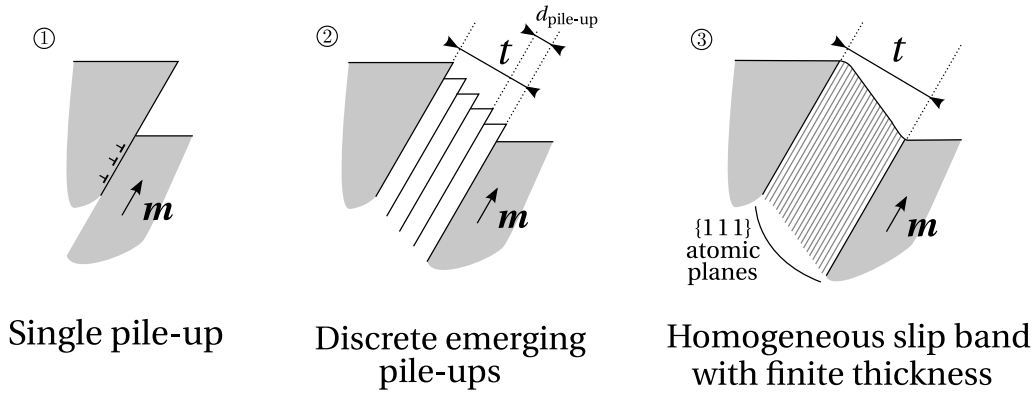


Figure 6.21: Different models for the plastic slip bands or clear channels for irradiated materials.

Basically, the slip band thickness results from the double cross slip frequency of glissile screw perfect dislocations leaving their original slip plane for an other parallel slip plane. The double cross slip elementary mechanism is depicted by figure 6.22, as extracted from [Hull and Bacon, 2011].

From that picture, two aspects can be considered during the onset of plasticity through the slip bands (or clear bands) development.

Firstly, cross slip is limited by the appearance of Shockley partial dislocations splitting along perfect screw dislocations thus impeding their advance in the new plane. Indeed, it is reminded that in FCC metals and alloys, the Burgers vector related to any partial dislocation is contained in only one slip plane, thus rendering impossible any cross slip mechanism for the partial dislocation line. The frequency of Shockley partials splitting sporadically along screw dislocations lines, is directly related to the stability of the stacking fault defect formed between the two partials separated by a mean distance d_{SF} . The value of the stacking fault energy γ_{SF} is inversely proportional to d_{SF} as a result of an equilibrium between the force tending to reduce the stacking fault surface and the repulsive elastic interactions between the two partials lines [Hull and Bacon, 2011]:

$$d_{SF} = \frac{Gb^2}{4\pi\gamma_{SF}} \quad (6.19)$$

b and G being the amplitude of the Burgers vector and the elastic shear modulus respectively. Hence, the lower the stacking fault energy, the larger the distance between two partial dislocations d_{SF} and the less frequent cross slip phenomena occur. Following this reasoning, it could be imagined that the slip band thickness could vary accordingly to the SFE ; with lower thicknesses for the most planar materials. Unfortunately, this particular point cannot be verified with the present data for unirradiated and irradiated stainless steels.

Secondly, it is easy to imagine that the extant of the double cross slips may be limited by defects such as irradiation-induced dislocation loops. Hence, clear bands are

6. DISCONTINUOUS SLIP BANDS MODEL FOR LOW STACKING FAULT ENERGY METALS AND ALLOYS

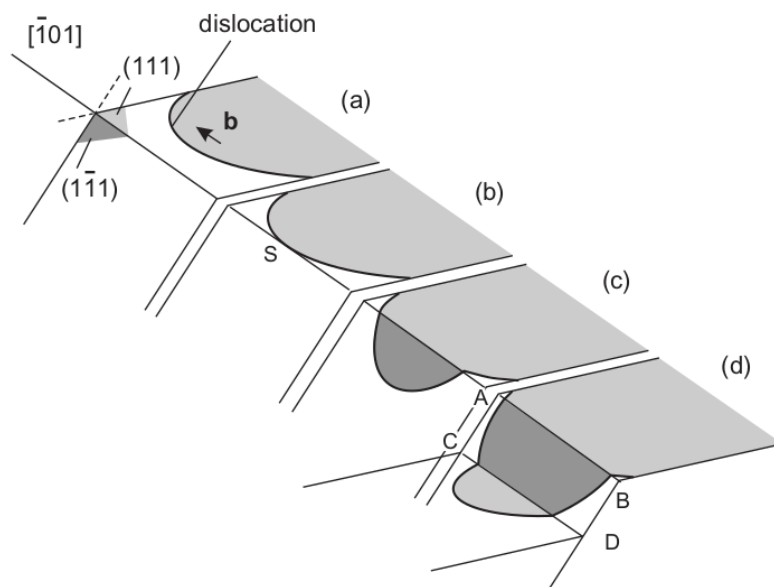


Figure 6.22: Cross slip mechanism (b) and (c) and subsequent double cross slip (d), of a screw perfect dislocation of Burgers vector $[101]$ gliding in the slip planes (111) (a) and $(1\bar{1}1)$ (c) and (d), as reproduced from [Hull and Bacon, 2011].

expected to be thinner in irradiated materials as compared to slip bands in unirradiated materials with a lower density of defects.

In conclusion, nothing can be clearly confirmed for choosing either one or the other model of slip band (or clear band) of finite thickness, presented in figure 6.21. Even though, as already pointed out, the homogeneous model would appear the most likely. Yet, it is indeed not obvious why specific atomic slip planes should be preferred by the dislocation gliding within both slip bands or clear bands, as proposed by the scheme 2.

Concerning this point, a final confirmation would necessitate to perform AFM acquisitions at higher resolution for several bands and for both irradiated and unirradiated materials.

6.3.1.2 Dislocation channelling

A major consequence of the irradiation of materials is the intensification of localised plasticity in the form of clear bands. As extensively described by [Was, 2007b], irradiation defects in metals and alloys are preliminary recombined during the onset of plasticity by initial groups of dislocations clearing these defects in the slip plane and leaving preferential paths for subsequent glissile dislocations. This process called dislocation channelling thus induces an increase of dislocations flow in a more narrow path as irradiation increases the defect density. It results in step heights significantly higher in irradiated materials with respect to its unirradiated counterpart for comparable plastic deformations as clearly evidenced by the \bar{h} column of data in table 6.4. For the same

6. DISCONTINUOUS SLIP BANDS MODEL FOR LOW STACKING FAULT ENERGY METALS AND ALLOYS

materials, the study C also shows that this effect is exacerbated with the irradiation dose.

The step height values ranging between 50–285 nm as proportionally compared to the typical clear bands thickness values of 50 nm roughly yields an assessment of plastic slip strains of at least 100 % in the clear bands as already pointed out by [Was, 2007b]. This assessment presents a striking contrast with the slip strain assessment of at most 17 % carried out in this chapter for an unirradiated stainless steels presenting a similar stacking fault energy at a slightly lower macroscopic plastic deformation. In comparison, study A seems to confirm these results in an unirradiated material with a comparable stacking fault energy and mean grain sizes ; considering similarly a low macroscopic deformation at strain rates between 1.0×10^{-6} – $1.0 \times 10^{-3} \text{ s}^{-1}$.

Therefore, from this simplified comparison, a ratio of around 10 seems to be reached between the plastic slip strain in clear bands and slip bands for similar materials and macroscopic deformations. From a prediction perspective, following the approach of Sauzay et al., it is clear that the plastic slip strain characterises the severity of the induced stress concentration. Consequently, this kind of ratio between plastic slip strain in clear bands and slip bands represents a clear and relevant indicator of the irradiation effect on intergranular fracture initiation.

However, in these assessments, it should be précised first that, more rigorously, the plastic slip strain in the bands determined from the actual total displacement step (u_{SB}) should rather be preferred for comparison purposes. Indeed the information of the step height may be insufficient to plainly characterise the shearing taking place for any slip bands or clear bands. For example, considering a population of slip bands near the type A configuration which are far from been uncommon, the shearing displacement actually occurs predominantly in the surface plane of the sample. The characterisation of the non negligible plastic slip strain by a simple step height measurement would therefore be unreliable since insignificant step heights would be detected.

It is admitted here that, statistically speaking, broad influences with respect to a phenomenon like dislocation channelling can be deciphered, with such step height measurements, considering the mean value of a significantly large population of bands. Nonetheless, their repartition would not render truthfully the characterisation of localised plasticity. It is clear that the mean plastic slip strain is a more reliable parameter for comparison purposes.

Secondly, a comparison between figures 6.20c and 6.20d seems to suggest that the population repartition of step heights and plastic slip strains strongly differ in nature (shape). As the plastic slip strain is partly derived from the slip band thickness, this emphasises the interest to understand the repartition of slip bands and clear band thickness and their relation with the corresponding plastic slip strains more thoroughly.

In that regard, it has already be pointed out here that the thicker slip bands seem to feature the highest plastic slip strains. This may seem paradoxical when a comparison is made with the elementary mechanism for dislocation channelling in clear bands. In that later case, an increase of irradiation evidently induces higher plastic slip strains for,

6. DISCONTINUOUS SLIP BANDS MODEL FOR LOW STACKING FAULT ENERGY METALS AND ALLOYS

in all likelihood, thinner channels.

But it is also clear from the preceding results, that the interband spacing and more precisely the repartition of slip bands (or clear bands) in the grains is intrinsically related to variations of the plastic slip strain observed. The interband spacing represents a key parameter to describe the localisation of plasticity and incidently the propensity to intergranular fracture initiation.

6.3.2 Interband spacing and plastic slip strain

6.3.2.1 Influence of the irradiation

Once again, the comparison of interband spacings between irradiated and unirradiated material with similar stacking fault energies (table 6.4) is striking. Significantly larger values are reported with mean distances between 3–4.42 μm for irradiated materials with doses between 1 and 5.5 dpa. In comparison, interband spacing values predominantly lower than 1 μm with some exceptions at around 1.5 μm are reported in studies †, A and B for macroscopic plastic deformation between 0.8–10 % with strain rates between 1.0×10^{-6} – $1.0 \times 10^{-3} \text{ s}^{-1}$.

Therefore, in irradiated stainless steels, clear bands spacings at least 3 times larger than slip bands spacing can roughly be retained here: using the mean interband spacing value of 0.64 μm from the present study for the six grains, a ratio of about 5–7 could be reported.

As schematically pictured in figure 6.23, one can consider the same grain solicited with the same plastic deformation E_G^p from an unirradiated polycrystal and its irradiated counterpart. It follows that, statistically speaking, the above interband spacing ratio would result in a 3:1 ratio (at least) for the number of slip bands with respect to the number of clear bands, considering the same grain size ϕ_G .

In both cases, assuming that the plastic deformation of the grain E_G^p results from the plastic slip strain through:

$$E_G^p = \mathbf{e}_f^T \cdot \left[f_{\text{SB}} \gamma_{\text{SB}}^p \frac{1}{2} (\mathbf{m}\mathbf{n}^T + \mathbf{n}\mathbf{m}^T) \right] \cdot \mathbf{e}_f \quad (6.20)$$

where γ_{SB}^p and f_{SB} are the plastic slip strain and the volume fraction of slip bands (or with γ_{CB}^p and f_{CB} for the clear bands). And since the volume fraction f_{SB} and the number of slip bands N_{SB} can be simplified by:

$$f_{\text{SB}} = \frac{N_{\text{SB}} t}{\phi_G} \quad N_{\text{SB}} \approx \frac{\phi_G}{t + d} \approx \frac{\phi_G}{d} \quad (6.21)$$

with ϕ_G the same grain size for both cases. For the same plastic deformation of the grain E_G^p and for about the same thickness for the slip bands and the clear bands, the ratio between the plastic slip strain, in both cases, follows from equation 6.20 and 6.21:

6. DISCONTINUOUS SLIP BANDS MODEL FOR LOW STACKING FAULT ENERGY METALS AND ALLOYS

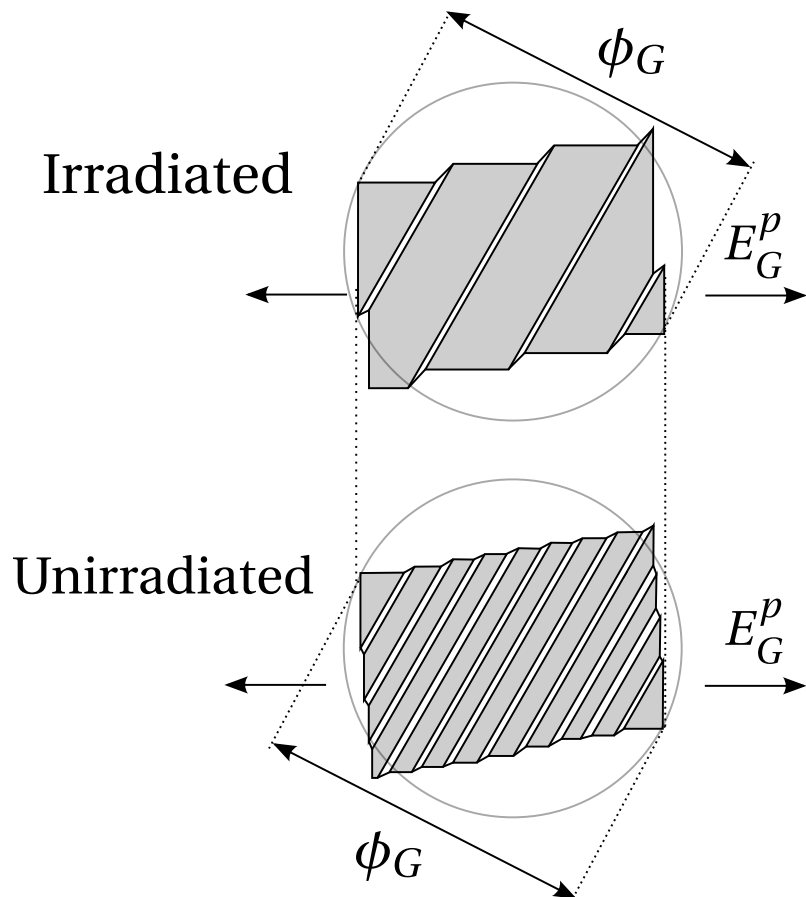


Figure 6.23: Theoretical grain of size ϕ_G plastically deformed at E^p after or without irradiation.

6. DISCONTINUOUS SLIP BANDS MODEL FOR LOW STACKING FAULT ENERGY METALS AND ALLOYS

$$R_\gamma = \frac{\gamma_{CB}^p}{\gamma_{SB}^p} = \frac{f_{SB}}{f_{CB}} = \frac{N_{SB}}{N_{CB}} \quad (6.22)$$

with N_{CB} the number of clear band in the irradiated grain. Therefore, from a statistical point of view, this very simplified reasoning and the above observations concerning the interband spacing would indicate that the plastic slip strain in the clear band is at least 3 times higher than for the slip bands.

Therefore, at a given grain size, the number of bands per grain and incidently the interband spacing are equivalent and key factors to explain the localisation of plasticity. Once again, it is not difficult to imagine that the density of irradiation defects is responsible for this effect. However, quantitatively speaking, it is not clear how this ratio R_γ could be predictable based on relevant initial parameters and with respect to the loading and the irradiation dose. The underlying mechanism behind the slip bands and clear bands formation are not completely understood yet despite some recent advances [Gururaj et al., 2015, Gussev et al., 2015].

In addition to the irradiation channelling, other effects might intervene.

6.3.2.2 Influence of the stacking fault

In particular, the results of study C referenced in table 6.4 show that for three stainless steels featuring increasing stacking fault energies, a clear increase of the clear bands step heights for the same imposed deformations and irradiation doses is recorded. Even if the step height might not be an indicator as relevant as the plastic slip strain, it is clear that the plastic localisation in the clear band intensifies with the decrease of the stacking fault energy. This intensification of the plastic localisation is accompanied by a clear increase of the interband spacing. This SFE effect could be similarly explained in comparison to the irradiation effect.

For unirradiated stainless steels, an intensification of the plastic slip strain seems to hold rather than a multiplication of the slip bands, as previously observed for the plastic deformation of 0.8 % and 2 % in this study. In comparison, studies A and B clearly show a decrease of the apparent interband spacing with a significant increase of the macroscopic plastic deformation which would indicate, in the contrary, a multiplication of the slip bands.

To confirm this trend, the present study would therefore necessitate more data with other interrupted test at higher macroscopic plastic deformations. However, at this point, it should be reminded that the actual interband spacing should be preferred contrary to the apparent measures of studies A and B. In particular, the missing data of orientation of the grains might be crucial to obtain reliable points of comparison.

6.3.2.3 Influence of the grain size

Finally, the grain size also constitutes a parameter of interest.

6. DISCONTINUOUS SLIP BANDS MODEL FOR LOW STACKING FAULT ENERGY METALS AND ALLOYS

For a plastic deformation $E^p = 2\%$ or 3% and at a strain rate of $1.0 \times 10^{-3} \text{ s}^{-1}$, studies A and B evidence interband spacings two times larger for a mean grain size twice larger (between $140 \mu\text{m}$ and $300 \mu\text{m}$).

This increase of interband spacing is accompanied by an increase of the mean step height by roughly the same ratio. This may indirectly indicate an increase of the plastic slip strain with the same ratio should the thickness of the band be considered constant between the two grain sizes. This last point is supported by the present results as indicated by the constant values of \bar{t} for the present study \dagger gathering grain sizes between $68\text{--}305 \mu\text{m}$.

Once again, the increase of the plastic slip strain with the grain size is readily understandable considering once again equations 6.20 and 6.21:

$$R_\gamma = \frac{\gamma_{SB}^p(\phi_{G2})}{\gamma_{SB}^p(\phi_{G1})} \approx \frac{\phi_{G1}}{d_1} \frac{t}{\phi_{G1}} \frac{d_2}{\phi_{G2}} \frac{\phi_{G2}}{t} \approx \frac{d_2}{d_1} = R_d \quad (6.23)$$

However, it is not obvious why the ratio R_d should be equal to the grain size ratio $R_\phi = \frac{\phi_{G2}}{\phi_{G1}}$.

This effect is clearly observed at the low deformations of 2% and 3% . However this effect seems to decrease at 10% macroscopic plastic deformation for which it can be assumed that the multiplication of other slip bands is triggered and might vary the above simplified ratio.

This particular point is not as significantly observed in this study \dagger at 0.8% . By averaging the interband distances over the 59 bands of grains 3b, 6b and 15b (all featuring large grains with a mean value of $285 \mu\text{m}$) and the 47 bands of grains 1g, 2g and 3g (all featuring lower grain sizes with a mean value of $100 \mu\text{m}$) average values of $0.79 \mu\text{m}$ and $0.53 \mu\text{m}$ are found respectively.

Nevertheless, it could rightfully be assumed here that the population of slip bands considered might not be statistically representative enough.

Therefore, the grain size effect should also be considered in order to provide a meaningful comparison. However, nothing is clear as whether this effect is also observed in irradiated materials and once again, no explanation can be given yet concerning the underlying mechanism that could explain it.

6.4 Summary of the results and conclusion

6.4.1 Results

In this chapter, the following results are found:

- Atomic force microscopy is successfully used on a preliminary acquisition to resolve the surface relief of emerging slip bands in a 316L unirradiated stainless steel pulled at a 17.4 % macroscopic plastic deformation.
- In order to assess the actual slip bands thickness and interband spacing, the need to cross the AFM data with supplementary EBSD data of the grains orientation is stressed. In particular, it is roughly assessed that considering apparent measures as obtained solely by AFM would yield a 20–45 % discrepancy with respect to the actual thickness and interband spacing.
- A geometrical model of slip bands or clear bands in a low stacking fault energy metals or alloys, as envisioned by the multiscale approach proposed by Sauzay et al., is supported by the AFM acquisitions. The finite nature of the slip bands thickness is clearly evidenced.
- A statistical characterisation of slip bands is successfully undertaken using AFM and EBSD data acquisitions on six selected grains after interrupted tensile tests at 0.8 % and 2 % macroscopic plastic deformation. One tracking of nine slip bands is achieved for one grain at both deformations.
- Evenly spaced clusters of about three slip bands are often observed. These clusters generally feature one or two large slip bands surrounded by significantly thinner slip bands. The thickest slip bands present the highest plastic slip strains, although the thinnest slip bands does feature non negligible plastic slip strains.
- Quantitatively, slip bands thickness values between 25–150 nm are recorded with a high frequency of thin slip bands between 25–90 nm and a lower frequency of thick slip bands between 90–150 nm. Nevertheless, the uncertainty over the assessment of the slip band thickness is not negligible and AFM acquisitions with higher resolutions might improve this point. The comparison between the tracked slip bands of the 0.8 % and 2 % AFM acquisitions of the same grain seems to indicate that the slip bands thickness do not vary significantly during the solicitation.
- At 0.8 % macroscopic plastic deformation, lognormal distribution are found for the interband spacing and the step height. The lower values of interbands spacings around 0.25 μm are the most frequent and are related to the thin slip bands in the clusters. The highest values between 1–1.5 μm are related to the space between the clusters.

6. DISCONTINUOUS SLIP BANDS MODEL FOR LOW STACKING FAULT ENERGY METALS AND ALLOYS

- The tracking AFM acquisitions of 0.8 % and 2 % may suggest that plasticity is occurring by the intensification of the plastic slip strain in the bands rather than by a multiplication of the slip bands. However, a more statistical assessment using a higher resolution for the AFM acquisitions, would be needed to confirm this preliminary observation.

The comparison between the present results with AFM and SEM data of literature yields the following observations:

- The present results underline the need to focus on the assessment of slip bands and clear bands thickness and actual interband spacings which are not taken into account in literature.
- In particular, it is not completely clear how slip bands and clear bands develop.
- The quantification of the localisation of plasticity should preferentially be undertaken through the determination of the plastic slip strain in the bands. Measurements solely based on the step height may not be relevant enough for that purpose.
- The interband spacing clearly constitute a key factor to explain and understand the localisation of plasticity in irradiated and unirradiated materials. The irradiation does, the stacking fault energy and the grain size constitute major influential parameters.
- For these three factors, the increase of the plastic slip strain in the bands is clearly induced by an increase of the interband spacing. Hence the importance to better understand the related underlying mechanisms of clear bands and slip bands formation in order to better predict this later parameter.

6.4.2 Conclusion

In this chapter, the multiscale approach and the related model proposed by Sauzay et al. is supported by AFM and EBSD experimental data obtained for a low stacking fault alloy. At the atomic scale, the finite nature of the slip bands thickness in a 316L austenitic stainless steel is clearly evidenced at low macroscopic plastic deformations. The model of homogenised plastic slip bands and clear bands could be also supported even though further investigations would be needed.

In that context, the sensibility to intergranular cracking initiation in irradiated stainless steels, with respect to their unirradiated counterpart, might be mostly explained by the variation of the interband spacing and the resulting variations of the plastic slip strain in the bands.

From a prediction perspective, the results of this chapter incite to undertake the above multiscale approach in the context of Finite Fracture Mechanics and a coupled

6. DISCONTINUOUS SLIP BANDS MODEL FOR LOW STACKING FAULT ENERGY METALS AND ALLOYS

criterion. A quantitative prediction of intergranular fracture initiation can therefore be proposed, along with evidences of the effect of localised plasticity in irradiated materials. These points are finally treated in te next chapter.

7

Intergranular fracture initiation in unirradiated and irradiated stainless steels

In this final chapter, it is proposed to focus on the characterisation and the use of a multiscale model proposing the prediction of a remote macroscopic critical stress to intergranular fracture initiation in the vicinity of discontinuous clear bands or slip bands.

In order to quantify the detrimental effect of the localisation of plastic deformation with the irradiation dose, the use of the model is extended to the case of multiple clear bands or slip bands, considering the interband spacings described in chapter 6.

A physical justification of the use of the coupled criterion at the atomic scale in this multiscale model is proposed. In that regard, the top-down approach presented in chapter 5 is adapted here. The results are compared to the multiscale model predictions (i.e. a bottom-up approach).

A final application of the model and its comparison with experimental results is provided considering the context of irradiated and unirradiated austenitic stainless steels pulled under simulated PWR or BWR environments by slow strain rate tensile testing.

7. INTERGRANULAR FRACTURE INITIATION IN UNIRRADIATED AND IRRADIATED STAINLESS STEELS

Contents

7.1	Introduction	247
7.2	Finite element computations of intergranular stress fields in the vicinity of slip bands or clear bands	249
7.2.1	Microstructures	249
7.2.2	Constitutive elastoplastic laws	252
7.2.2.1	Elasticity	252
7.2.2.2	Plasticity	252
7.2.3	Expected intergranular stress fields and scale effect	254
7.2.4	Computed stress fields for one or several slip bands	258
7.2.4.1	One slip band in a grain	258
7.2.4.2	Several slip bands in a grain	261
7.3	Criterion for intergranular crack initiation and multiscale chaining .	265
7.3.1	Application of the coupled criterion: a bottom-up approach . .	265
7.3.2	Bottom-up and top-down approaches for the failure of several CSL nickel grain boundaries	268
7.3.2.1	Configuration of the problem and CSL $\langle 211 \rangle$ symmetric tilt grain boundaries	269
7.3.2.2	Finite element computations	270
7.3.2.3	Molecular dynamics computations on bicrystals	272
7.3.2.4	Top-down approach	272
7.3.2.5	Results of the two approaches	276
7.4	Application of the multiscale model and comparison with experimental data	281
7.4.1	Molecular dynamics inputs for predicting the fracture of oxidized grain boundaries	281
7.4.1.1	Oxidized grain boundaries and MD simulations	281
7.4.1.2	Application to the intergranular failure of an irradiated austenitic stainless steel	282
7.4.2	Selection of experimental data	283
7.4.3	Application of the model	285
7.4.4	Results and discussion	287
7.4.4.1	Irradiated and non-irradiated stainless steels	287
7.4.4.2	Influence of the environment	288
7.4.4.3	Grain size effect	290

7. INTERGRANULAR FRACTURE INITIATION IN UNIRRADIATED AND IRRADIATED
STAINLESS STEELS

7.5 Summary of the results and conclusion 291
7.5.1 Results 291
7.5.2 Conclusion 292

7.1 Introduction

Stress corrosion cracking (SCC) is a fracture phenomenon whose prediction has been of particular interest in the nuclear industry for about half a century. In 1959, Coriou first demonstrated the detrimental use of nickel-based alloys Inconel 600 in nuclear reactors. Severe intergranular fractures were observed during tensile tests under water environment [Coriou et al., 1959, Coriou et al., 1966].

Since then, the susceptibility to SCC has been demonstrated for highly cold-worked austenitic stainless steels used in the primary circuit of pressurized water reactors (PWR) [Féron et al., 2012]. More extensively, several PWR vessels internal components fabricated from solution annealed (SA) 304 and cold-worked 316 alloys are subjected to heavy neutron irradiation doses over long periods of the reactor operation. These structural components experience intergranular failures through irradiation assisted stress corrosion cracking (IASCC) [Thomas and Bruemmer, 2002, Zinkle and Was, 2013, Tanguy, 2011]. In this phenomenon, irradiation has been shown to enhance intergranular cracking [Was and Andresen, 2007, Féron et al., 2012]. Irradiation hardening, radiation induced segregation (RIS), radiolysis and localized deformation are among the suspected influential factors over IASCC. This phenomenon is particularly difficult to anticipate as it involves synergistic influences of several multi-physical factors. Hence, IASCC is still not well understood. Numerous mechanisms have already been proposed [Bruemmer et al., 1999], however no mechanism permits to fully explain the intergranular cracking phenomenon. In particular, it is believed that more physically-based prediction models are still needed in that endeavour.

In the course of assessing a primary factor responsible for IASCC, Jiao et al. have shown that localised deformation through clear bands formation can be considered as the major contributor [Jiao and Was, 2011]. The mechanism of intergranular fracture initiation through grain boundary impact of clear bands, twin bands and slip bands for monotonic tensile tests [Sauzay et al., 2010, Jiao and Was, 2008, Jiao and Was, 2011, Chen et al., 1999, Bailat et al., 2000] or persistent slip bands for fatigue loadings [Zhang and Wang, 2008] is widely supported.

However, it is admitted that this mechanism alone can not fully explain the intergranular cracking phenomenon, considering the clear influence of the environment on IASCC.

Concerning the SCC phenomenon of nickel-based alloys, the selective internal oxidation proposed by Scott and Le Calvar [Scott and Le Calvar, 1993] is supported by FIB-SEM observations [Kruska et al., 2012, Caballero Hinostroza, 2016] of deep oxide penetrations at grain boundaries, inducing embrittlement of the interfaces.

For unirradiated austenitic stainless steels, it has been shown that the observed oxide penetrations at grain boundaries display significantly lower depth (few nanometres). In the particular case of irradiated austenitic stainless steels, radiation induced segregation (RIS) is widely evidenced [Was, 2007b] by local chromium depletions and nickel enrichments at grain boundaries. This effect could probably exacerbates the

7. INTERGRANULAR FRACTURE INITIATION IN UNIRRADIATED AND IRRADIATED STAINLESS STEELS

grain boundary preferential oxidation leading to deeper oxide penetrations. However, to our knowledge, no observations to support this hypothesis are available.

In fine, it is generally accepted that the implication of several mechanisms is necessary to describe the IASCC phenomenon.

Approaches for the understanding of the SCC and the IASCC underlying mechanisms is shifting toward high-resolution experimental techniques providing new insights of the problems as pointed out by Lozano-Perez et al. [Lozano-Perez et al., 2014]. Recently, micromechanical tests on bicrystal microcantilevers [Armstrong et al., 2009, Armstrong et al., 2011, Dugdale et al., 2013] provided a first quantitative measurement for the assessment of the oxidized grain boundary strength. Atom probe tomography and chemical analysis of grain boundary penetrations have further confirmed the oxide composition to be the same spinel type $\text{Ni}_x\text{Fe}_{(1-x)}\text{Cr}_2\text{O}_4$ [Kruska et al., 2012] as evidenced in the inner oxide layer formed on nickel-based alloys or austenitic stainless steels under PWR primary water environment [Marchetti et al., 2016, Dumerval et al., 2016].

Adopting the same approach, from continuum modelling to atomistic simulations via a multiscale transition, might contribute further in this process. The assessment of intergranular stress field with polycrystalline simulations [Hure et al., 2016] or high-resolution EBSD [Britton and Wilkinson, 2012, Johnson et al., 2016] have already been achieved. Molecular dynamics and ab initio computations, suggesting atomistic-based cohesive zone models toward more realistic finite element simulations at the continuum level [Spearot et al., 2004, Yamakov et al., 2006, Barrows et al., 2016], or improving our understanding of mechanical and fracture processes at the atomic scale [Janisch et al., 2010, Bitzek et al., 2015, Pokluda et al., 2015, Barbé et al., 2018], has also been investigated.

However, to our knowledge, no study has yet proposed a prediction of intergranular cracking initiation based on atomistic and microstructure parameters.

In this chapter, such approach is proposed with the use of a multiscale model, as previously derived by Sauzay et al. [Sauzay and Moussa, 2013], for the prediction of intergranular fracture initiation in water or inert environment. As previously introduced in chapter 6, this semi-analytical model takes into account the intergranular stress fields induced by discontinuous slip bands (or clear bands) of finite thickness. In that regard, finite element computations are used to provide a characterisation of the model. Interface debonding parameters obtained by molecular dynamics simulations are then embedded in the model through the use of finite fracture mechanics [Taylor et al., 2005] and a coupled criterion proposed by Leguillon et al. [Leguillon, 2002], similarly to the case of the V-notch described in chapter 5.

A first part of this chapter is dedicated to the finite element computations of intergranular stress fields in the vicinity of one or several slip bands or clear bands with a grain boundary. The above model is fully described for numerous configurations. In particular, the influence of the number of bands per grain and the interband spacing is investigated, as suggested in chapter 6.

A second part focuses on a validation of the use of the coupled criterion at the

7. INTERGRANULAR FRACTURE INITIATION IN UNIRRADIATED AND IRRADIATED STAINLESS STEELS

atomic scale from which the multiscale model proposed by Sauzay et al. is derived for the prediction of intergranular fracture initiation at slip bands or clear bands impacts.

A final part provides an application of the model using molecular dynamics results obtained from MD simulated tensile tests on a large variety of spinel oxide bicrystals by Van Brutzel et al. [Van Brutzel et al., 2019]. A comparison of the model prediction with numerous experimental data from literature is finally carried out.

7.2 Finite element computations of intergranular stress fields in the vicinity of slip bands or clear bands

Stress fields induced by one or several slip bands (or clear bands) impacting a grain boundary are calculated using the finite element code Cast3m [CAST3M,]. For this study, the calculations are carried out considering an austenitic stainless steel as necessary data are readily accessible. However, the following method could be used for any FCC material. In this part, the geometry of the problems to be solved and the behaviour model of the material are primarily described. The models and the expected features of the normal intergranular stress field are then detailed before the presentation of the results obtained from the FE computations.

7.2.1 Microstructures

As already introduced in chapter 6, type A and type B slip bands represent particular configurations where only one orientation parameter is needed to describe it. As displayed in figure 6.10:

1. The orientation of a type A slip band is such that the vectors (\mathbf{n}, \mathbf{m}) belong to the surface plane. The trace angle $\psi_{SB} = \alpha_{SB}$.
2. For a type B slip band the vectors (\mathbf{n}, \mathbf{m}) are in the plane defined by the two vectors $(\mathbf{e}_s, \mathbf{e}_f)$. The trace angle $\psi_{SB} = 90^\circ$.

In either cases, the Schmid factor is determined by the relation: $f = \cos(\alpha_{SB}) \sin(\alpha_{SB})$. A slip band is generally a combination of these two theoretical configurations. These two cases can be simulated by 2D finite element calculations choosing either a plane stress or a plane strain hypothesis for respectively type A and type B slip bands. The later case is theoretically considered to induce the most severe normal intergranular stress [Evrard and Sauzay, 2010]. In the context of finding a fracture criterion, type B slip bands are therefore at the centre of this study to consider the most conservative case. Simulations are thus carried out with the plane strain hypothesis using 2D finite element calculations.

However, as also pointed out before in several studies [Le Millier, 2014, McMurtrey et al., 2015, Was et al., 2012, Gupta et al., 2016], intergranular crack initiations are

7. INTERGRANULAR FRACTURE INITIATION IN UNIRRADIATED AND IRRADIATED STAINLESS STEELS

preferentially observed at discontinuous clear bands. Therefore, in this chapter, only a grain without slip transmission is modelled in order to consider, once again, the most conservative cases for both irradiated and unirradiated materials.

Following the AFM measurements presented in chapter 6, microstructures consisting in one or several slip bands of finite thickness t and interband spacing d are used.

The parameters and the notations of the models are shown in figure 7.1a. A monotonic uniaxial tensile loading with a remote macroscopic stress Σ is applied.

A large isotropic elastic matrix is employed in order to avoid possible size influences.

Plastic slip bands are embedded in an isotropic elastic grain with the same behaviour of the surrounding matrix. Therefore, the morphology of the grain does not impact the stress field along the grain boundary in the vicinity of the slip bands. The grain morphology shown in figure 7.1a is chosen to identify the length L of the slip bands, which crosses the entire grain and the orientation of the grain boundary α_{GB} with respect to the tensile axis. The length L corresponds to the average length of the two longer sides of the slip band. In the case of several slip bands, an average length \bar{L} is taken at the centre of the grain boundary as indicated in figure 7.1a resulting in a distribution of slip band lengths around this value.

The stacking sequence of elastoplastic and elastic behaviour is assumed, based on the hypothesis that when slip bands are formed during plastic deformation, few dislocation movements are expected outside the activated slip bands [Edwards et al., 2005]. It has already been reviewed that this behaviour is enhanced for irradiated materials as radiation-induced defects further impinge dislocation movements between clear channels.

In the case of several bands, the interband spacing d is varied between 1–20 μm in order to investigate its influence considering a grain size L of 40 μm which represents a widely used mean grain size for 316L SS. Furthermore, the number of slip bands N_{SB} , as defined on figure 7.1a, is chosen between 3 and 45 for $d = 1 \mu\text{m}$ and between 3 and 13 for $d = 2, 3$ and $4 \mu\text{m}$. These ranges of values encompass the cases of unirradiated and irradiated stainless steels as evidenced in chapter 6 and by other AFM studies [Jiao and Was, 2008, Menard, 2005, Aubert et al., 2010]. Despite the variations of the interband spacing reported before in the same grains, a constant value is considered here for one grain, as illustrated on figure 7.1a.

The models used consider only one slip system activated in the slip bands as mentioned before.

The orientation of the slip band, boils down here to the angle α_{SB} between the slip band and the tensile axis. The θ_{GBSB} angle (referenced in figure 7.1a), already used before in similar studies [Sauzay and Moussa, 2013, Sauzay and Vor, 2013], represents a parameter coupling the orientation of the grain boundary and the orientation of the band:

$$\theta_{GBSB} = \frac{\pi}{2} + \alpha_{GB} - \alpha_{SB} \quad (7.1)$$

α_{GB} being the angle of the grain boundary normal vector with respect to the tensile axis.

7. INTERGRANULAR FRACTURE INITIATION IN UNIRRADIATED AND IRRADIATED STAINLESS STEELS

The intensity of the singularity to be determined here by FE analysis is expected to depend only on the θ_{GBSB} angle [Sauzay and Vor, 2013].

A meshing code is implemented using the SALOME python library [SALOME, 2017] allowing to automatically mesh a large set of 2D microstructures for a large range of θ_{GBSB} angles. Several couples (α_{SB} , α_{GB}) are considered in the case of a single slip band. One mesh is shown in figure 7.1b in the case of 7 slip bands. Radial stress singularity are expected in the vicinity of the slip bands. Therefore disk-shaped partitions are used along with radial meshes. The mesh is strongly refined along the grain boundary on the close-field distance covering one tenth of the slip band thickness. The mesh size reaches typically 3 Å at the tips of the slip bands. A refinement up to 1 Å is also used for validating the independence of the approached solutions with respect to the mesh size. Regardless of the physicality underneath of these refinements, the aim is merely to approach the asymptotic solution of the mathematical problem.

7.2.2 Constitutive elastoplastic laws

The mechanical behaviour model for the simulation of a typical 316L stainless steel material is described in this section. A crystalline elastoplastic model for the simulated slip bands is used. As previously mentioned, the grain and the surrounded matrix are considered as isotropic elastic media.

7.2.2.1 Elasticity

The Young modulus $Y = 200$ GPa and the Poisson ratio $\nu = 0.3$ are used to model the elastic behaviour of an typical austenitic stainless steel. Using isotropic elasticity, it is reminded that the related shear modulus μ can be computed through:

$$\mu = \frac{Y}{2(1 + \nu)} \quad (7.2)$$

The same isotropic elasticity is achieved for the band with the following constants for cubic elasticity: $C_{11} = 269$ GPa, $C_{12} = 115$ GPa and $C_{44} = 77$ GPa.

7.2.2.2 Plasticity

A crystal viscoplastic law considering the model of Kocks for FCC metals or alloys is used for the mechanical behaviour of the slip bands. An implementation of the model is used in the Cast3m finite element code [CAST3M,] with a subroutine UMAT. The orientation of the twelve slip systems are described by their vectors ($\mathbf{n}_s, \mathbf{m}_s$). It is reminded that only one slip system activation is chosen for the slip band behaviour. The formulation of this crystalline model consists in:

7. INTERGRANULAR FRACTURE INITIATION IN UNIRRADIATED AND IRRADIATED STAINLESS STEELS

- The viscoplasticity flow equation governing the time evolution of the plastic slip strain γ_s^p for every slip system denoted s :

$$\dot{\gamma}_s^p = A \left\{ \sinh \left(\frac{\tau_s}{\tau_s^c} \right) \right\}^{\frac{1}{m}} \text{sgn}(\tau_s) \quad (7.3)$$

where τ_s is the shear stress resolved on the slip system: $\tau_s = \mathbf{m}_s^T \cdot \boldsymbol{\sigma} \cdot \mathbf{n}_s$ where $\boldsymbol{\sigma}$ is the stress field. The critical resolved shear stress τ_s^c represents a plasticity threshold beyond which dislocation movements are enabled in the corresponding slip plane. The values of the coefficients A and m listed in table 7.1 are chosen for removing viscosity effects which is verified for several strain rate solicitations.

- The hardening law, describing the variation of the critical resolved shear stress for each slip system through forest dislocation interactions is:

$$\dot{\tau}_s^c = \sum_i^{12} H_0 d_{si} |\dot{\gamma}_i^p| \quad (7.4)$$

$$\tau_s^c(t=0) = \tau_0 \quad (7.5)$$

$$d_{si} = \begin{cases} q & \text{if } i \neq s \\ 1 & \text{otherwise} \end{cases} \quad (7.6)$$

where d_{si} are the interaction matrix coefficients, H_0 the linear hardening slope. Choosing a high value to the latent hardening coefficient q numerically allows to activate exclusively the primary slip system. The activation of other systems is thus prevented by an important increase of their critical resolved shear stress as soon as the primary slip system is activated as indicated by equations (7.4) and (7.6). The initial critical stress τ_0 is chosen equal to 130 MPa, which is close to the computed value obtained by Nogaret et al. [Nogaret et al., 2008] in irradiated stainless steels using dislocation dynamics and considering dislocation interactions with irradiation induced Frank Loops.

The different coefficient values used for the calculations are summarised in table 7.1.

It is reminded that the Schmid factor can be used as an indicator for slip system activation regarding the following relation:

$$f = \max_{s \in \{1, \dots, 12\}} \frac{|\tau_s|}{\Sigma} \quad (7.7)$$

A maximum value of $f = 0.5$ is expected for the most well-oriented grain.

As the primary slip system (\mathbf{n} , \mathbf{m}) is the first and only activated system in the band it follows that its corresponding shear stress is $\tau_{SB} = f\Sigma$.

In the following sections, we denote $\tau_{\text{eff}} = f\Sigma - \tau_{SB}^c$ the effective shear stress actively responsible for the dislocation movements in the band where τ_{SB}^c is the critical remote shear stress of the primary slip system. This means that the slip band will be activated during the solicitation provided that the following condition is verified : $\tau_{\text{eff}} > 0$.

7. INTERGRANULAR FRACTURE INITIATION IN UNIRRADIATED AND IRRADIATED STAINLESS STEELS

A	$\frac{1}{m}$	τ_0 (MPa)	q	H_0 (MPa)	Y (GPa)	ν
1.0×10^{-10}	100	130	1.0×10^5	1	200	0.3

Table 7.1: Parameters used for the finite element calculations

The hardening in the band is assumed to be negligible considering that all the initial defects in the band are recombined or swept away by the initial dislocations movements. A low hardening slope $H_0 = 1$ MPa is therefore employed yielding the approximation: $\tau_{SB}^c \approx \tau_0$ thus $\tau_{eff} = f\Sigma - \tau_0$.

7.2.3 Expected intergranular stress fields and scale effect

Seeking for a characterization of the stress field induced by a slip band impacting a grain boundary, a crack analogy can be regarded for a better understanding of the problems to be solved. In the following paragraphs, the geometry of the different problems discussed encourages to adopt a polar coordinate system with the origin at the tip of the slip band.

As previously described by Sauzay et al. [Sauzay and Moussa, 2013, Sauzay and Vor, 2013], the crack analogy consists in comparing an activated slip band, sheared by its effective stress τ_{eff} , to a crack loaded by the same shear stress (i.e. in mode II) in an elastic medium as shown in figure 7.2a. Following this analogy and the work of Griffith [Griffith, 1921], Sauzay et al. showed that the stress singularity at the tip of a slip band with a finite thickness displays the same linear and square root dependence with the effective shear stress τ_{eff} and the slip band length L respectively.

Similarly, the pile-up theory based on the work of Eshelby [Eshelby et al., 1951], Stroh [Stroh, 1957] and Smith [Smith and Barnby, 1967], models a slip band as a single atomic plane in which all the dislocations of the activated slip system are gliding as depicted on figure 7.2a. This model is generally used for assessing stress concentrations at grain boundaries induced by a slip band impact [Britton and Wilkinson, 2012]. It proposes a radial asymptotic dependence with an exponent of 0.5:

$$\sigma_{nn}^{pile-up}(r, \theta_{GBSB}) = h(\theta_{GBSB}) \langle f\Sigma - \tau_0 \rangle \left(\frac{L^{pile-up}}{r} \right)^{\frac{1}{2}} + \Sigma_{nn}^{\infty} \quad (7.8)$$

as would similarly induce a perfect crack loaded in an elastic medium. In this model, the length of the pile-up $L^{pile-up}$ is considered to be about one half of the grain size. The normal stress expected far from the tip of the slip band is related to the remote stress by the relation $\Sigma_{nn}^{\infty} = \Sigma \cos(\alpha_{GB})^2$ and the geometrical pre-factor is determined by $h(\theta_{GBSB}) = \frac{3}{2} \sin(\theta_{GBSB}) \cos(\frac{\theta_{GBSB}}{2})$.

As previously mentioned in chapter 6, it is believed that the pile-up theory is not sufficient to predict an intergranular crack initiation. As mentioned in earlier studies [Sauzay and Vor, 2013, Sauzay and Moussa, 2013], using the pile-up theory at the atomic

7. INTERGRANULAR FRACTURE INITIATION IN UNIRRADIATED AND IRRADIATED STAINLESS STEELS

scale induces an underestimation of the remote critical stress to crack initiation. Indeed, these studies show that considering a band with negligible thickness and using the Griffith criterion lead to a predicted remote critical stress, 50 % lower than experimental values [Nishioka et al., 2008].

This discrepancy can be explained by an overestimation of the grain boundary normal stress singularity using the pile-up theory in a close vicinity of a slip band impacting a grain boundary.

As already addressed in chapter 6, if one considers the close vicinity of a slip band such that its finite thickness can not be neglected with respect to the distance from the slip band impact. Hence, it is natural to reject the hypothesis of an infinitesimal slip band thickness (single plane), assumed by the pile-up theory. However, this later hypothesis becomes more reliable when distances from the slip band increase as its geometry tends toward a pile-up shaped configuration. The pile-up solution is therefore expected far enough from the slip band impact. It constitutes the so-called far field solution.

Obviously, this change of scale must feature a continuous transition between the intergranular stress field solutions. Here, the context is clearly the asymptotic expansion to the close-field [Murer and Leguillon, 2010]. As presented earlier, in this part, the meshing refinement at the corner of the slip band grain boundary impact is purposely intended for catching this scale transition.

This transition is depicted further in figure 7.2c plotting the normal stress along the grain boundary in the close vicinity of an activated slip band from the FE-computed grain boundary normal stress field displayed in figure 7.2b. The configuration used for the calculation consists in one band with a θ_{GBSB} angle of 78° ($\alpha_{GB} = 33^\circ$, $\alpha_{SB} = 45^\circ$), a thickness $t = 200\text{ nm}$, a slip band length of $L = 10.7\text{ }\mu\text{m}$ and an effective shear stress of around 190 MPa . The choice of these specific parameters is somehow irrelevant to illustrate the above point.

Figure 7.2c shows a zone of discrepancy between the pile-up solution of equation 7.8 and the computed solution. This zone spreads along the grain boundary from the tip of the slip band ($r = 0$) to approximately one tenth of the slip band thickness ($r = \frac{t}{10}$). It could be referred to the close-field region where it is clear that the pile-up solution shows strong overestimation. At this scale, it is obvious that the finite thickness of the band and its influence can not be ignored. Then, the hypothesis of an infinitesimal thickness behind the pile-up theory does not hold.

A changing exponent of the singularity from the close-field to the far-field is clearly evidenced in figure 7.2d using a log-log scale, thus permitting to cover a slip band impact distance over several orders of magnitude. An exponent close to 0.5 is found far from the SB tip as reckoned by the pile-up theory for the reasons depicted above. Meanwhile, the computed FE solution clearly features a weak singularity with an exponent lower than 0.5.

In the vicinity of the slip band, depicted in figure 7.1b, other problems and their related solutions can be regarded in order to gain further insight into the hypothetical

7. INTERGRANULAR FRACTURE INITIATION IN UNIRRADIATED AND IRRADIATED STAINLESS STEELS

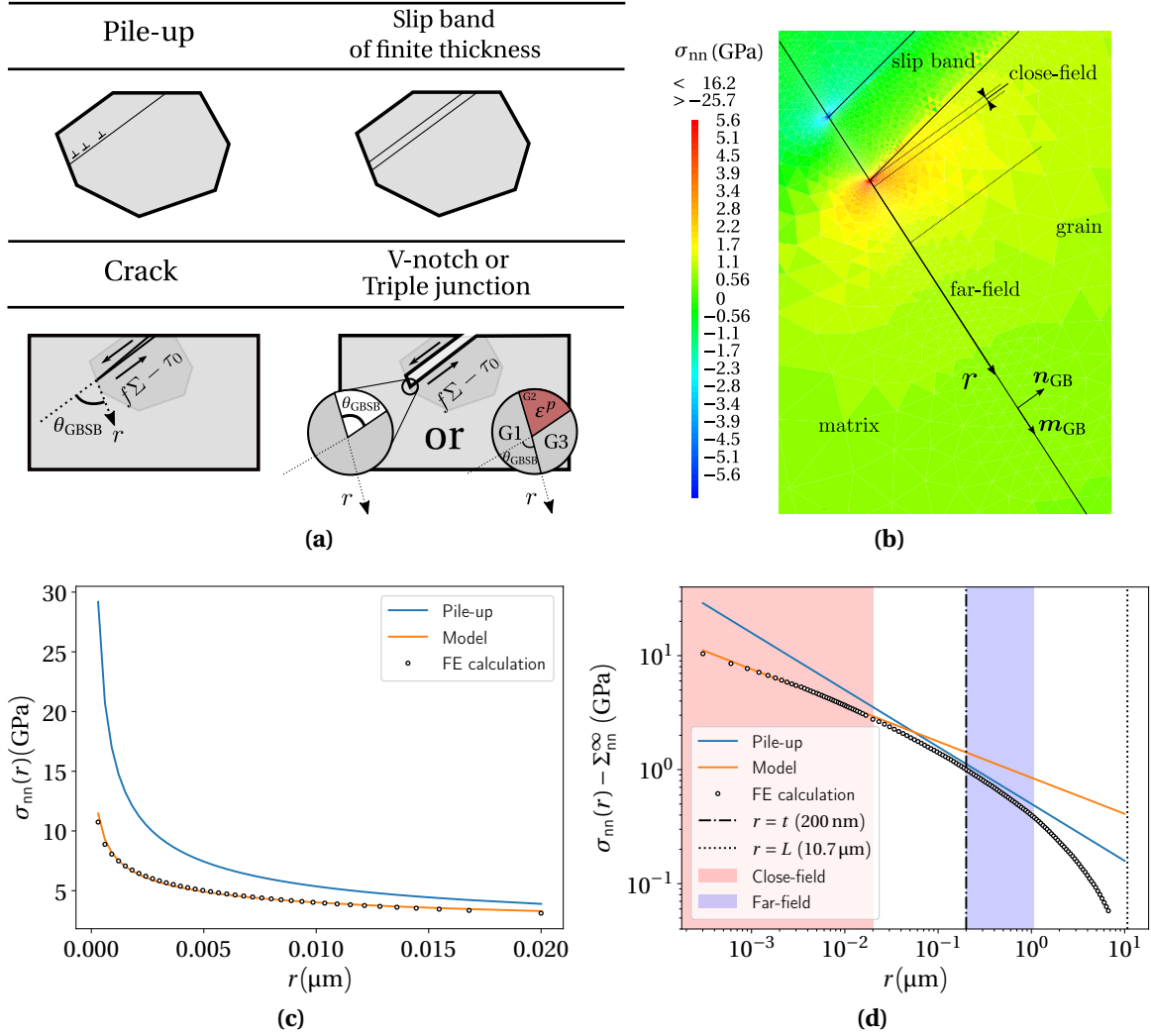


Figure 7.2: Crack analogy for one activated slip band (a). Normal stress field σ_{nn} computed for a macroscopic remote stress of $\Sigma_0 = 500$ MPa, $L = 10.7 \mu\text{m}$, $t = 200$ nm, $H_0 = 1.0$ MPa, $\tau_0 = 60$ MPa, $\theta_{GBSB} = 78^\circ$, \mathbf{n}_{GB} being the normal vector to the grain boundary (b). Normal stress profile extracted along the grain boundary in the close-field area and overestimation of the pile-up theory stress field model (c). The application of the model (equation 7.10, in yellow) [Sauzay and Vor, 2013] yields $A_{nn} = 1.01$ and a exponent $1 - \lambda = 0.3$. Normal stress profile along the grain boundary in a log-log scale and transition of the exponent of the singularity from the close-field to the far-field (d).

7. INTERGRANULAR FRACTURE INITIATION IN UNIRRADIATED AND IRRADIATED STAINLESS STEELS

close-field solutions that could be expected. As suggested by the sketch figure 7.2a, the V-notch problem, treated before in the context of a crack initiation criterion [Leguillon, 2002], shows similarly weak singularities when the θ_{GBSB} angle is not negligible. However, it is quite clear that many aspects (such as the boundary conditions for example) differs strongly between the two problems.

In that regard, the problem of the triple junction treated in thermo-elasticity [Saada, G., 1989, Laws and Lee, 1989, Rey, C. et al., 1985, Caré and Zaoui, 1996] should bring a more reliable comparison. Indeed, this triple junction analogy seems to be more relevantly comparable, should one consider, in that model, only one plastically and homogeneously deformed grain, as depicted on the lower right scheme of figure 7.2a. The solution of this problem, adapted in our case here, typically features a logarithm evolution:

$$\sigma_{\text{nn}}(r, \theta_{\text{GBSB}}) = \frac{\mu b_{\text{SB}}}{2\pi(1-\nu)} \left[\tilde{A}(\theta_{\text{GBSB}}) \ln \frac{R}{r} + \tilde{B}(\theta_{\text{GBSB}}) \right] \quad (7.9)$$

with $b_{\text{SB}} = \gamma^p \cos(\alpha_{\text{SB}} - \theta_{\text{GBSB}}) \sin(\alpha_{\text{SB}} - \theta_{\text{GBSB}})$, γ^p being the plastic slip strain homogeneous in the slip band corner, $\mu = \frac{Y}{2(1+\nu)}$ the shear modulus in isotropic elasticity, R a constant that could related to the length of the slip band and $\tilde{A}(\theta_{\text{GBSB}})$, $\tilde{B}(\theta_{\text{GBSB}})$ two geometrical functions.

The semi-analytical model proposed by Sauzay et al. [Sauzay and Vor, 2013] considers the influence of the thickness t and an asymptotic exponent $1 - \lambda < \frac{1}{2}$ according to the following formulation:

$$\sigma_{\text{nn}}(r) = A_{\text{nn}}(\theta_{\text{GBSB}}) \langle f\Sigma - \tau_0 \rangle \sqrt{\frac{L}{t}} \left(\frac{t}{r} \right)^{1-\lambda} + \Sigma_{\text{nn}}^{\infty} \quad (7.10)$$

where the intensity factor A_{nn} is assumed to only depend on the θ_{GBSB} angle. It is based on the asymptotic expansion of the stress singularity to the close-field of the slip band as proposed by Leguillon et al. [Murer and Leguillon, 2010].

Using this multiscale model, an exponent of $1 - \lambda = 0.3$ and a pre-factor $A_{\text{nn}} = 1.01$ can be deduced from the preceding GB normal stress profile (figures 7.2c and 7.2d) This first-hand computation agrees with a similar computation performed by Sauzay et al. [Sauzay and Moussa, 2013] which yields a slightly lower intensity factor $A_{\text{nn}} = 0.7$ using 3D calculations, with a lower viscoplastic exponent. In comparison, if one considers the preceding model of the triple junction of equation 7.9, the logarithm progression would similarly induce a fitted exponent lower than 0.5, which should therefore be constant whatever the θ_{GBSB} angle.

An extensive characterisation of the grain boundary normal stress field is subsequently carried out with the same multiscale model and method in the next subsection, considering the wide variety of configurations previously described.

7.2.4 Computed stress fields for one or several slip bands

7.2.4.1 One slip band in a grain

One slip band embedded in one grain is considered in the following paragraph. Calculations are carried out for a θ_{GBSB} angle between 20–160° by varying the orientation of the grain boundary α_{GB} with a fixed angle $\alpha_{\text{SB}} = 45^\circ$.

Similar calculations are realised for different orientations of the slip band (α_{SB} between 35–55°) covering Schmid factors between 0.47 and 0.5. Furthermore, different sets of θ_{GBSB} angles are used between each set of fixed α_{SB} configurations, thus permitting to consider a different θ_{GBSB} value at each calculation.

A final axial tensile stress of 600 MPa is chosen to ease the convergence of the computations. The GB normal stress fields in the close vicinity of the slip band are displayed with the same scale in figure 7.3a, at this final stress value and on several deformed configurations at $\alpha_{\text{SB}} = 45^\circ$ (using a 10 times amplification). It is important to remind here that the coordinate system (\mathbf{m}_{GB} , \mathbf{n}_{GB}) is fixed by the chosen θ_{GBSB} angle for each displayed field (i.e. the subscript n for the intergranular normal stress field σ_{nn} , is related to the fixed \mathbf{n}_{GB} direction for each configuration).

For each single computation (i.e. at α_{SB} and α_{GB} fixed), stress profiles are extracted every 10 MPa along the grain boundary as previously described. As before, the pre-factor A_{nn} and the exponent $1 - \lambda$ are then readily obtained from a simple linear regression based on the model described by equation (7.10). Satisfying squared correlation coefficient near 0.99 are obtained for each profile.

As expected, it is here verified for each configuration that these two parameters show weak variations according to the macroscopic stress Σ once the slip band is activated (i.e. $f\Sigma > \tau_0$, considering the chosen parameters of table 7.1: $\Sigma > 260$ MPa). From this result, it is then considered that an extrapolation of these parameters is fairly acceptable beyond the final loading of 600 MPa.

The pre-factor A_{nn} and the exponent $1 - \lambda$ are extracted and plotted according to the θ_{GBSB} angle in figure 7.3b. Master curves are found whatever the combination (α_{GB} , α_{SB}). This result confirms that the normal stress field solution only depends, geometrically, on the θ_{GBSB} angle (i.e. whatever the α_{SB} , α_{GB} angles and the related Schmid factor). Furthermore, results from the computations using the refined mesh of 1 Å clearly show negligible discrepancies, confirming the convergence of the computed solutions using a 3 Å mesh size.

A continuous function $A_{nn}(\theta_{\text{GBSB}})$ is found and clearly shows a maximum value at a θ_{GBSB} angle of 70°. In order to characterise the level of stress according to the considered configuration, the average normal stress value $\langle \sigma_{nn} \rangle_d$ is integrated on the elastic part of the refinement disk and plotted against the θ_{GBSB} angle on figure 7.3b:

$$\langle \sigma_{nn} \rangle_d = \frac{1}{S_d} \int_{S_d} \sigma_{nn}(r, \theta_{\text{GBSB}}) dS \quad (7.11)$$

with S_d the surface of the elastic part of the refinement disk. A similar variation of $\langle \sigma_{nn} \rangle_d(\theta_{\text{GBSB}})$ is found with respect to the $A_{nn}(\theta_{\text{GBSB}})$ prefactor. The maximum level of

7. INTERGRANULAR FRACTURE INITIATION IN UNIRRADIATED AND IRRADIATED STAINLESS STEELS

stress are found between 70° and 90° . More interestingly, the variation of the averaged stress $\langle\sigma_{nn}\rangle_d$ presents a clear discrepancy with the A_{nn} function which features a steep decreasing drop from 70° . This difference can be readily explained by the fact that the A_{nn} factor characterises mainly a stress profile extracted along the grain boundary, as presented figure 7.3a. Therefore, this pre-factor A_{nn} only takes into account the necessary information of the stress field along the grain boundary. It also displays a similar variation compared to the geometrical function $h(\theta_{GBSB})$ of the pile-up model (equation 6.1) even if clear discrepancies can be identified. In that regard, it should be emphasized that at each θ_{GBSB} value considered here corresponds a different problem whereas in the case of the pile-up the same solution is used with different profile directions according to the θ_{GBSB} angle. Therefore, these two geometrical prefactors are not comparable here. In the close-field solution, the prefactor $A_{nn}(\theta_{GBSB})$ embodies two information: the global stress intensity (normed) that could be illustrated by the averaged stress $\langle\sigma_{nn}\rangle_d$, and the GB direction. These two aspects are intrinsically linked by the θ_{GBSB} angle which therefore represents a fundamental parameter.

The exponent $1 - \lambda$ varies continuously between roughly 0 and 0.35. Its value increases as the θ_{GBSB} angle shrinks so that the slip band corner shape progressively tends toward the shape of a perfect crack. Conversely, a decrease of the exponent is found when the slip band corner shape tends toward a straight edge (at $\theta_{GBSB} = 180^\circ$). These variations are in agreement with the case of the V-notch. Similarly it is found that all the exponents reported here are lower than 0.5, confirming a departure from the problem of the pile-up. A local maximum value is obtained for a θ_{GBSB} angle around 90° . It is worth noticing that this later configuration yields the maximum normal stress values with respect to the other configurations (i.e. the highest stress profiles). Finally, a local minimum is found for a θ_{GBSB} angle around 70° . As evidenced on figure 7.3a, this later configuration does not yield the lowest normal stress values. It is important to note that the variation of the exponent alone does not provide a clear information for comparison purposes between the configurations. This point is evidenced by comparing the configurations with θ_{GBSB} angles of 40° and 80° featuring the same exponent of around 0.28 but clearly exhibiting (from figure 7.3a) clear discrepancies with the highest stresses in the later case.

The variation of the exponent further questions the comparison to the triple junction problem in thermo-elasticity for which the solution features a logarithm progression regardless of the θ_{GBSB} angle, as noted before. In order to bring more insight into that variation, the plastic slip deformation field γ^p is showed in figure 7.3b with the same scale, for a macroscopic stress of 600 MPa and for the 40° , 70° , 80° , 90° and 120° deformed configurations. Non negligible plastic slip deformation gradients are found with, for example, plastic slip deformation values ranging between 7 % and 56 % for the $\theta_{GBSB} = 90^\circ$ configuration. These deformation gradients are in disagreement with the use of the solution of the triple junction problem for which the hypothesis of an homogeneous plastic deformation is made. The plastic slip strain field could explain the variation of the exponent reported here.

7. INTERGRANULAR FRACTURE INITIATION IN UNIRRADIATED AND IRRADIATED STAINLESS STEELS

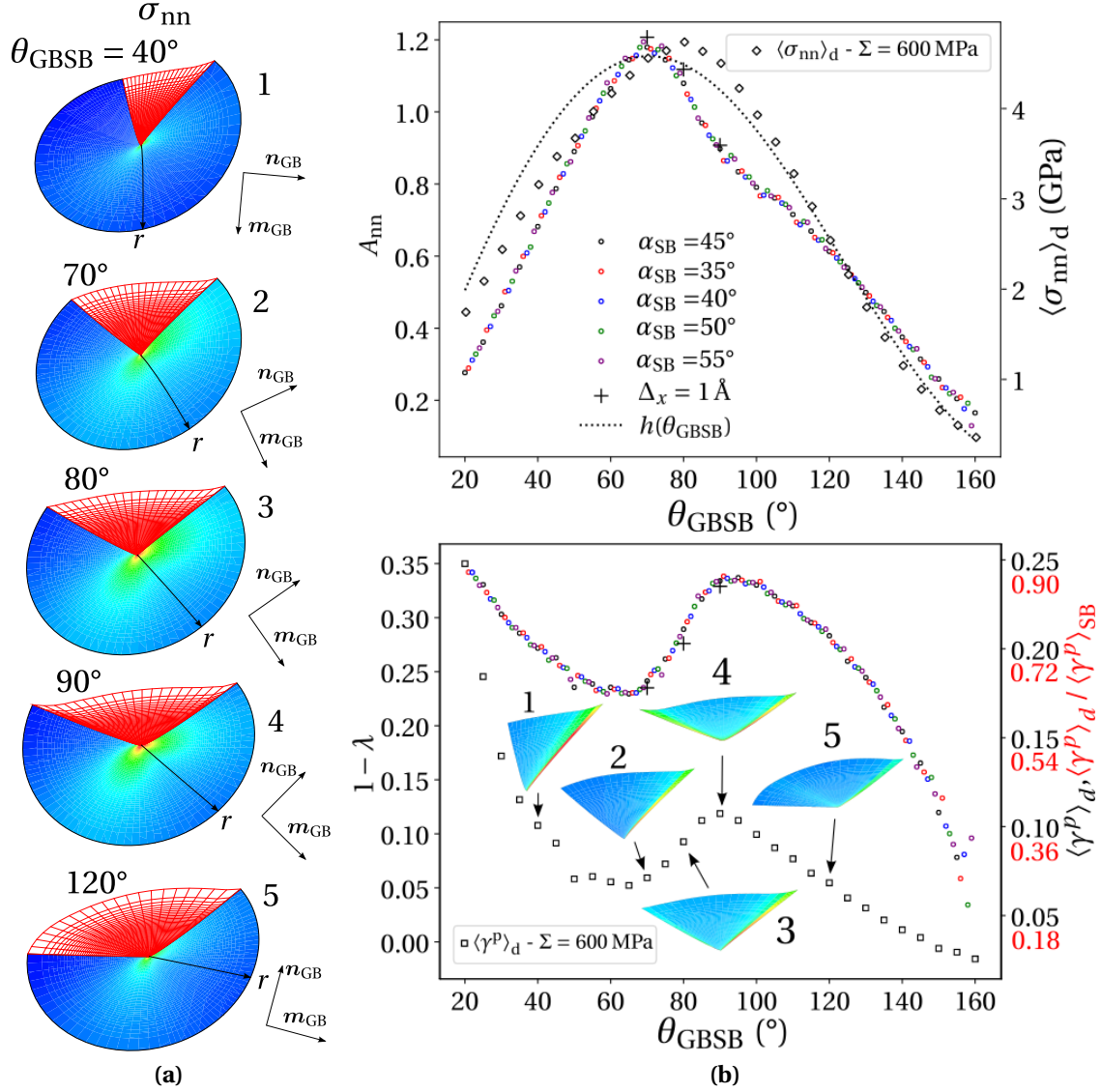


Figure 7.3: Stress fields σ_{nn} on the deformed structures (10 times amplification) of the refinement disk at the impact of the slip band with the grain boundary for a loading of $\Sigma = 600$ MPa and for different configurations with $\alpha_{SB} = 45^\circ$ and $\theta_{GBSB} = 40^\circ, 70^\circ, 80^\circ, 90^\circ$ and 120° (7.3a). Master curves for the intensity factor A_{nn} and the exponent $1 - \lambda$ according to the θ_{GBSB} angle for a single band with a parametrisation of the curves according to the α_{SB} angle. The averaged normal stress (to the grain boundary) $\langle \sigma_{nn} \rangle_d$ on the elastic part of the refinement disk and the plastic slip deformation field γ^p along with its mean value $\langle \gamma^p \rangle_d$ on the plastic part of the refinement disk are also displayed according to the θ_{GBSB} angle (7.3b).

7. INTERGRANULAR FRACTURE INITIATION IN UNIRRADIATED AND IRRADIATED STAINLESS STEELS

The mean value of the plastic slip $\langle \gamma^p \rangle_d$ integrated over the plastic part of the refinement disk are also plotted in figure 7.3b for each θ_{GBSB} configuration at 600 MPa. A mean plastic slip deformation of about 28 % is found in the slip band for every configuration and at the same effective shear stress of 170 MPa. Meanwhile, mean values between about 5 % and 10 % are found in the refinement disk and about 35 % are found near the surface. These results show that the exponent fitted by the model proposed by Sauzay et al. is in part correlated to the plastic slip deformation of the slip band corner. It is here logical to find mean plastic deformation values higher far away from the slip band corner, as plastic incompatibilities further restrain the deformations at the grain boundary. Finally, the same curve of $\langle \gamma^p \rangle_d(\theta_{\text{GBSB}})$ is found whatever the macroscopic stress applied by normalising the mean plastic slip deformation in the corner with the mean plastic slip deformation in the slip band $\langle \gamma^p \rangle_{\text{SB}}$. This can be related to the same Independence of the exponent with respect to the macroscopic stress. The scale of this later master curve is also provided in figure 7.3b on the right y-axis in red.

In conclusion, a comparison of the intergranular stress profiles between different θ_{GBSB} angles has to take into account both the A_{nn} and $1 - \lambda$ parameters in order to draw preliminary conclusions concerning the propensity to crack initiation depending on the microstructure geometry. A direct comparison can then be obtained with the use of the multiscale model described by equation 7.10 for a single slip band.

This semi-analytical model is here completely described to be used for a large variety of configurations. The computed values of $1 - \lambda$ and A_{nn} are gathered in appendix C.

It should be stressed at this point that these parameters are allegedly applicable with the model to any metal or alloy since these fitting parameters only originate from the geometry of the problem.

However, care would need to be taken with regard to the reliability of such applications provided that the material effectively features a localised plastic behaviour characterised by parallel slip bands (or clear channels) with negligible interactions between each other. Since this structural behaviour may not be expected in the general case, further results of computations considering modelled microstructures with several bands are presented in the following section.

For irradiated stainless steels, the large interchannel spacings confirmed by observations and measurements [Jiao et al., 2005, Jiao and Was, 2008] would tend to promote the use of this model considering isolated clear channels in a grain.

As suggested in chapter 6, the interest of the model lies further on an extended application to unirradiated stainless steels featuring narrower interband spacings and apparently no intergranular cracking initiations. In contrast, this application may shed more light on some of the underlying factors of intergranular cracking in agreement with the influence of the exacerbated plastic localisation in irradiated materials.

7.2.4.2 Several slip bands in a grain

Similar characterisations according to the θ_{GBSB} angle are performed on the configurations with $N_{\text{SB}} = 3, 5$ and 7 slip bands and a fixed interband spacing of $d = 1 \mu\text{m}$, as

7. INTERGRANULAR FRACTURE INITIATION IN UNIRRADIATED AND IRRADIATED STAINLESS STEELS

illustrated in figure 7.1.

As before, the θ_{GBSB} angle is varied between 20–120°, with a fixed $\alpha_{\text{SB}} = 45^\circ$.

A constant and homogeneous stress state is found in the elastic ligaments in between activated slip bands and far enough from the grain boundary where a shear stress value of $\tau_{\text{lig.}} = 130 \text{ MPa}$ is recorded whatever the applied macroscopic stress $\Sigma > f\tau_0$, with:

$$\tau_{\text{lig.}} = \mathbf{m}_s^T \cdot \boldsymbol{\sigma}_{\text{lig.}} \cdot \mathbf{n}_s \quad (7.12)$$

This is clearly linked to the initial critical resolved shear stress τ_0 , as the activation of the slip bands induces a screening effect between the bands preventing further deformation of the elastic ligaments in between, whatever the applied macroscopic stress Σ . The fitting procedure of the stress profiles in the vicinity of the slip bands is therefore applied considering the following modified remote stress along the grain boundary:

$$\Sigma_{\text{nn}}^\infty = \frac{\tau_0}{f} \cos(\alpha_{\text{GB}})^2$$

Profiles are extracted for macroscopic stresses between 260–450 MPa every 10 MPa in the vicinity of the first band (numbered 1) with a length \bar{L} at the centre of the grain boundary (see figure 7.1). As before, a fit is carried out with the model formulated by equation 7.10 with the introduction of the \tilde{A}_{nn} prefactor for several bands:

$$\sigma_{\text{nn}}(r) = \tilde{A}_{\text{nn}}(\theta_{\text{GBSB}}) \langle f\Sigma - \tau_0 \rangle \sqrt{\frac{\bar{L}}{t}} \left(\frac{t}{r} \right)^{1-\lambda} + \Sigma_{\text{nn}}^\infty \quad (7.13)$$

Once again it is verified that the exponent $1 - \lambda$ and the prefactor for several bands \tilde{A}_{nn} show very weak variations according to the macroscopic stress Σ .

The same master curve as previously shown in figure 7.3b is found for the exponent. This result confirms that the exponent is exclusively linked to the local plastic deformation of the slip band corner regardless of the number of stacked slip bands.

The prefactor evolutions parametrised by the number of slip bands, are displayed in figure 7.4 for the interband spacing of 1 μm . A similar shape and a decreasing amplitude of the prefactor are found with respect to the case of the single slip band which reveals a screening effect of the surrounding slip bands. These preliminary results would suggest a description of the prefactor \tilde{A}_{nn} with the following proportionality:

$$\tilde{A}_{\text{nn}}(\theta_{\text{GBSB}}, N_{\text{SB}}, \Theta_i) = r_{\text{scr}}(N_{\text{SB}}, \Theta_i) A_{\text{nn}} \quad (7.14)$$

introducing a screening ratio $r_{\text{scr}} < 1$, seemingly independent of the θ_{GBSB} angle and decreasing with N_{SB} , and with Θ_i , other influential parameters such as the interband spacing. Indeed, it is here verified for almost every θ_{GBSB} angles that the ratio between \tilde{A}_{nn} and A_{nn} is relatively close to the respective values of 0.48, 0.37 and 0.30 in the cases of 3, 5 and 7 slip bands. The related discrepancies with respect to some θ_{GBSB} configurations may certainly come from the fitting procedure applied on the solution computed here.

7. INTERGRANULAR FRACTURE INITIATION IN UNIRRADIATED AND IRRADIATED STAINLESS STEELS

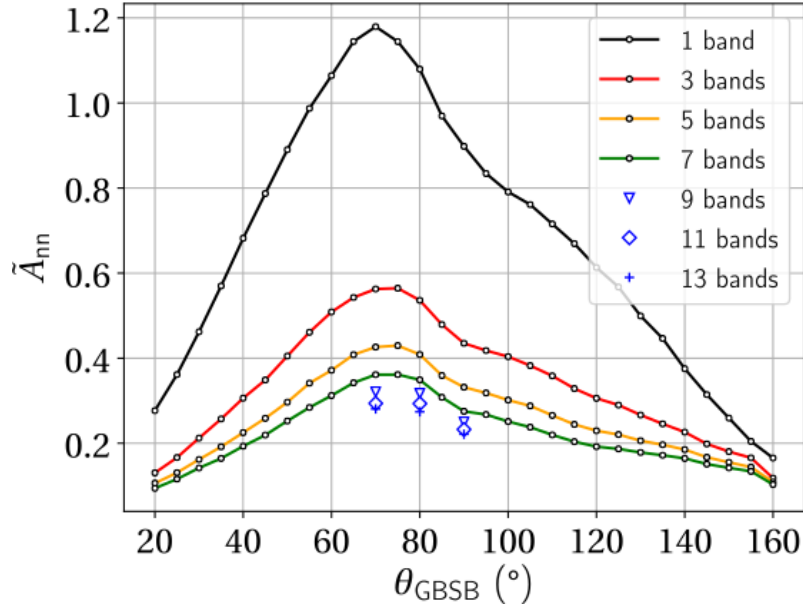


Figure 7.4: A_{nn} variation according to the θ_{GBSB} angle for one or several slip bands with an interband spacing of $1\ \mu\text{m}$.

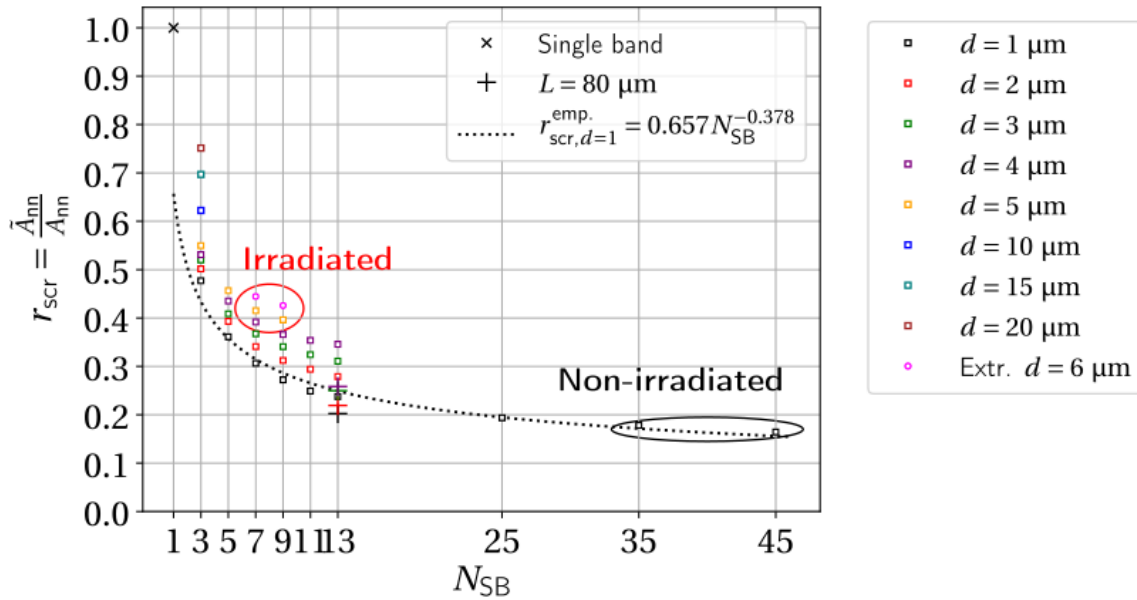


Figure 7.5: Variation of the screening ratio r_{scr} with respect to the number of slip bands N_{SB} and the interband spacing d .

7. INTERGRANULAR FRACTURE INITIATION IN UNIRRADIATED AND IRRADIATED STAINLESS STEELS

Further computational results at $N_{SB} = 9, 11$ and 13 slip bands are also provided for $\theta_{GBSB} = 70^\circ, 80^\circ$ and 90° . These results clearly indicate a progressive saturation of the prefactor \tilde{A}_{nn} with the increasing number of slip bands at one fixed θ_{GBSB} angle. This can be explained by the increase of the stacking sequence thickness, eventually reaching a value such that the influence of the two ends of the slip bands pile over the first band at the centre progressively vanishes.

In order to fully describe the evolution of the screening ratio r_{scr} for a possible extension of the model to unirradiated stainless steels, further computations are employed with 25, 35 and 45 slip bands in the stacking sequence, keeping a spacing of $1\ \mu\text{m}$ and a θ_{GBSB} angle of 70° .

In the case of irradiated stainless steels, a spacing of at most $5\text{--}6\ \mu\text{m}$ between clear channels is considered. Furthermore, it has been shown that the interchannel spacing decreases with the multiplication of clear channels during the accommodation of the plastic deformation. Therefore a complete set of configurations are used by varying the interband spacing between $2\text{--}5\ \mu\text{m}$, with a number of slip bands between 3 and 13 in the limits of the microstructure geometry. It is reminded that the grain size ϕ_G is assimilated to the size of the first slip band $\bar{L} = 40\ \mu\text{m}$.

The computed screening ratios are shown in figure 7.5 according to the number of slip bands and also reported in appendix C. Values between 15 % for unirradiated SS and 45 % for irradiated SS are reported. Concerning the influence of irradiation, these results therefore reveal that in the most detrimental case, a decrease of about 66 % of the A_{nn} prefactor could be considered for the intergranular normal stress induced by slip bands with respect to clear bands.

As stated before, a saturation of the decreasing ratio with the same number of bands seems to be evidenced even if a quasi-linear and steady progression seems to hold for stacking sequences between 25 and 45 slip bands.

A linear increase of the ratio is found with the increase of the interband spacing at a constant number of slip bands. It is believed that a linear extrapolation to higher values of d should be fairly acceptable. This linear progression is successfully verified further for a large variation of d between $2\text{--}20\ \mu\text{m}$ in the theoretical context of 3 parallel slip bands ; the case of the single band is clearly approached with the increase of d . Such an extrapolation is therefore used to deduce missing points at $d = 6\ \mu\text{m}$ for the cases with stacking sequences of $N_{SB} = 7$ and 9 clear channels.

Finally, similar calculations are performed with a mean grain size \bar{L} of $80\ \mu\text{m}$, a stacking sequence of 13 slip bands and interband spacings ranging between $2\text{--}4\ \mu\text{m}$. The influence of the mean grain size \bar{L} , is clearly not negligible.

In conclusion, the detrimental effect of the plastic localisation could be accounted for in the model via the screening ratio through the increase of the interband spacing, but also through the decrease of the number of slip bands which significantly raises the level of stress.

In fact, as suggested before in chapter 6, these two variables are intrinsically linked,

7. INTERGRANULAR FRACTURE INITIATION IN UNIRRADIATED AND IRRADIATED STAINLESS STEELS

through the grain size \bar{L} , considering a grain full of slip bands (or clear bands):

$$N_{SB} = \frac{\bar{L}}{d} \quad (7.15)$$

where d is presumably and primarily related to the material and to the irradiation dose. Should one consider an isolated grain without any plasticity in the neighbouring grains and a constant value of d related to the irradiated stainless steel considered, the model qualitatively and quantitatively confirms that the detrimental effect of irradiation could partly originate from the restrained number of clear channels that accommodate the same plastic deformation with respect to its unirradiated counterpart for the same grain size.

Special care should be taken with the number of slip bands N_{SB} in equation 7.15 when considering a variation of the grain size. Indeed, it was discussed in chapter 6, that the grain size may have an influence on the interband spacing d . The above equation should therefore be completed as follows:

$$N_{SB} = \frac{\bar{L}}{d(\bar{L})} \quad (7.16)$$

where the evolution $d(\bar{L})$ is still unclear.

The following section will then focus on the prediction of microcracks initiations based on the preceding stress field model and its characterisation in the context of several slip bands or clear channels in one isolated grain.

7.3 Criterion for intergranular crack initiation and multiscale chaining

7.3.1 Application of the coupled criterion: a bottom-up approach

Following the preceding results, the stress singularity exponents computed are lower than 0.5 for all the configurations. As extensively explained in chapter 5 and in the introduction of chapter 6, should a criterion for intergranular fracture initiation at a slip band (or clear band) impact be considered with the above model, the energy criterion of Griffith is not sufficient.

The use of the coupled criterion is then clearly indicated in these problems, as already advanced by Sauzay et al. [Sauzay and Vor, 2013, Sauzay and Moussa, 2013]. These later studies have shown, that similarly to the asymptotic expansion of the stress singularity to the close-field at the tip of a V-notch, the amount of energy per unit area $\gamma(a)$ released for the initiation of a finite crack increment of size a in the vicinity of the slip band, follows the formulation:

$$-\frac{\delta W}{A} = \gamma(A) = C(f\Sigma - \tau_0)^2 L \left(\frac{a}{t}\right)^{2\lambda-1} + .. \quad (7.17)$$

7. INTERGRANULAR FRACTURE INITIATION IN UNIRRADIATED AND IRRADIATED STAINLESS STEELS

considering the stress singularity of equation 7.10, with C , a prefactor similar to the $\mathcal{A}(\omega)$ prefactor computed by [Henninger, 2007] in the case of the V-notch (see chapter 5). As before, A corresponds to the area of the crack increment: $A = a \times e$, with e the thickness in the z direction perpendicular to the 2D plane.

In order to compute the C prefactor, Sauzay et al. have conveniently used the $G-\theta$ method implemented in Cast3m, to compute the energy release rate at the tip of a precrack of size a , introduced in the mesh along the grain boundary.

As already mentioned in chapter 5 in the case of the V-notch, it can be readily demonstrated that considering equation 7.17, the classical energy release rate $G(a)$ for crack of size a , which further grows continuously after initiation, follows from the derivate of the potential energy $W(a)$:

$$G(a) = - \lim_{\delta a \rightarrow 0} \frac{W(a + \delta a) - W(a)}{\delta A} \quad (7.18)$$

$$= 2\lambda C (f\Sigma - \tau_0)^2 L \left(\frac{a}{t} \right)^{2\lambda-1} + .. \quad (7.19)$$

$$= C' (f\Sigma - \tau_0)^2 L \left(\frac{a}{t} \right)^{2\lambda-1} + .. \quad (7.20)$$

with the crack area increment $\delta A = \delta a \times e$ and $C' = 2\lambda C$. Following the same $G-\theta$ method, the previous computations carried out for the single slip bands are reemployed by introducing a precrack in the different meshes. At each θ_{GBSB} angle, five computations are used with the different precrack sizes of 9, 12, 15, 18 and 21 nm.

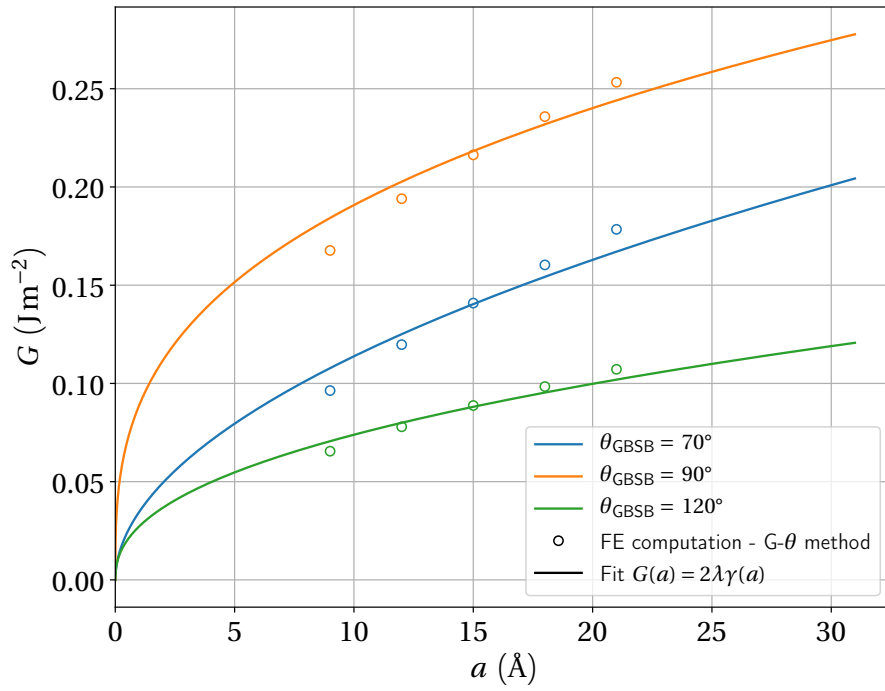
Figure 7.6a shows the results obtained for the θ_{GBSB} angles of 70°, 90° and 120°, along with the fit carried out using equation 7.20 with the same related exponents found before and displayed in figure 7.3b. The fitted C' prefactors (normalised by the shear modulus μ) are displayed in figure 7.6b according to the θ_{GBSB} angle of the configuration treated. The normalisation by the shear modulus μ clearly shows a rather satisfying agreement with the A_{nn} prefactor computed before on the intergranular stress profiles. It is therefore suggested that the following simplification can be made:

$$C' = \frac{A_{nn}}{\mu} \quad \text{or} \quad C = \frac{A_{nn}}{2\lambda\mu} \quad (7.21)$$

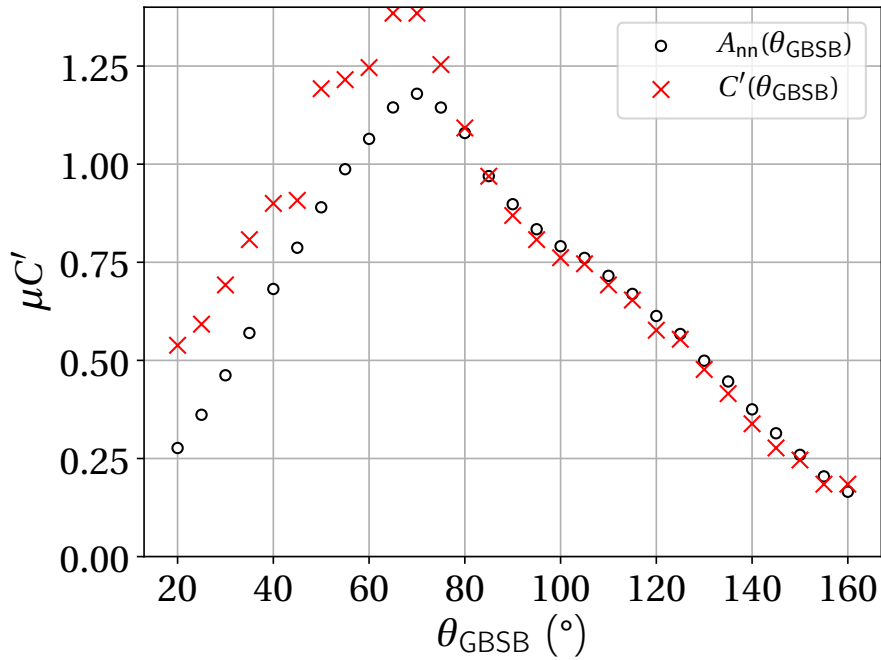
although figure 7.6b shows discrepancies for θ_{GBSB} angles between 20° and 75°. However, it is believed that the $G-\theta$ method and the fitting procedure may have an impact on the computed energy release rate depending on the configuration treated. For the remaining of this chapter, equation 7.21 is therefore considered to be acceptable. Due to the cost of the numerous computation that would be needed, the same fitting procedure is not carried out in the case of several slip bands. The hypothesis is made once again that equation 7.21 holds in these cases, although the related verifications are not provided here.

Finally, based on equations 7.10, 7.17, and on the application of the coupled criterion (annexe D), Sauzay et al. have deduced a model of a macroscopic critical stress Σ_c for

7. INTERGRANULAR FRACTURE INITIATION IN UNIRRADIATED AND IRRADIATED STAINLESS STEELS



(a)



(b)

Figure 7.6: Fit of equation 7.20 on the energy release rate computed in FE analysis using the G- θ method for precracks of size $a = 9, 12, 15$ and 21 nm (7.6a). Resulting C' prefactor normalised by the shear modulus μ and A_{nn} prefactor according to the θ_{GBSB} angle of the configuration (7.6b).

7. INTERGRANULAR FRACTURE INITIATION IN UNIRRADIATED AND IRRADIATED STAINLESS STEELS

the initiation of an intergranular crack of finite size a_c :

$$\Sigma_c = \frac{1}{f} \left[\tau_0 + \left(\frac{1}{C(\theta_{\text{GBSB}})} \right)^{1-\lambda} A_{nn}^{1-2\lambda}(\theta_{\text{GBSB}}) \sqrt{\frac{t}{L}} \sigma_c^{2\lambda-1} \left(\frac{\gamma_{\text{frac}}}{t} \right)^{1-\lambda} \right] \quad (7.22)$$

$$a_c = \frac{\gamma_c}{\sigma_c} \frac{A_{nn}^2}{C} \quad (7.23)$$

which clearly represents a multiscale model with microscopic and atomistic parameters:

- The Schmid factor f , the initial critical resolved shear stress τ_0 , the thickness t and the length L (or the averaged length \bar{L}) of the slip band(s) or clear channel(s).
- The atomistic critical stress to fracture initiation σ_c and the critical energy γ_c .

Following the work of Sauzay et al., this chapter therefore provides a full characterisation of the semi-analytical parameters A_{nn} , C and λ for numerous configurations. Furthermore, it is shown that, using equation 7.21, the above model can then be simplified:

$$\Sigma_c = \frac{1}{f} \left[\tau_0 + (2\lambda\mu)^{1-\lambda} A_{nn}^{-\lambda}(\theta_{\text{GBSB}}) \sqrt{\frac{t}{L}} \sigma_c^{2\lambda-1} \left(\frac{\gamma_{\text{frac}}}{t} \right)^{1-\lambda} \right] \quad (7.24)$$

$$a_c = \frac{\gamma_c}{\sigma_c^2} 2\lambda\mu A_{nn} \quad (7.25)$$

However, this simplification would need further computations involving different materials with different shear modulus, since it is not completely clear why equation 7.21 should hold.

This multiscale model is now used in the remaining of this chapter.

At first, a comparison of the model (which is a bottom-up approach) with adapted top-down simulations is carried out, similarly to the approach of chapter 5. As before, this part is intended to validate the use of the coupled criterion in conjunction with atomistic inputs. Finally, the model is then extensively employed for a comparison to numerous experimental data in the case of irradiated and unirradiated stainless steels pulled under oxidising environment.

7.3.2 Bottom-up and top-down approaches for the failure of several CSL nickel grain boundaries

This part focuses on the development of top-down simulations to be compared to the bottom-up approach using the coupled criterion, in the preceding context of a single slip band impacting a grain boundary. As before, a 2D plane strain hypothesis is made. In that regard, specific grain boundaries have to be considered for the simulations. Once again, pure nickel is chosen to model a FCC material in the MD simulations in order to access to a better understand the underlying mechanisms. Regardless of the discrepancies between austenitic SS and pure nickel, these simulations are merely

7. INTERGRANULAR FRACTURE INITIATION IN UNIRRADIATED AND IRRADIATED STAINLESS STEELS

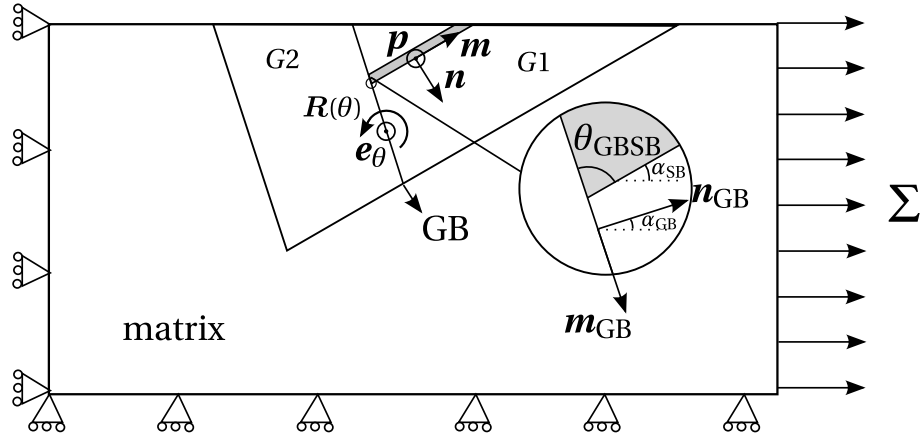


Figure 7.7: Scheme of the configuration considered for the simulations: one discontinuous slip band (or clear band) activated in the first grain (G1), impacting a grain boundary at an angle θ_{GBSB} without transmission in the neighbouring grain (G2). G1 and G2 crystallographic orientations are related by the rotation $R(\theta)$ around the unit rotation vector e_θ . n and m are the normal and unit slip vector of the activated slip system while n_{GB} and m_{GB} are the normal vector and direction of the grain boundary.

intended to validate the use of the coupled criterion at the atomic scale in the slip band/grain boundary interaction case.

It is finally reminded that, the finite element method and molecular dynamics simulations on bicrystals are also used to better decipher the GB behaviour subsequently assessed by the top-down simulations. These two aspects are presented in the next two subsections before the presentation of the top-down simulations and the related results in the remaining subsections.

7.3.2.1 Configuration of the problem and CSL $\langle 211 \rangle$ symmetric tilt grain boundaries

Figure 7.7 represents the configuration used for the finite element computations. A well-oriented slip band with $\alpha_{SB} = 45^\circ$ is considered. It is reminded that using a type B slip band induces the presence of the normal vector n and the unit slip vector m of the activated slip system, in the 2D plane.

In FCC materials, the slip systems are described by the pairs $(n, m) = \{111\} \langle 110 \rangle$. In the simulations, the vectors $n = \frac{1}{\sqrt{3}} [\bar{1}11]$ and $m = \frac{1}{\sqrt{2}} [110]$ are used for the example.

As illustrated in figure 7.7, this choice automatically induces a vector $p = n \wedge m = \frac{1}{\sqrt{6}} [\bar{1}1\bar{2}]$, perpendicular to the 2D plane. The CSL symmetric tilt grain boundaries that have to be considered in the MD simulations therefore impose a rotation axis along the vector $e_\theta = [\bar{1}1\bar{2}]$, partially defining the rotation $R(\theta)$, between the two grains G1 and G2.

The $\langle 211 \rangle$ symmetric tilt grain boundaries have been studied by Shimokawa [Shimokawa,

7. INTERGRANULAR FRACTURE INITIATION IN UNIRRADIATED AND IRRADIATED STAINLESS STEELS

2010] in pure aluminium. Among the numerous CSL grain boundaries treated in this study, the $\Sigma 5$ [02 1] and the $\Sigma 101$ [68 1] are chosen.

Considering the orientation of the slip system and the normal vector to the grain boundary, the α_{GB} angle and subsequently the θ_{GBSB} angle are deduced and reported in figure 7.9a for the two selected GBs.

Finite element computations can then be carried out using these parameters.

7.3.2.2 Finite element computations

As extensively explained in chapter 5, the present FE computations are used to extract the displacement fields to be used in the top-down approach at different macroscopic remote stresses Σ .

Two meshes are used for the two preceding configurations ($\Sigma 5$ and $\Sigma 101$ GBs) ; with the indicated parameters of figure 7.9a and a single slip band of length $L = 20 \mu\text{m}$ and thickness $t = 200 \text{ nm}$ at $\alpha_{SB} = 45^\circ$. A mesh size of 3 \AA is used in the refinement disk. The elastic constants for pure nickel $C_{11} = 241.3 \text{ GPa}$, $C_{12} = 150.8 \text{ GPa}$ and $C_{44} = 127.3 \text{ GPa}$ at 0 K (as reported using the MD potential of Mishin) are employed to consider cubic elasticity with the related grain orientations referenced in figure 7.9a.

As before, the same elastoplastic law is employed with the same parameters except for the cubic elasticity and the initial resolved shear stress τ_0 , which is chosen at 100 MPa. This particular choice is made to facilitate the convergence of the calculations. It is somehow irrelevant here, since only a comparison between two approaches using the same parameters is intended.

Solutions of the FE computations are recorded every $\Sigma = 50 \text{ MPa}$. Deformation profiles are extracted along the GB from the tip of the slip band corner. The variation of the ε_{nn} , ε_{mm} and γ_{nm} deformation components (in the $(\mathbf{m}_{GB}, \mathbf{n}_{GB})$ referential of figure 7.7) are displayed in figures 7.8a and 7.8b for the $\Sigma 5$ and $\Sigma 101$ GBs respectively at a macroscopic remote stress of $\Sigma = 1 \text{ GPa}$.

Additionally, the transverse/normal strain ratio $\alpha_\varepsilon = \frac{\varepsilon_{mm}}{\varepsilon_{nn}}$ and the shear/normal strain ratio $\eta_\varepsilon = \frac{\gamma_{nm}}{\varepsilon_{nn}}$ are plotted at $\Sigma = 1 \text{ GPa}$ according to the distance r along the GBs in figures 7.8c and 7.8d and at $r = 3 \text{ \AA}$ according to the macroscopic remote stress Σ in figure 7.8e and 7.8f. From the plane strain hypothesis, the transverse/normal strain ratio $\beta_\varepsilon = \frac{\varepsilon_{pp}}{\varepsilon_{nn}} = 0$ since $\varepsilon_{pp} = 0$.

From these results, it can be assessed that whatever the distance r between 0 and 1 nm and whatever the loading Σ above 500 MPa:

- For the $\Sigma 5$ GB: α_ε is between 0 and -0.05 and $|\eta_\varepsilon| > 1.5$.
- For the $\Sigma 101$ GB: α_ε and η_ε are at least above 0.4 with a mean value around 0.6.

These first-hand assessments are subsequently guiding the MD multiaxial strain loadings applied on the bicrystals containing the $\Sigma 5$ and the $\Sigma 101$ GBs.

7. INTERGRANULAR FRACTURE INITIATION IN UNIRRADIATED AND IRRADIATED STAINLESS STEELS

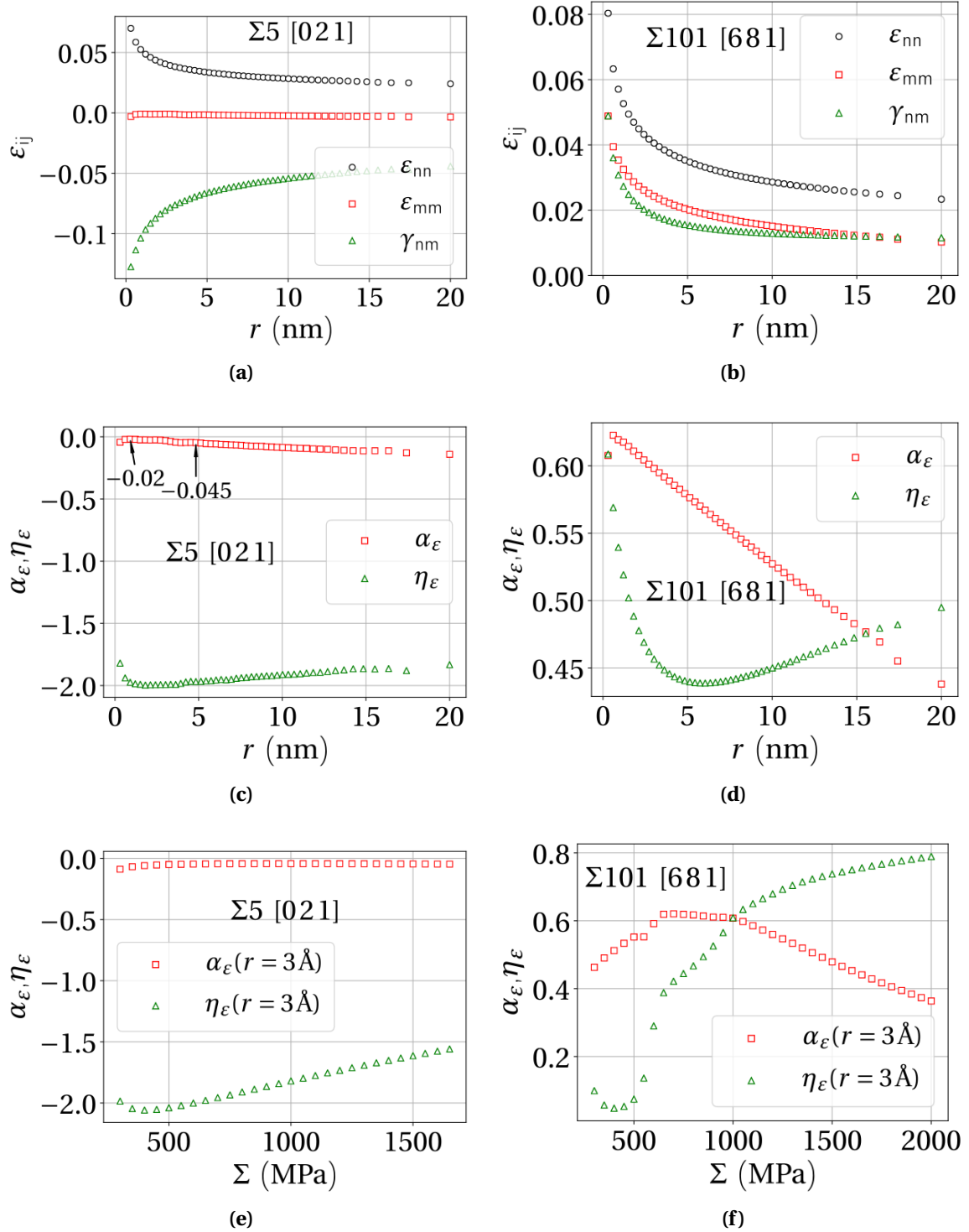


Figure 7.8: Deformation profiles along the two grain boundaries ($\Sigma 5$ and $\Sigma 101$) at a remote stress of $\Sigma = 1$ GPa (7.8a) and (7.8b) ; related α_ε (transverse deformation) and η_ε (shearing deformation) ratios profiles (7.8c) and (7.8d). The deformation components ε_{nn} , ε_{mm} and γ_{nm} are taken in the $(\mathbf{m}_{GB}, \mathbf{n}_{GB})$ referential. The evolution of the same ratios at a distance $r = 3 \text{ \AA}$ from the tip of the slip band are also given according to the remote applied stress Σ for the two GBs (7.8e) and (7.8f).

7. INTERGRANULAR FRACTURE INITIATION IN UNIRRADIATED AND IRRADIATED STAINLESS STEELS

7.3.2.3 Molecular dynamics computations on bicrystals

For the two bicrystals, the scheme and the table in figure 7.9a fully describe the two systems considered for the multiaxial loadings. In agreement with the atomic configurations obtained by Shimokawa in aluminum, the atomic structures of the $\Sigma 5$ and $\Sigma 101$ GBs are displayed in figure 7.9b after their formation at 10 K following the same method of chapter 2. In particular, the same structural units |C| and |AABAAAB| are found for the $\Sigma 5$ and $\Sigma 101$ respectively. Contrarily to the $\Sigma 5$ GB, the $\Sigma 101$ GB features a quite heterogeneous structure with A and B units scattered on an extended period along the grain boundary plane. The atomic stress fields $\sigma_{yy}^{at.}$ displayed in figure 7.9a further identify the disclination sites featuring the highest atomic stresses.

Following the same method extensively described in chapter 2 and the α_ε and η_ε ranges assessed before in the vicinity of the activated slip band, the multiaxial strain loadings performed on the bicrystals containing the $\Sigma 5$ and $\Sigma 101$ GBs yield the results presented in figures 7.10 and 7.11 respectively. Figures 7.10a and 7.11a present the behaviour maps introduced in chapter 2 which reference the critical stress to either partial dislocation nucleation ($\sigma_{yy}^{c,disl}$) or grain boundary decohesion ($\sigma_{yy}^{c,deco}$) according to the α_ε and η_ε strain ratios. Figures 7.10b and 7.11b, 7.11c, 7.11d provide the visualisation of the underlying mechanisms obtained at the critical events for ($\alpha_\varepsilon, \eta_\varepsilon$ ratios around the assessments previously obtained by FE analysis for the two GBs (at $(-0.1, -2)$ for the $\Sigma 5$ GB and at $(0.6, 0.6)$ for the $\Sigma 101$ GB).

Based on these behaviour maps, the following predictions on the GBs behaviour, subjected to the stress field previously assessed by FE computations, can be suggested:

- For the $\Sigma 5$ GB, a mixed behaviour between grain boundary sliding and decohesion or grain boundary sliding and heterogeneous dislocation nucleation is expected. Figure 7.10b typically shows such a behaviour.
- For the $\Sigma 101$ GB, a decohesion without any dislocation nucleation is expected. Figures 7.11b, 7.11c and 7.11d display the decohesion mechanism obtained for $\alpha_\varepsilon = \eta_\varepsilon = 0.6$. As previously observed in chapter 4 and 5 the GB decohesion is occurring by the debonding of the disclination sites through void nucleation and coalescence.

In both cases, it is clear that the shear strain γ_{nm} is not negligible and should have a significant influence on the GBs behaviours in the vicinity of the slip bands. In particular, grain boundary migrations after grain boundary sliding is evidenced in numerous cases when $\eta_\varepsilon > 0$.

7.3.2.4 Top-down approach

The top-down approach undertaken in the context of the slip band/grain boundary interaction is now succinctly described. The same steps indicated in chapter 5 are

7. INTERGRANULAR FRACTURE INITIATION IN UNIRRADIATED AND IRRADIATED STAINLESS STEELS

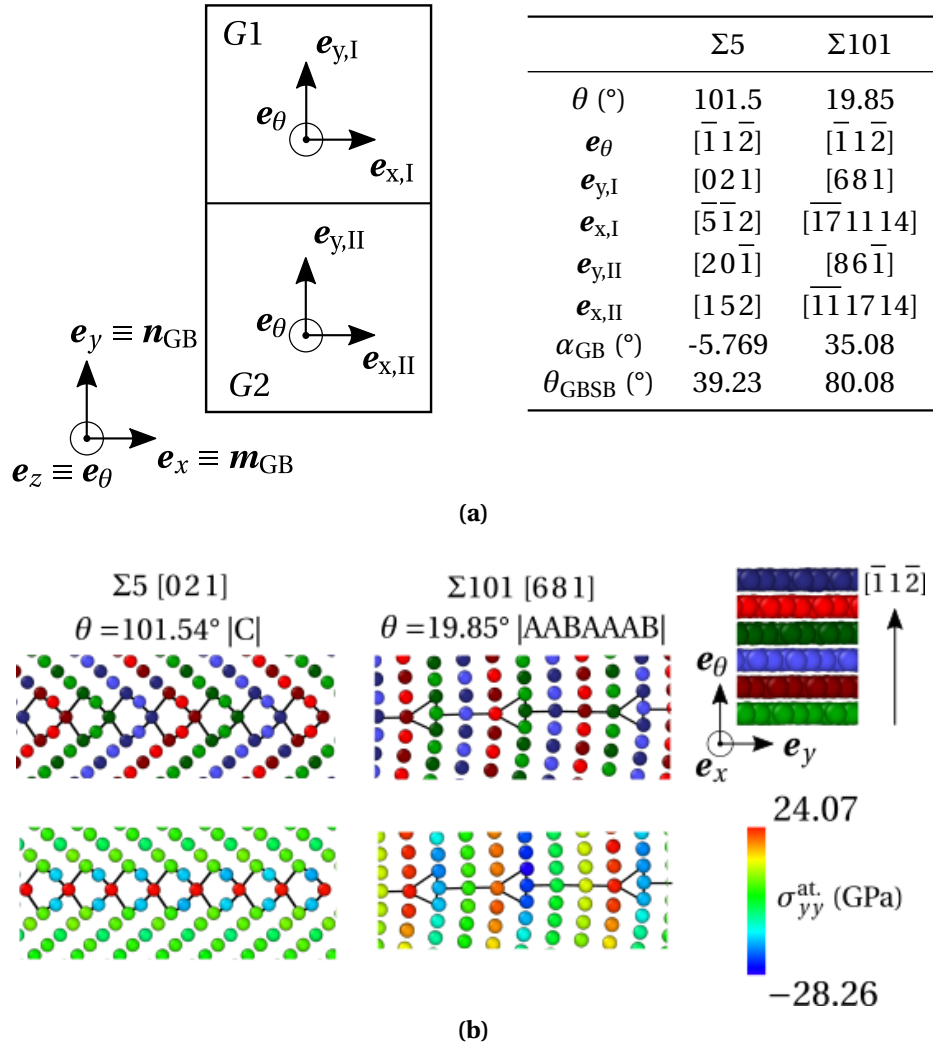
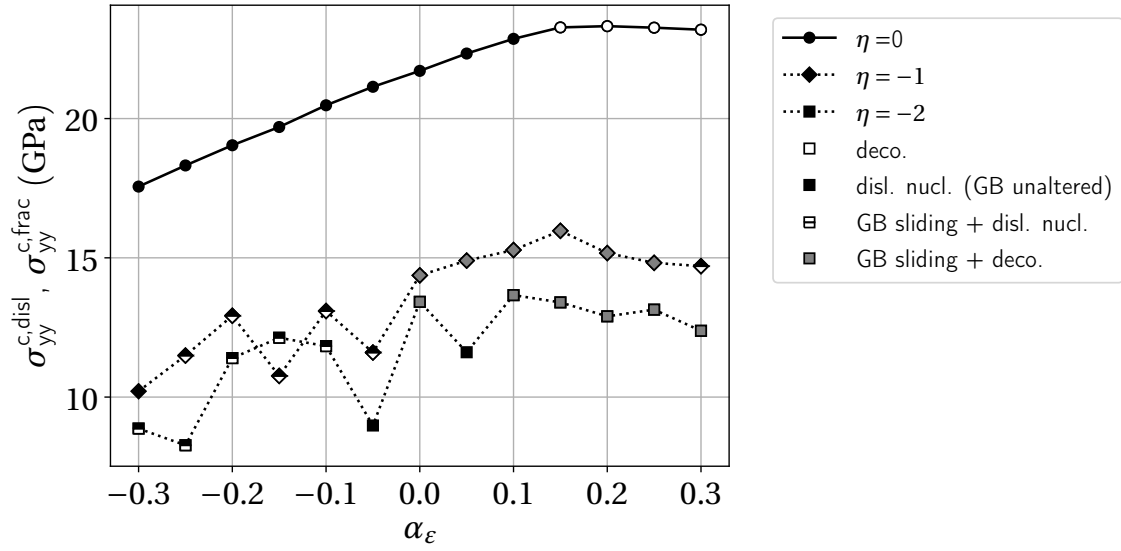
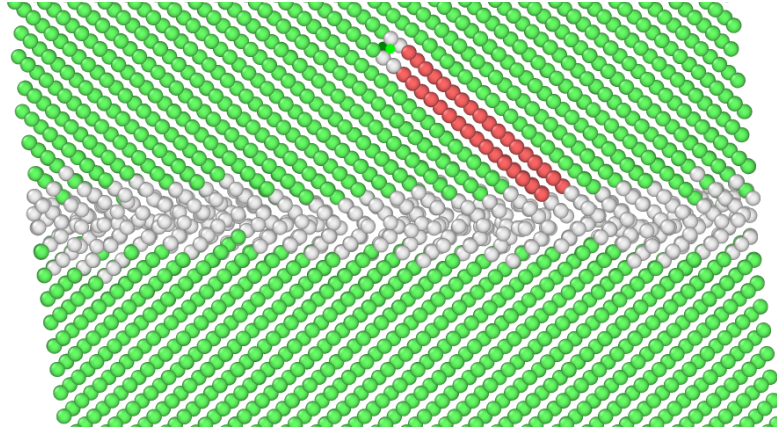


Figure 7.9: Scheme and parameters of the simulated bicrystals containing the $\Sigma 5$ and $\Sigma 101$ GBs (7.9a). Atomic structures and atomic stress field obtained after a GB formation at 10 K (7.9b).

7. INTERGRANULAR FRACTURE INITIATION IN UNIRRADIATED AND IRRADIATED STAINLESS STEELS



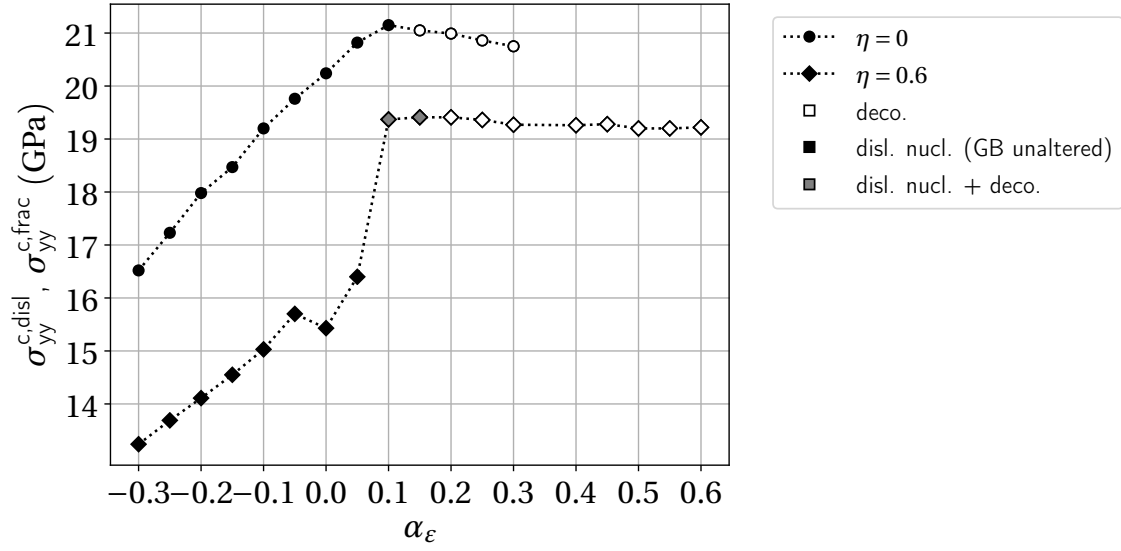
(a)



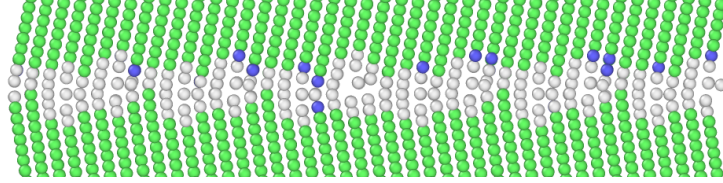
(b)

Figure 7.10: Behaviour map of the $\Sigma 5$ GB referencing the critical stress to GB dislocation nucleation or decohesion according to the α_ϵ and η_ϵ deformation ratios (7.10a). GB dislocation nucleation at $\alpha_\epsilon = -0.1$ and $\eta_\epsilon = -2$ (7.10b).

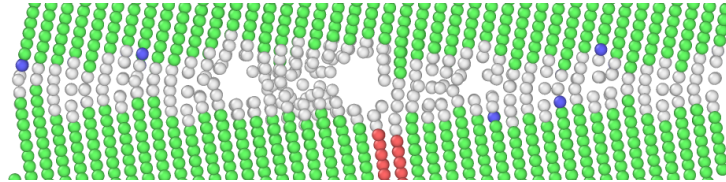
7. INTERGRANULAR FRACTURE INITIATION IN UNIRRADIATED AND IRRADIATED STAINLESS STEELS



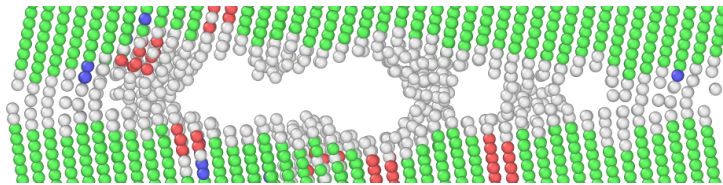
(a)



(b)



(c)



(d)

Figure 7.11: Behaviour map of the $\Sigma 101$ GB referencing the critical stress to GB dislocation nucleation or decohesion according to the α_ϵ and η_ϵ deformation ratios (7.11a). GB decohesion mechanism at $\alpha_\epsilon = 0.6$ and $\eta_\epsilon = 0.6$ (7.11b), (7.11c) (7.11d).

7. INTERGRANULAR FRACTURE INITIATION IN UNIRRADIATED AND IRRADIATED STAINLESS STEELS

followed. The only exception to the procedure, consists on the presence of the slip band in the refinement disk as illustrated (in red) in figure 7.12.

Since only the elastic part of the disk is under focus during the MD relaxation after predeformation, it is chosen to freeze the atoms (i.e. zero velocity vectors for the corresponding atoms) in the slip band part. In complement to the grey crown of frozen atoms, the atoms of the slip band will effectively contribute to the loading application on the elastic part of the disk during the relaxation. The presence of the slip band part is mandatory to prevent free surface boundary conditions that are not wanted here. Meanwhile, the strong plastic deformations mapped on the slip band part of the disk (from the FE computations of the displacement field), obviously lose their significance at the atomic scale, which further justifies the freezing of this group of atoms during the relaxation.

In this respect, the present top-down simulations obviously use strong hypothesis as the atomic structure of the slip bands part of the disk along with the GB structure resulting from numerous extrinsic dislocations flow at a particular given remote stress Σ are not considered here.

The bottom scheme in figure 7.12 illustrates the formation and the predeformation of the disk of atoms to be subsequently relaxed in the case of the $\Sigma 101$ GB at a macroscopic remote stress of 1050 MPa.

7.3.2.5 Results of the two approaches

The following results are found for the top-down simulations:

- For the $\Sigma 5$ GB, dislocation nucleation at the tip of the slip band are recorded first (figure 7.13) for a macroscopic remote stress of $\Sigma = 800$ MPa. As expected, grain boundary sliding is evidenced prior to the dislocation nucleation. It is verified for several loading inferior to 800 MPa that only grain boundary sliding without any critical events are observed. Since the relaxation are performed on predeformed atomic configurations every 50 MPa, the first dislocation nucleation is therefore located between 750 MPa (no critical events are recorded) and 800 MPa.
- For the $\Sigma 101$ GB, a grain boundary decohesion is recorded at 1050 MPa without dislocation nucleation or GB decohesion before this loading. Figure 7.14 shows several steps of the relaxation carried out at $\Sigma = 1050$ MPa, revealing a significant GB migration through GB sliding before decohesion. As expected, the decohesion mechanism is once again clearly correlated to the void nucleation and coalescence at the disclination sites previously identified in figure 7.9b and marked by the grid in figure 7.14. The crack initiation is also localised at the tip of the slip band.

Illustrations of the above results are provided in figures 7.13 and 7.14 after a 20 ps relaxation of the corresponding predeformed configurations.

Similarly to the V-notch case of chapter 5, the behaviour observed for the $\Sigma 5$ and $\Sigma 101$ are in agreement with the behaviours observed on bicrystals, considering the

7. INTERGRANULAR FRACTURE INITIATION IN UNIRRADIATED AND IRRADIATED STAINLESS STEELS

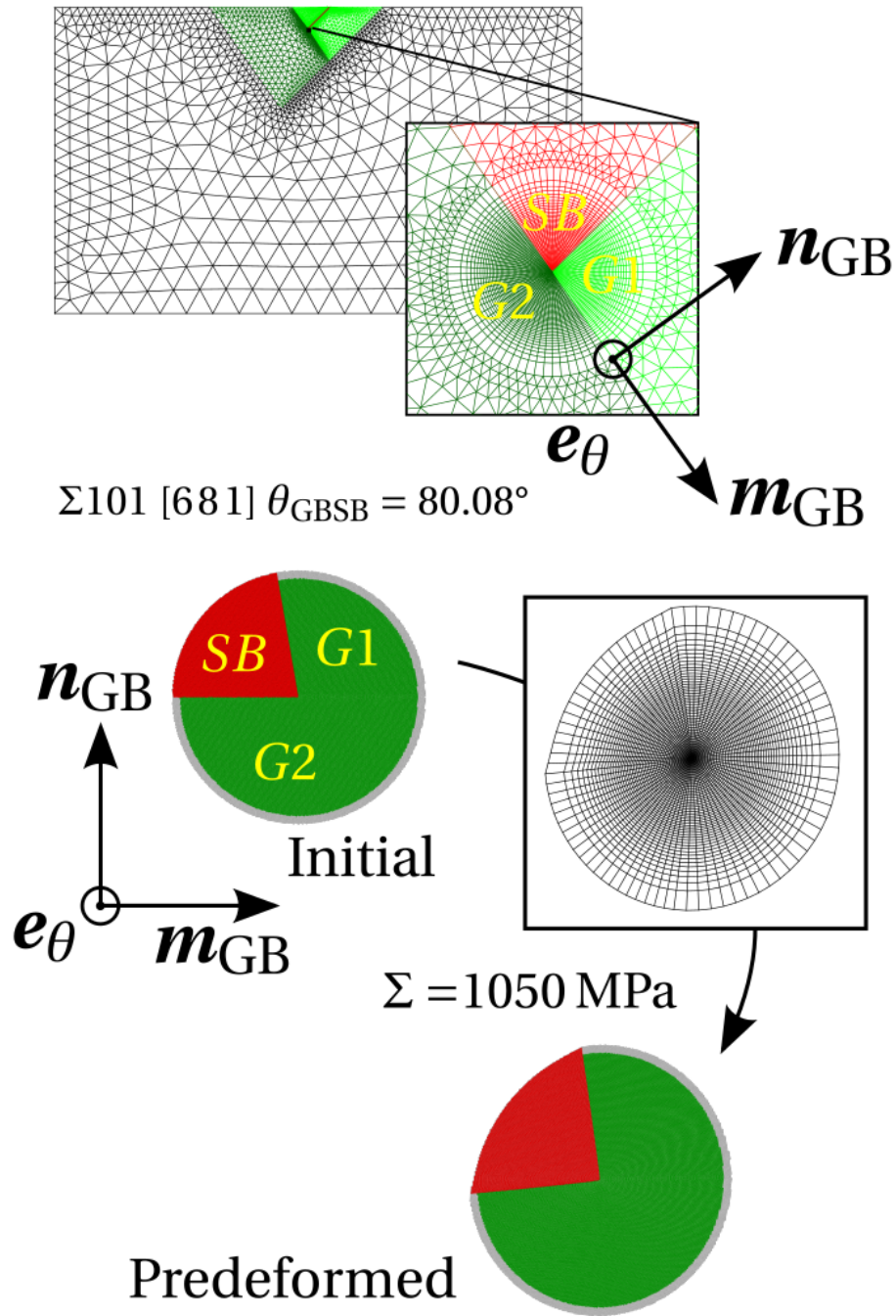


Figure 7.12: Finite element mesh used in the case of the $\Sigma 101$ GB considering a discontinuous slip band/grain boundary impact with a focus on the refinement disk (lower picture of 7.12). Predeformation process for the top-down simulations from the initial configuration of the $\Sigma 101$ GB, referencing the Slip Band (SB) part (in red), the two grains $G1$ and $G2$ (in green) and the crown of frozen atoms (in grey), to the predeformed configuration to be relaxed after the displacement mapping obtained at a 1050 MPa remote stress.

7. INTERGRANULAR FRACTURE INITIATION IN UNIRRADIATED AND IRRADIATED STAINLESS STEELS

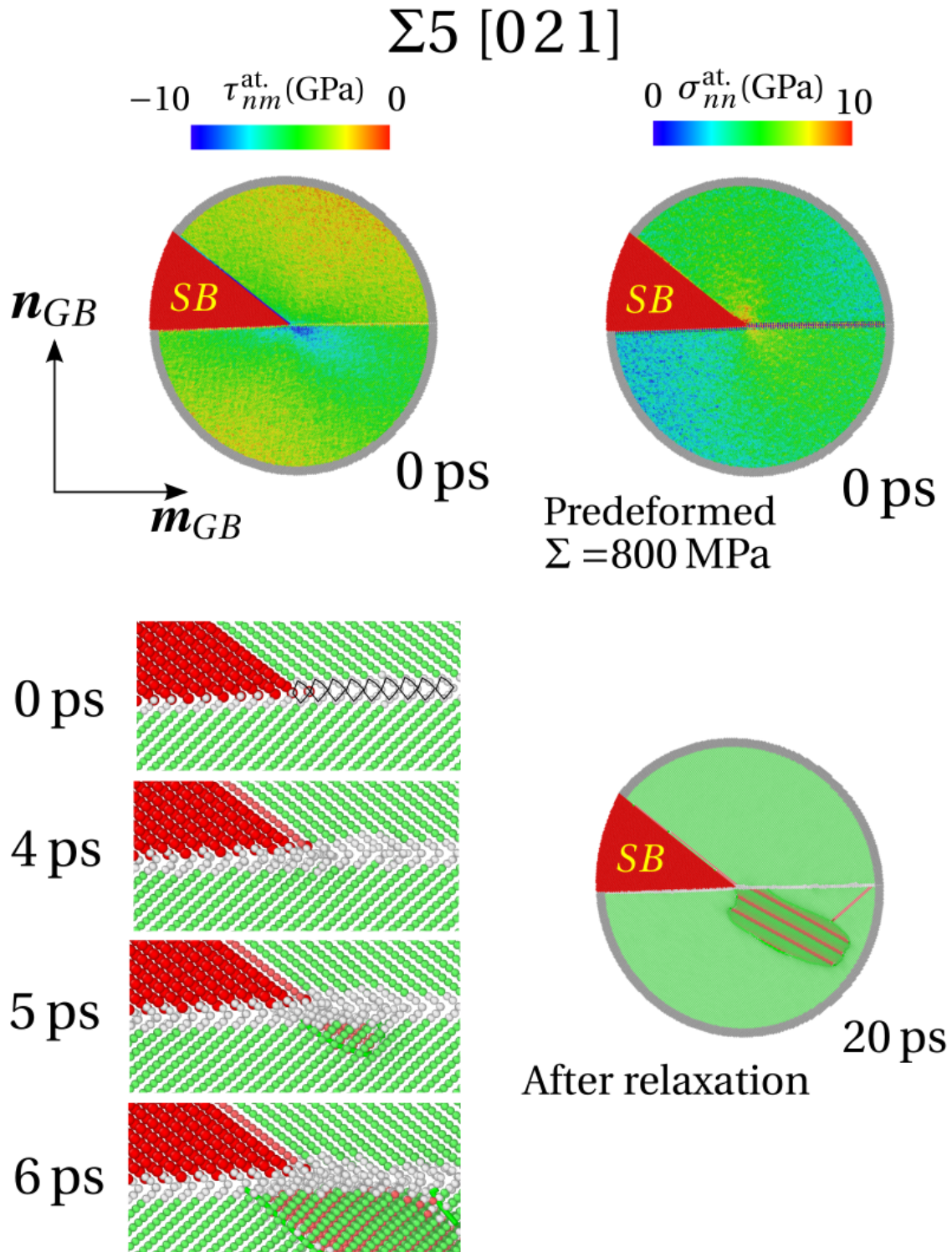


Figure 7.13: Atomic stress field $\tau_{nm}^{\text{at.}}$ and $\sigma_{nn}^{\text{at.}}$ components recorded on the predeformed atomic configurations of the $\Sigma 5$ GB at a $\Sigma = 800 \text{ MPa}$ loading (upper picture). Dislocation nucleation mechanism from the grain boundary computed at several relaxation steps (lower picture).

7. INTERGRANULAR FRACTURE INITIATION IN UNIRRADIATED AND IRRADIATED STAINLESS STEELS

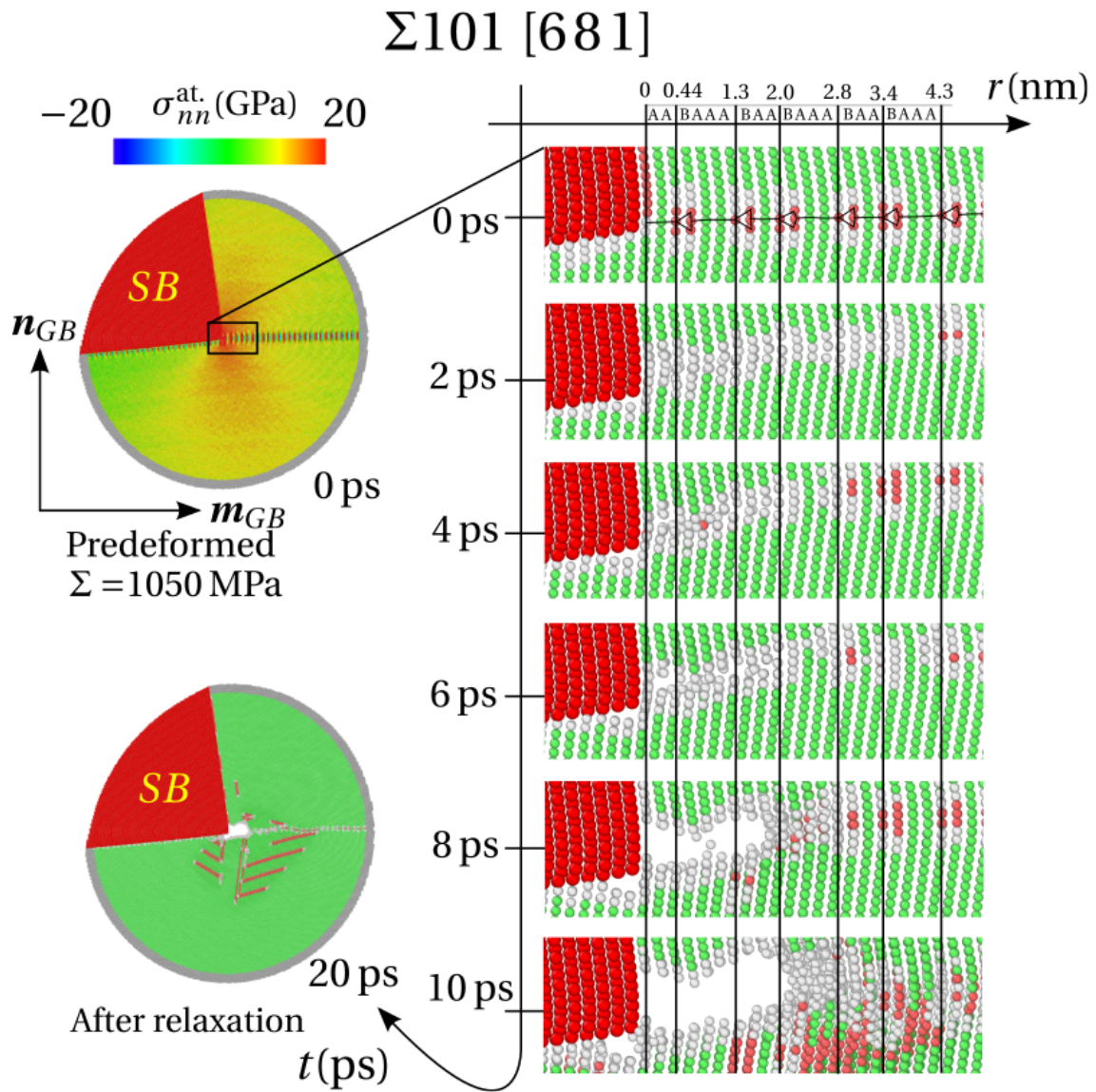


Figure 7.14: Atomic stress field $\sigma_{nn}^{at.}$ component recorded on the predeformed atomic configurations of the $\Sigma 101$ GB at a $\Sigma = 1050 \text{ MPa}$ loading along with the GB decohesion mechanism at several relaxation steps.

7. INTERGRANULAR FRACTURE INITIATION IN UNIRRADIATED AND IRRADIATED STAINLESS STEELS

μ (GPa)	f	τ_0 (MPa)	t (nm)	L (μm)	$1 - \lambda$	A_{nn}	σ_c (GPa)	γ_c (mJm^{-2})
48.2	0.5	100	200	20	0.289	1.079	19.28	3763

Table 7.2: Inputs used for the application of the multiscale model in the case of one discontinuous slip band impact a $\Sigma 101$ [681] grain boundary.

α_ε , β_ε and η_ε ratios assessed by FE computations. This point confirms once again the relevance of studying the GBs mechanical behaviour by MD multiaxial simulations on bicrystals.

In particular, it is interesting to note that the shearing deformation that are significantly higher for the case of the $\Sigma 5$ GB will preferentially trigger a dislocation nucleation mechanism. The influence of the stress field in the vicinity of the slip band/grain boundary is clearly underlined here. It is reminded that this stress field is actually intrinsically linked to the grain boundary by the geometrical constraints exposed before for the presentation of the FE model. But it is not linked to the intrinsic GB behaviour map presented before. Therefore, these two aspects (namely: the GB intrinsic behaviour and the intergranular stress field) have to be considered both when assessing and comparing the strength of grain boundaries.

An application of the multiscale model of equation 7.24 is carried out in the case of the $\Sigma 101$ grain boundary. As a reminder, the parameters of table 7.2 are used for that purpose, in coherency with the top-down simulations.

The shear modulus μ is obtained from the Voigth average:

$$\mu = \frac{1}{5} (C_{11} - C_{12} + 3C_{44}) \quad (7.26)$$

with the elastic constant C_{ij} at 0 K, recorded by the potential of Mishin for pure nickel. The λ and A_{nn} coefficients for a single band at $\theta_{\text{GBSB}} = 80^\circ$ plotted in figure 7.3 are used. The critical stress and critical energy are taken from the MD results on bicrystals at $\eta_\varepsilon = 0.6$, in coherency with the previous FE results.

Predicted values of $\Sigma_c = 911$ MPa and $a_c = 7.5 \text{ \AA}$ are obtained for the remote critical stress and the finite crack increment size at initiation. The remote critical stress predicted by this bottom-up approach is only 9–15 % lower than the range 1000–1050 MPa assessed by the top-down simulation. This comparison is rather satisfying. The discrepancies observed, could be explained either by the anisotropy, atomistic-related mechanisms or the non-linear elasticity that are taken into account in the top-down approach. Finally, the predicted value of the crack increment is far from being incoherent from an atomistic point of view (it is reminded that the lattice parameter of pure nickel at 0 K is at 3.52 \AA). Furthermore, it is small enough ($a_c < \frac{t}{10}$) so that the use of the coupled criterion in the close-field is still relevant. However, for the same reasons exposed in chapter 5, this crack increment a_c is not detectable in the top-down simulations. Indeed, considering the exponent $\lambda > \frac{1}{2}$, it is clear that the resulting crack size of roughly 2.7 \AA observed in figure 7.14 after the 20 ps relaxation at $\Sigma = 1050$ MPa, could probably

7. INTERGRANULAR FRACTURE INITIATION IN UNIRRADIATED AND IRRADIATED STAINLESS STEELS

results from the propagation of the initiated crack a_c that should probably happen at a lower stress value ($1000 \text{ MPa} < \Sigma < 1050 \text{ MPa}$). Even though more simulations involving more GBs for different θ_{GBSB} angles, would be needed to confirm it, the above results encourage and partly validate the use of the multiscale model of equation 7.24 with atomistic inputs from the application of the coupled criterion.

This model is finally used in the next section for a comparison to experimental results obtained on irradiated and unirradiated austenitic SS pulled under oxidising environment.

7.4 Application of the multiscale model and comparison with experimental data

7.4.1 Molecular dynamics inputs for predicting the fracture of oxidized grain boundaries

7.4.1.1 Oxidized grain boundaries and MD simulations

In this part, oxide penetrations are assumed to be developed at the grain boundaries of an alloy exposed to a PWR or BWR environment (or previously pre-oxidised) and subjected to a monotonic tensile loading during which slip bands or clear bands are formed and may interact with the metal/oxide interface at the oxidised GB. Figure 7.16a schematically illustrates this configuration which is evidently hypothetical: here, it is chosen to partly explain the detrimental effect of the environment on IG cracking by supposing an embrittlement of the GB through the oxide penetration coupled with the slip bands or clear bands/GB interactions.

The molecular dynamics results on oxide bicrystals [Van Brutzel et al., 2019], already briefly mentioned in chapter 1, are used in the above context, as inputs for the assessment of oxidised grain boundaries mechanical properties (σ_c and γ_{fac}).

These MD calculations are carried out with an empirical potential [Chartier et al., 2013] for two spinel type oxides: FeCr_2O_4 and NiCr_2O_4 , for which the lattice parameters and the cubic elastic constants are reproduced in normal and inverse spinel type configurations.

This choice of chemistry is in agreement with studies measuring a $\text{Ni}_{1-x}\text{Fe}_x\text{Cr}_2\text{O}_4$ composition for oxide grain boundary penetrations and Cr-rich internal oxide layers in oxidised nickel based alloys [Guerre et al., 2011, Marchetti et al., 2016, Jambon et al., 2011, Lozano-Perez et al., 2014]. The presence of chromite FeCr_2O_4 is further reported in internal oxide layers during SCC testing on irradiated and non-irradiated austenitic stainless steels 316 or 304 [Dumerval et al., 2016, Perrin et al., 2013, Lozano-Perez et al., 2010, Kruska et al., 2012, Lozano-Perez et al., 2011].

From these MD results, the entire set of grain boundaries mechanical properties presented in figure 7.15 is conveniently used, since, to our knowledge, the experimental

7. INTERGRANULAR FRACTURE INITIATION IN UNIRRADIATED AND IRRADIATED STAINLESS STEELS

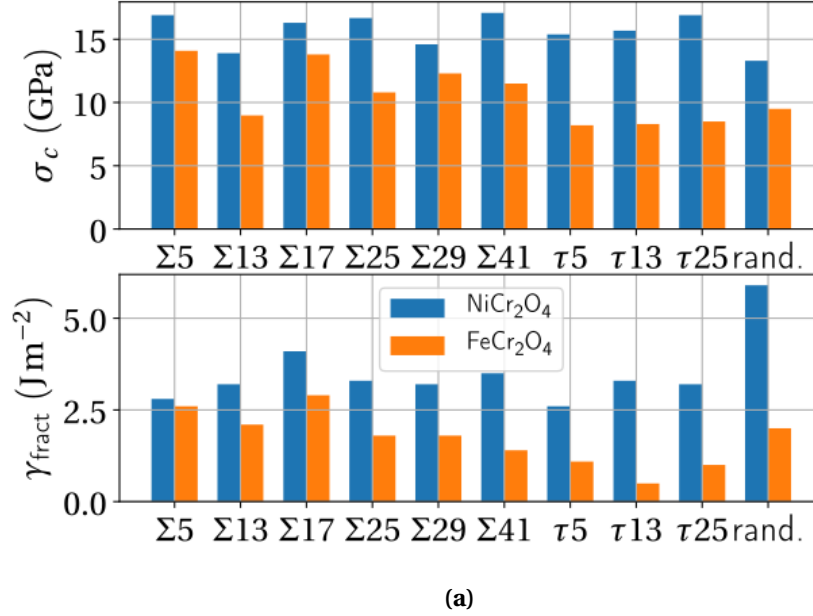


Figure 7.15: Mechanical properties of 10 spinel type oxide FeCr_2O_4 and NiCr_2O_4 GBs, from MD simulations of bicrystal tensile tests [Van Brutzel et al., 2019].

determination of the oxide nanograin misorientation in the penetrations or in the internal oxide layer has not been investigated yet. As already illustrated in chapter 1, all the bicrystals present a maximum a normal GB stress σ_c correlated to the systematic GB debonding. This mechanical property does not vary significantly with the loading (uniaxial deformation or uniaxial stress loadings).

From the scheme of figure 7.16a, it is clear that a more coherent application would rather consider the mechanical properties of various metal/oxide interfaces. However, these data are not yet available. It should also be stressed that the localisation of the IG fracture initiation (i.e. whether it is located at the metal/oxide interface or in the oxide) is still an open question.

7.4.1.2 Application to the intergranular failure of an irradiated austenitic stainless steel

The application of the intergranular fracture model of equation 7.24) using the MD results, is carried out with the microstructure parameters of a typical irradiated austenitic stainless steel to 35 dpa ($\tau_0 = 130$ MPa, $L = 50\mu\text{m}$, $t = 50$ nm) [Fukuya et al., 2008a]. A shear modulus of $\mu = 76.9$ GPa is taken using isotropic elasticity (equation 7.2 with $Y = 200$ GPa and $\nu = 0.3$). Several clear bands are considered here for taking into account the screening effects with a ratio of $r_{\text{scr}} = 0.45$ as previously computed. The most severe case is considered with a Schmid factor of 0.5 for the well oriented grain. Three

7. INTERGRANULAR FRACTURE INITIATION IN UNIRRADIATED AND IRRADIATED STAINLESS STEELS

grain boundary orientations ($\theta_{\text{GBSB}} = 70^\circ, 90^\circ$ and 120°) are examined to cover a large panel of configurations using the related $1 - \lambda$ exponents and A_{nn} prefactors previously referenced.

The distribution predicted by the model is shown in figure 7.16b for each oxide grain boundary and for each orientation.

Monotonic tensile tests performed with this material under a simulated PWR environment [Fukuya et al., 2008a] indicates in comparison a remote critical stress to failure of about 500 MPa and 700 MPa.

It is import to mention that the macroscopic critical stress predicted provides a lower bound with respect to experimental data. Indeed, in the model framework (with its related hypothesis), the microcracks length, typically measured on material surface after interrupted tensile tests, are in comparison several order of magnitude larger than the nanocrack initiation predicted (see for example [Jiao and Was, 2011], [Fukuya et al., 2008a], [Gupta et al., 2016]). It is also reminded that the model application considered is the most conservative.

A large scattering of the prediction is obtained for the different grain orientations and oxide chemistries. The magnitude of the prediction agrees reasonably well with experimental results but a significant overestimation is recorded, especially for the NiCr_2O_4 oxide GBs and the configurations at $\theta_{\text{GBSB}} = 130^\circ$. The prediction for $\theta_{\text{GBSB}} = 70^\circ$ and 90° shows the best agreement for the twist and random FeCr_2O_4 oxide GBs.

For a given oxide chemistry, little scattering is observed with the variation of the grain boundary type.

These results also indicate a non negligible influence of the oxide chemistry, the NiCr_2O_4 oxide displaying a better strength than the FeCr_2O_4 oxide.

In addition, it is also clear that the θ_{GBSB} angle also constitutes an influential factor, every other microstructural parameters being fixed.

In conclusion, the prediction of the multiscale model is shown to be relevant enough for studying influential factors over intergranular cracking phenomena.

In the following, it is assumed that the most common grain boundaries are random in the oxide penetration. The decohesion parameters (σ_c, γ_c) for the random grain boundaries are therefore chosen for further applications involving environmental effects.

7.4.2 Selection of experimental data

A comparison between the intergranular fracture model prediction and experimental data of numerous materials is proposed.

Results from constant extension rate tensile tests carried out on flat samples or tensile bar specimens exposed to simulated PWR or BWR environment, are referenced in tables 7.3 and 7.4. It is worth noticing that the majority of the tests are performed until failure of the entire specimen and do not provide a macroscopic critical stress for intergranular microcrack initiation as predicted by the model unlike interrupted

7. INTERGRANULAR FRACTURE INITIATION IN UNIRRADIATED AND IRRADIATED STAINLESS STEELS

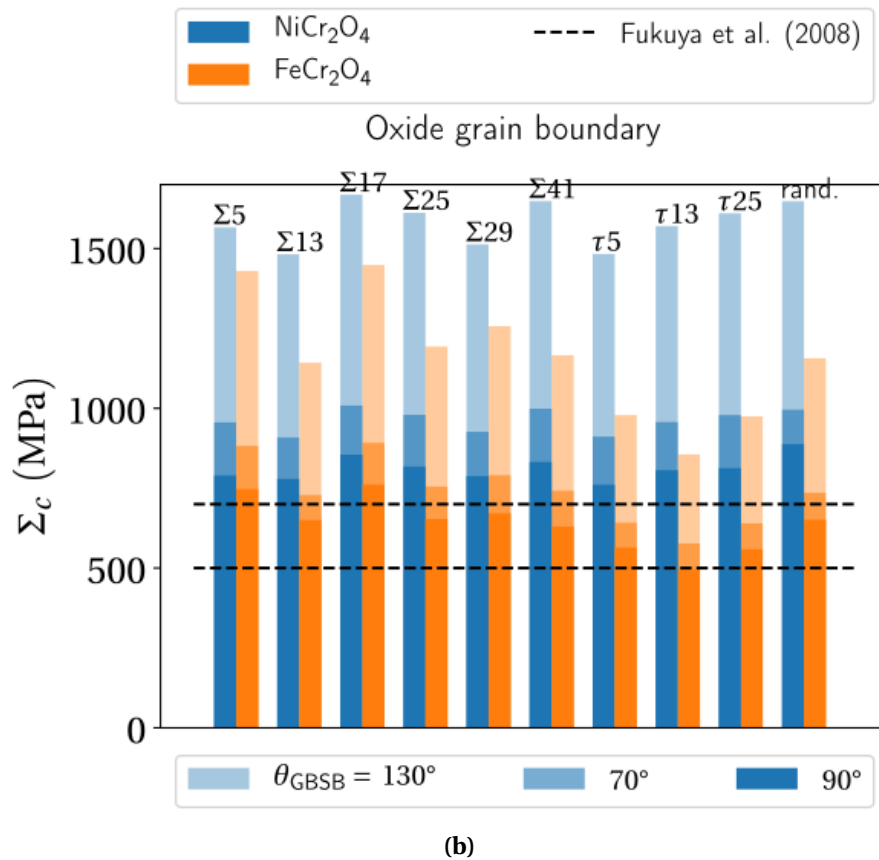
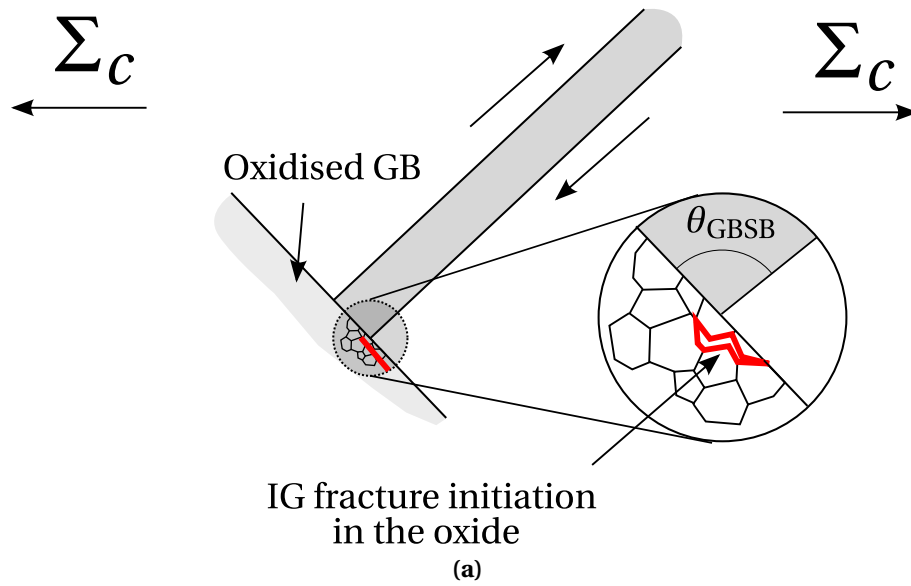


Figure 7.16: Intergranular fracture scenario at Σ_c , considering the initiation of a crack at an oxide grain boundary (7.16a). Distribution of remote critical stress to grain boundary fracture initiation Σ_c as predicted by the model for an irradiated austenitic stainless steel with a grain size $L = 50\mu\text{m}$, considering a well-oriented grain ($\alpha_{\text{SB}} = 45^\circ$) and several orientations of the oxidised grain boundary ($\theta_{\text{GBSB}} = 70^\circ, 90^\circ$ and 130°) (7.16b).

7. INTERGRANULAR FRACTURE INITIATION IN UNIRRADIATED AND IRRADIATED STAINLESS STEELS

tensile tests. The true stress at failure or the maximum stress as identified by the Considère criterion (in the case of ductile or no fracture) are systematically used for the comparison.

Particular care is taken concerning proton or ion pre-irradiated materials. Irradiation affected zones resulting from those particular types of expositions are restricted to a layer at the surface of the specimens and the thickness of the non-irradiated zones is generally significant. In those particular cases, the tensile behaviour of a typical neutron irradiated 304L stainless steel [Pokor, 2002] is used to assess the critical stress from the critical tensile deformation recorded in the original tested material.

The A-286 austenitic stainless steel, further referenced in the pre-irradiated category, constitutes a particular case. It is used by Fournier and Savoie [Savoie et al., 2007, Fournier et al., 2007] to investigate the influence of the localized deformation over IGSCC with a decorrelation of some irradiation effects such as radiation induced segregation. The A-286 referenced in table 7.3 features γ' precipitates with a mean diameter of 4.6 nm and a density of $1.6 \times 10^{23} \text{ m}^{-3}$, similar to the dislocations loops formed in a neutron irradiated stainless steel at 2 dpa [Savoie, 2007]. Precipitate-free clear bands are formed by low-cycle fatigue preloading (between 125–200 cycles), and are shown to present a mean thickness of 30 nm similar to clear channels width in irradiated stainless steels [Sauzay et al., 2010].

When available, fractography analyses permit to determine the nature of the crack initiation site and the propensity to intergranular brittle fracture. Intergranular (IG) initiation, transgranular (TG) initiation and ductile or absence of fracture (DNF) are further referenced in table 7.3 for each test.

7.4.3 Application of the model

The application of the model is carried out for two cases considering either irradiated or non-irradiated austenitic stainless steels tested under PWR or BWR simulated environment.

The environmental effects are taken into account through the nature of the oxide grain boundaries (supposedly formed at oxide GB penetrations) with its interface parameters σ_c and γ_c . The mechanical properties of the chromite oxide FeCr_2O_4 random grain boundary are chosen.

Averaged slip band thickness values are used according to the material considered:

- A thickness of about 50 nm can be derived for pre-irradiated austenitic stainless steels from transmission electron microscopy observations of clear channels [Sauzay et al., 2010].
- The value of 100 nm is used for the unirradiated material as reported in chapter 6.

As before, three orientations of the original grain boundary are considered for a Schmid factor of 0.5 with θ_{GBSB} angles of 70°, 90° and 120°, in order to take into account a repartition of grain boundary/slip band configurations.

7. INTERGRANULAR FRACTURE INITIATION IN UNIRRADIATED AND IRRADIATED STAINLESS STEELS

Mat./Ref.	Env.	\bar{L} (μm)	Σ_c (MPa)	Frac.	$\dot{\epsilon}$ (s ⁻¹)	T(°C)	dose (dpa)
A-286 [1,2]	PWR	6	1026	IG(16F)	1.5×10^{-7}	360	≡ 2
			1090	IG(5F)		360	
			1251	IG(1F)		320	
304L [3] †		10	583	IG	3.6×10^{-7}	288	1
304L [4] †		27	710	IG	5.0×10^{-8}	340	5
304 (SA) [5]		35	483	IG(90F)	2.5×10^{-7}	289	50
316 (15CW) [6]		30–40	946	IG	5.0×10^{-8}	320	5.4–5.6
304L (SA) [6]		40	670	TG	5.0×10^{-8}	320	4.3–4.5
			709	IG			
316 (15CW) [7]	(2.8DH)	50	490	IG(90F)	6.7×10^{-7}	320	35
	(0DH)		691	IG(54F)			
304 (TS) [8]	(8DO)	120	249	IG(100F)	4.2×10^{-7}	290	(f) 0.01–0.1
	(0.2DO)		310	IG(67F)			
	(0.001DO)		452	IG(19F)			
304 (SA) [9] †	BWR	40	366	IG(38.7F)	3.5×10^{-7}	320	5.5
			398	IG(58.6F)			
304 (SA) [10]		40–50	595	IG(42.8F)	3.5×10^{-7}	288	7.8
316L (SA) [10]			700	IG(50.5F)	3.5×10^{-7}	288	9.6
304L [3]	PWR	10	400	DNF	3.6×10^{-7}	288	-
304 (TS) [8]	(8DO)	120	208	IG(100F)	4.2×10^{-7}	290	-
	(0.2DO)		358	IG(53F)			
	(0.001DO)		536	TG			
304 (SA) [9] †	BWR	40	464	DNF	3.5×10^{-7}	320	

Table 7.3: Experimental results. (IG) intergranular fracture initiation. (TG) transgranular fracture initiation. (DNF) no fracture or ductile fracture initiation. (XF) X % IGSCC from fractography analysis (XCW) X % cold-worked. (XDO) X ppm dissolved oxygen (XDH) X ppm dissolved hydrogen (SA) solution-annealed. (TS) thermally sensitized. (RT) room temperature. (f) assessed from: a fluence 2.3×10^{23} – 3.8×10^{23} n/m² with $E_{\text{neutron}} > 1$ MeV [Was, 2007a]. † proton or ion irradiated specimen

7. INTERGRANULAR FRACTURE INITIATION IN UNIRRADIATED AND IRRADIATED STAINLESS STEELS

Notation of table 7.3	Ref.
[1]	[Fournier et al., 2007]
[2]	[Savoie et al., 2007]
[3]	[Cookson et al., 1993]
[4]	[Gupta et al., 2016]
[5]	[Chung et al., 2001]
[6]	[Massoud et al., 2005]
[7]	[Fukuya et al., 2008b]
[8]	[Hide et al., 1995]
[9]	[Busby and Was, 2003]
[10]	[Stephenson et al., 2012]

Table 7.4: References of table 7.3

The slip band length parameter L , corresponding to the grain size, is systematically varied between 5–300 μm .

Finally, in order to decipher the possible effect of irradiation, the single slip band or clear band cases are considered along with the cases of several bands with:

- A screening ratio $r_{\text{src}} = 0.45$ for irradiated austenitic SS.
- A screening ratio $r_{\text{src}} = 0.17$ for unirradiated austenitic SS.

7.4.4 Results and discussion

The comparisons are shown in figures 7.17a and 7.17b for the pre-irradiated and unirradiated stainless steels respectively.

7.4.4.1 Irradiated and non-irradiated stainless steels

The orders of magnitude of the model prediction are in satisfying agreement with the results from IASCC testing according to figure 7.17a, despite a clear overestimation for the irradiated cases with several clear bands and a large repartition of experimental data.

In the unirradiated case, data are too scarce and do not permit a relevant comparison with literature even if the model predicts high values of the remote macroscopic critical stress (e.g for the most detrimental case at $\theta_{\text{GBSB}} = 90^\circ$). This would confirm that slip band /GB interactions are significantly less prone to IG fracture initiation. This point is clearly illustrated by a comparison between this unirradiated case and the irradiated case for which significantly lower and more attainable macroscopic critical stresses are predicted. For example, in the θ_{GBSB} case at $L = 50 \mu\text{m}$, it is predicted that critical stresses of roughly 650 MPa and 1050 MPa are necessary to trigger IG cracking in irradiated and unirradiated austenitic SS respectively.

7. INTERGRANULAR FRACTURE INITIATION IN UNIRRADIATED AND IRRADIATED STAINLESS STEELS

In any cases, it is confirmed that the number of slip bands or clear bands and the related interband spacings are key quantitative factors to assess the susceptibility to IG cracking.

7.4.4.2 Influence of the environment

As reported in chapter 1, a clear detrimental influence of the PWR or BWR environment is reported in literature. IASCC and SCC tests demonstrate the fact that localized deformation can not explain alone the results obtained in primary water environments. Hide et al. IASCC study [Hide et al., 1995] shows for example a clear correlation between the concentration of dissolved oxygen (DO) and the propensity to IGSCC along with a decrease of the critical macroscopic stress. The same testing procedure in argon environment for the same low-irradiated material show in comparison substantially less intergranular cracking.

It is supposed here that grain boundary oxidation might influence the intergranular crack initiation. Here, the model applications are based on the presence of oxide penetrations at grain boundaries as a result of a preferential oxidation.

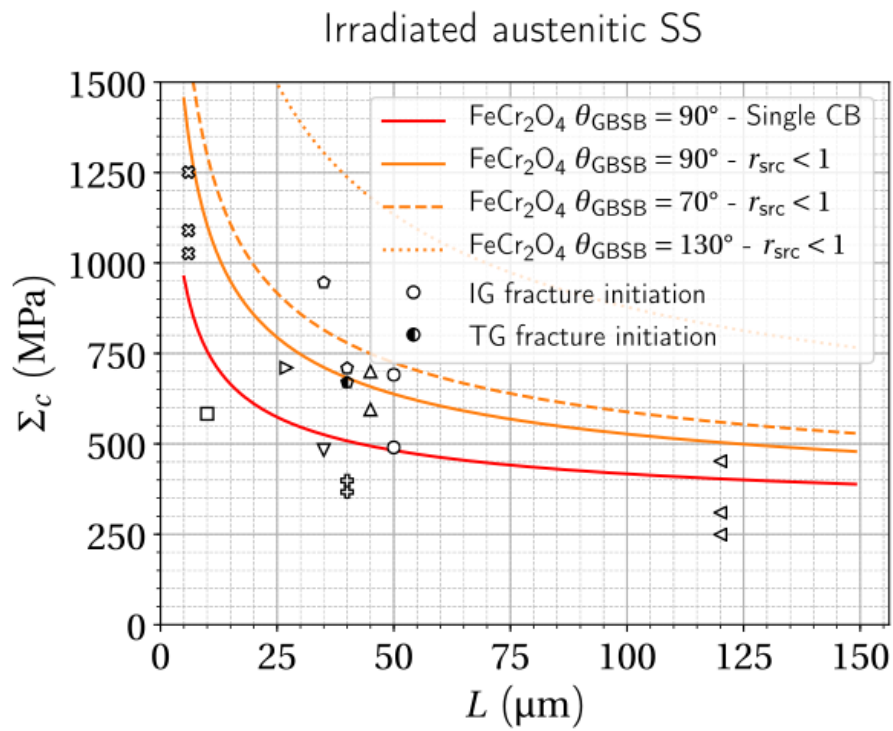
Results show that the multiscale model, chaining molecular dynamics computations on oxide grain boundaries yield an overestimation of the remote macroscopic critical stress.

However, it should be emphasised, once again, that the fracture initiation in the oxide penetration (figure 7.16a) is purely hypothetical. A more comprehensive study should rather focus on oxide/alloy interfaces as to our knowledge, it is not clear yet which is the most prone to microcrack nucleation.

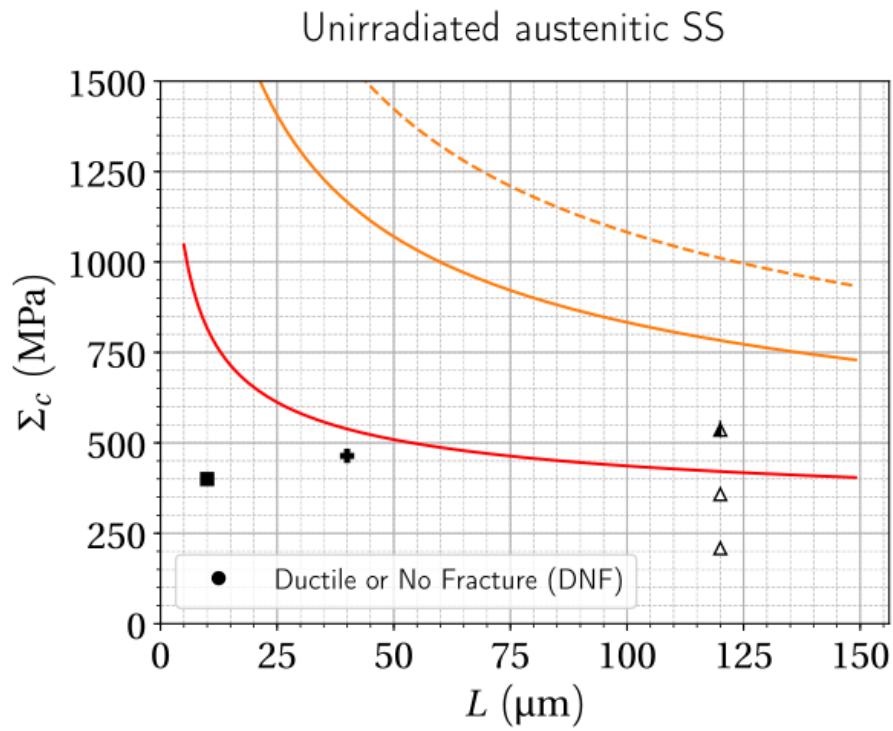
Oxide penetrations has been extensively observed in nickel-based alloys such as Inconel 600 alloys during SCC testing [Guerre et al., 2011, Caballero Hinostroza, 2016] displaying deep penetrations of several microns. In comparison, shallow penetrations (600 nm at most) are observed in cold-worked stainless steels after slow strain rate tensile tests and sometimes result from the asymmetrical formation of the Cr-rich surface oxide layer [Lozano-Perez et al., 2012b, Lozano-Perez et al., 2012a, Lozano-Perez et al., 2014]. However Cisse et al. [Cissé et al., 2013] reports the presence of intergranular oxidation several microns under the oxide surface layer of a A-286 precipitation-strengthened stainless steel after a slow strain rate tensile test. Once again, the hypothesis of the model, suggesting a scenario in which a clear band or a slip band impacts an oxide penetration, may therefore not be verified. Nevertheless it is not excluded that a microcrack initiations might occur at the impact of slip bands or clear channels with the surface oxide layer. Configurations studied here are very similar to this specific case even if surface effects and the presence of an oxide layer shall be considered for further FE computations.

Transgranular initiation are also reported in particular for unirradiated stainless steels [Couvant et al., 2005, Miwa et al., 2007] but also for irradiated stainless steels [Massoud et al., 2005]. For unirradiated materials oxide penetrations are observed at emerging slip bands from FIB-SEM slabs [Lozano-Perez et al., 2012b] and might induce

7. INTERGRANULAR FRACTURE INITIATION IN UNIRRADIATED AND IRRADIATED STAINLESS STEELS



(a)



(b)

Figure 7.17: Comparison of the model prediction with experimental test results for irradiated austenitic stainless steels in simulated PWR environment (7.17b) and for non-irradiated stainless steels (7.17b). 289

7. INTERGRANULAR FRACTURE INITIATION IN UNIRRADIATED AND IRRADIATED STAINLESS STEELS

microcrack initiations. Although this particular case is not considered in the FE model, a very similar case can be conceived. Secondary slip bands impacting an oxidized primary slip band could constitute a plausible mechanism to explain this phenomenon, formation of the primary slip bands being induced by cold-working.

7.4.4.3 Grain size effect

A tendency toward a significant influence of the grain size over intergranular crack initiation seems to be revealed here. However, it is clear that the comparison is not statistically representative as yet.

From the asymptotic variation of the prediction curves, it would be expected that the influence of the grain size is the most important toward the smallest values. Conversely, as much influence shall not be observed among the coarse-grain alloys (over 40–50 μm).

However, other effects are not taken into account in the model. For example, the dissolved hydrogen concentration is suspected to be a significant environmental factor promoting localisation of the deformation [Menard, 2005, Aubert et al., 2010] through thinner and more active slip bands as dislocation mobility increases [Robertson, 1999] and the stacking fault energy decreases. In the case of irradiated alloys, the radiation induced segregation (RIS) effect supposing the alteration of grain boundaries local properties or the acceleration of preferential oxidation through radiation-induced chromium depletion also be considered despite having a relatively minor contribution in comparison with the localised deformation effect [Jiao and Was, 2011]. As these detrimental factors have not been considered, it is not clear if these might challenge or mask the grain size effect proposed here.

7.5 Summary of the results and conclusion

7.5.1 Results

In this chapter, the following results are found:

- Once again, it is confirmed that the pile-up theory yields an overestimation of intergranular stress field in the vicinity of slip bands or clear bands of finite thickness. This last point is a necessity for the use of GB mechanical properties (σ_c, γ_c) at the atomic scale, since clear bands or slip bands thickness vary between 50–150 nm. In particular, stress exponents $1 - \lambda$ lower than 0.5 are found which indicates the necessity to use the coupled criterion presented in chapters 4 and 5 to predict fracture initiation.
- Following the above point, the present study provides a full characterisation and description of the multiscale model proposed by Sauzay and coworkers, which consider slip bands or clear bands with finite thickness and a coupled criterion to predict intergranular fracture initiation. In that regard, numerous finite element computations are employed, covering a large panel of configurations with one or several discontinuous slip bands or clear bands with GB impact angles between 20–160°.
- A screening ratio of about 45 % and 15 % of the intergranular normal stress induces by a single discontinuous slip band are found for the irradiated and unirradiated austenitic stainless steels, considering several clear bands and several slip bands respectively. These results quantify a 66 % stress increase that can be imputed to the effect of the localised plastic deformation for irradiated materials.
- Elements justifying the use of the coupled criterion in the close-field (vicinity) of a discontinuous slip band with atomistic inputs are provided. In that respect, the top-down approach used in chapter 5 is successfully adapted in the case of two pure nickel CSL $\langle 211 \rangle$ tilt GBs impacted by a single discontinuous slip band. Results are in a satisfying agreement with the multiscale model prediction (bottom-up approach) using MD results of multiaxial tensile loadings on the related bicrystals. In addition, the same behaviours are recovered in the bicrystals simulations and in the top-down simulations, further demonstrating the relevance of multiaxial loading studies on bicrystals at the atomic scale.
- Comparable orders of magnitude are found for the remote critical stress to IG fracture initiation from the proposed comparison between the predictions of the multiscale model using MD results on oxide GBs mechanical properties and experimental results on SSRT tests of irradiated and unirradiated austenitic stainless steels exposed to simulated PWR or BWR environments.

7. INTERGRANULAR FRACTURE INITIATION IN UNIRRADIATED AND IRRADIATED STAINLESS STEELS

- From the above comparison, the model points toward a clear influence of the slip band (or clear band)/GB impact angle (θ_{GBSB}) and confirms quantitatively the detrimental effect of the localisation of plastic deformation over the susceptibility to IG fracture initiation.
- A grain size effect predicted by the model seems to be reproduced by the experimental results on irradiated austenitic stainless steels, even if more data would be needed to confirm this trend.

7.5.2 Conclusion

This final chapter has permitted the capitalisation of the information and data provided in the previous chapters, in order to propose a justification and a coherent use of a multiscale model for the prediction of intergranular fracture initiation.

This multiscale model clearly demonstrates a capacity to reproduce relevant orders of magnitude for the predictions intended here, and using only intrinsic physical and geometrical parameters at different scales. In that respect, it is interesting to note that the inputs of the model can be readily obtained from simple measurements and atomistic simulations.

Despite the several simplifications and hypothesis used (e.g. perfect grain boundaries or interfaces, single slip system activated in the clear bands or slip bands, plane strain hypothesis, isotropic elasticity, and so on...), this model clearly possesses an interesting predictive potential. Since it relies on elementary inputs, its use is highly adaptable to numerous scenarios and can be further extended to take into account other multiphysical aspects. For example, it is easy to imagine that a kinetic oxidation model of grain boundaries could be readily coupled with this model from the varying (in time) mechanical properties of the grain boundaries. In that regard, a transition from a sound interface to a full oxidised GB with some transitional configurations could be envisioned through molecular dynamics, should relevant atomic potential be available for that purpose. This coupling could therefore yields a first consideration of some of the synergistic effects (mechanical and environmental effects).

Such a model is also highly valuable since it allows the the control over over numerous parameters, thus readily permitting parametric studies by coupling or decoupling various effects. For example, the model has permitted to study independently the effect of irradiation through the interband spacing and number of bands, or the effect of the grain size with results presented above. In addition, it could then be interesting to envision a statistical use of the the model through the various statistical data available on polycrystals (grain sizes, slip bands or clear bands interband spacings and number an so on...). This might enable to cover a more representative repartition of the prediction to be compared to the large scatter of data observed experimentally.

8

Conclusion and perspectives

8. CONCLUSION AND PERSPECTIVES

8.1 Conclusion

As a conclusion, a review of the main results of each chapter is provided in regards to the three points highlighted in chapter 1.

In the context of understanding and predicting IG fracture initiation in irradiated austenitic stainless steels pulled under simulated PWR, BWR or inert environment, it was pointed out from a brief literature review that:

1. More physically-based models are still needed
2. A model proposing a quantification of the irradiation influence on IG fracture initiation by taking into account the localisation of plastic deformation would be of great interest.
3. Intrinsic mechanical properties of grain boundaries and interfaces and a method for their use in a multiscale model could constitute an advance following the preceding points.

It was chosen to treat these points by a progressive simulation approach, beginning at the atomic scale and finishing at the microscopic scale.

Chapters 2, 3 and 4 were dedicated to the behaviour comprehension of bicrystals subjected to a wide variety of multiaxial loadings. Their purpose was to extract metals GBs mechanical properties and to provide a minimal understanding of the related underlying mechanisms keeping a predictive approach in mind for a subsequent use at upper scale.

For that purpose, pure FCC nickel was chosen as model to ease the comprehension of the mechanisms involved and thirteen CSL symmetric tilt GBs were selected for an extensive study. A behaviour transition between GB partial dislocation nucleation and GB debonding was found according to the multiaxial deformations imposed with a saturation at a constant critical stress recorded when decohesion was involved.

The importance of transverse and shear strain (or stress) components was clearly shown which pointed toward the necessity to take into account the full IG stress or strain tensor in any study focusing on GBs strength. The origin of both heterogeneous dislocation nucleation and GB decohesion were described. In particular, the influence of the lattice deformation on the homogeneous nucleation of partial dislocations and the influence of the GBs mechanical description were highlighted. The GBs debonding was related to the universal binding energy relation considering disclination atomic sites as the location of a void nucleation and coalescence mechanism. Thus, the related critical stresses assessed by molecular dynamics simulations were physically justified for their use in a coupled criterion to intergranular fracture initiation.

Chapter 5 has constituted a pivotal study and a first exercise to carry on the general IG fracture simulation approach toward upper scales. Two multiscale approaches were used to further justify the relevance of assessing GBs mechanical properties at

8. CONCLUSION AND PERSPECTIVES

the atomic scale and their use with a coupled criterion in the context of the V-notch problem.

Two bottom-up approaches were successfully employed in that regard, using the previous MD results which yielded coherent prediction in comparison to experimental results of tensile tests performed on notched bicrystals samples.

A top-down approach was introduced and has shown similar results but with significant discrepancies that could suggest the intervention of additional atomistic mechanisms in the fracture initiation process.

The importance of the strain (or stress) multiaxiality was confirmed and definitely constitutes a key point for the assessment of IG fracture initiation.

Chapters 6 and 7 were finally proposed in order to focus on the IG fracture initiation phenomenon observed in the vicinity of clear bands/GBs intersection in irradiated austenitic stainless steels pulled under PWR, BWR or inert environment.

A first experimental approach was pursued in order to characterise a geometrical model of plastic slip bands of finite thickness developed in a typical 316L unirradiated austenitic stainless steels after monotonic interrupted tensile tests.

This approach has focused on the measure of slip band thickness, interband spacing and plastic slip strain at low macroscopic plastic deformations. It was justified by the need to quantitatively decipher the origin of the IG fracture susceptibility in irradiated materials as opposed to the apparent mitigation of the phenomenon in unirradiated materials. In that regard, it was shown that a coupling of EBSD and AFM data is mandatory to obtain a quantitative assessment, necessary to pursue a comparison between unirradiated and irradiated austenitic stainless steels. Such comparison has shown that the interband spacing clearly constitutes a key parameter to understand the effect of the localisation of plastic deformation on IG fracture initiation in irradiated austenitic SS. This effect should be preferentially quantified by the plastic slip strain in the bands which is directly related to the severity of the intergranular normal stress components induced by slip bands or clear band/GB intersections.

This experimental characterisation was subsequently used to quantitatively assess the influence of localised deformation on the IG fracture initiation using a multiscale model.

For that final purpose, numerous FE computations were employed to fully characterise this multiscale model based on the assessment of IG stress field in the vicinity of slip bands or clear band/GB interactions and a coupled criterion for IG fracture initiation using MD results on bicrystals at the atomic scale. The model was extended for its use to a wide range of microstructure configurations of slip bands and clear bands.

Following the approach of chapter 5, a physical justification of this multiscale model was proposed and successfully achieved with an adapted top-down approach.

In the wake of the general approach undertaken from the atomic scale of chapters 2, 3 and 4 to the microscopic scales of chapters 6 and 7 with a bridge of scale suggested in chapter 5, the multiscale model proposed by Sauzay and coworkers was confidently used to propose a comparison of its prediction with several results from IASCC experimental

8. CONCLUSION AND PERSPECTIVES

studies.

A grain size effect was proposed and a confirmation of the major influence of clear band/GB interaction on IG fracture initiation through dislocation channelling was obtained from the model predictions in the cases of unirradiated and irradiated austenitic stainless steels and their comparison to experimental results.

8.2 Perspectives

In this study, it is obvious that many aspects of the IG fracture phenomenon have been discarded but could constitute key points of interest from both the industrial and scientific perspectives.

Nevertheless, one of the advantages of the multiscale model employed in chapter 7 relies on its ability to be adaptative, since it essentially deals with intrinsic inputs of the materials involved in the IG fracture phenomenon. In particular, the following future perspectives could be envisioned in order to extend and improve the use of this multiscale model:

- The mechanical properties of metal/oxide interfaces at the atomic scale would be complementary and necessary to the present study. It was clearly shown that using oxide GB properties yield to slightly overestimate the predictions with respect to experimental data. It is believed that metal/oxide interfaces at the atomic scale may present lower mechanical properties. In addition, as expressed in chapter 7, the use of the multiscale model would be more coherent. Undertaking this aspect may necessitate at least a rough knowledge of the interface structure (crystal orientations, composition of the oxide and of the alloy in the vicinity of the interface). and a reliable potential able to reproduce the bond transition between oxide and metal phase and the mechanical properties of both phases (intrinsic SFE for the metal, elastic constants etc..). In that regard, the ReaxFF potential [van Duin et al., 2001] was originally considered to be a good candidate, but subsequent improvements may be needed to fulfil the above conditions. Ab initio computations of interface debonding would also yield to valuable inputs in that regard. Finally, it is reminded that the localisation of the IG fracture initiation in irradiated austenitic SS or nickel-based alloys still constitutes an open question. In that regard, it was suggested from FIB SEM observations [Lozano-Perez, 2017] that metal/oxide interfaces (in pre-oxidised unirradiated austenitic SS) may present a rough structure with for example the presence of cavities. Should it be confirmed, and depending on the cavity size and shape, MD or FE computations could be employed to relate their influence on the possible IG fracture initiations at the metal/oxide interface or in the oxide penetration. In that scenario, the slip band or clear band impact may or may not play a significant role.
- Similarly, atomistic mechanical properties of GBs in austenitic SS are also of great interest, using for example MD simulations with Fe-Ni-Cr EAM potential recently

8. CONCLUSION AND PERSPECTIVES

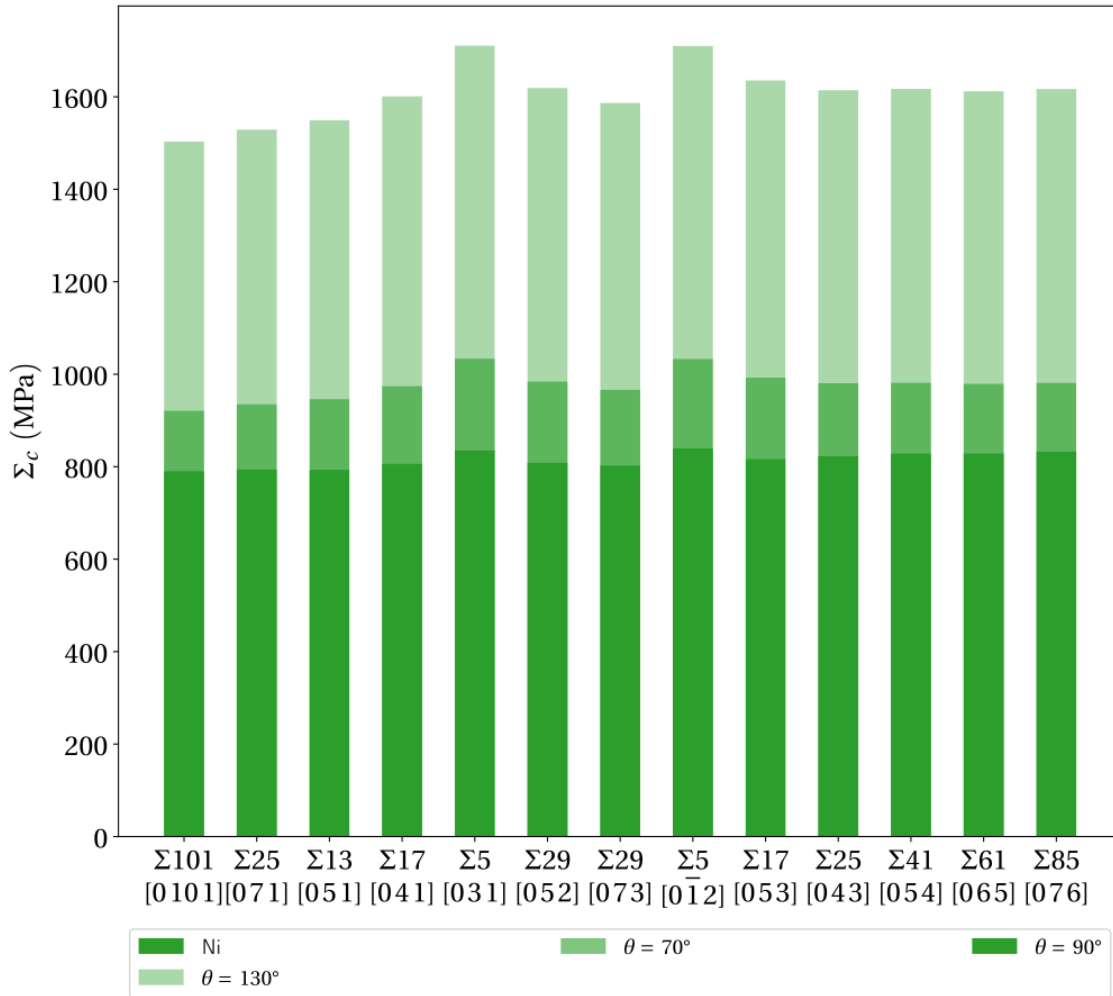


Figure 8.1: Application of the multiscale model using the GB mechanical properties of pure Ni CSL tilt symmetric GBs assessed by MD simulations in chapter 2 and reported in chapter 4. The same inputs used before for the application of figure 7.16b are used for the case of an irradiated austenitic stainless steels with a mean grain size of 50 μm .

8. CONCLUSION AND PERSPECTIVES

available [Béland et al., 2017]. In this study, only pure nickel was considered for the GB simulation, however, it is suspected that the potential of Béland may yield similar results (in order of magnitude). For coherency purposes, the data on this GBs obtained in chapter 2 were not used here with the model for the prediction of IG fracture initiation in austenitic SS pulled under simulated inert environment. In order to provide an idea of the macroscopic critical remote stress involved for a sound metal GB (not oxidised), figure 8.1 presents an application of the multi-scale model similar to figure 7.16b but using the mechanical properties obtained previously on Ni CSL GBs and presented in table 4.2. These predictions are to be compared with the macroscopic remote critical stress of 1 GPa determined after IASCC testing under inert environment of an irradiated austenitic SS to 35 dpa [Nishioka et al., 2008]. A study on Fe-Ni-Cr systems may improve these predictions. An additional interest would lie on the influence of the chromium depletion and nickel enrichment (due to RIS) on the GB mechanical properties and its consequences on the model predictions.

- Tending toward a probabilistic approach using the model could permit to decipher some of the different data scattering typically observed in SSRT testing.

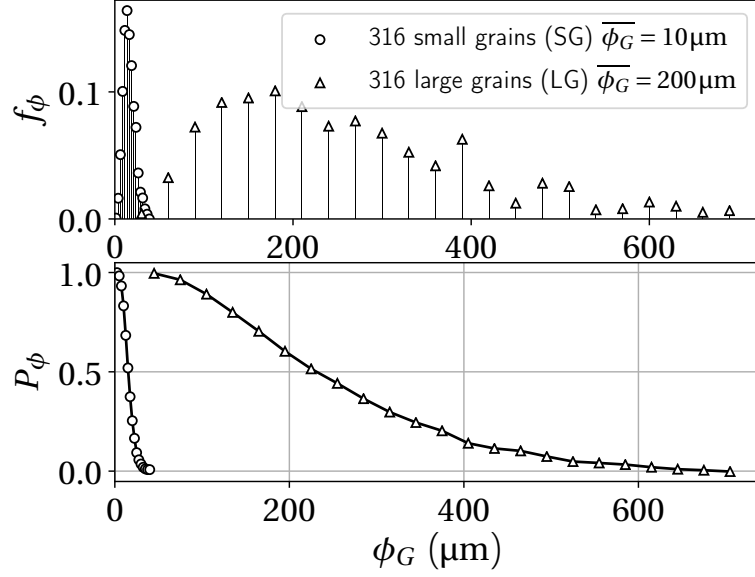
For a first example, several studies focus on the slip transmission probability at GBs, proposing criteria in that regard. Following these studies, it could be interesting to extend further the multiscale model to the different cases of clear band/GB interactions, as classified by [Le Millier, 2014] (chapter 1), thus permitting to statistically predict the propensity to IG fracture based on the above criteria and the statistical data on a given material microstructure (grains orientation or Schmid factor, GB plane, etc.).

For a second example, it was pointed out in chapter 7, that the grain size may have a strong detrimental effect on IG fracture initiation. Then, it could be envisioned that, from representative grain size distribution of a given material of interest, the application of the model could yield to a percentage of IG fracture repartition as illustrated in figure 8.2, following the steps:

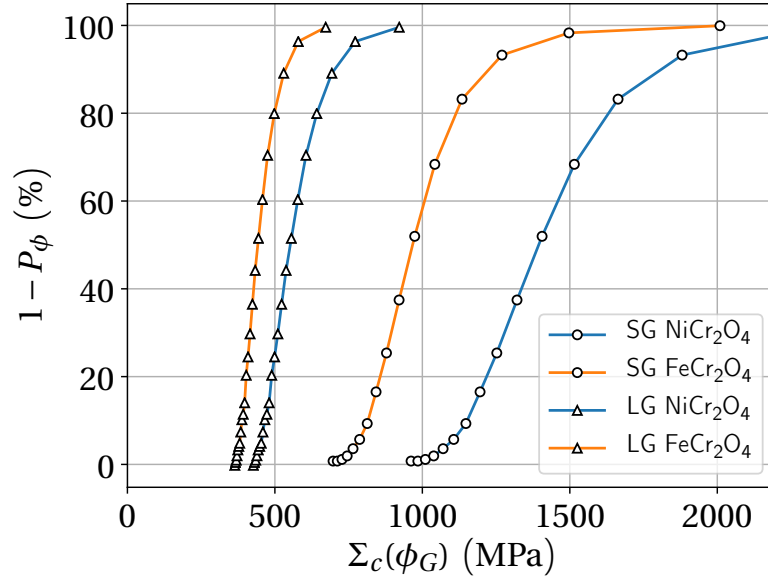
1. Derive the cumulative probability P_ϕ from the grain size distribution f_ϕ .
2. Deduce the remote critical stress to IG fracture initiation related to each grain size ϕ_G .
3. Following step 2, the grain size cumulative probability can be directly related to the IG fracture propensity by association with the above predictions of the model.

For a third example, it was shown in chapters 6 and 7 that the interband spacing may also play a key role on the IG fracture initiation according to the grain size, the irradiation dose, the stacking fault energy and the macroscopic plastic deformation. A prediction of the distribution of the interband spacing per grain could be

8. CONCLUSION AND PERSPECTIVES



(a)



(b)

Figure 8.2: Probability density f_ϕ and related cumulative probability P_ϕ of grain sizes for two 316 austenitic steels featuring small grains and large grain with mean grain sizes of $10\mu\text{m}$ and $200\mu\text{m}$ respectively (8.2a) (from [Hazan, 2019]). Corresponding propensity to IG fracture $1 - P_\phi$, according to the macroscopic remote stress imposed (8.2b).

8. CONCLUSION AND PERSPECTIVES

highly rewarding by combining these interband spacing predictions with the use of the multiscale model. A direct probabilistic prediction could then be achieved solely based, once again, on intrinsic material properties and on engineering and physical parameters readily accessible (macroscopic plastic deformation irradiation dose, etc.). However, such a description of the interband spacing is not yet available. Should such endeavour be undertaken experimentally and/or with simulation tools, it is believed that EBSD and AFM data along with dislocation dynamics simulations involving various Frank loop densities would be interesting to combine.

- An other aspect of improvement could rely on the validation of the intergranular stress or strain fields computed in chapter 7. In that regard, two approaches could be considered:
 1. It was shown in chapter 7 that the stress field is partly related to the plastic slip strain field in the slip band or clear band corner, which in turn is directly linked to the dislocation flow in the band and in the vicinity of the grain boundary. However, these FE computations may neglect several atomistic aspects such as the actual dislocation flow, or the effect of extrinsic dislocations on the GB structure. In order to tackle this issue, a chaining of dislocation dynamics and MD simulations might be envisioned for getting access to: a representative flow of dislocations during the activation of the slip bands or clear bands, and the representative mechanisms of GB interactions with these numerous dislocation impacts.
 2. Recent advances in high-resolution electron back scatter diffraction has allowed to get access to IG strain and stress field measure in the vicinity of impacting slip bands or clear bands up to several nanometre resolutions. A direct experimental comparison with the stress fields model presented in chapters 6 and 7 may be envisioned, but could be limited to a comparison in the far-field where the pile-up solution holds.
- As already pointed out in the conclusions of chapter 7, the oxidation kinetics at grain boundaries could also be readily taken into account in the multiscale model. A model of GB oxidation kinetic has been developed by Couvant and coworkers [Couvant et al., 2015] for nickel-based alloys and could be adapted to austenitic SS [Couvant et al., 2017]. Using the multiscale model, the effect of oxidation kinetics coupled to the mechanical loading could be taken into account by the simultaneous variations (in time) of the local critical stress $\sigma_c(t)$, the critical energy γ_c and the IG stress field via the time variation of the effective shear stress $\tau_{\text{eff}}(t) = f\Sigma(t) - \tau_0$. This endeavour would however require an extensive atomistic study of the mechanical properties of a wide variety of different interfaces.
- The detrimental influence of hydrogen on the IG fracture susceptibility was also discarded here. However, it could be taken into account with the model through

8. CONCLUSION AND PERSPECTIVES

the related intensification of the plastic localisation in the slip bands, as reported by Menard, Aubert and coworkers [Menard, 2005, Aubert et al., 2010] or by an hydrogen embrittlement of grain boundaries through atomistic studies on bicrystal. Once again, ab initio computations results would constitute valuable assets in that regard.

Finally, the general approach follows from chapters 2 to chapter 7 could be adapted to scenarios that would not necessary involve slip band or clear band/GB interactions as a precursor to IG fracture initiations:

- The susceptibility of nickel-based alloys to stress corrosion cracking by IG fracture initiation and propagation is well-known since the work of Coriou. In particular, it has been shown that deep oxide penetration occurring during SCC tests under simulated PWR environments are the location of IG Fracture initiation, as evidence in figure 8.3a.

Unlike the IASCC phenomenon occurring in austenitic SS, slip band impacts has not been observed and correlated to the SCC initiation in nickel-based alloys. In addition, the oxide penetration depth seems to be linked to the IG fracture initiation. Therefore, in complement to the SCC predictive models already existing [Couvant et al., 2015], following a similar multiscale approach could also be interesting, from a scientific point of view, by focusing on stress fields induced by this oxide penetration in conjunction with the use of a criterion for fracture initiation at the atomic scale. From an atomistic point of view, and based on the oxide nanograin observations in these penetrations, MD simulations could be envisioned involving various multiaxial loadings on representative volumes of oxide nanograin polycrystals using the potential of [Chartier et al., 2013] for FeCr_2O_4 or NiCr_2O_4 in coherency with FE assessed strain or stress fields. In particular this potential was already used by [Van Brutzel et al., 2019] on MD simulations of uniaxial loading performed on cuboid oxide nanograin polycrystals with random orientations as illustrated in figure 8.3c. A typical nanograin polycrystal used in MD computations on pure nickel is also shown in figure 8.3d for the sake of illustration. In that particular case, simulation of about 4.6 million atoms is achieved with a box size of 37 nm and a mean grain size of 10 nm. This approach could also be adopted in the case of oxide penetrations at slip bands (see TEM observations of [Lozano-Perez et al., 2014] in figure 8.3b) which are suspected to be responsible for the SCC transgranular initiations in highly cold-worked austenitic SS.

- Finally, it is believed that the multiscale approach initiated in chapter 5 on the V-notched bicrystal tensile test simulations could be greatly improved. Different notch tip geometries should be considered along with a larger and more representative distribution of grain boundaries. In addition, the use of cohesive zone models with atomistic parameters of fracture could be improved, in particular regarding the fracture propagation phase after initiation. Should FE

8. CONCLUSION AND PERSPECTIVES

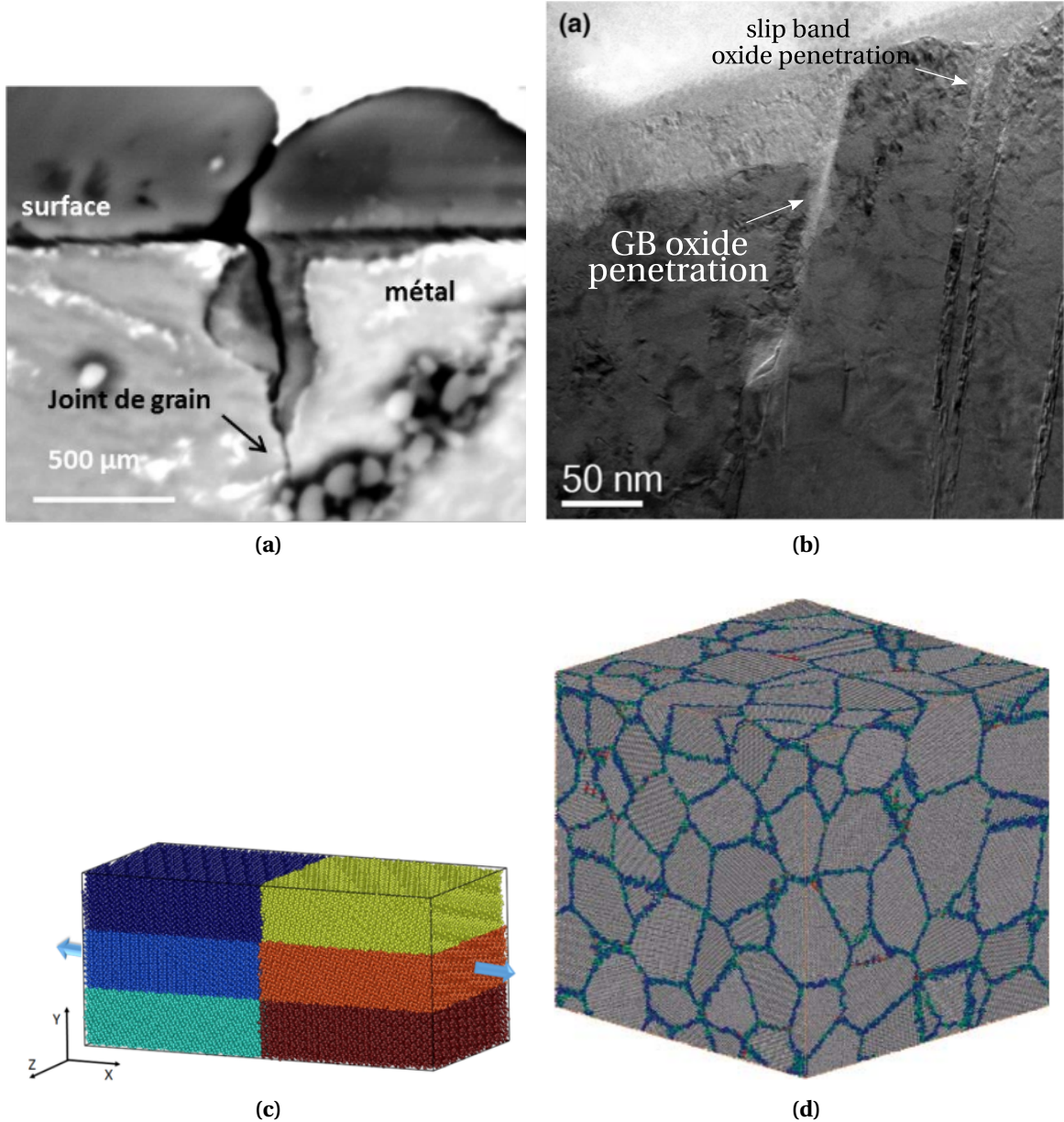


Figure 8.3: FIB-SEM observation of an IG fracture initiation at an oxide penetration in a nickel-based alloy (8.3a) [Caballero Hinostroza, 2016]. TEM observations of oxide penetrations at a GB and slip bands in a highly cold-worked 304 unirradiated austenitic stainless steels (8.3b) [Lozano-Perez et al., 2014]. Spinel type FeCr_2O_4 oxide polycrystal with random grain orientations, used in MD simulations of uniaxial tensile loading (8.3c) [Van Brutzel et al., 2019]. Typical polycrystals of nanograins used in MD simulations (here for pure nickel) (8.3d) [Van Swygenhoven, 2002].

8. CONCLUSION AND PERSPECTIVES

computations be achieved for IG fracture propagations over several micrometers (e.g. with crack sizes that could be typically detected experimentally), the related microscopic critical stress predictions could be directly validated by experimental microscopic tensile tests. In the most idealistic view, this could be achieved through a complementary experimental study involving micromechanical testing on notched bicrystal samples with a high resolution control or characterisation of the manufactured notch geometry, along with a high resolution characterisation of the grain boundary structure. Such characterisation is nowadays possible using high resolution transmission electron microscopy. The advantages of performing microtensile tests would also rely on the direct observations of the material behaviour that could eventually be compared by results of a top-down approach involving large scale simulations. This approach could then be adapted to the assessment of other interfaces strength.

Appendices

Appendix A

Universal binding energy relation model

This appendix provides some details for the derivation of the various formula related to the universal binding energy relation.

The universality evidenced by Rose et al. is described by the following fitting function $E^*(a^*)$:

$$\frac{E}{-E_0} = E^* = -(1 + a^*)e^{a^*} \quad (\text{A.1})$$

$$a^* = \frac{r_{\text{WS}} - r_{\text{WS0}}}{l} = \frac{\delta}{l} \quad (\text{A.2})$$

hence:

$$da^* = \frac{dr_{\text{WS}}}{l} = \frac{d\delta}{l} = \frac{1}{4\pi l r_{\text{WS}}^2} dV \quad (\text{A.3})$$

with V the atomic volume such that:

$$r_{\text{WS}} = \left(\frac{3}{4\pi} V \right)^{\frac{1}{3}} \quad (\text{A.4})$$

For a given system, the cohesive energy E follows:

$$E(\delta) = E_0(1 + a^*)e^{-a^*} \quad (\text{A.5})$$

with its first derivatives:

$$\frac{dE}{d\delta} = \frac{da^*}{d\delta} \frac{d}{da^*} (E_0(1 + a^*)e^{-a^*}) \quad (\text{A.6})$$

$$= \frac{E_0}{l} [e^{-a^*} - (1 + a^*)e^{-a^*}] \quad (\text{A.7})$$

$$= \frac{-E_0}{l} a^* e^{-a^*} \quad (\text{A.8})$$

APPENDIX A. UNIVERSAL BINDING ENERGY RELATION MODEL

and second derivatives:

$$\frac{d^2 E}{d\delta^2} = \frac{da^*}{d\delta} \frac{d}{da^*} \left(-\frac{E_0}{l} a^* e^{-a^*} \right) \quad (\text{A.9})$$

$$= \frac{-E_0}{l^2} \left[e^{-a^*} - a^* e^{-a^*} \right] \quad (\text{A.10})$$

$$= \frac{-E_0}{l^2} (1 - a^*) e^{-a^*} \quad (\text{A.11})$$

$$= \frac{-1}{l^2} E(\delta) \quad (\text{A.12})$$

Evaluating the second derivatives at $\delta = 0$ leads to:

$$l = \sqrt{\frac{-E_0}{\left(\frac{d^2 E}{d\delta^2} \right)_{\delta=0}}} \quad (\text{A.13})$$

The equivalent of a pressure P is then obtained from the first derivative of E with respect to the atomic volume V :

$$P(V) = \frac{dE}{dV} = \frac{da^*}{dV} \frac{d}{da^*} \left(E_0 (1 + a^*) e^{-a^*} \right) \quad (\text{A.14})$$

$$= \frac{-E_0}{4\pi l r_{\text{WS}}^2} a^* e^{-a^*} \quad (\text{A.15})$$

and its derivatives:

$$\frac{dP}{dV} = \frac{d^2 E}{dV^2} = \frac{dr_{\text{WS}}}{dV} \frac{d}{dr_{\text{WS}}} \left(\frac{-E_0}{4\pi l r_{\text{WS}}^2} a^* e^{-a^*} \right) \quad (\text{A.16})$$

$$= \frac{-E_0}{4\pi l r_{\text{WS}}^2} \left[\frac{-2}{4\pi l r_{\text{WS}}^3} a^* e^{-a^*} + \frac{1}{4\pi l r_{\text{WS}}^2} \frac{1}{l} e^{-a^*} - \frac{1}{4\pi l r_{\text{WS}}^2} \frac{1}{l} a^* e^{-a^*} \right] \quad (\text{A.17})$$

$$= \frac{-E_0}{(4\pi l r_{\text{WS}}^2)^2} \left[-\frac{2la^*}{r_{\text{WS}}} + 1 - a^* \right] e^{-a^*} \quad (\text{A.18})$$

Evaluating this last derivatives in $\delta = 0$ (or $V = V_0$) yields:

$$\left(\frac{dP}{dV} \right)_{V=V_0} = \frac{-E_0}{(4\pi l r_{\text{WS}0}^2)^2} \quad (\text{A.19})$$

Since

$$\left(\frac{d^2 E}{d\delta^2} \right)_{\delta=0} = \frac{-E_0}{l^2} \quad (\text{A.20})$$

$$= (4\pi l r_{\text{WS},0^2})^2 \left(\frac{dP}{dV} \right)_{V=V_0} \quad (\text{A.21})$$

APPENDIX A. UNIVERSAL BINDING ENERGY RELATION MODEL

And from the definition of the bulk modulus:

$$B = V_0 \left(\frac{dP}{dV} \right)_{V=V_0} \quad (\text{A.22})$$

then:

$$\left(\frac{d^2 E}{d\delta^2} \right)_{\delta=0} = \frac{1}{l^2} (4\pi l r_{\text{WS},0}^2)^2 \frac{B}{V_0} \quad (\text{A.23})$$

$$= 12\pi r_{\text{WS},0} B \quad (\text{A.24})$$

Hence the assessment of Rose et al.:

$$l = \sqrt{\frac{-E_0}{12\pi r_{\text{WS},0} B}} \quad (\text{A.25})$$

The maximum of the pressure function P_c is found at the critical volume V_c , corresponding to the positive root of the derivatives $\frac{dP}{dV}$. For finding the root, $r_{\text{WS}} \geq r_{\text{WS},0}$, then:

$$\frac{dP}{dV} = 0 \Leftrightarrow -\frac{2la^*}{r_{\text{WS}}} + 1 - a^* = 0 \quad (\text{A.26})$$

or with $r_{\text{WS}} = la^* + r_{\text{WS},0}$:

$$(1 - a^*)(la^* + r_{\text{WS},0}) - 2la^* = 0 \quad (\text{A.27})$$

$$-l(a^*)^2 - (l + r_{\text{WS},0})a^* + r_{\text{WS},0} = 0 \quad (\text{A.28})$$

which admits two real solutions since:

$$\Delta = l^2 + r_{\text{WS},0}^2 + 6lr_{\text{WS},0} > 0 \quad (\text{A.29})$$

The roots are then:

$$a_{\pm}^* = \frac{l + r_{\text{WS},0} \pm \sqrt{(l + r_{\text{WS},0})^2 + 4lr_{\text{WS},0}}}{-2l} \quad (\text{A.30})$$

Choosing the positive root finally yields the critical volume desired:

$$V_c = \frac{4}{3}\pi r_c^3 \quad r_c = r_{\text{WS},0} + la_-^* \quad (\text{A.31})$$

since we know that such positive solution exists (physically) and since $l + r_{\text{WS},0} + \sqrt{\Delta} > 0$ necessarily implicates that $a_+^* < 0$.

Appendix B

Tensile test

This appendix provides details for the correction performed on the raw tensile curve to obtain the material engineering curve.

In the elastic regime, let's consider the complete loading line as two series springs as displayed in figure B.1.

The total displacement imposed U_{tot} comprises the displacement due to the sample U_{mat} and the displacement due to the apparatus U_{app} :

$$U_{\text{tot}} = U_{\text{mat}} + U_{\text{app}} \quad (\text{B.1})$$

Normalising by the initial length of the gauge:

$$\begin{aligned} \frac{U_{\text{tot}}}{L_0} &= \frac{U_{\text{mat}}}{L_0} + \frac{U_{\text{app}}}{L_0} \\ \frac{F}{L_0 K_{\text{tot}}} &= E_{\text{eng}}^{\text{mat}} + \frac{F}{L_0 K_{\text{app}}} \\ \frac{RS_0}{L_0 K_{\text{tot}}} &= E_{\text{eng}}^{\text{mat}} + \frac{RS_0}{L_0 K_{\text{app}}} \end{aligned} \quad (\text{B.2})$$

where R is the engineering stress considering the sample such that $F = RS_0$.

Specific modulus can then be considered conveniently:

$$\frac{RS_0}{L_0 K_{\text{app}}} = \frac{F}{L_0 K_{\text{tot}}} - E_{\text{eng}}^{\text{mat}} \quad (\text{B.3})$$

$$\frac{R}{Y_{\text{app}}} = \frac{R}{Y_{\text{tot}}} - \frac{R}{Y_{\text{mat}}} \quad (\text{B.4})$$

And a Young modulus of the apparatus can be deduced assuming the Young modulus Y of the material to be known (expected value) and extracting the total Young modulus from the original curve:

$$Y_{\text{app}} = \left(\frac{1}{Y_{\text{tot}}} - \frac{1}{Y_{\text{mat}}} \right)^{-1} \quad (\text{B.5})$$

APPENDIX B. TENSILE TEST

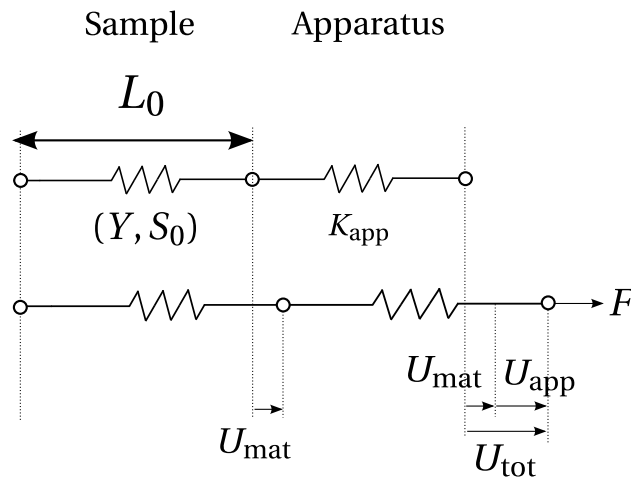


Figure B.1

The material engineering curve can then be obtained recovering the engineering deformation of the gauge:

$$E_{eng}^{mat} = \frac{U_{tot}}{L_0} - \frac{R}{Y^{app}} \quad (B.6)$$

Appendix C

Stress field solutions at intergranular slip band(s) or clear band(s) impacts

This appendix provides the FE computed exponents $1 - \lambda$, prefactors A_{nn} and screening ratio r_{scr} of the intergranular stress fields in the vicinity of the slip bands or clear bands. Table C.1: $1 - \lambda$ and A_{nn} parameters in the case of a single discontinuous band (notations: $\theta \equiv \theta_{\text{GBSB}}$). Table C.2: Screening ratio r_{scr} in the case of multiple slip bands or clear bands (notations: N_{SB} number of slip bands, d interband spacing).

APPENDIX C. STRESS FIELD SOLUTIONS AT INTERGRANULAR SLIP BAND(S) OR CLEAR BAND(S) IMPACTS

θ	$1-\lambda$	A_{nn}	θ	$1-\lambda$	A_{nn}	θ	$1-\lambda$	A_{nn}	θ	$1-\lambda$	A_{nn}	θ	$1-\lambda$	A_{nn}
20	0.349	0.276	21	0.342	0.289	22	0.341	0.311	23	0.336	0.328	24	0.329	0.345
25	0.330	0.361	26	0.323	0.395	27	0.317	0.404	28	0.316	0.434	29	0.309	0.446
30	0.303	0.462	31	0.300	0.501	32	0.295	0.504	33	0.290	0.530	34	0.290	0.559
35	0.285	0.569	36	0.285	0.599	37	0.281	0.608	38	0.274	0.625	39	0.274	0.668
40	0.271	0.681	41	0.273	0.712	42	0.268	0.722	43	0.260	0.747	44	0.262	0.776
45	0.262	0.787	46	0.255	0.818	47	0.253	0.828	48	0.253	0.856	49	0.242	0.861
50	0.235	0.890	51	0.246	0.906	52	0.245	0.931	53	0.241	0.947	54	0.240	0.983
55	0.238	0.987	56	0.232	1.009	57	0.233	1.030	58	0.231	1.051	59	0.229	1.080
60	0.235	1.064	61	0.233	1.086	62	0.234	1.103	63	0.229	1.126	64	0.230	1.148
65	0.229	1.144	66	0.230	1.148	67	0.230	1.156	68	0.233	1.179	69	0.235	1.194
70	0.241	1.179	71	0.247	1.174	72	0.251	1.162	73	0.252	1.173	74	0.247	1.182
75	0.261	1.144	76	0.262	1.148	77	0.269	1.122	78	0.276	1.100	79	0.282	1.107
80	0.289	1.079	81	0.296	1.049	82	0.301	1.034	83	0.310	1.013	84	0.319	0.982
85	0.317	0.969	86	0.323	0.962	87	0.324	0.935	88	0.331	0.925	89	0.333	0.908
90	0.334	0.897	91	0.338	0.864	92	0.336	0.864	93	0.333	0.879	94	0.334	0.869
95	0.336	0.834	96	0.334	0.835	97	0.331	0.819	98	0.332	0.819	99	0.332	0.802
100	0.330	0.790	101	0.333	0.766	102	0.328	0.769	103	0.322	0.781	104	0.323	0.766
105	0.319	0.761	106	0.315	0.763	107	0.314	0.747	108	0.311	0.743	109	0.313	0.734
110	0.310	0.715	111	0.311	0.694	112	0.303	0.687	113	0.299	0.695	114	0.297	0.693
115	0.295	0.669	116	0.294	0.651	117	0.291	0.644	118	0.287	0.645	119	0.289	0.620
120	0.283	0.613	121	0.276	0.608	122	0.273	0.595	123	0.270	0.584	124	0.271	0.569
125	0.259	0.567	126	0.261	0.548	127	0.254	0.537	128	0.253	0.525	129	0.250	0.513
130	0.244	0.499	131	0.240	0.489	132	0.238	0.474	133	0.232	0.462	134	0.226	0.458
135	0.217	0.446	136	0.219	0.429	137	0.209	0.421	138	0.206	0.399	139	0.197	0.392
140	0.194	0.375	141	0.186	0.362	142	0.185	0.349	143	0.172	0.341	144	0.161	0.343
145	0.165	0.314	146	0.157	0.305	147	0.150	0.293	148	0.152	0.264	149	0.136	0.260
150	0.119	0.259	151	0.133	0.235	152	0.107	0.234	153	0.100	0.218	154	0.090	0.222
155	0.078	0.204	156	0.058	0.208	157	0.080	0.176	158	0.034	0.191	159	0.096	0.129
160	-0.015	0.165	-	-	-	-	-	-	-	-	-	-	-	-

Table C.1: $1-\lambda$ and A_{nn} parameters in the case of a single discontinuous band (notations: $\theta \equiv \theta_{\text{GSB}}$).

APPENDIX C. STRESS FIELD SOLUTIONS AT INTERGRANULAR SLIP BAND(S) OR CLEAR BAND(S) IMPACTS

N_{SB} $d(\mu\text{m})$	1	3	5	7	9	11	13	25	35	45
1		0.477	0.361	0.306	0.272	0.249	0.238	0.194	0.178	0.165
2		0.502	0.393	0.341	0.312	0.294	0.279			
3		0.520	0.409	0.367	0.341	0.324	0.310			
4		0.531	0.435	0.392	0.366	0.354	0.346			
5		0.550	0.457	0.415	0.396					
10		0.622								
15		0.697								
20		0.751								
∞	1									

Table C.2: Screening ratio r_{scr} in the case of multiple slip bands or clear bands (notations: N_{SB} number of slip bands, d interband spacing).

Appendix D

Multiscale model of the macroscopic remote stress for intergranular fracture initiation at clear channels impact

This appendix provides the details for the derivation of the multiscale model of the macroscopic critical stress for intergranular finite fracture initiation using the coupled criterion, as proposed by Sauzay et al.

The close-field solution of the related problem is the following:

$$\sigma_{nn}(r) = A_{nn} \langle f\Sigma - \tau_0 \rangle \sqrt{\frac{L}{t}} \left(\frac{t}{r} \right)^{1-\lambda} + .. \quad (D.1)$$

confounding the distance r from the tip of the slip band and a the finite crack size increment for which a potential energy quantity - δW for the finite area increment $A = a \times e$ is needed:

$$-\frac{\delta W}{A} = \gamma(a) = C(f\Sigma - \tau_0)^2 L \left(\frac{a}{t} \right)^{2\lambda-1} + .. \quad (D.2)$$

The coupled criterion proposes the initiation of a finite crack of size a_c when a critical stress σ_c and a critical energy γ_c are simultaneously reached over a_c :

$$\begin{cases} \sigma_{nn}(r \equiv a) \geq \sigma_c \\ \gamma(a) \geq \gamma_c \end{cases} \quad (D.3)$$

$$\quad (D.4)$$

As extensively shown in chapter 5, the initiation of a finite crack of size a_c is enabled when the equality holds in equations D.3 and D.4 at a critical remote stress Σ_c , which combined with equations D.1 and D.2, yields:

First

$$A_{nn}(f\Sigma_c - \tau_0) \sqrt{\frac{L}{t}} \left(\frac{t}{a_c} \right)^{1-\lambda} = \sigma_c \quad (D.5)$$

APPENDIX D. MULTISCALE MODEL OF THE MACROSCOPIC REMOTE STRESS FOR INTERGRANULAR FRACTURE INITIATION AT CLEAR CHANNELS IMPACT

from equation D.3.

Isolating the critical effective shear stress ($f\Sigma_c - \tau_0$) at the crack initiation:

$$f\Sigma_c - \tau_0 = \frac{1}{A_{nn}} \sigma_c \sqrt{\frac{t}{L}} \left(\frac{a_c}{t} \right)^{1-\lambda} \quad (\text{D.6})$$

And, secondly, from equation D.4:

$$C(f\Sigma_c - \tau_0)^2 L \left(\frac{a_c}{t} \right)^{2\lambda-1} = \gamma_c \quad (\text{D.7})$$

Replacing equation D.6 in equation D.7 gives access to the increment crack size a_c :

$$a_c = \frac{\gamma_c}{\sigma_c^2} \frac{A_{nn}^2}{C} \quad (\text{D.8})$$

which can be used in equation D.6:

$$f\Sigma_c - \tau_0 = \frac{1}{A_{nn}} \sigma_c \sqrt{\frac{t}{L}} \left(\frac{\gamma_c}{\sigma_c^2} \frac{A_{nn}^2}{C} \right)^{1-\lambda} \left(\frac{1}{t} \right)^{1-\lambda} \quad (\text{D.9})$$

$$= A_{nn}^{1-2\lambda} \sigma_c^{2\lambda-1} \left(\frac{1}{C} \right)^{1-\lambda} \sqrt{\frac{t}{L}} \left(\frac{\gamma_c}{t} \right)^{1-\lambda} \quad (\text{D.10})$$

This finally leads to the critical remote stress to crack initiation:

$$\Sigma_c = \frac{1}{f} \left[\tau_0 + \left(\frac{1}{C} \right)^{1-\lambda} A_{nn}^{1-2\lambda} \sqrt{\frac{t}{L}} \sigma_c^{2\lambda-1} \left(\frac{\gamma_c}{t} \right)^{1-\lambda} \right] \quad (\text{D.11})$$

Bibliography

- [P. H. Pumphrey, 1975] P. H. Pumphrey (1975). Observations of the interaction of lattice dislocations with high angle grain boundaries. *J. Phys. Colloques*, 36:C4–23–C4–33.
- [Alers et al., 1960] Alers, G., Neighbours, J., and Sato, H. (1960). Temperature dependent magnetic contributions to the high field elastic constants of nickel and an fe-ni alloy. *Journal of Physics and Chemistry of Solids*, 13(1):40 – 55.
- [Andric et al., 2019] Andric, P., Yin, B., and Curtin, W. (2019). Stress-dependence of generalized stacking fault energies. *Journal of the Mechanics and Physics of Solids*, 122:262 – 279.
- [ANS, 2019] ANS (2019). New approach to internals inspections saves dose and time. *Nuclear News*.
- [Armstrong et al., 2009] Armstrong, D., Rogers, M., and Roberts, S. (2009). Micromechanical testing of stress corrosion cracking of individual grain boundaries. *Scripta Materialia*, 61(7):741–743.
- [Armstrong et al., 2011] Armstrong, D., Wilkinson, A., and Roberts, S. (2011). Micro-mechanical measurements of fracture toughness of bismuth embrittled copper grain boundaries. *Philosophical Magazine Letters*, 91(6):394–400.
- [Aubert et al., 2010] Aubert, I., Olive, J.-M., and Saintier, N. (2010). The effect of internal hydrogen on surface slip localisation on polycrystalline AISI 316L stainless steel. *Materials Science and Engineering: A*, 527(21):5858–5866.
- [Aubert et al., 2012] Aubert, I., Saintier, N., and Olive, J.-M. (2012). Crystal plasticity computation and atomic force microscopy analysis of the internal hydrogen-induced slip localization on polycrystalline stainless steel. *Scripta Materialia*, 66(9):698 – 701.
- [Aubert et al., 2016] Aubert, I., Saintier, N., Olive, J.-M., and Plessier, F. (2016). A methodology to obtain data at the slip-band scale from atomic force microscopy observations and crystal plasticity simulations. application to hydrogen-induced slip localization on aisi 316l stainless steel. *Acta Materialia*, 104:9 – 17.

BIBLIOGRAPHY

- [Bailat et al., 2000] Bailat, C., Gröschel, F., and Victoria, M. (2000). Deformation modes of proton and neutron irradiated stainless steels. *Journal of Nuclear Materials*, 276(1):283 – 288.
- [Banerjea and Smith, 1988] Banerjea, A. and Smith, J. R. (1988). Origins of the universal binding-energy relation. *Phys. Rev. B*, 37(0):6632–6645.
- [Barbé et al., 2018] Barbé, E., Fu, C.-C., and Sauzay, M. (2018). Fracture of coherent interfaces between an fcc metal matrix and the $cr_{23}c_6$ carbide precipitate from first principles. *Phys. Rev. Materials*, 2:023605.
- [Barrows et al., 2016] Barrows, W., Dingreville, R., and Spearot, D. (2016). Traction–separation relationships for hydrogen induced grain boundary embrittlement in nickel via molecular dynamics simulations. *Materials Science and Engineering: A*, 650:354 – 364.
- [Binnig et al., 1986] Binnig, G., Quate, C. F., and Gerber, C. (1986). Atomic force microscope. *Phys. Rev. Lett.*, 56(9):930–933.
- [Bitzek et al., 2015] Bitzek, E., Kermode, J. R., and Gumbsch, P. (2015). Atomistic aspects of fracture. *International Journal of Fracture*, 191(1):13–30.
- [Bollmann, 1970] Bollmann, W. (1970). *Crystal defects and crystalline interfaces*. Springer.
- [Borovikov et al., 2017] Borovikov, V., Mendelev, M. I., and King, A. H. (2017). Effects of solutes on dislocation nucleation from grain boundaries. *International Journal of Plasticity*, 90:146 – 155.
- [Britton and Wilkinson, 2012] Britton, T. B. and Wilkinson, A. J. (2012). Stress fields and geometrically necessary dislocation density distributions near the head of a blocked slip band. *Acta Materialia*, 60(16):5773 – 5782.
- [Bruemmer et al., 1999] Bruemmer, S., Simonen, E., Scott, P., Andresen, P., Was, G., and Nelson, J. (1999). Radiation-induced material changes and susceptibility to intergranular failure of light-water-reactor core internals. *Journal of Nuclear Materials*, 274(3):299 – 314.
- [Bruker,] Bruker. <http://www.brukerafmprobes.com>.
- [Bulatov et al., 2014] Bulatov, V. V., Reed, B. W., and Kumar, M. (2014). Grain boundary energy function for fcc metals. *Acta Materialia*, 65:161 – 175.
- [Busby and Was, 2003] Busby, J. and Was, G. (2003). *Irradiation-Assisted Stress Corrosion Cracking in Model Austenitic Alloys with Solute Additions*, pages 995–1014. TMS.

BIBLIOGRAPHY

- [Béland et al., 2017] Béland, L. K., Tamm, A., Mu, S., Samolyuk, G., Osetsky, Y., Aabloo, A., Klintonberg, M., Caro, A., and Stoller, R. (2017). Accurate classical short-range forces for the study of collision cascades in fe–ni–cr. *Computer Physics Communications*, 219:11 – 19.
- [Caballero Hinostroza, 2016] Caballero Hinostroza, J. (2016). *Modélisation de l'amorçage de la corrosion sous contrainte de l'alliage 600 en milieu primaire*. Theses, Ecole Nationale Supérieure des Mines de Paris.
- [Cahn et al., 2006] Cahn, J. W., Mishin, Y., and Suzuki, A. (2006). Coupling grain boundary motion to shear deformation. *Acta Materialia*, 54(19):4953 – 4975.
- [Cai et al., 2018] Cai, Y., Wu, H., and Luo, S. (2018). A loading-dependent model of critical resolved shear stress. *International Journal of Plasticity*, 109:1 – 17.
- [Cao et al., 2008] Cao, A., Wei, Y., and Ma, E. (2008). Grain boundary effects on plastic deformation and fracture mechanisms in cu nanowires: Molecular dynamics simulations. *Phys. Rev. B*, 77:195429.
- [Caré and Zaoui, 1996] Caré, S. and Zaoui, A. (1996). Cavitation at triple nodes in α -zirconium polycrystals. *Acta Materialia*, 44(4):1323 – 1336.
- [CAST3M,] CAST3M. Cast3m – <http://www-cast3m.cea.fr>.
- [Chartier et al., 2013] Chartier, A., Golovchuk, B., Gossé, S., and Brutzel, L. V. (2013). Disorder and grain boundaries of (Ni,Fe)Cr₂O₄ spinels from atomistic calculations. *The Journal of Chemical Physics*, 139(13):134702.
- [Chen et al., 1999] Chen, Y., Spätig, P., and Victoria, M. (1999). The mechanical properties of 590 mev proton irradiated iron. *Journal of Nuclear Materials*, 271-272:128 – 132.
- [Chung et al., 2001] Chung, H., Strain, R., and Shack, W. (2001). Tensile and stress corrosion cracking properties of type 304 stainless steel irradiated to a very high dose. *Nuclear Engineering and Design*, 208(3):221 – 234.
- [Cissé et al., 2013] Cissé, S., Laffont, L., and Lafont, M.-C., T. B. (2013). Influence of localized plasticity on oxidation behaviour of austenitic stainless steels under primary water reactor. *J. Nucl. Mater.*, 433:319 – 328.
- [Cookson et al., 1993] Cookson, J., Carter, R., Damcott, D., Atzmon, M., and Was, G. (1993). Irradiation assisted stress corrosion cracking of controlled purity 304l stainless steels. *Journal of Nuclear Materials*, 202(1):104 – 121.
- [Coriou et al., 1959] Coriou, Grall, Gall, L., and Vettier (1959). Stress corrosion cracking of inconel in high temperature water. Technical report, CEA Saclay - Third Metallurgy Conference on Corrosion.

BIBLIOGRAPHY

- [Coriou et al., 1966] Coriou, H., Grall, L., Mahieu, C., and Pelas, M. (1966). Sensitivity to stress corrosion and intergranular attack of high-nickel austenitic alloys. *CORROSION*, 22(10):280–290.
- [Couvant et al., 2005] Couvant, T., Legras, L., Vaillant, F., Boursier, J., and Rouillon, Y. (2005). *Effect of strain-hardening on stress corrosion cracking of AISI 304L stainless steel in PWR primary environment at 360C*, pages 1069–1079. TMS.
- [Couvant et al., 2017] Couvant, T., Wehbi, M., Caballero, J., Duhamel, C., and Crépin, J. (2017). Journées des jeunes chercheurs 2017 dijon - workshop cnrs modélisation et simulation de la csc.
- [Couvant et al., 2015] Couvant, T., Wehbi, M., Duhamel, C., Crépin, J., and Munier, R. (2015). Development of a local model to predict scc: preliminary calibration of parameters for nickel alloys exposed to primary water. In *17th International Conference on Environmental Degradation of Materials in Nuclear Systems-Water Reactors*, pages 1955–1973.
- [Cui et al., 2014] Cui, B., Kacher, J., McMurtrey, M., Was, G., and Robertson, I. (2014). Influence of irradiation damage on slip transfer across grain boundaries. *Acta Mater.*, 65:150 – 160.
- [Daw and Baskes, 1984] Daw, M. S. and Baskes, M. I. (1984). Embedded-atom method: Derivation and application to impurities, surfaces, and other defects in metals. *Phys. Rev. B*, 29:6443–6453.
- [Dingreville et al., 2017] Dingreville, R., Aksoy, D., and Spearot, D. E. (2017). A primer on selecting grain boundary sets for comparison of interfacial fracture properties in molecular dynamics simulations. *Scientific report*, 7.
- [Dugdale, 1960] Dugdale, D. (1960). Yielding of steel sheets containing slits. *Journal of the Mechanics and Physics of Solids*, 8(2):100 – 104.
- [Dugdale et al., 2013] Dugdale, H., Armstrong, D. E., Tarleton, E., Roberts, S. G., and Lozano-Perez, S. (2013). How oxidized grain boundaries fail. *Acta Mater.*, 61(13):4707 – 4713.
- [Dumerval et al., 2016] Dumerval, M., Perrin, S., Marchetti, L., Sennour, M., Jomard, F., Vaubaillon, S., and Wouters, Y. (2016). Effect of implantation defects on the corrosion of 316L stainless steels in primary medium of pressurized water reactors. *Corrosion Science*, 107:1 – 8.
- [EDF, 2018] EDF (2018). Training school on safe long-term operation of light water reactors through the improvement of understanding of radiation effects, 3-7 september 2018, polytechnic university of valencia, soteria.

BIBLIOGRAPHY

- [Edwards et al., 2001] Edwards, D., Garmer, F., Simonen, E., and Bruemmer, S. (2001). Characterization of neutron-irradiated 300-series stainless steels to assess mechanisms of irradiation-assisted stress corrosion cracking: Volume 2: Core components. Technical report, EPRI, Palo Alto, CA.
- [Edwards et al., 2005] Edwards, D., Singh, B., and Bilde-Sørensen, J. (2005). Initiation and propagation of cleared channels in neutron-irradiated pure copper and a precipitation hardened CuCrZr alloy. *J. Nucl. Mater.*, 342(1–3):164 – 178.
- [Edwards et al., 2003] Edwards, E., Simonen, E., and Bruemmer, S. (2003). Evolution of fine-scale defects in stainless steels neutron-irradiated at 275 degree celsius. *Journal of Nuclear Materials*, 317(1):13 – 31.
- [Eshelby et al., 1951] Eshelby, J., Frank, F., and Nabarro, F. (1951). Xli. the equilibrium of linear arrays of dislocations. *The London, Edinburgh, and Dublin Philosophical Magazine and Journal of Science*, 42(327):351–364.
- [Evrard and Sauzay, 2010] Evrard, P. and Sauzay, M. (2010). Modelling of the effect of dislocation channel on intergranular microcrack nucleation in pre-irradiated austenitic stainless steels during low strain rate tensile loading. *Journal of Nuclear Materials*, 405(2):83–94.
- [Fournier et al., 2007] Fournier, L., Savoie, M., and Delafosse, D. (2007). Influence of localized deformation on A-286 austenitic stainless steel stress corrosion cracking in PWR primary water. *Journal of Nuclear Materials*, 366(1):187 – 197.
- [Frenkel, 1926] Frenkel, J. (1926). Zur theorie der elastizitätsgrenze und der festigkeit kristallinischer körper. *Zeitschrift für Physik*, 37(7):572–609.
- [Fukuya, 2013] Fukuya, K. (2013). Current understanding of radiation-induced degradation in light water reactor structural materials. *Journal of Nuclear Science and Technology*, 50(3):213–254.
- [Fukuya et al., 2008a] Fukuya, K., Nishioka, H., Fujii, K., Kamaya, M., Miura, T., and Torimaru, T. (2008a). Fracture behavior of austenitic stainless steels irradiated in PWR. *J. Nucl. Mater.*, 378(2):211 – 219.
- [Fukuya et al., 2013] Fukuya, K., Nishioka, H., Fujii, K., Miura, T., and Kitsunai, Y. (2013). Local strain distribution near grain boundaries under tensile stresses in highly irradiated {SUS316} stainless steel. *J. Nucl. Mater.*, 432(1–3):67 – 71.
- [Fukuya et al., 2011] Fukuya, K., Nishioka, H., Fujii, K., Miura, T., and Torimaru, T. (2011). An {EBSD} examination of {SUS316} stainless steel irradiated to 73 dpa and deformed at 593 k. *J. Nucl. Mater.*, 417(1–3):958 – 962. Proceedings of ICFRM-14.

BIBLIOGRAPHY

- [Fukuya et al., 2008b] Fukuya, K., Nishioka, H., Fujji, K., and Torimaru, T. (2008b). Effects of dissolved hydrogen and strain rate on IASCC behavior in highly irradiated stainless steels. *Journal of Nuclear Science and Technology*, 45(5):452–458.
- [Féron et al., 2012] Féron, D., Herms, E., and Tanguy, B. (2012). Behavior of stainless steels in pressurized water reactor primary circuits. *Journal of Nuclear Materials*, 427(1):364 – 377.
- [Féron and Staehle, 2016] Féron, D. and Staehle, R., editors (2016). *Stress Corrosion Cracking of Nickel Based Alloys in Water-cooled Nuclear Reactor - The Coriou Effect*. Woodhead Publishing.
- [Genée, 2017] Genée, J. G. (2017). *Statistical and Numerical Study of Slip Bands-Grain Boundaries Interactions : Case of Nickel Based Superalloys*. Theses, ISAE-ENSMA Ecole Nationale Supérieure de Mécanique et d'Aérotechnique - Poitiers.
- [Genée et al., 2017] Genée, J., Signor, L., and Villechaise, P. (2017). Slip transfer across grain/twin boundaries in polycrystalline ni-based superalloys. *Materials Science and Engineering: A*, 701:24 – 33.
- [Gertsman et al., 1989] Gertsman, V. Y., Nazarov, A. A., Romanov, A. E., Valiev, R. Z., and Vladimirov, V. I. (1989). Disclination-structural unit model of grain boundaries. *Philosophical Magazine A*, 59(5):1113–1118.
- [Griffith, 1921] Griffith, A. A. (1921). The phenomena of rupture and flow in solids. *Philosophical Transactions of the Royal Society of London. Series A, Containing Papers of a Mathematical or Physical Character*, 221:163–198.
- [Guerre et al., 2011] Guerre, C., Laghoutaris, P., Chêne, J., Marchetti, L., Molins, R., Duhamel, C., and Sennour, M. (2011). *Stress corrosion cracking of alloy 600 in PWR primary water: influence of chromium, hydrogen and oxygen diffusion*, pages 1477–1488. TMS.
- [Gupta et al., 2016] Gupta, J., Hure, J., Tanguy, B., Laffont, L., Lafont, M.-C., and Andrieu, E. (2016). Evaluation of stress corrosion cracking of irradiated 304l stainless steel in pwr environment using heavy ion irradiation. *Journal of Nuclear Materials*, 476:82 – 92.
- [Gururaj et al., 2015] Gururaj, K., Robertson, C., and Fivel, M. (2015). Channel formation and multiplication in irradiated fcc metals: a 3d dislocation dynamics investigation. *Philosophical Magazine*, 95(12):1368–1389.
- [Gussev et al., 2015] Gussev, M. N., Field, K. G., and Busby, J. T. (2015). Deformation localization and dislocation channel dynamics in neutron-irradiated austenitic stainless steels. *J. Nucl. Mater.*, 460:139 – 152.

BIBLIOGRAPHY

- [Hayes et al., 2004] Hayes, R. L., Ortiz, M., and Carter, E. A. (2004). Universal binding-energy relation for crystals that accounts for surface relaxation. *Phys. Rev. B*, 69:172104.
- [Hazan, 2016] Hazan (2016). Private communication.
- [Hazan, 2019] Hazan, J. (2019). *Etude de la durée de vie et de l'endommagement intergranulaire par fatigue des métaux cubiques à faces centrées: influence de la taille de grains et de l'épaisseur d'éprouvette*. PhD thesis, Université Paris Sorbonne.
- [Henninger, 2007] Henninger, C. (2007). *Prise en compte des contraintes résiduelles dans un critère d'amorçage en rupture fragile*. PhD thesis. Thèse de doctorat dirigée par Leguillon, Dominique Mécanique Paris 6 2007.
- [Henninger et al., 2007] Henninger, C., Leguillon, D., and Martin, E. (2007). Crack initiation at a v-notch– comparison between a brittle fracture criterion and the dugdale cohesive model. *Comptes Rendus Mécanique*, 335(7):388 – 393.
- [Hide et al., 1995] Hide, K., Onchi, T., Mayuzumi, M., Dohi, K., and Futamura, Y. (1995). Intergranular cracking of irradiated thermally sensitized type 304 stainless steel in high-temperature water and inert gas. *CORROSION*, 51(10):757–766.
- [Hirth and Lothe, 1982] Hirth, J. P. and Lothe, J. (1982). *Theory of dislocations*. Kriger publishing company Malabar Florida.
- [Hosemann, 2018] Hosemann, P. (2018). Small-scale mechanical testing on nuclear materials: bridging the experimental length-scale gap. *Scripta Materialia*, 143:161 – 168.
- [Hull and Bacon, 2011] Hull, D. and Bacon, D. (2011). *Introduction to dislocations*. Elsevier.
- [Huntington, 1958] Huntington, H. (1958). The elastic constants of crystals. volume 7 of *Solid State Physics*, pages 213 – 351. Academic Press.
- [Hure et al., 2016] Hure, J., Shawish, S. E., Cizelj, L., and Tanguy, B. (2016). Intergranular stress distributions in polycrystalline aggregates of irradiated stainless steel. *Journal of Nuclear Materials*, 476:231 – 242.
- [IAEA, 2020] IAEA (2020). *Nuclear Power Reactors in the World*. Number 2 in Reference Data Series. International Atomic Energy Agency (IAEA), V.
- [Isamu and Tsurekawa, 2019] Isamu, K. and Tsurekawa, S. (2019). Incipient plasticity near the grain boundary in pure and in sulfur-segregated nickel bicrystals. International Student Conference on Advanced Science and Technology - Kumamoto University - Japan.

BIBLIOGRAPHY

- [Jambon et al., 2011] Jambon, F., Marchetti, L., Jomard, F., and Chêne, J. (2011). Mechanism of hydrogen absorption during the exposure of alloy 600-like single-crystals to pwr primary simulated media. *Journal of Nuclear Materials*, 414(3):386 – 392.
- [Janisch et al., 2010] Janisch, R., Ahmed, N., and Hartmaier, A. (2010). Ab initio tensile tests of al bulk crystals and grain boundaries: Universality of mechanical behavior. *Phys. Rev. B*, 81:184108.
- [Jiao et al., 2005] Jiao, Z., Busby, J., Obata, R., and Was, G. (2005). *Influence of Localized Deformation on Irradiation-assisted Stress Corrosion Cracking of Proton-irradiated Austenitic Alloys*, pages 379–388. TMS.
- [Jiao et al., 2007] Jiao, Z., Busby, J., and Was, G. (2007). Deformation microstructure of proton-irradiated stainless steels. *Journal of Nuclear Materials*, 361(2):218 – 227. TMS 2007:Wechsler Symposium.
- [Jiao and Was, 2008] Jiao, Z. and Was, G. (2008). Localized deformation and iascc initiation in austenitic stainless steels. *Journal of Nuclear Materials*, 382(2):203 – 209. Microstructural Processes in Irradiated Materials.
- [Jiao and Was, 2010] Jiao, Z. and Was, G. (2010). The role of irradiated microstructure in the localized deformation of austenitic stainless steels. *Journal of Nuclear Materials*, 407(1):34 – 43. Proceedings of the Symposium on Microstructural Processes in Irradiated Materials and on Reactor Pressure Vessel (RPV) Embrittlement and Fusion Materials: Measuring, Modeling and Managing Irradiation Effects.
- [Jiao and Was, 2011] Jiao, Z. and Was, G. (2011). Impact of localized deformation on IASCC in austenitic stainless steels. *J. Nucl. Mater.*, 408(3):246 – 256.
- [Johnson et al., 2016] Johnson, D., Kuhr, B., Farkas, D., and Was, G. (2016). Quantitative analysis of localized stresses in irradiated stainless steels using high resolution electron backscatter diffraction and molecular dynamics modeling. *Scripta Materialia*, 116:87 – 90.
- [Kacher et al., 2014] Kacher, J., Eftink, B., Cui, B., and Robertson, I. (2014). Dislocation interactions with grain boundaries. *Current Opinion in Solid State and Materials Science*, 18(4):227 – 243. Slip Localization and Transfer in Deformation and Fatigue of Polycrystals.
- [Kelly and MacMillan, 1986] Kelly, A. and MacMillan, N. (1986). *Strong Solids*, chapter 1, pages 24–34. Clarendon Press - Oxford, third edition edition.
- [Kittel and McEuen, 1996] Kittel, C. and McEuen, P. (1996). *Introduction to solid state physics*, volume 8. Wiley New York.

BIBLIOGRAPHY

- [Kruska et al., 2012] Kruska, K., Lozano-Perez, S., Saxey, D. W., Terachi, T., Yamada, T., and Smith, G. D. (2012). Nanoscale characterisation of grain boundary oxidation in cold-worked stainless steels. *Corrosion Science*, 63:225 – 233.
- [Kurzydowski et al., 1984] Kurzydowski, K., Varin, R., and Zielinski, W. (1984). In situ investigation of the early stages of plastic deformation in an austenitic stainless steel. *Acta Metallurgica*, 32(1):71–78.
- [LAMMPS,] LAMMPS. <http://lammps.sandia.gov>.
- [Laws and Lee, 1989] Laws, N. and Lee, J. (1989). Microcracking in polycrystalline ceramics : Elastic isotropy and thermal anisotropy. *Journal of the Mechanics and Physics of Solids*, 37(5):603 – 618.
- [Lazar and Podloucky, 2008] Lazar, P. and Podloucky, R. (2008). Cleavage fracture of a crystal: Density functional theory calculations based on a model which includes structural relaxations. *Phys. Rev. B*, 78:104114.
- [Le Millier, 2014] Le Millier, M. (2014). *Fragilisation des aciers inoxydables austénitiques sous irradiation : évolution de la microstructure et amorçage de la corrosion sous contrainte assistée par l'irradiation en milieu REP*. Theses, Ecole Nationale Supérieure des Mines de Paris.
- [Lee and Vermilyea, 1971] Lee, D. and Vermilyea, D. A. (1971). The initiation of intergranular failure in inconel-600. *Metallurgical Transactions*, 2(9):2565–2571.
- [Leguillon, 2002] Leguillon, D. (2002). Strength or toughness? a criterion for crack onset at a notch. *European Journal of Mechanics - A/Solids*, 21(1):61 – 72.
- [Leguillon and Sanchez-Palencia, 1987] Leguillon, D. and Sanchez-Palencia, E. (1987). *Computation of singular solutions in elliptic problems and elasticity*. John Wiley & Sons, Inc.
- [Lim and Raj, 1985] Lim, L. and Raj, R. (1985). Continuity of slip screw and mixed crystal dislocations across bicrystals of nickel at 573 K. *Acta Metallurgica*, 33(8):1577 – 1583.
- [Linne et al., 2019] Linne, M., Venkataraman, A., Sangid, M., and Daly, S. (2019). Grain boundary sliding and slip transmission in high purity aluminum. *Experimental Mechanics*, 59(5):643–658.
- [Lozano-Perez, 2017] Lozano-Perez, S. (2017). private communication.
- [Lozano-Perez et al., 2014] Lozano-Perez, S., Dohr, J., Meisnar, M., and Kruska, K. (2014). SCC in PWRs: Learning from a bottom-up approach. *Metallurgical and Materials Transactions E*, 1(2):194–210.

BIBLIOGRAPHY

- [Lozano-Perez et al., 2012a] Lozano-Perez, S., Kruska, K., Iyengar, I., Terachi, T., and Yamada, T. (2012a). The role of cold work and applied stress on surface oxidation of 304 stainless steel. *Corrosion Science*, 56:78 – 85.
- [Lozano-Perez et al., 2012b] Lozano-Perez, S., Ni, N., Kruska, K., Grovenor, C., Terachi, T., and Yamada, T. (2012b). *Characterizing Environmental Degradation in PWRs by 3D FIB Sequential Sectioning*, pages 993–1004. John Wiley & Sons, Inc.
- [Lozano-Perez et al., 2011] Lozano-Perez, S., Rodrigo, P., and Gontard, L. C. (2011). Three-dimensional characterization of stress corrosion cracks. *Journal of Nuclear Materials*, 408(3):289 – 295.
- [Lozano-Perez et al., 2010] Lozano-Perez, S., Saxey, D. W., Yamada, T., and Terachi, T. (2010). Atom-probe tomography characterization of the oxidation of stainless steel. *Scripta Materialia*, 62(11):855 – 858.
- [Malis et al., 1972] Malis, T., Lloyd, D., and Tangri, K. (1972). Dislocation generation from grain boundaries in nickel. *Physica status solidi (a)*, 11(1):275–286.
- [Marano et al., 2019] Marano, A., Gélébart, L., and Forest, S. (2019). Intragranular localization induced by softening crystal plasticity: Analysis of slip and kink bands localization modes from high resolution fft-simulations results. *Acta Materialia*, 175:262–275.
- [Marchetti et al., 2016] Marchetti, L., Perrin, S., Jambon, F., and Pijolat, M. (2016). Corrosion of nickel-base alloys in primary medium of pressurized water reactors: New insights on the oxide growth mechanisms and kinetic modelling. *Corrosion Science*, 102:24 – 35.
- [Massoud et al., 2005] Massoud, J.-P., Zamboch, M., Brabec, P., Shamardin, V., Prokhorov, V., and Dubuisson, P. (2005). *Influence of the neutron spectrum on the tensile properties of irradiated austenitic stainless steels, in air and in PWR environment*, pages 357–363. TMS.
- [McMurtrey et al., 2015] McMurtrey, M., Cui, B., Robertson, I., Farkas, D., and Was, G. (2015). Mechanism of dislocation channel-induced irradiation assisted stress corrosion crack initiation in austenitic stainless steel. *Current Opinion in Solid State and Materials Science*, 19(5):305 – 314.
- [McMurtrey and Was, 2012] McMurtrey, M. and Was, G. (2012). *Role of Slip Behavior in the Irradiation Assisted Stress Corrosion Cracking in Austenitic Steels*, pages 1383–1394. John Wiley & Sons, Inc.
- [McMurtrey et al., 2011] McMurtrey, M., Was, G., Patrick, L., and Farkas, D. (2011). Relationship between localized strain and irradiation assisted stress corrosion cracking in an austenitic alloy. *Materials Science and Engineering: A*, 528(10–11):3730 – 3740.

BIBLIOGRAPHY

- [Menard, 2005] Menard, M. (2005). *Effets de l'hydrogène absorbé sur la localisation de la déformation plastique d'un acier inoxydable 316L*. PhD thesis.
- [Mishin, 2004] Mishin, Y. (2004). Atomistic modeling of the γ and γ' -phases of the ni-al system. *Acta Materialia*, 52(6):1451 – 1467.
- [Mishin and Farkas, 1998] Mishin, Y. and Farkas, D. (1998). Atomistic simulation of [001] symmetrical tilt grain boundaries in nial. *Philosophical Magazine A*, 78(1):29–56.
- [Mishin et al., 2001] Mishin, Y., Mehl, M. J., Papaconstantopoulos, D. A., Voter, A. E., and Kress, J. D. (2001). Structural stability and lattice defects in copper: Ab initio, tight-binding, and embedded-atom calculations. *Phys. Rev. B*, 63:224106.
- [Miwa et al., 2007] Miwa, Y., Tsukada, T., and Jitsukawa, S. (2007). Scc behavior of solid-HIPED and irradiated type 316LN-IG stainless steel in oxygenated or hydrhydrogen water at 423-603K. *J. Nucl. Mater.*, 367 - 370:1175 – 1179.
- [Murer and Leguillon, 2010] Murer, S. and Leguillon, D. (2010). Static and fatigue failure of quasi-brittle materials at a V-notch using a dugdale model. *European Journal of Mechanics - A/Solids*, 29(2):109 – 118.
- [Murr, 1981] Murr, L. (1981). Strain-induced dislocation emission from grain boundaries in stainless steel. *Materials Science and Engineering*, 51(1):71 – 79.
- [Murr, 1974] Murr, L. E. (1974). Yielding and grain-boundary ledges: Some comments on the hall-petch relation. *Applied Physics Letters*, 24(11):533–536.
- [Mykura, 1980] Mykura, H. (1980). A checklist of cubic coincidence site lattice relations. *Grain Boundary Structure and Kinetics*, pages 445–456.
- [Möller et al., 2013] Möller, J. J., Prakash, A., and Bitzek, E. (2013). Fe2at – finite element informed atomistic simulations. *Modelinf and Simulation in Materials Science and Engineering*, 21(5).
- [Nazarov et al., 2000] Nazarov, A., Shenderova, O., and Brenner, D. (2000). On the disclination-structural unit model of grain boundaries. *Materials Science and Engineering: A*, 281(1):148 – 155.
- [Nečas and Petr, 2012] Nečas, D. and Petr, K. (2012). Gwyddion: an open-source software for SPM data analysis. *Central European Journal of Physics*, 10:181–188.
- [Nishioka et al., 2008] Nishioka, H., Fukuya, K., Fujji, K., and Kitsunai, Y. (2008). Deformation structure in highly irradiated stainless steels. *Journal of Nuclear Science and Technology*, 45(4):274–287.

BIBLIOGRAPHY

- [Nogaret et al., 2008] Nogaret, T., Rodney, D., Fivel, M., and Robertson, C. (2008). Clear band formation simulated by dislocation dynamics: Role of helical turns and pile-ups. *Journal of Nuclear Materials*, 380(1):22 – 29.
- [Ogata et al., 2002] Ogata, S., Li, J., and Yip, S. (2002). Ideal pure shear strength of aluminum and copper. *Science*, 298(5594):807–811.
- [Olmsted et al., 2009] Olmsted, D. L., Foiles, S. M., and Holm, E. A. (2009). Survey of computed grain boundary properties in face-centered cubic metals: I. grain boundary energy. *Acta Materialia*, 57(13):3694 – 3703.
- [Onchi et al., 2003] Onchi, T., Dohi, K., Soneda, N., Cowan, J., Scowen, R., and Castano, M. (2003). Fractography and microstructural characterization of irradiated 304 stainless steel intergranular fractured in inert gas. *Journal of Nuclear Materials*, 320(3):194–208.
- [OVITO,] OVITO. <http://ovito.org/>.
- [Perrin et al., 2013] Perrin, S., Marchetti, L., Duhamel, C., Sennour, M., and Jomard, F. (2013). Influence of irradiation on the oxide film formed on 316L stainless steel in PWR primary water. *Oxidation of Metals*, 80(5):623–633.
- [Pickering, 1976] Pickering, F. (1976). Physical metallurgy of stainless steel developments. *Int. Met. Rev., Dec. 1976*, 21, 227-268.
- [Plimpton, 1995] Plimpton, S. (1995). Fast parallel algorithms for short-range molecular dynamics. *Journal of Computational Physics*, 117(1):1 – 19.
- [Pokluda et al., 2015] Pokluda, J., Černý, M., Šob, M., and Umeno, Y. (2015). Ab initio calculations of mechanical properties: Methods and applications. *Progress in Materials Science*, 73:127 – 158.
- [Pokor, 2002] Pokor, C. (2002). *Caractérisation microstructurale et modélisation du durcissement des aciers austénitiques irradiés des structures internes des réacteurs à eau pressurisée*. PhD thesis. Thèse de doctorat dirigée par Bréchet, Yves Science et génie des matériaux Grenoble INPG 2002.
- [Pond and Smith, 1977] Pond, R. C. and Smith, D. A. (1977). On the absorption of dislocations by grain boundaries. *The Philosophical Magazine: A Journal of Theoretical Experimental and Applied Physics*, 36(2):353–366.
- [Priester, 2006] Priester, L. (2006). *Les joints de grains: de la théorie à l'ingénierie*. L'Editeur: EDP Sciences.
- [Priester, 2013] Priester, L. (2013). *Grain boundaries and crystalline plasticity*. John Wiley & Sons.

BIBLIOGRAPHY

- [Pumphrey and Gleiter, 1974] Pumphrey, P. H. and Gleiter, H. (1974). The annealing of dislocations in high-angle grain boundaries. *The Philosophical Magazine: A Journal of Theoretical Experimental and Applied Physics*, 30(3):593–602.
- [Read and Shockley, 1950] Read, W. T. and Shockley, W. (1950). Dislocation models of crystal grain boundaries. *Phys. Rev.*, 78:275–289.
- [Rey, C. et al., 1985] Rey, C., Mussot, P., Vroux, A. M., and Zaoui, A. (1985). Effects of interfaces on the plastic behaviour of metallic aggregates. *J. Phys. Colloques*, 46:C4–645–C4–550.
- [Rice, 1992] Rice, J. R. (1992). Dislocation nucleation from a crack tip: An analysis based on the peierls concept. *Journal of the Mechanics and Physics of Solids*, 40(2):239 – 271.
- [Rittner and Seidman, 1996] Rittner, J. D. and Seidman, D. N. (1996). $\langle 110 \rangle$ symmetric tilt grain-boundary structures in fcc metals with low stacking-fault energies. *Phys. Rev. B*, 54:6999–7015.
- [Robertson, 1999] Robertson, I. (1999). The effect of hydrogen on dislocation dynamics. *Engineering Fracture Mechanics*, 64(5):649 – 673.
- [Rose et al., 1981] Rose, J. H., Ferrante, J., and Smith, J. R. (1981). Universal binding energy curves for metals and bimetallic interfaces. *Phys. Rev. Lett.*, 47:675–678.
- [Rose et al., 1983] Rose, J. H., Smith, J. R., and Ferrante, J. (1983). Universal features of bonding in metals. *Phys. Rev. B*, 28:1835–1845.
- [Rose et al., 1984] Rose, J. H., Smith, J. R., Guinea, F., and Ferrante, J. (1984). Universal features of the equation of state of metals. *Phys. Rev. B*, 29:2963–2969.
- [Saada, G., 1989] Saada, G. (1989). Edges and wedges. *J. Phys. France*, 50(18):2505–2517.
- [SALOME, 2017] SALOME (2017). Salomé : The open source integration platform for numerical simulation.
- [Sangid et al., 2011] Sangid, M. D., Ezaz, T., Sehitoglu, H., and Robertson, I. M. (2011). Energy of slip transmission and nucleation at grain boundaries. *Acta Materialia*, 59(1):283 – 296.
- [Sansoz and Molinari, 2005] Sansoz, F. and Molinari, J. (2005). Mechanical behavior of σ tilt grain boundaries in nanoscale cu and al: A quasicontinuum study. *Acta Materialia*, 53(7):1931 – 1944.
- [Sauzay et al., 2010] Sauzay, M., Bavard, K., and Karlsen, W. (2010). Tem observations and finite element modelling of channel deformation in pre-irradiated austenitic stainless steels – interactions with free surfaces and grain boundaries. *J. Nucl. Mater.*, 406(1):152 – 165.

BIBLIOGRAPHY

- [Sauzay and Gilormini, 2002] Sauzay, M. and Gilormini, P. (2002). Influence of surface effects on fatigue of microcracks nucleation. *Theoretical and Applied Fracture Mechanics*, 38(1):53–62.
- [Sauzay and Moussa, 2013] Sauzay, M. and Moussa, M. O. (2013). Prediction of grain boundary stress fields and microcrack initiation induced by slip band impingement. *International Journal of Fracture*, 184(1):215–240.
- [Sauzay and Vor, 2013] Sauzay, M. and Vor, K. (2013). Influence of plastic slip localization on grain boundary stress fields and microcrack nucleation. *Engineering Fracture Mechanics*, 110:330 – 349.
- [Savoie, 2007] Savoie, M. (2007). *Influence de la localisation de la déformation sur la corrosion sous contrainte de l'acier inoxydable austénitique A-286 en milieu primaire des REP*. PhD thesis, École Nationale Supérieure des Mines de Saint-Étienne.
- [Savoie et al., 2007] Savoie, M., Esnouf, C., Fournier, L., and Delafosse, D. (2007). Influence of ageing heat treatment on alloy A-286 microstructure and stress corrosion cracking behaviour in PWR primary water. *Journal of Nuclear Materials*, 360(3):222 – 230.
- [Scott and Le Calvar, 1993] Scott, P. and Le Calvar, M. (1993). Some possible mechanisms of intergranular stress corrosion cracking of alloy 600 in pwr primary water. In R.E., G. and Simonen, E., editors, *Proceedings of the 6th International Conference on Environmental Degradation of Materials in Nuclear Power Systems – Water Reactors*, pages 657–665. Minerals, Metals and Materials Society.
- [Sharp, 1967] Sharp, J. V. (1967). Deformation of neutron-irradiated copper single crystals. *Philos. Mag.*, 16(139):77–96.
- [Shimokawa, 2010] Shimokawa, T. (2010). Asymmetric ability of grain boundaries to generate dislocations under tensile or compressive loadings. *Phys. Rev. B*, 82:174122.
- [Simmons and Wang, 1971] Simmons, G. and Wang, H. (1971). *Single crystal elastic constants and calculated aggregate properties*. MIT Press, Cambridge.
- [Singh et al., 2019] Singh, D., Parashar, A., Kedharnath, A., Kapoor, R., and Sarkar, A. (2019). Effect of symmetrical and asymmetrical tilt grain boundaries on the tensile deformation of zirconium bicrystals: a md-based study. *Journal of materials science*, 54(4):3082–3095.
- [Singh and Tangri, 1970] Singh, R. and Tangri, K. (1970). Deformation faulting in the premacroyield region of polycrystalline nickel. *Metallurgical Transactions*, 1(11):3151–3157.

BIBLIOGRAPHY

- [Smith and Barnby, 1967] Smith, E. and Barnby, J. T. (1967). Crack nucleation in crystalline solids. *Metal Science Journal*, 1(1):56–64.
- [Spearot et al., 2008] Spearot, D., Capolungo, L., Qu, J., and Cherkaoui, M. (2008). On the elastic tensile deformation of $\langle 100 \rangle$ bicrystal interfaces in copper. *Computational Materials Science*, 42(1):57 – 67.
- [Spearot et al., 2009] Spearot, D., Tschopp, M., and McDowell, D. (2009). Orientation and rate dependence of dislocation nucleation stress computed using molecular dynamics. *Scripta Materialia*, 60(8):675 – 678.
- [Spearot et al., 2004] Spearot, D. E., Jacob, K. I., and McDowell, D. L. (2004). Non-local separation constitutive laws for interfaces and their relation to nanoscale simulations. *Mechanics of Materials*, 36(9):825 – 847.
- [Spearot et al., 2005] Spearot, D. E., Jacob, K. I., and McDowell, D. L. (2005). Nucleation of dislocations from $[001]$ bicrystal interfaces in aluminum. *Acta Materialia*, 53(13):3579 – 3589.
- [Spearot et al., 2007a] Spearot, D. E., Jacob, K. I., and McDowell, D. L. (2007a). Dislocation nucleation from bicrystal interfaces with dissociated structure. *International Journal of Plasticity*, 23(1):143 – 160.
- [Spearot et al., 2007b] Spearot, D. E., Tschopp, M. A., Jacob, K. I., and McDowell, D. L. (2007b). Tensile strength of $\langle 100 \rangle$ and $\langle 110 \rangle$ tilt bicrystal copper interfaces. *Acta Materialia*, 55(2):705 – 714.
- [Stephenson et al., 2012] Stephenson, K. J., Ashida, Y., Busby, J. T., and Was, G. S. (2012). *Stress Corrosion Crack Initiation Susceptibility of Irradiated Austenitic Stainless Steels*, pages 1187–1199. John Wiley & Sons, Inc.
- [Stroh, 1957] Stroh, A. (1957). A theory of the fracture of metals. *Advances in Physics*, 6(24):418–465.
- [Stukowski, 2009] Stukowski, A. (2009). Visualization and analysis of atomistic simulation data with OVITO—the open visualization tool. *Modelling and Simulation in Materials Science and Engineering*, 18(1):015012.
- [Stukowski et al., 2012] Stukowski, A., Bulatov, V. V., and Arsenlis, A. (2012). Automated identification and indexing of dislocations in crystal interfaces. *Modelling and Simulation in Materials Science and Engineering*, 20(8):085007.
- [Sutton et al., 1995] Sutton, A. P., Balluffi, R. W., and Sutton, A. (1995). Interfaces in crystalline materials.

BIBLIOGRAPHY

- [Sutton et al., 1983] Sutton, A. P., Vitek, V., and Christian, J. W. (1983). On the structure of tilt grain boundaries in cubic metals i. symmetrical tilt boundaries. *Philosophical Transactions of the Royal Society of London. Series A, Mathematical and Physical Sciences*, 309(1506):1–36.
- [Suzuki et al., 2011] Suzuki, A., Gigliotti, M., and Subramanian, P. (2011). Novel technique for evaluating grain boundary fracture strength in metallic materials. *Scripta Materialia*, 64(11):1063 – 1066.
- [Tadmor et al., 1999] Tadmor, E. B., Miller, R., Phillips, R., and Ortiz, M. (1999). Nanoin-dentation and incipient plasticity. *Journal of Materials Research*, 14(6):2233–2250.
- [Tadmor et al., 1996a] Tadmor, E. B., Ortiz, M., and Phillips, R. (1996a). Quasicontinuum analysis of defects in solids. *Philosophical Magazine A*, 73(6):1529–1563.
- [Tadmor et al., 1996b] Tadmor, E. B., Phillips, R., and Ortiz, M. (1996b). Mixed atomistic and continuum models of deformation in solids. *Langmuir*, 12(19):4529–4534.
- [Tanguy, 2011] Tanguy, B. (2011). Corrosion sous contrainte assistée par l’irradiation des aciers inoxydables austénitiques (IASCC). *Revue de Métallurgie*, 108(1):39–46.
- [Tanguy and Hure, 2016] Tanguy, B. and Hure, J. (2016). Intergranular stress distributions in polycrystalline aggregates of irradiated stainless steels. In *3ieme Workshop du GIS, Modélisation des champs mécaniques et interaction avec les joints de grains*.
- [Taylor et al., 2005] Taylor, D., Cornetti, P., and Pugno, N. (2005). The fracture mechanics of finite crack extension. *Engineering Fracture Mechanics*, 72(7):1021 – 1038.
- [Terachi et al., 2008] Terachi, T., Yamada, T., Miyamoto, T., Arioka, K., and Fukuya, K. (2008). Corrosion behavior of stainless steels in simulated pwr primary water—effect of chromium content in alloys and dissolved hydrogen—. *Journal of Nuclear Science and Technology*, 45(10):975–984.
- [Thomas and Bruemmer, 2002] Thomas, L. and Bruemmer, S. (2002). Analytical transmission electron microscopy characterization of stress corrosion cracks in an irradiated type 316 stainless steel core component of PWR. In *Fontevraud 5 International symposium; Fontevraud*, pages 347 – 359. Société Française d’Énergie Nucléaire - SFEN.
- [Tokuda et al., 2018] Tokuda, Y., Tsurekawa, S., and Molodov, D. A. (2018). Local mechanical properties in the vicinity of $(1\bar{1}0)\sigma_3/[111]$ symmetric tilt grain boundary in aluminum bicrystal. *Materials Science and Engineering: A*, 716:37 – 41.
- [Tschopp and McDowell, 2007] Tschopp, M. A. and McDowell, D. L. (2007). Structures and energies of σ_3 asymmetric tilt grain boundaries in copper and aluminium. *Philosophical Magazine*, 87(22):3147–3173.

BIBLIOGRAPHY

- [Tschopp et al., 2007] Tschopp, M. A., Spearot, D. E., and McDowell, D. L. (2007). Atomistic simulations of homogeneous dislocation nucleation in single crystal copper. *Modelling and Simulation in Materials Science and Engineering*, 15(7):693–709.
- [Tschopp et al., 2008] Tschopp, M. A., Spearot, D. E., and McDowell, D. L. (2008). Chapter 82 - influence of grain boundary structure on dislocation nucleation in fcc metals. In Hirth, J., editor, *A Tribute to F.R.N. Nabarro*, volume 14 of *Dislocations in Solids*, pages 43 – 139. Elsevier.
- [Van Brutzel et al., 2019] Van Brutzel, L., Chartier, A., Sicaud, B., and Sauzay, M. (2019). Mechanical behavior of (ni, fe)cr₂o₄ spinel grain boundaries studied by molecular dynamics simulations. *The Journal of Chemical Physics*, 151(1):014701.
- [van Duin et al., 2001] van Duin, A. C. T., Dasgupta, S., Lorant, F., and Goddard, W. A. (2001). Reaxff: a reactive force field for hydrocarbons. *The Journal of Physical Chemistry A*, 105(41):9396–9409.
- [Van Swygenhoven, 2002] Van Swygenhoven, H. (2002). Grain boundaries and dislocations. *Science*, 296(5565):66–67.
- [Van Swygenhoven and Derlet, 2008] Van Swygenhoven, H. and Derlet, P. (2008). Chapter 81 - atomistic simulations of dislocations in fcc metallic nanocrystalline materials. In Hirth, J., editor, *A Tribute to F.R.N. Nabarro*, volume 14 of *Dislocations in Solids*, pages 1 – 42. Elsevier.
- [Van Swygenhoven et al., 2002] Van Swygenhoven, H., Derlet, P. M., and Hasnaoui, A. (2002). Atomic mechanism for dislocation emission from nanosized grain boundaries. *Phys. Rev. B*, 66:024101.
- [Van Swygenhoven et al., 1999] Van Swygenhoven, H., Spaczer, M., and Caro, A. (1999). Microscopic description of plasticity in computer generated metallic nanophase samples: a comparison between cu and ni. *Acta Materialia*, 47(10):3117 – 3126.
- [Victoria et al., 2000] Victoria, M., Baluc, N., Bailat, C., Dai, Y., Luppo, M., Schäublin, R., and Singh, B. (2000). The microstructure and associated tensile properties of irradiated fcc and bcc metals. *Journal of Nuclear Materials*, 276(1):114 – 122.
- [Vo et al., 2017] Vo, H., Reichardt, A., Frazer, D., Bailey, N., Chou, P., and Hosemann, P. (2017). In situ micro-tensile testing on proton beam-irradiated stainless steel. *Journal of Nuclear Material*, 493:336–342.
- [Vitek, 1968] Vitek, V. (1968). Intrinsic stacking faults in body-centred cubic crystals. *The Philosophical Magazine: A Journal of Theoretical Experimental and Applied Physics*, 18(154):773–786.

BIBLIOGRAPHY

- [Was, 2003] Was, G. (2003). *Recent Developments in Understanding Irradiation Assisted Stress Corrosion Cracking*, pages 965–985. TMS.
- [Was, 2007a] Was, G. (2007a). *Fundamentals of Radiation Materials Science: Metals and Alloys*. Springer Berlin Heidelberg, Berlin, Heidelberg.
- [Was and Jiao,] Was, G. and Jiao, Z. Private communication.
- [Was, 2007b] Was, G. S. (2007b). *Fundamentals of Radiation Materials Science*. Springer-Verlag Berlin Heidelberg.
- [Was and Andresen, 2007] Was, G. S. and Andresen, P. L. (2007). Stress corrosion cracking behavior of alloys in aggressive nuclear reactor core environments. *CORROSION*, 63(1):19–45.
- [Was et al., 2012] Was, G. S., Farkas, D., and Robertson, I. M. (2012). Micromechanics of dislocation channeling in intergranular stress corrosion crack nucleation. *Current Opinion in Solid State and Materials Science*, 16(3):134 – 142. Material Challenges for Advanced Nuclear Power Systems.
- [Weinberger and Cai, 2012] Weinberger, C. R. and Cai, W. (2012). Plasticity of metal nanowires. *J. Mater. Chem.*, 22:3277–3292.
- [West and Was, 2013] West, E. and Was, G. (2013). Strain incompatibilities and their role in intergranular cracking of irradiated 316l stainless steel. *Journal of Nuclear Materials*, 441(1):623–632.
- [Wilkinson and Britton, 2012] Wilkinson, A. J. and Britton, T. B. (2012). Strains, planes, and ebsd in materials science. *Materials today*, 15(9):366–376.
- [Wolf, 1989] Wolf, D. (1989). A read-shockley model for high-angle grain boundaries. *Scripta Metallurgica*, 23(10):1713 – 1718.
- [Wolf, 1990] Wolf, D. (1990). Structure-energy correlation for grain boundaries in f.c.c. metals—iii. symmetrical tilt boundaries. *Acta Metallurgica et Materialia*, 38(5):781 – 790.
- [Wyman et al., 2017] Wyman, R. D., Fullwood, D. T., Wagoner, R. H., and Homer, E. R. (2017). Variability of non-schmid effects in grain boundary dislocation nucleation criteria. *Acta Materialia*, 124:588 – 597.
- [Yamakov et al., 2006] Yamakov, V., Saether, E., Phillips, D., and Glaessgen, E. (2006). Molecular-dynamics simulation-based cohesive zone representation of intergranular fracture processes in aluminum. *Journal of the Mechanics and Physics of Solids*, 54(9):1899 – 1928.

BIBLIOGRAPHY

- [Yamakov et al., 2002] Yamakov, V., Wolf, D., Phillpot, S. R., Mukherjee, A. K., and Gleiter, H. (2002). Dislocation processes in the deformation of nanocrystalline aluminium by molecular-dynamics simulation. *Nature materials*, 1(1):45–49.
- [Yamakov et al., 2003] Yamakov, V., Wolf, D., Phillpot, S. R., Mukherjee, A. K., and Gleiter, H. (2003). Deformation-mechanism map for nanocrystalline metals by molecular-dynamics simulation. *Nature Materials*, 3:43 – 47.
- [Zhang et al., 2014] Zhang, L., Lu, C., and Tieu, K. (2014). Atomistic simulation of tensile deformation behavior of $\sigma 5$ tilt grain boundaries in copper bicrystal. *Scientific reports*, 4:5919.
- [Zhang et al., 2015] Zhang, L., Lu, C., Tieu, K., Zhao, X., and Pei, L. (2015). The shear response of copper bicrystals with $\sigma 11$ symmetric and asymmetric tilt grain boundaries by molecular dynamics simulation. *Nanoscale*, 7:7224–7233.
- [Zhang and Wang, 2008] Zhang, Z. and Wang, Z. (2008). Grain boundary effects on cyclic deformation and fatigue damage. *Progress in Materials Science*, 53(7):1025 – 1099.
- [Zinkle and Was, 2013] Zinkle, S. and Was, G. (2013). Materials challenges in nuclear energy. *Acta Materialia*, 61(3):735 – 758. The Diamond Jubilee Issue.
- [Černý and Pokluda, 2007] Černý, M. and Pokluda, J. (2007). Influence of superimposed biaxial stress on the tensile strength of perfect crystals from first principles. *Phys. Rev. B*, 76:024115.
- [Černý et al., 2010] Černý, M., Šesták, P., and Pokluda, J. (2010). Influence of superimposed normal stress on shear strength of perfect bcc crystals. *Computational Materials Science*, 47(4):907 – 910.
- [Černý et al., 2016] Černý, M., Šesták, P., Řehák, P., Všianská, M., and Šob, M. (2016). Ab initio tensile tests of grain boundaries in the fcc crystals of ni and co with segregated sp-impurities. *Materials Science and Engineering: A*, 669:218 – 225.
- [Černý et al., 2019] Černý, M., Šesták, P., Řehák, P., Všianská, M., and Šob, M. (2019). Atomistic approaches to cleavage of interfaces. *Modelling and Simulation in Materials Science and Engineering*, 27(3):035007.